CRANFIELD UNIVERSITY

JASON BARDEN

ACTIVE AERODYNAMIC CONTROL OF HEAVY GOODS VEHICLES

SCHOOL OF ENGINEERING

PhD THESIS

This page intentionally left blank.

CRANFIELD UNIVERSITY

SCHOOL OF ENGINEERING

Ph.D. THESIS

Academic Year: 2009-2013

JASON BARDEN

Active Aerodynamic Control of Heavy Goods Vehicles

Supervisors: Prof. K.P.Garry and Dr. J.Whidborne

April 2013

This thesis is submitted in partial fulfilment of the requirements for the degree of Doctor of Philosophy

Abstract

Most heavy goods vehicles in service today are fitted with add-on aerodynamic devices. The most common of which is the cab-mounted roof deflector. Such devices provide appreciable drag savings, however, they are often not optimised for the trailer. When a wind yaw angle is present, their savings also diminish as the yaw angle increases.

The work conducted within this thesis investigated the possibility of using an adjustable deflector for active flow control. The optimum deflector height for a given trailer height was initially investigated using wind tunnel testing. The variation of this optimum with yaw angle and container separation was then investigated. From the results a 3D look-up table was generated.

A control scheme was proposed that used the 3D look-up table requiring only three measurable inputs. The three inputs required were: the wind yaw angle, the container height and the container separation. A pressure differential located on the deflector was found to linearly relate to the wind yaw angle. This relationship allowed on-road measurement of the wind yaw angle and therefore enabled the development of a prototype controller.

Extensive on-road testing and unsteady computational simulation were conducted. The results obtained indicated a mean yaw angle magnitude of around 5° perturbed by four fundamental low frequencies. These frequencies were identified in the runs conducted over the test period and an average frequency established. Higher frequency disturbances were attributed to the wakes of leading heavy goods vehicles and were filtered by a suitably chosen numerical filter.

Finally, an estimation of the efficiency of the active device was made using a combination of simulation and full scale testing.

From the results obtained, an optimised deflector generated an average drag reduction of 7.4%. An estimated additional drag reduction of 1.9% over the optimised deflector was predicted through use of an active system.

Acknowledgements

I am very thankful to a great number of people who have helped me throughout the project. I wish to thank my supervisors Prof. K.P.Garry and Dr. J.Whidborne for their guidance and support from the outset. I would like to thank Jenny Holt, Lynton Banks-Davies and Paul for running the Cranfield wind tunnel. I am very grateful to the Technology Strategy Board for the sponsorship that enabled the academic research. I am also thankful to Nick Blake and Chris Griffiths from Mercedes - Benz UK, Brian Getley and the Hatcher Components staff and Lindsay from Suffonics for their technical guidance with the project. The people who have helped me outside of the writing of the thesis, notably Stefan Velikov and Quintain Mcenteggart for use of their couch. Roy Chamberlain and Craig Wilde from the Cranfield Fitness Centre, without whom I would have been much poorer. My friends from the first and second year: Remi Lansiaux, Remi Cackel, Cedric Galichon, Marjorie Rossi, Marie Luneau, Fran Mena, Marie Masselot, Julie Audouit, Robin Waluschnig and Jeremy Appleyard, without whom I could not be without. Matyas Benke for his expert guidance on meshing. I wish to thank my parents for their financial support for my many years at Cranfield University.

Finally I wish to dedicate my thesis to my wife Klementina Gerova, for her love and support throughout and in particular during the writing stages.

Contents

This page intentionally left blank.

List of Figures

This page intentionally left blank.

This page intentionally left blank.

List of Tables

This page intentionally left blank.

This page intentionally left blank.

Nomenclature

A	Reference Area
B	Bluff Body Width
C	Sutherland's Constant
C_D	Drag Coefficient
$\overline{C_D}$	Wind Averaged Drag Coefficient
$C_{D(Max)}$	Maximum Drag Coefficient Measured
$C_{D(Min)}$	Minimum Drag Coefficient Measured
C_f	Skin Friction Coefficient
C_P	Pressure Coefficient
ΔC_P	Pressure Coefficient Differential
$\Delta C_{P(Max)}$	Largest Pressure Coefficient Differential
$\Delta C_{P(Min)}$	Smallest Pressure Coefficient Differential
C_v	Specific Heat at Constant Volume
f^*	Plant Optimum
F_B	Body Force per Unit Mass
f	Frequency
f_c	Cutoff Frequency
F_D	Force of Drag
f_{Noise}	White Noise Frequency
F_S	Surface Force per Unit Volume
g/d_2	Container Separation
$G(s)$	Plant Controller
$H(s)$	Feedback Controller
j_m	Mass Flux
k	Constant of Proportionality
l	Characteristic Length
L	Bluff Body Length
M	Molar Mass
Ma	Mach Number
p	Measured Pressure

P	Static Pressure
P_0	Total Pressure
p_∞	Freestream Pressure
$P(V_W, \phi)$	Probability distribution of V_W and ϕ
q	Dynamic Pressure
q_∞	Freestream Dynamic Pressure
R	Universal Gas Constant
Re	Reynolds Number
$Re_{(FS)}$	Full Scale Reynolds Number
$Re_{(Model)}$	Model Scale Reynolds Number
St	Strouhal Number
T	Absolute Temperature
T_B	Bluff Body Height
T_0	Reference Temperature
U	Local Velocity Measurement
U_C	Wake Centre Line Velocity Deficit
U_{inj}	Injected Velocity
U_s	Plant Input
U_0	Freestream Velocity
U_∞	Freestream Velocity
V	Vehicle Velocity Vector
V_{Ave}	Average Wind Speed
V_R	Resultant Velocity of Air Relative to Vehicle
V_{ref}	Reference Velocity
V_{Truck}	Truck Velocity
V_W	Wind Velocity Vector
$V_{W(\mathrm{Max})}$	Maximum Wind Speed
V_{Wind}	Wind Velocity Vector
$\overline{V}_{(x)Wind}$	Average X-Component Wind Speed
$\overline{V}_{(y)Wind}$	Average Y-Component Wind Speed
V_∞	Freestream Velocity
W	Trailer Width
X_b	Reverse Bubble Flow Length
y	Plant Output
$Y(s)$	Plant Output
$Y_{W1/2}$	Wake Width

α	Road Gradient
β	Wind Yaw Angle
$\|\beta\|$	Magnitude of Wind Yaw Angle
β_{Est}	Estimated Wind Yaw Angle
δ_H	Deflector Height Ratio
$\hat{\delta_H}$	Estimation of Optimum Deflector Height Ratio
δ_{Hopt}	Optimum Deflector Height Ratio
μ	Dynamic Viscosity
μ_0	Reference Viscosity
Ω	Rotation Frequency
Φ_{Truck}	Truck Direction
Φ_{Wind}	Wind Direction
ρ	Fluid Density
ρ_∞	Freestream Fluid Density
τ_w	Local Wall Shear Stress
θ	Plant Feedback
θ^*	Optimal Plant Input
υ	Relative Velocity
φ	Angle between V and V_W

This page intentionally left blank.

Abbreviations

AFC	Active Flow Control
$ActiveFREDDIE$	Active Fuel REDucing DevIcE
CAD	Computer-Aided Design
CBE	Cab Behind Engine
CF	Compact Flash
CFD	Computational Fluid Dynamics
CH	Container Height
CHS	Container Height Sensor
COE	Cab Over Engine
DBD	Dielectric Barrier Discharge
DC	Direct Current
DHS	Deflector Height Sensor
$EIDs$	Energy Injection Devices
$FREDDIE$	Fuel REDucing DevIcE
GCM	Generic Conventional Truck Model
GPS	Global Positioning System
GTS	Ground Transportation System
GUI	Graphic User Interface
HGV	Heavy Goods Vehicle
$ICAO$	International Civil Aviation Organisation
IDE	Integrated Development Environment
$IGES$	Initial Graphics Exchange Specification
LA	Linear Actuator
LAH	Linear Actuator Height
LCV	Low Carbon Vehicles
LUT	Look-Up Table
$MIDs$	Mass Injection Devices
$NASA$	National Aeronautics and Space Administration
NRC	National Research Council of Canada

ODE	Ordinary Differential Equations
$ODHS$	Optimum Deflector Height
OEM	Original Equipment Manufacturer
$OPEC$	Organisation of the Petroleum Exporting Countries
PI	Proportional Integral
PID	Proportional Integral Derivative
PIV	Particle Imaging Velocimetry
PWM	Pulse Width Modulated
$RANS$	Reynolds-Averaged Navier-Stokes
$SaOB$	Suction and Oscillatory Blowing Actuators
TSB	Technology Strategy Board
USB	Universal Serial Bus
$WADC$	Wind Averaged Drag Coefficient
X_m	Defined Container Separation
YAS	Yaw Angle Sensor
ZYO	Zero Yaw Optimised

Definitions

A	Reference Area, defined as: trailer width x trailer height for ($\delta_H \leq 1.0$) and trailer width x deflector height for ($\delta_H > 1.0$)
C_D	Drag Coefficient, defined as the drag force divided by (q_∞A)
$\overline{C_D}$	Wind Averaged Drag Coefficient is defined in Sec.(2.4.5.4)
δ_H	Deflector Height Ratio, defined as the deflector height (d_1) divided by the trailer height (d_2): $\delta_H = \frac{d_1}{d_2}$
Re	Reynolds Number, based on V_∞ and overall vehicle length (L): $Re = \frac{\rho V_\infty L}{\mu}$
St	Strouhal Number, based on V_∞ and overall vehicle length (L): $St = \frac{fL}{V_\infty}$

This page intentionally left blank.

Chapter 1

Introduction

Heavy Goods Vehicles (HGVs) are comprised of a tractor and trailer unit. Within the United Kingdom there is no limit to the maximum height of the rear trailer unit [1]. The trailer height and shape also change due to varying transportation requirements from different operators. Due to time constraints, commercial haulage companies often use various trailer units with the same tractor unit. In addition, the cab to container gap can also be varied each time a new trailer is coupled to the tractor unit.

In an effort to reduce the aerodynamic drag on commercial vehicles, the vehicle manufacturers along with aftermarket companies produce a variety of add-on aerodynamic devices. One such device is the cab mounted roof deflector. Deflectors of this type have been shown to provide an appreciable drag reduction of around 20% [2] over the baseline vehicle. The deflector geometry produced by the manufacturers or other aftermarket companies, however, is usually optimised for a specific tractor-trailer configuration. Due to variation in configuration during the operation of the vehicle, the initial optimised design will not always be optimal.

The possibility of an optimal deflector geometry as a function of varying tractor configurations prompted investigation into the optimal deflector height (δ_{Hopt}). The optimal deflector height was defined as the height of the deflector that produced the lowest aerodynamic drag (C_D) on the vehicle. In addition to varying container heights and separations on HGVs, the wind direction also varies during on-road operation.

Due to HGVs operating for extended periods of time on the road, the wind direction and speed contribute to an effective yaw angle (β). The drag coefficient of a HGV is known to increase as the yaw angle increases. Due to the on-road variation of the wind yaw angle, investigation was extended into the optimum deflector height as a function of the wind yaw angle ($\delta_{Hopt}(\beta)$). It was proposed that if the optimum deflector height varied with β, an additional drag reduction over the already zero yaw optimised deflector could be achieved.

1.1 Motivation for an Optimum (δ_{Hopt})

The nature of commercial transportation ensures the primary design criterion is to maximise transportation volume whilst minimising unused space. European Union laws dictate that the maximum length of a Heavy Goods Vehicle (HGV) includes the cab and the trailer. In North America, however, the maximum length applies only to the length of the trailer. European Union HGVs are, as a result, of cab-over-engine (COE) design and storage space is maximised through use of a rectangular cuboid shaped trailer. An example of the design differences between the vehicles used in North American and Europe is shown in Fig.(1.1).

Figure 1.1: Typical North American (Left) and European (Right) Commercial Heavy Goods Vehicle Designs [3].

European Union law imposes a maximum trailer height no larger than 4.10 m, with the majority of manufacturers producing trailers of 4.0 m in height. This law arose to allow for clearance of bridges located within Continental Europe. In the United Kingdom, however, there is no limit on the maximum height of the trailer [1]. In addition there is no regulation or specification on the cab to trailer separation. Current manufacturers therefore produce trailers ranging in height from 3.95 m to 4.95 m [4].

Fleet operators often do not use the same tractor-trailer combination due to a variety of reasons. The primary reason is due to the truck and trailer manufacturers usually being independent entities. This results in the trailer manufacturer producing generic trailer designs for use with various truck designs. Trailer manufacturers also produce a variety of trailer heights to accommodate various storage volumes required by different fleet operators. The fleet operators also usually have, due to

cost, multiple trailers used in combination with the same truck. The reason for this is driven by the turnaround time being greatly reduced at the operator station if the truck arrives, decouples and re-couples to a new trailer compared to the waiting time of unloading and reloading the same trailer. The use of varying trailer heights along with varying trailer separations each time the trailer is coupled to the truck gives rise to large height and separation mismatches.

Prior work by Hucho et al. [2] has shown a reduction in the aerodynamic drag coefficient (C_D) of a HGV of around 20% shown in Fig.(1.2). The reduction was achieved via the addition of a simple add-on aerodynamic deflector. The deflectors tested, however, were designed for a specific tractor, trailer height and separation. Due to the variation of the height and separation of the trailers used within the UK, the drag reduction achieved from a non-optimised static deflector would therefore be expected to be lower than those tested by Hucho et al. [2].

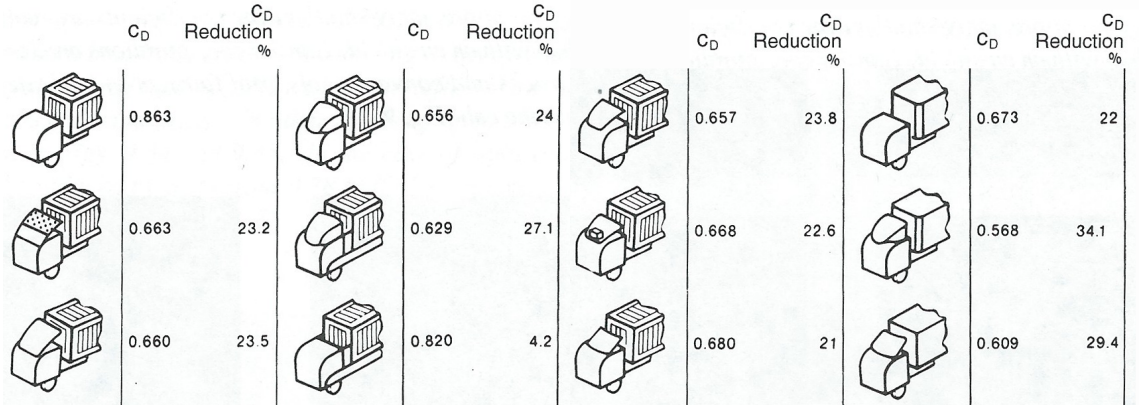

Figure 1.2: Performance Evaluation of Tractor-Trailer Add-on Aerodynamic Devices [2].

The inconsistent trailer height (a problem specific to the UK only) and separation (a worldwide problem) prompted investigation into the feasibility of an actively adjusting deflector. An actively adjusting or "active" deflector would allow for height adjustment of the deflector and enable the deflector to adjust to the optimum height (δ_{Hopt}), a function of both the trailer height and the trailer separation. The deflector adjusting to the δ_{Hopt} for a given trailer configuration would therefore be expected to provide an additional drag reduction over a non-optimised static deflector.

1.2 Motivation for an Active System ($\delta_H(\beta)$)

Research conducted in the 1970's by Buckley et al. [5] at the University of Maryland focused on reducing the aerodynamic drag on HGVs. The results revealed the benefits that could be obtained from simple streamlining of commercial vehicles. Using wind tunnel evaluation of $1/10^{th}$ scale models, this work focused on quantifying the component contributions from the main areas associated with the aerodynamic drag on a commercial vehicle.

The results identified that the container forebody was a major contributor towards the aerodynamic drag on the vehicle. A cab mounted roof-fairing was shown to provide a drag saving of up to 25% at zero wind yaw angle (β) over the baseline model.

The results also revealed the sensitivity of β on the drag coefficient (C_D) of the vehicle and demonstrated a 70% increase in the coefficient for a 20° increase in β for the baseline model configuration. Figure (1.3) shows the effect of β for various truck and trailer designs.

The on-road flow field experienced by a vehicle is subject to the changes in the wind speed (V_W) and direction (Φ_{Wind}). At constant vehicle velocity this generates a change in the effective wind yaw angle (β) that the vehicle is subjected to. As the C_D of a vehicle depends on both V_W and β, an estimation to the on-road performance is required through use of a wind averaged drag coefficient (WADC or $\overline{C_D}$). The WADC takes into account the C_D of the vehicle as a function of β. Wind statistics from annualised meteorological data along with annualised vehicle densities along particular routes are used to determine the probability that a vehicle will experience a particular wind direction and speed. The wind direction probability and C_D as a function of β are then multiplied together and integrated over both V_W and β. This results in the WADC providing a better estimation to the on-road performance of the test vehicle. (See Sec.(2.4.5.4) for more details on the WADC).

Research by Buckley et al. [5] showed that the aerodynamic drag reduction achieved from a simple fixed-position deflector reduced from 25% at zero yaw to a wind-averaged estimated saving of around 15%. This result highlighted the importance of accounting for β when estimating the performance of add-on devices.

The result of the reduction in efficiency when β was non-zero prompted investigation into the variation of δ_{Hopt} with β. If δ_{Hopt} varied with β, i.e if the optimal deflector height with a wind yaw present is different from the zero yaw case, a further reduction in the WADC over a static deflector would be achieved. This reduction could be achieved through use of an active system, whereby the deflector height would adjust to the optimal height based on β.

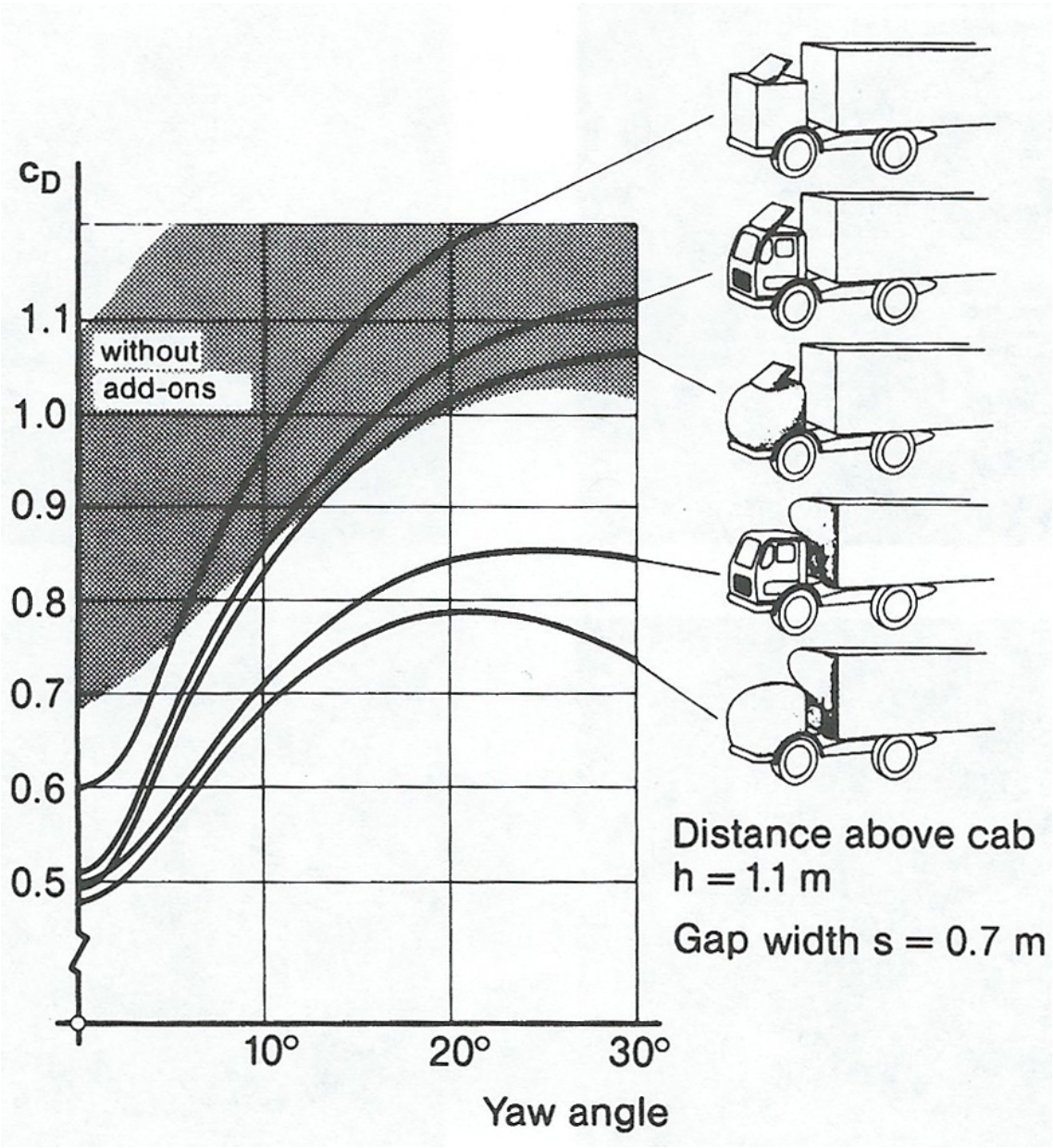

Figure 1.3: Performance Evaluation of Various Cab and Tractor-Trailer Add-on Aerodynamic Devices with Yaw Angle [2].

1.3 Financial Motivation

Many factors contribute towards the profile drag on commercial vehicles, the aerodynamic drag at normal operating speeds accounts for over two thirds of the power required for operation of the vehicle. Research into reducing the drag of HGV's has therefore historically received significant interest with rises in the cost of fuel. One such example of the financial link is shown in the research conducted in the 1970's by Buckley et al. [5] shortly after the oil crisis.

The oil crisis in 1973 was a result of the Organisation of the Petroleum Exporting Countries (OPEC) raising the price of oil by 70%. This resulted in the price of fuel (adjusted for inflation) rising by 475% from $20/Barrel in 1973 to $115/Barrel in 1979. This higher cost of fuel lead to a significant contribution towards the operating cost of the commercial vehicle.

Since the oil crisis, the fuel price has decreased to an inflation-adjusted $80/Barrel, however, this still contributes to a significant percentage of the total operational cost of the vehicle. The fuel contribution towards the total cost of vehicle and driver is shown in Fig.(1.4).

	Low mileage (miles p.a.)	Fuel costs as a percentage of total cost of vehicle and driver	Average mileage (miles p.a.)	Fuel costs as a percentage of total cost of vehicle and driver	High mileage (miles p.a.)	Fuel costs as a percentage of total cost of vehicle and driver
32t rigid	50,000	37	55,000	33	65,000	31
33t (2+2) artic	65,000	37	75,000	36	85,000	35
38t (2+3) artic	65,000	36	75,000	36	85,000	36
38t (3+2) artic	50,000	34	70,000	35	85,000	36
32t drawbar	45,000	32	60,000	34	80,000	36
40t (2+3) artic	50,000	34	70,000	36	80,000	35
44t (3+3) artic	70,000	39	85,000	38	100,000	38

* Includes vehicle standing costs, vehicle running costs and driver costs.

Fuel prices based on bulk prices and exclude VAT.

Cost data as at 1 January 2013. Source: FTA's Manager's Guide to Distribution Costs - January 2013 Update Report.

Figure 1.4: Fuel Consumption as a Proportion of Total Annual Vehicle and Driver Cost for a Range of Heavy Goods Vehicles [6].

Although the cost of fuel has decreased from the historic maximum in 1979, Fig.(1.4) shows that fuel still contributes to between 31% and 39% of the total

operational cost. The high contribution of the fuel cost towards the overall operating costs places a strong emphasis on fuel efficiency. Figure (1.5), shows that for an average speed of 72 km/hr (approximately 45 mph), the drag of the vehicle accounts for 38% of the fuel consumption on a heavy goods vehicle.

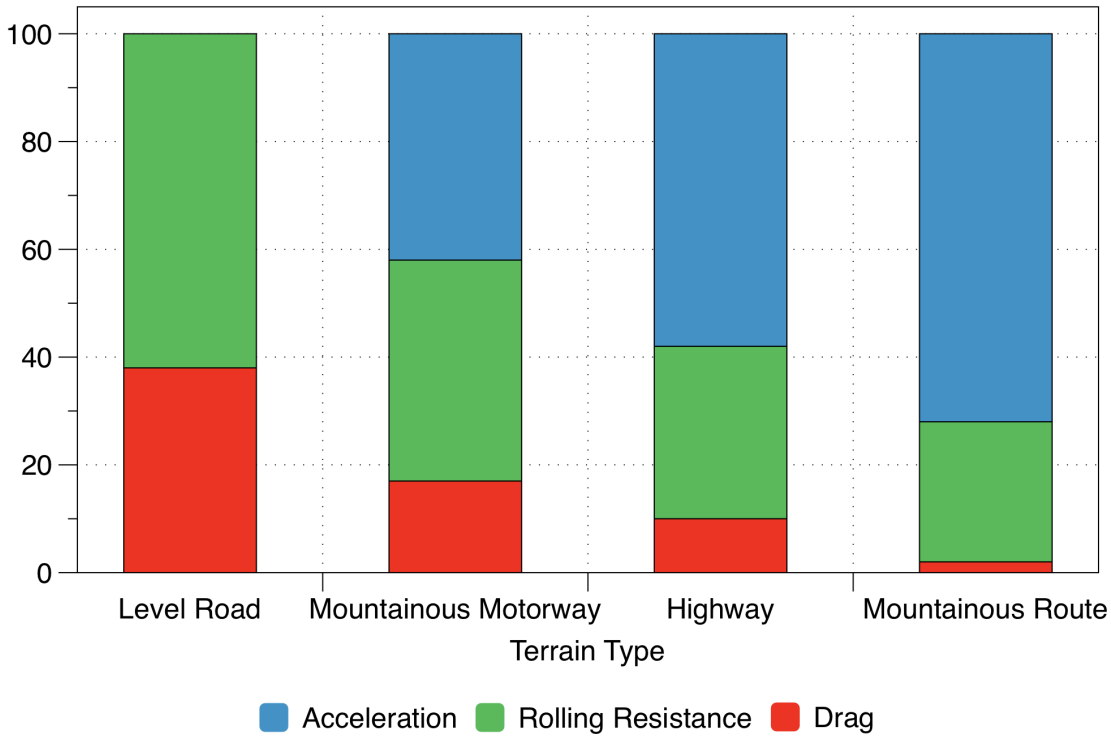

Figure 1.5: Fuel Consumption of a 40-ton Tractor-Semitrailer to Overcome Tractive Resistance Components for Different Route Profiles. Data Reproduced from Hucho et al [2].

An estimation of the fuel saving as a function of drag reduction was also made by Hucho et al. [2] and is shown in Fig.(1.6). A C_D reduction of 35% on a level road at an average speed of approximately 45 mph equated to a fuel saving of 12%. This equates to an approximate C_D to Fuel Saving ratio of 3:1, respectively.

The Department for Transport within the United Kingdom publishes annual statistics associated with HGVs [7]. The total annual mileage for heavy goods vehicles used within the UK in 2010 was $1{,}759\times10^6$ miles. The average fuel consumption for each vehicle was estimated to be around 6.5 MPG or 1.4 MPL, equating to a total consumption of $1{,}230\times10^6$ litres per year.

Financially this equates to around £1.1 Billion annually (current commercial fuel price of £1.11 per litre as of August 2013). For an active system with an estimated performance equating to a 3% reduction in C_D this would (using the empirical 3:1,

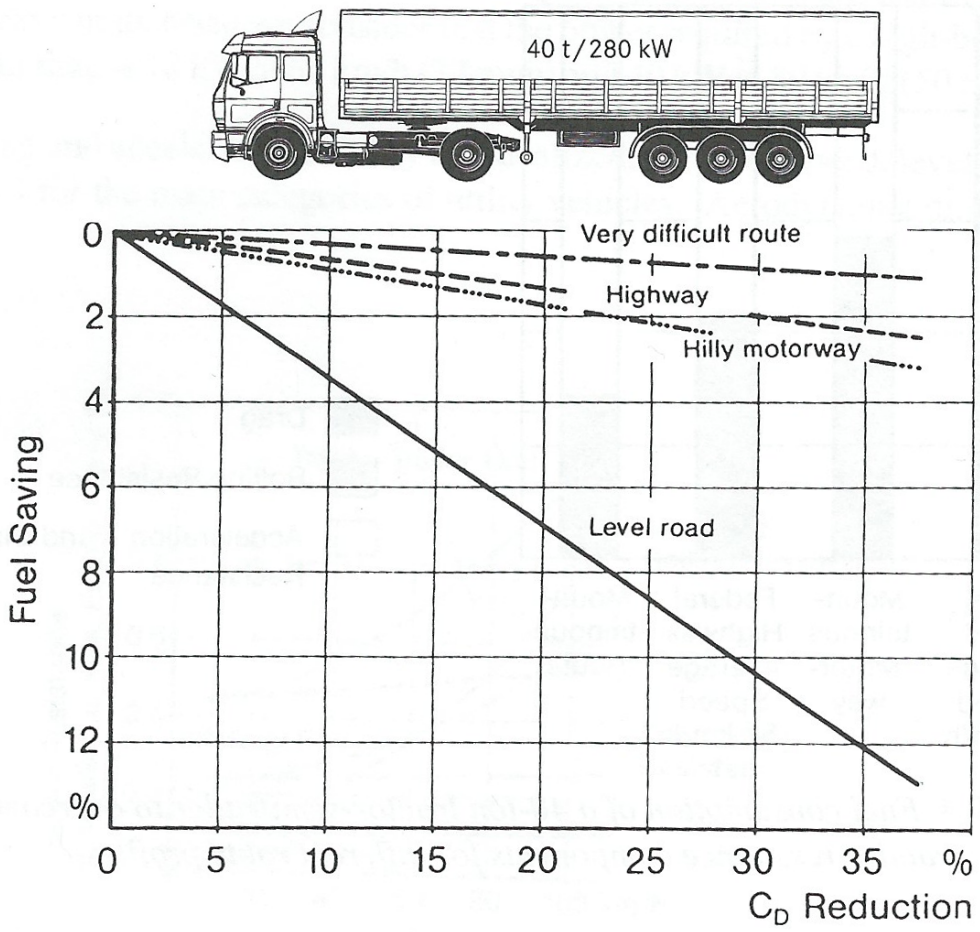

Figure 1.6: Fuel Saving as a Function of Aerodynamic Drag (C_D) Reduction for Varying Road Types [2].

C_D : Fuel formula) generate a 1% reduction in fuel. Under the assumption that the system would be adopted by the entire UK fleet of HGVs, this would equate to an annual saving of £110 Million.

The substantial financial savings for minimal reductions in C_D combined with pressure to curb climate change provided sufficient financial motivation for the project to obtain funding through a government carbon reduction scheme. The Technology Strategy Board (TSB) funded the project under the Low Carbon Vehicles (LCV) initiative.

The project's title was "Drag Reduction of Heavy Goods Vehicles Using Active Control" and was deemed applicable to the UK market in an effort to reduce the carbon emissions produced by HGVs operating within the UK.

1.4 Project Aims

The research was sponsored under the Technology Strategy Board (TSB) 'Low Carbon Vehicles Innovation Platform'. The primary aim was to develop a commercially viable active aerodynamic device. Commercial partners Mercedes-Benz UK and Hatcher Components Ltd were jointly involved with Cranfield University in the TSB project. Their role was to comment on the commercial practicality of the commercial controller and provide the resources needed to produce the prototype controller. This included the use of a full scale vehicle to test the prototype controller.

The purpose of the research topic was to investigate the aerodynamic characteristics of heavy goods vehicles and develop a control scheme to adjust to the optimal deflector height, irrespective of the cost of the equipment required for implementation.

The aim of the aerodynamic aspect of the research was to determine if a cab mounted roof deflector had an optimum height (δ_{Hopt}) for a given trailer height and separation. The optimum deflector height was defined as the deflector height that minimised the vehicle's drag coefficient (C_D). Investigation then continued to determine if the optimum deflector height was a function of the wind yaw angle (β). Once the relationship was determined it allowed investigation into whether an actively adjusting system could provide additional drag reduction over a zero yaw optimised (ZYO) deflector.

Once δ_{Hopt} and its variation with β had been determined and provided δ_{Hopt} was a function of β, a suitable control scheme was to be designed to control the movement of the deflector. The control scheme used in the academic research and the control scheme used in the commercial implementation, however, differed. The commercial controller was limited to being "commercially practical", with a limit on the expense of sensors and equipment required for implementation. The research controller, however, had no financial limitation.

The primary aim of the research controller was to test the suitability of Extremum-Seeking Control (ESC) applied to aerodynamics. Active Flow Control (AFC) has previously been applied to ESC, however, the implementation of most controllers did not result in a net energy saving. The main aim of the research controller was therefore to determine if AFC in conjunction with the use an adjustable control surface (the cab mounted roof deflector) could produce a net energy saving.

1.5 Project Objectives

The project objectives performed in this research were identified as:

- To determine the optimum deflector height (δ_{Hopt}) for a given trailer height. The optimum deflector height was defined as the height ratio between the deflector and trailer height that resulted in the minimum vehicle C_D.
- To determine the variation of the δ_{Hopt} with the container separation (g/d_2) and the wind yaw angle (β).
- Determine measurement methods for the variables β, g/d_2 and δ_H required for the control scheme.
- Construct a numerical model of the vehicle to enable full-scale simulation within *Simulink*®.
- Production of a full-scale prototype of the active system.
- Design and implement a full scale test program to correlate parameters measured in the wind tunnel test with the on-road data.
- Estimation of the performance of the control algorithm/active device using on-road data within *Simulink*®.
- CFD simulation of two commercial vehicles in tandem to attribute on-road signal 'noise' to a parameter associated with the steady-state operation of the full-scale vehicle.
- Production of a commercial active control system from the obtained data.

1.6 Project Limitations

Due to the project requiring a full scale, commercially viable working prototype, certain constraints were placed upon the project. As a result of these limitations, the research was split into several Technology Readiness Levels (TRLs) [8] shown in Fig.(1.7).

TRLs are an aerospace gauge developed by the National Aeronautics and Space Administration (NASA) to determine how ready a technology is for operational use. TRLs range from TRL 1 $\rightarrow$ TRL 9, with TRL 1 being the basic principle and TRL 9 "flight proven". The NASA TRLs were chosen as they provided a suitable partition of the work between research and production. Other TRLs exist for various industries such as oil and gas, however, the NASA levels were chosen as their level's were the closest match for the aerodynamic requirements of the project.

The project was therefore split into three TRL level groups with the academic research investigated in levels TRL1 - TRL4, a prototype controller generated in levels TRL4 - TRL7 and a production controller in levels TRL7 - TRL9. Details of each project group is outlined in the following subsections.

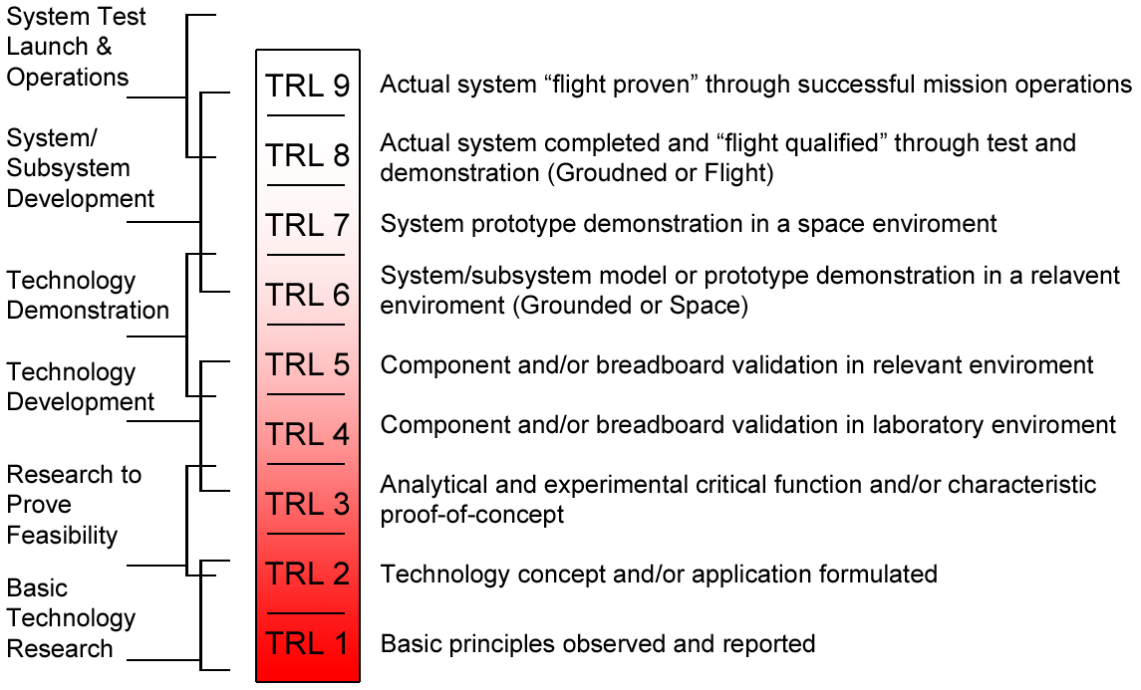

Figure 1.7: NASA Technology Readiness Levels [8].

1.6.1 Research Controller (TRL1 - TRL4)

The research controller used an Extremum Seeking Control (ESC) algorithm, whereby a measured parameter was driven to a minimum. For a HGV with an active deflector, this equated to the aerodynamic vehicle drag (C_D). The C_D, however, was a parameter that was difficult and impractical to measure directly on-road, therefore a measurable parameter that related to the drag was measured instead.

An example of this parameter could be a pressure tapping located on the vehicle or measurement of the engine load. If the C_D of the vehicle could be inferred through measurement of another parameter, it would offer superior performance over a look-up table as it would not require prior knowledge or assumption about the vehicle configuration.

The investigation into determining a parameter that related to C_D was difficult to achieve for commercial application. The associated costs of the sensors required to measure the parameters used by the controller eliminated it as a viable controller for the higher TRL levels.

The variables required for the research controller are shown in Fig.(1.8).

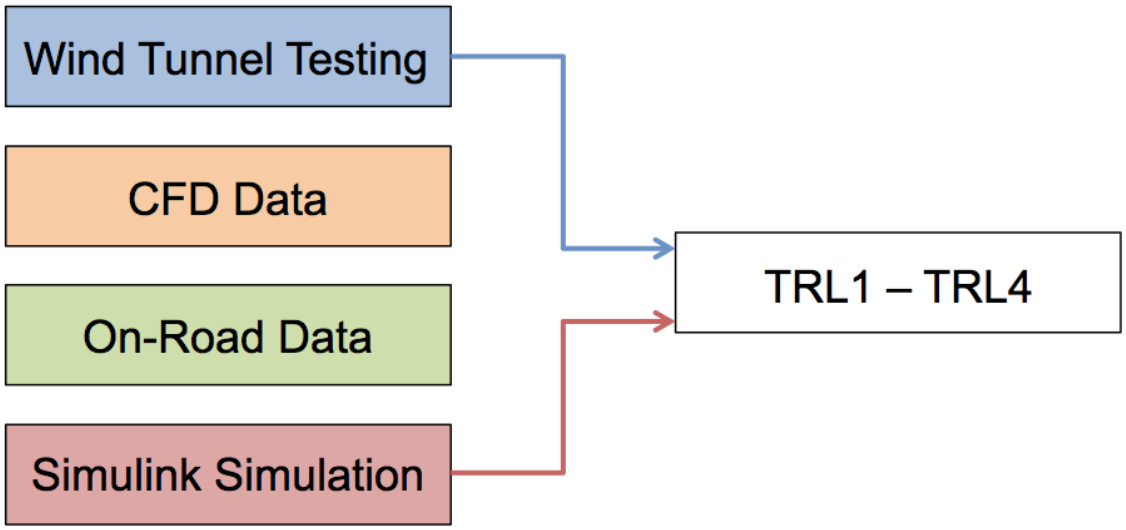

Figure 1.8: Data Required by TRL1 - TRL4 Control Scheme.

The research controller was a proof of concept controller and therefore only required wind tunnel data for the *Simulink*® simulation. *Simulink*® is a Graphic User Interface (GUI) that allows block diagrams of various systems to be created. The block diagrams of the systems are visual representation of computer code used to simulate complex mechanical systems (see [9] for further information). The simulation used in the project was a numerical representation of the HGV where parameters

such as engine power, torque and wheel speed could be calculated as functions of various variable parameters such as wind speed.

1.6.2 Prototype Controller (TRL4 - TRL7)

The prototype controller used a look-up table to determine the optimum deflector height (δ_{Hopt}). As a result, wind tunnel testing was required to populate the table with data to determine δ_{Hopt} as a function of the trailer height and separation.

Due to the on-road conditions at this phase of the project being unknown, the accuracy of the data contained within the table was of paramount importance. Investigation into larger container separations (g/d_2) was therefore required to extend the range of data contained within the look-up table. Computational Fluid Dynamics (CFD) simulations were therefore used to model configurations that could not be tested in the wind tunnel and therefore extended the range of the look-up table data.

The variables required for the prototype controller are shown in Fig.(1.9).

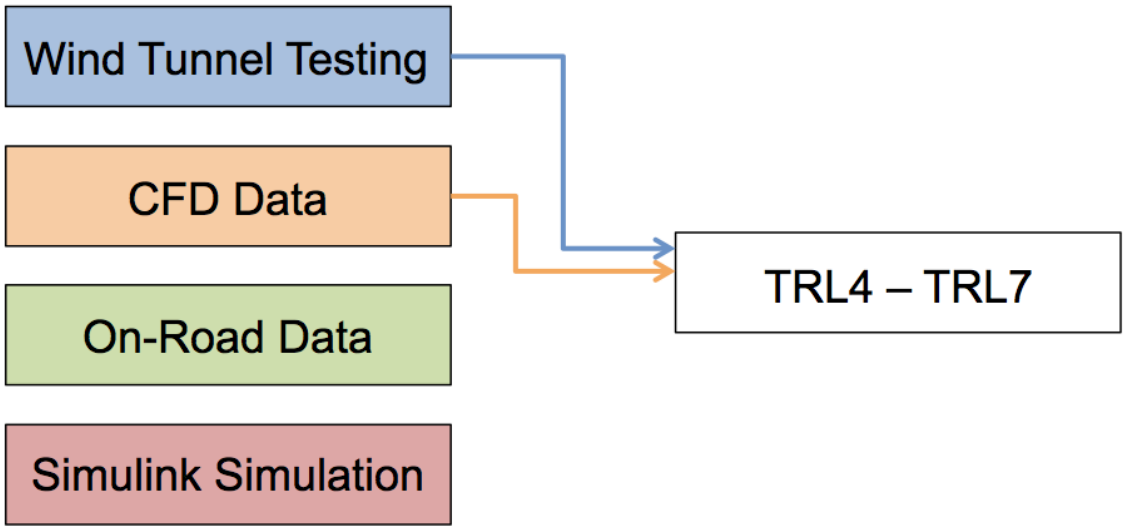

Figure 1.9: Data Required by TRL4 - TRL7 Control Scheme.

The prototype controller used for on-road data accusation had no prior information about the on-road conditions. As a result the adjustment frequency of the actuators was set to the minimum adjustment period of 300 seconds determined by the manufacturer (From Fig.(B.22) in Sec.(B.9.8) of Appendix B).

1.6.3 Production Controller (TRL7 - TRL9)

The production controller used on-road data obtained during testing of the prototype controller. The on-road variation of the wind direction (β) and wind speed (V_W) was measured during the prototype controller testing phase. As a result, an estimation of the optimal adjustment frequency and performance of the active system was made through simulation in *Simulink*®. The production controller therefore required on-road data in order to perform this simulation.

The variables required for the production controller are shown in Fig.(1.10).

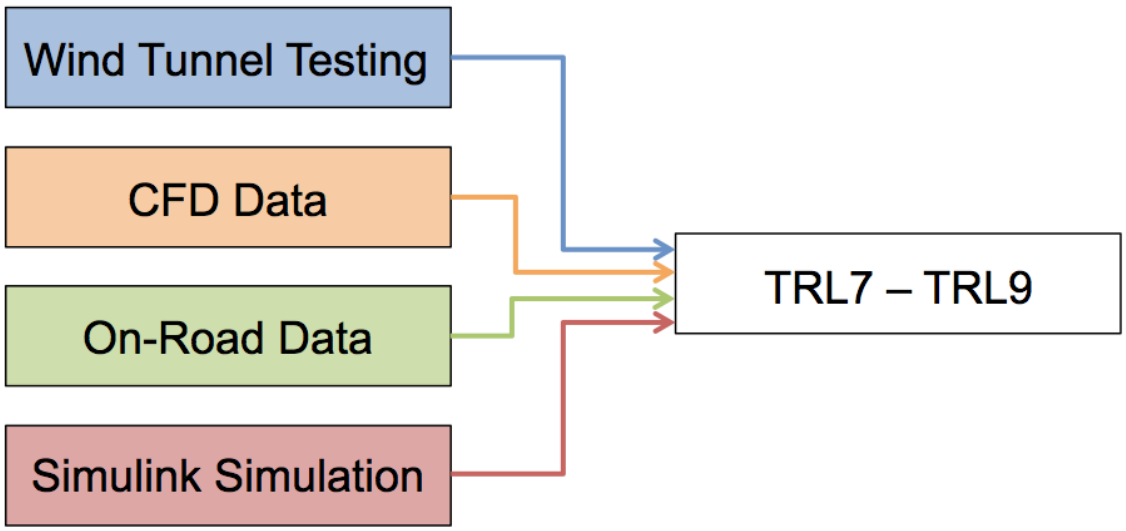

Figure 1.10: Data Required by TRL7 - TRL9 Control Scheme.

The production controller had knowledge about the on-road environment as well as the vehicle response from the variation of the deflector height (δ_H). The data used within the look-up table was previously generated data used for a specific cab/trailer shape. As a result the commercial controller is more robust than the research controller, however, the research controller has the potential to achieve superior performance.

The increase in performance is achieved due to the research control not requiring a priori estimation of the behaviour of the system. The research controller reduces the measured drag to the actual, rather than the wind tunnel estimated, minimum. The wind tunnel model used was a simplified approximation of a full scale vehicle. The estimated optimal height achieved from the simplified flow filed may not therefore correspond to the optimal height of the full scale vehicle.

1.7 Deflector Design

The basis for the active deflector design was the static deflector designed in 2003 by Cranfield University named "FREDDIE" or Fuel REDucing DevIcE. FREDDIE was designed as an optimal shape over a yaw range of ($-5° \leq \beta \leq +5°$) for a Mercedes-Benz cab shape and a common trailer height and trailer gap separation.

The method of actuation used for the active system was imposed by Hatcher Components, one of the project's partners. A design criterion was therefore placed upon the project that required four linked, non-feedback, linear actuators to be used, therefore eliminating independent actuator control. The deflector was required to adjust by 300 mm (full scale) linearly at a deflection angle of 10° measured from the vertical plane. An example of the actuator and actuation method used on the prototype system is shown in Fig.(1.11).

Figure 1.11: Actuator and Actuation Method Used in ActiveFREDDIE Prototype.

The adjustment angle of 10° was required to account for material tolerance due to expansion and contraction of the fibreglass used for the static skirt and deflector. The adjustment range was chosen based on load calculations and physical tests made

on the actuators. It was found that the larger the actuation range, the weaker the actuator and the greater the probability of distortion of the actuator extension rod due to the aerodynamic load placed of the deflector.

In 2011 the deflector was redesigned to account for these changes resulting in an ActiveFREDDIE design. The differences between the static and active deflectors are shown in Fig.(1.12).

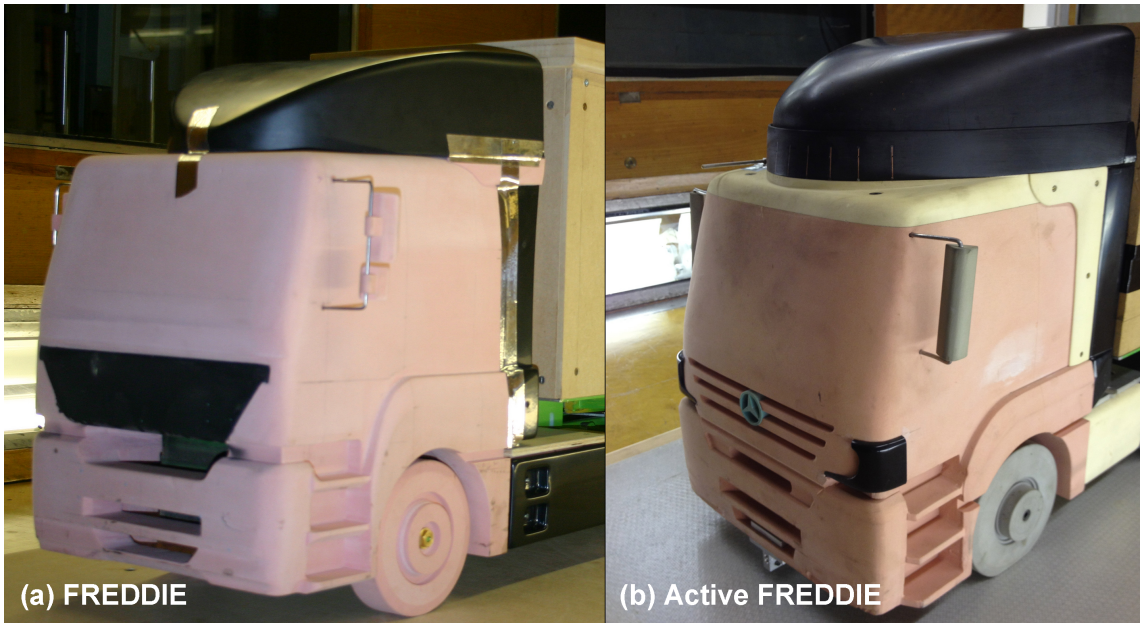

Figure 1.12: Design of (a) FREDDIE vs. (b) ActiveFREDDIE.

The prior FREDDIE design shown in Fig.(1.12) does not have a static skirt around the base of the deflector. The ActiveFREDDIE centre line geometry is also modified slightly to account for the 10° actuation angle. The sharp contour line present between the side and top of the deflector was also removed due to aerodynamic advantages obtained during CFD optimisation.

The limitation of a constant pitch angle on the deflector caused by linked actuators meant the deflector geometry was possibly not the absolute optimal. Independent actuator control would have allowed for pitch compensation which in theory could provide additional drag reduction when the shape of the trailer roof is considered. Section (7.2) details further scope on the project provided by relaxed commercial constraints.

The prototype ActiveFREDDIE deflector had a full scale actuation range of 300 mm, when used in conduction with a 4.00 m trailer provided a deflector height range of (3.9 - 4.2 m). This actuation range equated to a deflector height ratio (δ_H) of

$0.929 \rightarrow 1.050$. The prototype deflector is shown in lowest (3.9 m) and highest (4.2 m) configurations in Fig.(1.13).

Figure 1.13: ActiveFreddie Prototype in (Left) Lowest and (Right) Highest Configurations.

1.8 Thesis Structure

The thesis is divided into seven chapters with chapter introductions presented within each chapter. Due to the length of Chapter 6, subsection summaries are presented at the end of each section in order to aid the reader.

The main chapters within the thesis are organised as follows:

Chapter 1 gives an introduction to the motives associated for the project and the aims and objectives of the project.

Chapter 2 presents the reader with a review of prior research in the fields associated with the project.

Chapter 3 outlines the experimental equipment used and the associated accuracy of the measurements made and details the methodology of the experimental tests.

Chapter 4 continues with the numerical methodology for the computational study.

Chapter 5 focuses on the controller selection and design.

Chapter 6 presents the results and analysis associated with the experimental, numerical, control simulations and full-scale testing.

Chapter 7 presents the reader with a conclusion of the work conducted and scope for future work.

The references are located after Chapter 7 of the thesis, with the appendices located at the end of the thesis. The appendices and are organised as follows:

Appendix A provides the mathematics associated with the extremum-seeking algorithm.

Appendix B contains details of the experimental apparatus used for the wind tunnel and on-road tests.

Appendix C provides the mathematical background for the Computational Fluid Dynamics (CFD) Reynolds-Averaged Navier-Stokes (RANS) and Large Eddy Simulation (LES) solvers used for the numerical simulations.

Appendix D contains the embedded C/C++ ActiveFREDDIE control code used in the prototype controller.

Appendix E contains results from the experimental wind tunnel tests.

Appendix F contains results from the numerical simulations.

Appendix G contains the results from the full scale testing.

Chapter 2

Literature Review and Background

2.1 Background

In the 1930's shortly after the end of prohibition in the United States of America, the Labatt's brewery company changed its shipping from rail to road. Whilst the end of prohibition meant that the sale of alcohol was again legal, the advertisement of alcohol wasn't. As a result, brewers decided on alternate, legal methods of advertisement.

The Lebatt's brewery company commissioned Count Alexis de Sakhnoffsky to design a streamlined heavy goods delivery vehicle. The radical design was created as a method of mobile advertising. Development of the Lebatt's Streamliner began in 1935 and four generations later, the most radical and final incarnation, the 1947 Streamliner shown in Fig.(2.1).

The 1947 Streamliner featured a cab-over-engine tractor unit, enclosed rear tractor and trailer wheel arches and a curved aluminium trailer roof. The design of the Streamliner allowed for larger payloads due to the reduction in size of the cab and increased length of the trailer and also a higher top speed. The payload of 8.5 tonnes was 3.5 tonnes more than the maximum payload of other heavy goods vehicles at the time. The Streamliner also reached a top speed of 80 kmh^{-1} compared to most only obtaining 56 kmh^{-1} with the same engine capacity.

Despite the aerodynamic benefits obtained from the streamlined bodies, the aluminium bodies were expensive and time consuming to produce. The side-opening trailer doors precluded conventional pallet loading. As a result of the operational inefficiency compared to more conventional bluff body tractor-trailer designs, the Streamliner ceased production in the mid 1950's.

Due to the low petrol prices at the time and the resultant low contribution to

Figure 2.1: The 1947 Labatt Streamliner [10].

the operational cost of the vehicle, the Streamliner design was largely forgotten until the 1970's oil crisis.

2.2 Aerodynamic Fundamentals

When an object moves through a viscous fluid, a force resisting the motion of that object is applied in the direction countering its velocity. For subsonic velocities the drag forces on a heavy goods vehicle can be classified into the following categories:

Parasitic Drag
- Pressure Drag: Sec.(2.2.1)
- Interference Drag: Sec.(2.2.2)
- Skin Friction Drag: Sec.(2.2.3)

Lift-Induced Drag: Sec.(2.2.4)

2.2.1 Pressure Drag

Form drag or pressure drag arises due to the shape of an object and contributes significantly towards the overall aerodynamic drag of bluff body shaped objects. On the forebody of an object the incoming air is brought to rest at a stagnation point generating a region of high pressure, static air. As the air accelerates from the front

of the body to a mid point on the object, there is an increase in velocity of the air and hence a reduction in pressure. At the rear of the of the object the airflow detaches from the body generating an area of recirculating air within a "wake". This area of recirculation generates a region of high negative pressure at the rear of the object.

The pressure differential between the front and rear of the object creates a resulting net force in the direction of high to low pressure (from the front of the object towards the rear), opposing the direction of motion of the object. The larger the pressure differential is, due to the shape of the object, the larger the pressure drag experienced by the object.

An example of various objects and the associated wakes is shown in Fig.(2.2)

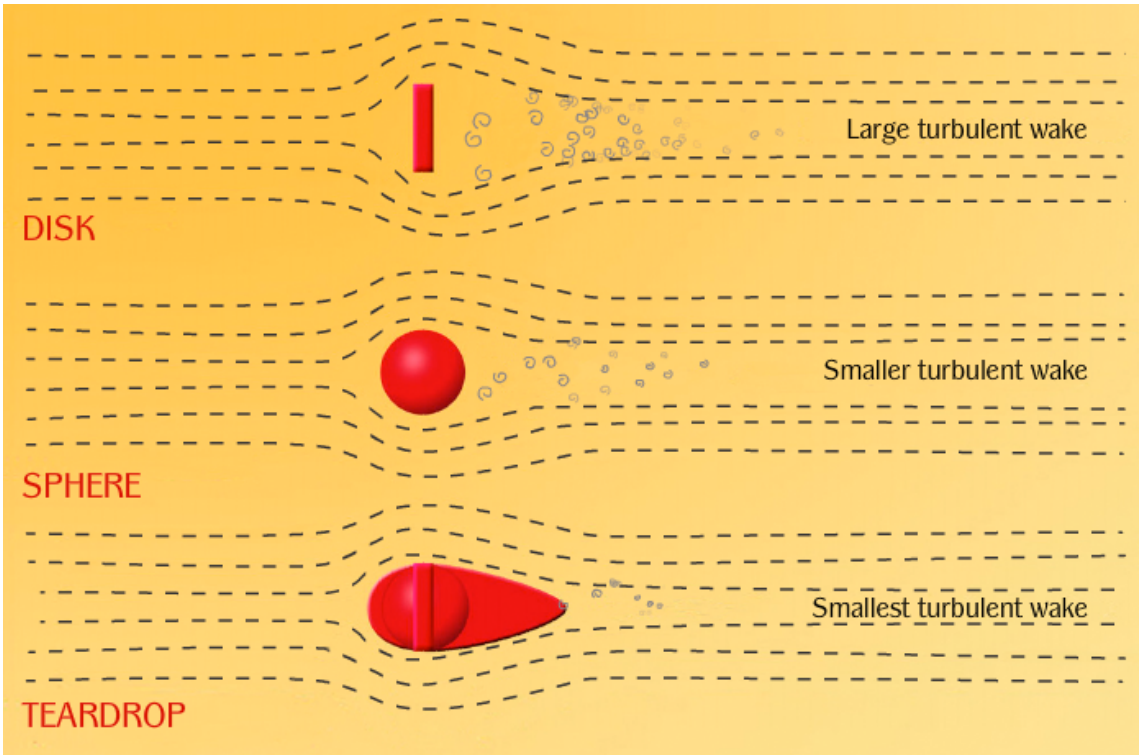

Figure 2.2: Characteristic Airflow Around Various Shapes [11].

Figure (2.2) contains three objects: a disk, a sphere and a teardrop. The object with the greatest recirculation and largest wake is the disk, with the least recirculation and lowest wake being the teardrop. The lower negative pressure gradient on the teardrop reduces the flow velocity and delays flow separation. This results in a reduction in the negative flow velocity, reducing the size of the recirculation region behind the object. This reduction in the pressure difference accounts for the reduction in the pressure drag. The streamlining on the rear of the object, however, adds

additional material, this in turn causes an increase in the skin friction component of the aerodynamic drag force.

For a heavy goods vehicle, where the overall length of the tractor and trailer is regulated, the reduction in pressure drag is usually achieved by tapering the rear of the trailer whilst minimising the container forebody pressure. The pressure distribution around an optimised trailer design [12] is shown in Fig.(2.3).

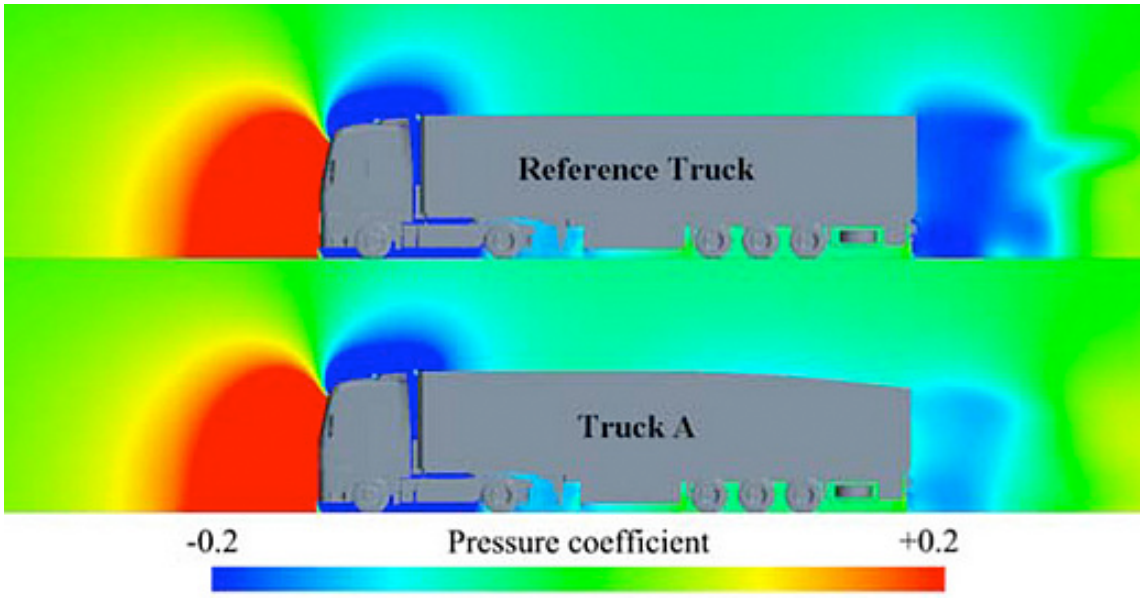

Figure 2.3: CFD Simulation of Truck and Trailer Pressure Distribution [12].

The image shows areas of low pressure coloured blue with areas of high pressure coloured red. The optimised trailer increases the positive pressure on the rear of the trailer by reducing the velocity of the flow via a negative pressure gradient.

The result is a reduced vehicle wake with the wake pressure closer to freestream compared to the baseline trailer. Due to the loading capability of the vehicle being negatively impacted with tapering on the rear of the trailer, work is primarily focused on reducing the container forebody pressure rather than increasing the pressure on the rear of the container. Limited shaping of the cab is achieved due to length restrictions on the overall vehicle, placing great emphasis on storage volume rather than aerodynamic optimisation.

The effects of shaping the front and rear end of a vehicle on the adverse pressure gradient and the resulting C_D change is shown in Fig.(2.4).

An estimated reduction of between 10 - 38% over the baseline (square front) C_D could be achieved from the front roof and vertical edges being rounded.

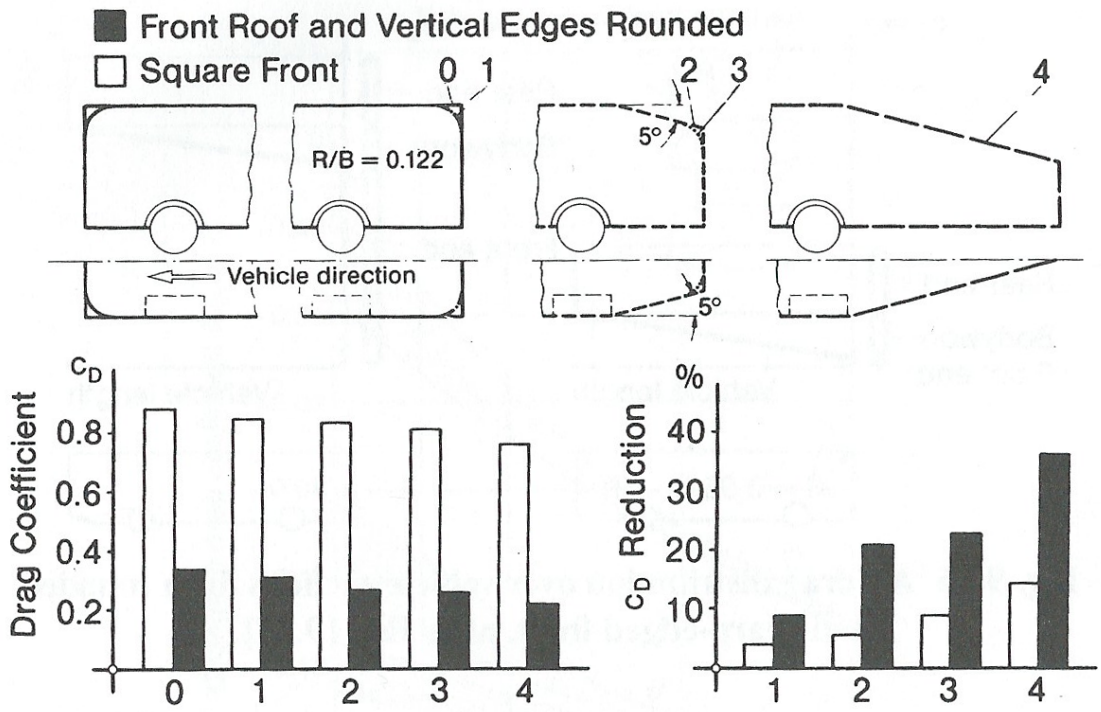

Figure 2.4: Influence of Front and Rear End Vehicle Design on C_D [2].

2.2.2 Interference Drag

Interference drag occurs when two or more sources of airflow combine at a point on the body resulting in a turbulent mixing of the flows. On a heavy goods vehicle the two main sources that contribute to interference drag are the wheels and the outlets from the cooling ducts used for the radiator.

The rotation of the wheels adds energy to the flow and results in "viscous pumping". This phenomenon leads to a C_P much greater than 1.0 in front of the wheels. This results in a high stagnation point ($C_P > 2.0$) on the front of the wheels and air is ejected outwards from the wheels shown in Fig.(2.5).

The effect of this within closed wheel wells is to eject turbulent air along the sides of the vehicle. This turbulent air mixes with the air passing along the sides of the vehicle resulting in vortices traversing the sides of the vehicle.

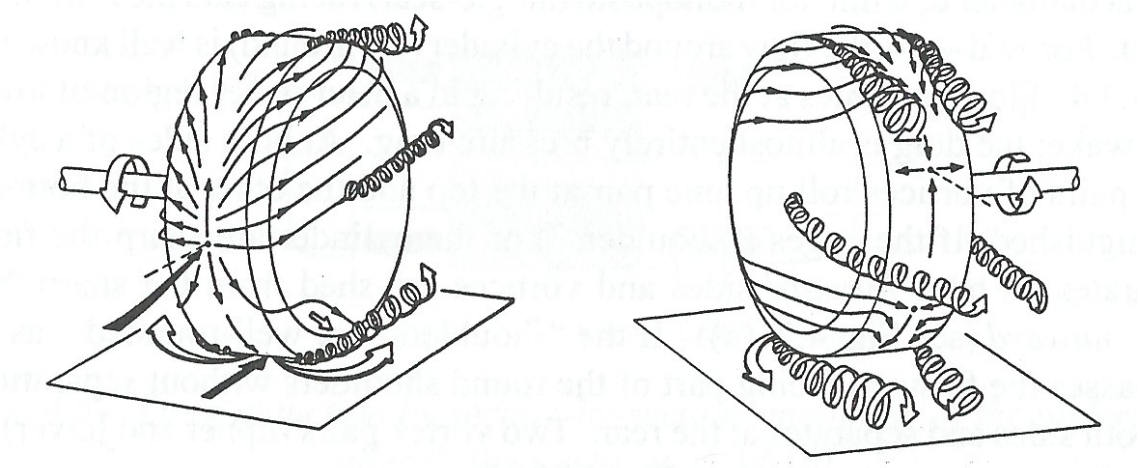

Figure 2.5: Flow Patter of a Wheel Rotating on the Ground [2].

2.2.3 Skin Friction Drag

Skin friction arises due to surface roughness present in the body's molecular composition. It is directly proportional to the amount of surface area in contact with the fluid and increases as the velocity squared. The equation for the coefficient of friction (C_f) is given by

$$C_f = \frac{\tau_w}{\frac{1}{2}\rho U_\infty^2} \tag{2.1}$$

where τ_w is the local wall shear stress, ρ is the fluid density and U_∞ is the freestream velocity.

Skin friction drag is created in the boundary layer, it is generated due to the viscosity of the air interacting with the surface roughness of the object. The air molecules closest to the surface of the body are therefore most affected. The greater the surface roughness, the greater the surface friction and as a result the greater the shear stress. The viscous resistance due to the increased shear stress creates a friction drag.

An increase in surface roughness reduces the transition length from laminar to turbulent flow. Turbulent flow has increased interaction with the body's surface due to the viscous sub layer and as a result the friction drag increases. Skin friction can be reduced by using materials with lower coefficients of friction, smoothing surfaces and coating components.

The more streamlined an object, however, the greater the contribution of skin friction to the overall drag force on the object. A heavy goods vehicle has little

streamlining present and hence the predominant aerodynamic drag arises due to pressure drag.

2.2.4 Lift-Induced Drag

Lift-induced drag is generated when an object redirects the incident airflow. For an aeroplane wing at an angle of attack, lift is generated due to the pressure differential between the upper and lower wing surfaces. Spillover of the high pressure air at the edge of the wing establishes a trailing vortex at each wing tip. This vortex drags the surrounding air in a downwards motion called downwash (shown in Fig.(2.6)).

This downwash creates an effective relative airflow incident to the wing resulting in a vertical tilting of the effective lift vector by an amount equal to the induced downwash angle. The tilting of the effective lift vector away from vertical creates a horizontal vector component called the induced drag.

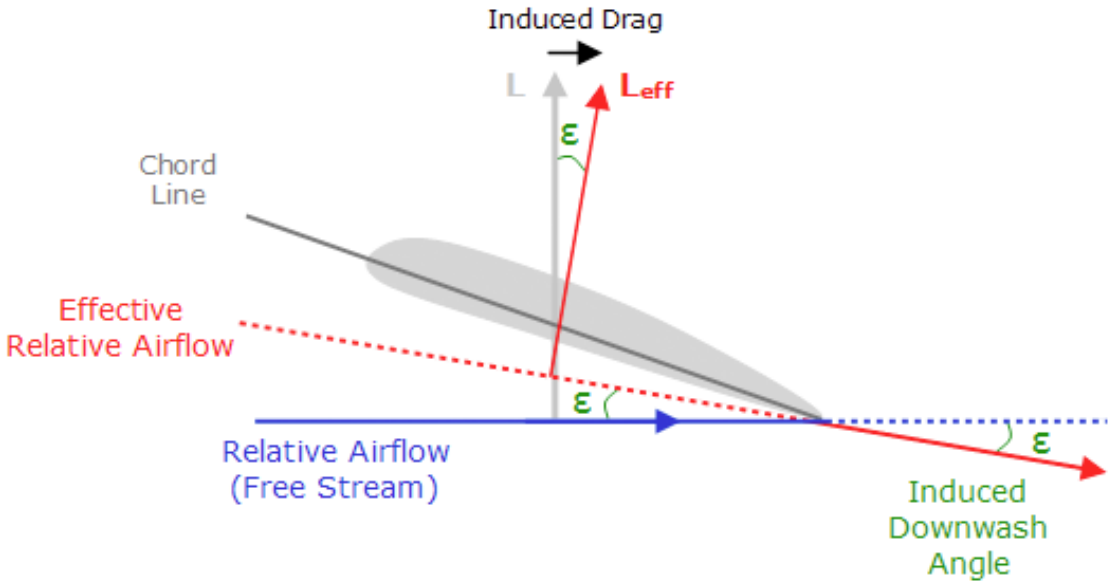

Figure 2.6: Lift Induced Drag Around an Aerofoil [13].

The edge vortices that contribute towards lift-induced drag on a vehicle can be seen in Fig.(2.7). The rearward slope of the passenger vehicle contributes significantly to the generation of these vortices. Most commercial trailers, however, do not contain this negative pressure gradient and as a result, the contribution of lift-induced drag on a heavy goods vehicle is much smaller than that of a passenger car.

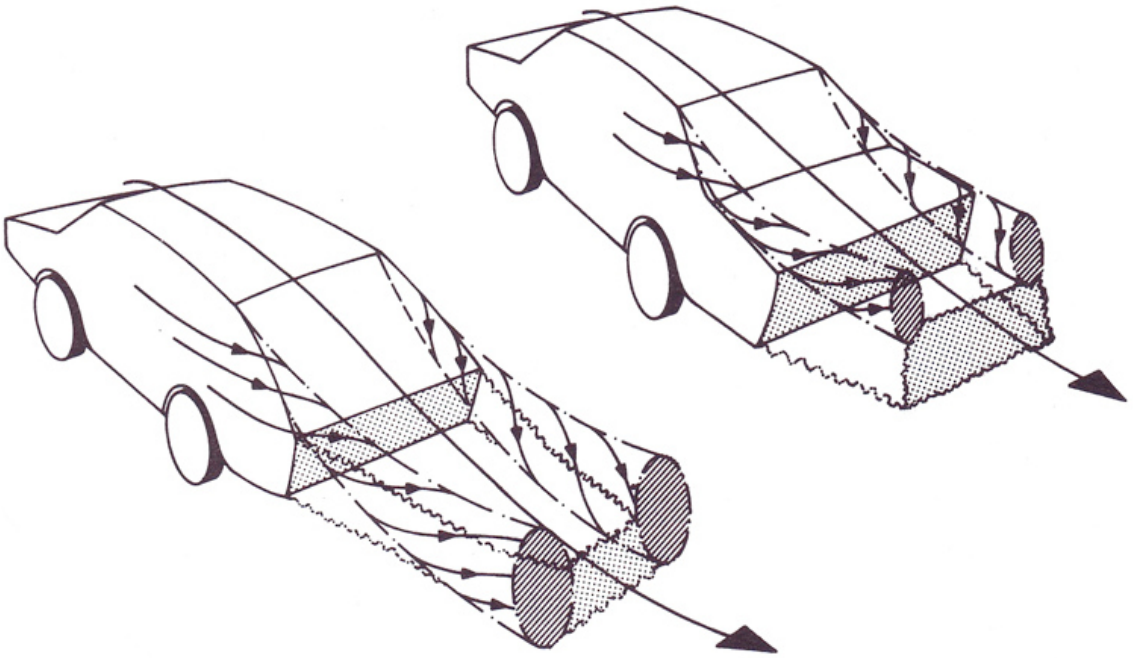

Figure 2.7: Vortex Formation Around a Vehiclel [14].

The major contributions towards the C_D of a HGV is predominately pressure drag. This results in current and prior aerodynamic research focusing on minimising the major component contributors towards the pressure drag on the vehicle.

2.3 Previous Aerodynamic Research

In the 1950's, research at the University of Maryland by Sherwood [15] provided in-depth research into simple add-on devices designed to improve the fuel consumption of HGVs. These devices consisted of a deflector (shown in the upper right section of Fig.(2.8)) and a nose cone (shown in the lower right section of Fig.(2.8)). The lower and upper left hand sections of Fig.(2.8) show the baseline van and truck, respectively.

The research also focused on areas of HGVs research with lower drag savings such as: edge rounding, rounded trailer faces, trailer skirts and boat-tailing.

This early work provided the scientific basis and prompted the development of an air deflector by Saunders [16] in 1966.

Due to the low fuel costs at the time, new aerodynamic devices were not readily adopted. The 1970's oil crisis, however, lead to larger operating costs as a result

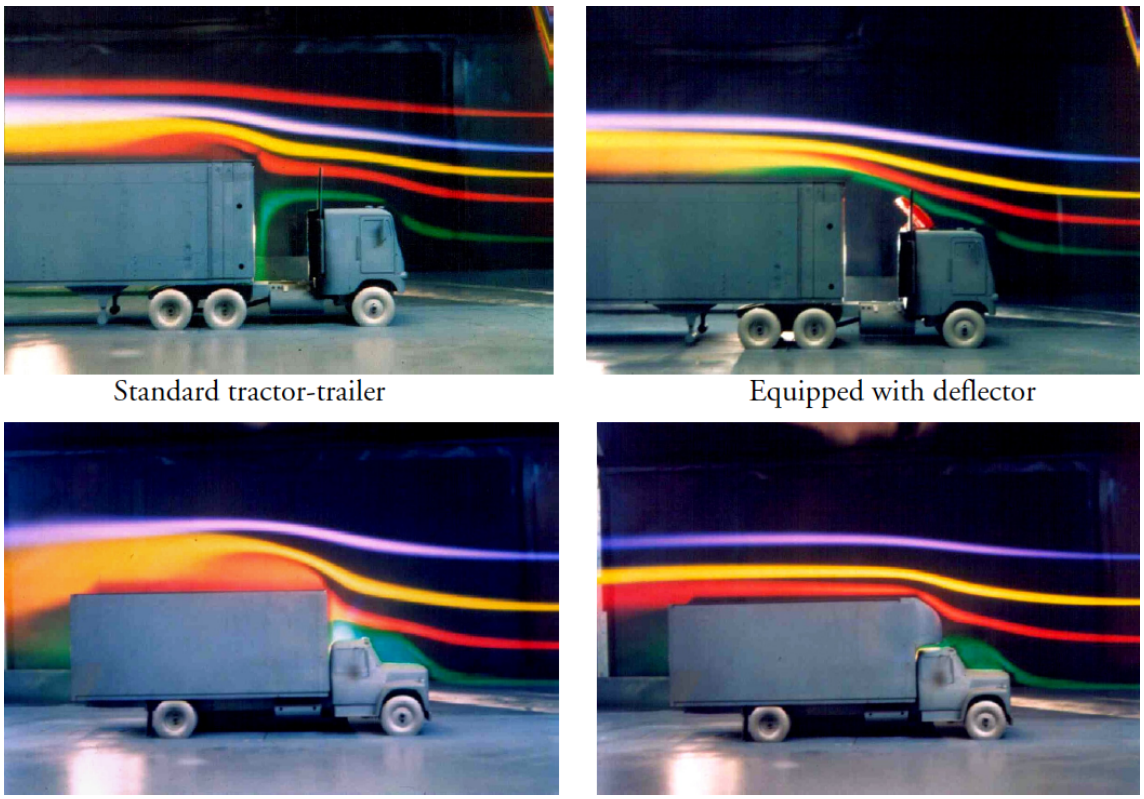

Figure 2.8: Smoke Flow Over (Left) Baseline and (Right) Modified Trucks [15].

of the aerodynamic inefficiency of the vehicles. During the mid 1970's widespread adoption of add-on deflectors was made within the haulage industry.

Further research made in 1970's, again by Sherwood [17] at the University of Maryland continued the early work conducted in the 1950's. The later work focused on a more in-depth analysis on the aerodynamic add-on devices. The aerodynamic configurations tested were baseline, baseline with 12" radius side posts, deluxe trailer front, 3/4 trailer skirts, 3/4 trailer skirts + roof fairing, faired tractor-trailer gap, streamlined tractor, streamlined + boat tailed, fully streamlined and fully streamlined + boat tailed (shown in Figs.(2.9 and 2.10)).

The results obtained from the second test provided comprehensive details on the drag savings achieved through various combinations of aerodynamic devices. The baseline model consisted of a cab and trailer with no aerodynamic aids, the resulting drag coefficient (C_D) of 1.00 at 0° yaw angle increased by 70% to 1.70 at 15° yaw. This resulted in a Wind Averaged Drag Coefficient (WADC) of 1.41. The WADC is an estimation of the aerodynamic performance allowing for variation in the wind yaw angle (see Sec.(2.4.5.4) for more details). The average wind direction (Φ_{Wind}) within the United Kingdom is $\simeq$ 257.5° with an average wind speed (V_W) of 3.5

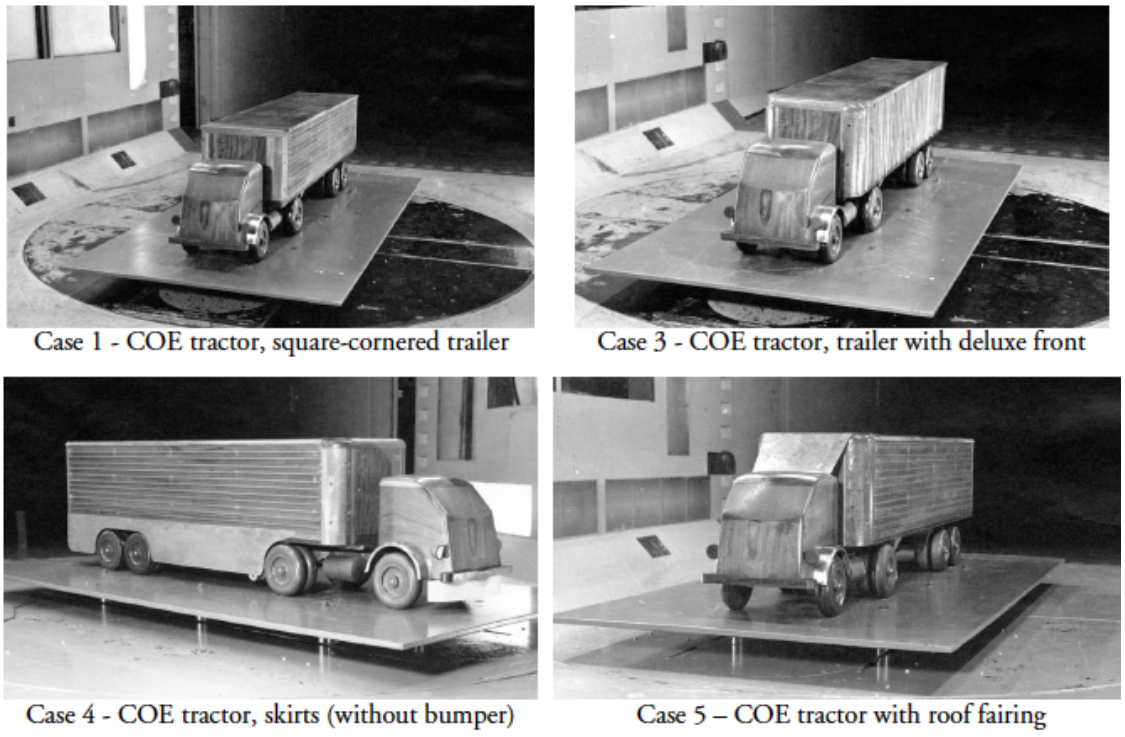

Figure 2.9: University of Maryland Aerodynamic Device Testing, Cases: 1, 3, 4 and 5 [17].

ms^{-1} [18]. The average direction of travel of a heavy goods vehicle (Φ_{Truck}) within the UK is either 360° or 180° (South to North or North to South, respectively). As a result, there is a resultant non-zero yaw angle present (β), the 0° yaw angle performance of a vehicle does not therefore reflect the actual on-road performance.

The dramatic increase of the C_D at yaw, highlighted the contribution of the wind yaw angle towards the overall drag of the vehicle. The roof fairing provided a large drag saving of 35% over the baseline at zero yaw. This saving was achieved by removing the area of high pressure on the container forebody caused by stagnation and also by reducing the amount of recirculated air in the gap between the tractor and trailer. The savings achieved by the deflector decreases past 5° yaw angle to 23% at 20° yaw angle, highlighting the optimum operating range of the deflector to be between ($-5° \leq \beta \leq +5°$).

The largest saving obtained at the yaw angles tested was provided by a fully streamlined and skirted boat tailed model (case 10 in Fig.(2.10)), highlighting the importance of streamlining the base configuration. The fully streamlined model

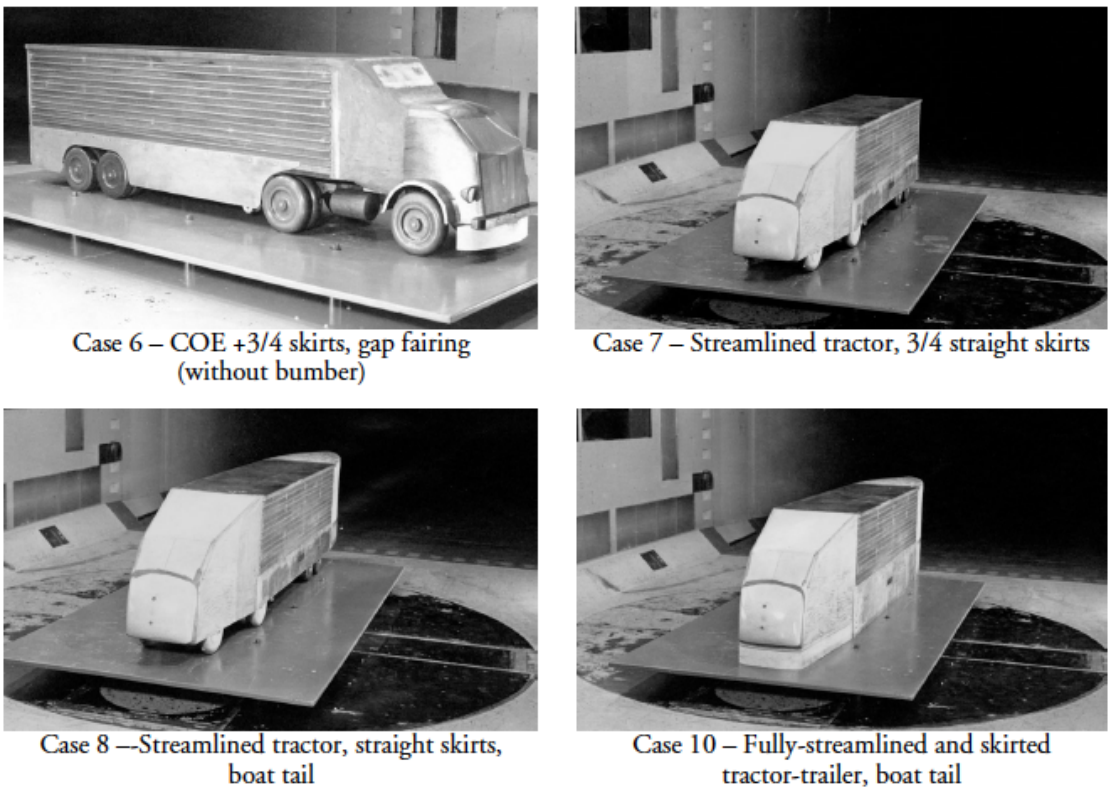

Figure 2.10: University of Maryland Aerodynamic Device Testing, Cases: 6, 7, 8 and 10 [17].

tested provided a drag saving of 82% at zero yaw angle and a WADC reduction of 84%. Certain configurations tested included a full sealed cab-to-trailer (cases 6, 7, 8 and 10 in Fig.(2.10)), are not practical for an articulated vehicle, but highlighted the contributions of these areas to the overall drag on the vehicle.

From the research conducted in the 1970's, it was apparent that there were two main areas of research to pursue. Based upon this, current research is divided between that of optimising the shape of existing vehicles via aerodynamic add-on devices and the development of a leading-edge Ground Transportation System (GTS) [19]. The GTS is an idealised tractor-trailer configuration shown in Fig.(2.11) and is the basis for both computational fluid dynamics (CFD) and experimental research.

The benefits of add-on devices are that they are relatively inexpensive compared to both the capital and operational costs of the vehicle. The downside is that add-on devices will not yield the highest drag reduction when compared to a purpose-built vehicle. The benefits of a GTS are highlighted by the largest overall drag reduction

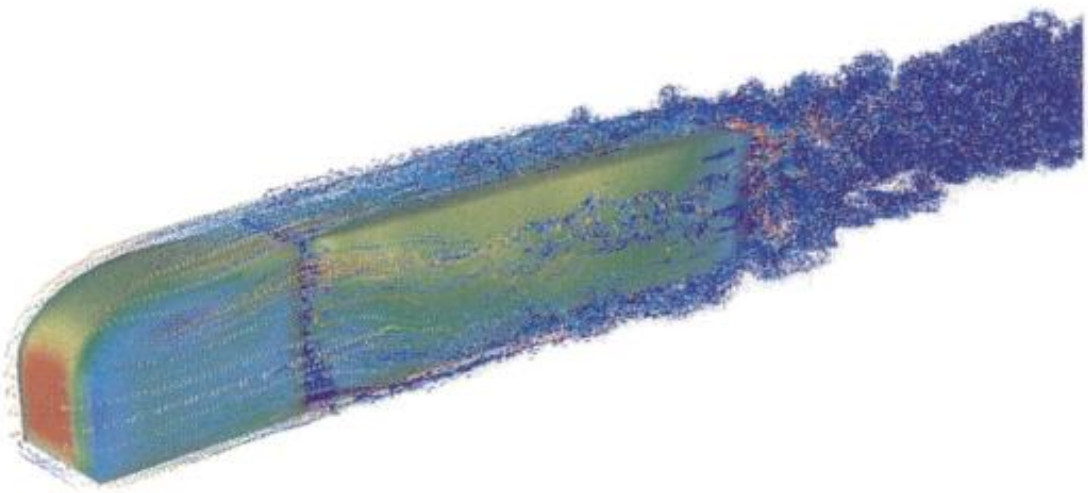

Figure 2.11: CFD Flow Visualisation on a Ground Transportation System (GTS) Model [20].

at any yaw, however, the downside is that such a system would require replacement of all current vehicles in favour of a new vehicle which has not been commercially tested.

The influence of the GTS research can be seen in Fig.(2.12), which shows a Penske Racing truck fitted with aerodynamic add-on devices to modify the shape towards the optimum GTS design. The truck, however, is not in wide spread commercial use and like the Labatt Streamliner, is a mobile advertisement. The GTS styled Penske Racing truck is an advert for Penske's commercial truck rentals, which differ vastly from the optimum GTS shape and resemble the baseline shape tested by Sherwood [17].

Early notable work was also conducted by Cooper [22], whose work focused on the contribution of front edge rounding and rear edge shaping on the aerodynamic drag associated with bluff vehicles [23]. This work supported the initial work conducted by Sherwood [15], Buckley et al. [5] and Mason & Beebe [24]. These works looked into aerodynamic devices for improving truck fuel economy by identifying and optimally shaping the areas that contributed greatest towards the drag on bluff bodied vehicles.

Climate change and the accompanying drive to reduce carbon emissions has instigated renewed interest in the field of HGV drag reduction. There are now Industry, Research and Government backed research programs such as: Truck Manufacturers Association (TMA) [25], Society of Automotive Engineers (SAE) [26] and Department of Energy (DOE) [27]. The reports published by these organisations give a

Figure 2.12: Penske Racing Truck Fitted with Aerodynamic Devices [21].

comprehensive overview into HGV related research via excerpts from relevant aerodynamic research. In line with this, one of the main tenets of current research is to work with and gain support from industry. This is achieved primarily with involvement of vehicle manufacturers in the testing of aerodynamic devices. Involvement of the manufactures during the research phase enables commercial input to be made on the practicality of the research towards the conditions experienced by a HGV during its operating life cycle. This enables focus on practical solutions to be researched rather than idealised research, which in turn leads to improved commercial adoption of products generated from the research.

2.4 Current Aerodynamic Research

2.4.1 Aerodynamics of Heavy Goods Vehicles

From early research conducted on commercial vehicles, several main areas were identified as contributing significantly towards the aerodynamic drag on a heavy

goods vehicle. As a result, current research is focused on design optimisation of the identified areas to improve aerodynamic efficiency. The identified areas of research are:

Cab Design: Sec.(2.4.2)
- Mirrors: Placement and optimisation
- Aerodynamic Add-on Devices: Cab deflector, side fairings and cab skirts

Cab and Trailer Gap: Sec.(2.4.3)
- Cab to Trailer Separation: Optimal separation
- Active Suction and Blowing: Rear of cab and forebody of container

Trailer Design: Sec.(2.4.4)
- Aerodynamic Add-on Devices: Leading edge fairings, side skirts, trailer underbody, wheel covers vortex generators and boat tailing
- Active Aerodynamics: Energy Injection Devices and Dielectric Barrier Discharge

Other Contributing Factors: Sec.(2.4.5)
- Engine Cooling Ventilation: Design and optimisation
- Tyre Spray Suppression
- On-Road Conditions
- On-Road Performance

There have been significant advances in computational power since the original studies conducted by Sherwood [17]. This has enabled detailed computer simulation of complicated mechanical devices and their impacts on the system. As a result, there is a growing research field in the use of Active Flow Control (AFC). Active Flow Control [28] is a method of controlling the fluid flow by perturbing the flow by either suction or blowing or via mechanical adjustment of the physical shape of the object using actuators. Control is achieved through use of a reference value or "target value" where a measured value on the object is then driven to the desired value via a feedback controller (see Fig.(2.32 in Sec.(2.5))).

The advances in computational power have also meant that Computational Fluid Dynamics (CFD) is becoming an evermore powerful tool used for investigation of HGVs. The advantage of CFD over experimental wind tunnel testing is the ability to overcome the Reynolds effect associated with scale models [2]. Due to the physical restrictions from the dimensions of most wind tunnel working sections, either $1/8^{th}$ or $1/10^{th}$ scale models are used. The large size of HGVs and their relatively high operating speeds means that the wind tunnel speed required to accurately model the flow exceeds the limit at which compressibility effects are no longer negligible.

Most research areas are therefore investigated using both computation fluid dynamics [29] and wind tunnel testing, with both active and passive devices investigated.

Due to the physical size of a HGV, simulation of all the turbulence length scales present in the vehicle flows via Direct Numerical Simulation (DNS) is not possible with current computational power. This has meant that certain modelling of the sub-grid scale turbulence is required. Sub-grid scale turbulence is the turbulence with length scales less than the resolution of the computational cell. Using Reynolds-Averaged Navier-Stokes (RANS) solvers, they are averaged out within the cell and their effects cannot be accounted for and must therefore be estimated using turbulence models.

The requirement of turbulence modelling results in wind tunnel testing still being required to validate the CFD results. Once the model has been validated to ensure the turbulence is accurately modelled, faster optimisation of the geometry is possible. The validation phase requirement has lead to an increased partnership between CFD and experimental testing.

2.4.2 Cab Design

A typical EU tractor unit is shown in Fig.(2.13). As a result of a non-standard trailer height within the UK, various tractor-trailer combinations are used resulting in a height difference between cab and trailer. The driver requirement of numerous viewing angles results in the cab manufacturer attaching multiple mirrors to the vehicle. The position of the mirrors on the vehicle is due to driver comfort, with little aerodynamic consideration given for the placement. The large engine capacities required to haul a loaded trailer unit means that multiple inlets are required for engine and transmission cooling.

As a result of these criteria, the baseline unit produced by the manufacturer can be improved, however, their primary goal is to focus on driver comfort rather than an aerodynamically optimised vehicle.

2.4.2.1 Cab Mirrors

The contribution to drag attributed to an outboard mirror has been well documented by Leuschen et al. [31], whose paper "Summary of Full-Scale Wind Tunnel Test of Aerodynamic Drag-Reducing Devices for Tractor-Trailers" investigated the full-scale component's contributions to aerodynamic drag on a standard North American cab. The results obtained from the National Research Council of Canada (NRC) using a full scale tunnel, indicated that Original Equipment Manufacturers (OEM) cab-mounted mirrors contributed to a C_D of 0.010, approximately 2% of the total

Figure 2.13: Example of a Typical EU Tractor Unit Produced by Mercedes-Benz [30].

aerodynamic drag on the vehicle. If the mirrors were removed and replaced by video cameras, it was estimated that an annual fuel saving of 588 Litres (US Annual mileage of 81,000 miles at a speed of 62 mph) could be achieved. The paper also concluded the drag achieved by the mirrors was due to current US safety regulations that dictate a minimum size of the mirrors which must enable a 95% field of view. This regulation was therefore the main driving force in the design rather than the aerodynamic optimisation.

The result of this limitation imposed by safety standards and driver comfort, the current area of research on cab mirrors focuses on minimising aero-acoustic noise and reducing material deposit by adjusting the flow field around the mirrors. Research by Khalighi et al. [32] used Particle Imagining Velocimetry (PIV) to investigate the mean velocity field obtained in the wake of several tested mirrors. The results highlighted the importance of the design of the mirror on the resulting wake structure. The mirrors, however, were tested in isolation and hence the complex flow fields around the cab and the resulting cab to mirror interaction were not investigated.

Investigation into self (resulting from the flow field of the vehicle, such as tyre

rotation) and foreign (resulting from the flow field of other vehicles, such as trailer wakes) soiling was conducted by Urban [33] of Daimler Chrysler. Initial design of an A-pillar flap was achieved using the results from CFD optimisation simulations in an attempt to reduce foreign soiling. The concept of an A-pillar flap is to prevent water droplets and spray from entering the region between the side window and side mirror. Figure (2.14) shows an extended separation bubble caused by the flap, which prevents the water from entering this region.

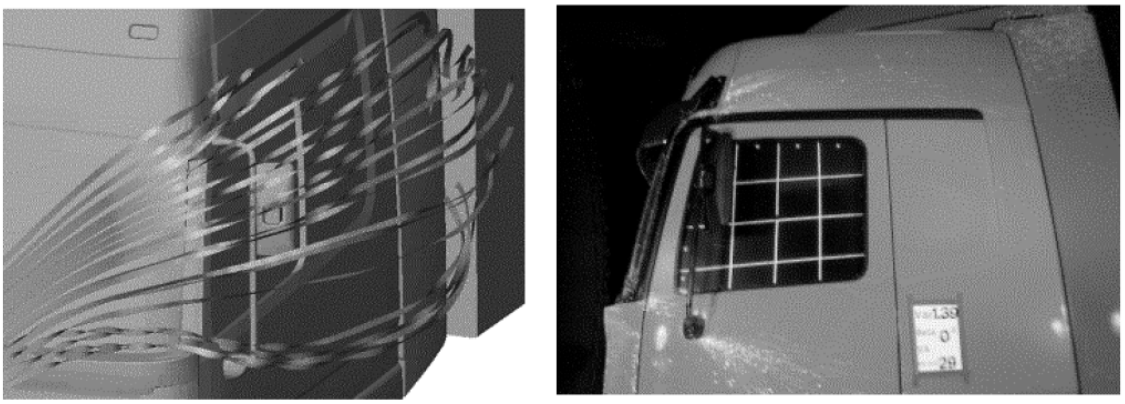

Figure 2.14: CFD (Left) and Experimental (Right) Foreign Soiling on a Mercedes-Benz Actros, Investigated by Urban [33].

Final optimisation of the design and testing of the flap was achieved by full scale wind tunnel testing. In an effort to reduce self-soiling around the door handle and cabin entry points, the addition of a side vent (shown in Fig.(2.15)) was made to the vehicle. The design of the side vent prevents flow separation around the lower A-pillar region of the vehicle and generates a flow along the side of the vehicle, suppressing the road spray generated from the front wheels.

The results from the wind tunnel test showed that both the A-pillar and side vent contribute to an increase in overall drag of the vehicle, but were chosen for driver visibility and safety over the aerodynamic penalty associated with the fitment of the devices.

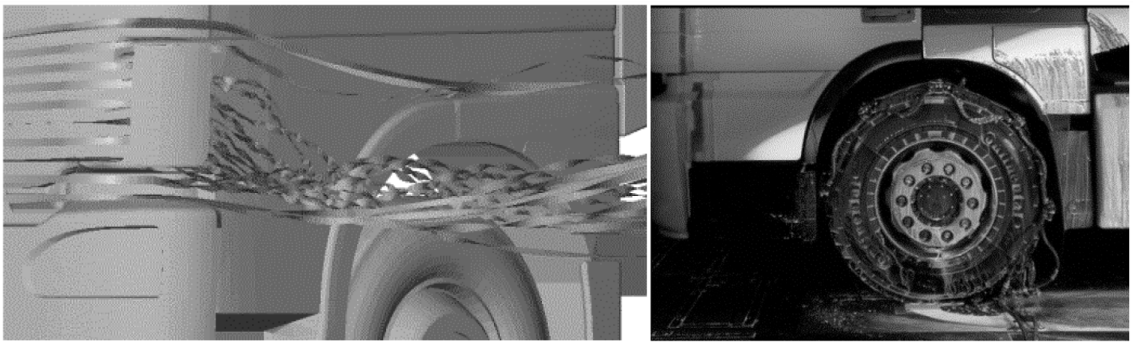

Figure 2.15: CFD (Left) and Experimental (Right) Self Soiling on a Mercedes-Benz Actros, Investigated by Urban [33].

2.4.2.2 Cab Aerodynamic Add-on Devices

The use of air deflectors on modern HGVs can be attributed to Saunders [16]. Designed in 1966 for a company called 'Air-Shield', the trailer mounted deflector was based on earlier work conducted at the University of Maryland [5]. The trailer deflector can be seen in Fig.(2.16).

Since the release of the 'Air-Shield' deflector, various cab mounted designs have been suggested. Beers [34] and Lambie et al. [35] in the late 1970's proposed various deflector geometries for diverting the air flow around the vehicle. These designs can be seen in Figs.(2.17 and 2.18), respectively.

The variations in these cab deflector designs have been tested by Hucho [14]. The results (shown in Fig.(2.19)) show that the drag reduction achieved depends heavily on the deflector design. The efficiency of the deflector varied by 19% solely due to the geometry of the deflector.

The most efficient deflector test contained a 3D profile, accounting for the air flow both over the top and around the side of the container. This resulted in a drag coefficient reduction of 30% over the baseline [14]. The baseline configuration test was a cab without a deflector.

The various deflector designs primarily arose due to the variation of their intended purpose. The deflector designed by Beers [34] (shown in Fig.(2.17)) was designed for a standard tractor-trailer configuration. The deflector was therefore designed to remove the area of high pressure located on the container forebody and reduce the effects of cavity recirculation between the tractor and trailer.

The air deflector designed by Lambie et al. [35] (shown in Fig.(2.18)), however, was designed for a refrigerated trailer unit. Due to the trailer refrigeration unit containing an inlet suction required for the refrigeration compressor, the area of high pressure that is usually present on the container forebody is removed. The deflector was therefore designed to direct air into the refrigeration unit and around

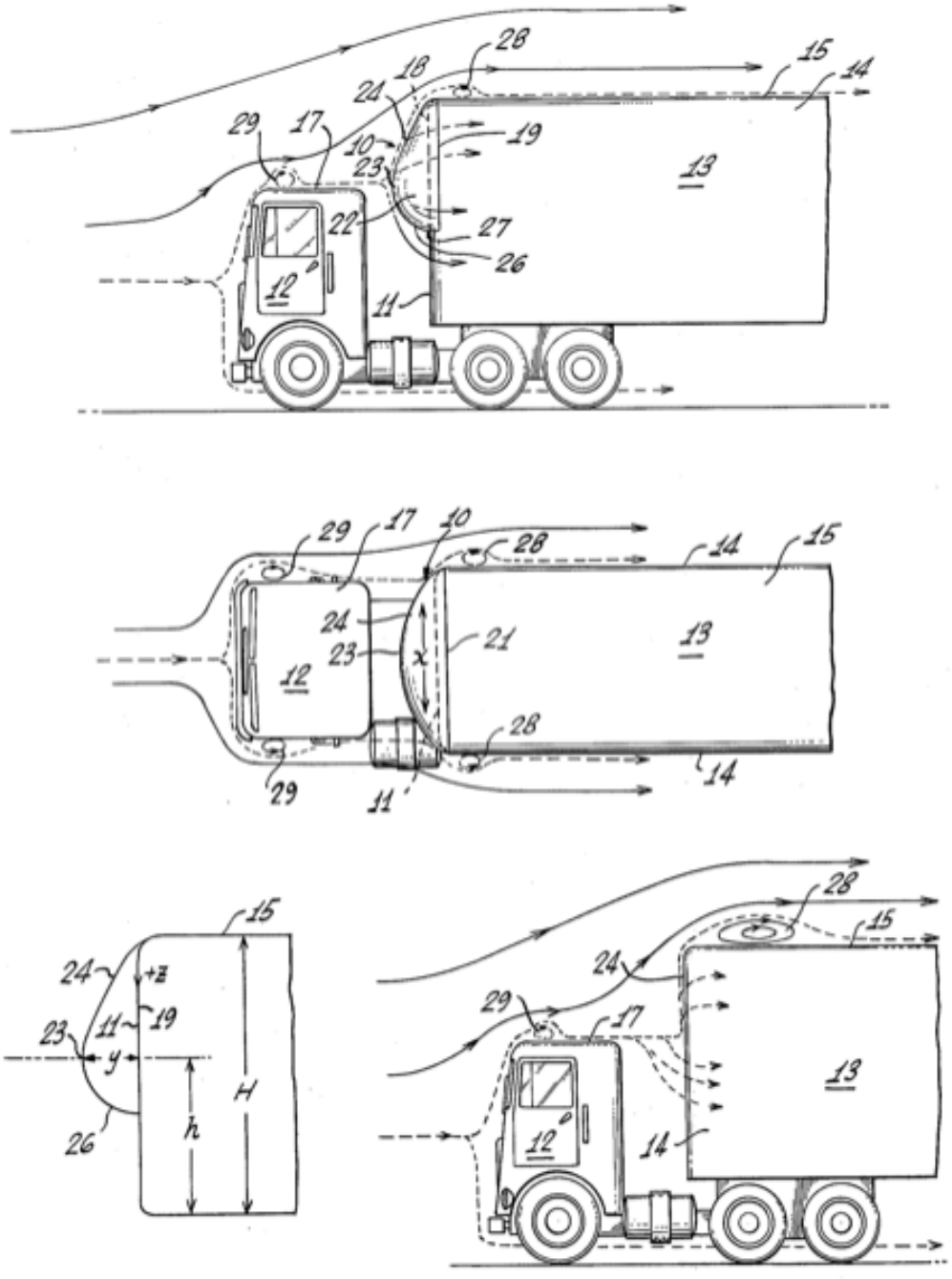

Figure 2.16: 'Air-Shield' Trailer Deflector [16].

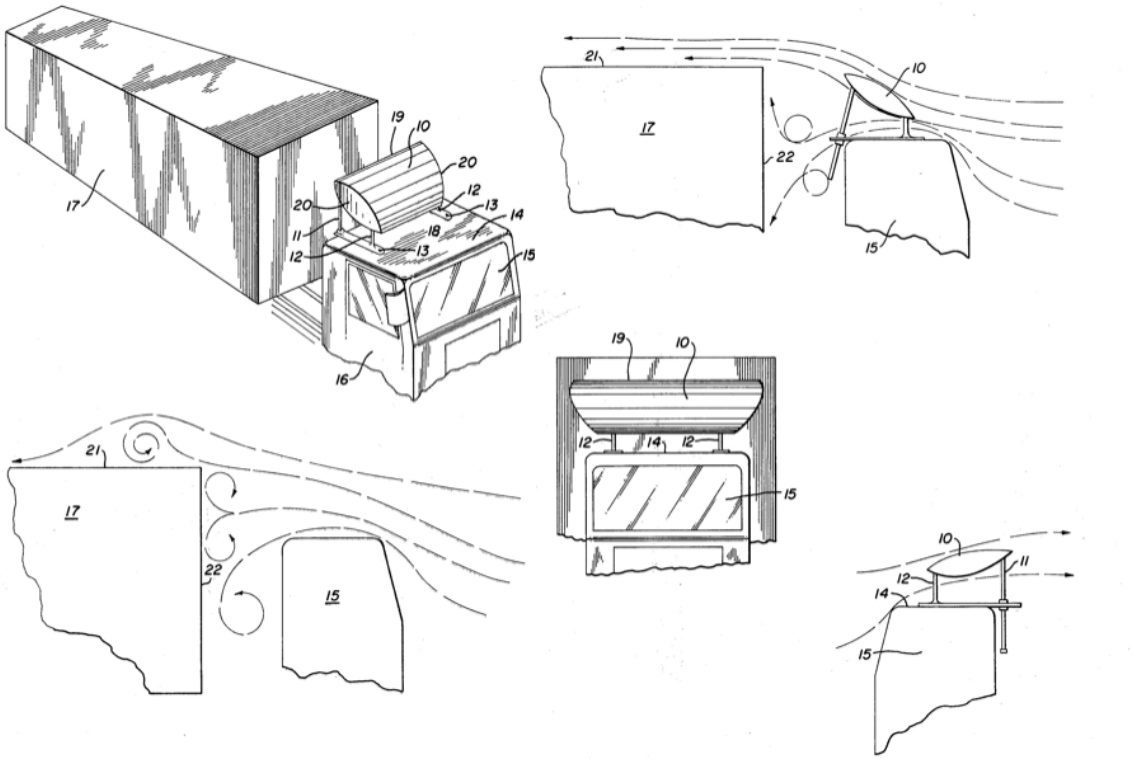

Figure 2.17: Cab Mounted Aerodynamic Device [34].

the trailer where the refrigeration unit is not present.

Whilst many various deflector designs exist (shown in Fig.(2.20)), the majority vary due to their intended application rather than for their aerodynamic performance. Due to the wide range of truck models available from different manufacturers, deflectors vary in design due to the physical differences in the baseline vehicle.

To minimise the cost of production due to varying moulds required during the construction of the fibreglass deflectors, deflector manufacturers often limit their designs to single manufacturers. This results in deflector manufacturers catering their designs to a specific HGV marque.

As a result of the relationship between vehicle and deflector manufacturers, little progress since that of Saunders [16] has been made on aerodynamic cab devices. This is primarily due to the shape of the cab being dictated by safety and human factors rather than by aerodynamic drag reduction. Currently only passive cab mounted deflectors have been investigated. The most recent design being Volvo's adjustable deflector [36]. The deflector, when connected to a compatible trailer, can be adjusted to a predetermined optimal height evaluated previously through exten-

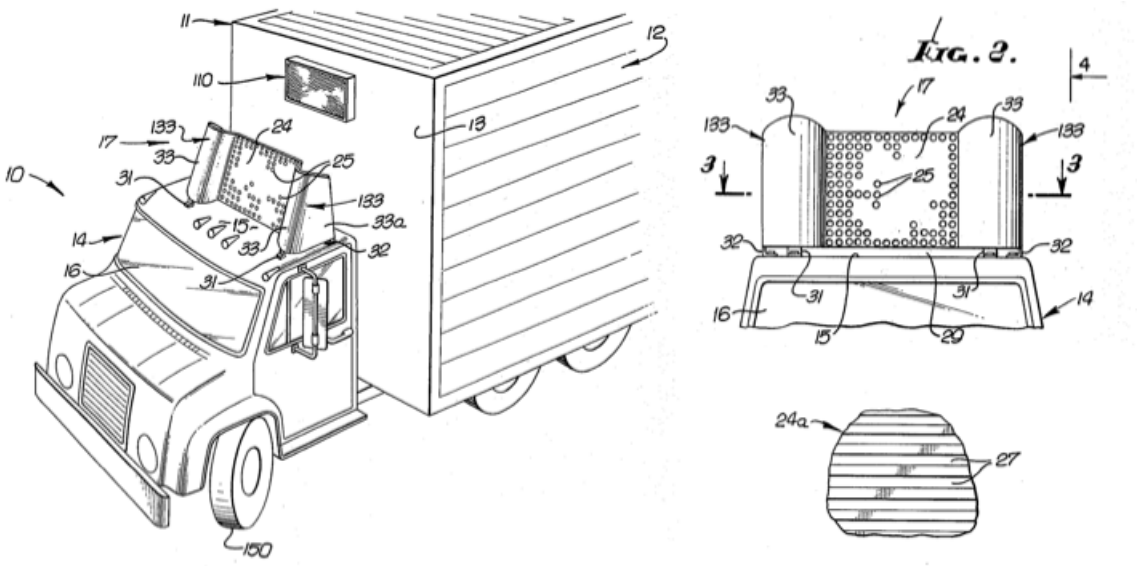

Figure 2.18: Cab Mounted Aerodynamic Device for a Refrigerated Truck [35].

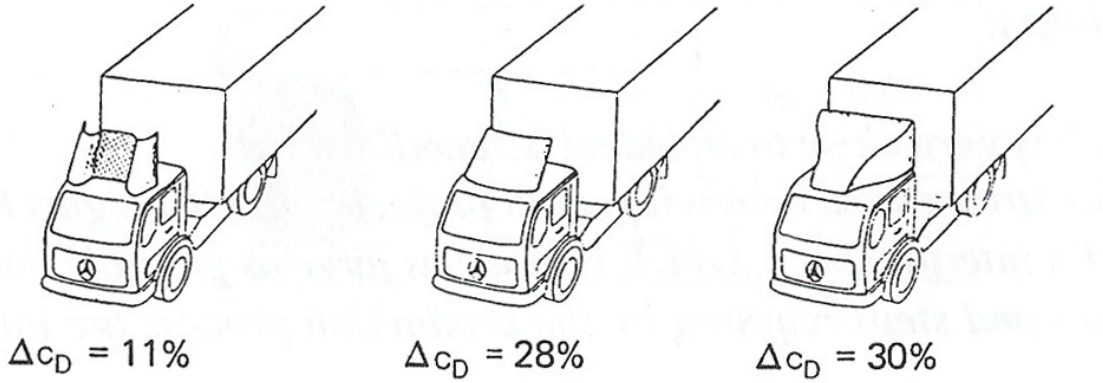

Figure 2.19: Drag Reduction Achieved for Various Cab Deflectors Designs [14].

sive wind tunnel testing. Such deflectors offer an appreciable potential aerodynamic drag saving of between 20 - 30% [22] over the baseline model. Static deflectors, however, such as the one developed by Volvo [37], only provide a significant saving whilst the flow field is at zero yaw angle and do not offer the lowest drag configuration when a significant wind yaw angle is present. A 10% [22] reduction in efficiency is experienced at yaw between the optimum deflector height and the optimum height with no wind yaw present. This reduction in efficiency highlights the importance of active control to ensure the vehicle is at the optimum, minimum drag configuration.

Figure 2.20: Various Aftermarket Deflector Designs.

Notable later work has been conducted by Leuschen et al. [31]. Their paper "Summary of Full-Scale Wind Tunnel Test of Aerodynamic Drag-Reducing Devices for Tractor-Trailers", provided full scale wind tunnel test results on roof deflectors, side extenders and cab skirts. Their work serves to further validate the savings predicted by Sherwood [17]. The results obtained from the full aero package consisted

of a roof deflector, side extenders and cab skirt. The aero package resulted in a C_D saving of 0.141, compared to the scale model prediction of 0.153 by Sherwood [17]. The difference arose due to the less aerodynamic baseline of the cab used by Sherwood [17]. The work, however, did not investigate optimum designs of any of the add-on devices tested, but simply the contribution towards the drag of the vehicle.

Currently there is no focus on the optimum shape of aerodynamic add-on devices for modern HGVs. This in part due to the significant amount of prior work. The second reason is that greater focus is being employed on cab design. As a result of varying cab designs, each manufacturer has an associated aerodynamic add-on device specific for their cab and investigation into an overall shape is only achieved through the generic GTS geometry.

2.4.3 Cab and Trailer Gap

The flow field within the Tractor-Trailer gap has been previously investigated using Particle Imaging Velocity (PIV), notable research has been conducted by Heineck et al. [38] at the National Aeronautics and Space Administration (NASA) Ames Research Centre. The surface pressure results from their investigation are shown in Figs.(2.21 and 2.22). This experiment provided a practical source for experimental validation of the CFD predicted flow structures. It also formed the basis for the development of side extenders to reduce the effects of the vortices contained within the gap. The effect on the side extenders on the vortices produced within the gap was significant, with a reduction in C_P from 1.0 to around 0.1 on the forebody of the container. The reduction in forebody pressure and the resulting drop in the aerodynamic drag coefficient (C_D) from 0.75 to 0.5 at 10° yaw angle was achieved primarily by bounding the asymmetric vortex between the side extenders. The resulting symmetrically bound vortex imposed less disturbance on the freestream flow parallel to the truck and hence a reduction in the interference drag generated by the cavity.

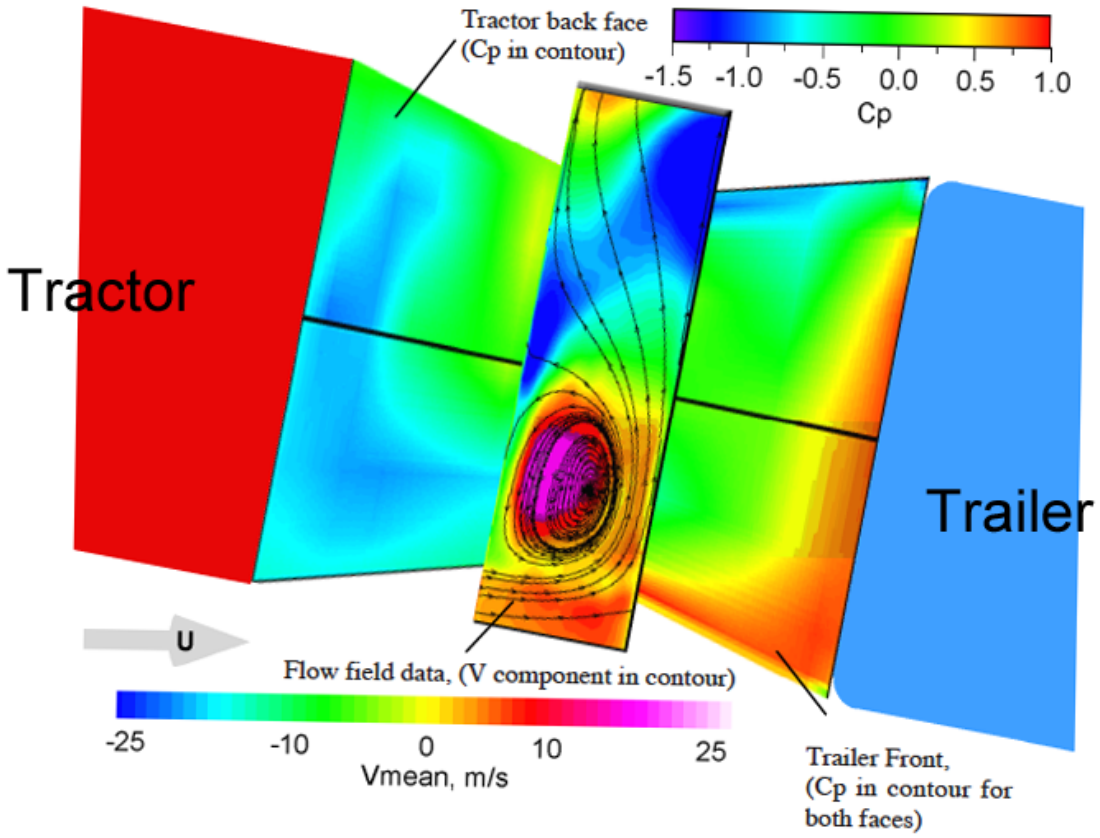

Figure 2.21: Cavity Flow Shown Between Tractor Rear (Red, Left) and Container Forebody (Blue, Right) [38].

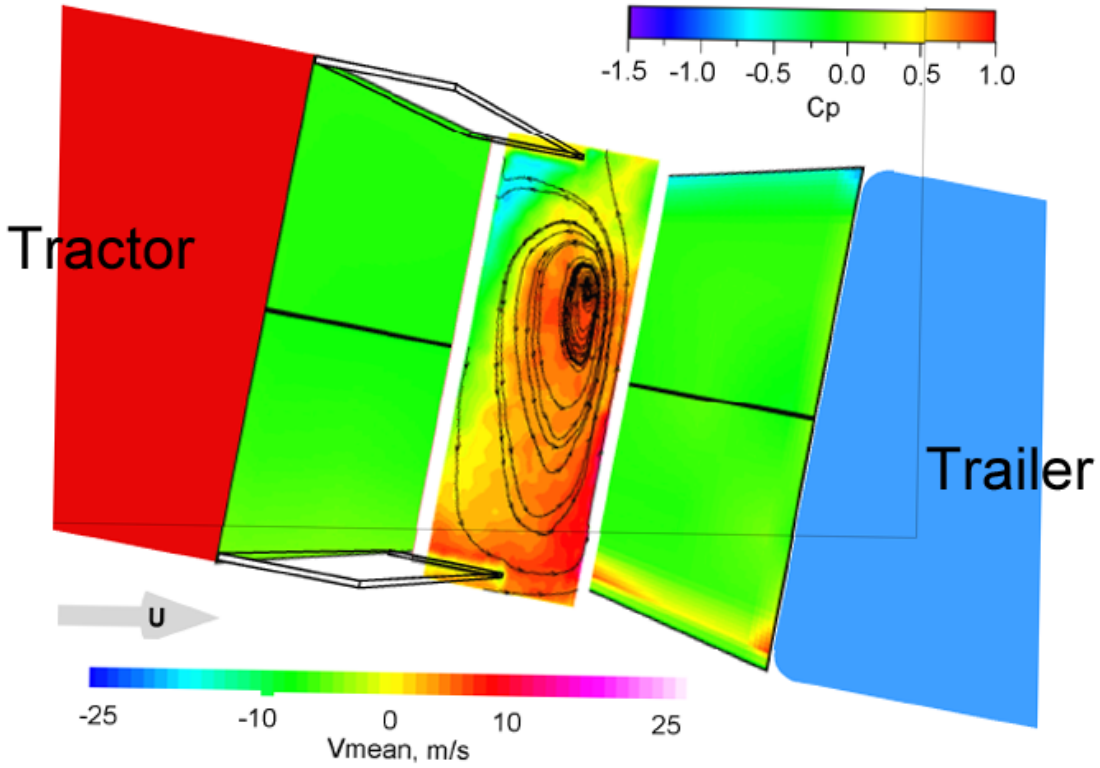

Figure 2.22: Cavity Flow Shown Between Tractor Rear (Red, Left) and Container Forebody (Blue, Right) with Addition of Side Extenders [38].

2.4.3.1 Cab to Trailer Separation: Optimal separation

The effect of the tractor-trailer separation distance on the flow structure has been investigated by Hammache et al. [39]. The investigation was conducted to determine how the vortices produced within the gap varied with the gap separation. The experiment was conducted, again using PIV to give insight into the flow structure contained within the tractor-trailer cavity.

The experiment also highlighted the time varying and unpredictable nature of the flow field within the cavity. The dependence on the cavity dimensions was found to determine the modes present within the cavity. The optimum normalised gap width is shown in Fig.(2.23), which shows a dramatic increase in the drag coefficient when the normalised gap width ($\frac{G}{\sqrt{A}}$) exceeds 0.5. G is the gap between cab rear and container forebody and A is the frontal area of the container forebody.

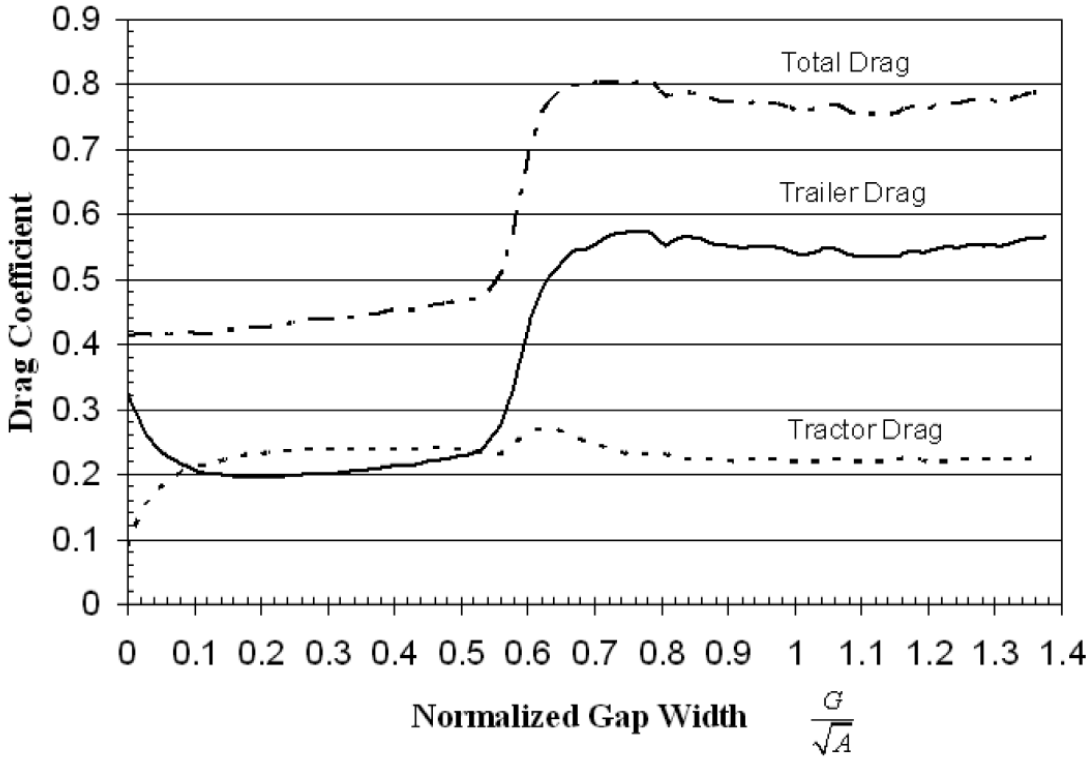

Figure 2.23: Tractor-Trailer Cavity Separation [39].

The variation of the flow structure within the tractor-trailer gap was also noted by Hammache et al. [39] and can be seen in Fig.(2.24). The experiment was conducted for a single yaw angle of zero degrees. Thus far the experiments conducted

on the cab-trailer gap have not sought to determine if the optimum cab-trailer separation is a function of the yaw angle. The time variation for a critical gap is shown in Fig.(2.25), highlighting a 15% increase in the aerodynamic drag force recorded for around one second for the critical gap separation.

The experiment investigated the effects of the gap separation on the time variation of the vortices produced within the cavity. For a sub-critical gap ($\frac{G}{\sqrt{A}} \leq 0.5$), this corresponded to either a symmetric or asymmetric flow field within the cavity. These flow fields have very little time variation and the drag force due to these vortices is approximately constant. Increasing the gap separation above the sub-critical gap ($\frac{G}{\sqrt{A}} > 0.5$) causes the symmetric or asymmetric flow field to change from a "cavity mode" to a "wake mode".

This wake mode is caused by the wake due to vortex shedding from the rear of the cab. In wake mode, the truck and trailer are effectively bluff bodies in tandem. The flow filed in wake mode exhibits a time variation and as a result the drag force varies considerably compared to the sub-critical case.

The sub-critical gap, as expected exhibits little drag fluctuation as a function of time. The sub-critical gap acts in the same manner as a large gap with side extenders, producing stable vortices within the gap that have little interaction with the side flow field around the cab.

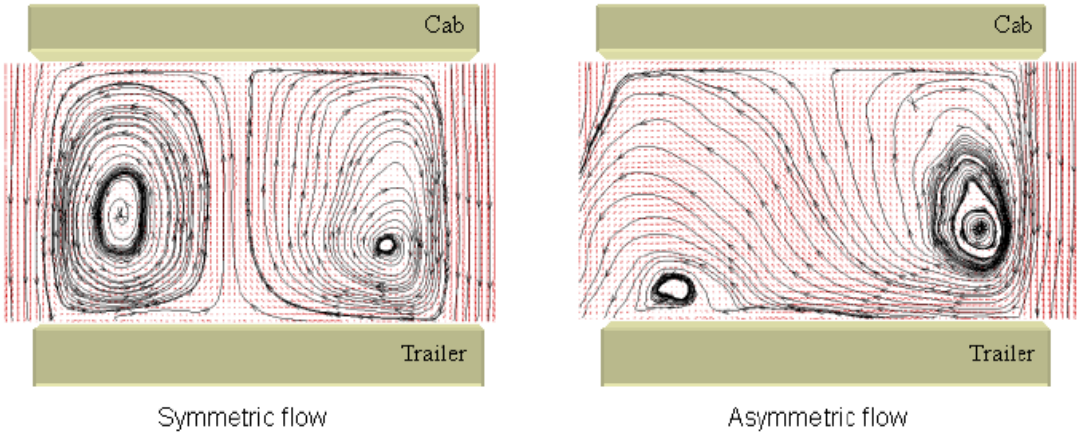

Ensemble-averaged streamline patterns of the flow in the gap at zero yaw, G/√A = 0.55. (a) symmetric flow, (b) asymmetric flow.

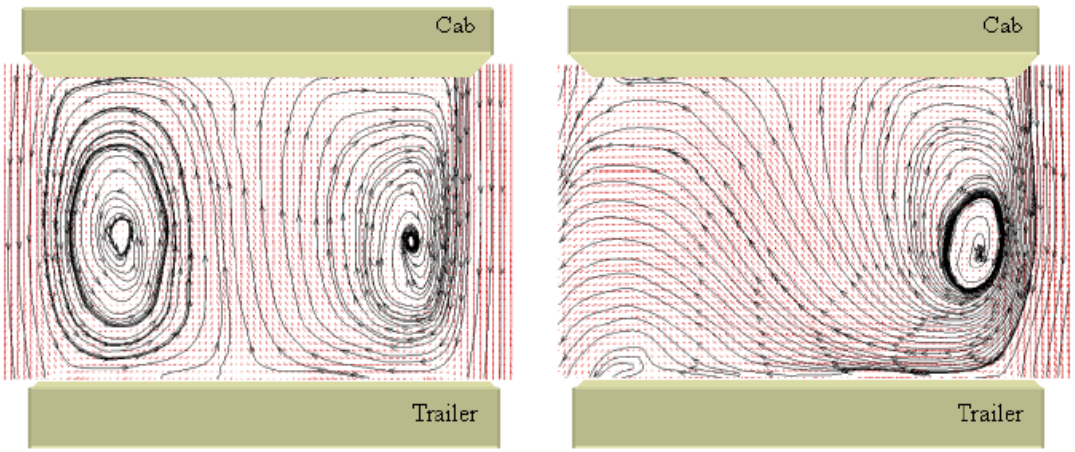

. Ensemble-averaged streamline patterns of the flow in the gap at zero yaw, G/√A = 0.65. (a) symmetric flow, (b) asymmetric flow.

Figure 2.24: C_D Variation within the Tractor-Trailer Gap [39].

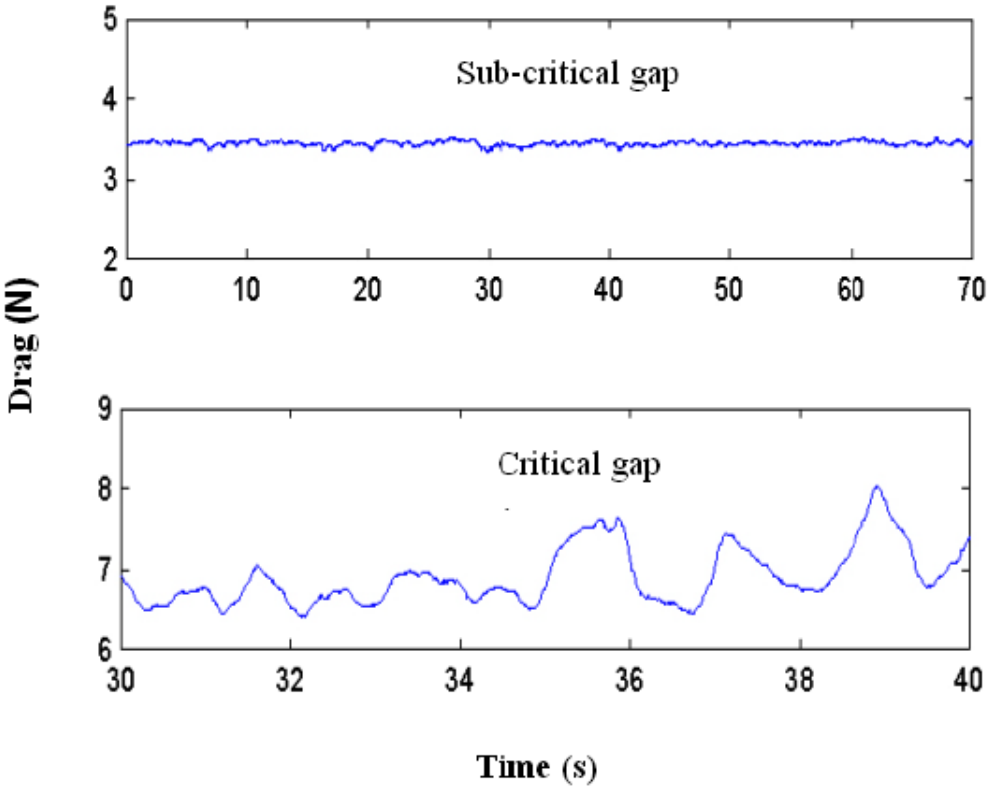

Figure 2.25: Tractor Trailer Cavity Flow Drag Time Variation [39].

2.4.3.2 Active Suction and Blowing

Active suction and blowing is the ability to change the pressure contained within the flow field at certain location on the vehicle. This is achieved through use of mass injection actuators, whereby the local flow field is "sucked" creating a reduction in pressure from areas of high pressure, usually at the front of the vehicle. The air is then compressed and "injected" into an area of low pressure within the flow field, usually at the rear of the vehicle. The result is a reduction in the areas where the velocity of the flow field significantly deviates from freestream, thereby reducing the pressure drag on the vehicle.

From the results of vorticity based flow, both active and passive forms of control have been developed. Active control has been achieved through Suction and Oscillatory Blowing (SaOB) and has been investigated by Seifert et al. [28]. The work investigated pulsed suction and blowing on the rear of a 2D GTS model. The suction created on the rear trailing edge of the trailer reduced the angle of separation and hence the effective form drag of the vehicle. The results from the study indicated that SaOB actuators, could provide a maximum net saving of around 6 - 7%, after the power expenditure used to drive the actuators is considered. The work also concluded that the position of the actuators was critical to the performance of the actuators.

The cab rear has also been investigated by Ortega et al. [40] using wind tunnel measurements and CFD simulation. The work conducted by Ortega et al. investigated blowing on the rear of the tractor to generate an area of low pressure in the tractor-trailer gap which reduced the rate of fluid entrainment from the freestream, greater than that achieved by passive cab extenders. A C_D reduction of 0.146 was achieved for the maximum flow rate tested. This reduction was significantly greater than passive side extenders tested which produced a reduction of 0.049. The experiment, however, did not take into account the energy required to drive the flow on the rear of the cab.

Active Flow Control (AFC) is currently in the early stages of development, with the primary focus on the position and design of the actuators. Whilst significant savings have been achieved experimentally by Ortega et al. [40], careful consideration of the net energy saving must be made in order to reduce the overall drag of the vehicle.

2.4.4 Trailer Design

The primary design criterion of a trailer is the transportation of physical goods, as a result trailers are optimised for maximum internal storage. In the UK various trailer heights exist ranging from 3.95 m to 4.95 m [4]. The articulated couplings between cab and trailer place a restriction on the devices that can be placed on the forebody

of the container. To minimise drag, a small cab to trailer gap should be chosen and a cab mounted deflector used to remove the container forebody pressure. Current research is therefore primarily focused on the top and rear shape of the container.

An example of a trailer design currently in production is the DON-BUR 'teardrop' trailer [41] (shown in Fig.(2.26)).

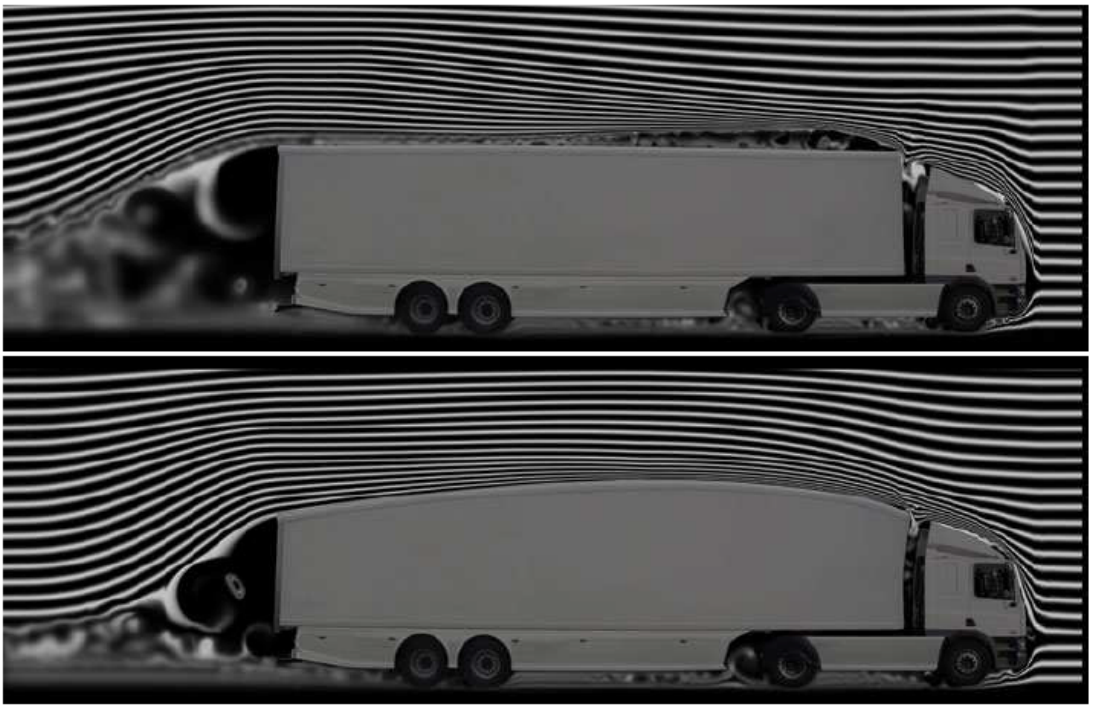

Figure 2.26: Standard Trailer (Above) and DON-BUR Aerodynamic Teardrop Trailer (Below) [41].

The design of the 'teardrop' results in an increased vertical height from 4.0 m to 4.5 m, resulting in a 12.5% frontal area increase over the baseline. This has the benefit of increasing internal storage volume by 10%, however, the load carried must be arranged in a novel orientation to take advantage of the additional space.

Limited independent data exists on the performance of the 'teardrop' shape, data published by DON-BUR indicated a drag reduction of 43% over a standard trailer with zero wind yaw angle. Marks & Spencer PLC have reported an average fuel consumption saving of 10% [41].

2.4.4.1 Trailer Aerodynamic Add-on Devices

Passive aerodynamic add-on devices for trailers have been investigated experimentally by Leuschen et al. [31] shown in Fig.(2.27) and computationally by Pankajashan et al. [42]. Results from these studies showed an increase in the WADC of 0.0195 over baseline for trailer vortex strakes. The side skirts tested provided a WADC of 0.0367, equating to a annual fuel saving of around 2,264 Litres (US Annual mileage of 81,000 miles at a speed of 62 mph).

A reduction in the WADC of 0.0438 and 0.0506 was achieved for the boat tail designs: 'Aerovolution' inflatable rear boat tail and the 'Transtex Composite' folding rear trailer deflector respectively. As a result of the requirement to access the rear for loading and unloading of the trailer, current research is focused on more practical, collapsible rear boat tails.

Passive devices have also been investigated in scale form by Garry [43] and full scale by Coon et al. [44] (shown in Fig.(2.28)). This later work generated a reduction in drag through use of the addition of a centre and tractor-trailer plates. The add-on passive devices achieved a total drag reduction over baseline of 9%.

Transtex Composites folding rear trailer deflector

Aerovolution inflatable boattail

NXT leading edge fairing

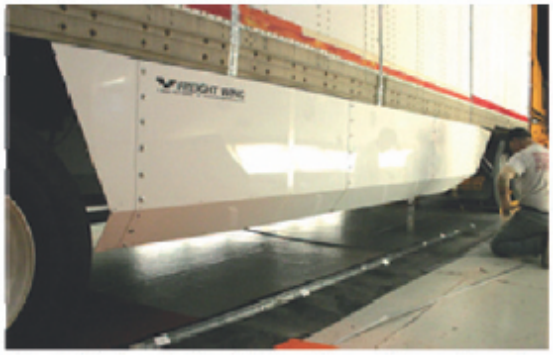

Freightwing belly fairing

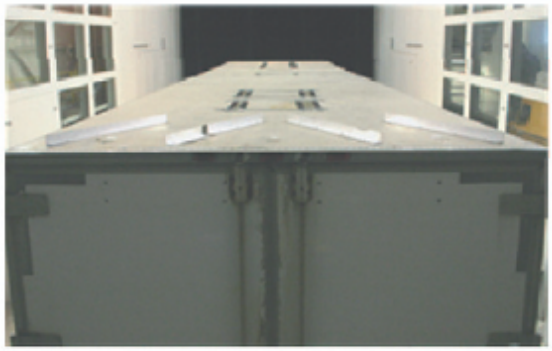

Vortex generators (top)

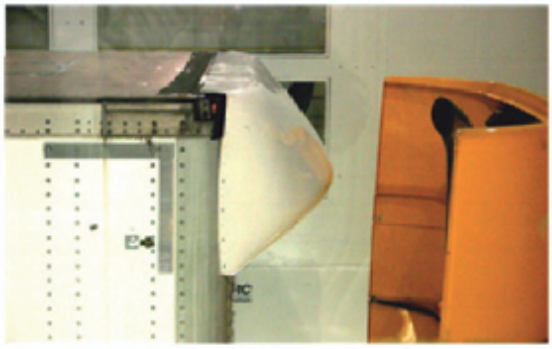

Menac leading edge fairing

Figure 2.27: Various Trailer Aerodynamic Devices [31].

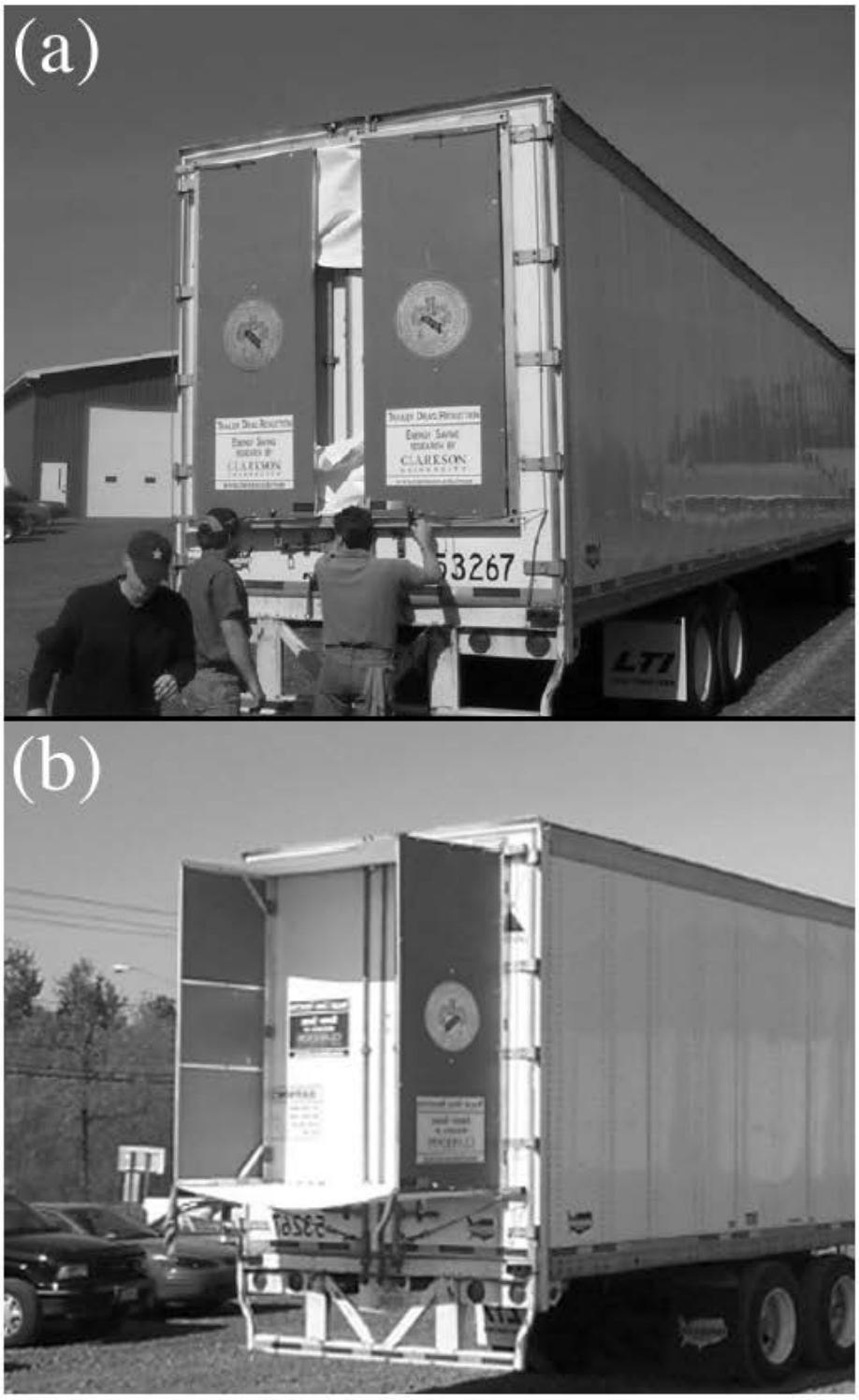

Figure 2.28: Full Scale (a) Closed and (b) Open Trailer Plates [44].

2.4.4.2 Active Aerodynamics

Active control is achieved through various Mass Injection Devices (MIDs), primarily through Suction and Oscillatory Blowing Actuators (SaOB) mounted on the rear surface of the trailer or in conjunction with Boat Tails. Initial integration of control theory with aerodynamics was conducted by Taubert et al. [45] in "Applying Active Flow Control to a $1/24^{th}$ Scale Model of a Semi-Trailer Truck". An image of the experimental arrangement is shown in Fig.(2.29).

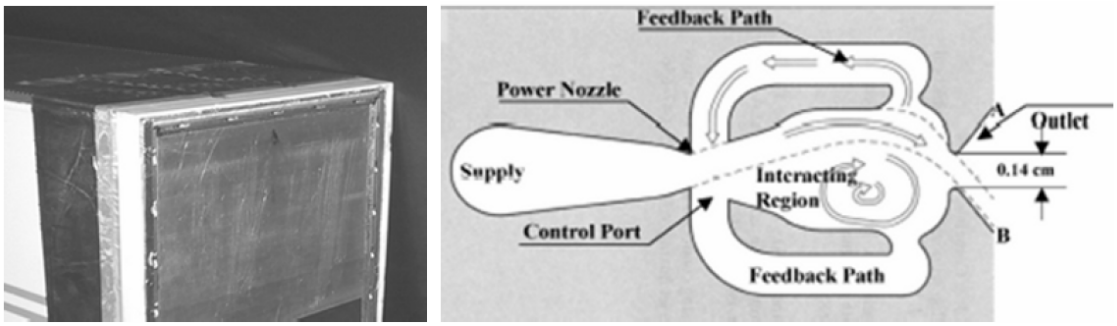

Figure 2.29: Active Flow Control to a $1/24^{th}$ Scale Model of a Semi-Trailer Truck [45].

Results obtained from this study, supported the savings achieved through boat tailing recorded by Leuschen et al. [31]. The active control achieved a reduction in aerodynamic drag of 1% over baseline. The study highlighted the importance of SaOB actuator design and placement for future studies to try and improve the effectiveness of actuators.

Another recent area of research has focused on Dielectric Barrier Discharge (DBD) plasma actuators [37]. Initially developed by Ernst Werner von Siemens in 1857, DBD are comprised of two electrodes, one in air and one covered by a dielectric layer. An alternating current supplies the electrodes resulting in a charge build up in the dielectric medium. The continued discharge from the dielectric medium causes the surrounding air to ionize and form a plasma. The asymmetrical design of the actuators generates a body force vector acting on the surrounding, neutrally charged air. This force vector accelerates the surrounding air with minimal thermal energy transfer. When applied to boundary layer separation, DBD Plasma Actuators stabilise the flow, promoting attachment and delaying separation of the boundary layer and hence a reduction in the aerodynamic drag.

Energy Injection Devices (EIDs) and DBD Plasma Actuators should provide a greater drag reduction compared to passive devices, however, further research is required on energy optimisation and actuator design in order to achieve a net energy saving that currently, has not been sufficiently tested. Most MIDs are therefore

usually investigated for purely academic purposes rather than for commercial implementation.

2.4.5 Other Contributing Factors

2.4.5.1 Engine Cooling Ventilation

The inlet cooling ducts on commercial vehicles have been shown to have no significant contribution [31] to the overall drag on a commercial vehicle. As a result of the minor contribution of the inlets on the drag of the vehicle, current experiments are focused on optimising the airflow around the engine compartment to provide sufficient cooling. Experiments by Sofu et al. [46] focused on using CFD and full scale testing to determine the thermal distribution within the engine bay. The primary focus on modern tractor units is to provide sufficient cooling for the power train whilst minimising thermal stress on critical components.

2.4.5.2 Tyre Spray Suppression

Despite the area of high pressure generated from uncovered wheel arches which contributes significantly towards the aerodynamic drag of the vehicle, current research is focused on safety rather than on drag reduction. Modern research is focused on tyre suppression, with focus on preventing hazardous spray patterns generated from the arches [47]. The large quantity of spray generated from a HGV significantly reduces the visibility of trailing passenger vehicles.

Current research is therefore focused on methods for replicating and improving tyre spray measurements on commercial vehicles. Results from such studies show little effect on the drag reduction capabilities of the devices tested, however, a reduction of up to 30% [47] in the spray generated from the vehicle can be achieved.

2.4.5.3 On-Road Conditions

Aerodynamic devices are currently designed and tested using wind tunnel and CFD simulation. The unsteady nature of on-road flows provides time varying conditions that differ from those obtained using either CFD or wind tunnel testing. The purpose of a low speed wind tunnel is to create a low turbulence environment. Whilst this offers an accurate measurement of the pressure distribution and drag on the vehicle, this does not accurately represent the turbulent flow fields experienced during on-road testing.

Comparisons made by Watkins et al. [48] have highlighted the differences in a drag measurements obtained from a low turbulence wind tunnel to those obtained from turbulent on-road measurements. The unsteady flow experienced by a vehicle

is comprised of many contributing factors. These major contributing factors have been outlined by Gaylard et.al [49] and are listed below:

- Turbulence of the Natural Wind
- Unsteady Wakes Produced by Other Vehicles
- Traversing Through Stationary Wakes of Roadside Obstacles

Two key points about the on-road conditions have been highlighted by Gaylard et.al [49], the first is that the yaw angle (lateral velocity) fluctuations will be of greatest importance. Secondly, that the greatest proportion of unsteadiness encountered will occur at frequencies below 10 Hz. These points remove the need for high frequency ($>$ 200 Hz) investigation into yaw angle variation. A data logging device with a minimum sample frequency of 20 Hz could therefore be used to investigate these effects. This places a large relaxation on the size of data obtained per second and hence increases the sample time available for each test.

2.4.5.4 On-Road Performance

The transition from wind tunnel performance to full scale testing is governed by many factors, one of which is the variation of the wind direction. The wind averaged drag coefficient (WADC) formulated by Ingram [18], is the current basis for estimating the full scale performance from wind tunnel obtained vehicle data.

The WADC is given by

$$\overline{C_D} = \int_0^{2\pi} \int_0^{V_{Max}} C_D(\psi)[1 + (V_W/V_R)^2 + 2(V_W/V)\cos(\phi)]P(V_W, \phi)\,\mathrm{d}\phi dV_W \quad (2.2)$$

where V is the wind velocity vector, V_W is the wind velocity, V_R is the resultant velocity of the air relative to the vehicle, V_{Max} is the combined maximum velocity of the vehicle and wind, ϕ is the wind angle and $P(V_W, \phi)$ is the probability distribution of V_W and ϕ.

The WADC uses wind speed (V_W) and direction (β) probabilities obtained from 19 meteorological test stations located in the UK between 1966 - 1975. This data is then weighted with the corresponding vehicle population density for each test station and a probability function of speed and direction obtained. The "compass card" generated from this data is shown in Fig.(2.30).

If this probability function is then coupled with the drag coefficient of the vehicle at these angles, an estimation for the vehicle's on-road performance can subsequently be made. The results obtained between 1966-1975 indicated a mean wind direction

(Φ_{Wind}) within the United Kingdom of $\simeq 257.5°$ with an average wind speed (V_W) of 3.5 ms^{-1} [18]. The average direction of a heavy goods vehicle (Φ_{Truck}) within the UK is was found to be 360° or 180° (South to North or North to South, respectively).

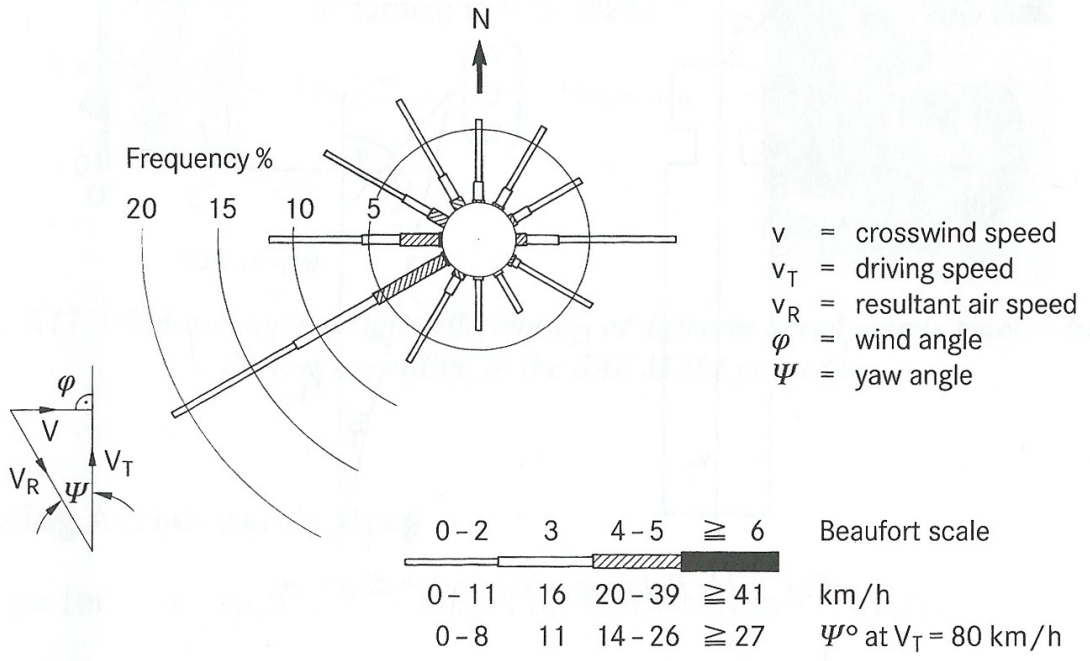

Figure 2.30: Averaged Annual Wind Direction, Speed and Associated Frequency [18].

The WADC is a standard used for an estimation of the performance of the vehicle traveling in an "on-road" environment from wind tunnel data. The equation formulated by Ingram [18] uses extensive wind data, this data however is for the macro flow fields surrounding the vehicle.

The micro flow fields generated due to scenery and vehicle interaction were not considered in the data. A more recent publication by Wordley et al. [50] has focused on the on-road turbulence due to the micro flow fields. The experiment used a four-hole dynamic pressure "Cobra" probe to measure the wind environment. The experiment investigated the wind speed and turbulence intensities as a function of the terrains.

The experiment was conducted in Australia and various terrains such as city canyon, smooth open terrain and freeway traffic were investigated. The largest variation in turbulence intensity was experienced under traffic conditions.

This later study revealed the importance of the flow field around a vehicle when in the presence of other vehicles. The macro effects of the wind can be estimated

using the probabilities contained within the WADC, the micro flow field effects, however, cannot be related to the wind tunnel environment. This study highlighted the importance of full scale testing in the required environment.

2.5 Control Systems

2.5.1 Introduction

A control system is defined as a device or a set of devices used to manage the behaviour of a known system, process or "plant". An example of a common control system is a human being controlling the temperature within a shower. Initially without prior information about the system, it can be difficult to obtain the required temperature. Over time, however, knowledge about how the temperature varies with the angular rotation of the temperature controller is gained. After a certain time period, accurate temperature control can be achieved with minimal input.

The input can be considered to be the human, the controller is the temperature control wheel and the output is the water temperature. The purpose of the controller is to drive the known system to a desired output by a control scheme, in this example, to the desired water temperature.

Control systems can be classified into two primary groups. These groups are closed or open loop, depending on if feedback is used or not, respectively. The shower example can be considered as feedback control. The user can feel the temperature of the water and adjust via addition or subtraction of warm water the to get the desired output temperature from the shower head.

The block diagram showing open loop control is shown in Fig.(2.31), with closed loop feedback shown in Fig.(2.32). The controller, plant and sensor blocks are assumed linear, hence their input/output relationship is denoted by the Laplace transform transfer function, $C(s)$, $P(s)$ and $F(s)$, respectively. The Laplace transformed signals, $R(s)$, $E(s)$, $U(s)$ and $Y(s)$ denote the reference signal, the measured, the controller output and the plant output respectively.

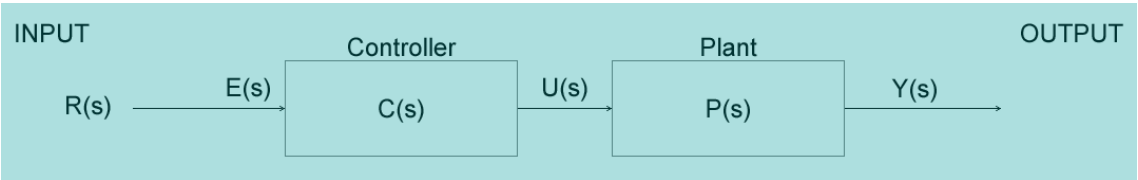

Figure 2.31: Simple Open Loop Control.

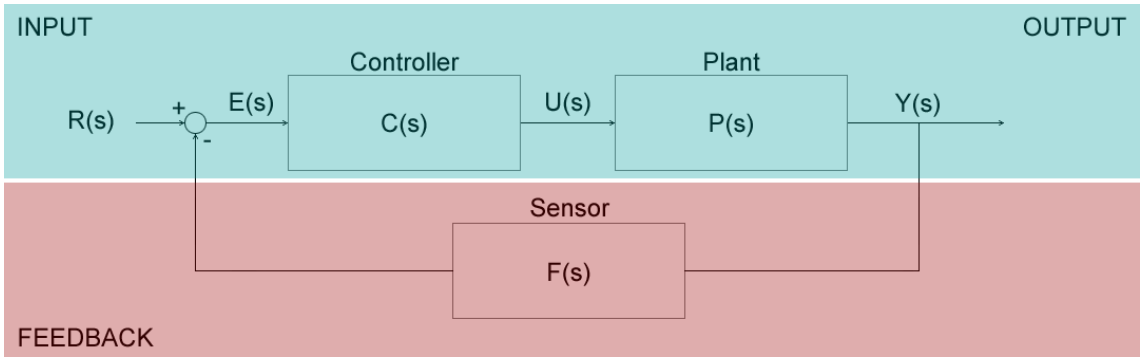

Figure 2.32: Simple Feedback Control.

The output from the plant is given by

$$Y(s) = P(s)U(s) \tag{2.3}$$

The output from the controller is given by

$$U(s) = C(s)E(s) \tag{2.4}$$

The measured error is calculated by

$$R(s) = E(s) - F(s)Y(s) \tag{2.5}$$

The closed loop transfer function, $H(s)$ is therefore given by

$$H(s) = \frac{Y(s)}{R(s)} = \frac{C(s)P(s)}{(1 + C(s)P(s)F(s))} \tag{2.6}$$

Further details on the standard feedback structure explained in this section may be found in numerous texts, e.g. [9].

2.5.2 Closed Loop Control

Closed loop control schemes feed a measured output from the system ($Y(s)$) back against a reference input in order to drive the system to the desired output. Open loop systems do not employ feedback and hence the controller does not know the state of the output. This imposes a requirement of good knowledge of the system and as a result, they do not deal well with any system model uncertainties. Open loop systems as a result, are often used in non-critical applications due to the relatively low cost and simplicity of design. Closed loop or feedback controllers offer the following advantages over open loop controllers:

- Good disturbance rejection: Removal of any undesired inputs from the system to enable the output to follow the desired output.
- Good performance with model uncertainties: The approximation of the system may not be accurately known. Tuning of the control can improve the performance of the system even if not exactly known.
- Improved reference tracking: Improvement in following the desired output, even if the desired output is time varying.

An example of a Proportional Integral Derivative (PID) controller is shown in Fig.(2.33).

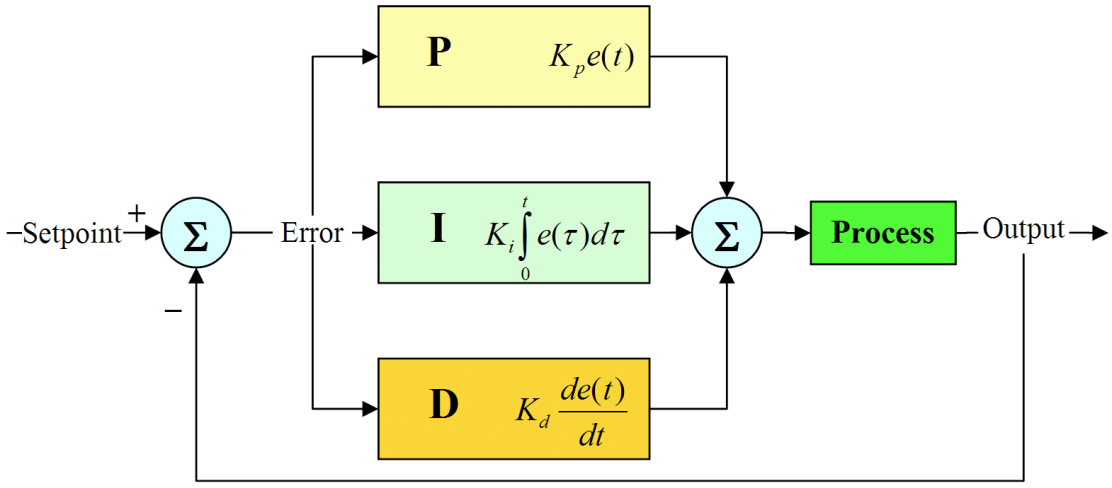

Figure 2.33: Proportional Integral Derivative Control [51].

A PID controller is a generic feedback controller that is widely used in industrial control systems. Over 90% of the controllers in operation today are some form of PID controller [52]. A PID controller calculates the difference between the reference value or 'setpoint' and the measured output value. The difference between these two values is known as the "error", the controller then attempts to reduce this error by adjusting the inputs to the control system. As the name suggests, the PID controller calculation algorithm involves three separate parameters. The proportional term (P) that depends on the present error, the integral term (I) that depends on the accumulation of past errors and derivative term (D) that depends on the prediction of future errors. The weighted sum of these terms is then used as feedback control for the system.

PID systems are widely used due to their tuning simplicity and effectiveness for plants with model uncertainties. Certain applications, however, require that the

controller must adapt to a control system with varying parameters. Such control is known as adaptive control. An example of this is Extremum Seeking Control (ESC).

2.5.3 Extremum Seeking Control

Many methods exist for adaptive control, both linear [53] and nonlinear [54]. These methods, however, rely on known 'setpoints' for regulation. A setpoint is a desired process output that an automatic control system will aim to reach. Certain applications have an extremum, requiring adaptation to find the set point at which the output is driven to its extremity. Such adaptation is called extremum seeking control. Consider a plant represented by $y = f(\theta)$, the extremum or optimal output is given by $f^*(\theta^*)$ whereby $f^*(t)$ is minimal (or maximal) generated from the optimal input (θ^*).

Extremum or self-optimising control schemes have received significant interest since the 1950's and 1960's [55] even prior to the theoretical breakthroughs in adaptive linear control during the 1980's. The first emergence of extremum control being in 1922 [56] by Leblanc's adaptive controller. Difficulty in implementing the optimising controllers led to a decline after the 1960's. With increased computational power came renewed interest. The most widely adopted scheme has been proposed by Ariyur and Krstic [57] and is shown in Fig.(2.34).

The scheme uses a sinusoidal perturbation signal $(a \sin \omega t)$ with angular frequency (ω) to generate an estimation of the gradient information of the static cost function $(f(\theta))$. The purpose of the algorithm is to minimise $(\theta - \theta^*)$, the difference between the plant output (y) and the optimal input, respectively. This results in the output $f(\theta)$ being driven to its minimum (f^*).

Also present in the scheme is a gain compensator and washout compensator $(-k/s)$ and $(s/s + h)$ respectively, the washout compensator serves to remove f^* (the plant optimum) from the output signal. It is the only method to permit fast adaptation without the imposed limitation of requiring the plant dynamics to settle prior to optimisation [57]. The mathematics associated with the algorithm is shown in Sec.(A.1) of Appendix A.

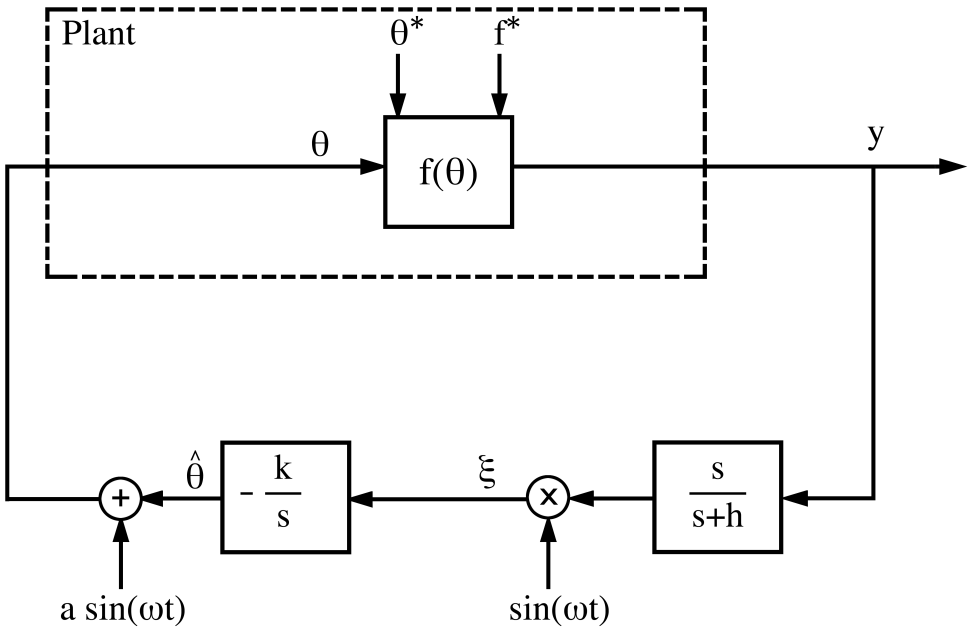

Figure 2.34: Extremum Seeking Control Scheme [57].

2.5.4 Active Flow Control

Active Flow Control (AFC) has been applied successfully in the past to control aerodynamic vehicle drag [28]. Current vehicle drag control research is focused on two primary areas. The first area uses pressure sensors in conjunction with Energy Injection Devices (EIDs) to control flow detachment. The second area uses pressure sensors in conjunction with actuators to change the physical shape of the object. Muminovic et al. [58] concluded that a suitable plant output for active control was a pressure coefficient located on the vehicle. Other papers such as "Feedback shear layer control for bluff body drag reduction" [59], used pressure coefficients in conjunction with the extremum-seeking control scheme proposed by Ariyur and Krstic [57]. Other authors such as Beaudoin et al. [60] have used an actuator in conjunction with extremum-seeking control as a demonstration of the diverse application of extremum-seeking control. The experimental configuration used by Beaudoin et al. [60] is shown in Fig.(2.35).

The experiment conducted by Beaudoin et al. [60] involved a bluff-body with a rotating cylinder located on the upper rear (shown in Fig.(2.35)). The basic configuration is similar to the classic backwards facing step. The freestream velocity range of ($U_0 = 2.0 \rightarrow 12$ ms^{-1}) used for the experiment equated to a Reynolds

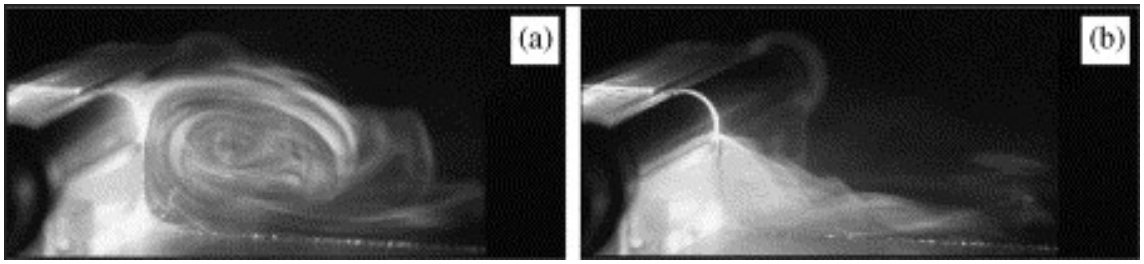

Figure 2.35: Visualisation of the separated flow downstream of a bluff-body for U_0 = 2 ms^{-1}, (a) without and (b) with Extremum Seeking Control [60].

number (R_e) range of 3,500 $\rightarrow$ 20,000. The maximum rotation frequency (Ω_{Max}) of the cylinder was 250 Hz, which equated to a maximum injection velocity (U_{inj}) of 7.5 ms^{-1}.

The active control used for this experiment required energy to rotate the actuator. The cost function (J) used in the experiment was therefore a combination of the aerodynamic power ($P = F_D U_0$) and the power required by the actuator for rotation. The minimum of J used in the experiment therefore created a net energy saving. The results from the experiment are shown in Fig.(2.36).

The upper figure shows the time varying cost function J represented by a solid line time with the plateau of J shown by the dashed line. The lower figure shows the time variation of the cylinder rotation frequency (Ω_0) represented by a solid line with the corresponding plateau of Ω_0 shown by the dashed line.

The results show the baseline average cost function of the model to be $J = 0.98$ W. The baseline cost function value is due solely to the aerodynamic drag force and therefore $\Omega = 0$. Between 80s and just after 500s open loop control was applied with $\Omega_0 = 45$ Hz. The open loop control reduced the cost function to an average of $J =$ 0.96 W. Shortly after 500s the closed loop, extremum-seeking control algorithm was enabled. This further reduced the average open loop cost function from $J = 0.96$ W to J = 0.95 W. The optimal input frequency of the actuator (Ω_0) fluctuated between 50 - 100 Hz with an average of 100 Hz. This large variation in Ω_0 corresponded to a poorly defined J [60].

The implementation of the extremum seeking algorithm by Beaudoin et al. [60] sought to find the optimal actuator frequency (Ω_0) that corresponded to the minimal total power. The total power was a combination of the aerodynamic and actuator power, as a result, the control algorithm sought to drive the frequency of the actuator (Ω_0) to an optimal frequency. The optimal frequency resulted in a net energy saving over the baseline (static) model. This provided a significant result for active flow control due to the ability of the controller to provide a net energy saving.

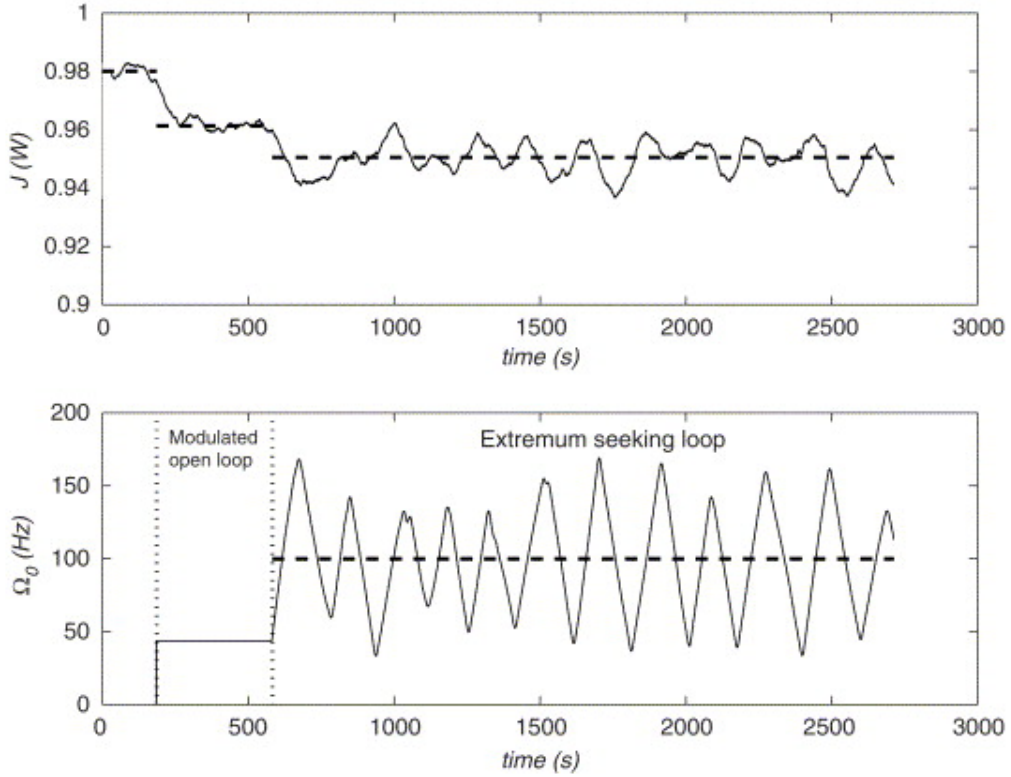

Figure 2.36: Open-loop and Closed-loop Control Experiment for $U_0 = 12$ ms^{-1} [60].

2.5.5 Extremum Seeking Applied to Active Flow Control

The ability of an extremum seeking controller to drive the system to an optimal output, without prior knowledge of the optimal input is useful for Active Flow Control (AFC). The requirement from the system, however, is the ability to measure the output from the system. For a drag reducing device, this would be the drag of a vehicle. For an AFC system to be employed, the drag of the vehicle or another parameter that achieves a minimum for the optimal input must be measurable. Certain parameters on the vehicle could correlate to the optimal input and could be used instead of the drag force. An example of a parameter that could be used instead of the drag force is the power output required from the engine. These parameters, however, would be commercially difficult to measure on-road due to large and potentially unknown disturbances on the measured signal(s).

Another parameter that could correlate to the drag of the vehicle is the trailer forebody pressure, shown in Fig.(2.37).

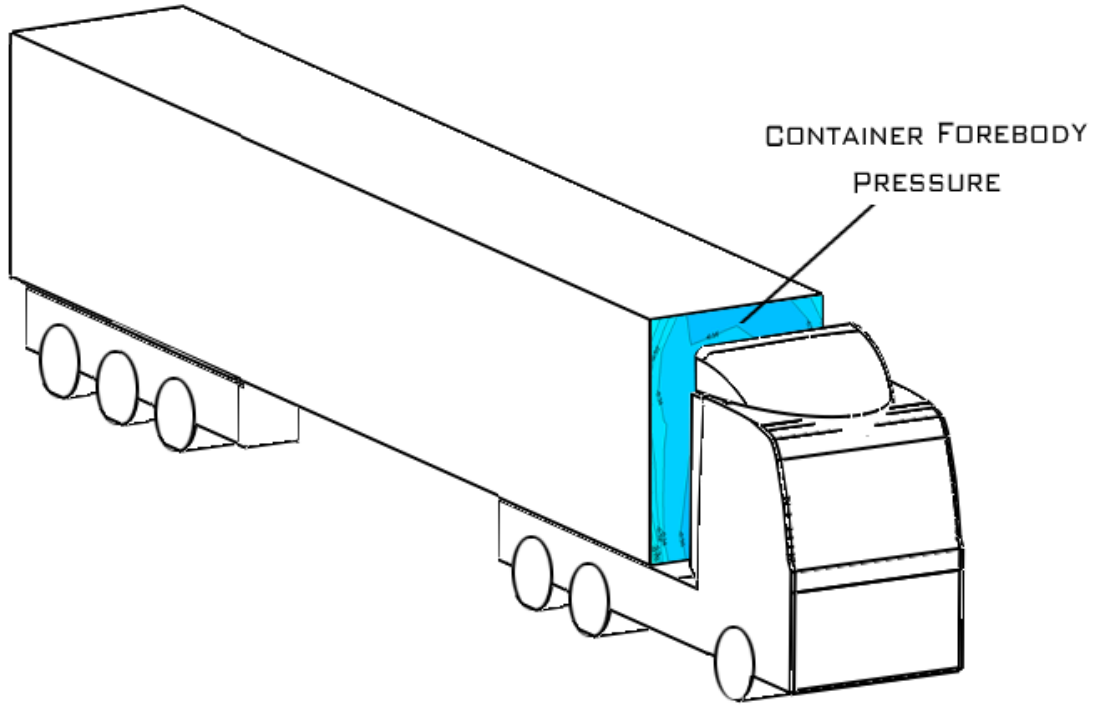

Figure 2.37: Trailer Forebody Pressure Measurement.

The force due to the forebody pressure on the trailer is given by

$$\overrightarrow{F_D} = -\oiint p \cdot \overrightarrow{n}\, dA \tag{2.7}$$

where F_D is the drag force on the trailer forebody, p is the surface pressure normal to the surface ($\overrightarrow{n}$) and dA is the surface area. If the surface area of the forebody can discretised into equal areas equal to $dA = dL^2$ shown in Fig.(2.38).

The container forebody force can then be approximated by

$$F_D = -\sum_{(i,j)=0}^{i=n,j=N} p_{(i,j)} \times dL^2 \tag{2.8}$$

where i and j are the pressure tapping numbers in the x (horizontal) and y (vertical) direction, respectively.

Due to the pressure drag associated with the container forebody contributing significantly to the total drag on the heavy goods vehicle, it was predicted that the container forebody would be a suitable position for pressure tappings. The pressure tappings would enable the forebody force to be estimated and used as a

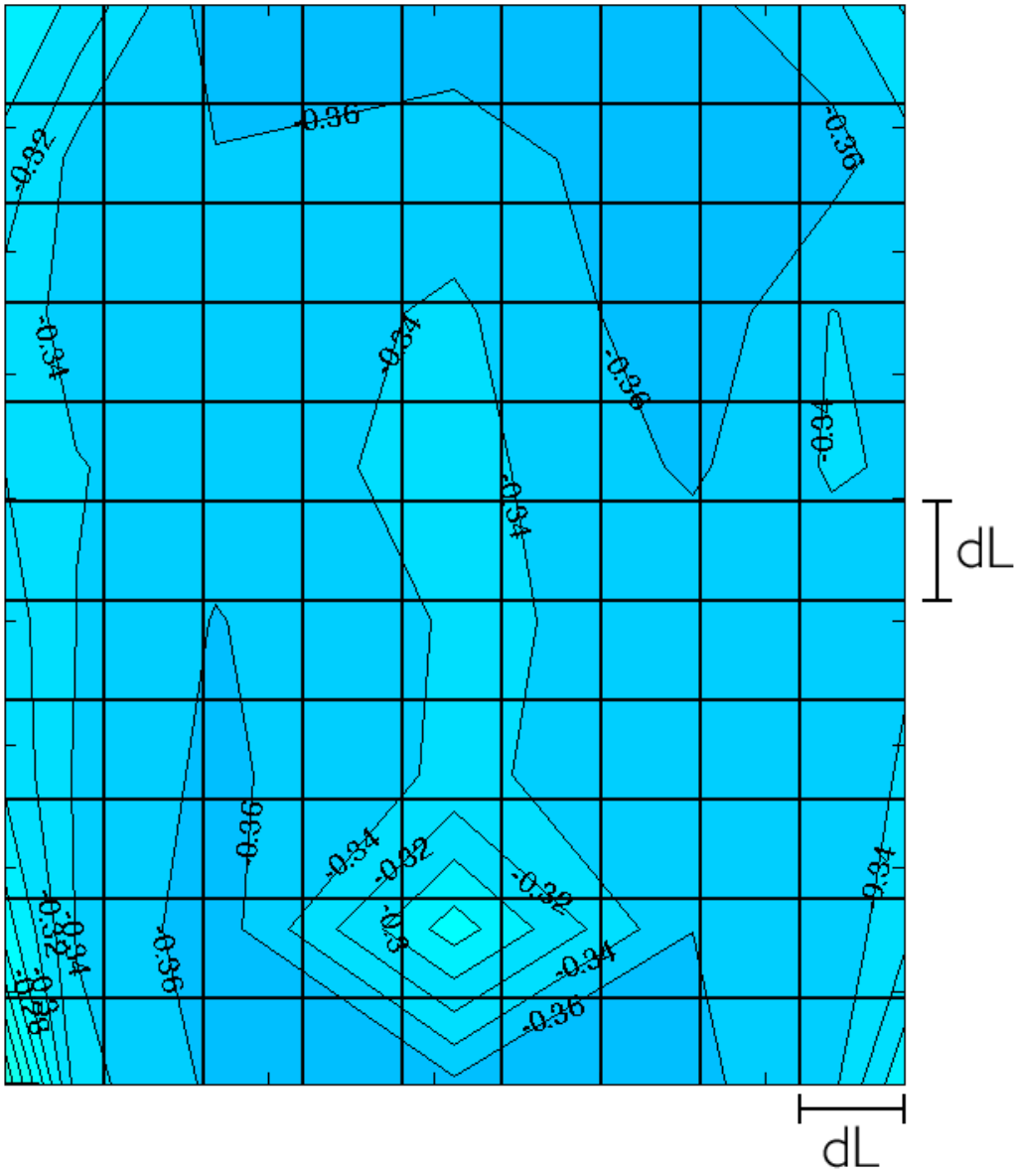

Figure 2.38: Trailer Forebody Pressure Measurement Discretisation.

parameter input for the extremum seeking controller. The modified ESC scheme using the pressure tappings as a plant input is shown in Fig.(2.39). The Plant is the heavy goods vehicle, the measurable output (y) from the vehicle is the forebody container pressure F_D (related to the forebody pressure using Eq.(2.7)). $F_{D(Min)}$ is the minimum forebody drag on the container due to the optimal plant input (the optimum deflector height, δ_{Hopt}). The feedback fed into the plant is the optimum

deflector height (δ_{Hopt}) generating the difference between the current output and the desired output of $F_D - F_{D(Min)}$. The estimate of the optimal deflector height ($\hat{\delta_H}$) converges to δ_H.

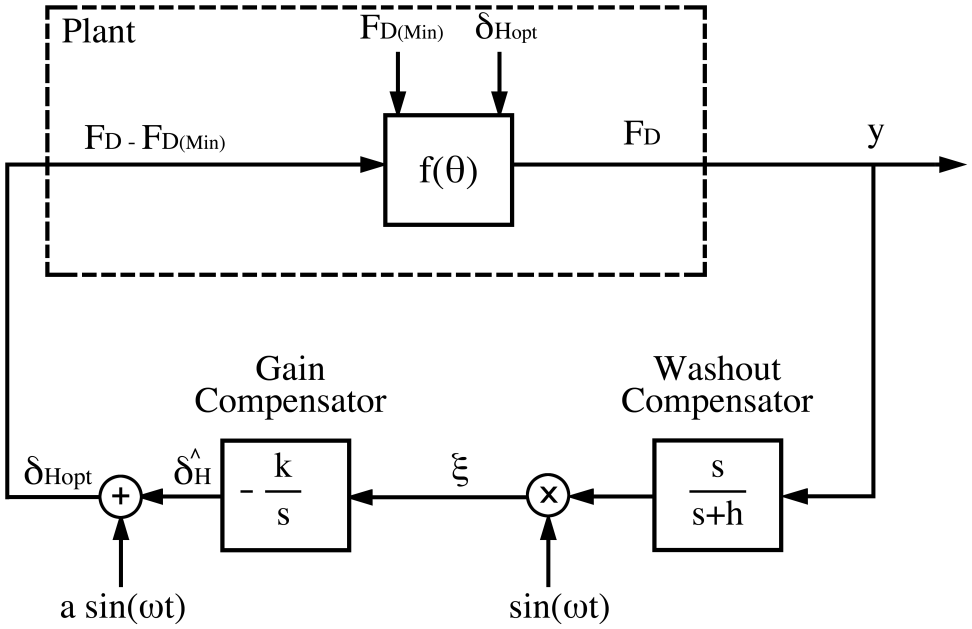

Figure 2.39: Extremum Seeking Control Scheme [57] Using Container Forebody Pressure Measurements.

2.6 Conclusions

The current pressure to curb climate change has renewed interest in the field of HGV aerodynamics. The current field focuses on three primary areas located on the vehicle: the cab design, the tractor-trailer gap and the trailer design. With Original Equipment Manufacturers (OEM) and fleet operators primarily dictating the design of the cab and trailer, current research is focused on the aerodynamic add-on devices to these areas. The field is split into either active or passive devices for use on heavy goods vehicles.

Active control is employed with a focus on research orient publications rather than commercial implementation. The primary goal of current active control research is in the design and positioning of the actuators [28]. Passive devices have previously been tested in full-scale tunnels [31] which attributed the component saving of add-on devices. As a result the current focus on passive devices is in commercial implementation rather than on design optimisation.

Previous wind tunnel experiments such as those by Leuschen et al. [31] used vehicles of North American design and as a result used a constant trailer height. In the United Kingdom there is no limit on the maximum height of a trailer [1]. Current manufacturers therefore produce trailers ranging in height from 3.95 m to 4.95 m [4]. Fleet operators also do not use the same tractor-trailer combination, giving rise to large height mismatches. The current most advanced semi-active deflector design is Volvo's adjustable deflector [36]. The deflector, when connected to a compatible trailer, can be adjusted to a pre-determined optimal height evaluated from prior wind tunnel tests. Such deflectors offer an appreciable saving of an estimated 20% - 30% [22] over the baseline model. Static deflectors, however, such as the one developed by Volvo [37], only provide an appreciable zero yaw saving and do not offer the lowest drag configuration when a significant wind yaw is present. A 10% [22] reduction in efficiency is experienced at yaw between the optimum yaw configuration and optimum zero yaw configuration. This reduction in efficiency highlights the importance of active control whilst the vehicle is in use to ensure the optimum minimum drag profile is constantly maintained.

The results from the literature review indicated that at present, there are no active aerodynamic devices that are able to deal with the truck and trailer height mismatch present within the UK. The literature also revealed whilst the deflector design and general trends associated with container separation have been identified [22], there is no current investigation into the optimum deflector height (δ_{Hopt}).

The lack of an active aerodynamic applied to cab mounted roof deflectors prompted the research into active flow control on HGVs. The active flow control is achieved through use of a height adjustable deflector which can adjust to the optimum height based on the container height, container separation and yaw angle.

This page intentionally left blank.

Chapter 3

Experimental Details

The primary purpose of the experimental testing within the research was to determine the optimal deflector height (δ_{Hopt}) as a function of the container height, the cab to container separation and the wind yaw angle.

The secondary purpose of the wind tunnel testing was to determine if a measurable pressure location that related to the overall drag on the vehicle existed. The pressure measurement was required as a measurable parameter feedback for the extremum-seeking control algorithm.

Due to the lack of a suitable measurement location on the vehicle, the control algorithm was changed to an alternate method. The alternate method used a static look-up table in conjunction with the wind tunnel data obtained from the preliminary wind tunnel investigation. The look-up table, however, required the wind yaw angle (β) to be measured. This modified the purpose of the secondary wind tunnel test to determining an estimate for β using pressure differentials (ΔC_P) located on the deflector geometry.

The final purpose of the wind tunnel test was to determine the effects of the vehicle's flow field on the sensor mounting locations. During the on-road tests, sensors were mounted to measure the wind speed (V_W) and wind yaw angle (β). Due to the geometry of the vehicle, the mounting locations generated offset errors that were measured and account for.

3.1 Low Speed Wind Tunnels Overview

The common usage for the term "low speed wind tunnel", is that the maximum velocity of the tunnel should not exceed $Ma \simeq 0.4$ or 134 ms^{-1} [61]. As a result, the equations used in "low-speed" flows are listed in Eq.(3.1). The full equations are listed in Eqs.(B.1 - B.3) in Sec.(B.1) of Appendix B.

1. Conservation of mass.

2. Force and motion are related by Newton's Second Law.

3. Energy equations are governed by the First Law of Thermodynamics.

An incompressible version of Bernoulli's equation is therefore the basis for the dynamics of the flow within a low speed wind tunnel and is given by

$$P_0 = P + \frac{1}{2}\rho v^2 \tag{3.1}$$

where P_0 is the total pressure, P is the static pressure, ρ is the density of the fluid and v is the velocity of the fluid.

3.2 The Cranfield $8' \times 6'$ Low Speed Wind Tunnel

The Cranfield $8' \times 6'$ low speed wind tunnel used in the experimental testing is an academic and commercial wind tunnel test facility. The arrangement of the wind tunnel is shown in Fig.(B.3) in Sec.(B.2.1) of Appendix B, with airflow in the clockwise direction.

It is a closed return wind tunnel driven by a five bladed electric fan. The maximum wind tunnel speed generated by the motor under operation at ambient temperature and pressure is 55 ms^{-1} (Fig.(B.2) in Sec.(B.2) of Appendix B).

Downstream of the motor are two diffusers. The power loss at any point in the tunnel is proportional to the velocity cubed [61]. The diffusers are designed to reduce the flow velocity with minimal energy loss and are therefore usually placed prior to turning vanes. Minimal energy loss corresponds to maximum pressure recovery and as a result, a reduction in the power required to drive the tunnel.

Downstream of the diffusers are two turning vanes, fitted in order to minimise the pressure loss due to sharp bends and also act as flow straighteners. Downstream of the turning vanes is the settling chamber. The settling chamber is the largest cross sectional area of the tunnel containing a control gauze screen. The control gauze screen in the settling chamber reduces fluctuating variations in transverse velocity with little effect on the streamwise velocity.

A contraction ratio of 7:1 after the settling chamber ensures sufficient acceleration of the flow into the test section to minimise pressure loss from the control gauze whilst minimising wall flow separation. The losses due to the cross-sectional shape of the test section can be considered negligible [61], as a result, it is designed primarily to accommodate the aerodynamic models tested.

A closed working section of 2.4 m x 1.8 m is fitted with corner fillets with an average height to width ratio of 0.3 to reduce boundary layer effects. Boundary layer suction is also fitted to minimise the effects of the boundary layer growth on the ground board when used for force measurements.

Downstream of the working section are wire cutters fitted to protect the engine blades in case of model breakaway. Two further diffusers are fitted prior to two further corner vanes, one after the test section and one prior to the motor inlet to ensure minimal energy loss prior to returning to the motor inlet. A control room isolated from the freestream velocity is used to monitor the wind tunnel test. The wind tunnel test procedure was conducted in accordance to SAE standard J1252 [62]. National Instruments LabVIEW® control software was used in order to automate the wind tunnel data acquisition.

3.3 Model Description

3.3.1 Cranfield Deflector

The deflector used for the experiments was an active version of a Cranfield designed deflector named '$FREDDIE$' or Fuel REDucing DevIcE, shown in Fig.(3.1). The profile of FREDDIE was generated in 2003 at Cranfield University to be optimised for a yaw angle range of ($-5° \leq \beta \leq +5°$). Section (1.7) details further information on the deflector profile.

The revised $ActiveFREDDIE$ shown in Fig.(3.2) was designed in 2011 for a maximum height adjust of 300 mm corresponding to a trailers range of 3.9 m - 4.1 m, a value set by the manufacturers of $FREDDIE$, Hatcher Components Ltd.

$ActiveFREDDIE$ was designed to be adjusted by four linear actuators along the vertical z-axis at an incline of 10°. A 300 mm static 'skirt' was added to the base of the deflector to account for the raising of the deflector from the cab roof. The skirt prevents any flow underneath the gap that would be generated from the extension of the spoiler from the cab roof. Flow underneath the spoiler would generate considerable aerodynamic drag and as a result the skirt is fitted at the expense of a minor drag increase over the static FREDDIE.

The linear extension of the deflector ensured the deflector profile remained optimised for each container height connected. The method of actuator extension was deemed the most robust for the fibreglass mounting fixtures by Hatcher Components Ltd.

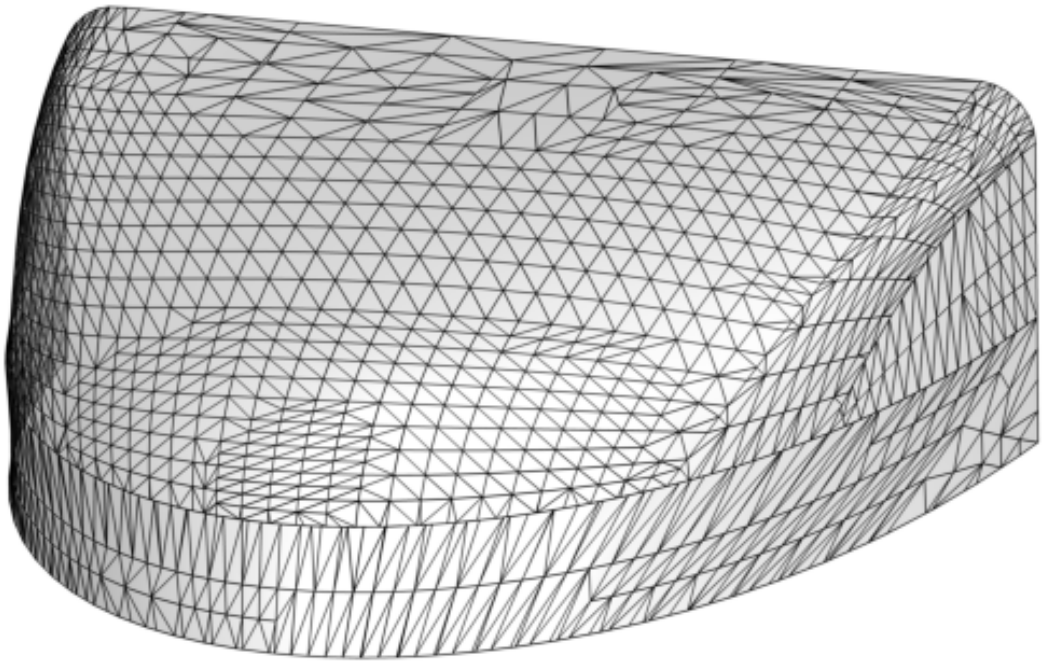

Figure 3.1: Cranfield Designed FREDDIE Deflector.

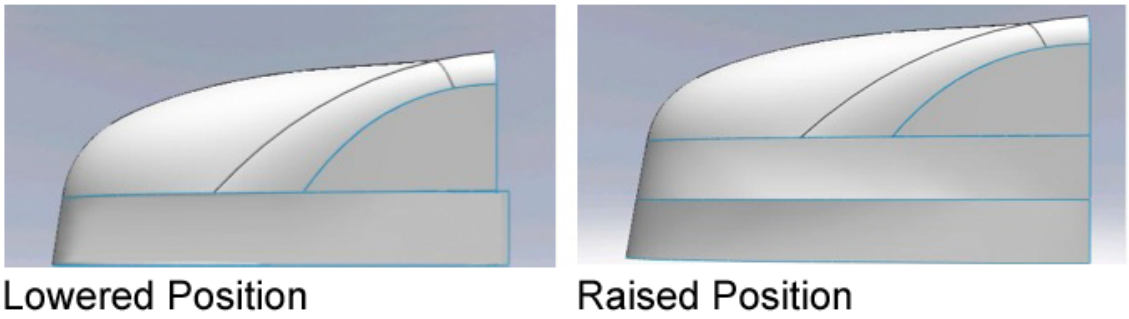

Figure 3.2: ActiveFREDDIE Redesigned Deflector.

3.3.2 Wind Tunnel Model Description

A $1/8^{th}$ scale model of a Mercedes-Benz Actros commercial vehicle (shown in Fig.(3.3)) made from high density modelling foam was used in the experimental test. The vehicle was fitted with a cab mounted, adjustable deflector made from vacuum formed high impact polystyrene sheet.

The "FREDDIE" deflector could be varied between its lowest and highest con-

figuration of 484 mm and 514 mm measured from the ground to the top of the deflector. This corresponded to a full scale height range of 3.9 m - 4.1 m, respectively. The deflector was adjusted using 3 mm medium-density fibreboard spacers. with a total of 10 spacers for a maximum extension of 30 mm. A $1/8^{th}$ scale MDF trailer with adjustable spacers was connected in tandem with the cab, it was varied in height to give the following trailer heights: 437,489,500,517,529 and 557 mm. These heights corresponded to 3.5 m, 3.9 m, 4.0 m, 4.1 m, 4.2 m and 4.5 m full scale, respectively. The cab to trailer separation varied between 50 mm - 146 mm during the experimental tests, corresponding to a full scale separation range of 0.4 m - 1.2 m.

3.3.2.1 Model Dimensions

The model used in the wind tunnel testing is shown in Fig.(3.3). The corresponding technical drawing of the arrangement used in the wind tunnel tests is shown in Fig.(3.4).

Figure 3.3: A $1/8^{th}$ Scale Model of a Mercedes Actros Commercial Vehicle.

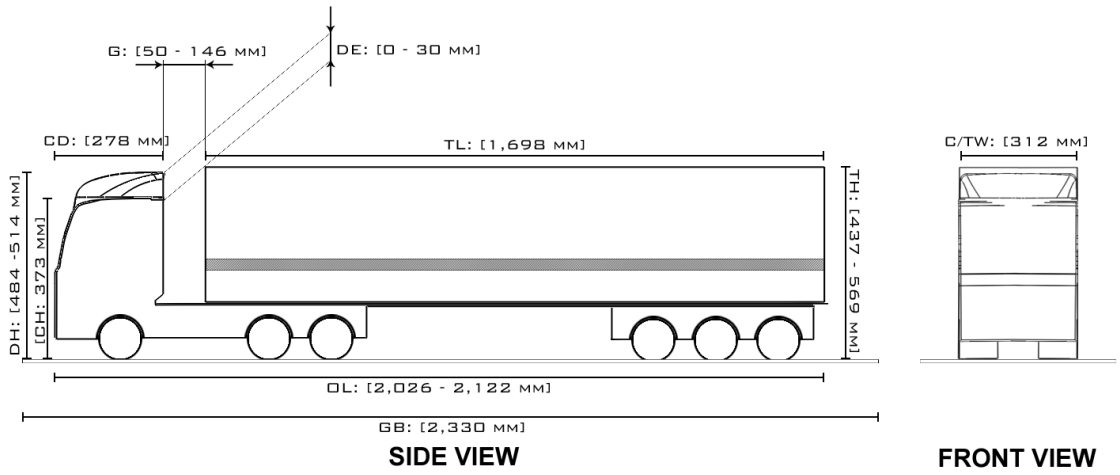

Figure 3.4: Technical Drawing of the $1/8^{th}$ Scale Model Mercedes Actros Commercial Vehicle.

Table (3.1) shows the notation used in Fig.(3.4).

Abbreviation	Item	Dimensions (mm)
CD	Cab Depth	278
CH	Cab Height	373
C/TW	Cab/Trailer Width	312
DE	Deflector Extension	0 - 30
DH	Deflector Height	484 - 514
G	Cab to Trailer Gap	50 - 146
GB	Ground Board Length	2,330
TH	Trailer Height	437 - 569
TL	Trailer Length	1698
OL	Overall Length	2,026 - 2,122

Table 3.1: $1/8^{th}$ Scale Model Dimensions.

3.4 Model Arrangement

3.4.1 Force Arrangement

For drag force measurements, the scale model was placed on a rotating ground board with force-torque sensors, shown in Fig.(3.5). The ground board was used

as the flow field around the base of the geometry was not of interest for pressure measurements. The boundary layer generated by the ground board results in a sufficient approximation to the boundary layer generated on-road [62].

The six component force-torque sensors used in the wind tunnel are JR3 monolithic aluminium devices instrumented with metal foil strain gauges which sense the imposed loads. The strain gauge signals are then connected to an external amplifier and signal conditioning equipment. The strain gage signals are amplified and combined to produce signals representing the force and moment loads for all axes. Further information can be obtained from the JR3 website [63]. The ground board was then mounted on a rotating force balance and rotated over the following yaw angle range: $(-17.5^\circ \leq \beta \leq +17.5^\circ)$. Further yawing was not possible due to risk of model breakaway as well as non-negligible wall interference effects at larger yaw angles.

The output from the sensors has the following convention, shown graphically in Figs.(3.5 and 3.6) with the installation photograph in Fig.(3.7):

- Longitudinal axis: Positive drag force is parallel to the airflow direction, rolling moment is positive for anti-clockwise roll parallel to the airflow and negative for clockwise roll.
- Lateral axis: Side force is positive for the model's starboard direction and negative for the port direction, pitching moment is positive for nose-up and negative for nose-down.
- Yawing moment: yaw angle is defined as positive for the port side of the model and negative for the starboard.

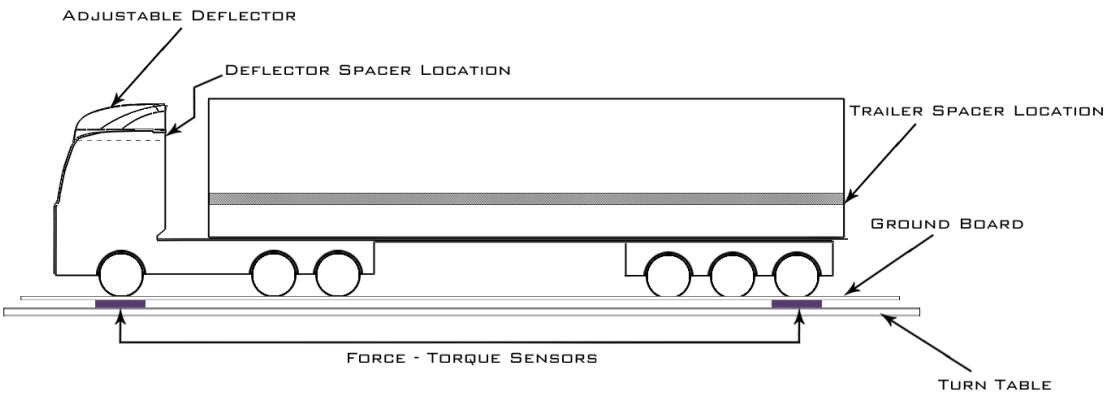

Figure 3.5: Diagram of Experimental Configuration.

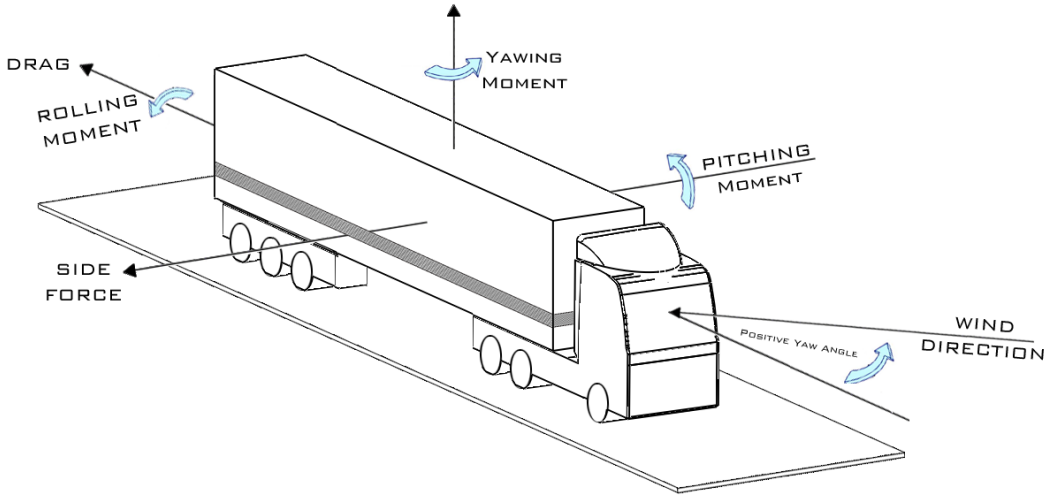

Figure 3.6: Cranfield 8′ x 6′ Force and Moment Orientation.

Figure 3.7: Cranfield 8′ x 6′ Model Installation Arrangement.

The methodology for force measurements is shown in Sec.(B.4) of Appendix B.

3.4.2 Pressure Arrangement

For pressure measurements, the force-torque sensors were removed. This was due to the external running of the cabling required by the transducers causing erroneous results when used in conduction with the force-torque sensors. The model was again yawed over the yaw angle range: $(-17.5° \leq \beta \leq +17.5°)$.

The methodology for force measurements is shown in Sec.(B.3) of Appendix B. The data acquisition methodology and error calculation is shown in Sec.(B.5) and Sec.(B.6) of Appendix B, respectively.

3.5 Reynolds Number Influence

From the definition of Reynolds number (R_e)

$$Re = \frac{\rho V_\infty l}{\mu} \tag{3.2}$$

where ρ is the density of the fluid, V_∞ is the freestream fluid velocity, l is the characteristic length and μ is the dynamic viscosity of the fluid. "Flows around geometrically similar bodies are called mechanically similar if the Reynolds number has the same value for different characteristic lengths, air speed and fluid properties. Mechanic similarity is the basis for model tests" [14].

During the experiments, the tunnel was run at it's maximum operating velocity of 40 ms^{-1}. For a $1/8^{th}$ scale model with l =1,827 mm, ρ = 1.205 kgm^{-3}, $\mu = 1.51 \times 10^{-5}$ $kgm^{-1}s^{-1}$ at 20°C this equated to a Reynolds number for the model of $Re_{(Model)} = 5.8 \times 10^5$. A full scale truck operating at 55 mph or 24.5 ms^{-1} equates to a full scale Reynolds number of $Re_{(FS)} = 2.8 \times 10^7$.

As a result of not being able to match the Reynolds number even at maximum permissible tunnel velocity, a Reynolds number independence test was not conducted.

Prior Reynolds number tests conducted by Hucho et al. [14] noted that "On commercial vehicle models, unlike car models, this behaviour [the effect of the drag coefficient with Reynolds number] is essentially dependent on the vehicle front end".

This statement has been validated by Cooper [64] with tests conducted at the full scale National Research Council (NRC) Low Speed Wind Tunnel. Results were conducted at both the 2 m x 3 m (in model form) and at the 9 m x 9 m (full scale vehicle) wind tunnels. The results obtained at model scale in the wind tunnel were "virtually identical to the results obtained from full scale testing" [64]. As a result Reynolds transition effects were not investigated during the experimental testing.

3.6 Experimental Methodology

Wind tunnel testing was conducted on a scale model to determine the vehicle drag and its variation with the wind yaw angle (β), deflector height (δ_H) and container separation (g/d_2). This enabled the optimum deflect height (δ_{Hopt}) for a given container separation to be determined as a function of β.

Pressure measurements were made on the rear of the truck, trailer forebody and trailer centre line. The measurements were made to determine if δ_{Hopt} could be related to a pressure measurement located on the vehicle. The control scheme required a measurable parameter to minimise, for the HGV this was the drag of the vehicle. Due to the drag coefficient (C_D) of a vehicle being difficult to measured on-road, another measurable parameter that correlated to the C_D had to be measured instead.

A correlation between a simple pressure differential (ΔC_P) on the vehicle and the C_D did not exist. As a result, investigation was extended into relating β to a ΔC_P located on the deflector. Measurement of β enabled the use of a look-up table to estimate the C_D of the vehicle from prior wind tunnel testing. A final test was then conducted to determine the suitability of mounting locations for sensors to be used on the full scale vehicle.

Full scale testing was conducted to determine the accuracy of the predicted ΔC_P obtained from wind tunnel measurements.

3.6.1 Wind Tunnel Testing at the Cranfield $8' \times 6'$ Low Speed Wind Tunnel

3.6.1.1 Optimum Deflector Height (δ_H)

A $1/8^{th}$ scale model of a Mercedes-Benz Actros (see Section(3.3) for more details on the model configuration) fitted with an adjustable deflector was connected in tandem to a height adjustable trailer. Prior to placing the model on the ground board, a tare run was conducted. A tare run is a run without a model on the ground board and allows for the aerodynamic forces solely due to the presence of the ground board to be recorded and removed from the subsequent results. The only method outlined by SAE Standard J2084-1993 [65] to accurately match the on-road boundary layer for straight flow is through the use of a moving ground belt. The standard also states: "Principle shape optimisations without special interest in the vehicle's underside, it is generally sufficient to use a stationary ground board with a scoop to peel off the incoming boundary layer". A static ground board was therefore used in conduction with boundary layer suction prior to the board.

After the tare run, the model was attached to the ground board and rotated through the test angle range of: $(-17.5^\circ \leq \beta \leq +17.5^\circ)$ to record the values on the force-moment sensors with no aerodynamic load. The recorded values were then stored as "zero values" to be subtracted from the measured values, this is conducted prior to the start of each run.

A tunnel velocity of $V = 40$ ms^{-1}, equating to $Re_{(Model)} = 7.2 \times 10^5$ was selected, the model was then rotated through the yaw angle range, $(\beta : -17.5^\circ \rightarrow +17.5^\circ)$. Sensor measurement was automatically recorded using LabVIEW®.

The deflector was adjusted in height via the addition of spacers and the method repeated until the maximum deflection height was achieved. The method employed was then repeated for varying trailer heights and trailer separations.

3.6.1.2 Pressure Signal Location

The flow contained within the tractor-trailer gap was assumed to be approximated by a simple cavity. The assumption about the flow field within the cavity was that the recirculation would generate a pressure signature at optimal deflection height. The result of this approximation was that the pressure tappings were to be located at suitable points within the generated cavity between the rear of the truck and the container forebody.

Due to the movement of the deflector, nine static pressure tappings were made on the rear of the deflector (shown in Fig.(3.8)). This enabled measurement of the pressure within the cavity for varying deflector heights.

Eight pneumatically averaged tappings were made on the rear of the cab (shown in Fig.(3.8)) to determine if any averaged effects on the rear of cavity were present. Gotz et al. [2] identified pressure variations on the container forebody and the centre line of the container roof relating to the addition of a cab mounted deflector.

An Array of fifty-five tappings were made on the container forebody (shown in Fig.(3.10)) to allow for any yaw effects on the flow within the cavity.

Six pressure tappings were made along the container centre line (shown in Figs.(3.9) and 3.11), to determine the reattachment point of the flow field.

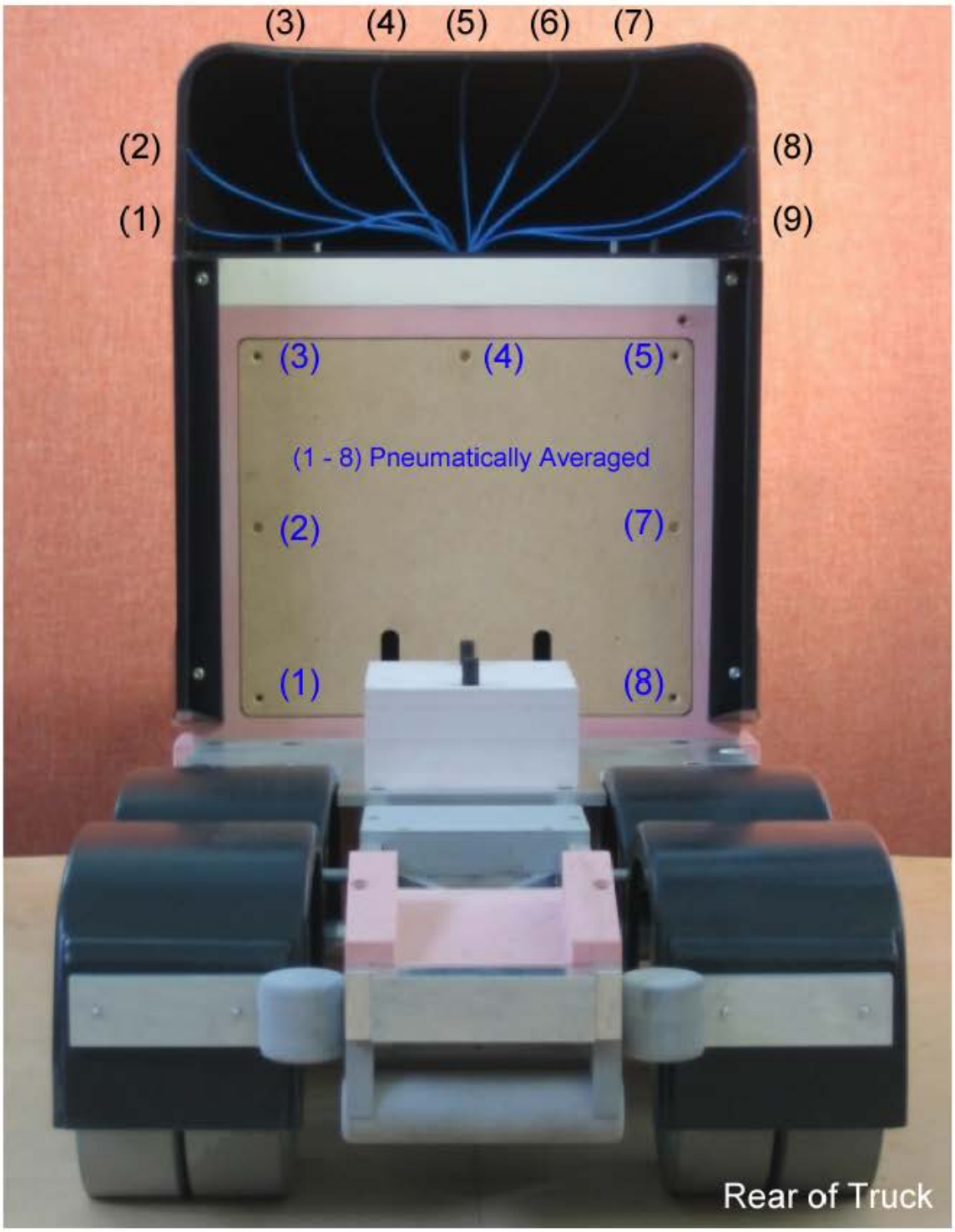

Figure 3.8: Deflector and Pneumatically Averaged Cab Rear Pressure Tapping Locations.

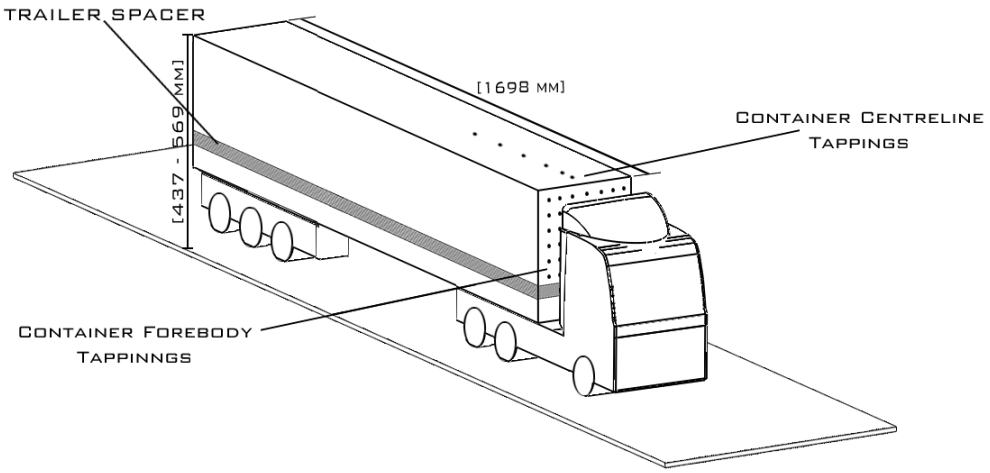

Figure 3.9: Trailer Centre Line and Forebody Pressure Tapping Locations.

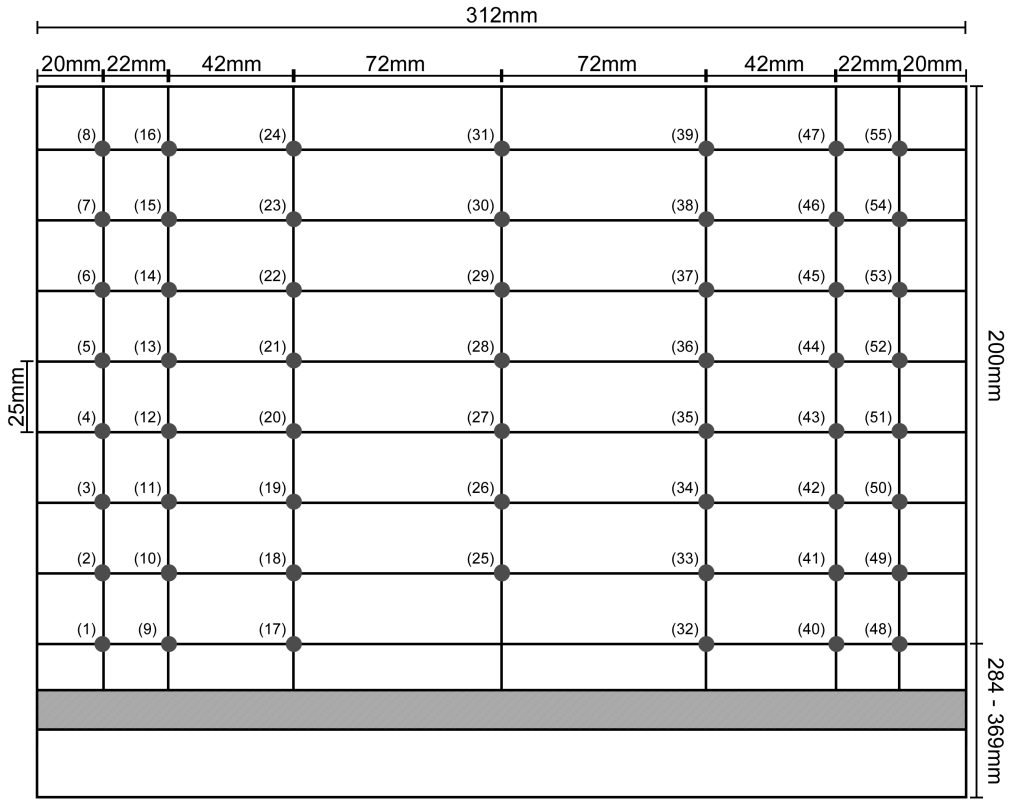

Figure 3.10: Trailer Face Pressure Tapping Locations.

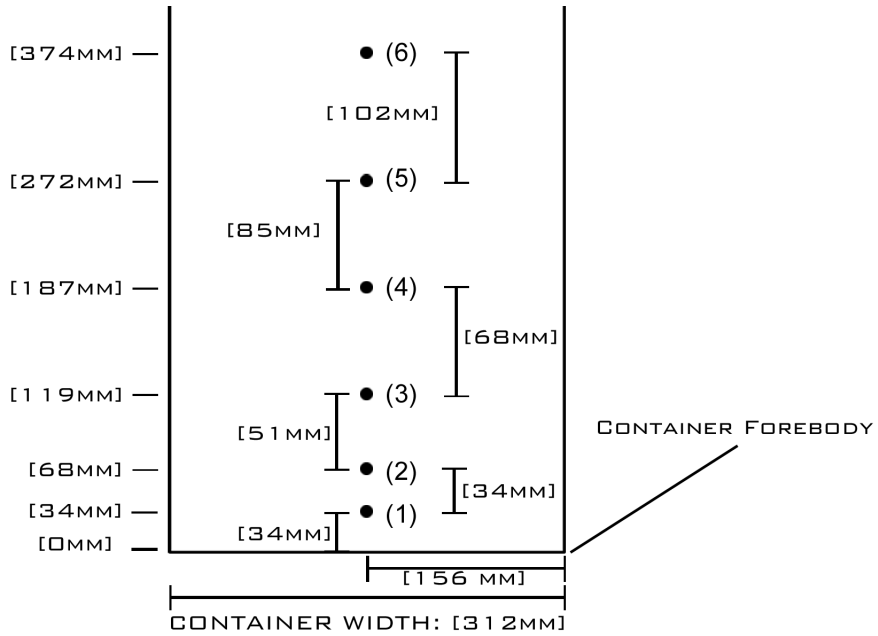

Figure 3.11: Plan View of Trailer Centre Line Pressure Tapping Locations.

The pressure tappings were connected to Furness FC018 differential pressure transducers referenced to an upstream static pressure. The same method for the adjustment of the deflector and trailer heights and trailer separations used for the force measurements was employed for the pressure measurements.

3.6.1.3 Yaw Angle Determination from Pressure Differentials

The control algorithm used for determining the optimum deflector height required the wind yaw angle (β) as an input parameter. As a result, β was required to be measured on the full scale vehicle. A common method for determining β and the pitch angle (α) in low speed flows is through the use of a 5-hole probe, shown in Fig.(3.12).

Restrictions were imposed by the deflector manufacturer on the mounting of external sensors. Research was therefore conducted into the feasibility of creating a measurement system utilising the deflector geometry as a 3-hole probe. The removal of the pitch compensation found on a 5-hole probe sensor would introduce an error on the estimated yaw angle (β_{Est}).

The error associated with the removal of pitch compensation could only be evaluated after full scale testing had been conducted.

From Eq.(B.33), the pressure coefficient (C_P) is defined as: $C_P = \frac{p-p_\infty}{\frac{1}{2}\rho_\infty V_\infty^2}$

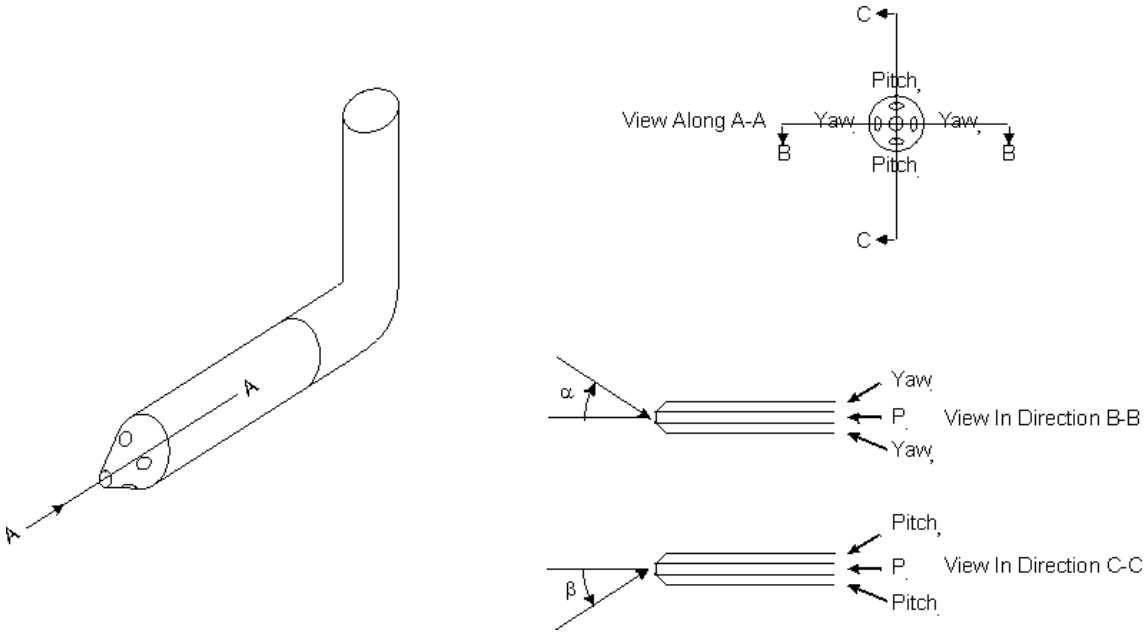

Figure 3.12: Five Hole Pressure Probe [66].

Therefore, measurement of pressure coefficient located at a tapping on the (left) and (right) side of the deflector can be given by

$$C_{P(left)} = \frac{p_{(left)} - p_\infty}{\frac{1}{2}\rho_\infty V_\infty^2} \tag{3.3}$$

$$C_{P(right)} = \frac{p_{(right)} - p_\infty}{\frac{1}{2}\rho_\infty V_\infty^2} \tag{3.4}$$

By defining $\Delta C_P =\mid C_{P(left)} - C_{P(right)} \mid$ and $\Delta P =\mid P_{(left)} - P_{(right)} \mid$, Eq.(3.3) - Eq.(3.4) gives

$$\Delta C_P = \frac{\Delta P}{\frac{1}{2}\rho_\infty V_\infty^2} \tag{3.5}$$

For temperature compensating transducers

$$\Delta C_P \propto \frac{\Delta P}{V_\infty^2} \tag{3.6}$$

Therefore, if a relationship between ΔP and the wind angle (β) exists and the total velocity (V_∞) is measured, the yaw angle can be inferred by a pressure differential located on the vehicle.

Most commercial 5-hole probes have ports located at an angle of 30° relative to half the length of the probe head, shown in Fig.(3.13).

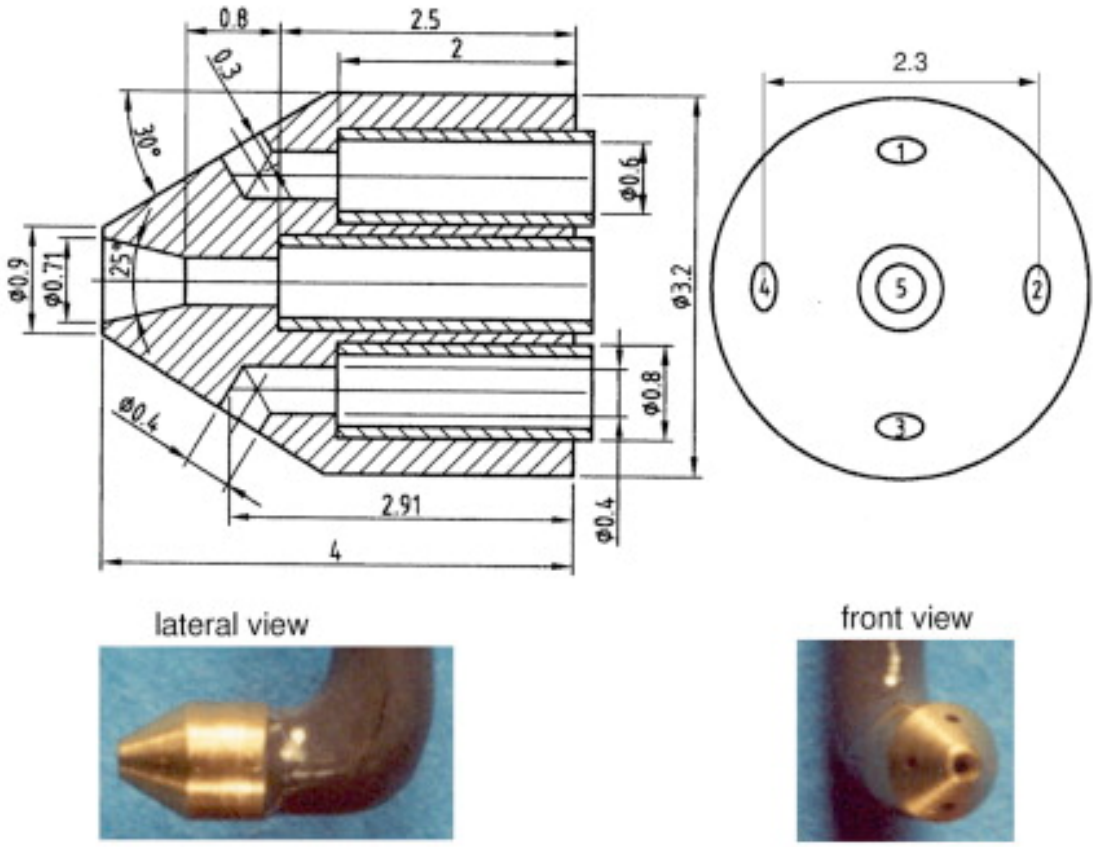

Figure 3.13: Five Hole Pressure Probe Technical Drawing [67].

The curved profile of the deflector (in plan view) does not follow the chamfered profile on a typical probe. As a result the optimum locations of the ports were unknown for the deflector profile. Four tappings were therefore made either side of the centre line at 10° intervals. This resulted in nine tappings located on the static skirt over an angular range of: (-40° → +40° with reference to the centre line of the deflector). The tapping locations are shown in Fig.(3.16).

Figure 3.14: Deflector Pressure Tapping Locations.

Three additional rows of tappings were made on the deflector to determine the

sensitivity of deflector height (δ_H) on the accuracy of the pressure differential (ΔC_P), the locations are shown in Figs.(3.15 and 3.14). Table (3.2) shows the nomenclature used in Fig.(3.15).

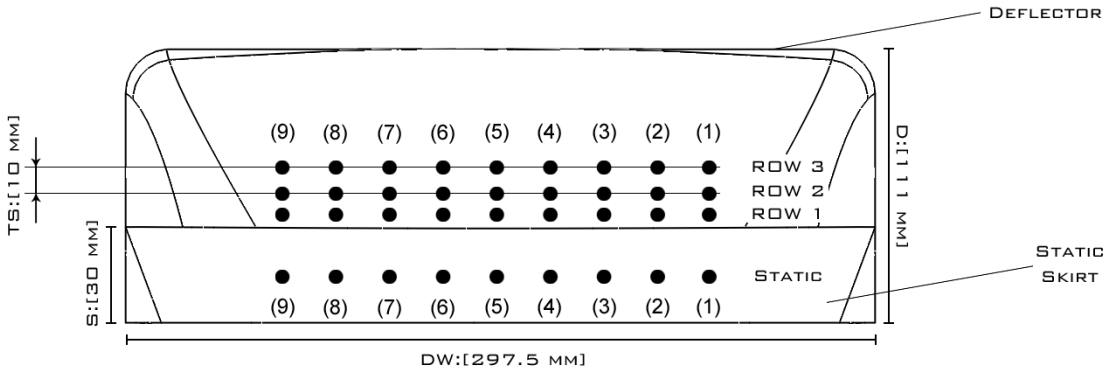

Figure 3.15: Technical Drawing of Deflector Pressure Tapping Locations.

Abbreviation	Item	Dimensions (mm)
D	Deflector Height	111.0
DW	Deflector Width	297.5
S	Static Skirt Height	30.0
TS	Tapping Separation	10.0

Table 3.2: Deflector Pressure Tapping Notation.

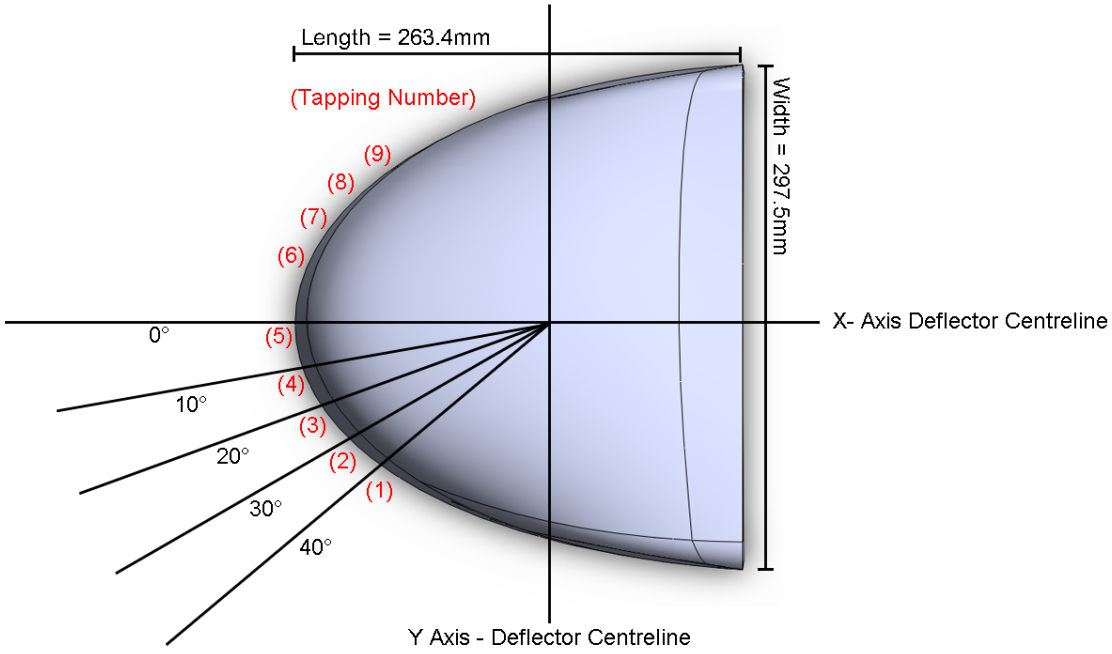

Figure 3.16: Angular Pressure Tapping Location on Deflector.

The model was again mounted on a turn-table and rotated through a yaw angle range of $(-17.5° \leq \beta \leq +17.5°)$ and the zeros recorded. The negative yaw range allowed for any asymmetry present within the model to be determined. The pressure tappings on the static skirt and deflector were recorded as a function of the yaw angle and the pressure differentials calculated. The results for this test are shown in Sec.(6.1.10) of Chapter 6.

3.6.2 Flow Field Measurement

After calibration of the five-hole probe (details are shown in Sec.(B.7) of Appendix B) and calibration maps of $C_{P\alpha}$, $C_{P\alpha}$, $C_{P(Total)}$ and $C_{P(Static)}$ (shown in Figs.(B.8 - B.11) in Secs.(B.7.1.1 - B.7.4.1) of Appendix B, respectively) obtained for the sensor, the sensor was mounted on the top and side of the deflector. The mounting locations are shown in Figs.(3.17 - 3.20), with corresponding nomenclature for the technical diagrams shown in Tabs.(3.3 and 3.4), respectively.

3.6.2.1 Deflector Top Mounting Location

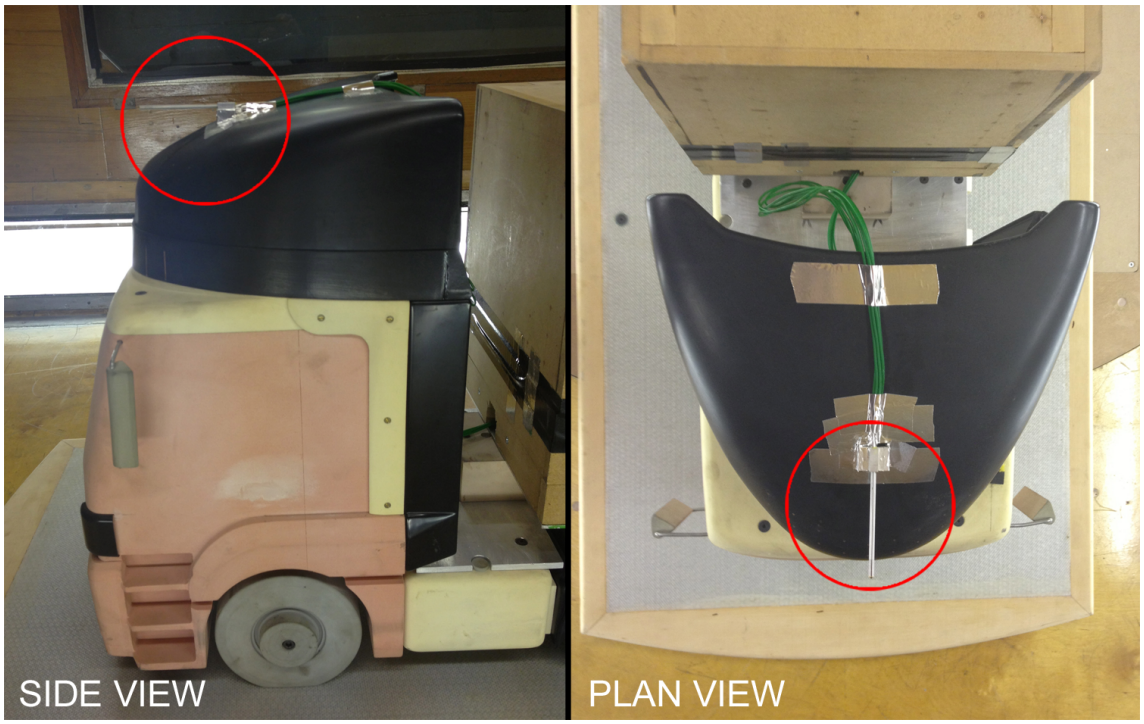

Figure 3.17: Five Hole Pressure Probe Deflector Mounting Location.

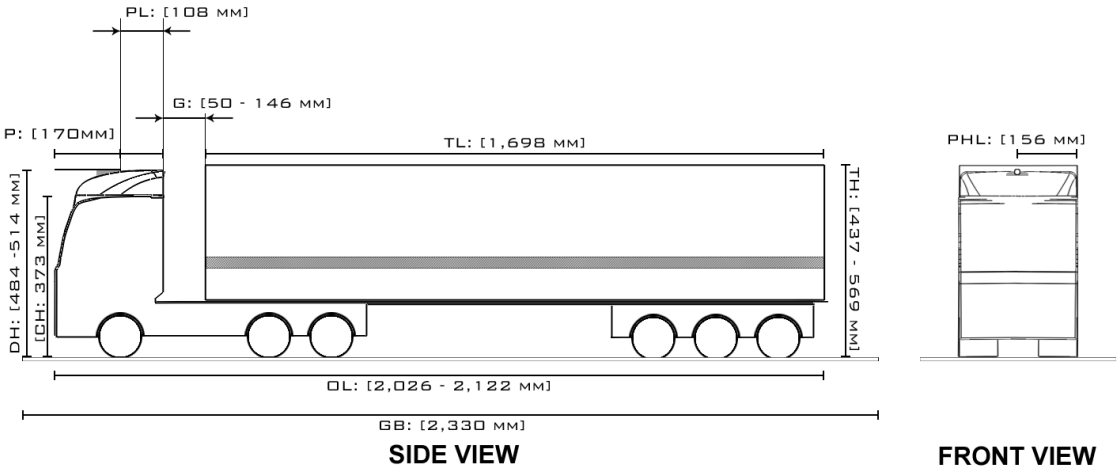

Figure 3.18: Five Hole Pressure Probe Deflector Mounting Location Schematic.

Abbreviation	Item	Dimensions (mm)
CH	Cab Height	373
G	Cab to Trailer Gap	50 - 146
DH	Deflector Height	484 - 514
GB	Ground Board Length	2,330
OL	Overall Length	2,026 - 2,122
P	Probe Length	170
PHL	Probe Horizontal Location	158
PL	Probe Location	108
TH	Trailer Height	437 - 569
TL	Trailer Length	1698

Table 3.3: Five Hole Pressure Probe Deflector Mounting Location Notation.

3.6.2.2 Deflector Side Mounting Location

Figure 3.19: Five Hole Pressure Probe Side Deflector Mounting Location.

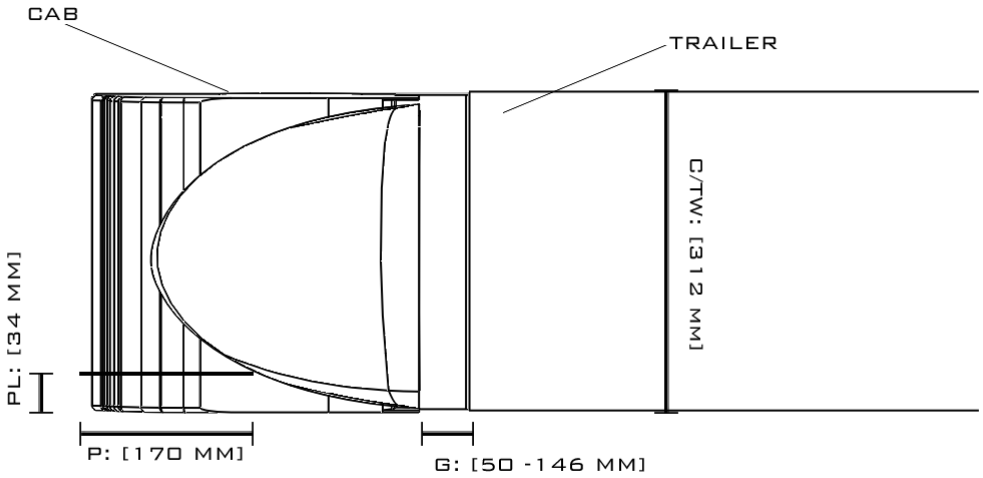

Figure 3.20: Five Hole Pressure Probe Side Deflector Mounting Location Schematic.

Abbreviation	Item	Dimensions (mm)
C/TW	Cab/Trailer Width	312
G	Cab to Trailer Gap	50 - 146
P	Probe Length	170
PL	Probe Location	34

Table 3.4: Five Hole Pressure Probe Side Deflector Mounting Location Notation.

The location on top of the deflector was chosen to determine the mounting location for a total pressure measurement probe (Kiel probe) on the full scale vehicle. The mounting location on the side of the deflector was chosen to determine the effect of any upwash or flow disturbance on the wind vane sensor (see Sec.(6.1.11 for more information)).

3.7 Full Scale On-Road Testing

3.7.1 Experimental Measurements Overview

Notation

The notation used for parameter measurement is shown in Fig.(3.21).

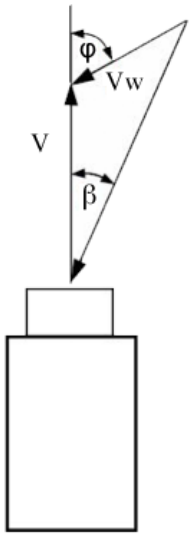

Figure 3.21: Yaw Angle Notation.

where β is the resultant/effective yaw angle (measured directly on the vehicle), φ is the wind angle (calculated) relative to the vehicle direction of motion, V is the vehicle velocity and V_W is the wind velocity.

Vehicle

The vehicle used for full scale testing was a 2008 Mercedes-Benz 2543 Axor. The manufacturer's specification sheet of the Axor is shown in Fig.(B.12) and the cab dimensions in Fig.(B.13) in Secs.(B.8.1 and B.8.2) of Appendix B. The vehicle used was equipped with a 4.5L inline 6 turbo-diesel engine, with a maximum output of 315 kW and a permitted gross combination weight of 40,000 kg.

Driver

The Axor is aimed at local delivery and short haulage transportation, with a maximum non-stop driving time of 4.5 hours as required by EU regulation (EC) Nº 561/2006 and a daily driving time not exceeding 9 hours.

The vehicle used for full scale testing, fitted with sensors are shown in Fig.(3.22) with the notation shown in Tab.(3.5)

Sensors

Figure 3.22: HGV Used for Testing, a 2008 Mercedes-Benz 2543 Axor.

Item Number	Description
{1}	Wind Cup Anemometer
{2}	Wind Vane Sensor
{3}	GPS Receiver
{4}	Pressure Transducer (Right)
{5}	Pressure Transducer (Left)

Table 3.5: Full Scale Sensor Mounting Location.

Data Logger

The data logger used was a Race Technology DL1 MK2 [68] shown in Fig.(3.23). The data logger comprised of 13 external inputs with 100 Hz logging frequency on each channel. To avoid aliasing the signals were passed through a 50 Hz low-pass filter. The logger connected to a 20 Hz GPS input used in conjunction with a 2g 3-axis accelerometers to determine the precise motion of the vehicle. The logger records directly to a compact flash (CF) card with analysis software provided by Race Technology [68]. The full specification sheet provided by the manufacturer is shown in Fig.(B.14) in Sec.(B.9.1) of Appendix B.

Figure 3.23: Race Technology DL1 MK2 Data logger [68].

Wind Speed (V_W): Item Number {1}

Relative wind speed experienced by the truck was measured by an InSpeed [69] "vortex wind sensor", shown in Fig.(3.24) which measured the combined wind and truck flow speed through a rotating cup anemometer. The anemometer contains a reed switch/magnet and provides one pulse per rotation and can measure total speed from 5 mph to over 125 mph. The accuracy of the anemometer has been tested by the manufacturer and is within ± 4% of the velocity above 40 mph. The full specification sheet provided by the manufacturer is shown in Fig.(B.17) in Sec.(B.9.4) of Appendix B.

Figure 3.24: inSpeed Vortex Wind Sensor [69].

Relative Wind Direction (β): Item Numbers $\{2, 4, 5\}$

The wind direction was measured by two sensors, the first, an InSpeed [70] "wind vane sensor" shown in Fig.(3.25), with a 360° zero dead band range. The manufacture specification sheet is shown in Fig.(B.18) in Sec.(B.9.5) of Appendix B.

Figure 3.25: inSpeed Wind Vane Sensor [69].

The second measurement was obtained by 2 x PX138-0.3D5V temperature compensated, differential pressure transducers shown in Fig.(3.26). Manufactured by Omega Engineering [71], the accuracy of the transducers is ± 2 Pa and the full specification sheet is shown in Fig.(B.19) in Sec.(B.9.6) of Appendix B. The transducers are used in conjunction with a Kiel Probe shown in Fig.(3.27), the specification sheets are shown in Figs.(B.20 and B.21) in Sec.(B.9.7) of Appendix B. The Kiel probe could measure total pressure over a a yaw angle range (β) of $\pm 63^{\circ}$ and pitch angle range (α) of $\pm 58^{\circ}$ [72]. This allowed determination of the pressure differential (ΔC_P) between the left and right tappings and therefore the relative yaw angle of the wind.

Figure 3.26: Omega Engineering PX138-0.3D5V Transducer [71].

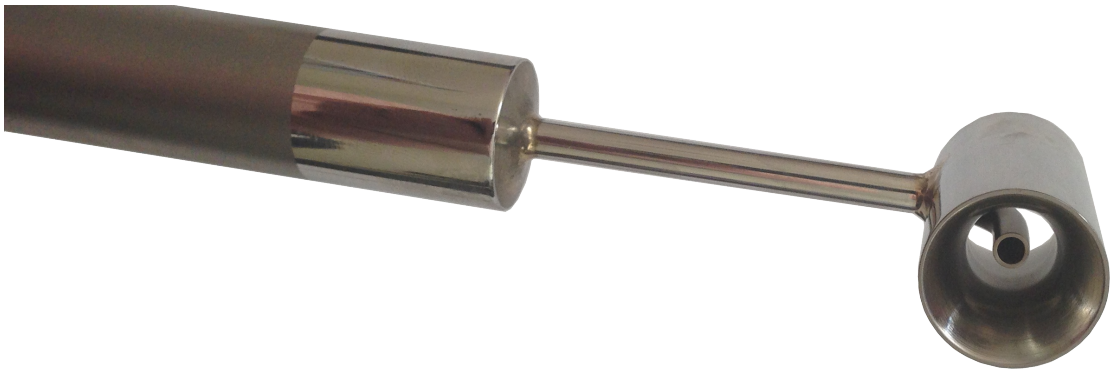

Figure 3.27: United Sensor Corp. KFE-12-N-10 Kiel Probe [72].

Vehicle Speed (V_{Truck}): Item Number {3}

The vehicle speed was derived from data obtained using the 20 Hz GPS sensor, shown in Fig.(3.28) and used in conduction with the 2g 3-axis sensors fitted to the data logger [68]. The accuracy of the GPS receiver has been tested by the manufacturer and is within ± 0.13 mph shown in Fig.(B.16) in Sec.(B.9.3) of Appendix B.

Figure 3.28: Race Technology GPS Receiver [68].

3.7.2 Full Scale Experimental Test Procedure

***Prior Experimental Research*:**

Prior experimental research on the on-road conditions experienced by vehicles has been conducted by Watkins et al. [73]. The research identified the main sources of turbulence experienced by a moving vehicle to be:

- Vehicle traversing the turbulence field associated with the atmospheric wind.
- Vehicle traversing the wakes of local roadside objects (e.g. trees and buildings) in the atmospheric wind.
- Effect of wakes from other road users, recognising that vehicles can pass in the same, or opposing, directions.

The paper outlined a chosen sampling frequency for static atmospheric wind conditions of 5.7 Hz. This value was based on the minimum required sampling frequency of 1.88 Hz at 10 ms^{-1} wind near the ground determined by Flay [74]. The moving sampling data was conducted at 55 Hz using a Gill propeller-vane anemometer and averaged over 74 seconds. The rational for time averaging was

that fluctuations in wind or vehicle speed of a period greater than 10 seconds could be considered as quasi-steady.

Two test routes were chosen for the experiment, the first a 2 km stretch of smooth terrain with no obstacles and the second a 20 km open terrain with scattered objects.

Results obtained from the on-road data indicated a road vehicle could experience varying wind speeds in the range of 1-10 ms^{-1} depending on location. The paper also concluded that the atmospheric wind energy was present at frequencies of the order of 0.002 Hz and below.

***Test Outline*:**

Due to the limited information on the time variation of the on-road wind conditions and interference effects, a large sample size logged at high frequency was deemed necessary to provide a enable identification of a broad frequency range. The constraint of a minimum logging frequency of 1.88 Hz determined by Flay [74] was well exceeded when logging at 100 Hz. Commercial transportation schedules vary daily, however, on average around 6 hours of vehicle operation time could be expected. A restriction imposed by logging to a Compact Flash (CF) card at high frequency was that vast amounts of data was generated whilst sampling. The CF card that could be used within the logger was limited to 2GB and therefore storage space had to be considered for the long term logging.

In an effort to maximise the useful data obtained from a CF card to reduce post-processing time, the data logger was set to auto-log data provided that $V_{(Truck)} > 13$ ms^{-1} (29 mph). This requirement meant that the data logger would only obtain data when the vehicle is approaching normal operating velocities and would discard low velocity data. A 100 Hz logging frequency provided on average 2.2×10^6 data points. The 2 GB CF card could hold approximately 80 hours of logging and was removed from the vehicle weekly and the data extracted to a computer for analysis.

The data analysis used for the full scale testing is shown in Sec.(B.10) with error calculations in Sec.(B.11.3) of Appendix B.

Chapter 4

Computational Fluid Dynamics Simulation Details

The role of Computational Fluid Dynamics (CFD) in this research was initially to extend the range of tractor-trailer gaps explained earlier and secondly to enable comparison with the full scale, on-road data. The control scheme used in the full scale application required a look-up table, this resulted in the requirement of extensive data to populate the table. The accuracy of the data contained within the look-up table contributed significantly to the overall accuracy of the system.

The optimum deflector height ratio (δ_{Hopt}) for a given trailer height was known from wind tunnel testing to depend on the wind yaw angle (β) and the gap to container height ratio (g/d_2). Tractor-trailer separations over 146 mm (1.2 m full scale) could not be tested in the wind tunnel due to experimental constraints. The variation of δ_H with large g/d_2 could not therefore be experimentally tested.

The CFD used within this research was employed to determine δ_{Hopt} for larger g/d_2. Wind tunnel testing provided a tractor-trailer gap range of 50 mm - 146 mm, corresponding to a full scale separation of 0.4 m - 1.2 m. CFD simulations were therefore used to extend the data within the look-up table to a tractor-trailer separation of 250 mm corresponding to a full scale separation of 2.0 m. The time averaging of data collected from the wind tunnel meant that time averaged Reynolds-Averaged Navier-Stokes (RANS) was used in the CFD simulation. on-road The second stage of CFD within the research was for comparison with full scale, on-road data. Due to the results from the on-road data containing large amounts of high frequency noise, investigation into the source of this noise was conducted. The frequency spectrum of the on-road signal was obtained by application of a Fourier transformation on the time series data, as a result, the time variation of the flow was required in the CFD simulations. The most accurate, computationally feasible time varying simulation technique available was via Large Eddy Simulation (LES).

LES was therefore applied to two tractor-trailer vehicles in tandem with investigation into the effects of the lead trailer wake on the trailing tractor unit. The trailer wake was investigated to determine if the on-road 'signal noise' frequency could be attributed to the vortex shedding from the wake of a leading vehicle.

The techniques used for the research were therefore an initial time averaged RANS investigation on a tractor-trailer separation and a second time varying LES on the trailer wake of two heavy goods vehicles in tandem.

4.1 Solver Overview

Computational simulation was conducted using the commercial flow solver ANSYS Fluent 12.1 [75]. The governing equations and the associated turbulence models used by the solver is shown in Appendix C. Mesh generation was achieved using ANSYS ICEM CFD and post-processing was conducted in Tecplot 360.

4.1.1 Fluent Solution Procedure

The procedure to obtaining a CFD solution with Fluent is as follows:

1. Pre-Processing: Geometry positioning, surface mesh generation/volume mesh generation (3D).
2. Mesh Generation: Definition of initial conditions and boundary conditions.
3. Mesh Export: Conversion of mesh to unstructured format (for Fluent 12.1).
4. Fluent: Iteration of solution until point of convergence.
5. Post-Processing: Visualisation of the flow field.

Each of the above are described in detail in the following sub-sections.

4.1.2 Pre-Processing: 2D

Geometry generation was achieved by importing a Mercedes-Benz supplied Parasolid CAD model into ANSYS ICEM CFD. Data points on the model were then extracted to form a 2D outline of the geometry shown in Fig.(4.1). The truck and trailer wheel cavities were simplified to enable a structured mesh to be used, shown in Fig.(4.2). The underside of the vehicle was simplified to include only the first wheel on the cab and the cavity simplified to form a sealed cavity.

The vehicle was situated one truck length 1.0 × L (where L = 17.8 m) from the domain inlet, 3.0 × L from the outlet, 0.1 × L from the bottom wall and 1.0 × L from the top wall. A detailed description of the geometry distribution is presented in Tab.(4.1).

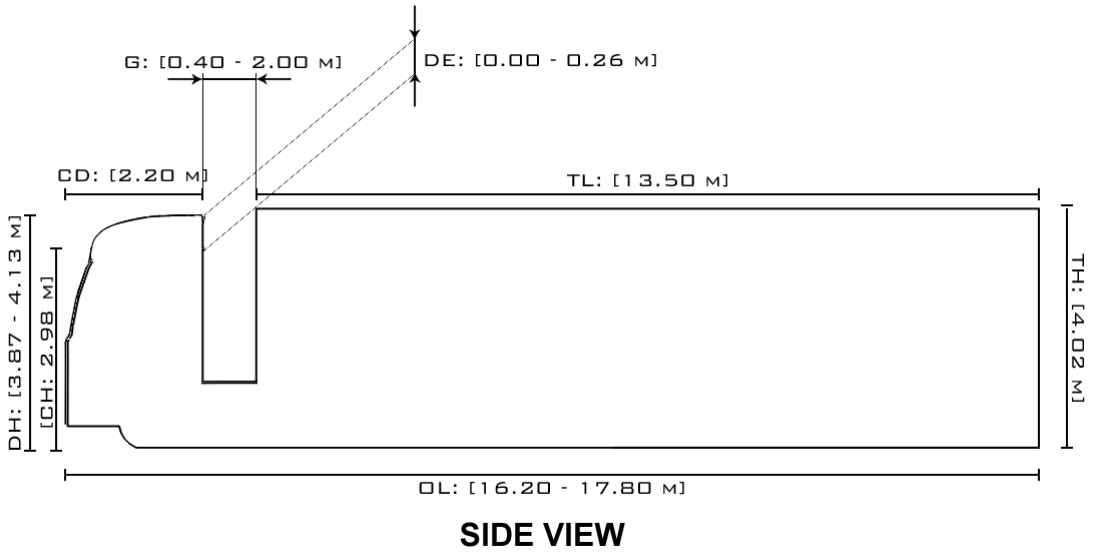

Figure 4.1: 2D Mercedes-Benz Technical Geometry.

Abbreviation	Item	Dimensions (m)
CD	Cab Depth	2.20
CH	Cab Height	2.98
DE	Deflector Extension	0.00 - 0.26
DH	Deflector Height	3.87 - 4.13
G	Cab to Trailer Gap	0.40 - 2.00
TH	Trailer Height	4.02
TL	Trailer Length	13.50
OL	Overall Length	16.20 -17.80

Table 4.1: 2D Geometry Distribution.

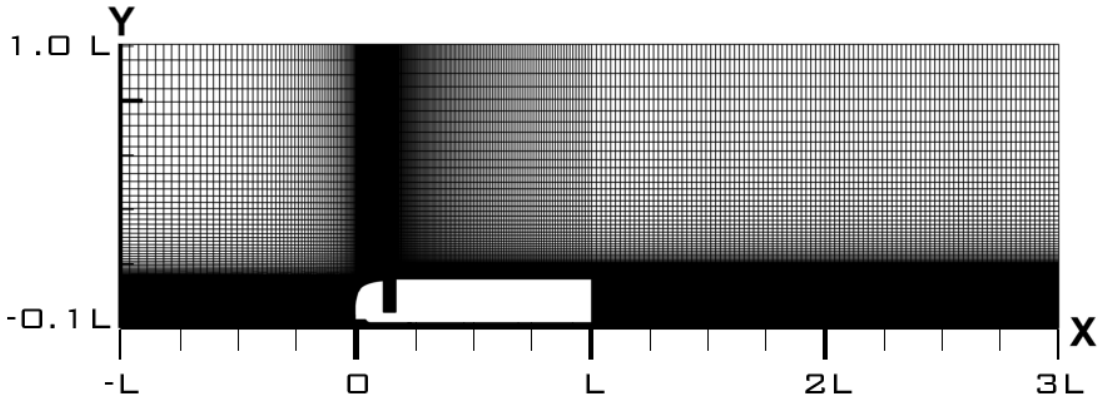

Figure 4.2: 2D Mercedes-Benz Domain Layout.

The result of this simplification was to incorrectly estimate the trailer wake structure on the vehicle and over predict the cavity pressures. The drag coefficient on bluff bodies is mainly due to profile drag and the simplified geometry should under predict this value. The geometry should, however, be able to predict the best RANS model for use within the 3D simulations.

4.1.3 Mesh Generation: 2D

After the 2D geometry had been generated, the mesh was then constructed in ANSYSY ICEM CFD. Details of the generated meshes are shown in Tab.(4.2) with images of the resulting meshes shown in Figs.(4.3 - 4.5). The y^+ distribution around the model for Case 2 is shown in Tab.(4.3).

	Number of Grid Cells				
Case	Front	Top	Bottom	Rear	Total
Case 1	112	196	192	165	21132
Case 2	112	392	385	165	42929
Case 3	224	392	385	330	84528

Table 4.2: Mesh Distribution Around Model.

Dimensionless Wall Distance

The dimensionless wall distance, y^+ is defined by

$$y^+ \equiv \frac{u_* y}{\nu} \tag{4.1}$$

where $u_* \equiv \sqrt{\frac{\tau_\omega}{\rho}}$, τ_ω = wall shear stress, ρ = fluid density, y = distance to nearest wall and ν = local kinematic viscosity.

Fluent uses a logarithmic law for mean velocity in the region: $30 < y^+ < 300$. For $y^+ < 11.225$, Fluent applies a laminar stress-strain relationship.

Section	y^+ Value
Front	$32 \sim 50$
Top	$34 \sim 100$
Bottom	$34 \sim 90$
Rear	$30 \sim 70$

Table 4.3: y^+ Distribution Around Model (Case 2).

The meshes used in the simulations are shown in Fig.(4.3 - 4.5), the frontal section of the vehicles are shown in detail in Sec.(C.10.1) of Appendix C. The rear section of the vehicle is shown in detail in Sec.(C.10.4) of Appendix C

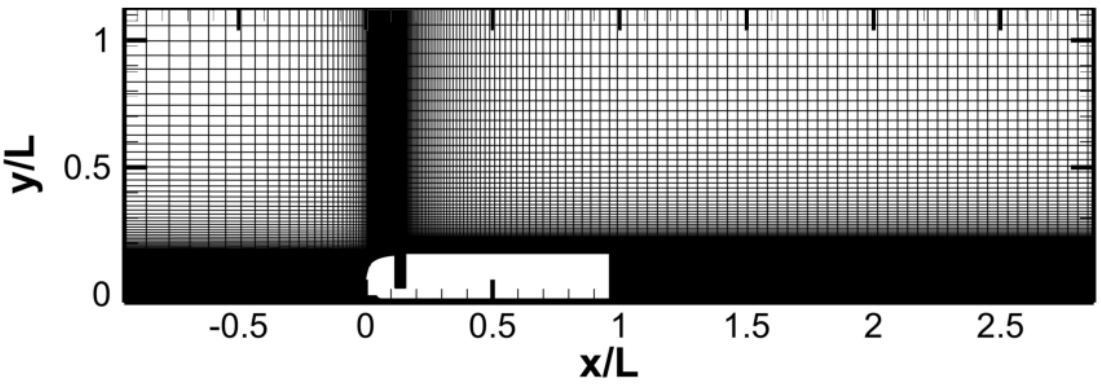

Figure 4.3: 20k Grid Cell Mesh.

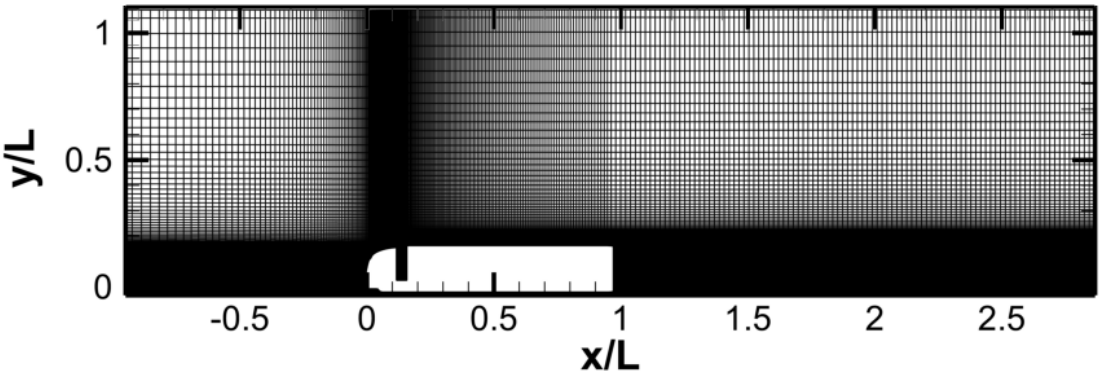

Figure 4.4: 40k Grid Cell Mesh.

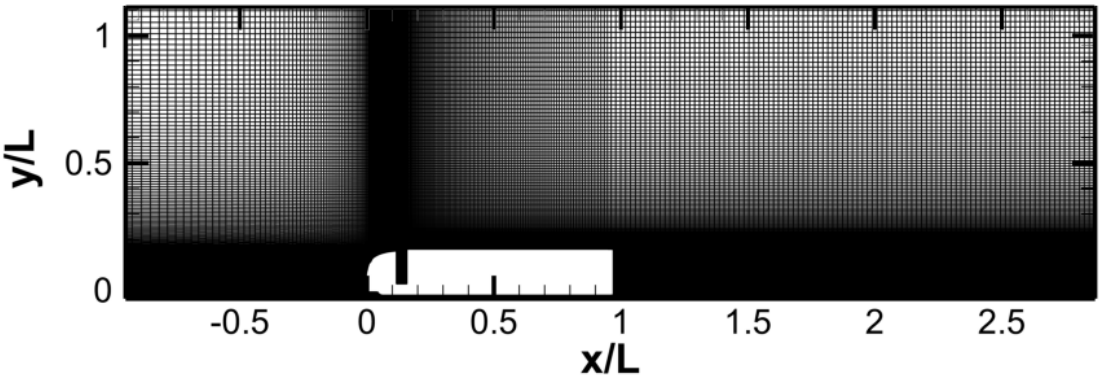

Figure 4.5: 80k Grid Cell Mesh.

4.1.4 Pre-Processing: 3D

The Mercedes-Benz supplied Parasolid CAD model of the vehicle was then imported into Solidworks and the geometry simplified. The ActiveFREDDIE deflector geometry was added to the vehicle and connected to a simplified trailer. The resulting assembly is shown in Figs.(4.6 and 4.7). The resulting geometry differs from the 2D case through the addition of cab side extenders, a non-sealed tractor-trailer cavity, tractor wheels and a wheel cavity. This improved the accuracy of the model and allowed for comparison with the full scale vehicle.

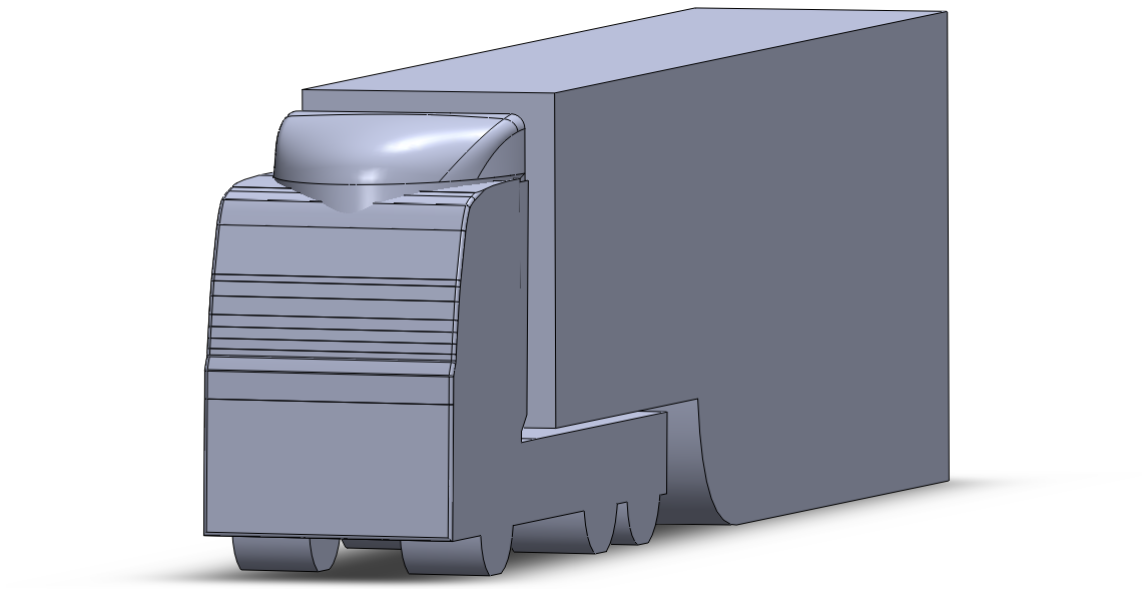

Figure 4.6: 3D Mercedes-Benz Geometry.

The vehicle is situated one truck length 1.0 × L (where L = 17.8 m) from the domain inlet, 3.0 × L from the outlet, 2.5 × L from either side wall, 0.1 × L from the bottom wall and 1.0 × L from the top wall. A detailed description of the geometry distribution is presented in Tab.(4.4).

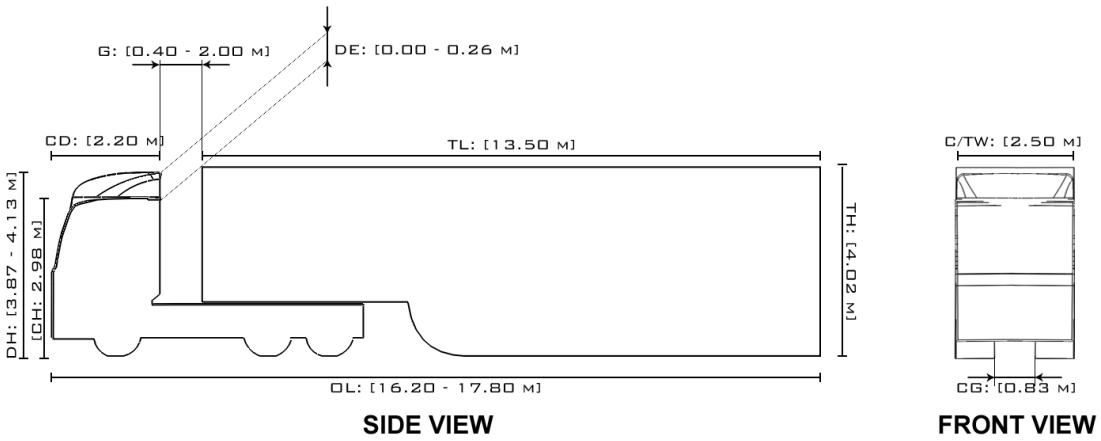

Figure 4.7: 3D Mercedes-Benz Technical Geometry.

Abbreviation	Item	Dimensions (m)
CD	Cab Depth	2.20
CG	Cavity Gap	0.83
CH	Cab Height	2.98
C/TW	Container/Trailer Width	2.50
DE	Deflector Extension	0.00 - 0.26
DH	Deflector Height	3.87 - 4.13
G	Cab to Trailer Gap	0.40 - 2.00
TH	Trailer Height	4.02
TL	Trailer Length	13.50
OL	Overall Length	16.20 -17.80

Table 4.4: 3D Geometry Distribution.

4.1.5 Pre-Processing: 3D Tandem

In order to simulate the effect of a heavy goods vehicle in the presence of a trailer wake, two trucks in tandem were required for the simulation. The 3D generated geometry was therefore duplicated and placed behind a lead vehicle. The two vehicles in tandem were separated by a gap of 0.5 × L (8.30 m).

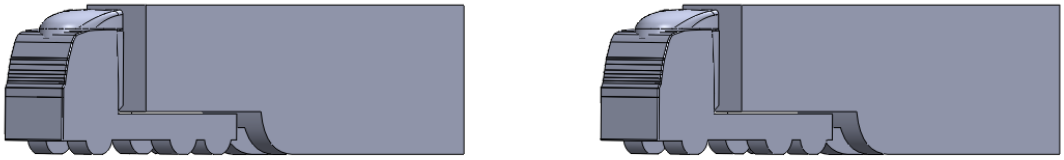

Figure 4.8: 3D Tractor-Trailer Tandem Configuration Front 3/4 View.

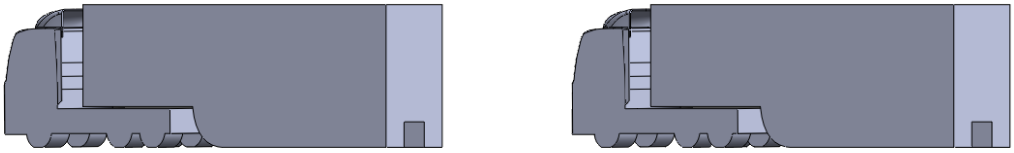

Figure 4.9: 3D Tractor-Trailer Tandem Configuration Rear 3/4 View.

Figure 4.10: 3D Tractor-Trailer Tandem Configuration Plan View.

The leading vehicle was situated one truck length 1.0 × L (where L = 17.8 m) from the domain inlet, the following vehicle was separated by 0.5 × L from the rear

of the leading trailer. The following vehicle was located 3.0 × L from the outlet, both vehicles are located 2.5 × L from either side wall, 0.1 × L from the bottom wall and 1.0 × L from the top wall. A detailed description of the geometry distribution is presented in Fig.(4.11).

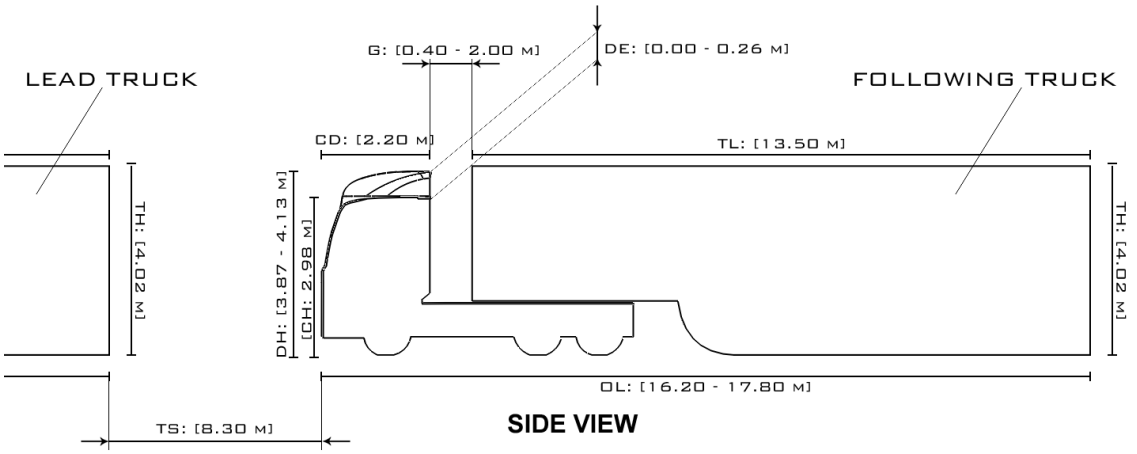

Figure 4.11: 3D Tractor-Trailer Tandem Configuration Side View Technical Drawing.

Abbreviation	Item	Dimensions (m)
CD	Cab Depth	2.20
CH	Cab Height	2.98
DE	Deflector Extension	0.00 - 0.26
DH	Deflector Height	3.87 - 4.13
G	Cab to Trailer Gap	0.40 - 2.00
TH	Trailer Height	4.02
TL	Trailer Length	13.50
TS	Truck Separation	8.30
OL	Overall Length	16.20 -17.80

Table 4.5: 3D Tandem Tractor-Trailer Geometry Distribution.

4.1.6 Mesh Generation: 3D

Due to the complexity of the three dimensional geometry, automatic volume meshing was used to generate the meshes for both the single and vehicles in tandem cases. Pointer et al. [76] reported that the near-vehicle cell size plays an important role of the k-ϵ turbulence model's ability to accurately predict the vehicle's C_D. Pointer et al. [76] concluded that a reduction in the average cell size lead to a C_D convergence towards the experimental C_D. With a suitable geometry and RANS model, the values predicted were within 3.0% of experimental data. Several cell sizes were chosen to determine the optimum cell sizing required to reduce the error in the predicted C_D, these are shown in Tab.(4.6).

Near-Vehicle Cell Size (mm)	Approximate Mesh Size
2000	0.5×10^6
1000	2.0×10^6
250	5.0×10^6
50	10.0×10^6
25	20.0×10^6

Table 4.6: Mesh Distribution Around 3D Model.

Figure (4.12) shows the 10 Million cell volume mesh of the vehicle.

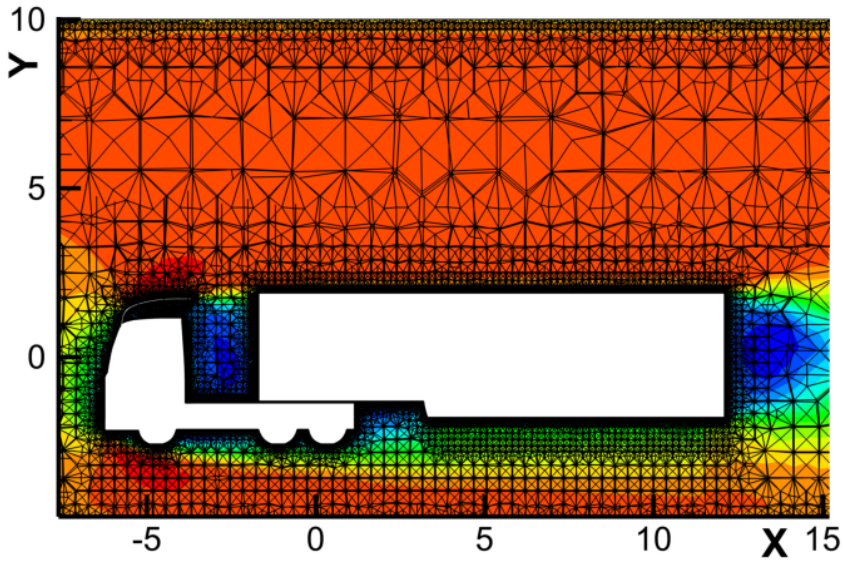

Figure 4.12: 10 Million Grid Cell Mesh, Slice Extracted Along Vehicle Centre Line.

Figures.(4.13 - 4.17) show the volume mesh at different viewing angles and positions around the geometry.

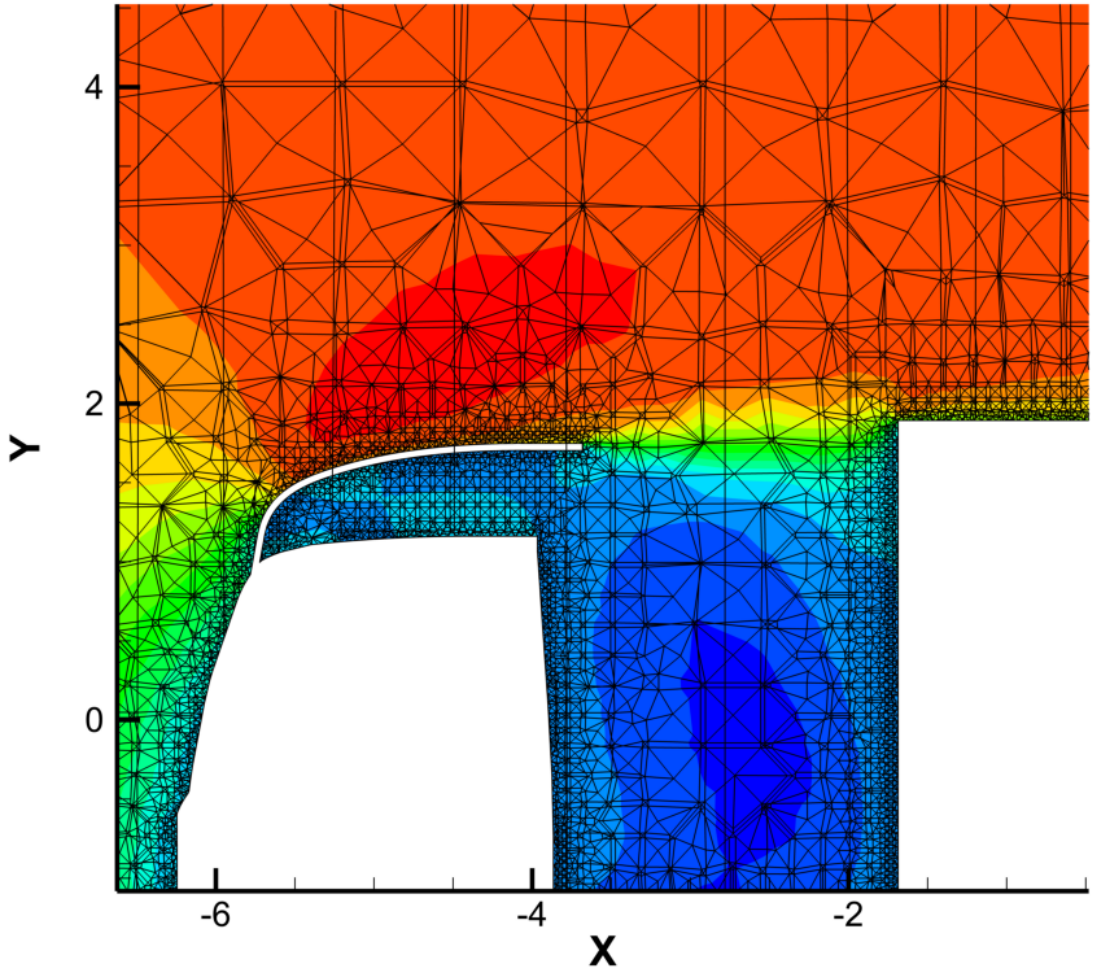

Figure 4.13: 10 Million Grid Cell Volume Mesh Around Deflector and Trailer Geometry.

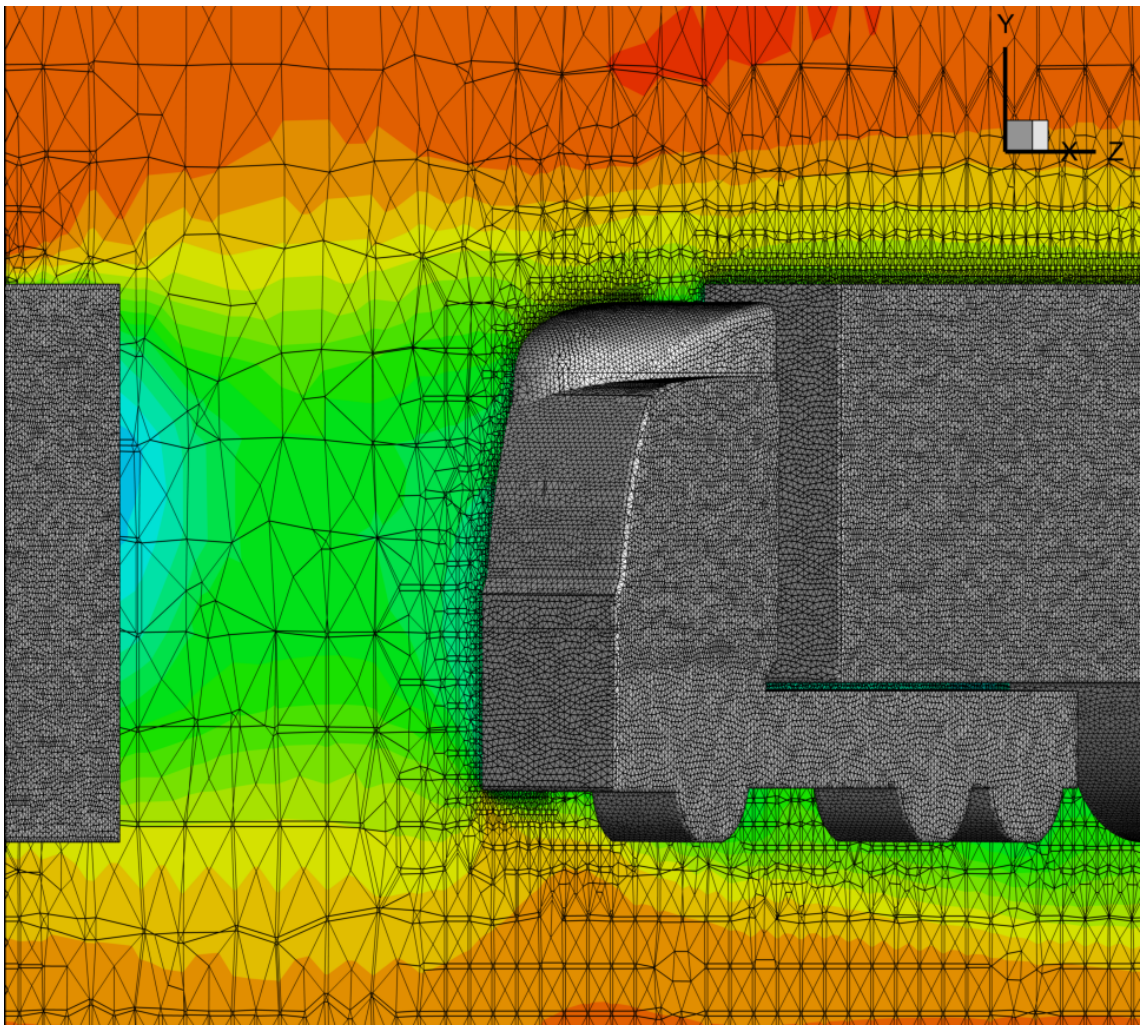

Figure 4.14: 10 Million Grid Cell Surface Mesh Around Vehicle Gap and Trailing Vehicle.

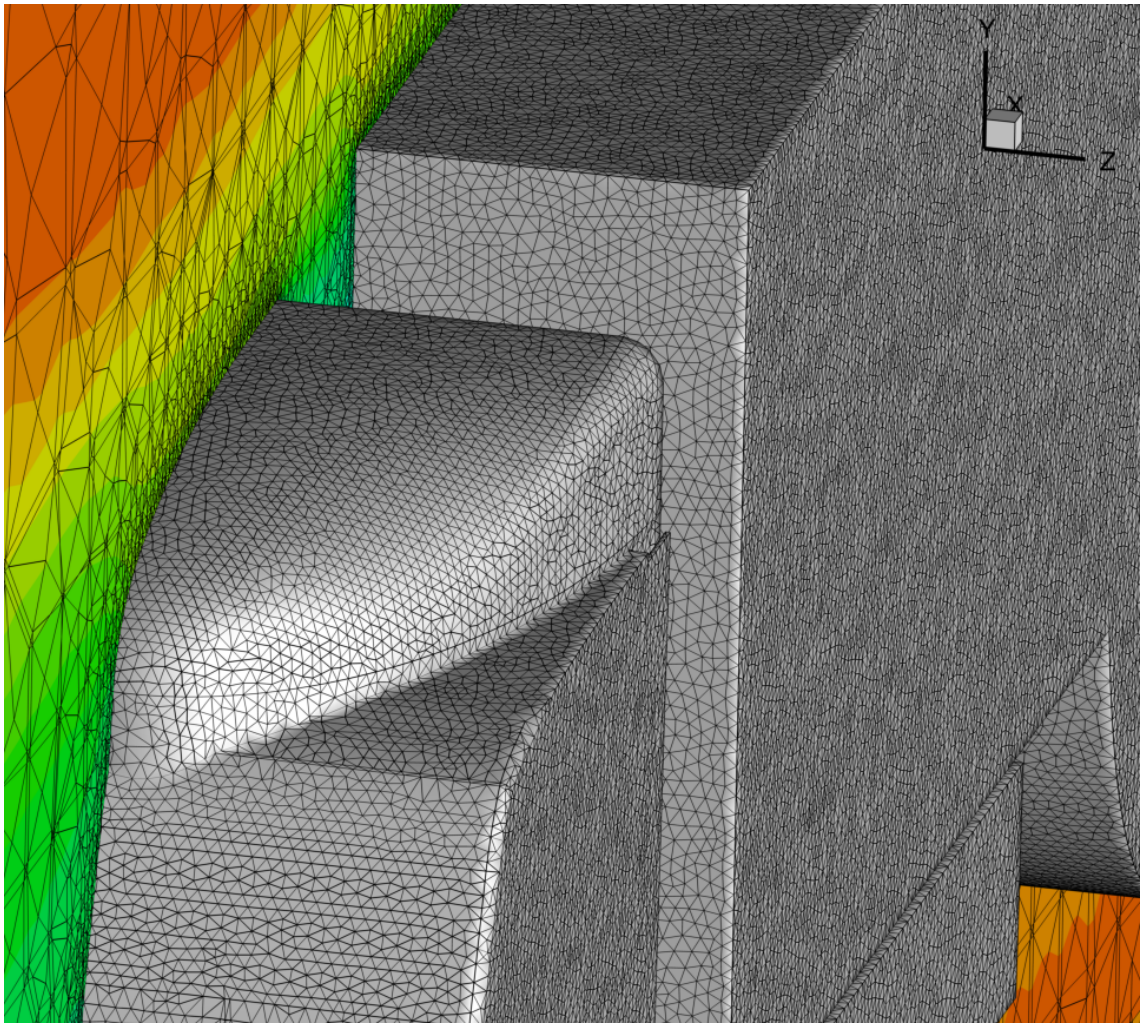

Figure 4.15: 10 Million Grid Cell Surface Mesh Around Deflector.

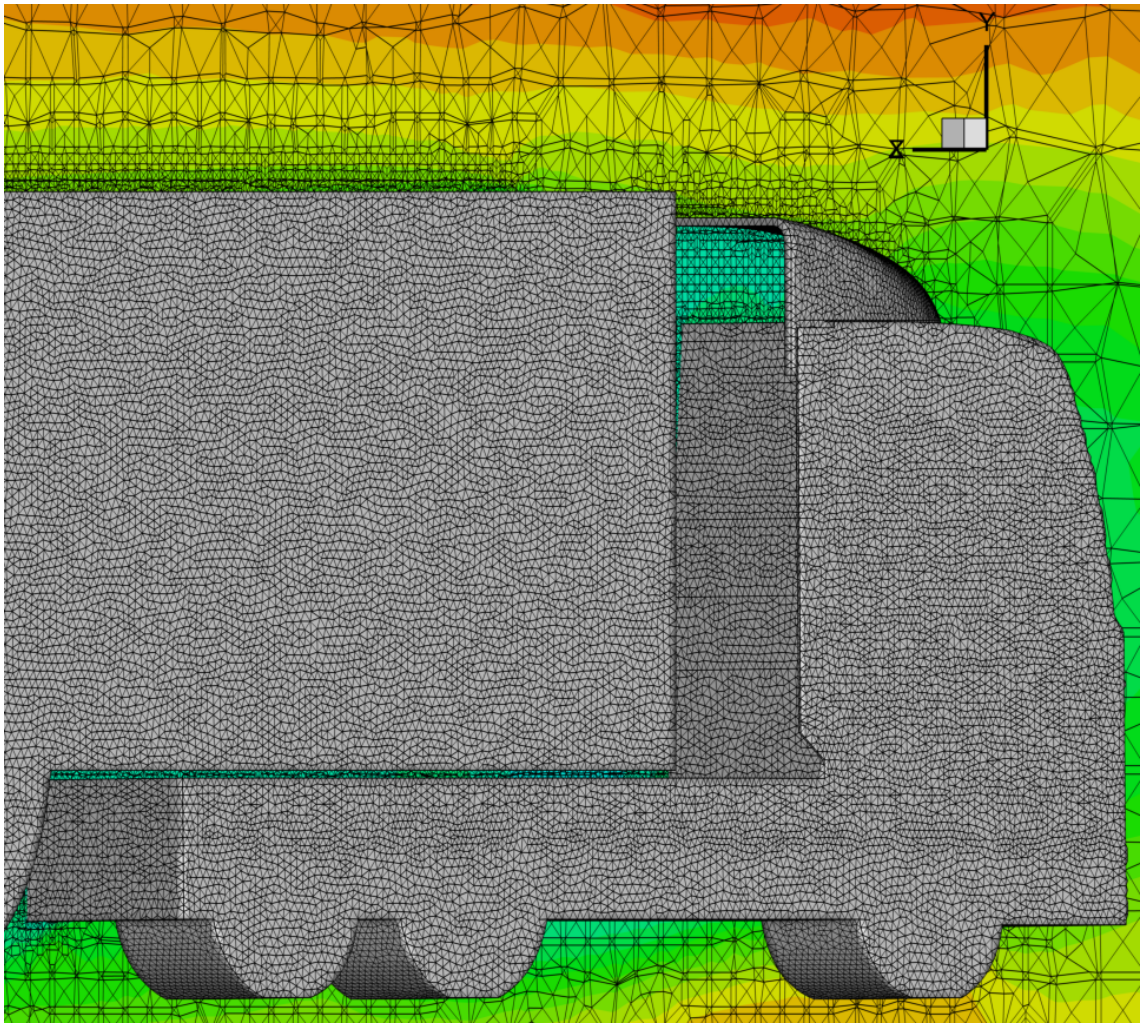

Figure 4.16: 10 Million Grid Cell Surface Mesh Around Deflector and Trailer Geometry (Rear View).

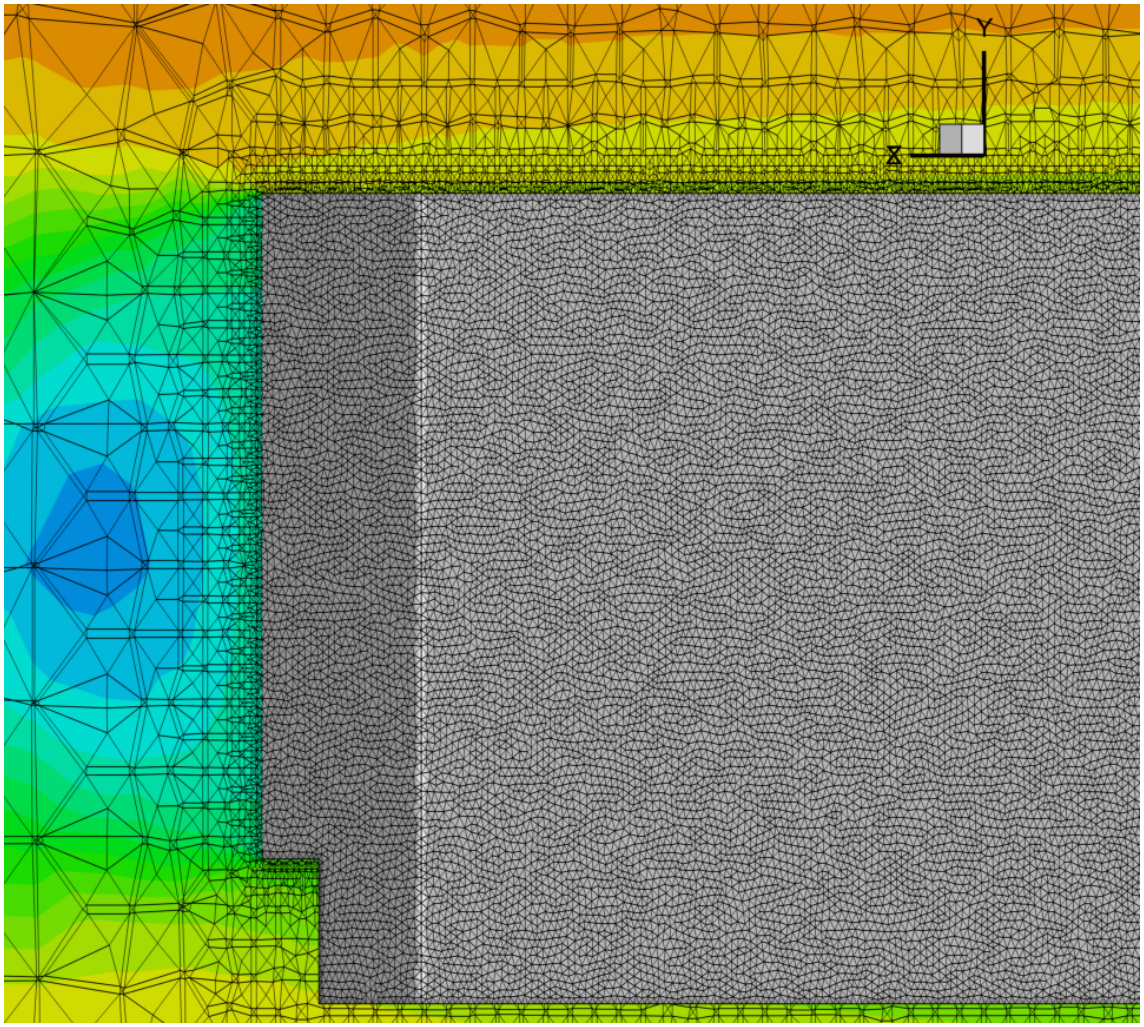

Figure 4.17: 10 Million Grid Cell Surface Mesh Around Rear of Trailer.

The process of exporting the mesh along with the numerical solvers used within Fluent is shown in Secs.(C.6 - C.9) of Appendix C.

4.1.7 2D Fluent Initialisation

General Details	
Solver	ANSYS Fluent 12.1, Pressure Based, Steady, Implicit, Node-Based.
Mesh Type	Structured.
Number of Cells	
	Case 1 - 21132
	Case 2 - 42929
	Case 3 - 84528
Solver Controls	
Turbulence Model	All Available Models
Near-Wall Treatment	Standard Wall Treatment
Discretisation (Under Relaxation)	
Pressure	Second Order (0.3)
Momentum	Second Order Upwind (0.4)
Turbulent Kinetic Energy	Second Order (0.4)
Turbulent Dissipation Rate	Second Order Upwind (0.4)
Materials	
Fluid	Air
Density	1.225 kgm^{-3}
Viscosity	1.7894×10^{-5} $kgm^{-1}s^{-1}$
Boundary Conditions	
Inlet	Velocity Inlet (5 ms^{-1})
Outlet	Pressure Outlet
Top	Wall
Bottom	Wall
Truck	Wall

Table 4.7: 2D Fluent Initialisation Computational Configuration.

4.1.8 3D Fluent Initialisation

General Details	
Solver	ANSYS Fluent 12.1, Pressure Based, Steady, Implicit, Node-Based.
Mesh Type	Unstructured.
Cell Size (mm)	
	Case 1 - 2000
	Case 2 - 1000
	Case 3 - 250
	Case 4 -50
	Case 5 - 25
Solver Controls	
Turbulence Model	S-A and Realizable k-ϵ
Near-Wall Treatment	Standard Wall Treatment
Discretisation (Under Relaxation)	
Pressure	Second Order (0.3)
Momentum	Second Order Upwind (0.4)
Turbulent Kinetic Energy	Second Order (0.4)
Turbulent Dissipation Rate	Second Order Upwind (0.4)
Materials	
Fluid	Air
Density	1.225 kgm^{-3}
Viscosity	1.7894×10^{-5} $\text{kgm}^{-1}\text{s}^{-1}$
Boundary Conditions	
Inlet	Velocity Inlet (5 ms^{-1})
Outlet	Pressure Outlet
Top	Wall
Bottom	Wall
Truck	Wall

Table 4.8: 3D Fluent Initialisation Computational Configuration.

4.1.9 3D LES Fluent Initialisation

General Details	
Solver	ANSYS Fluent 12.1, Pressure Based, Unsteady, Implicit, Node-Based.
Mesh Type	Unstructured.
Cell Size (mm)	Case 1 - 25
Solver Controls	
Subgrid Model	Dynamic Kinetic Energy Subgrid-Scale Model
Near-Wall Treatment	Standard Wall Treatment
Discretisation (Under Relaxation)	
Pressure	Second Order (0.3)
Momentum	Bounded Central Differencing (0.7)
Subgrid Kinetic Energy	Bounded Central Differencing (0.8)
Transition Formulation	Second-Order Implicit (1.0)
Time Step	
Time Stepping Method	Fixed
Time Step Size (Seconds)	0.01
Materials	
Fluid	Air
Density	1.225 kgm^{-3}
Viscosity	1.7894×10^{-5} $kgm^{-1}s^{-1}$
Boundary Conditions	
Inlet	Velocity Inlet (35 ms^{-1})
Outlet	Pressure Outlet
Top	Wall
Bottom	Wall
Truck	Wall

Table 4.9: 3D LES Fluent Initialisation Computational Configuration.

4.1.10 Fluent Execution

Once the variables to initialise the solution had been inputted into Fluent, Fluent executed a pressure-based segregated algorithm. The algorithm is used in order to solve governing equations and is iterative (until convergence). The algorithm is outlined below:

1. Solve discretised momentum equations.
2. Solve pressure correction equation.
3. Correct Pressure and velocities.
4. Solve all other discretised equations.
5. Test convergence, if converged solution has finished otherwise the process is repeated.

4.1.11 Computational Specifications

Computer-Aided Design (CAD) model generation, meshing and the 2D simulations were conducted on a Dell Precision 490 Workstation. The workstation specifications are listed in Tab.(4.10).

Manufacturer	Dell
Model	Precision 490
CPU Manufacturer	Intel
CPU Model	Xeon X5365
CPU Numbers	2
CPU Cores	4
CPU Clock Speed	3.00 GHz
RAM	16 GB DDR2 667 MHz

Table 4.10: Meshing Computer.

The 3D cases were run on the Cranfield University supercomputer "Astral - 2" (shown in Fig.(4.18)), the specifications of the supercomputer are listed in Tab.(4.11).

Figure 4.18: Astral-2 Supercomputer.

Name	Astral-2
Manufacturer	Hewlett-Packard
CPU Manufacturer	Intel
CPU Model	E5-2660
CPU Cores	1280
RAM	5120 GB
Theoretical Peak (Rpeak)	22.5 TFlops
Linpack Performance (Rmax)	19.9 TFlops

Table 4.11: Simulation Supercomputer.

In order to run on the supercomputer, a bash submission script and Fluent batch script were required. An example of these scripts are shown in Figs.(C.11.1 and C.11.2) in Sec.(C.11) of Appendix C, respectively.

This page intentionally left blank.

Chapter 5

Control System Design

Due to restrictions placed upon the project, several concurrent control schemes were required to be developed (see Sec.(1.6) for more information on the restrictions and Technology Readiness Levels (TRLs)).

The control system design was therefore split into three separate controllers, detailed below:

Research Controller (TRL1 - TRL4) (Sec.(5.1)): Used an Extremum Seeking Control algorithm and required wind tunnel and on-road data in conjunction with a mathematical simulation for the vehicle dynamics. Parameters that were used in the simulation were deemed to be too small to allow practical measurement on-road.

Prototype Controller (TRL4 - TRL7) (Sec.(5.2)): Used wind tunnel data only, on-road conditions were unavailable at this stage of the research and were therefore assumed to be time invariant.

Production Controller (TRL7 - TRL9) (Sec.(5.3)): Used CFD, wind tunnel and on-road data. On-road data enabled estimation of the performance of the active system. Estimation was conducted on the optimal frequency of adjustment of the deflector and into a suitable filtration method for signal noise.

5.1 Research Controller (TRL1 - TRL4)

The research controller used for the (TRL1 - TRL4) levels used an Extremum Seeking Control (ESC) algorithm. The control algorithm drives a measured parameter (such as the drag of the vehicle) to a minimum. For a HGV fitted with an adjustable deflector, this corresponded to driving the deflector to an optimum height (δ_{Hopt})

that generated the lowest drag (C_{DMin}) on the vehicle. Since the drag of the vehicle is a difficult and impractical variable to measure directly on-road, a measurable parameter that related to the drag was measured instead.

The investigation into determining a parameter that related to C_D was difficult to achieve with budget limitations placed by the commercial partners. The associated costs of the sensors required to measure the parameters required for the controller eliminated it as a viable controller for the higher TRL levels.

The data required for the research controller were wind tunnel testing and *Simulink*® simulation. Further information about the research controller is shown in Fig.(1.8) in Sec.(1.6.1). The research controller was a proof of concept controller and therefore only required wind tunnel data for the *Simulink*® simulation.

5.1.1 Extremum Seeking Background

The research control system design is based on the extremum seeking algorithm developed by Krstic et al. [54]. Figure (5.1) shows Extremum Seeking Control (ESC) for a static map.

The extremum seeking algorithm has five main components, these are:

Plant (Sec.5.1.2): The system or systems to be modelled (the vehicle and on-road conditions).

Optimal Input (θ^*) (Sec.5.1.3): The value of an input variable (the optimum deflector height (δ_{Hopt})) that creates the optimum of the plant.

Optimum of Plant (f^*) (Sec.5.1.4): The value of the plant generated by the optimal input (the vehicle's C_{DMin}).

Output (y) (Sec.5.1.5): The output from the system (C_D of the vehicle).

Plant Feedback (θ) (Sec.5.1.6): The difference arising between the current output and the desired output (C_D - $C_{D(Min)}$).

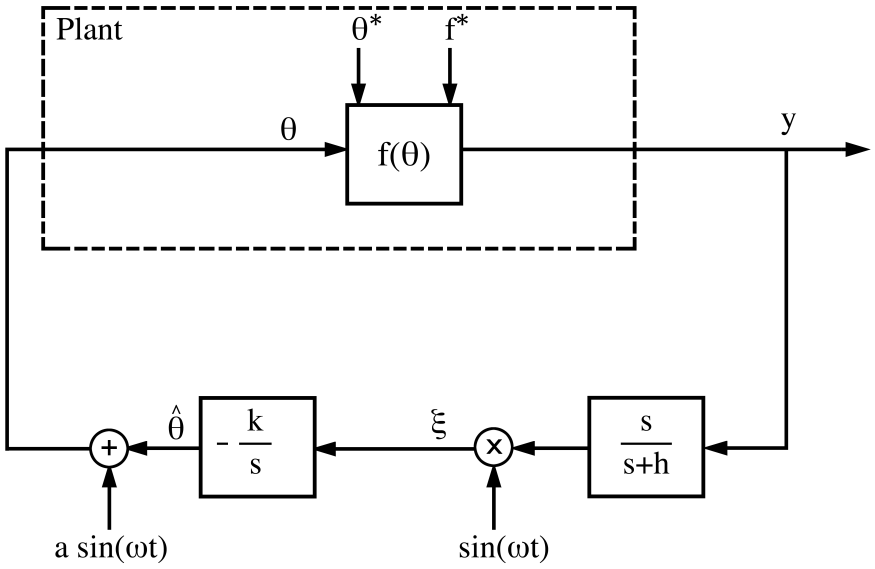

Figure 5.1: Extremum Seeking Control Scheme [54].

5.1.2 Plant

The plant used in the ESC was a combination of a model approximation of the heavy goods vehicle and data obtained from on-road testing. The on-road testing recorded the road gradient (α), the wind speed (V_W) and wind direction (β). The vehicle parameters are shown in Fig.(5.2) with the associated block diagram representation used for the simulation shown in Fig.(5.3).

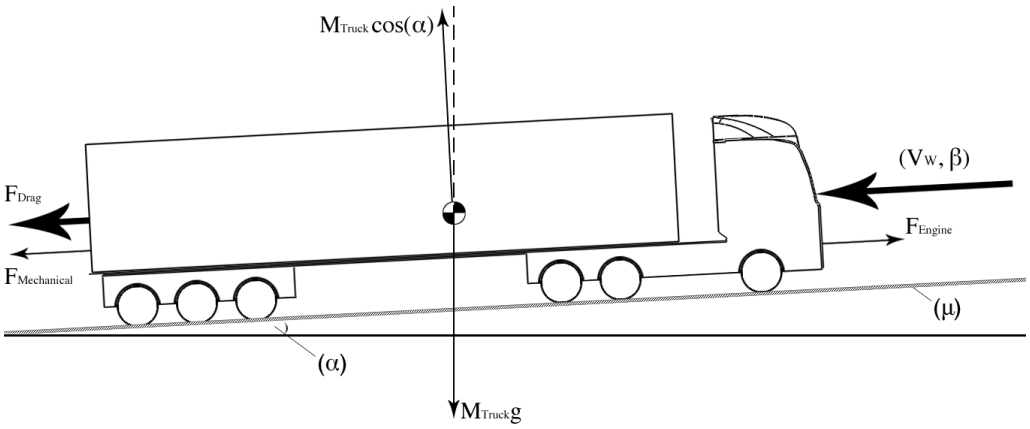

Figure 5.2: Plant Model (Heavy Goods Vehicle).

where V_W is the wind speed, β is the wind direction, $M_{Truck}g$ is the weight of the vehicle, μ is the coefficient of friction between the tyres and the road and α is the gradient of the road with respect to the horizon. F_{Drag}, $F_{Mechanical}$ and F_{Engine} are the forces arising due to the aerodynamic drag, mechanical resistance and the power from the engine, respectively. The centre of gravity of the vehicle is denoted by: ◒.

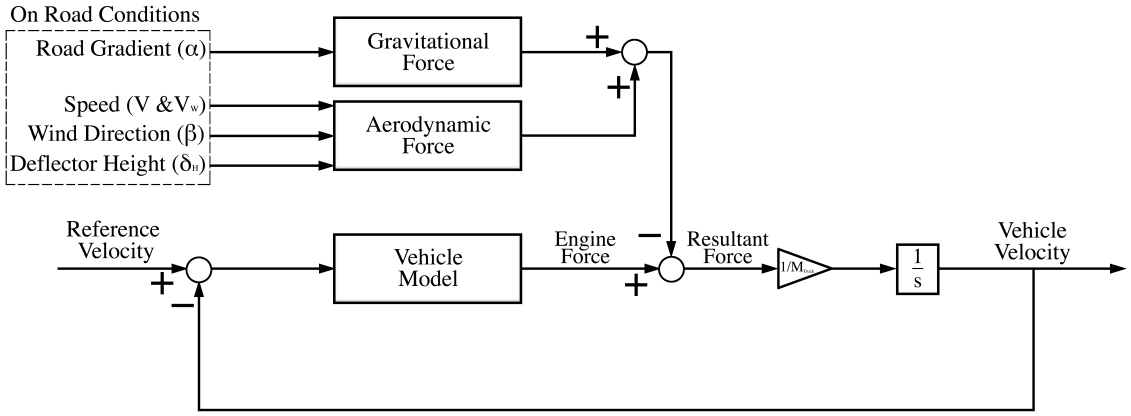

Figure 5.3: *Simulink*® Block Diagram of a HGV Plant.

The vehicle model is an idealised version of the vehicle with certain factors removed. Certain factors such as tyre pressure, the coefficient of friction of the tyre and vehicle suspension were not modelled. The simplification caused certain on-road conditions to differ greatly from that predicted by the model. An example is the heavy goods vehicle accelerating from rest at full power. The power applied on-road would cause slippage of the driving tyres and hence a reduction in the acceleration. The model, however, would predict a perfect adhesion and therefore constant acceleration.

Due to the active system operating only during steady state vehicle operation, the vehicle simplifications for ESC does not result in significant data loss. The on-road variables did not require a model as they were independent and therefore measured during the full scale testing phase of the research.

5.1.2.1 Vehicle Model

The vehicle model used within the plant (shown in Fig.(5.3)) is shown in Fig.(5.4).

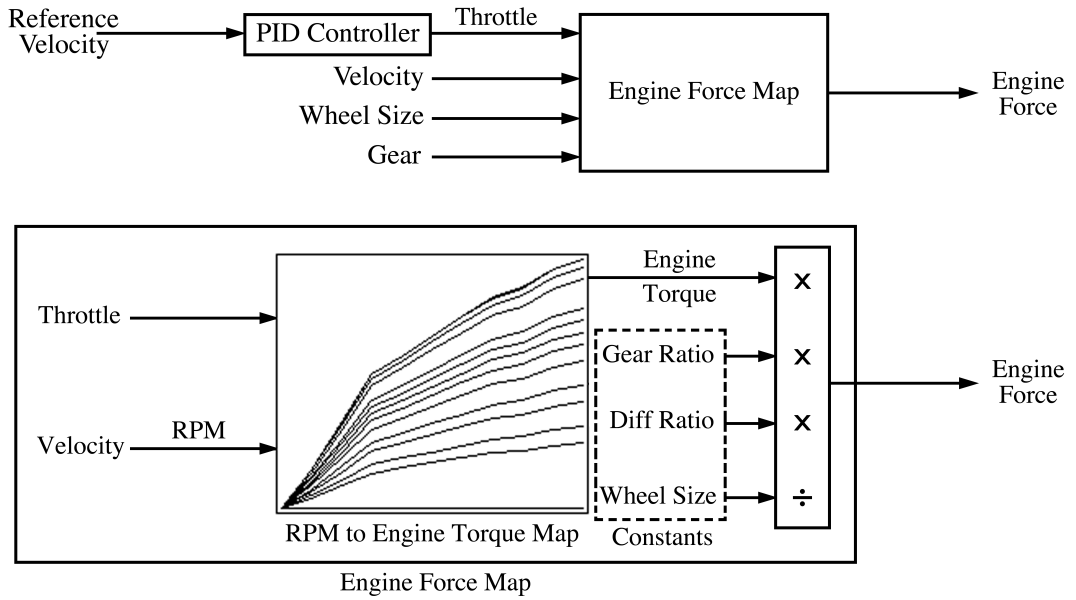

Figure 5.4: *Simulink*® Throttle and Velocity to Engine Force Map.

5.1.2.2 PID Speed Controller

The vehicle model used a reference input (the desired vehicle velocity) and a PID velocity controller to maintain this velocity (see Sec.(2.5.2 for more information on PID control)). The output from the PID controller is a throttle input into the engine force map. This output was either to increase, decrease or maintain the engine power depending on the requirement for more, less or constant speed, respectively.

Vehicles weighing over 7.5 tonnes within the EU are required by law to have a maximum velocity not exceeding 56 mph or 25 ms^{-1} [77]. Commercial vehicles therefore are fitted with speed restrictors limiting their maximum velocity. This results in the velocity of the vehicle, when not influenced by traffic or weather conditions operating at close to constant (maximum permissible) velocity for the duration of their journey.

5.1.2.3 Velocity to RPM

The velocity to RPM relation [78] is given by

$$RPM = \frac{V_{Truck} \times \text{Gear Ratio} \times \text{Diff Ratio}}{2\pi r_{Wheel}} \tag{5.1}$$

5.1.2.4 Engine Force

The throttle, velocity, wheel size and gear were then fed into an engine force map. In order to adjust the required engine force from the controller a conversion between velocity and RPM was required. This was required for the throttle output from the PID controller to have the correct engine force map for the RPM range the engine was operating at. Figure(5.5) shows the engine torque (T) as a function of the engine speed (RPM) for (a) Petrol and (b) Turbo Diesel engines.

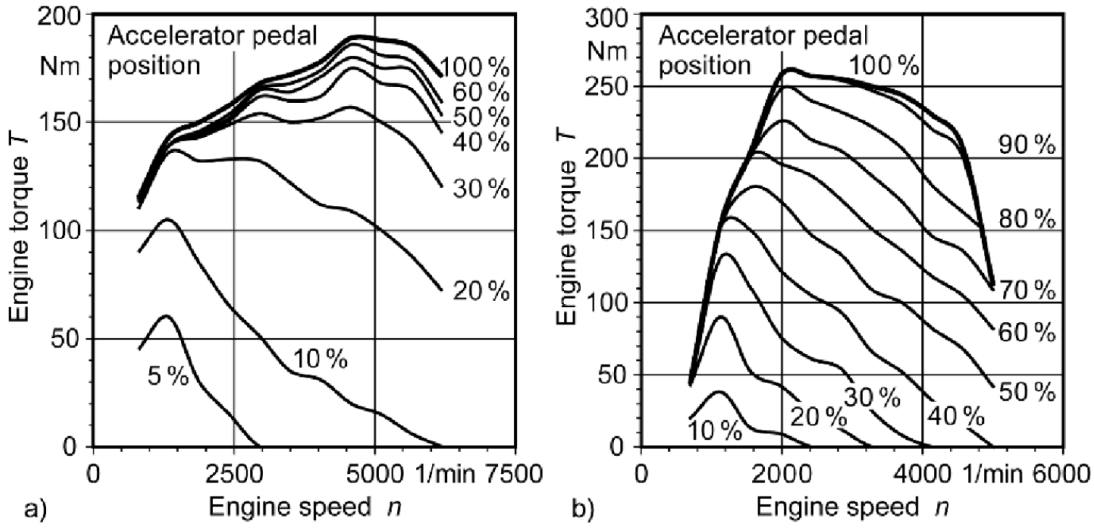

Figure 5.5: Engine Torque vs. RPM Map [78].

The turbo diesel engine map for the on-road vehicle, a Mercedes-Benz 2543 Axor was supplied the commercial partner Mercedes-Benz.

5.1.2.5 Resultant Force

The acceleration of a HGV can be obtained from Newton's Second Law

$$M_{Truck}\frac{dV_{Truck}}{dt} = F_{Total} \tag{5.2}$$

where F_{Total} is the total force acting on the vehicle and is given by

$$F_{Total} = F_{Engine} - [F_{Drag} + F_{Mechanical}] \tag{5.3}$$

where F_{Engine} is the engine force, $F_{Drag} = \frac{1}{2}\rho V_{Total}^2 C_D A$ and $F_{Mechanical} = M_{Truck}(g\sin(\alpha) + \mu g\cos(\alpha))$. $V_{Total} = V_{Truck} + V_{Wind}$, C_D is a function of the deflector height (δ_H) and

the wind yaw angle (β). C_D is determined through experimental wind tunnel testing of the vehicle. M_{Truck} is the mass of the truck, μ is the road friction coefficient and α is the road gradient.

Therefore the truck can be modelled by[1]

$$F_{Engine} - \left[\frac{1}{2}\rho(V_{Truck} + V_{Wind})^2 C_D(\delta_H, \beta)A + M_{Truck}(g\sin(\alpha) + \mu g\cos(\alpha))\right] = M_{Truck}\frac{dV_{Truck}}{dt} \quad (5.4)$$

5.1.3 Optimal Input (θ^*)

The optimal input (θ^*) or for a HGV, the optimal deflector height (δ_{Hopt}) is calculated based on data obtained from the wind tunnel testing. The aero look-up table shown in Figs.(5.6 and 5.7) was populated by the following on-road variables: wind direction (β), wind speed (V_W) and vehicle velocity (V_{Truck}).

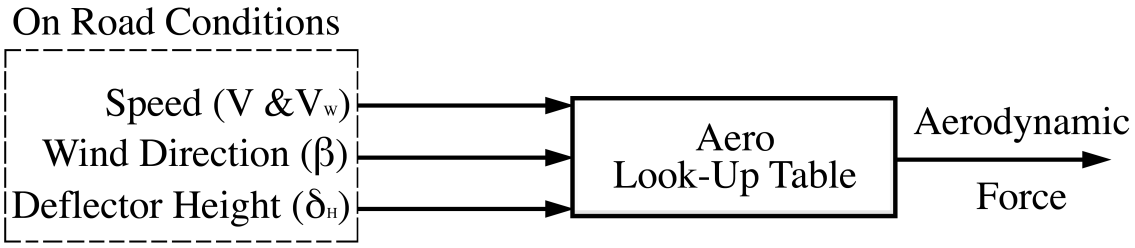

Figure 5.6: *Simulink*® Block Diagram of Aerodynamic Force.

[1]The total force should include an efficiency term that is a function of the vehicle velocity (V), however, this term is unknown. The system is therefore assumed to have no losses, whilst this was not a physically realistic assumption, it does not affect the accuracy of the results obtained from the extremum seeking control simulations [79].

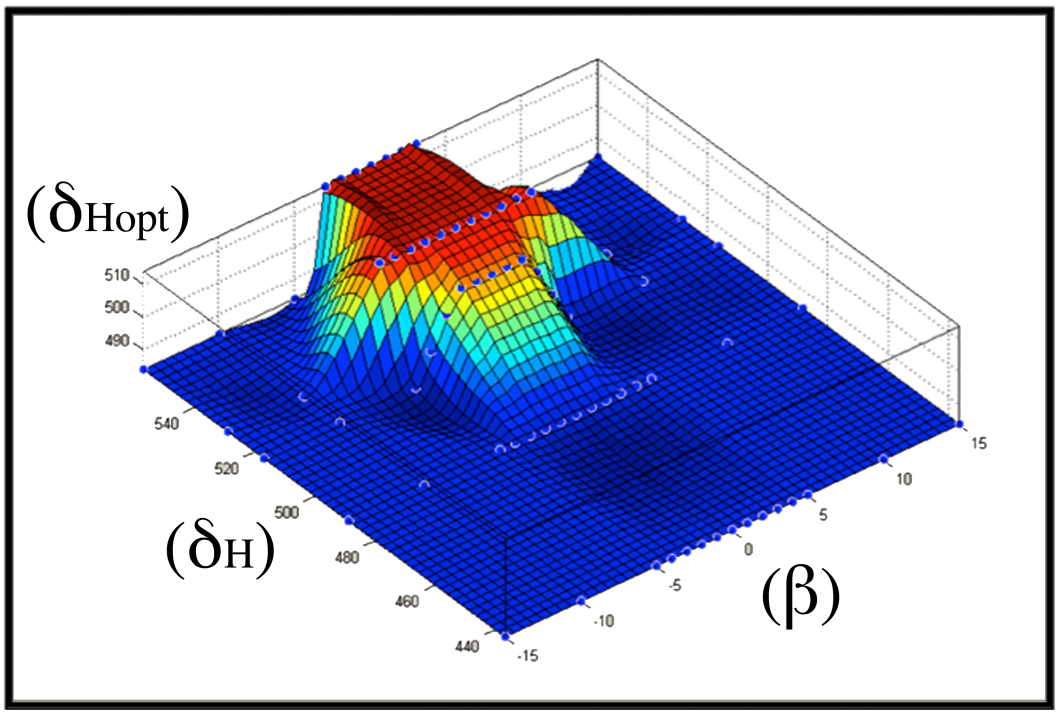

Figure 5.7: Aero Look-Up Table Used within *Simulink*® Model.

The aero look-up table determines δ_{Hopt} based on β, with cubic spline interpolation between wind tunnel data points.

5.1.4 Optimum of Plant (f^*)

Once δ_{Hopt} had been calculated the associated plant optimum (f^*) or $C_{D(Min)}$ is also known from the aero look-up table.

5.1.5 Output (y)

After f^* ($C_{D(Min)}$) has been calculated, the aerodynamic force can be calculated as an output from the aero look-up table. The aerodynamic force is given by

$$F_D = \frac{1}{2}\rho V_{Total}^2 C_{D(Min)} A \tag{5.5}$$

Therefore the instantaneous power required by the engine to overcome the aerodynamic force is given by

$$P_D = F_D \times V_{Total} = \frac{1}{2}\rho V_{Total}^3 C_{D(Min)} A \tag{5.6}$$

Using Eq.(5.3), the total force required by the engine is therefore a combination of the aerodynamic and mechanical force.

5.1.6 Plant Feedback (θ)

After calculation of the total engine force, the acceleration of the vehicle is then known. Using an integrator term in the *Simulink*® blockset, the velocity of the vehicle can be fed back to the speed controller in Sec.(5.1.2.2).

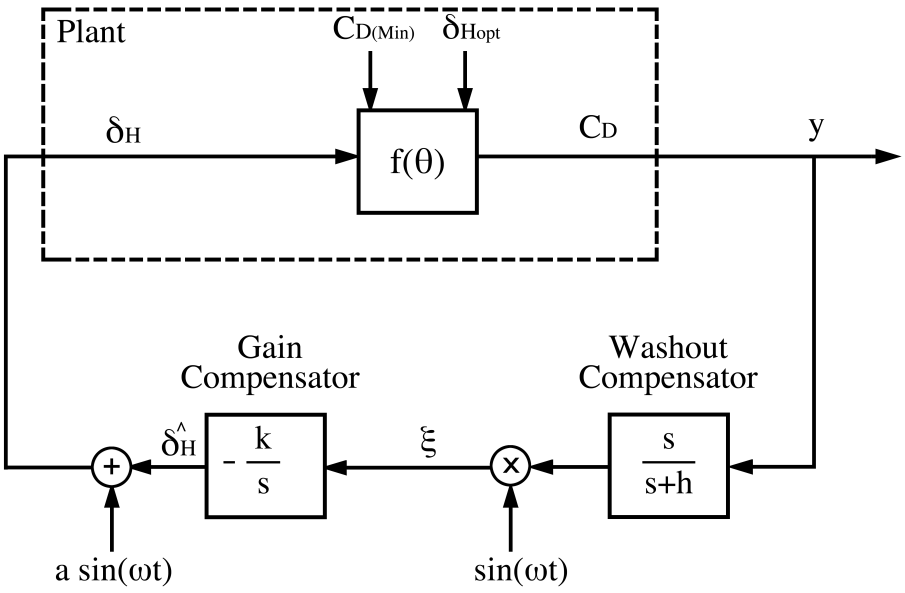

Figure 5.8: Extremum Seeking *Simulink*® Block Diagram for HGV Plant.

The output from the plant (θ), is then fed back into the system as a plant input. This input is then compared against the optimal input (θ^*) and if different, will adjust δ_H to reach the new δ_{Hopt}. The ESC algorithm is shown in Fig.(5.8) with the associated mathematics in Sec.(A.1) of Appendix A.

5.2 Prototype Controller (TRL4 - TRL7)

The prototype controller used a look-up table to determine the optimum deflector height (δ_{Hopt}). Wind tunnel testing was required to generate a look-up table containing δ_{Hopt} as a function of the container height, container separation (g/d_2) and yaw angle (β).

Due to the on-road conditions at this phase of the project being unknown, the accuracy of the data contained within the look-up table was of paramount importance. Investigation into larger container separations (g/d_2) was required to extend the range of available data. CFD simulations were used to model configurations that could not be experimentally tested.

The variables required for the prototype controller are shown in Fig.(1.9) in Sec.(1.6.2).

The prototype controller used for on-road data accusation had no prior information about the on-road conditions. The adjustment frequency of the actuators was therefore set to the minimum adjustment period of 300 seconds determined by the manufacturer (From Fig.(B.22) in Sec.(B.9.8) of Appendix B).

5.2.1 Hardware Overview

The hardware used in the development of the prototype controller is listed in Tab.(5.1).

Item	Description
Transducers	Omega Engineering PX138-0.3D5V
Linear Actuators	HIWIN LAS3
Microcontroller	Pi Innovo M100
H Bridge Controller	Devantech MD03
Range Sensor	SHARP IR GP2Y0A710K0F

Table 5.1: Prototype Controller Hardware.

5.2.1.1 Transducers

The transducers used for the on-road testing were PX138-0.3D5V produced by Omega Engineering, shown in Fig.(5.9).

Figure 5.9: Omega Engineering PX138-0.3D5V Transducer [71].

For further information about the transducers see Sec.(3.7) and Sec.(B.9.6) of Appendix B for the technical specifications.

5.2.1.2 Linear Actuators

The linear actuators used in the prototype controller were HIWIN LAS3 actuators, shown in Fig.(5.10).

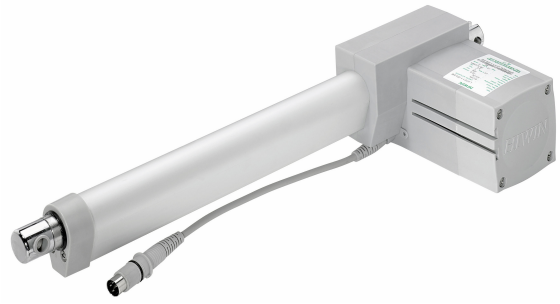

Figure 5.10: HIWIN LAS3 Actuators [80].

For the technical specification of the actuators see Sec.(B.9.8) of Appendix B.

5.2.1.3 Microcontroller

The microcontroller used for the controller prototype was a Pi Innovo M100 shown in Fig.(5.11).

Figure 5.11: Pi Innovo M100 Controller Unit [81].

The technical specifications of the ECU are shown in Sec.(B.9.9) of Appendix B. Due to the external mounting location of the ECU, the ECU was encased in a weatherproof protective casing shown in Fig.(5.12).

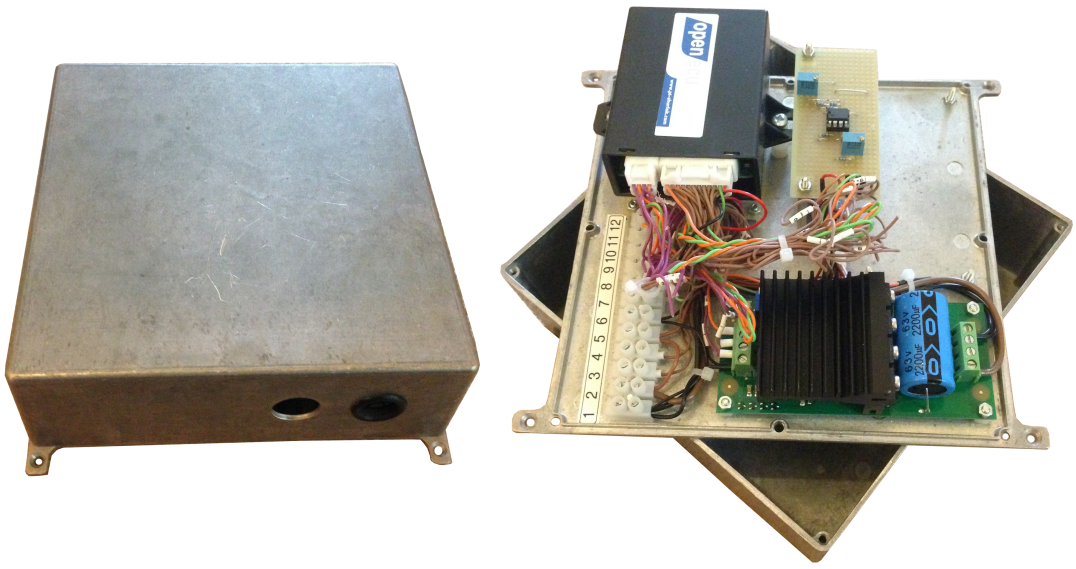

Figure 5.12: Weatherproof M100 ECU Case.

5.2.1.4 H Bridge Controller

To control the Direct Current (DC) actuators a 24 V H Bridge controller was required, shown in Fig.(5.13). A H Bridge controller allows a DC actuator to either extend or retract by reversing the polarity of the voltage applied to the actuator through use of internal switches.

The voltage required by the actuators was 24 V with the microcontroller requiring 12 V with a 5 V output for the logic gates. The H Bridge required a 5 V Pulse-Width Modulated (PWM) signal. PWM enabled the extension speed of the actuators to be controlled by selecting the desired pulsing frequency of the control signal. The H Bridge therefore used the 5 V logic output from the M100 ECU to supply 24 V to the actuators at the required extension speed.

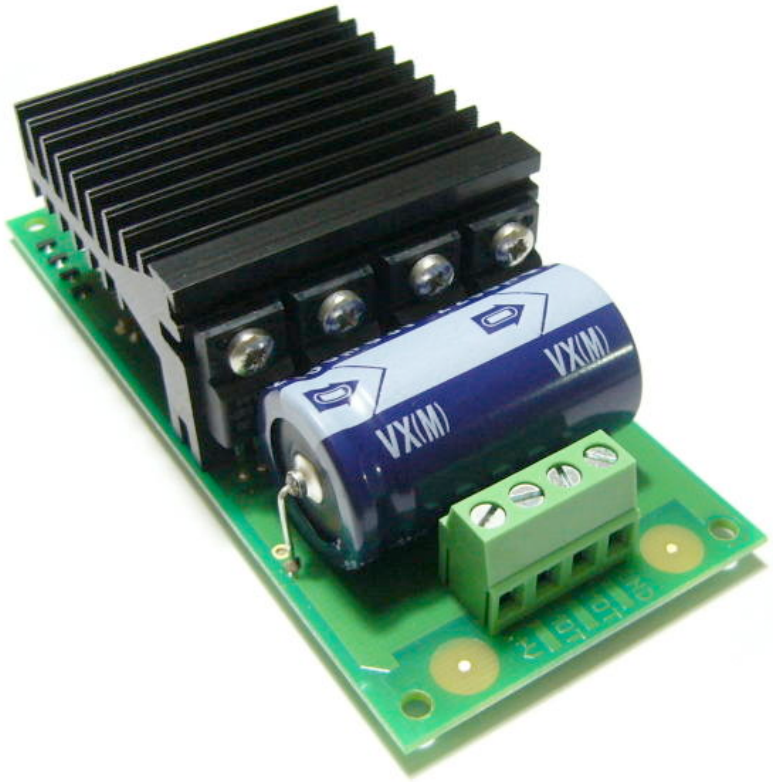

Figure 5.13: Devantech MD03 [82].

For the circuit diagram of the H bridge controller see Sec.(B.9.10) of Appendix B.

5.2.1.5 Range Sensor

The range sensor required to determine the container height and separation (g/d_2) was a Sharp GP2Y0A710K0F Infrared sensor. The sensor is shown in Fig.(5.14), the sensors required a 5 V excitation voltage supplied by the M100 ECU. The output from the sensor was 0 V - 5 V which was non linear with respect to distance. The output voltage corresponded to 0.00 m - 2.00 m, with the usable sensor range being 0.15 m - 2.00 m. Due to the voltage being non linear a calibration chart (shown in Fig.(B.27) in Sec.(B.9.11) of Appendix B) was programmed into the M100 ECU.

Figure 5.14: SHARP R GP2Y0A710K0F IR Sensor [83].

For the specification sheet of the range sensor see Sec.(B.9.11) of Appendix B.

5.2.2 Code Overview

The conversion of the control algorithm developed in Sec.(5.2.3) was achieved using Freescale™ Code Warrior. The code was written by the author in embedded C/C++ and complied using Python™. The code was debugged using a Pi Innovo M100 debugging board shown in Fig.(5.15). The ActiveFREDDIE control code is shown in Sec.(D.1) of Appendix D.

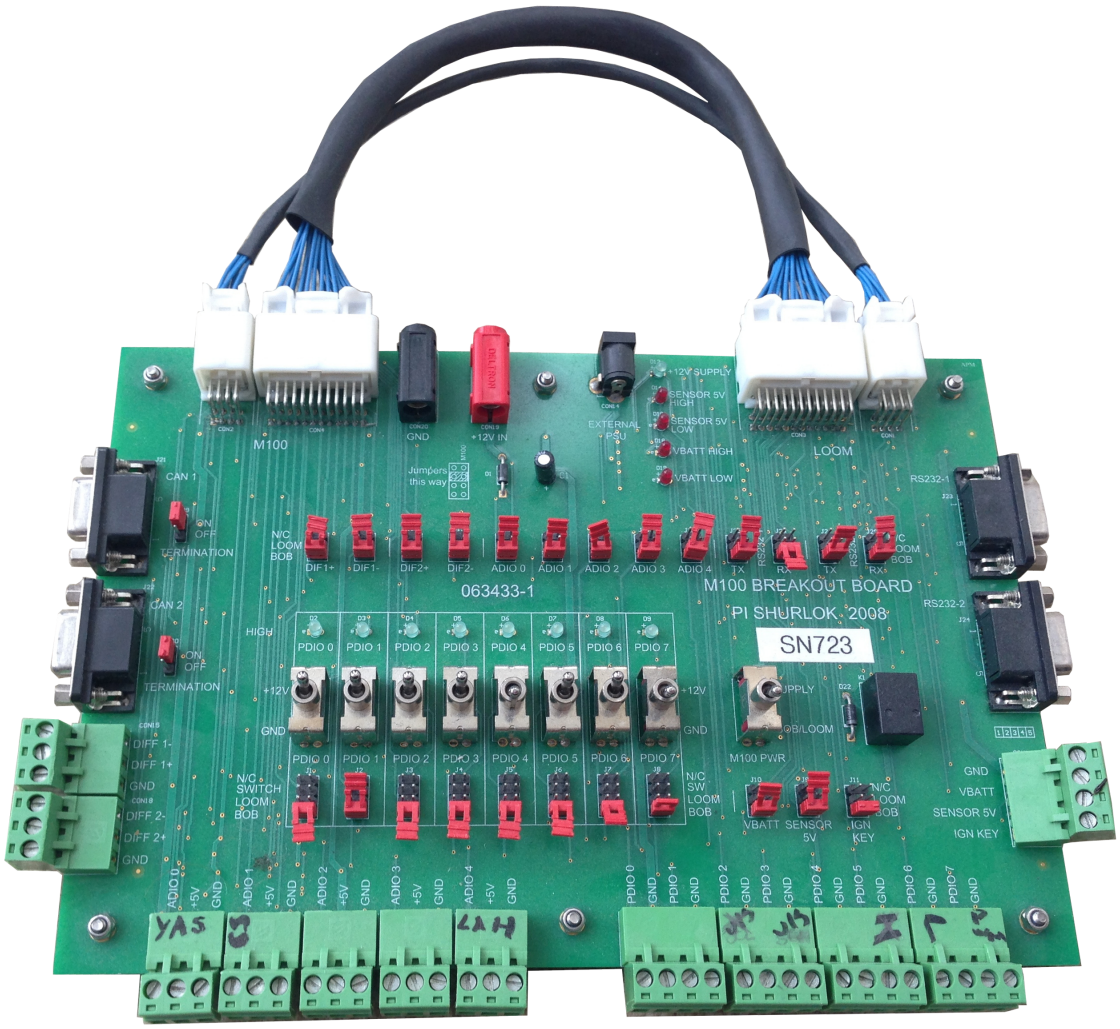

Figure 5.15: M100 ECU Debugging Board [81].

5.2.3 Prototype Controller Overview

The control algorithm used in the prototype controller is summarised below with a flowchart of the algorithm shown in Fig.(5.16). The acronyms used in the flowchart are shown in Tab.(5.2).

1. ***Initialisation:*** The initialisation occurs when the ignition line supplied to the microcontroller is raised to the high state (+24 V). The Container Height Sensor (CHS) begins pulsating infrared light, the time difference between emission and reception determines the distance the beam has travelled. Inserting

a distance (X m) corresponding to the minimum distance in meters the beam must travel in order to begin the control scheme.

This minimum distance imposes the criterion that a container must be present in order for the deflector to be active. If this criterion is not met, the scheme will then determine if the actuators are at the lowest position. If the actuators are not at the lowest position the microcontroller will lower the deflector to the minimum height where it will remain until the ignition line is grounded (ignition off) and the vehicle restarted.

If a container is detected the linear actuators are driven to minimum height. The actuators have pulse modulated feedback, providing a high accuracy of 1 pulse per 0.33 mm stroke. A result of no reference position feedback (e.g. a Hall sensor), is the requirement to drive the actuators to minimum position in order to reset the pulse counter to re-sync with the microcontroller. The deflector is then raised to the maximum height, if the deflector determines the container is no longer detected (i.e. the beam reports a distance $> X$ m) the deflector will stop at this height.

From the pulse accumulation, the height of the container (CH) is determined and is inserted into the control scheme. If the deflector extends to maximum extension without reporting a loss of container, the system will assume the maximum height of the container is the maximum height of the deflector.

2. ***Variable Collection:*** The variables collected are: CH and the container separation (CHS). These variables are then fed into the control scheme. After the CH and CHS variables have been inserted into the control scheme, the controller begins the periodic function of the routine.

   The Yaw Angle Sensor (YAS) and Deflector Height Sensor (DHS) begin periodic sampling. The Yaw angle sensor samples every 5 seconds and is averaged over 300 seconds (5 minutes). The DHS is sampled every processor cycle, the transition between high (+5 V) and low (0 V) states is then recorded as a single pulse and converted into a distance/extension.

   Periodic: The values of DHS and YAS are then inserted into the periodic control scheme ever 300 seconds, the look-up table determines the optimum deflector height (ODHS) and compares the current deflector height (DHS).

3. ***Control Scheme:*** If the optimum deflector height is lower than the current deflector height, the actuators will lower the deflector until the optimum is met. If the optimum is higher than the current deflector height, the actuators will extend until the deflector is at the optimum height. If the deflector is currently at the optimum, the actuators will not adjust the height of the deflector.

The control scheme repeats this sequence every 300 seconds, until the vehicle ignition line is grounded, whereby the actuators are driven to the minimum height and the controller reset.

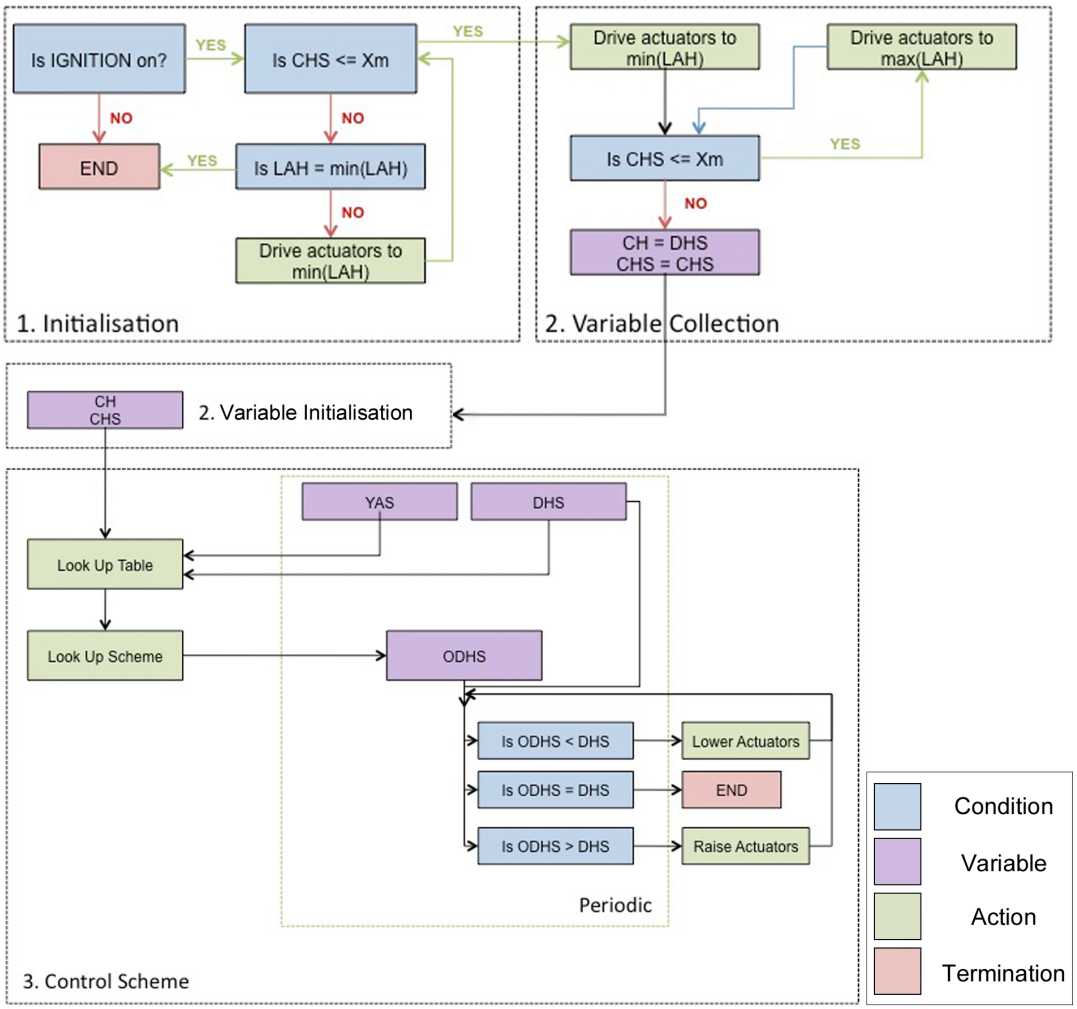

Figure 5.16: Control Scheme Flow Chart.

Acronym	Definition
CH	Container Height
CHS	Container Height Sensor
DHS	Deflector Height Sensor
ODHS	Optimum Deflector Height
LAH	Linear Actuator Height
Xm	Minimum Container Distance
YAS	Yaw Angle Sensor

Table 5.2: Control Scheme Flow Chart Key.

5.3 Production Controller (TRL7 - TRL9)

The production controller used on-road data obtained during testing of the prototype controller. The on-road variation of the wind direction (β) and wind speed (V_W) were measured during the prototype controller testing phase. The data obtained from this testing enabled estimation of the optimal adjustment frequency and also an estimation of the performance of the active system. The production controller required on-road data in order to perform these simulations.

The variables required for the production controller are shown in Fig.(1.10) in Sec.(1.6.3).

5.3.1 Full Scale Performance Estimation

The aim of control theory in the production level controller is to provide an estimation of the performance of the active system. In order to provide a net energy saving, the energy expended in moving the actuators must be less than the energy saved from the reduction in drag force. Section (5.3.1.1) details an estimation of the power required by the actuators whilst Sec.(5.3.1.2) simulates the energy saving as a function of the frequency of actuation.

5.3.1.1 Power Expenditure Estimation

The power required to operate an actuator is listed by the manufacturers specification sheet, shown in Fig.(B.22) in Sec.(B.9.8) of Appendix B.

Actuator Power Usage

$P_{Actuator} = I \times V$

where $I = 1.5$ Amps and $V = 24$ Volts.

Therefore: $P_{Actuator} = 36$ Js^{-1}

Drag Power Reduction

The force due to the drag of the vehicle is given by:

$F_D = \frac{1}{2}\rho v^2 C_D A$

The instantaneous power is therefore given by:

$P_D = F_D \times v = \frac{1}{2}\rho v^3 C_D A$

The resulting instantaneous power saving is given by:

$\Delta P_D = \frac{1}{2}\rho v^3 A(\Delta C_D)$

where $C_D = F_D/q_\infty A$, $\Delta C_D = C_{D(Non-Optimised)} - C_{D(Optimised)}$ and A = trailer width $\times$ trailer height for ($\delta_H \leq 1.0$) and trailer width x deflector height for ($\delta_H > 1.0$).

Total Power Expenditure

The total power expenditure for a given movement is therefore given as:

$$P_{Required} = \left(\Delta P_D \times \frac{1}{\text{frequency of adjustment}}\right) - (P_{Actuator} \times t_{Operation}) \qquad (5.7)$$

Example

An example of Eq.(5.7), is a zero yaw optimised deflector at a height ratio (δ_H) of 0.994 from Table(6.1) in Chapter 6, requiring movement to $\delta_H = 0.988$ for a $+1^\circ$ yaw angle. For the 517 mm deflector tested, this equates to a full scale change of 24 mm in the deflector height.

- $\Delta C_D = 0.7\%$ (A reduction from 0.544 to 0.540 at $+1^\circ$ yaw).
- $t_{Operation} = 1.2$ seconds (From Fig.(B.22) in Sec.(B.9.8) of Appendix B), the actuators are able to move at 20 mm per second with the supplied power, therefore a full scale height change of $8\times$(514 mm - 511 mm) = 24 mm, would take $\frac{24}{20} = 1.2$ seconds.
- $P_{Actuator} = 36$ Js^{-1}

Therefore the minimum frequency of adjustment would relate to zero total power expenditure from the four actuators, which is given by:

frequency of adjustment = $f_{adjustment} = \left(\Delta P_D \times \frac{1}{(4\times P_{Actuator}\times t_{Operation})}\right)$

Substituting in the values gives:

$f_{adjustment} = \frac{266.9\text{Js}^{-1}}{(4\times 36\text{Js}^{-1}\times(1.2s))}$

$f_{adjustment} = 1.54$ Hz or 0.65 seconds.

This result implies that during operational velocities, any frequency less than 1.5 Hz will result in a net energy saving. As a result the limiting factor on the adjustment rate is not the energy expenditure on adjusting the actuators.

5.3.1.2 Optimal Adjustment Frequency

Results obtained from the full scale on-road testing in Sec.(3.7) were used in conjunction with the *Simulink*® model created in Sec.(5.1). The wind speed (V_W), wind angle (β) and truck velocity (V) values recorded by the data logger were used as inputs for the model, shown in Fig.(5.17).

The model compared the difference in drag coefficient (C_D) of the optimised vs. non-optimised deflector obtained from wind tunnel testing (shown as the wind tunnel look-up table in Fig.(5.17)). The resultant reduction in the drag force (F_D) due to optimisation was then multiplied by the total velocity to obtain the instantaneous power.

Therefore by varying the frequency of adjustment of the deflector, the total energy saved over a typical vehicle operational run could be estimated and the optimum adjustment time could be determined.

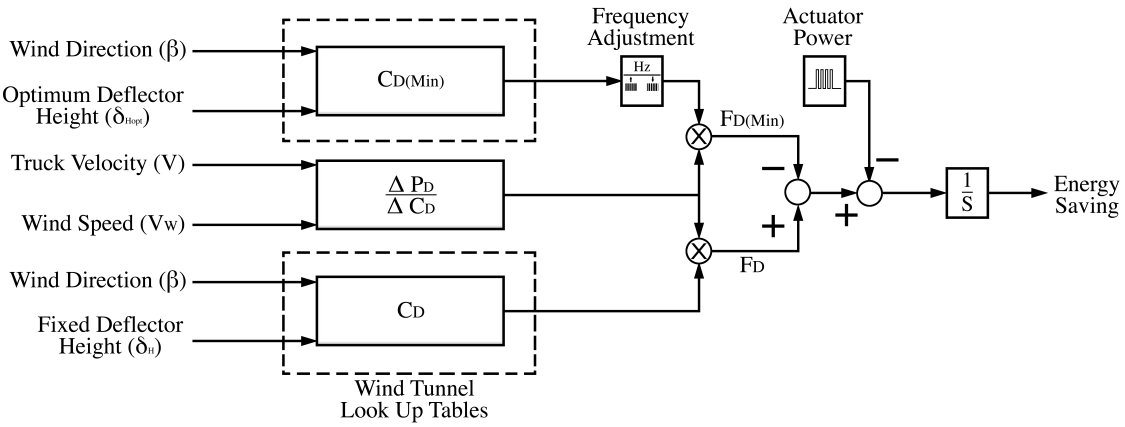

Figure 5.17: *Simulink*® Estimation of Optimal Adjustment Frequency.

Chapter 6

Results and Data Analysis

The results section is divided into four subsections with details on the objectives of each subsection listed below:

Experimental Testing (Sec.(6.1)): Wind tunnel testing at the Cranfield $8' \times 6'$ low speed wind tunnel. Testing was conducted to obtain the optimum deflector height ratio (δ_H) and determine its relationship with yaw angle (β) and container separation (g/d_2). Investigation into the pressure distribution on the vehicle and establish a suitable location for a differential pressure coefficient (ΔC_P) that relates to β. Determine suitable location for the instrumentation used for full scale testing.

3D Computational Results (Sec.(6.2)): Computational Fluid Dynamics (CFD) simulations to enable prediction of larger values of (g/d_2) that could not be experimentally tested. Reynolds-Averaged Navier-Stokes (RANS) model chosen from 2D computational results are shown in Sec.(F.1) of Appendix F.

Full Scale Testing (Sec.(6.3)): Investigation into road variation of β, wind speed (V_W) and the estimated yaw angle (β_{Est}) predicted from ΔC_P. Comparison of frequencies obtained from on-road and Large Eddy Simulation (LES) of trailer wakes. Estimation of the accuracy of β_{Est}. On-road and off-road fuel efficiency tests on the prototype controller.

Control Scheme (Sec.(6.4)): Evaluation of Extremum Seeking Control (ESC) algorithm applied towards Active Flow Control (AFC). Determination of optimal actuator adjustment frequency of production control scheme. Full scale testing of semi-active system vs. static system and estimation of the performance of the fully active system compared to the static system.

6.1 Experimental Testing

6.1.1 The Effect of Yaw Angle on the Vehicle's C_D

A preliminary wind tunnel test was conducted to ensure the results obtained were in good agreement with previous values obtained by Cooper [64]. The initial results were compared to measurements obtained in the National Research Council (NRC) 2 m x 3 m wind tunnel in model form and also at full scale in the NRC 9 m x 9 m Low Speed Wind Tunnel.

The test conducted in the NRC 2 m x 3 m tunnel used a $1/8^{th}$ scale model (shown in Fig.(6.1)) at 30 ms^{-1} over a yaw angle range of $(-20° \leq \beta \leq +20°)$. The model dimensions used in the test were similar to the Cranfield model and the results obtained by Cooper using a wind tunnel velocity of 30 ms^{-1} were 'virtually identical to the results obtained from full scale testing' [64]. The results for the scale tests are shown in Fig.(6.2).

Figure 6.1: Cranfield Scale Model (Left) and NRC Scale Model (Right) [64].

The results obtained from the preliminary test were in good agreement with those obtained by Cooper [64]. The Cranfield model exhibited a lower drag coefficient (C_D) of 0.54, compared to the NRC model C_D of 0.57 for zero degrees yaw angle. This lower drag coefficient continued over the yaw angle range of $(-5° \leq \beta \leq +5°)$.

The lower drag of the Cranfield model was partly due to the more aerodynamic design of the cab over engine (COE) configuration, compared to the cab behind engine (CBE) design of the North American tractor-trailer unit. The decrease in drag coefficient for the NRC vehicle at greater yaw angles was achieved through the addition of cab side extenders. The NRC vehicle was fitted with an "aero package" consisting of a roof fairing, cab side extenders and cab skirts.

[1]* Reproduced from Cooper [64]

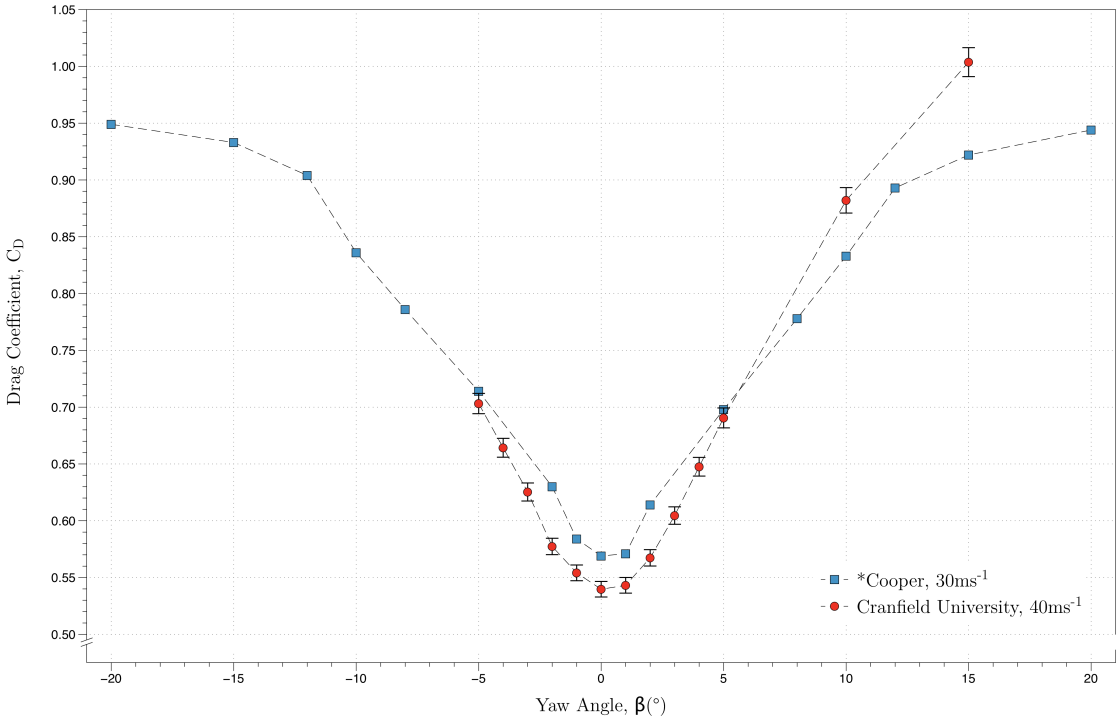

Figure 6.2: C_D[1]Variation with β.

The NRC vehicle as a result, had additional cab side extenders compared to the Cranfield baseline model. The side extenders have been found to give a wind-averaged drag reduction ($\overline{C_D}$) of 0.0123 by Leuschen et al. [31], which could account for the deviation from the Cranfield model at higher yaw angles.

6.1.2 The Effect of the Deflector Height on the Vehicle's C_D

Due to most UK commercial vehicles employing varying trailer heights, a relationship between the trailer and deflector height mismatch has been used to non-dimensionalise the data. The mismatch between container and deflector height is given by

$$\delta_H = \frac{d_1}{d_2} \tag{6.1}$$

where d_1 and d_2 are defined as half the deflector height and half the trailer height

respectively (shown in Fig.(6.3)). The tractor to trailer separation (g) was fixed at 345 mm, equating to a g/d_2 value of 1.335 for the preliminary tests. A value of 1.0 for δ_H infers a matched cab to trailer height, 0.9 and 1.1 correspond to a 10% lower and 10% higher trailer, respectively.

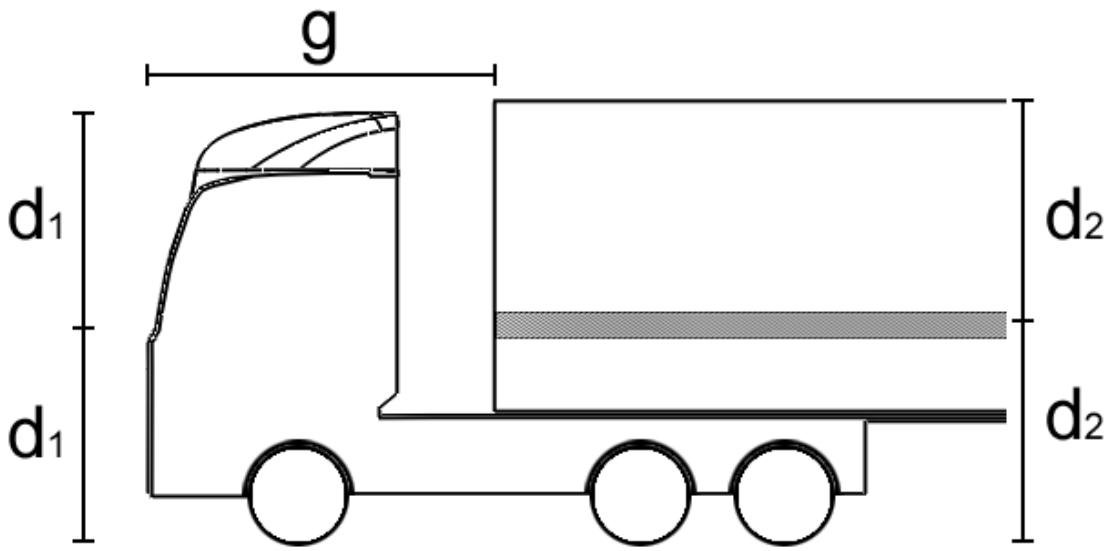

Figure 6.3: Tractor-Trailer in Tandem Notation.

The results obtained from the variation of the deflector height for given deflector to trailer height ratios using a fixed separation are shown in Fig.(6.4).

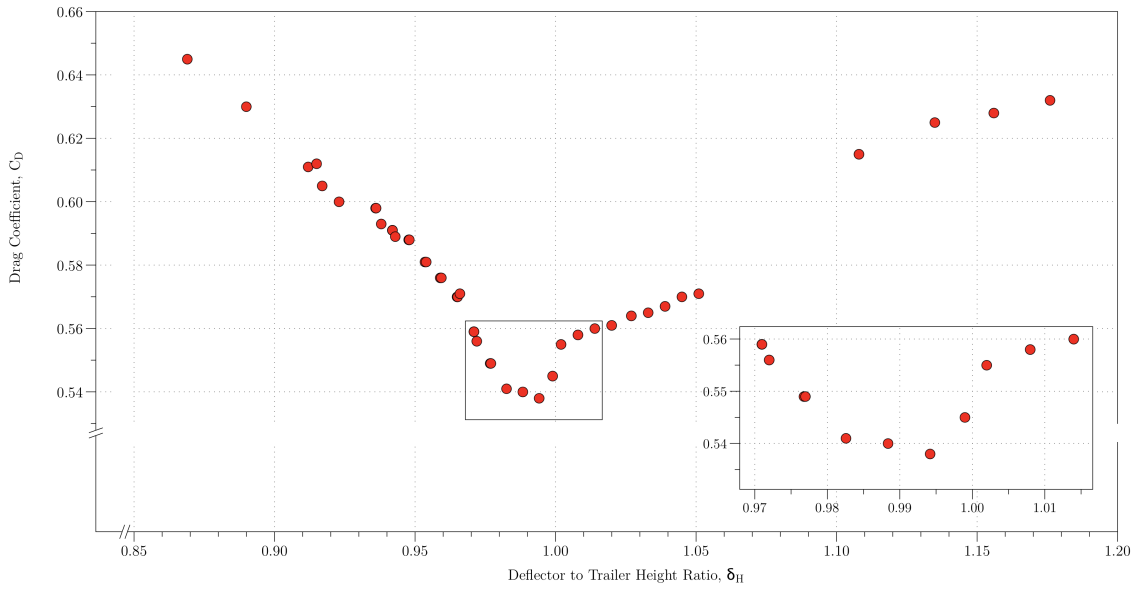

Figure 6.4: C_D Variation with δ_H for $\beta = 0°$ and $g/d_2 = 1.335$.

The results indicated that for a given trailer height and separation, at 0° yaw angle, there exists an optimum deflector height that produces the lowest drag configuration. The deflector height ratio (δ_H) that produced the lowest C_D was 0.994, approximately the same height as the container (a difference of 2.4 cm at full scale compared to the trailer height and equating to 8% of the actuator extension length). A sharp rise in the C_D was achieved either side of this optimum, a rise in the C_D of 18% was achieved for a 0.1 (10%) change in δ_H. This result highlights the importance of the optimum deflector height on the overall aerodynamic drag of the vehicle.

The results also highlight the importance of accurate extension measurement. If the error on the measurement of the actuator extension is significant, the drag increase due to an incorrectly aligned deflector would therefore be significant. The actuators used for the full scale testing were Hiwin LAS3 pulse feedback actuators (shown in Fig.(B.22) in Sec.(B.8) of Appendix B). The resolution of the sensors was 0.3175 mm per pulse, with a 300 mm total extension, this equated to a full scale error measurement of 0.1% or ± 0.317 mm. The high accuracy of the actuators ensured precise deflector positioning was achieved.

6.1.3 The Effect of Yaw Angle on the Optimum Deflector Height

The results from the optimum deflector height experiment indicated that an optimum height exists that minimises the C_D for 0° yaw angle. The effect of yaw angle on this optimum height was then investigated. The trailer and deflector height mismatch ratio (δ_H) was limited to the range ($0.94 \leq \delta_H \leq 0.99$) to give an achievable test matrix.

Figure (6.5) shows the 0° and +5° yaw angle effects on the C_D and optimum deflector height, respectively. The results from other yaw angles tested is shown in Fig.(E.1) in Sec.(E.1) of Appendix E.

Figure(6.5) shows clearly that for a fixed yaw angle (+5°) there is an optimum deflector height (δ_H) in the range ($0.965 \rightarrow 0.977$). The graph shows an increase in the drag coefficient for a deviation in deflector height away from this minimum. The results revealed that an increase in 5° yaw angle reduces the optimum deflector height (δ_{Hopt}) by 3.0%. The result of a different optimum deflector height from the Zero Yaw Optimised (ZYO) height arises due to the three dimensional geometry of the deflector. The three dimensional geometry resulted in a steeper velocity profile for the freestream velocity at increased yaw angle. Due to the deflector geometry, it was found that the optimum deflector height decreased for increasing β.

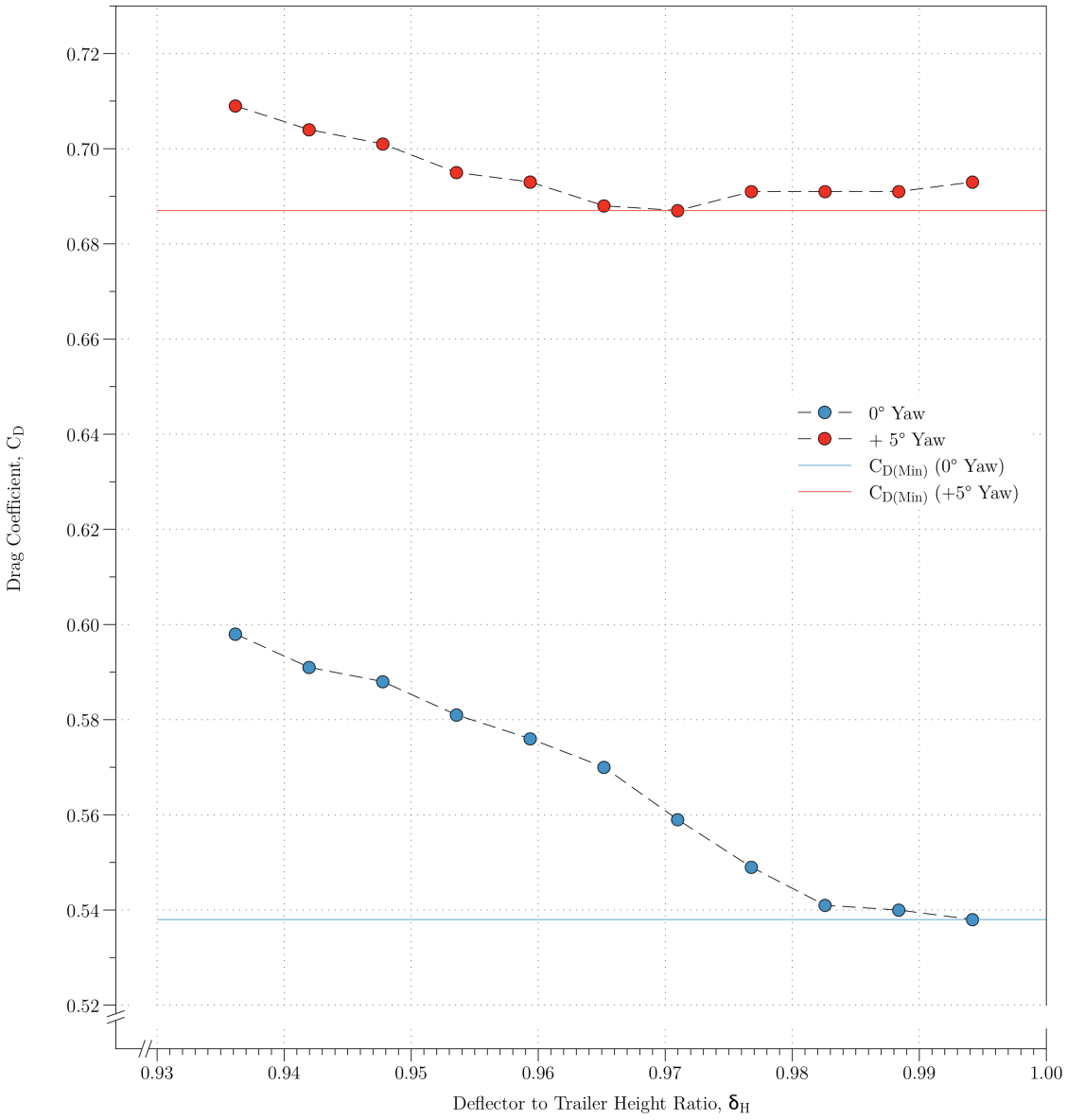

Figure 6.5: C_D Variation with Deflector Height Ratio (δ_H) for $\beta = 0°$ and $\beta = +5°$.

6.1.4 The Variation of C_D for δ_H and δ_{Hopt}

The variation of the deflector height provided a range of drag coefficients. When the deflector was at the optimum height (δ_{Hopt}) it corresponded to the minimum drag coefficient ($C_{D(Min)}$). The δ_H that corresponded to the Zero Yaw Optimised case provided ($C_{D(ZYO)}$) and the δ_H that created the highest drag coefficient ($C_{D(Max)}$).

Figure(6.6) shows the variation of three deflector heights used: the optimum deflector height ($\delta_{Hopt}(\beta)$), the zero yaw optimised deflector height (δ_{Hopt}) and the deflector height that generated the largest aerodynamic drag (δ_H). The data is shown in tabular form in Tab.(E.1) in Sec.(E.1) of Appendix E. The results are summarised in Tab.(6.1) with the maximum C_D as a percentage savings shown in Tab.(6.2) with the wind-averaged drag coefficients shown in Tab.(6.3).

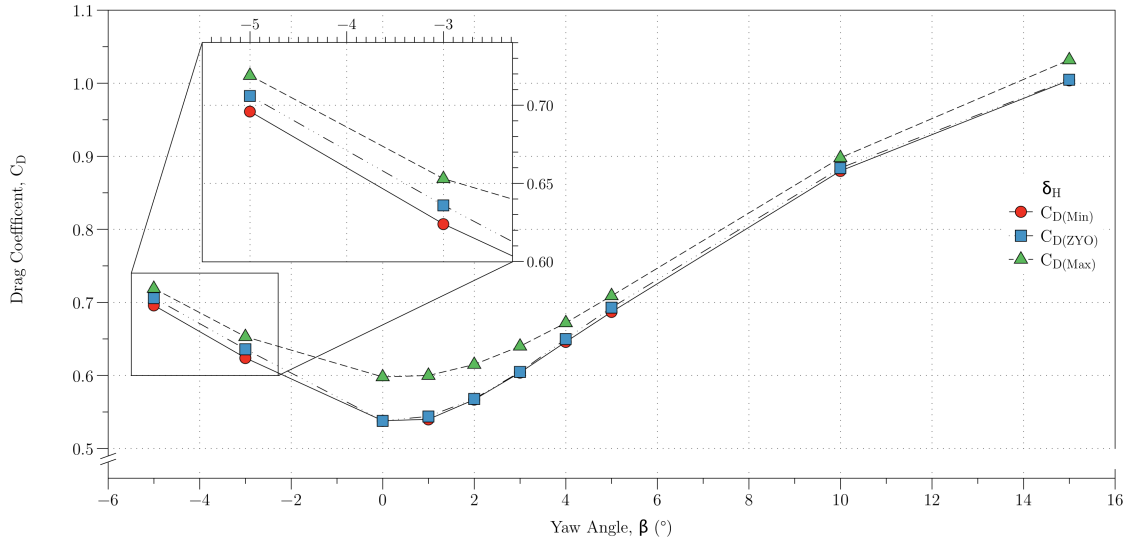

Figure 6.6: C_D Variation with Yaw Angle (β) for Various Deflector Height Ratios (δ_H).

$\beta(^\circ)$	Optimum Deflector Height Ratio (δ_{Hopt})	C_D
-5	0.965	0.696
-3	0.971	0.624
0	0.994	0.538
1	0.988	0.540
2	0.983 & 0.988	0.567
3	0.983	0.604
4	0.983 & 0.971	0.646
5	0.971	0.687
10	0.965	0.880
15	0.988	1.004

Table 6.1: Optimum Deflector Height Ratio as a Function of Yaw Angle (β).

The result obtained from Tab.(6.1) show that the optimum deflector height ratio (δ_{Hopt}) drops as the yaw angle increases up to +10°. The difference in optimum deflector height for +5° and -5 ° yaw angle is likely due to an asymmetry present within the model. The dual optimum achieved for +2° and +4° implies that the optimum deflector height is located between these values (if a local minimum exists), but cannot be determined from the experimental results without the use of a thinner ($< 3mm$) deflector spacer. The increase in optimum deflector height from +10° to +15° is unexpected and is likely a 3D effect present due to the tractor-trailer cavity's vortices interaction with the local flow velocity field.

	Yaw Angle $\beta(^\circ)$									
C_D	-5	-3	0	1	2	3	4	5	10	15
$C_{D(Max)}$	0.719	0.653	0.598	0.600	0.615	0.640	0.672	0.709	0.898	1.032
$C_{D(ZYO)}$	0.706	0.626	0.538	0.544	0.567	0.605	0.650	0.693	0.884	1.005
$C_{D(Min)}$	0.696	0.624	0.538	0.540	0.567	0.604	0.646	0.687	0.880	1.004
$\delta C_{D(Max-Min)}$	0.023	0.029	0.060	0.060	0.048	0.036	0.026	0.022	0.018	0.028
$\delta C_{D(ZYO-Min)}$	0.010	0.002	0.000	0.004	0.000	0.001	0.004	0.006	0.004	0.001
$C_{D(Max-Min)}\%$	3.2	4.5	10.1	10.0	7.8	5.6	3.8	3.0	2.0	2.7
$C_{D(ZYO-Min)}\%$	1.4	0.3	0.0	0.8	0.0	0.2	0.6	0.9	0.4	0.1

Table 6.2: C_D Coefficients and Percentage Saving for Max, Zero Yaw Optimised and Min Configurations.

$\overline{C_D}$	Value
$\overline{C_{D(Max)}}$	1.507
$\overline{C_{D(ZYO)}}$	1.395
$\overline{C_{D(Min)}}$	1.388
$\overline{C_{D(Max-Min)}}\%$	7.4
$\overline{C_{D(ZYO-Min)}}\%$	0.5

Table 6.3: Wind-Averaged Drag Coefficients and Percentage Saving for Max, Zero Yaw Optimised and Min Configurations.

The wind-averaged drag coefficient (WADC) is described in further detail in Section (2.4.5.4), with the WADC calculation shown in Sec.(E.5) of Appendix E.

Table (6.2) shows a summary of the potential percentage reduction in drag coefficient (C_D) for various configurations. Table (6.3) shows that a wind-average drag coefficient reduction of up to 7.4% could be achieved if the deflector is set to the optimum configuration when compared to the highest drag configuration. If the deflector is already adjusted to zero yaw optimum (ZYO), a further wind-averaged drag reduction of 0.5 % could be achieved through active control.

Due to the different tractor-trailer combinations, the assumption that the cab deflector is at ZYO is a very improbable one and as such the actual saving through active control will be closer to the highest drag configuration ($\overline{C_{D(Max-Min)}}$) of 7.4%.

6.1.5 The Effect of Container Separation on the Optimum Deflector Height

To investigate the effect of container separation on the optimum deflector height three additional container separations of 50.8 mm, 121.0 mm and 146.0 mm were used in conjunction with an additional trailer height of 500.0 mm.

The effect of separation of two bluff bodies on the drag coefficient was investigated by Koenig et al. [84]. The notation used to relate the ratio of frontal area and gap separation is shown in Fig.(6.7) with the experimental results shown in Figs.(6.9 and 6.10).

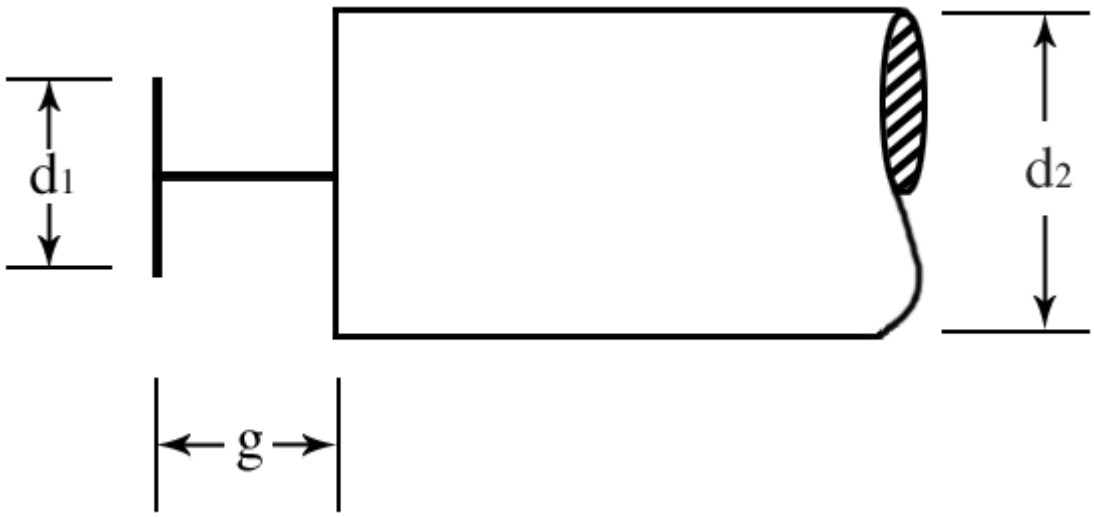

Figure 6.7: Bluff Bodies in Tandem Notation [84].

Thus for a model truck and trailer in tandem, g = (container to trailer separation + cab depth (278.0 mm)).

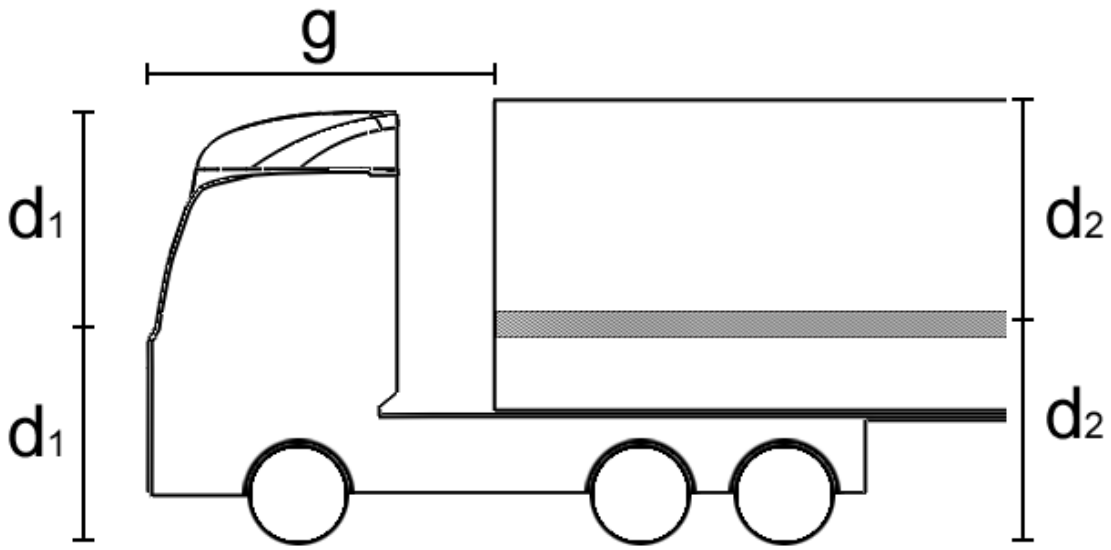

Figure 6.8: Notation used for Tractor-Trailer in Tandem.

For a variable height deflector and fixed trailer height, the d_1/d_2 ratio of

$$\delta_H = \frac{d_1}{d_2} = 0.968 \rightarrow 1.034 \tag{6.2}$$

For the three separations tested, this equated to g values of 328.8, 399.0 and 419.0 mm. This gave a g/d_2 ratio of

$$g/d_2 = 1.315 \rightarrow 1.676 \tag{6.3}$$

The variation of C_D with g/d_2 is shown in Fig.(6.10). The d_1/d_2 values for the model configurations have been plotted along with the data obtained by Koenig [84] in Fig.(6.11) for comparison.

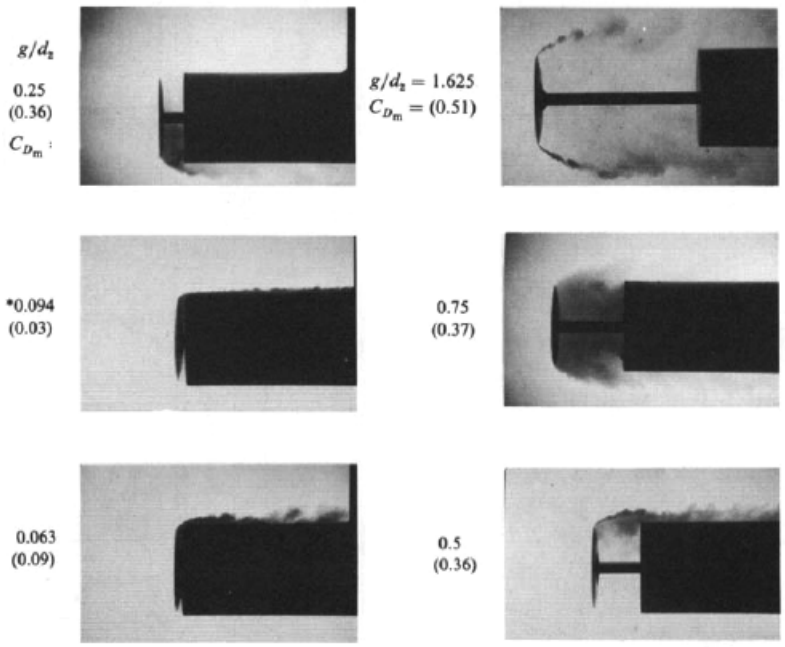

Figure 6.9: C_D Variation with g/d_2 [84].

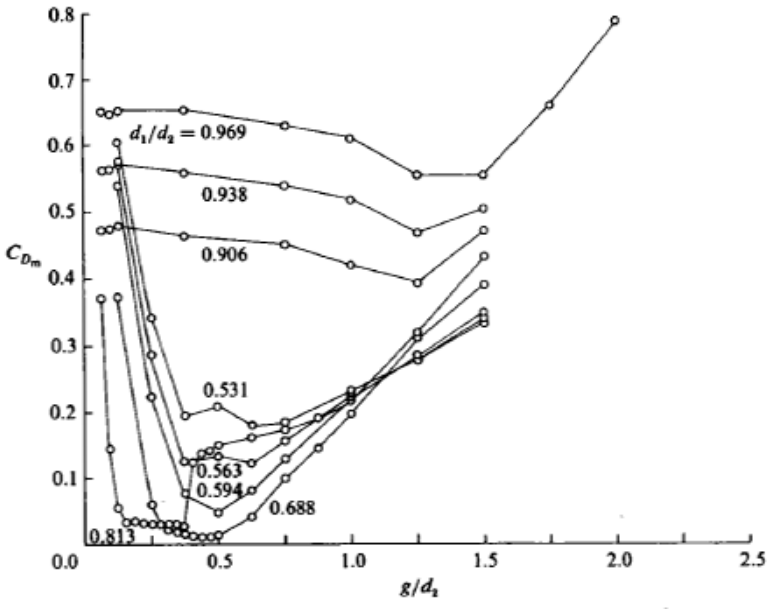

Figure 6.10: C_D Variation with g/d_2 for Various d_1/d_2 Configurations [84].

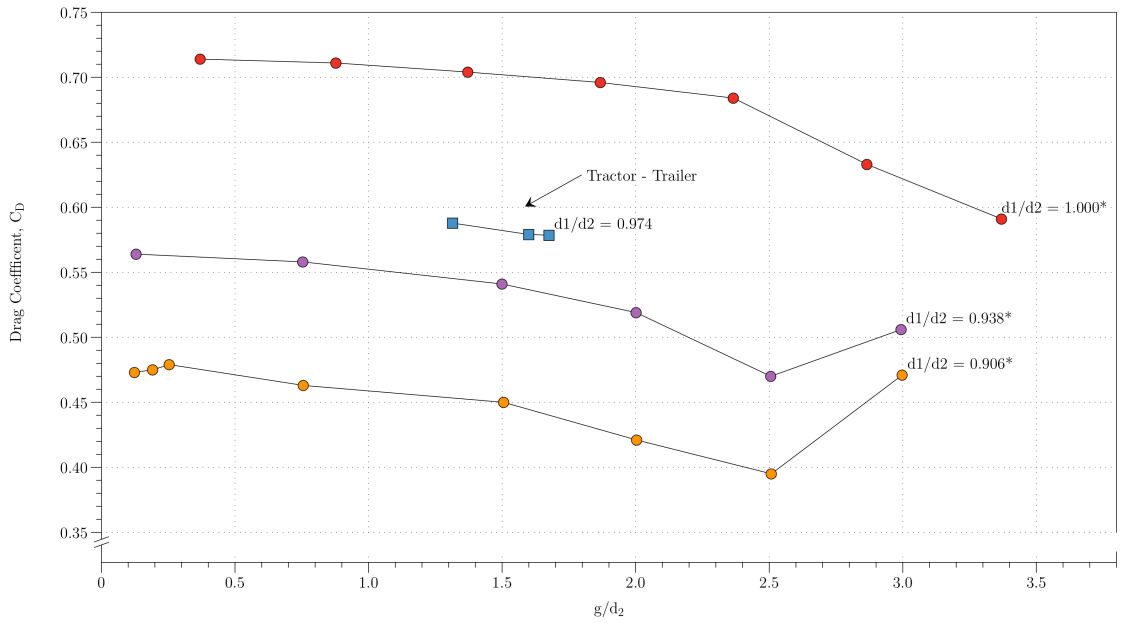

Figure 6.11: Comparison[2]of Tractor-Trailer C_D Variation with Varying g/d_2.

6.1.6 Variation of C_D with g/d_2 for Various δ_H

The variation of C_D with g/d_2 is shown in Fig.(6.12). Data obtained by Koenig et al. [84] showed a strong dependence on the gap spacing (g/d_2) on the C_D produced by bluff bodies. Comparison of the results obtained from variation of the container separation, showed that the C_D values obtained for the separations tested lie within the linear region shown in Fig.(6.11), predicted by Koenig et al [84].

From the container separations tested (g/d_2), the C_D variation revealed that an optimum deflector height ratio (δ_H) existed for each separation. An increase of 5.0% in the C_D over the optimum height ratio was achieved at $g/d_2 = 1.315$. An increase in C_D of 2.3% and 2.5% was obtained from the 1.600 and 1.676 container separations, respectively. The results are shown in Tab.(E.2) in Sec.(E.2) with the results plotted in Figs.(E.2 - E.4) in Sec.(E.2) of Appendix E.

[2]Data Denoted with * Reproduced from Koenig et al. [84]

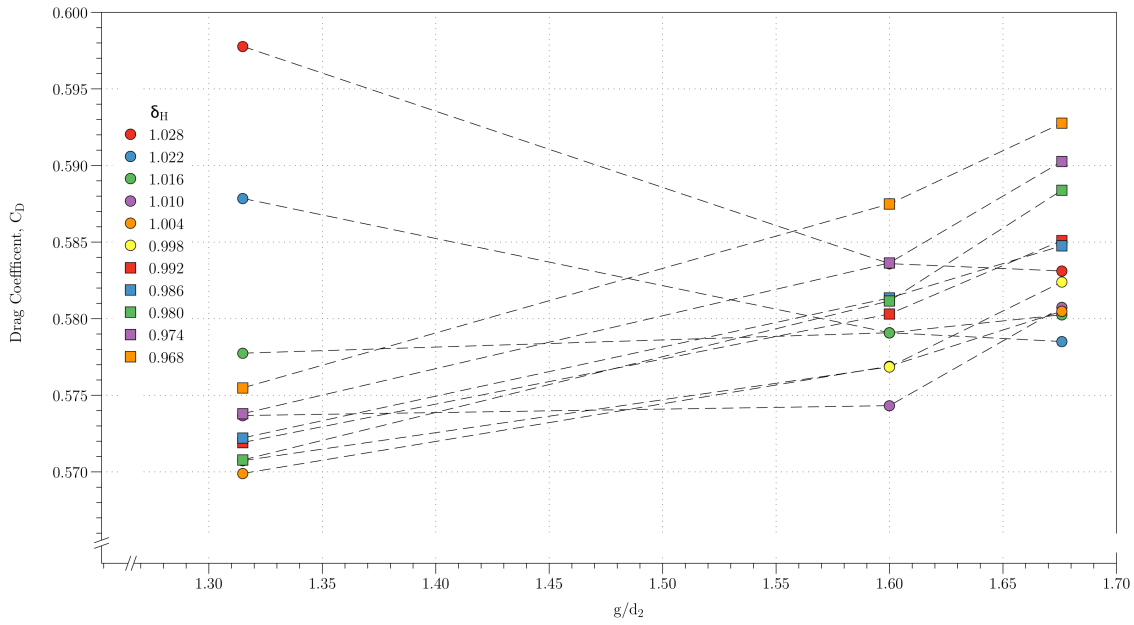

Figure 6.12: Tractor-Trailer C_D Variation with Varying g/d_2.

$\beta(^\circ)$	Optimum δ_H (g/d_2)		
	1.315	1.600	1.676
-17.5	0.968	1.022	1.028
-15	0.980	1.022	1.028
-10	0.968	0.980	0.992
-5	0.992	0.968	0.968
0	0.992	0.986	0.974
5	0.992	0.968	0.968
10	0.986	0.986	0.968
15	0.992	1.022	1.028
17.5	0.986	1.028	1.028

Table 6.4: Optimum δ_H vs. Yaw Angle (β) for Various g/d_2.

Figure (6.13) shows the optimum deflector height from Tab.(6.4) with the corresponding C_D in Fig.(6.14).

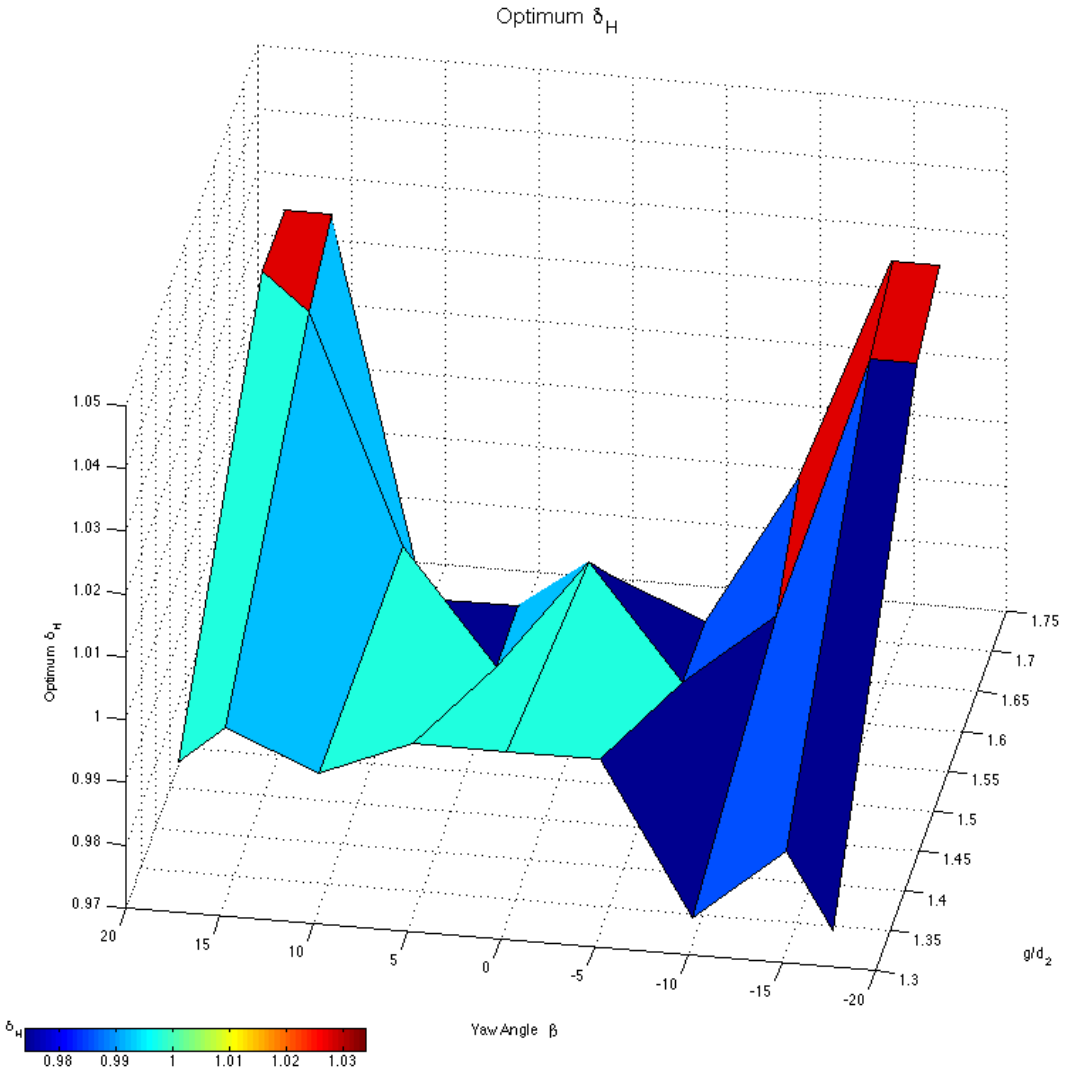

Figure 6.13: Optimum δ_H as a Function of β and g/d_2.

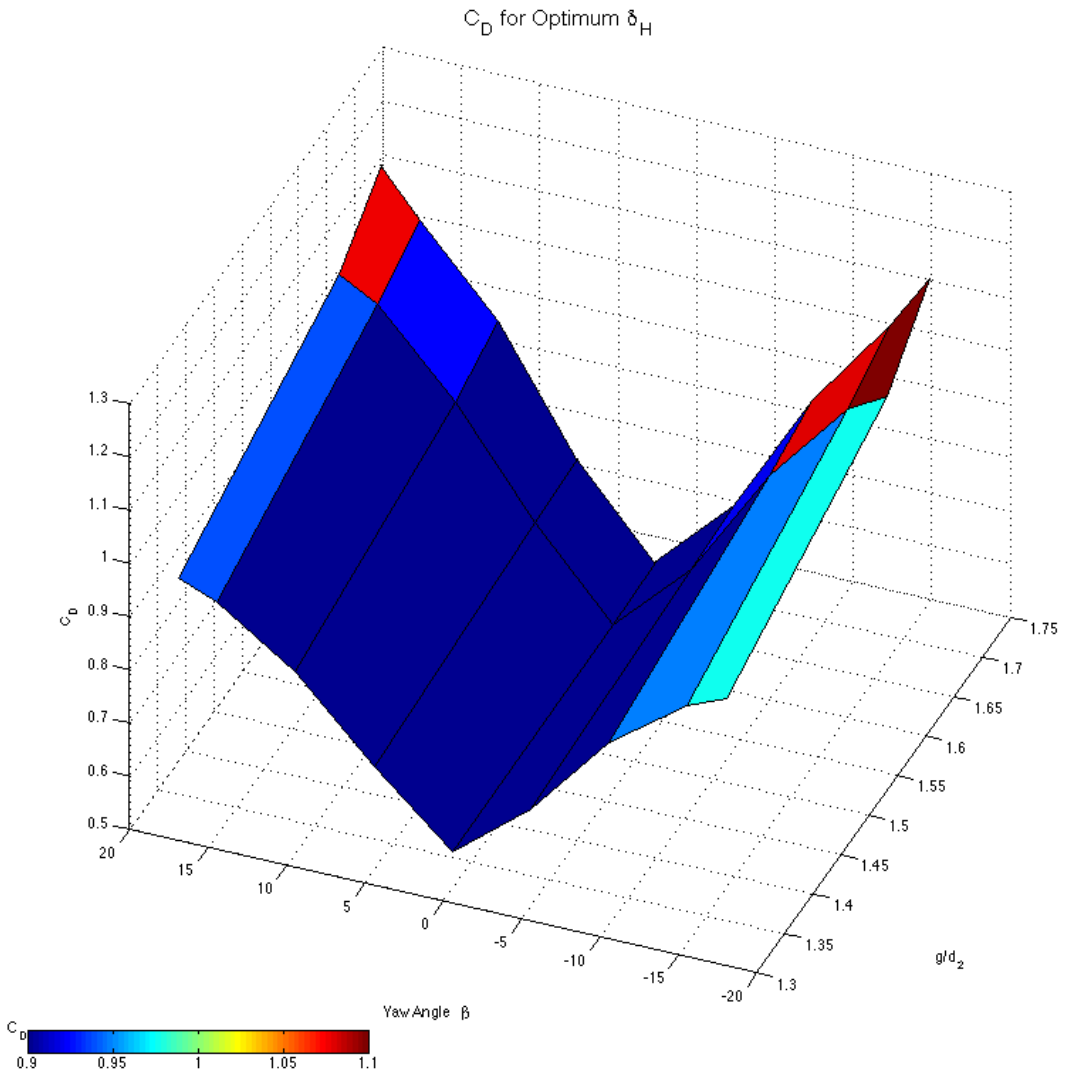

Figure 6.14: Tractor-Trailer C_D Variation with β and g/d_2 for δ_{Hopt}.

6.1.7 Subsection Summary

Initial testing for the baseline C_D of the vehicle showed good agreement with prior experimental work conducted by Cooper [64]. Further investigation revealed that the optimum deflector height ratio (δ_H) depended on three variables. These variables were the wind yaw angle (β), the container height (d_2) and the tractor-trailer separation (g).

Initial calculations showed for a fixed container separation, a wind-averaged drag saving of 7.4% could be achieved due to an optimised configuration. This saving was reduced to a wind-averaged drag saving of 0.5% when the baseline was changed to the zero yaw optimised deflector height.

The result of a dependence on the wind yaw angle for the optimum deflector height (δ_{Hopt}) provided the motivation and data required for investigation into an active deflector. Further investigation was therefore conducted to investigate the pressure distribution on the vehicle.

Pressure tappings located on the vehicle were used to relate the C_D of the vehicle to a measurable pressure. This relationship was required by the control algorithm to enable active flow control.

6.1.8 Pressure Signature Location

The effect of a cab mounted roof deflector on the pressure distribution located on the container forebody has been tested by Gotz et al. [2] and is shown in Fig.(6.15).

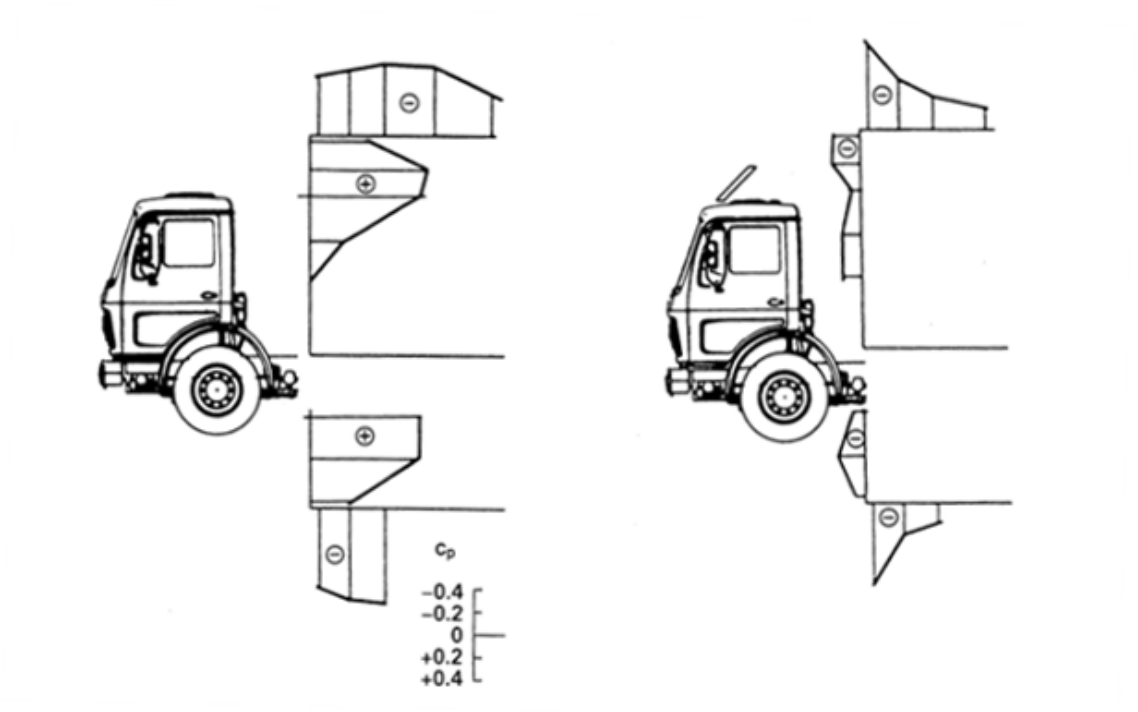

Figure 6.15: C_P Distribution on Container Forebody and Centre Line [2].

The addition of a deflector to the roof of a heavy goods vehicle serves to remove the area of high pressure due to air stagnation on the forebody of the container. The problem in two dimensions can therefore be considered similar to flow over an open cavity, thus there is an area of recirculation within the cab-trailer gap.

Investigation into the pressure distribution as a function of deflector height was therefore conducted to determine if the lowest drag configuration exhibited a pressure signature within the gap. The main aim of the project was to reduce the effects of the tractor-trailer height mismatch, thus the main area of interest was the cab. The addition of transducers to a location on the container imposed the condition that all trailers connected to the cab would require retrofitting of transducers. This would result in extra cabling added to the wiring harness and this requirement was deemed commercial impractical by the commercial project partners. Investigation into locations on the trailer for a pressure signature was therefore only conducted for the TRL1 - TRL4 research control system.

For the 517 mm trailer tested, the cab to trailer gap width (G) remained constant at 67 mm, the width of the trailer tested was 308 mm giving an area (A) of 161,304 mm^2 and $\sqrt{A}$ = 401.6 mm. This resulted in a normalised gap width ($\frac{G}{\sqrt{A}}$) = 0.17. The 502 mm trailer tested had a cab to trailer gap width range of G = (50 mm $\rightarrow$ 146 mm), combined with a width of 308 mm resulted in an area, A of 154,616 mm^2. The normalised gap width was within the range: $\frac{G}{\sqrt{A}} = (0.1 \rightarrow 0.4)$.

The range of separations tested was below the critical gap of: $\frac{G}{\sqrt{A}} \approx 0.5$ determined by Hammache et al. [39]. The normalised gap width for the experiment was below the critical gap implying that the flow within the cavity was considered symmetric and in a "cavity mode" instead of in a "wake mode".

If the gap had been increased beyond a $\frac{G}{\sqrt{A}}$ ratio of 0.5, the flow could no longer have been considered to be within a "cavity mode" and the trailer would have to have been assumed to be a trailing bluff body with time varying vortex shedding from the rear of the tractor.

Figures.(6.16 and 6.17) show the "cavity mode" flow for sub critical gap and "wake mode" flow for post critical gap, respectively.

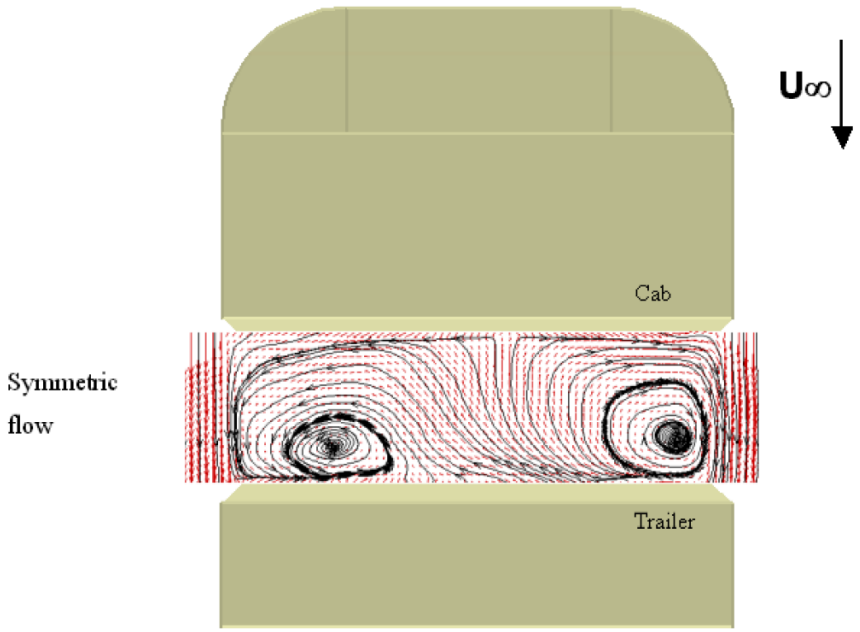

Figure 6.16: Symmetric Flow Pattern for Sub Critical Normalised Gap Width ($\frac{G}{\sqrt{A}}$) = 0.28.

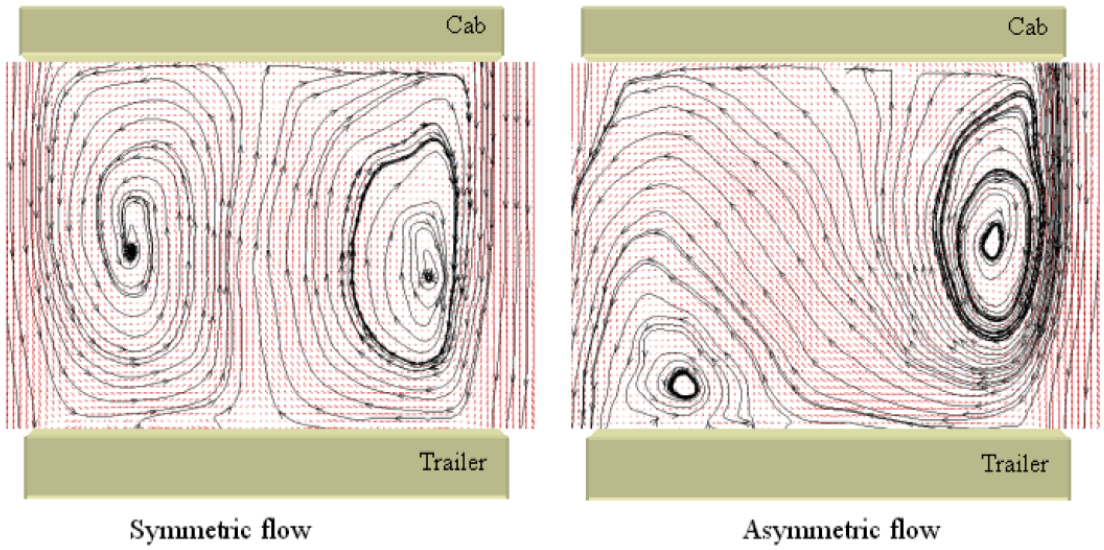

Figure 6.17: Symmetric and Asymmetric Flow Pattern for Post Critical Normalised Gap Width ($\frac{G}{\sqrt{A}}$) = 0.65.

6.1.8.1 Pneumatically Averaged Cab Rear

A selection of the results from the pneumatically averaged tappings located on the rear of the cab are shown in Fig.(6.18). The corresponding C_D graphs are shown in Fig.(6.19) for comparison.

The initial result provided by the zero yaw case shown in Fig.(6.18), appeared to follow the C_D graph with the maximum negative C_P achieved at the optimum deflector height ratio (δ_{Hopt}) of 0.99. This trend, however, was not exhibited when the δ_{Hopt} was no longer at maximum, as shown for the $+5°$ yaw angle case, where the optimum deflector height ratio is 0.98. The pressure coefficient C_P located on the rear of the cab did not track δ_{Hopt}, but instead tracked the height of the deflector (δ_H).

The extension of the deflector to the maximum height provided the greatest recirculation within the cavity and hence the largest negative C_P, however, the lowest drag configuration had no effect on the pressure coefficient.

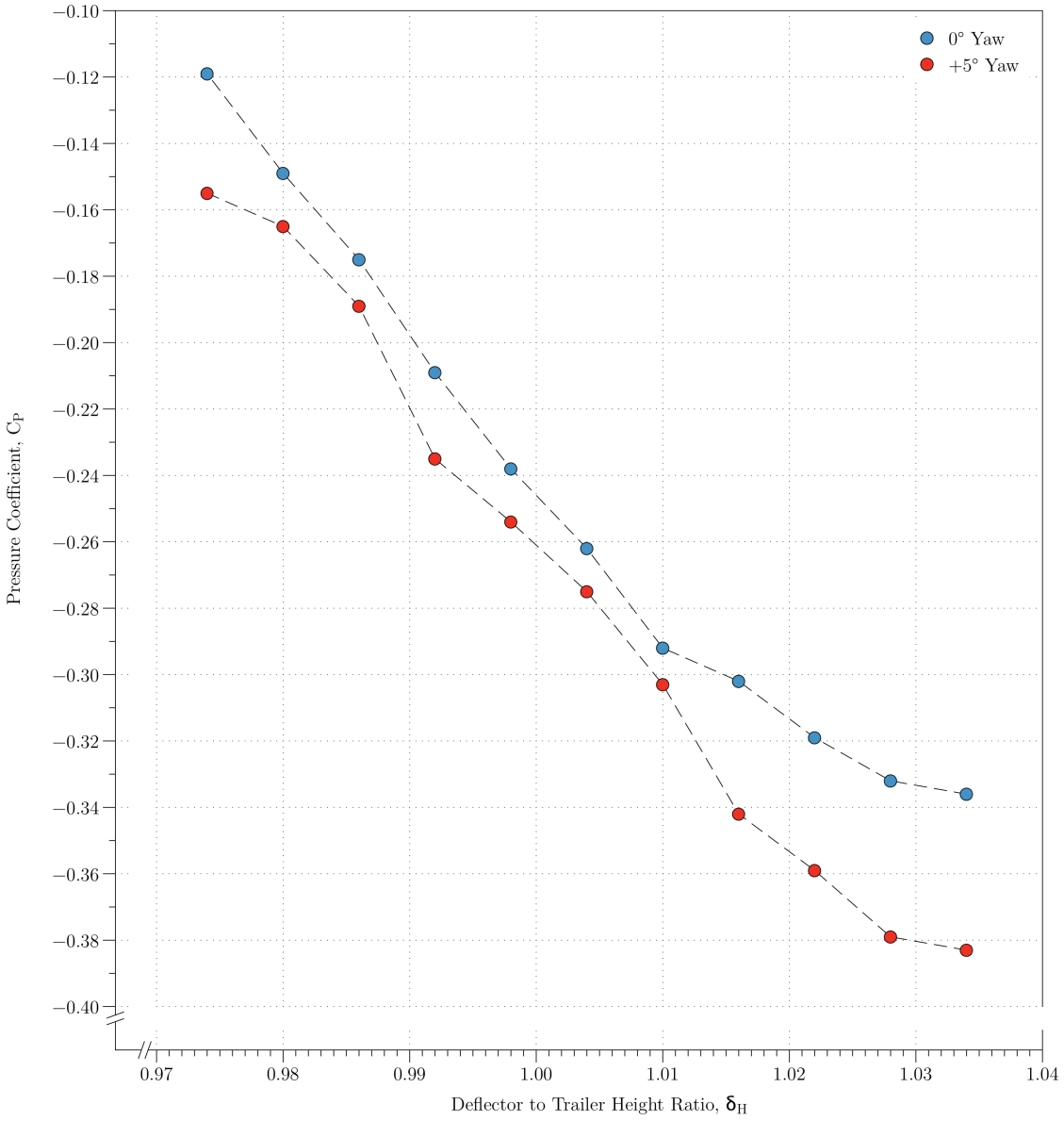

Figure 6.18: C_P Variation with Deflector to Trailer Ratio (δ_H) for $\beta = 0°$ and $\beta = +5°$.

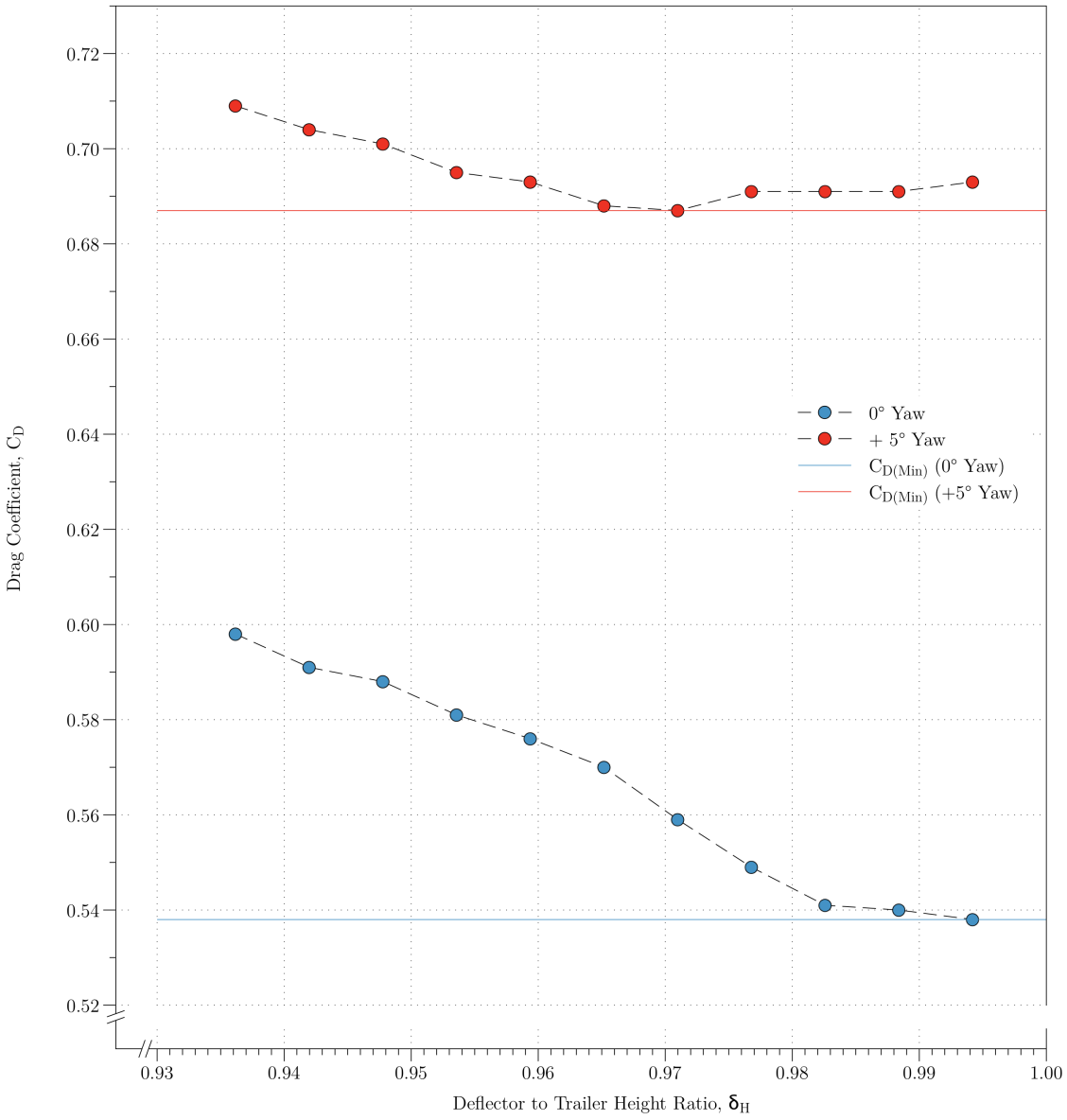

Figure 6.19: C_D Variation with Deflector Height Ratio (δ_H) for $\beta = 0°$ and $\beta = +5°$.

6.1.8.2 Deflector Rear Tappings

A selection of tapping pressures from the rear of the deflector are shown in Fig.(6.20). The tapping numbering used for the rear of the deflector is shown in Fig.(3.8) in Sec.(3.6.1.2). The pressures recorded from all of the tappings are shown for $\beta = 0°$ and $\beta = +5°$ in Figs.(E.5 and E.6) in Sec.(E.3) of Appendix E, respectively.

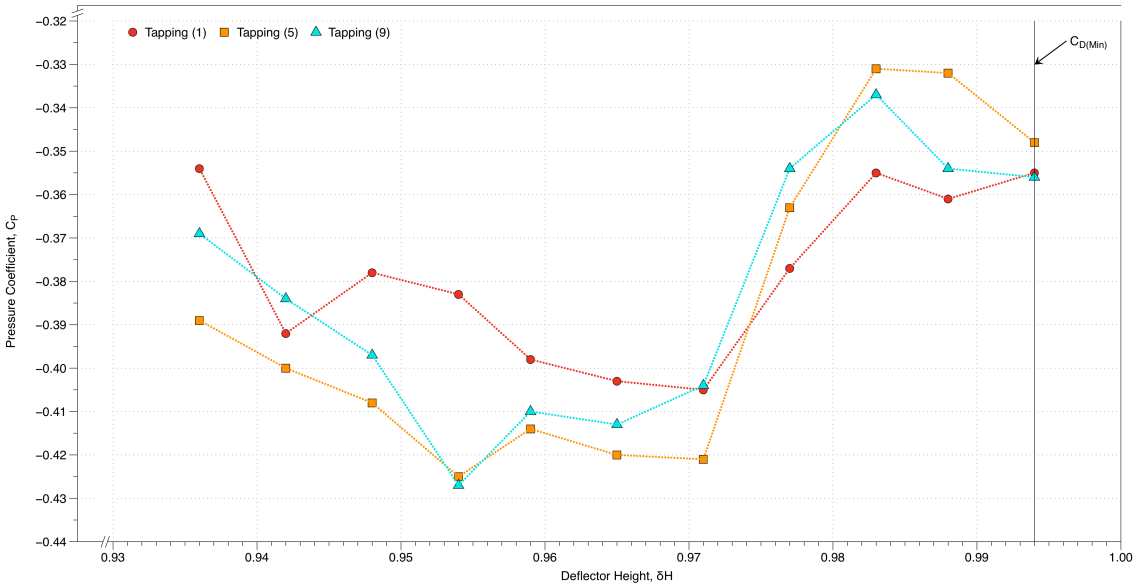

Figure 6.20: C_P Distribution on Rear of Deflector for Tappings: (1), (5) and (9) for $\beta = 0°$.

Initially the results from the pressure tappings on the rear of the deflector appeared to have a pressure signature. The pressure tappings were approaching close to a minimum C_P value of -0.33, this minimum at zero yaw corresponding to the minimum C_D. Due to the variation between ports at lower δ_H it was expected that the pressure fluctuations could be averaged out via pressure differentials (ΔC_P) between pairs of tappings.

Investigation into ΔC_P between pairs of tappings was then conducted in an effort to produce a smoother, unique optimum with minimal disturbance. The pressure differential between pairs of tappings and averages of tappings did not produce a trend relating the C_P, $\overline{C_P}$ or $|\Delta C_P|$ to the vehicle's C_D for any yaw angle tested.

The lack of pressure signature located on the cab led to investigation on the pressure distribution on the trailer for the TRL1 - TRL4 research control system. The higher TRL levels required an alternate control system based on the results obtained from the cab pressure measurements.

6.1.8.3 Container Roof Centre Line

The container roof centre line pressure has been previously investigated for zero yaw by Gotz et al. [2]. The plot style has been reproduced with the wind tunnel pressure data and is shown in Fig.(6.21). The variation of the centre line pressure as a function of deflector height is shown in Figs.(6.22 and 6.23). The graphs for $\beta =$

$-5°$, $+5°$, $+10°$ and $+15°$ are shown in Figs.(E.7, E.8, E.9 and E.10) in Appendix E, respectively.

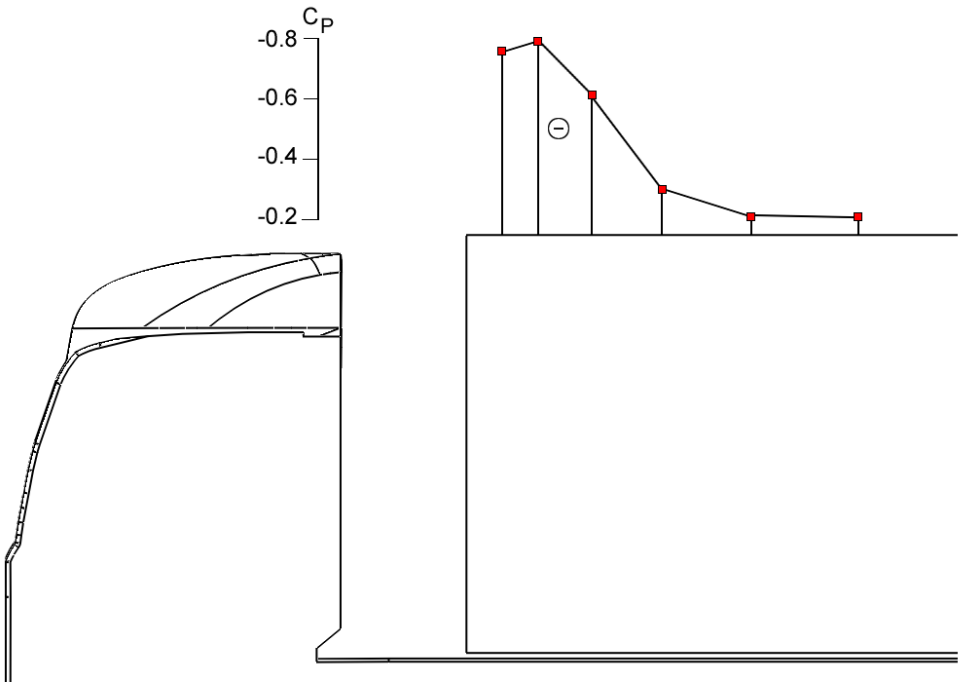

Figure 6.21: C_P Distribution Along Trailer Centre Line for $\beta = 0°$ and $\delta_H = 0.936$.

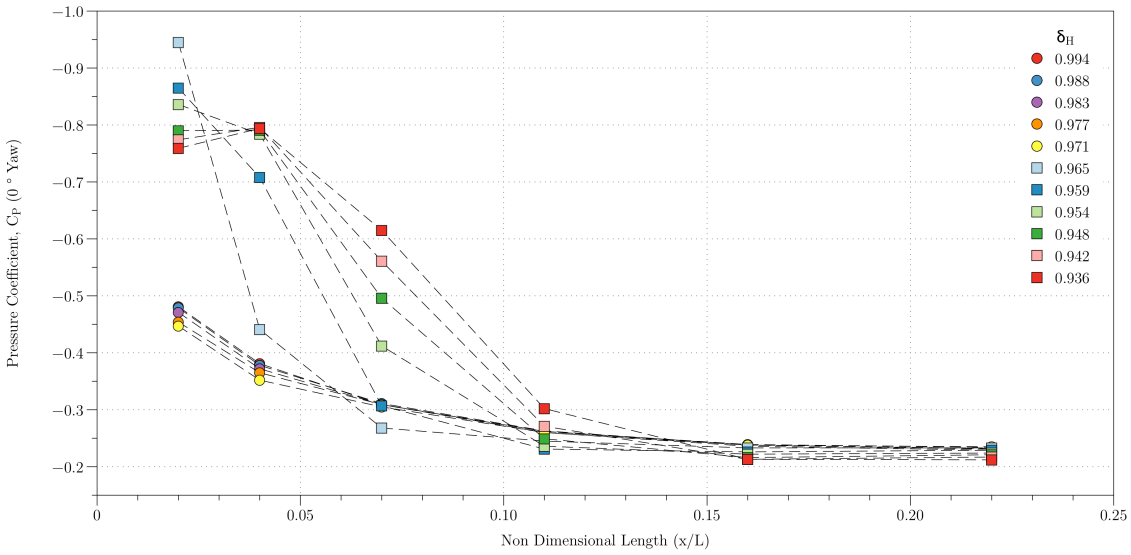

Figure 6.22: C_P Variation vs. Displacement Along Trailer Centre Line for $\beta = 0°$.

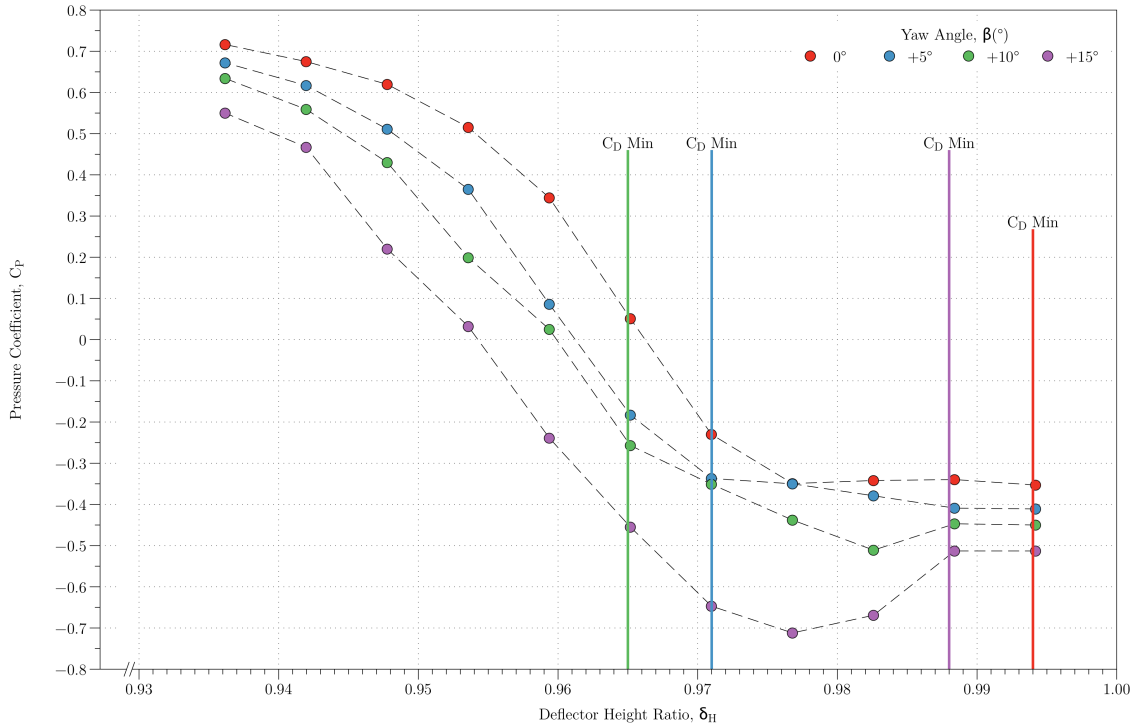

Figure 6.23: C_P Variation vs. δ_H.

The results obtained from the centre line pressure tappings exhibited, for a deflector height ratio in the range of 0.936 to 0.965 similar C_P values to those obtained by Gotz et al. [2]. For zero yaw angle, the results obtained indicate a C_P on the first tapping of around -0.45 decreasing to around -0.20 at 0.16 (x/L) displacement along the trailer.

The effect of the deflector was to remove the area of high pressure on the forebody of the container, the deflector achieved this by diverting the airflow above the top of the trailer. This resulted in an acceleration of the flow due to the positive velocity gradient caused by the geometry of the deflector. Reattachment occurred downstream of the trailer as the C_P value tends to zero and the velocity of the diverted air returns to freestream.

A large increase in the negative pressure coefficient occurred when the deflector height ratio was decreased below 0.971, shown in Fig.(6.22). At $\delta_H = 0.965$ the C_P decreased from -0.45 to -0.95 whilst maintaining the C_P vs. displacement form indicated by Gotz et al. [2].

For $\delta_H \leq 0.959$, however, the graph suddenly changed to a shape similar to cab mounted without a deflector, shown in Fig.(6.15).

The height of the deflector was too low to direct the airflow above the trailer and the high pressure area on the forebody of the container was again generated. This

resulted in a shift in the maximum negative C_P of -0.2 to a point further downstream on the trailer centre line.

The optimum deflector height had no effect on the C_P distribution along the trailer centre line. The largest increase in C_P occurred at a consistent height ratio of 0.971 which was a significant difference from optimum height ratio of 0.994 for zero yaw.

The yaw angle did not have an appreciable effect on the pressure distribution. Due to this yaw insensitivity, if a pressure signature had been located it would have been a suitable mounting location for the experimental control system.

6.1.8.4 Container Forebody

The initial container forebody pressure measurements are shown in Fig.(6.24). The C_P distribution was for zero yaw angle and δ_{Hopt}. Initial results could not be compared with the "Tractor Trailer Cavity Flow" PIV conducted by Heineck et al. [38] as the normalised gap width ($\frac{G}{\sqrt{A}}$) did not exceed the critical gap of 0.5, tested by Hammache et al. [39].

The pressure distribution on container forebodies has been investigated by Garry [85] in the paper: "A Summary of the Scale Model Wind Tunnel Measurements and Full Scale Surface Pressure Tests on the Leyland T45 and DAF3300 Vehicles Used for the TRRL Spray Dispersion Programme". The pressure measurements from this experiment are shown in Fig.(6.24).

The results obtained by Garry [85] showed a similar C_P distribution to the results obtained from the forebody pressure measurements. Differences, however, do arise due to the different values of g/d_2 used in the tests. The technical report published by Garry [85] did not specify the deflector height or container separation. Differences due to δ_H and g/d_2 were therefore present and the specific effect of these variables on the C_P forebody distribution are shown in the following sections.

Table (6.5) is presented to remind the reader of the effect of δ_H, β and g/d_2 on the vehicle's C_D.

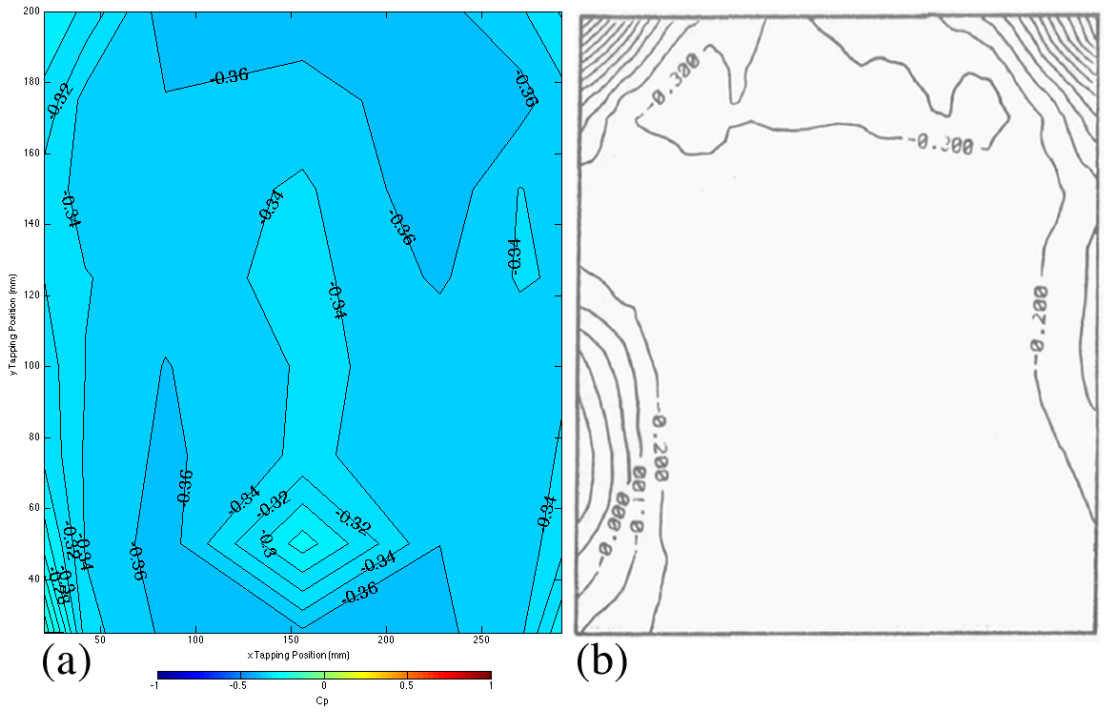

Figure 6.24: C_P Distribution on Container Forebody for (a) $\delta_H = 0.998$ and $\beta = 0°$, (b) δ_H = Unknown and $\beta = 0°$ [85].

$\beta(°)$	Optimum δ_H (g/d_2)		
	0.658	0.798	0.838
-17.5	0.968	1.022	1.028
-15	0.980	1.022	1.028
-10	0.968	0.980	0.992
-5	0.992	0.968	0.968
0	0.992	0.986	0.974
5	0.992	0.968	0.968
10	0.986	0.986	0.968
15	0.992	1.022	1.028
17.5	0.986	1.028	1.028

Table 6.5: Optimum δ_H as a Function of Yaw Angle (β) and g/d_2.

6.1.8.5 Container Forebody C_P Variation with δ_H

The variation in the C_P distribution on the container forebody with δ_H is shown in Fig.(6.25). The associated C_D variation with δ_H is shown in Tab.(6.6).

The results obtained from the forebody pressure measurements illustrated that the below optimum deflector height (shown in Fig.(6.24) (a)) has areas of high pressure "spill over". These areas of high pressure (C_P = +0.20) arise due to a mismatch in the cab to trailer heights. Increasing the deflector to the optimum δ_H and therefore lowest C_D (Fig.(6.24)) served to remove these areas of high pressure (C_P = -0.32). Further extension beyond the optimum deflector height (δ_{Hopt}) (Fig.(6.24) (b)), continued to reduce the forebody pressure to around C_P = -0.34 over the container face.

The optimum deflector height (δ_{Hopt}) was achieved at the minimum deflector height that removed the forebody stagnation, further extension reduced the forebody C_P but at the expense of a rise in the vehicle's C_D.

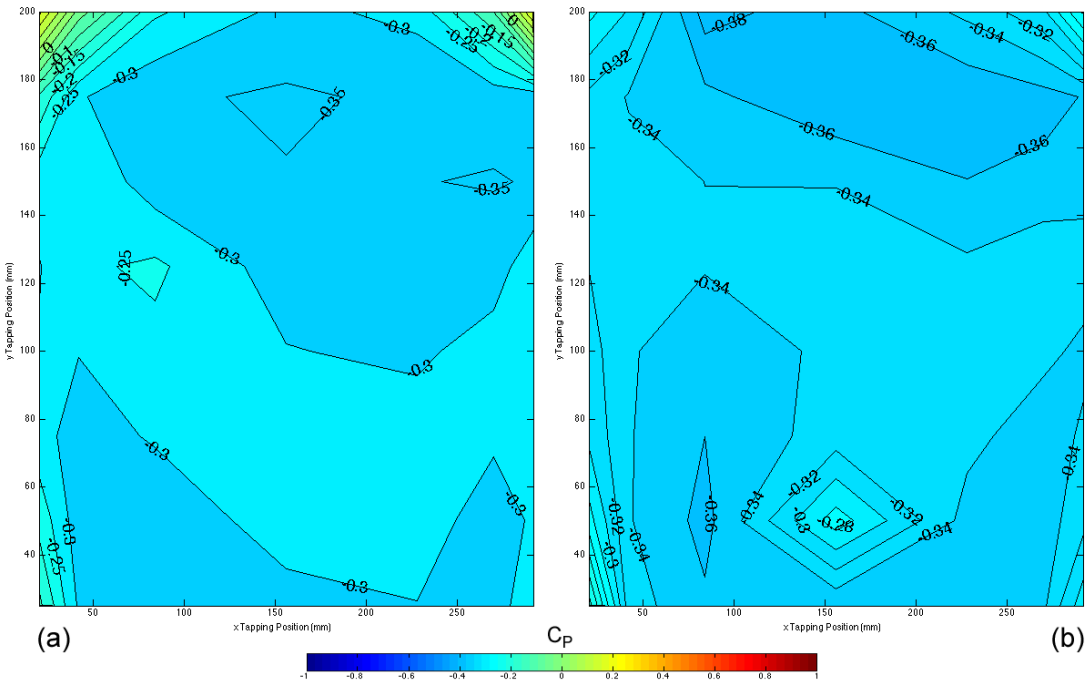

Figure 6.25: C_P Distribution on Container Forebody, $g/d_2 = 0.798$ and $\beta = 0°$ for (a) $\delta_H = 0.968$ and (b) $\delta_H = 1.028$.

Deflector Height Ratio, δ_H	Drag Coefficient (C_D)
0.968	0.584
0.974	0.579
0.980	0.579
0.986	0.574*
0.992	0.577
0.998	0.577
1.004	0.580
1.010	0.581
1.016	0.581
1.022	0.584
1.028	0.587†

Table 6.6: C_D[3]Coefficients for Various δ_H Values, $g/d_2 = 0.798$ and $\beta = 0°$.

6.1.8.6 Container Forebody C_P Variation with β

The variation in the C_P distribution on the container forebody with β is shown in Fig.(6.26). The associated C_D variation with δ_H is shown in Tab.(6.7).

$\beta(°)$	Optimum δ_H
-17.5	1.022
-15	1.022
-10	0.98
-5	0.968
0	0.986
5	0.968
10	0.986
15	1.022
17.5	1.028

Table 6.7: Optimum δ_H vs. Yaw Angle.

[3]* Denotes Lowest and † Denotes Highest C_D Value Obtained Respectively.

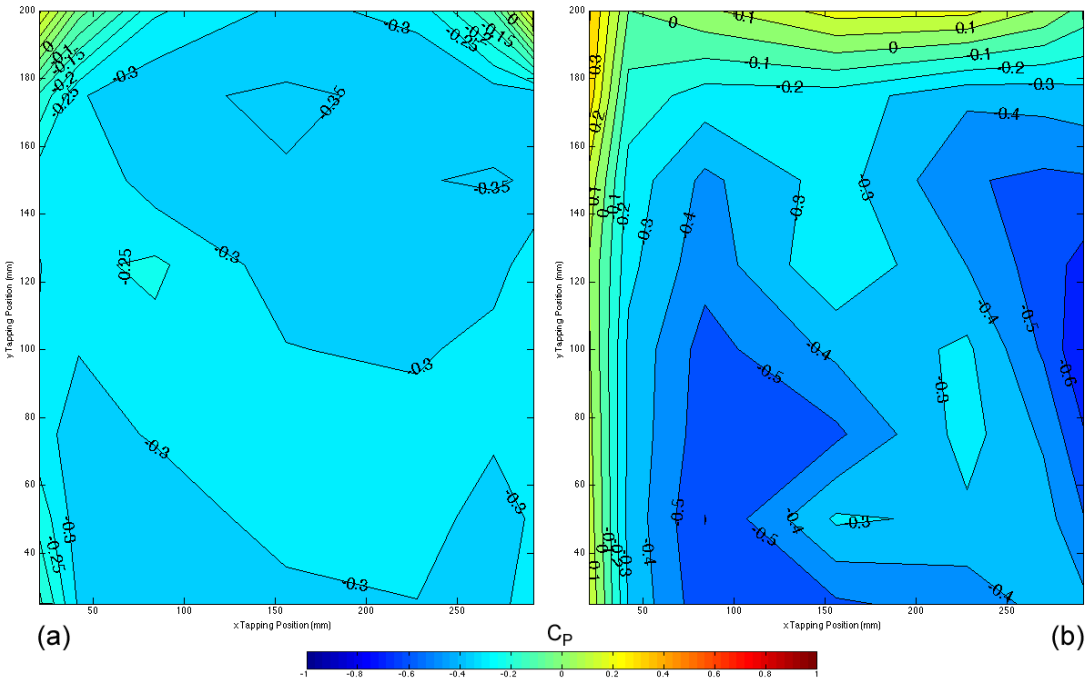

Figure 6.26: C_P Distribution on Container Forebody, $\delta_H = 0.968$, $g/d_2 = 0.798$ and $\beta =$ (a) 0° and (b) $\beta = +17.5°$.

The results obtained from the forebody pressure measurements showed that an increase in β for a given δ_H and g/d_2 results in an increase in the forebody pressure.

An increase in the C_P from -0.3 to 0.3 was obtained on the container side exposed to the freestream velocity at yaw. Conversely a reduction from -0.3 to -0.6 for C_P was achieved on the side shielded from the freestream velocity. There was an asymmetric growth in the "spill over" region on the top of the container. This implied that δ_H should have increased at increased β to remove the stagnation point at the top of the container. This result was in agreement with the C_D results that δ_{Hopt} increased from 0.986 to 1.028 for increased β from 0° to +17.5°.

6.1.8.7 Container Forebody C_P Variation with g/d_2

The variation in the C_P distribution on the container forebody with g/d_2 is shown in Fig.(6.27). The associated C_D variation with δ_H is shown in Tab.(6.8).

Optimum δ_H (g/d_2)		
0.658	0.798	0.838
0.992	0.986	0.974

Table 6.8: Optimum δ_H for Various g/d_2.

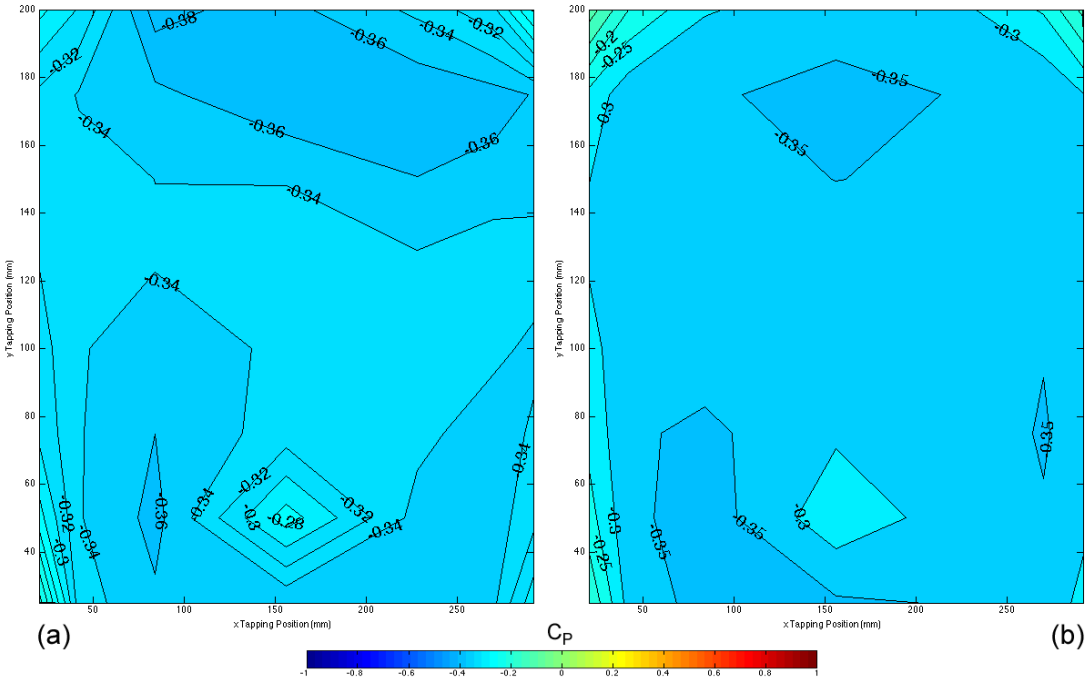

Figure 6.27: C_P Distribution on Container Forebody, $\delta_H = 0.986$, (a) $g/d_2 = 0.798$ and (b) $g/d_2 = 0.838$ and $\beta = 0°$.

The results obtained from the forebody pressure measurements showed that an increase in g/d_2 for a given δ_H results in a higher C_P region on the corners of the container top. The result was similar to those obtained in Fig.(6.24) (a), the result indicated that the deflector was too low and that the optimum δ_H was larger than for smaller g/d_2. The C_D measurements revealed, however, that δ_{Hopt} lowered for an increase in g/d_2. Despite lowering the forebody pressure distribution, the optimum drag configuration was not related to the forebody pressure measurements.

6.1.9 Subsection Summary

The results obtained from the averaged cab rear, deflector rear, container centre line and forebody pressure measurements showed that there was a variation in the pressure distribution with a varying deflector height ratio (δ_H). The pressure measured at points on the vehicle depended on the δ_H, as well as the wind yaw angle (β) and the container separation (g/d_2). The variation of δ_H was related to changes in the C_P measured at certain points on the container centre line and forebody.

The optimum deflector height (δ_{Hopt}), however, could not be related to a pressure measurement. This posed a serious problem for the suitability of the system for use in the prototype control system. The pressure on the forebody of the container was reduced with an increase in the deflector height as expected, however, there was not an increase above the optimum deflector height. This imposed the condition that the control scheme would not be able to identify the minimum drag configuration. The scheme would therefore seek to extend the deflector to a maximum height in order to minimise the forebody pressure. This would have the effect of increasing drag due to a non optimised deflector height.

As the "target" pressure for the optimum deflector height varies due to both the δ_H and β, for a control scheme to be employed, both variables must be known.

Investigation therefore began into determining the wind yaw from a pressure differential (ΔC_P) at a location on the vehicle. It was concluded that if ΔC_P could be related to β, a static look-up table could be used in conjunction with wind tunnel data obtained to determine $\delta_H(\beta)$. This would enable the prototype controller to be constructed and therefore allow the higher TRL levels of research to continue.

6.1.10 Pressure Differential Location

The results from the pressure signature measurements concluded that a tapping location or array of tappings located on the cab or trailer did not provide a suitable signature for the optimum deflector height (δ_{Hopt})/lowest drag configuration ($C_{D(Min)}$). Due to the yaw angle (β) influencing the pressure distribution on the vehicle, investigation into determining β from pressure differentials was conducted.

It was concluded that if β was known, δ_{Hopt} for a given trailer height could be determined from wind tunnel tests results. The control scheme could therefore be modified to use a static look-up table with β and the trailer height as input variables.

Investigation into tapping locations on the front of the deflector was therefore conducted. If a significant pressure differential (ΔC_P) existed that was a function of β, the deflector geometry would effectively act as a three-hole yaw probe. A five hole yaw probe (accounts for pitch angle (α) using ports (1) and (3)) is shown in Fig.(6.28).

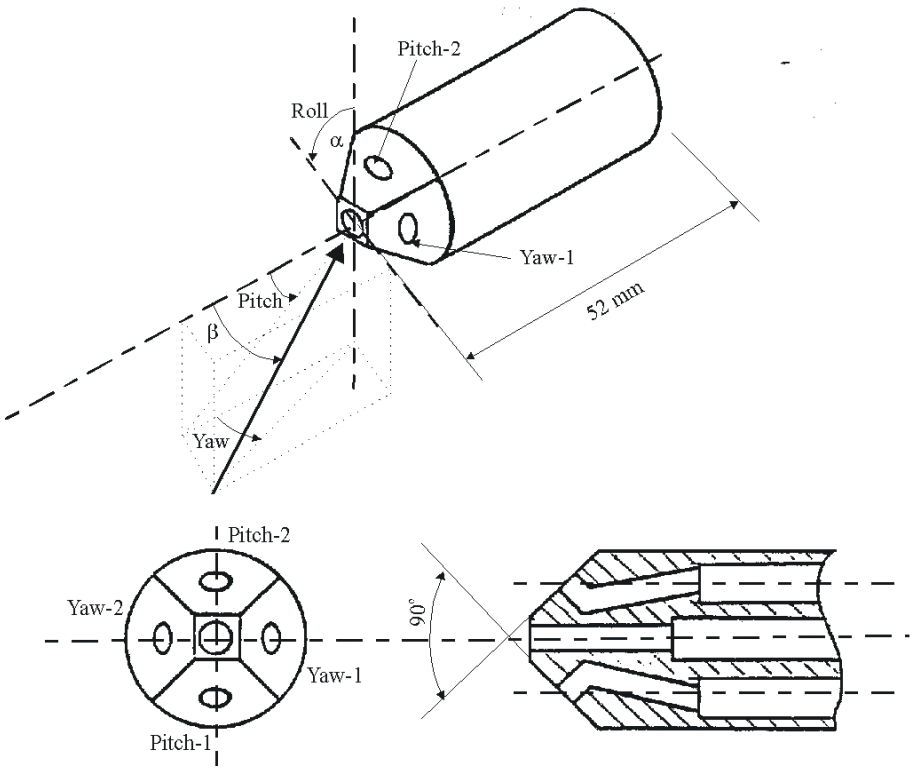

Figure 6.28: Five Hole Pressure Probe Design [66].

The calibration for a five hole yaw probe has been conducted by Pisasale et al. [86] and is shown in Fig.(6.29).

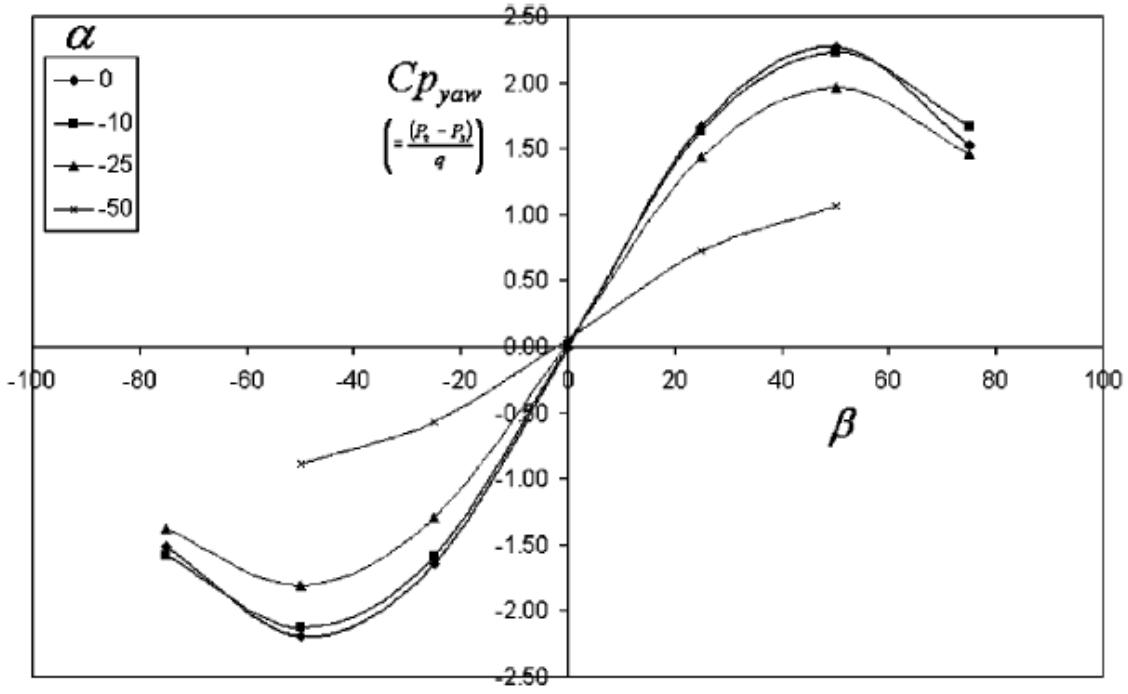

Figure 6.29: Five Hole Yaw Probe Calibration Sheet [86].

The results from the static skirt and the first row tappings are shown in Figs.(6.30 and 6.31) respectively. The second and third row tappings are shown in Figs.(6.32 and 6.33). The tappings that provided the most accurate data were tapping pairs (1) and (9) (shown in Fig.(3.15) of Chapter 3). The ports were separated by the furthest physical distance with angular separation of 80° between the two ports. The data presented in Figs.(6.30 - 6.34) is therefore with respect to the ΔC_P between these ports.

Fig.(6.34) shows the ΔC_P variation for a single δ_H of 0.994 for the static skirt. This allowed a linear relationship between β and ΔC_P to be generated.

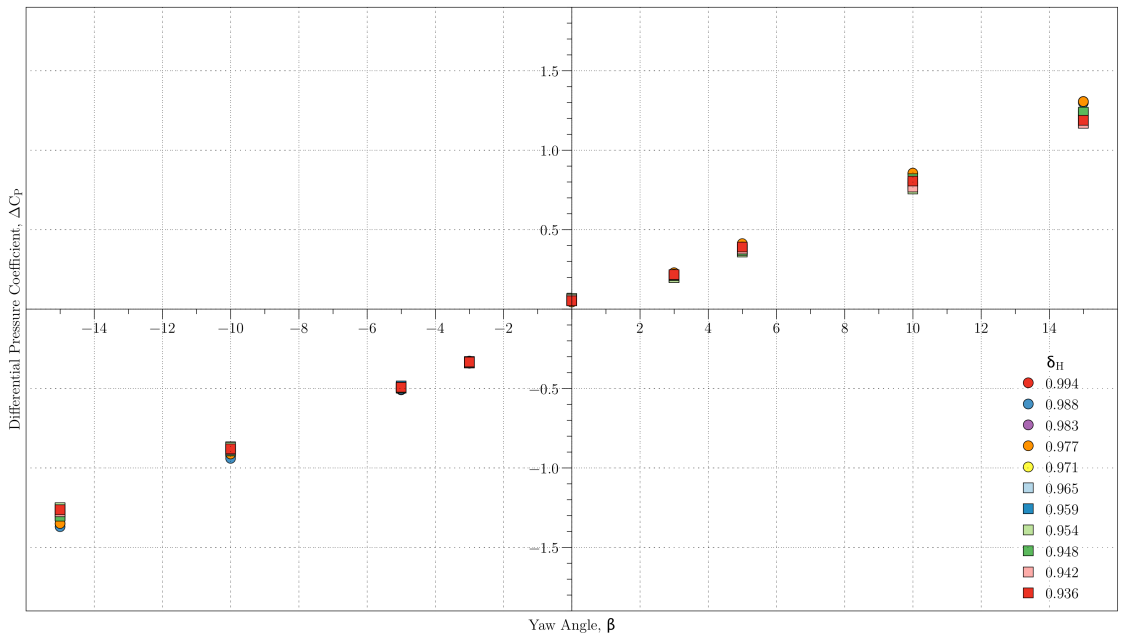

Figure 6.30: ΔC_P Variation with Yaw Angle (β), Static Row.

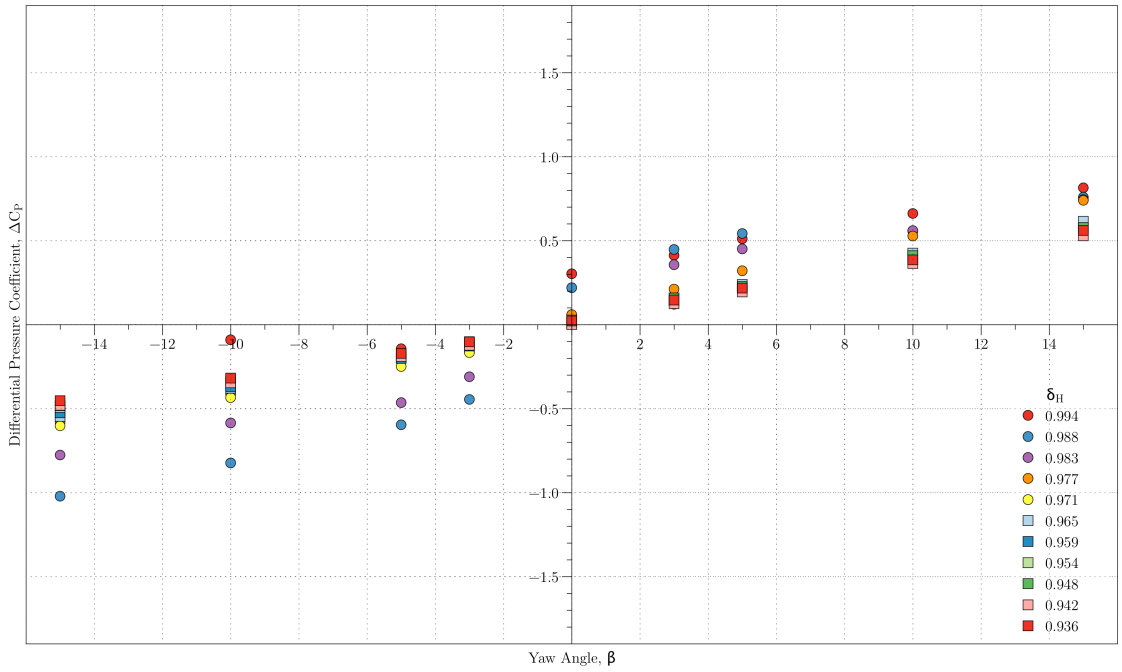

Figure 6.31: ΔC_P Variation with Yaw Angle (β), First Row.

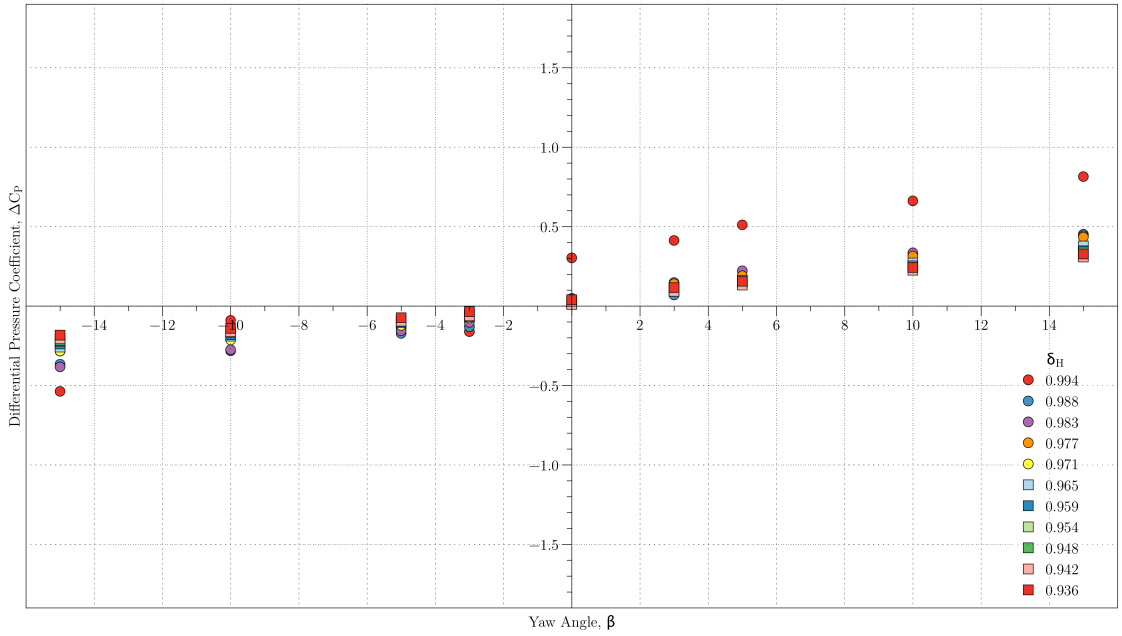

Figure 6.32: $|\Delta C_P|$ Variation with Yaw Angle (β), Second Row.

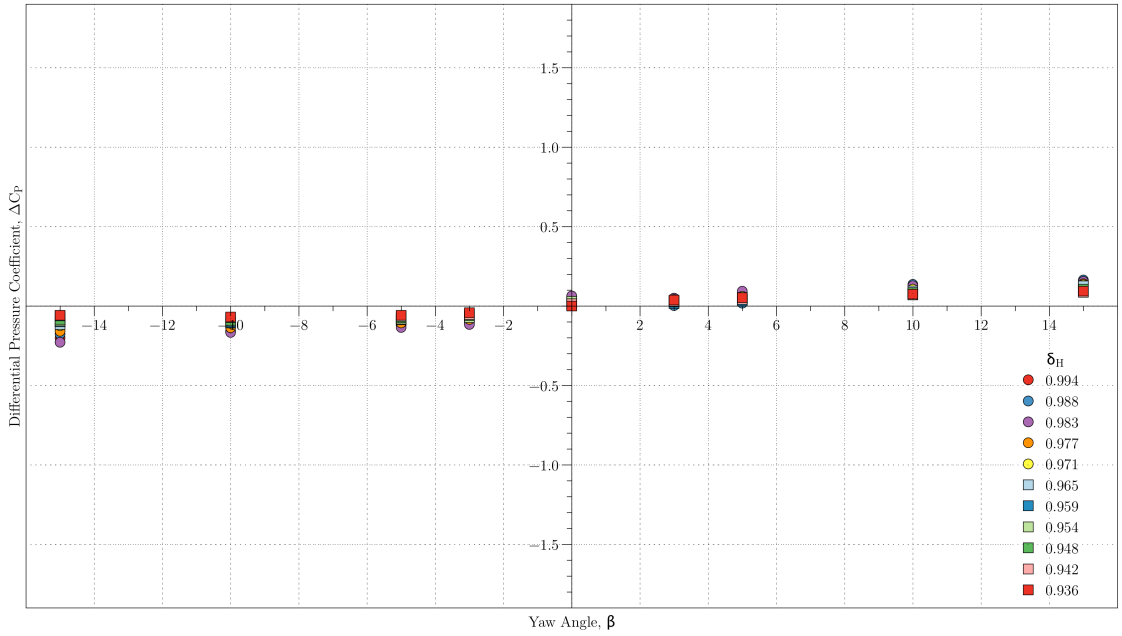

Figure 6.33: $|\Delta C_P|$ Variation with Yaw Angle (β), Third Row.

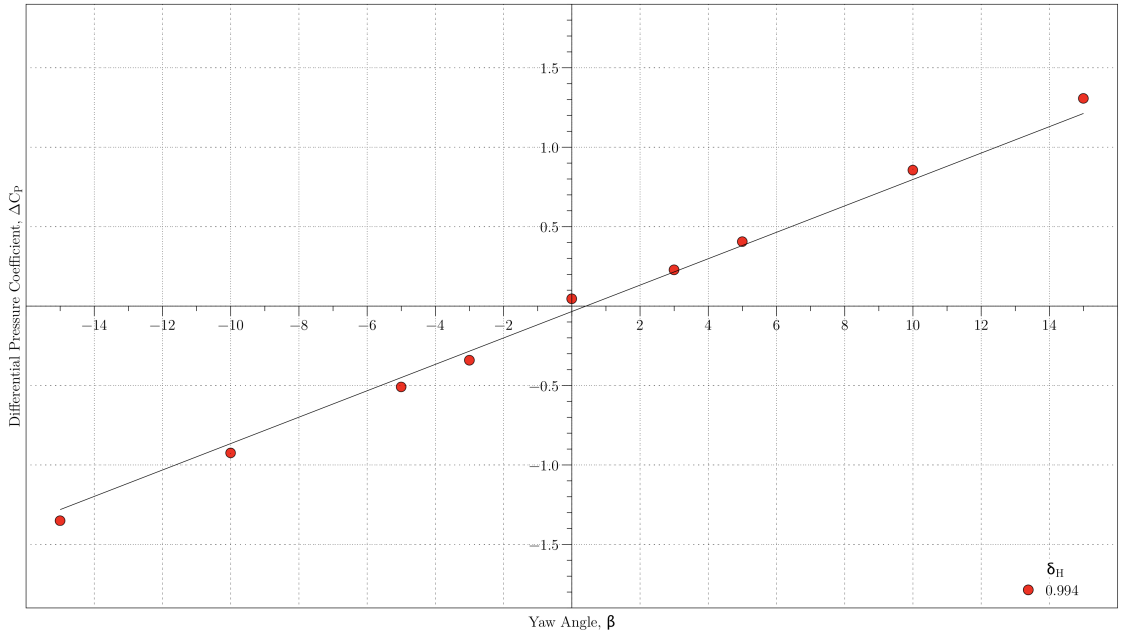

Figure 6.34: ΔC_P Variation with Yaw Angle (β), Static Row for $\delta_H = 0.994$.

The results obtained from the pressure differential tapping locations agreed strongly with previously recorded data by Pisasale et al. [86]. The data obtained from the static skirt tappings at zero yaw resulted in a ΔC_P of 0.03 (shown in Fig.(6.34)) compared to 0.00 for Pisasale et al. [86]. At 20° yaw, the ΔC_p obtained by Pisasale et al. was 1.50, extrapolation from the experimental data gives a theoretical ΔC_P of 1.62 calculated by

$$y = 0.083127x - 0.03407 \tag{6.4}$$

hence the estimated yaw angle (β_{Est}) could be written as

$$\beta_{Est} = \Delta C_{P(\text{offset})} - C_1 \tag{6.5}$$

where $\Delta C_{P(\text{offset})} = \Delta C_P / 0.083$ and $C_1 = 0.410$.

The results obtained from tappings located on the deflector (shown in Figs.(6.31 - 6.33)) showed that the three rows tested on the deflector were affected by the movement of the deflector. The changes in deflector geometry with height affected the pressure coefficient such that, the difference no longer tracked the yaw angle accurately. The static skirt tracked the yaw angle for all deflector heights tested with a 4% variation from previous yaw sensor calibrations [86].

6.1.11 Full Scale Instrumentation Location

The vehicle geometry affects the flow field around the vehicle resulting in a disturbance to sensors placed within close proximity to the vehicle. Manufacturer and legal constraints placed a restriction on the mounting locations of the sensors. This resulted in no external sensors being allowed to be placed further forward that the cab or higher than the deflector's minimum height. Due to the constraints, investigation into possible mounting locations around the top of the cab, close to the deflector were conducted.

To determine the flow field around the sensor location, a five hole probe was mounted to the model vehicle used in the wind tunnel. The experimental arrangement is shown in Section(3.6.2). The mounting location is shown in Fig.(6.35). The wind tunnel data was used in conjunction with 3D RANS and LES CFD simulations to aid in the identification of the flow field around the deflector whilst the vehicle was under both freestream and wake velocity profiles. The CFD methodology used within the thesis is shown in Chapter 4. The processed results obtained are shown in Tab.(6.9) and the raw data are shown in Tab.(E.5) in Sec.(E.6) of Appendix E.

Figure 6.35: 5 Hole Pressure Probe Mounting Location.

A single time step from the LES simulation is shown in Fig.(6.36). The RANS

slice extraction for $\beta = 0°$ and $\beta = +20°$ are shown in Figs.(6.37 and 6.38), respectively.

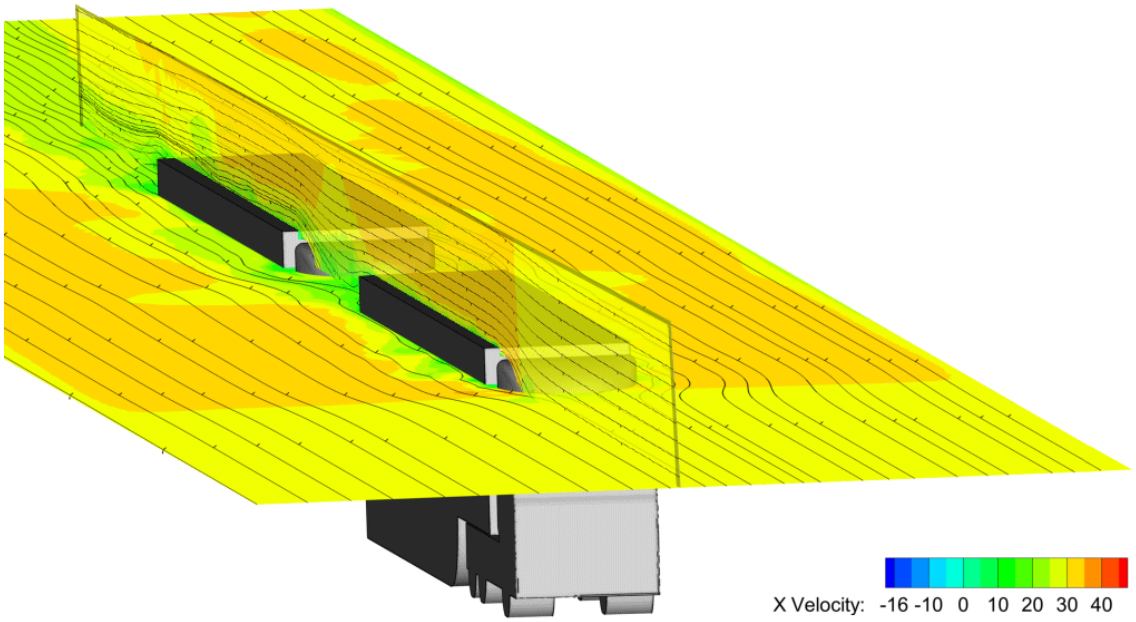

Figure 6.36: Wind Vane and Wind Anemometer CFD Simulation, Slice Extraction at $z/W = 1.20$ and $y/W = 0.11$.

Fig.(6.36) shows a significant change in the air speed around the deflector, the lead vehicle has a speed close to the inlet velocity (35 ms^{-1}). The trailing vehicle, however, has a significantly lower speed closer to 10 ms^{-1} in the presence of the lead vehicle's wake. The stream traces of the trailing vehicle also indicate the wake of the trailing vehicle has a significant effect on the flow field around the deflector of the trailing vehicle.

Figs.(6.37 and 6.38) show the deflector geometry accelerates the flow around the position of the sensors. This acceleration leads to an angular offset for the wind vane at zero (inlet) yaw, the sensor therefore would overpredict the yaw angle of the wind if left unaccounted for. The cup anemometer could also overpredict the total velocity due to the flow acceleration.

The results from the experimental and CFD sensor positioning are shown in Tab.(6.9). The velocity profile extracted from the vertical slice is shown in Fig.(6.39) for -20° yaw angle.

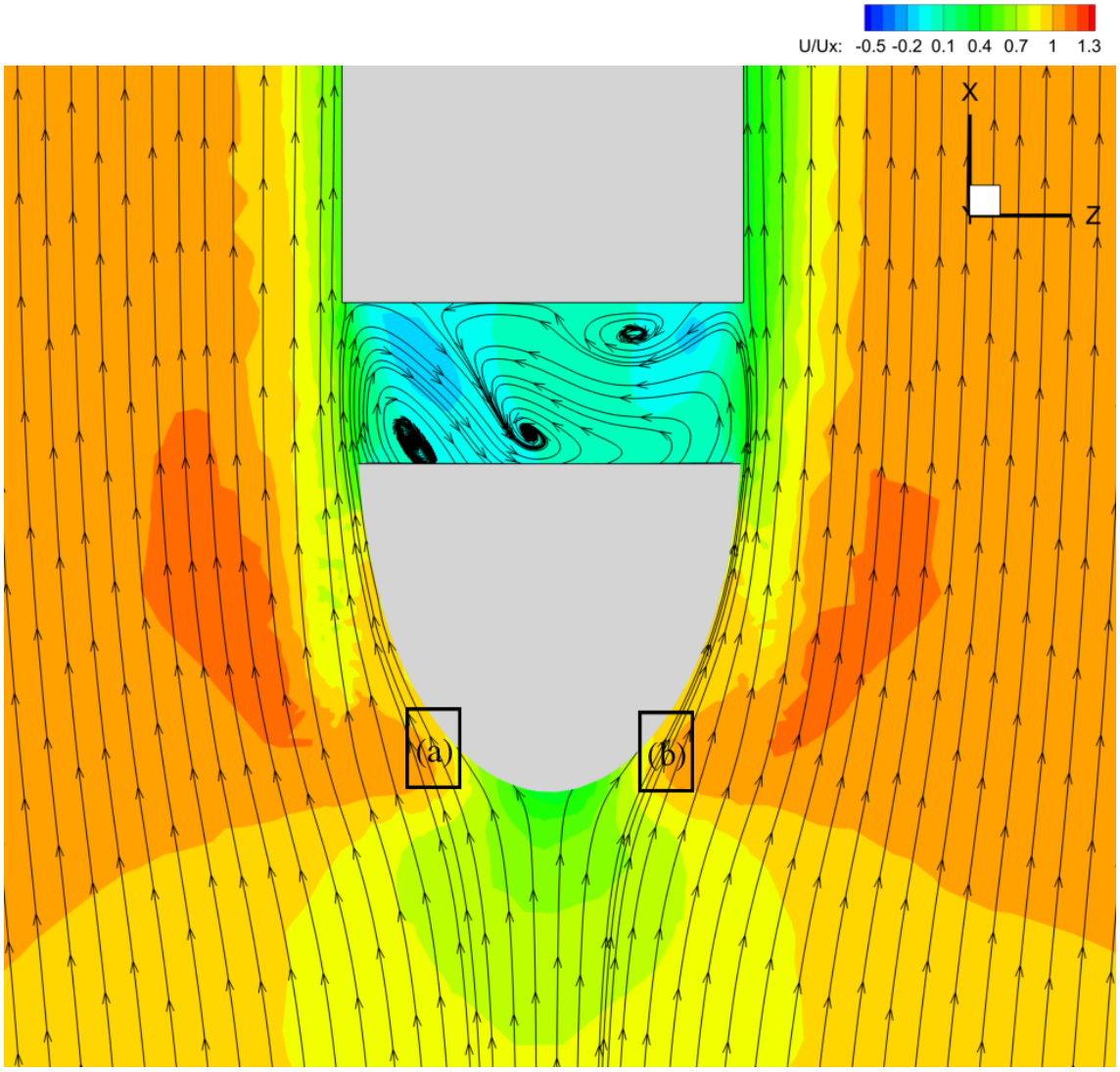

Figure 6.37: Wind Anemometer and Wind Vane (a) and (b) Mounting Locations (β = 0° Yaw) Slice Extraction at $z/W = 1.20$.

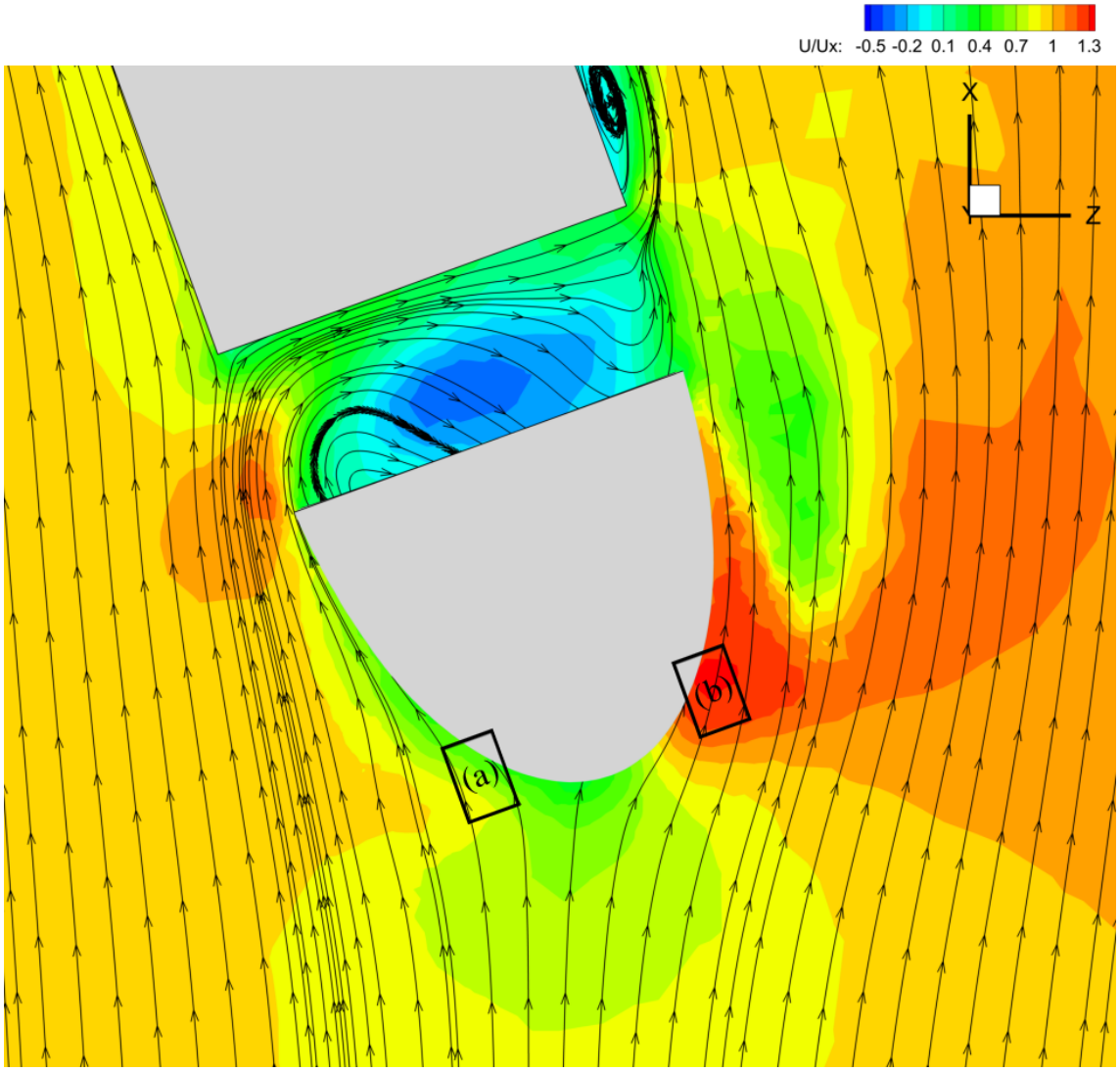

Figure 6.38: Wind Anemometer and Wind Vane (a) and (b) Mounting Locations (β = +20° Yaw) Slice Extraction at $z/W = 1.20$.

Item	Wind Tunnel	CFD
Yaw Angle (0°)	-15.0°	-14.7°
Yaw Angle (+20°)	-25.0°	-24.8°
Correct Yaw Angle (+20°)	-0.7°	-0.1°
Correct Yaw Angle (-20°)	-	+1.2°
Pitch Angle (0°)	-25.0°	-24.8°
Pitch Angle (+20°)	-16.0°	-16.0°
Pitch Angle (-20°)	-28.0°	-28.2°

Table 6.9: Wind Vane Sensor Offset due to Mounting Location.

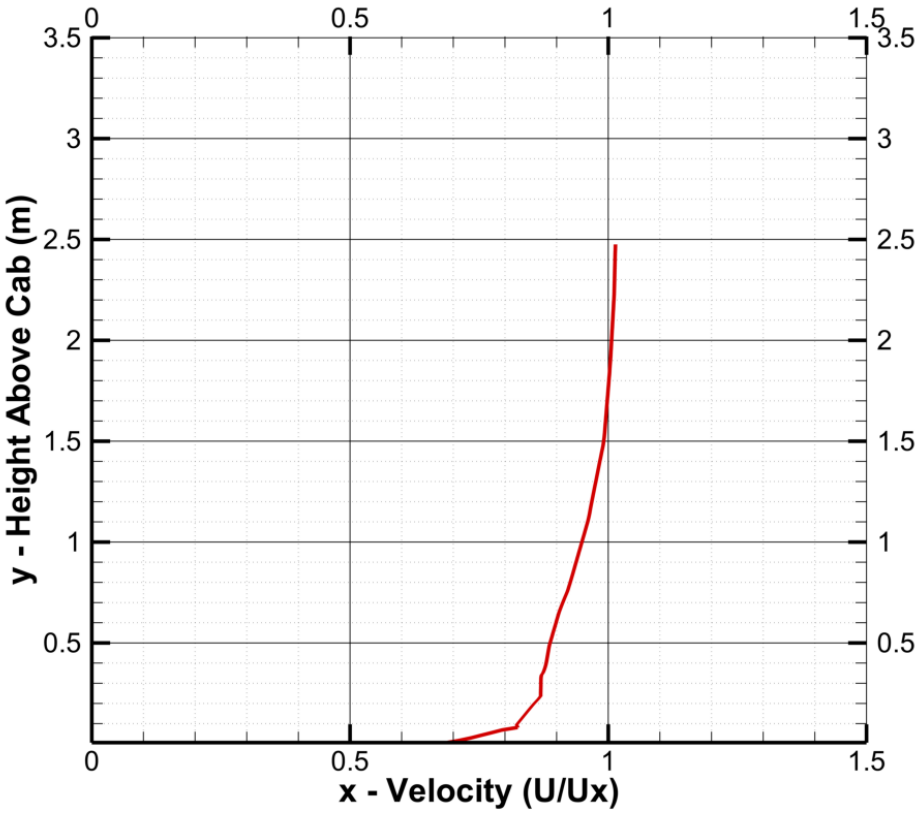

Figure 6.39: CFD x-Velocity Profile Above HGV Cab at -20° Yaw Angle.

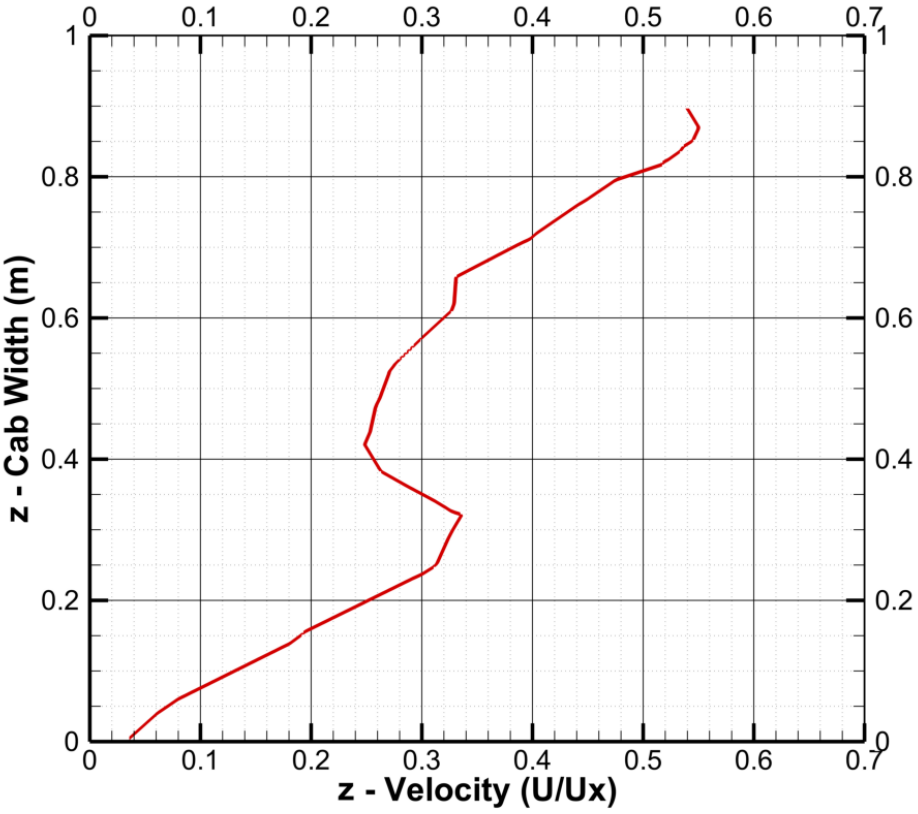

Figure 6.40: CFD z-Velocity Profile Above HGV Cab at -20° Yaw Angle.

The pitch angle (α) was found to be -25.0° at 0.0° yaw at the probe location tested. This pitch angle varied over the range (-16.0° $\rightarrow -28.0°$) for the ($-20.0° \rightarrow +20.0°$) yaw angle range tested. The wind vane used for full scale testing was a 2D rotary, pitch independent potentiometer. The wind vane therefore did not require pitch correction for the measurements taken during on-road measurements. The yaw angle (β) offset at 0.0° was found to be -15.0°, once accounted for this generated a maximum error of +1.2° at -20.0° yaw angle, corresponding to a 6% error on the full scale measurements.

Fig.(6.39) shows that at a yaw angle of -20.0°, the velocity is only at freestream at 1.5 m above the cab. The limitation by the vehicle suppliers eliminated this height as a viable test location. The rotary cup anemometer used for on-road testing was mounted 0.18 m above the cab, corresponding to a normalised x-velocity (U/Ux) of 0.85 (29.75 ms^{-1} for a 35 ms^{-1} inlet velocity). Due to the rotary cup anemometer combining the x-velocity and y-velocity flow fields, the wind speed measured at 0.18

m was the resultant of measuring 0.85% of freestream (x-velocity) and 0.42% of freestream (z-velocity). The resultant velocity vector equated to a speed of 33.2 ms^{-1}, created a -5.1% error on the wind speed measurement at -25.0° yaw angle.

The errors associated with the other yaw angles tested are shown in Tab.(6.10).

Yaw Angle (°)	Error(%)
-20.0	-5.1%
0.0	1.3%
+20.0	+5.6%

Table 6.10: Wind Anemometer Sensor Offset due to Mounting Location.

The maximum error in wind speed measurement due to the mounting location was +5.6% at +20.0° yaw angle.

6.1.12 Subsection Summary

The results obtained from the pressure differential location indicated a linear relationship between a pressure coefficient differential (ΔC_P) and the wind yaw angle (β). Four rows of pressure tappings were measured, each containing nine individual tappings. One row was located on the static skirt of the deflector, with the remaining three rows located on the deflector.

The static skirt tappings provided the most accurate relationship between ΔC_P and β. Pressure tapping pairs (1) and (9) located on the static skirt were found to have the least variation with δ_H.

The linear relationship formed from these tapping was: $\beta_{Est} = \Delta C_{P(\text{offset})} - C_1$, where: $\Delta C_{P(\text{offset})} = \Delta C_P / 0.083$ and $C_1 = 0.410$.

From wind tunnel and CFD measurements the mounting location of the wind vane and wind anemometer was found to have an effect on the sensors. The zero yaw offset on the wind vane was found to be approximately -15.0°. Once the zero yaw offset had been accounted for, the accuracy was around 6% at the maximum yaw angle tested of 20.0°. This equated to a maximum full scale error of ±1.2° on the measurement of β. The error on the anemometer was found to be approximately 5.3% at ±20.0° equating to ± 1.8 ms^{-1} (4.0 mph) on a total velocity (V) of 35 ms^{-1} (78.2 mph).

This page intentionally left blank.

6.2 Computational Results

The aim of the 3D Computational Fluid Dynamics (CFD) simulations were to investigate the accuracy of the chosen 2D Reynolds-Averaged Navier-Stokes (RANS) model with the obtained experimental results (the 2D CFD results are shown in Sec.(F.1) of Appendix F). More information on the model arrangement and computational methodology is shown in Chapter 4.

6.2.1 3D Cell Size Conversion

Due to the complexity of the 3D geometry an unstructured mesh was chosen, as a result the effect of cell size on the numerical convergence was investigated. Initially a series of five meshes with varying near vehicle cell size were chosen, shown in Tab.(6.11). The purpose of the study was to investigate the effect of the near vehicle cell size on the accuracy of the C_D prediction. The Spalart-Allmaras solver was again chosen as it is a single equation model, providing the lowest execution time for convergence.

Case Number	Near Vehicle Cell Size (mm)	Mesh Size (Cells)	C_D
3D Case 1	2000	2.5×10^6	0.583
3D Case 2	1000	2.0×10^6	0.567
3D Case 3	250	5.0×10^6	0.525
3D Case 4	50	10.0×10^6	0.521
3D Case 5	25	20.0×10^6	0.521

Table 6.11: Spalart-Allmaras 3D Cell Size Convergence Study.

The results indicated that a near vehicle cell size of 50 mm was sufficient to provide C_D convergence. This agrees well with Pointer et al. [76] near vehicle cell size value of 6 mm for a $1/8^{th}$ scale model, equated to 48 mm for a full scale vehicle.

6.2.2 3D Container Centre Line Pressure Distribution

The 2D container centre line pressure distribution failed to accurately predict the drop in C_P for an increase in the non dimensional length (x/L) along the container.

For an increasing (x/L) the C_P was expected to drop to close to 0.0 indicating that the flow was returning to freestream velocity. Fig.(6.42) shows a comparison between 2D and 3D k-$\epsilon_{(Realizable)}$ and the wind tunnel data from Sec.(3.6.1.2). The experimental points are limited due to extensive prior work on the centre line trends on HGVs (shown in Fig.(6.41)).

The results indicated an improvement in the centre line pressure distribution predicted by the 3D k-$\epsilon_{(Realizable)}$ turbulence model. The 3D model underpredicted the experimental C_P of around -0.95 at the leading edge of the trailer by almost half (C_P = -0.5). The prediction of the increase in C_P for increasing (x/L), however, was estimated more accurately with the 3D case with a minimum of C_P = -0.05 compared to the experimental C_P of -0.2. Due to the improved accuracy of the centre line pressure distribution, the forebody pressure distribution was then investigated. The container forebody had a larger array of tappings to enable a more detailed comparison. The layout for experimental tapping array is shown in Chapter 3.

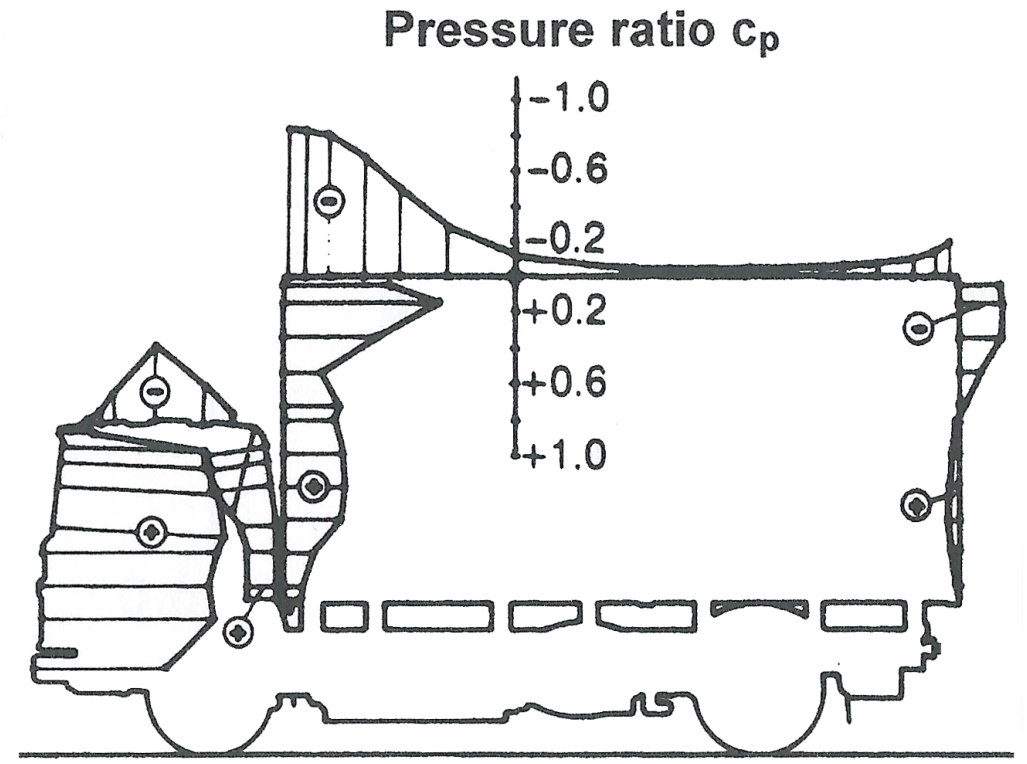

Figure 6.41: Truck Centre Line Pressure Distribution [87].

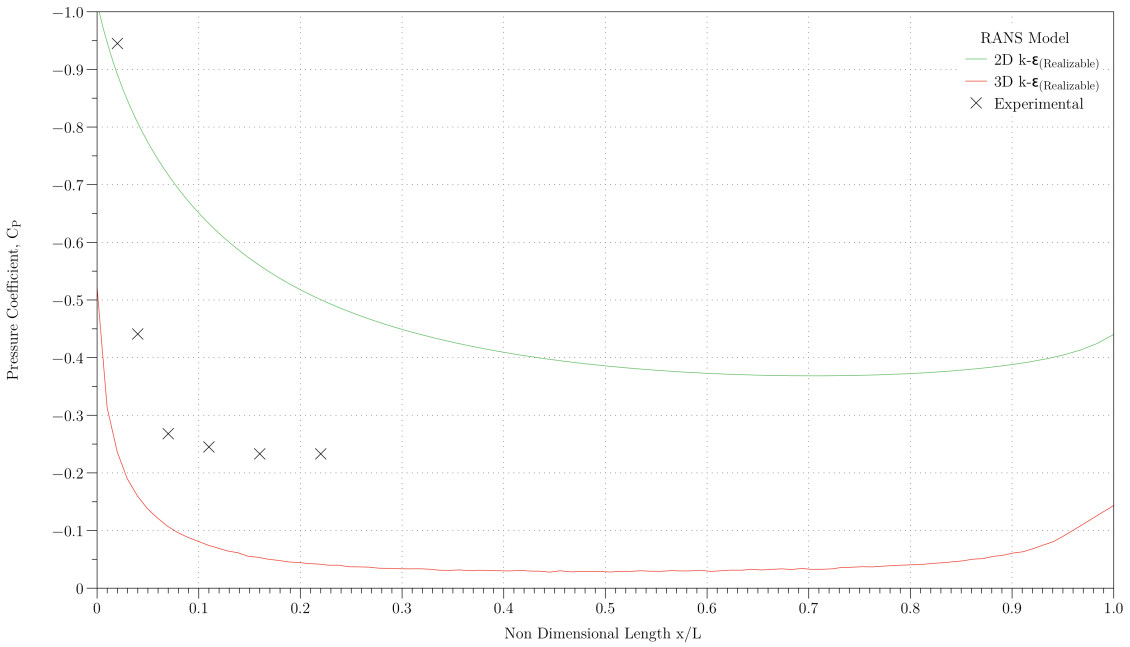

Figure 6.42: 2D and 3D k-$\epsilon_{(Realizable)}$ CFD vs. Experimental - Centre Line Pressure, $\delta_H = 0.968$ and $g/d_2 = 0.838$.

6.2.3 3D Container Forebody Pressure Distribution

6.2.3.1 3D Container C_P Distribution vs. Experiment

Initial comparison with experimental data was made and the resulting contour plots are shown in Fig.(6.43). The 3D k-$\epsilon_{(Realizable)}$ turbulence model showed a good prediction of the forebody pressure distribution. The model correctly predicted an area of higher pressure on the top corners of the container due to 'spill-over' from the rear of the deflector.

An area of significant recirculation was present at the upper half central region of the container, predicted correctly by the model. The model, however, underpredicted the C_P, with a value of -0.2 compared to the experimental value of -0.3. The flow structure of the lower section of the forebody was also predicted correctly. Two asymmetrical peaks of lower C_P with a slight underprediction in the C_P from the model of -0.2 compared to the experimental value of -0.3.

The accuracy of the structure of the forebody pressure distribution implied the flow geometry within the cavity was sufficiently modelled. Direct comparison with experimental values showed an underprediction in the magnitude of the C_P values.

This correlated to an underprediction from the CFD simulation on the C_D values. Comparison of the relative changes, between container separations and deflector heights, however, revealed more accurate trends.

The prediction of the forebody pressure for $g/d_2 = 1.056$ is shown in Fig.(6.44), comparison was made against $g/d_2 = 0.798$ using the same turbulence model.

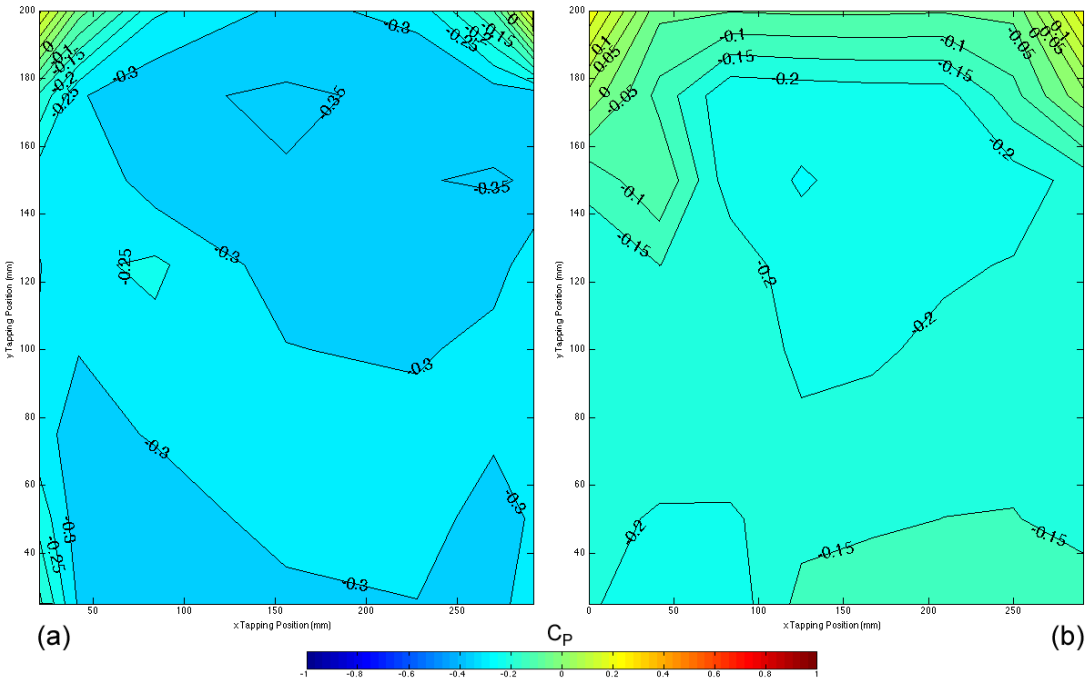

Figure 6.43: C_P Distribution on Container Forebody, (a) Experimental, (b) k-$\epsilon_{(Realizable)}$, $\delta_H = 0.968$, $g/d_2 = 0.798$ and $\beta = 0°$.

6.2.3.2 3D Container C_P Distribution for Varying g/d_2

Increasing container separation resulted in the shear layer separating from the top of the deflector onto the container forebody. The result was an increase in the C_P on the top of the container from C_P = -0.1 at $g/d_2 = 0.798$ to C_P = +0.1 at g/d_2 = 1.056. The increase in forebody pressure and additional cavity recirculation lead to an increase in C_D for increased g/d_2.

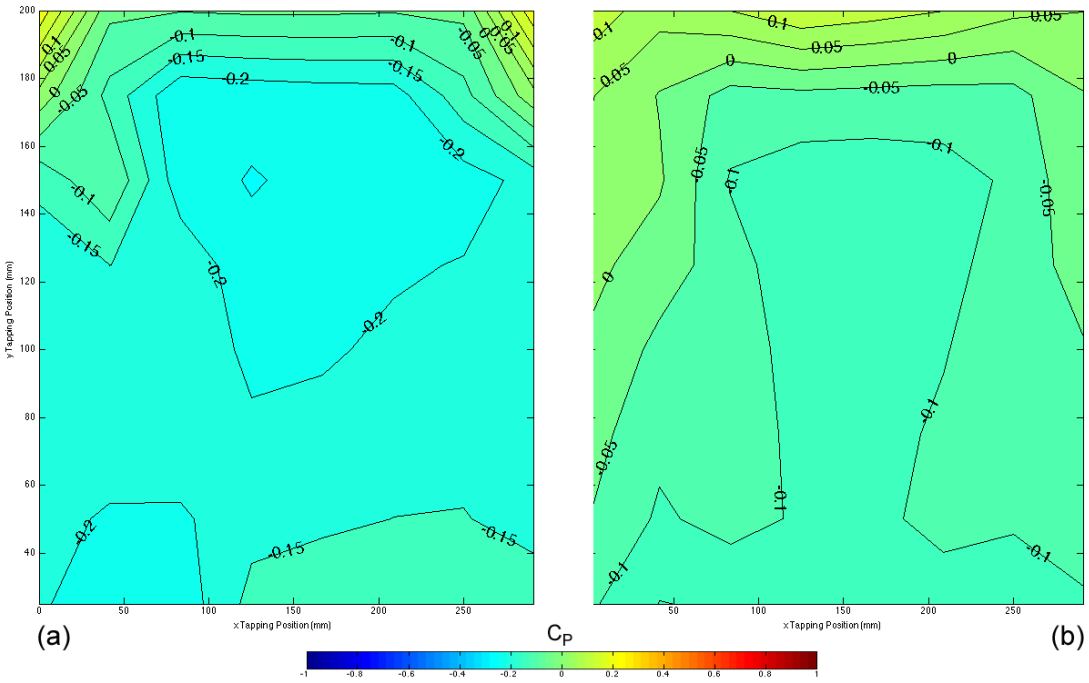

Figure 6.44: k-$\epsilon_{(Realizable)}$ C_P Distribution on Container Forebody, (a) $g/d_2 = 0.798$, (b) $g/d_2 = 1.056$, $\delta_H = 0.968$ and $\beta = 0°$.

6.2.4 3D k-$\epsilon_{(Realizable)}$ Prediction of ΔC_D vs. g/d_2

The wind tunnel data is shown in Tab.(6.12 and 6.13), the corresponding k-$\epsilon_{(Realizable)}$ predicted C_D and ΔC_D are shown in Tab.(6.14 and 6.15) respectively.

	g/d_2			
δ_H	0.658	0.798	0.838	1.056
0.968	0.598	0.584	0.583	-

Table 6.12: Wind Tunnel C_D Results Summary.

	g/d_2			
δ_H	0.658	0.798	0.838	1.056
0.968	-	-2.3%	-2.5%	-

Table 6.13: Wind Tunnel ΔC_D Results Summary.

	g/d_2			
δ_H	0.658	0.798	0.838	1.056
0.968	0.507	0.505	0.504	0.527

Table 6.14: k-$\epsilon_{(Realizable)}$ C_D Prediction.

	g/d_2			
δ_H	0.658	0.798	0.838	1.056
0.968	-	-0.4%	-0.6%	+5.2%

Table 6.15: 3D k-$\epsilon_{(Realizable)}$ ΔC_D Predication.

The results obtained from the simulation showed accurate prediction of the C_D dropping for increasing g/d_2 from 0.658 to 0.838. The RANS simulation also correctly predicted an increase in the C_D as the normalised gap width ($G/\sqrt{A}$) (Shown in Tab.(6.14)) exceeded the critical value of 0.5, determined by Hammache [39] (Shown in Fig.(6.45)).

The g/d_2 value of 1.056 corresponds to a $G/\sqrt{A}$ value of 0.64, above 0.5 the trailer drag contributes significantly to the overall drag of the vehicle. The resulting 3D effect meant that the 2D model could not accurately predict the flow field for $g/d_2 \geq 0.8$ and was only useful for the prediction of trends.

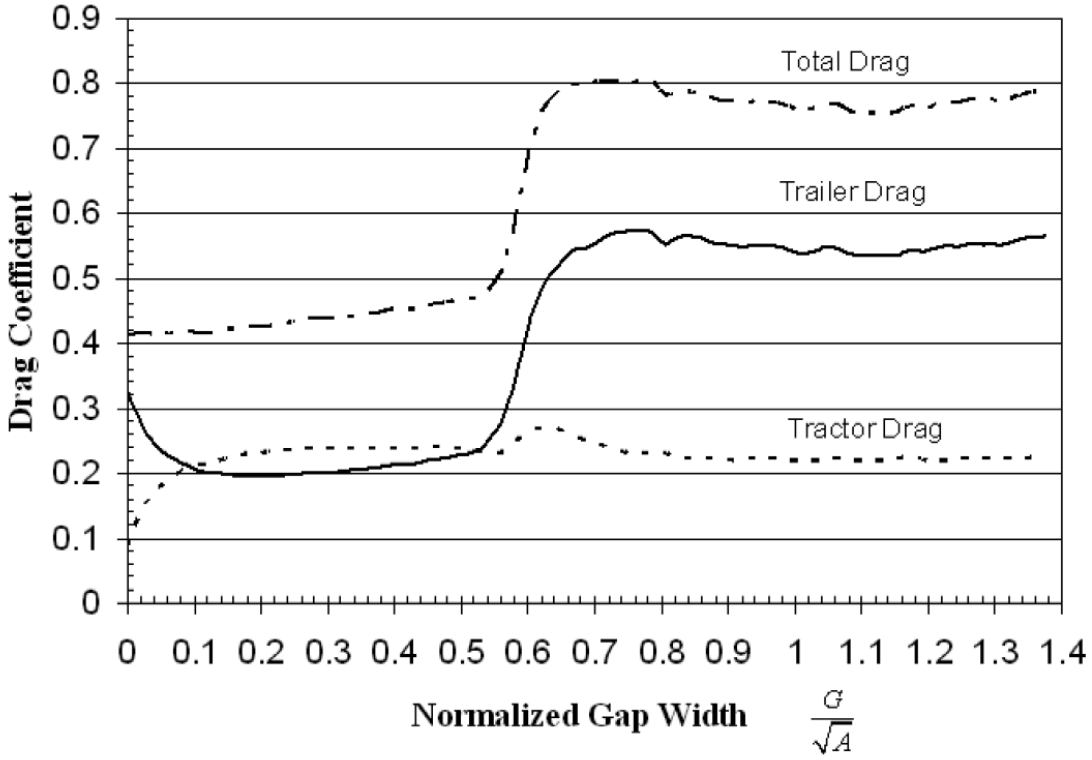

Figure 6.45: Tractor Trailer Cavity Separation [39].

6.2.5 3D Flow-Field Visualisation

The flow field associated with the 3D geometry is shown in Fig.(6.46), the 3D tractor-trailer cavity recirculation and cab deflector recirculation is shown in Fig.(6.47). Comparison was made of the tractor-trailer cavity (shown in Fig.(6.48)) with prior experimental data obtained by Hammache [39] (shown in Fig.(6.49)).

The 3D k-$\epsilon_{(Realizable)}$ accurately predicted a pair of symmetric vortices present within the cavity. The RANS averaging, however, removed the time-variation of these vortices present within the experimental data. In order to predict the transient effects of the larger cavity, Large Eddy Simulation (LES) was required. Due to relatively short period of approximately 2 seconds determined by Hammache [39], averaging was sufficient for determining the optimum deflector height ratio (δ_{Hopt}).

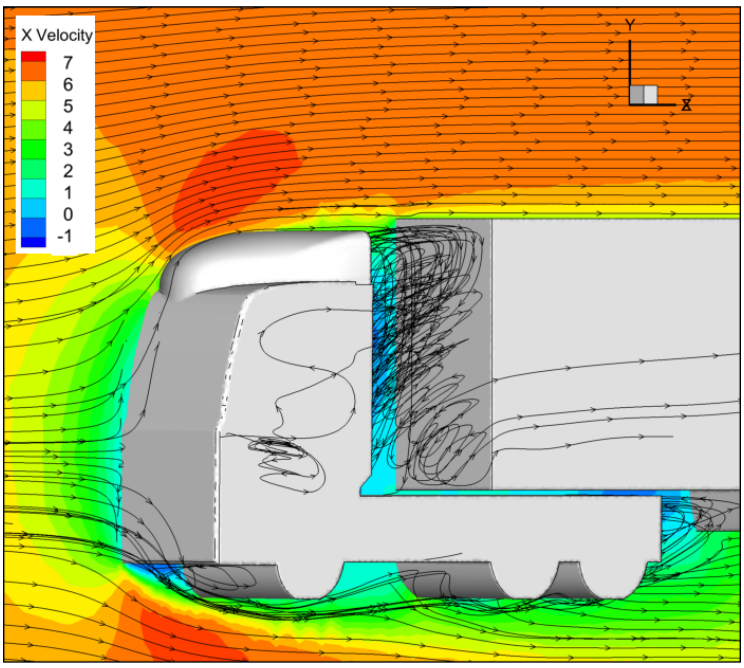

Figure 6.46: CFD Velocity Flow-Field, $\delta_H = 0.968$ and $g/d_2 = 1.056$.

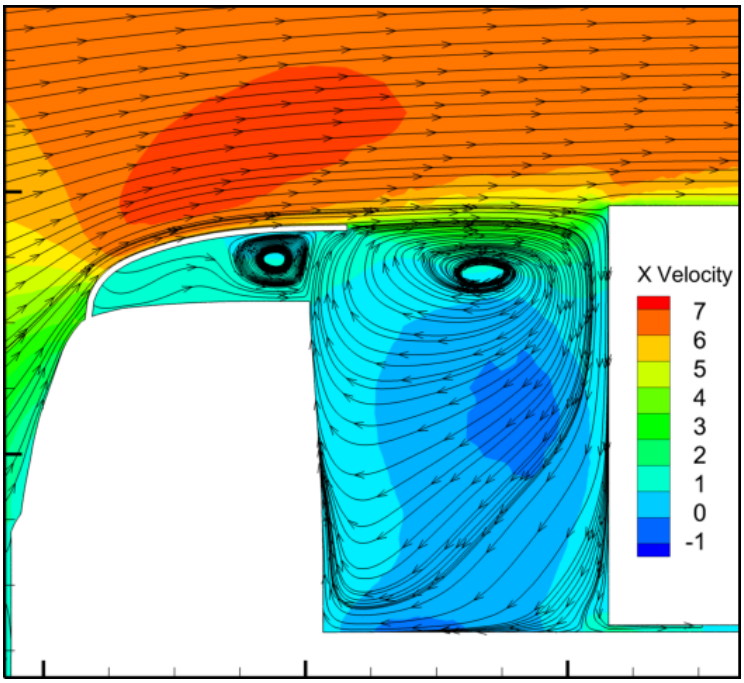

Figure 6.47: CFD Velocity Flow-Field, $\delta_H = 0.968$ and $g/d_2 = 1.056$.

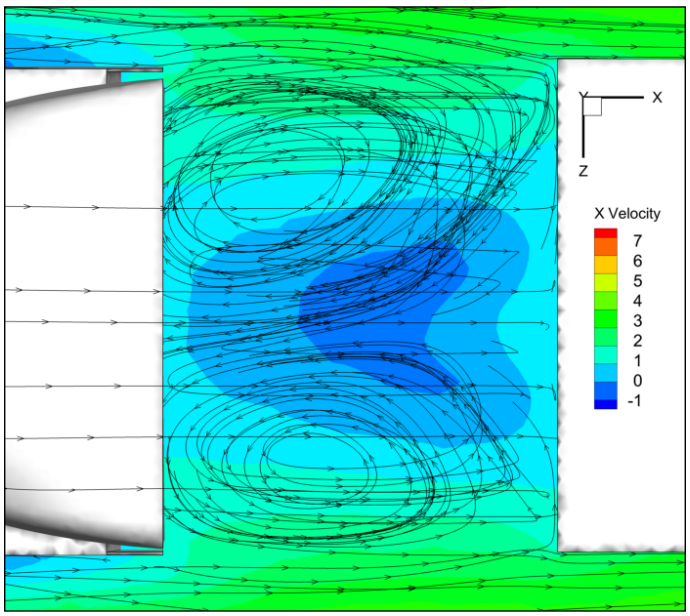

Figure 6.48: CFD Velocity Flow-Field, $\delta_H = 0.968$, $g/d_2 = 1.056$ and $G/\sqrt{A} = 0.64$.

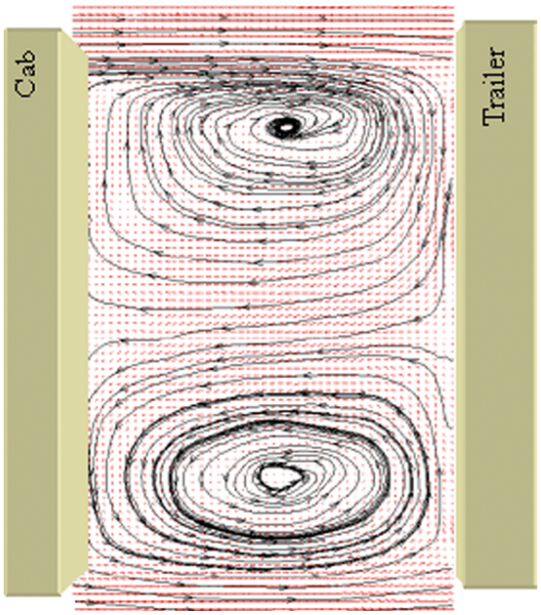

Figure 6.49: Experimental Tractor-Trailer Flow-Field [39] for $G/\sqrt{A} = 0.65$.

6.2.6 Subsection Summary

The results obtained from the numerical investigation revealed the optimum RANS solver for the experiment to be the k-$\epsilon_{(Realizable)}$. The k-$\epsilon_{(Realizable)}$ correctly predicted the structure of the wake vortices when comparing with the experimental data.

The k-$\epsilon_{(RNG)}$ model most accurately predicted the ΔC_D but added a non-physical additional recirculation region to the lower side of the tractor. The k-$\epsilon_{(Realizable)}$ model was shown to offer better performance over both k-ϵ and k-$\epsilon_{(RNG)}$ as it satisfies mathematical constraints on the Reynolds stresses consistent with the flow physics of turbulent flows. The RANS model to most accurately model the deflector flow field and recirculation within the cavity flow is therefore the k-$\epsilon_{(Realizable)}$ turbulence model.

The 2D k-$\epsilon_{(Realizable)}$ model, however, failed to correctly predict the trailer centre line or container forebody pressure distribution. The 2D geometry was therefore only sufficient for predicting the optimum deflector height ratio up until the critical value of $g/d_2 < 0.8$. For $g/d_2 \geq 0.8$ the cavity effect dominated and the tractor contributed significantly to the overall drag of the vehicle.

The 3D k-$\epsilon_{(Realizable)}$ turbulence model was therefore required to accurately model the flow physics of the tractor-trailer. The 3D model accurately predicted the structure of the container centre line and forebody container pressures, resulting in an strong improvement in accuracy of the cavity flow field compared to the 2D case. The resulting C_D prediction offered by the 3D model was therefore sufficient to allow prediction of the optimum deflector height using only computational simulation.

6.3 Full Scale Testing

Wind tunnels are designed to be low in turbulence to enable accurate, repeatable data measurement. This stable environment, however, does not reflect the nature of the on-road, turbulent flow. Full scale on-road testing was conducted to determine the effects that the real-world turbulence had on the estimated yaw angle (β_{Est}). The estimated yaw angle was predicted from a wind tunnel pressure differential (ΔC_P). The predicted relationship obtained in Eq.(6.5) on page 177 relates a ΔC_P generated from two static tappings located on the static skirt of the deflector to the wind yaw angle (β). The accuracy of estimating β via β_{Est} directly relates to the efficiency of the control scheme used in the production controller.

The aim of the full scale testing was to identify and filter out any high frequencies present in the data that did not relate to the macro flow field. Numerical simulation using Large Eddy Simulation (LES) of two truck-trailer units in tandem was also conducted for comparison and to aid identification of the frequency spectrum obtained from the micro flow field.

6.3.1 Overview of Test Programme

Full scale on-road testing was conducted over a period of approximately four weeks covering a total of 766 miles (1,232 km), resulting in just under 14h worth of data. The tests were conducted over a variety of different delivery routes, shown in Figs.(6.50 and 6.51). A more detailed view of the individual runs along with the route statistics are shown in Secs.(G.4.2 - G.4.14.1) of Appendix G. The test route road type associated with the runs is shown in Tab.(6.16) with the test route statistics shown in Tab.(6.17).

The experimental configuration used for the full scale tests is shown in Sec.(3.7). Wind speed (V_{Wind}), yaw angle (β), vehicle speed (V_{Truck}) and two pressure tappings ($P_{(1,2)}$) were logged at 100 Hz with vehicle position at 20 Hz. Testing was automatically started once the vehicle's velocity exceeded 30 mph or 13 ms^{-1} and stopped when the vehicle's velocity dropped below 20 mph or 9 ms^{-1}. The automation used for data recording prevented large amounts of dead-zone (irrelevant data) being logged when the vehicle was stationary. The result of the automatic logging was that certain test routes shown in Fig.(6.51) were split into sections (a) and (b) where logging stopped and then recommenced. Due to delivery routes containing repeat deliver locations, certain routes (such as Run [4a] have been repeated at a later date in another run, e.g. Run [8]).

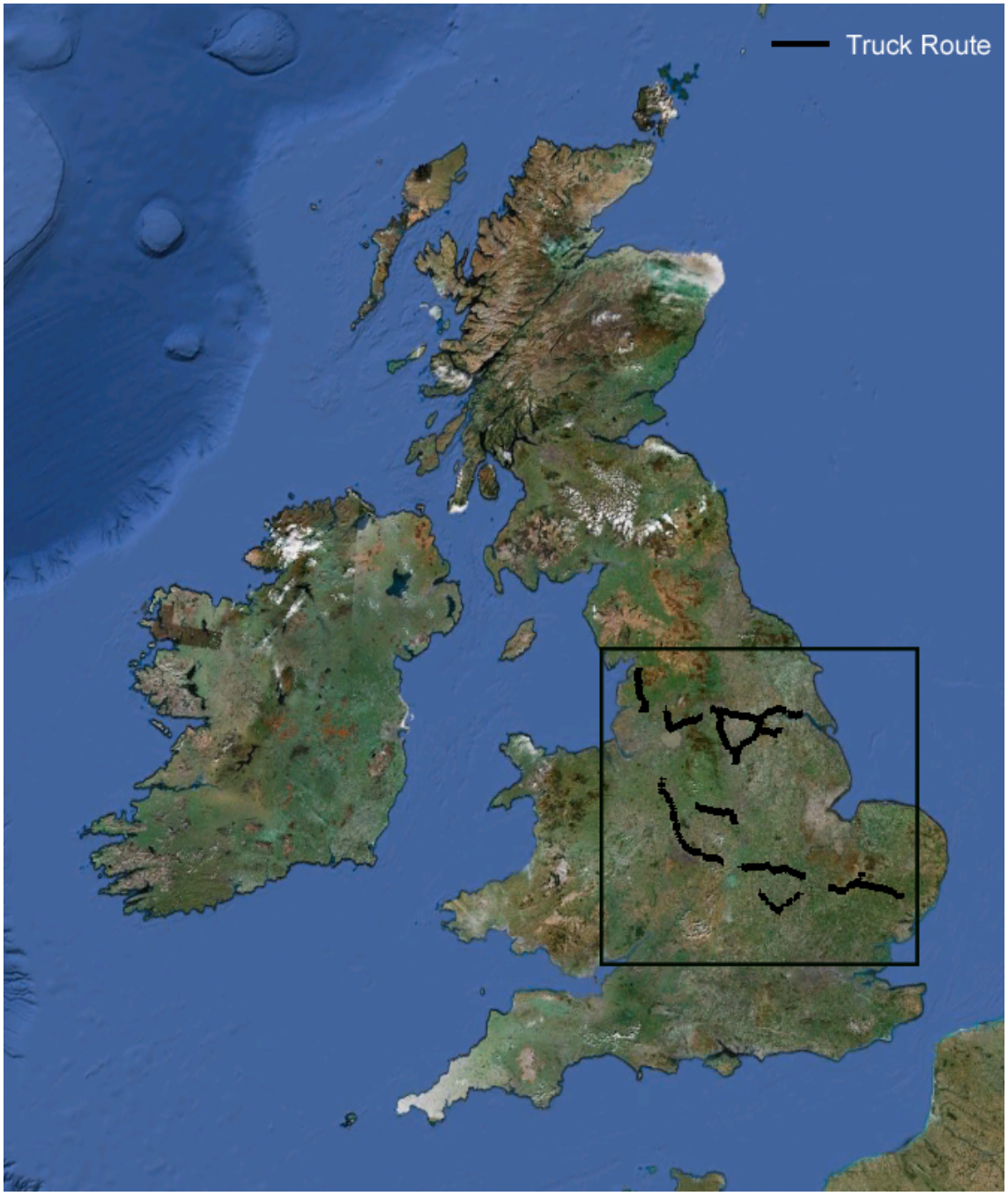

Figure 6.50: Vehicle Test Routes.

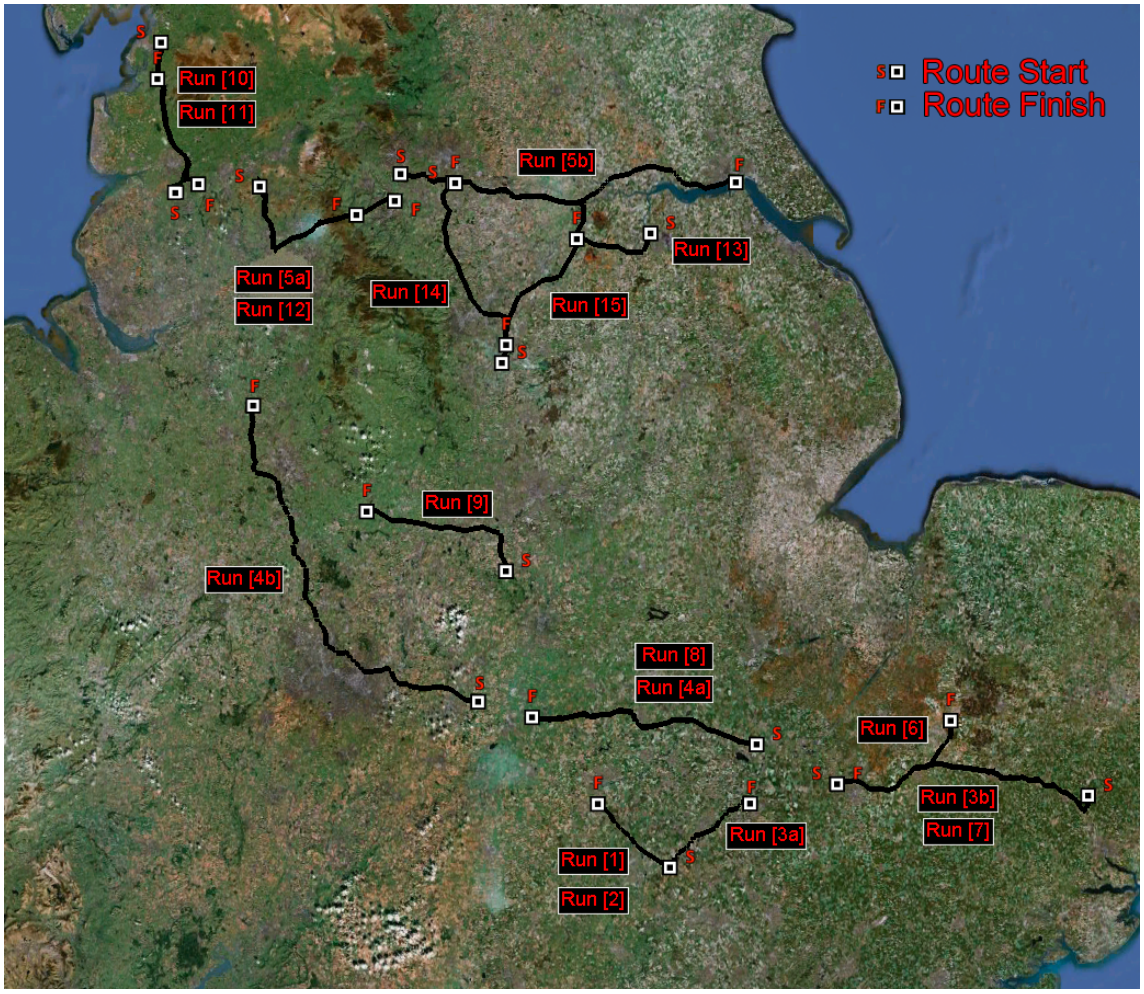

Figure 6.51: Annotated Vehicle Test Route.

Run Number	Terrain Type	Road Name
Run [1]	Motorway	(M1)
Run [2]	Motorway	(M1)
Run [3]	Dual Carriageway	(A14)
Run [4]	Motorway	(M6)
Run [5]	Motorway	(M18)
Run [6]	A-Road (3 Lanes)	(A14)
Run [7]	A-Road (3 Lanes)	(A14)
Run [8]	Dual Carriageway	(A14)
Run [9]	Dual Carriageway	(A50)
Run [10]	Motorway	(M6)
Run [11]	Motorway	(M6)
Run [12]	Motorway	(M62)
Run [13]	Motorway	(M18)
Run [14]	Motorway	(M1)
Run [15]	Motorway	(M18)

Table 6.16: Test Route Road Type.

A typical UK Motorway and Dual Carriageway are shown in Figs.(G.1 and G.2) respectively in Sec.(G.1) of Appendix G.

Run Number	Date (dd/mm/yyyy)	Test Length (km)	Test Duration (hh:mm:ss)
Run [1]	22/08/2012	56.5	00:27:11
Run [2]	22/08/2012	50.1	00:21:27
Run [3]	22/08/2012	140.3	01:34:52
Run [4]	23/08/2012	188.7	02:12:45
Run [5]	23/08/2012	196.0	03:09:17
Run [6]	05/09/2012	44.8	00:32:12
Run [7]	06/09/2012	84.3	00:58:22
Run [8]	06/09/2012	69.4	00:48:12
Run [9]	06/09/2012	51.9	00:36:30
Run [10]	07/09/2012	56.2	00:38:31
Run [11]	07/09/2012	36.8	00:25:21
Run [12]	14/09/2012	79.6	00:56:24
Run [13]	14/09/2012	74.3	00:51:53
Run [14]	14/09/2012	58.7	00:39:39
Run [15]	14/09/2012	45.1	00:31:20
Total:	-	1232.1	13:51:09

Table 6.17: Vehicle Test Route Statistics.

The GPS coordinates of the start and finish locations of the test routes are shown in Tabs.(G.4 - G.40) in Secs.(G.4.2 - G.4.14.1) of Appendix G.

6.3.2 Probability Distributions of Test Sample

Statistical analysis of the wind speed and direction for all the test routes are shown in Tab.(6.18 and 6.22) respectively. The wind speed histogram is shown in Fig.(6.52) with the histogram for wind direction shown in Fig.(6.55). Secs.(G.4.2 - G.4.14.1) of Appendix G contain the statistics associated with individual runs.

6.3.2.1 Wind Speed

Analysis of the wind speed of all the runs revealed a large range of velocities associated with the data set, a range of 0 ms^{-1} to 19.9 ms^{-1} with minor negative skewness and a mean of 8.7 ms^{-1}. Average annual wind speeds were recorded at various sites throughout the UK, an example of the annual average wind speed for 1999 is shown in Fig.(6.53).

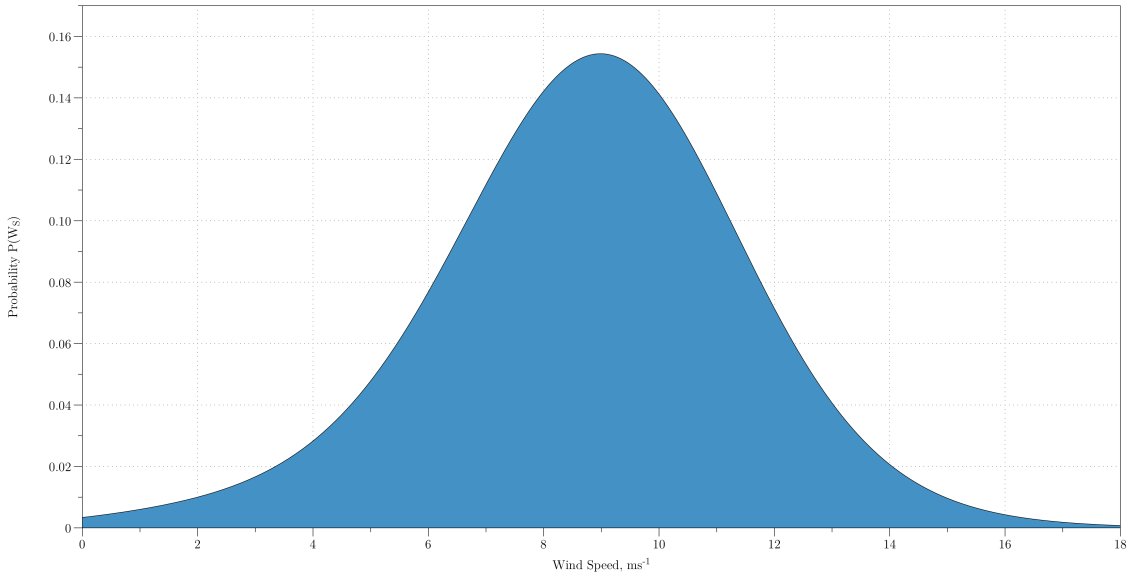

Figure 6.52: Wind Speed (V_{Wind}) Probability Distribution.

Item	Value
Minimum	0.0
Maximum	19.9
Range	19.9
Standard Deviation (σ)	2.3
Skewness	-0.5
Kurtosis	1.5
Q1	7.6
Median	8.9
Q3	10.0
Average	8.7
Sample Points	5.0×10^6

Table 6.18: Wind Speed Histogram Statistical Values.

The majority of the on-road data was collected from motorway or dual carriage driving (see table Tab.(6.16)). The wind shear coefficient (n) used to extrapolate the wind speed to 4.0 m was therefore chosen to be 0.1 (smooth-hard ground), shown in Fig.(6.19). The resulting extrapolated annual mean wind speed for the areas associated with the test route is shown in Fig.(6.54). The individual wind speeds for each run are shown in Tab.(6.20).

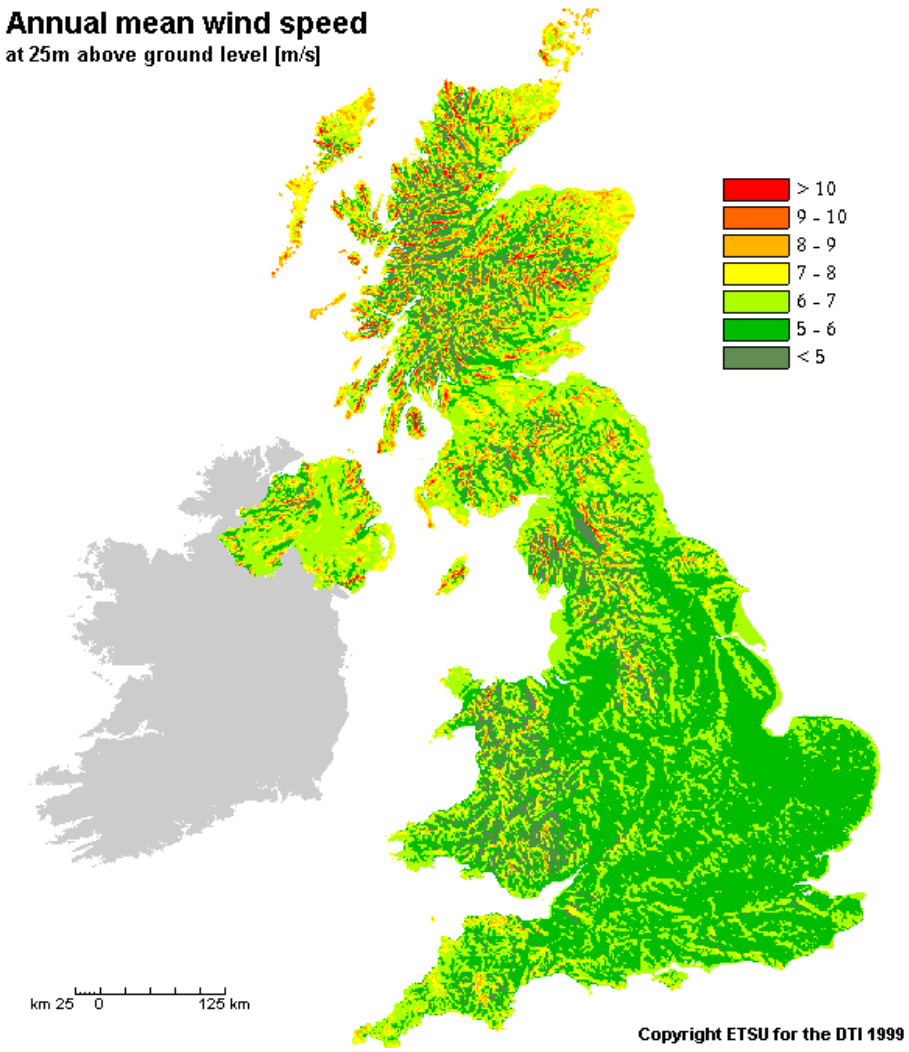

Figure 6.53: UK Annual Mean Wind Speed [88].

Estimation for the wind speed at vehicle level (4 m) is given by a simple power law extrapolation [89]

$$\left(\frac{Z_1}{Z_2}\right)^n = \left(\frac{V_1}{V_2}\right) \tag{6.6}$$

where Z_1 is the height of required wind data (4 m), Z_2 is the height of measured wind data (25 m), V_1 is the required velocity, V_2 is the velocity of measured wind data and n is the wind shear coefficient (terrain depended, shown in Tab.(6.19)).

Terrain Type	n
Lake, Ocean, and Smooth-Hard Ground	0.10
Foot-High Grass on Level Ground	0.15
Tall Crops, Hedges, and Shrubs	0.20
Wooded Country with Many Trees	0.25
Small Town with Some Trees and Shrubs	0.30
City Area with Tall Buildings	0.40

Table 6.19: Wind Shear Coefficient of Various Terrains [90].

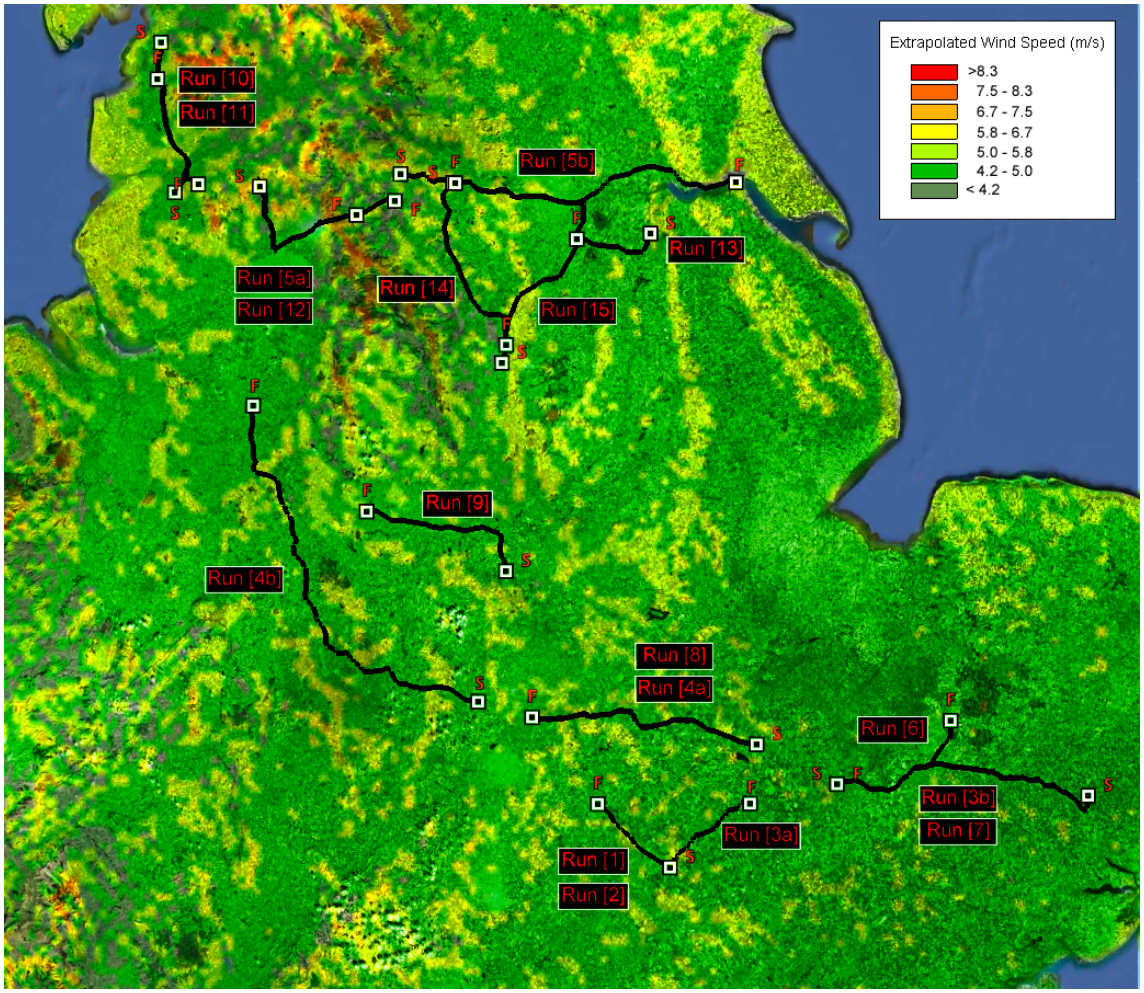

Figure 6.54: Extrapolated Annual Mean Wind Speed.

Run Number	$\overline{V}_{Wind}$ (ms^{-1})	Extrapolated V_{Wind} (ms^{-1})
Run [1 & 2]	7.1	4.2 - 6.7
Run [3]	7.0	4.2 - 5.8
Run [4b]	7.4	4.2 - 6.7
Run [5b]	9.0	6.7 - 8.3+
Run [6]	9.9	5.0 - 5.8
Run [7]	7.7	5.0 - 5.8
Run [8]	8.7	5.0 - 6.7
Run [9]	8.1	5.0 - 6.7
Run [10]	8.2	6.7 - 8.3+
Run [11]	8.9	6.7 - 8.3+
Run [12]	8.1	6.7 - 8.3+
Run [13]	8.2	5.0 - 6.7
Run [14]	8.4	6.7 - 8.3+
Run [15]	9.3	4.2 - 6.7

Table 6.20: Test Route Average Wind Speed.

The results obtained from the on-road test showed that for a one month test period, an average wind speed of 8.2 ms^{-1} was obtained. Individual analysis of the runs revealed that the majority of the runs lie above the predicted velocity range based on annualised data. Run [5], Run [10] - Run [12] and Run [14] do, however, lie within the extrapolated velocity range.

The differences arose due to the comparison of daily data with mean annual data. Section (G.2) of Appendix G compares Met Office [91] data with the data obtained from the on-road tests. The summarised results are shown in Tab.(6.21).

The results show closer agreement than the annualised data. This indicated that during the period of on-road testing, the UK experienced a higher than average level of wind speed on the majority of test routes. Table (6.21) show a maximum difference between the Met Office [91] data and the data obtained from the anemometer of 3.7 ms^{-1} with an average difference of 1.5 ms^{-1}.

The cup anemometer used for the on-road testing measured the total speed (the speed due to the vehicle combined with the wind speed), this equated to an average percentage error of 4.9%. This value is in agreement with the measurement errors supplied by the manufacturer (see Fig.(B.17) in Sec.(B.8) of Appendix B).

Run Number	$\overline{V}_{Wind}$ (ms^{-1})	Weather Station $\overline{V}_{Wind}$ (ms^{-1})	$\lvert\Delta\overline{V}_{Wind}\rvert$ (ms^{-1})
Run [1 & 2]	7.1	6.2	0.9
Run [3]	7.0	7.4	0.4
Run [4b]	7.4	5.1	2.0
Run [5b]	9.0	7.7	1.3
Run [6]	9.9	6.2	3.7
Run [7]	7.7	4.7	3.0
Run [8]	8.7	6.1	2.0
Run [9]	8.1	4.8	3.3
Run [10]	8.2	8.1	0.1
Run [11]	8.9	6.6	2.3
Run [12]	8.1	7.0	1.1
Run [13]	8.2	7.8	0.4
Run [14]	8.4	9.2	0.8
Run [15]	9.3	8.6	0.7

Table 6.21: Test Route and Weather Station Average Wind Speed [91].

6.3.2.2 Wind Direction

The results obtained from the on-road wind measurements indicated an average yaw angle of -0.45° with a standard deviation (σ) of 12.4. The average magnitude of the wind direction ($|\beta|$) was 4.6°. The results showed, at normal operating vehicle velocities the effective yaw angle that the vehicle was subject to over the period of operation was approximately symmetric. This result was to be expected as the routes will often have a prevailing wind direction (Φ_{Wind}) and the vehicle will usually traverse the road in both directions, cancelling out the yaw angle due to the wind direction.

The chosen location of the wind vane mounting location used to record the wind angle is shown in Sec.(6.1.11) of Chapter 6. The wind tunnel yaw angle sign convention is reversed when compared to the on-road yaw notation.

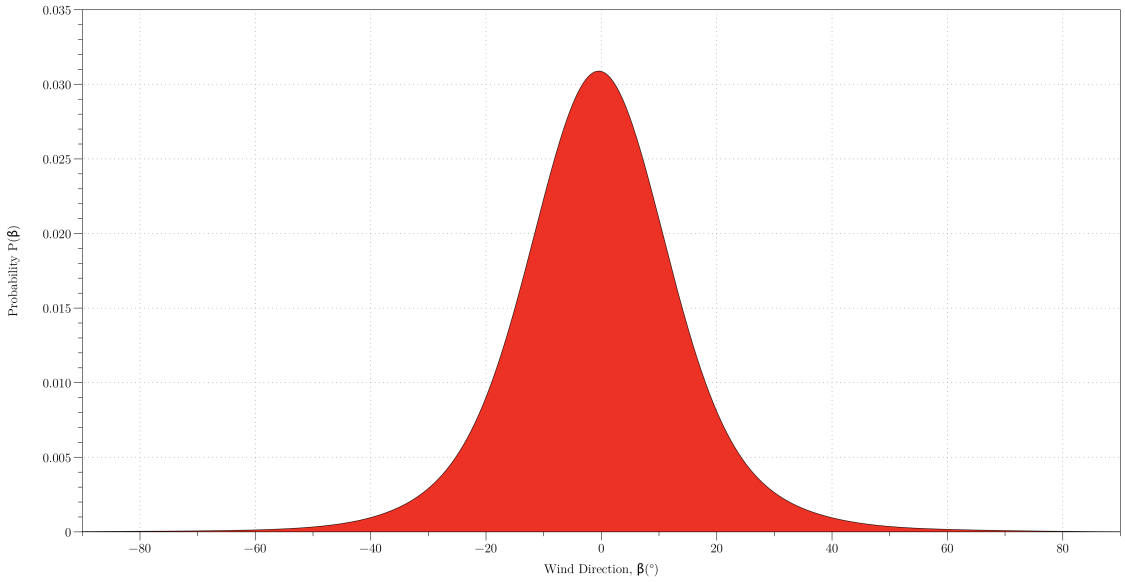

Figure 6.55: Wind Yaw Angle (β) (°) Probability Distribution.

Item	Value
Minimum	-90.0
Maximum	90.0
Range	180.0
Standard Deviation (σ)	12.4
Skewness	0.1
Kurtosis	5.7
Q1	-5.8
Median	-0.5
Q3	5.0
Average	-0.5
Sample Points	5.0×10^6

Table 6.22: Wind Yaw Angle Statistical Values.

Table (6.23) shows summarised comparison results from the data obtained from the Met Office [91]. Section (G.3) of Appendix G provides an example calculation for calculating the wind yaw angle (β) along with data obtained from meteorological sites within the UK.

Run Number	$\overline{\beta}(^\circ)$	Weather Station $\overline{\beta}(^\circ)$	$\lvert\Delta\overline{\beta}\rvert(^\circ)$
Run [1]	-9.9	-11.0	1.1
Run [2]	10.5	11.3	0.8
Run [3]	2.2	2.0	0.2
Run [4b]	-3.9	-8.7	4.8
Run [5b]	0.0	1.1	1.1
Run [6]	-2.2	-6.6	4.4
Run [7]	-5.6	-9.9	4.3
Run [8]	-4.8	-5.2	0.4
Run [9]	-4.9	-10.2	5.8
Run [10]	-2.2	-2.5	0.3
Run [11]	2.3	2.3	0.0
Run [12]	3.2	3.1	0.1
Run [13]	-5.1	-7.0	1.9
Run [14]	10.3	8.0	2.3
Run [15]	2.2	6.2	4.0

Table 6.23: Test Route and Weather Station Average Wind Direction [91].

Table (6.23) shows a maximum difference of 5.8° with an average difference on $\overline{\beta}$ of 2.1°. Whilst this appears to be a large difference in values, this is attributed to directional changes in the vehicle during the run. Run [9] as an example has a 5.8° difference between the measured values, however, the vehicle rotates through 90° during the journey. The vectors used to calculate (β) use an average truck direction along with average speeds of V_{Truck} and V_{Wind}, as a result any significant changes in the vehicle direction will alter the calculation of $\overline{\beta}$. Journeys where the direction of the vehicle does not alter significantly (for example Run [1 & 2]) show a significantly lower difference between the measured values.

6.3.3 Time Variation of V_W, β, ΔP, ΔC_P and β_{Est}

To investigate the effects of the on-road turbulent environment on the measured data, the time variation of the measured variables from Run [4] are shown in Figs.(6.56 - 6.60). The estimated wind direction (β_{Est}) shown in Fig.(6.60) was calculated using Eq.(6.5) derived in Chapter 6. Run [4] was chosen as it contained the largest continuous sample of around 91 minutes worth of data. This enabled a theoretical frequency as low as 0.00036 Hz to be calculated from the data.

Wind Speed (V_{Wind})

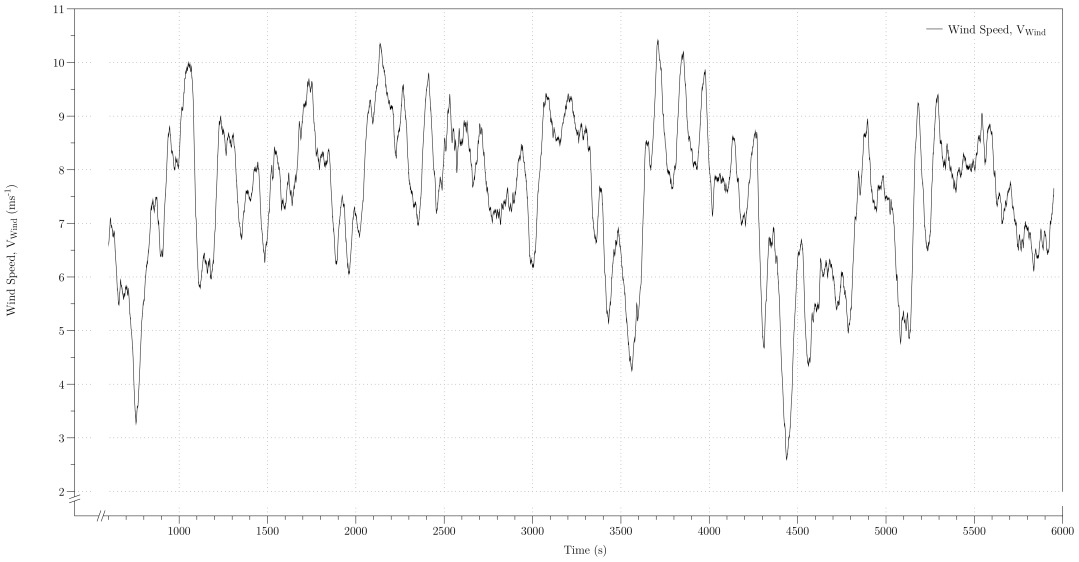

Figure 6.56: Wind Speed (V_{Wind}) Time Variation.

Wind Direction (β)

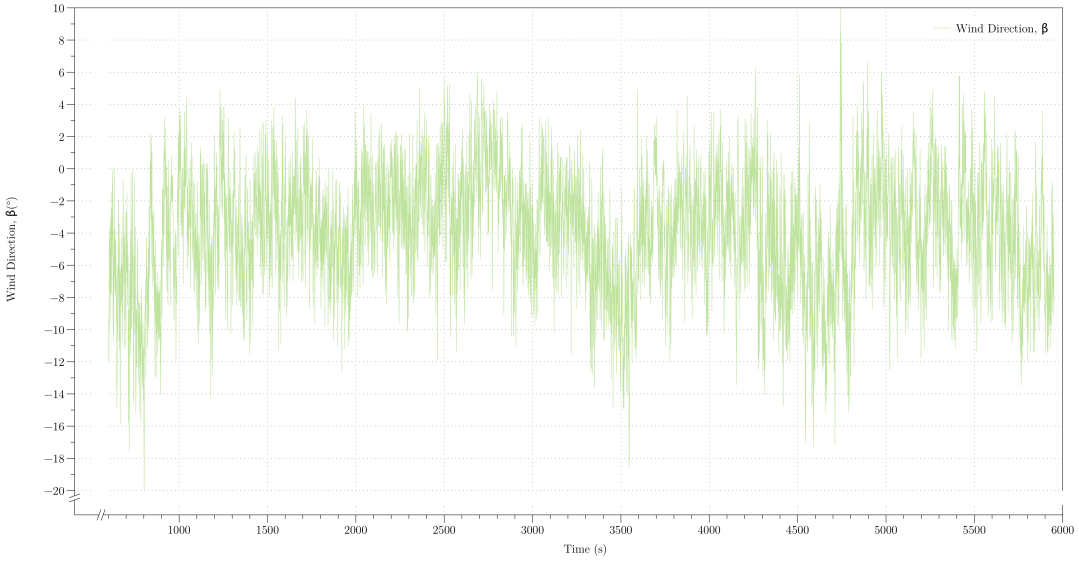

Figure 6.57: Wind Yaw Angle (β) (°) Time Variation.

Pressure Differential (ΔP)

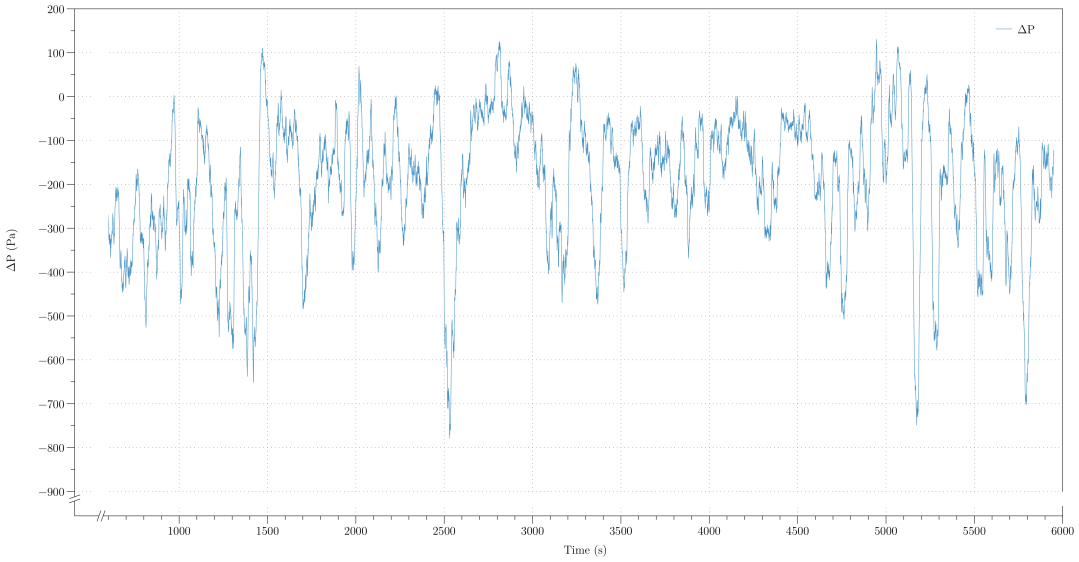

Figure 6.58: Pressure Differential (ΔP) Time Variation.

Pressure Coefficient Differential (ΔC_P)

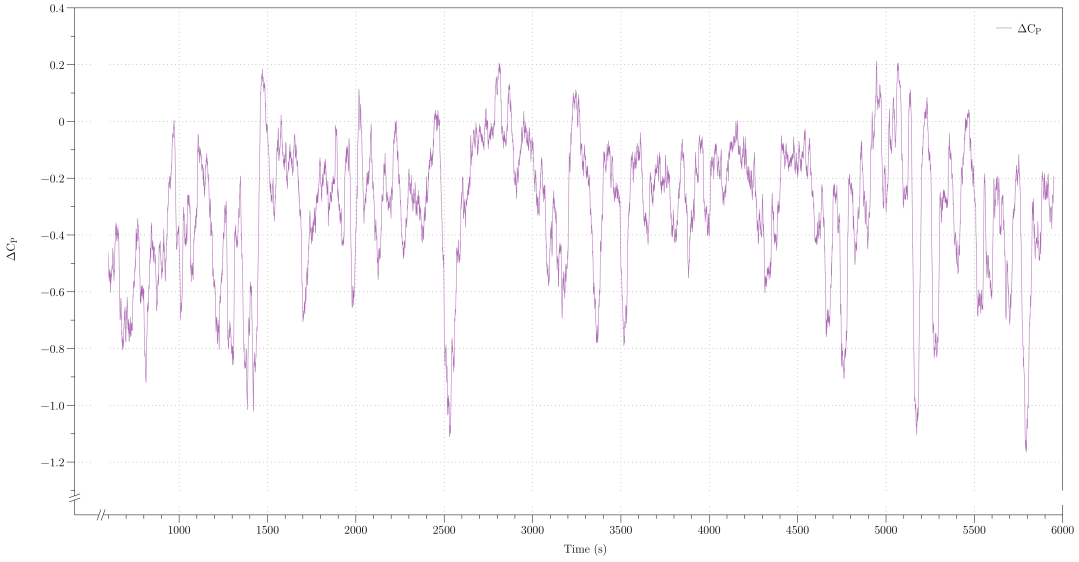

Figure 6.59: Pressure Coefficient (ΔC_P) Time Variation.

Estimated Wind Direction (β_{Est})

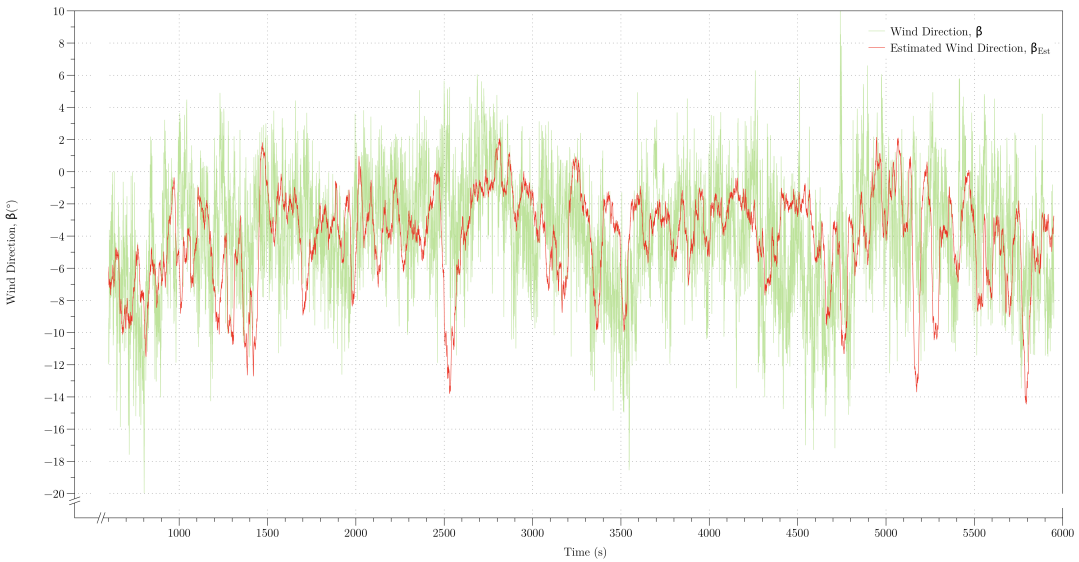

Figure 6.60: Estimated vs. Wind Yaw Angle (β) Time Variation.

Whilst the results displayed for time variation are easy to conceptualise, Fourier analysis was applied to the time series in the form of a Discrete Fourier Transform (DFT). This enabled the underlying frequencies contained within the time series to be determined. Section (G.5) of Appendix G contains details on the DFT and the method of application to the measured data.

6.3.4 Frequency Variation of β

The discrete Fourier transform applied to Run [4] (Fig.(6.57)) is shown in Fig.(6.61). The power spectrum of the remaining runs are shown in Figs.(G.12 - G.62) in Secs.(G.4.2 - G.4.14.1) of Appendix G.

The four frequencies with greatest power contained within the signal are located at low frequencies and are shown in Tab.(6.24). The frequency identification for the remaining runs are summarised in Tab.(6.25).

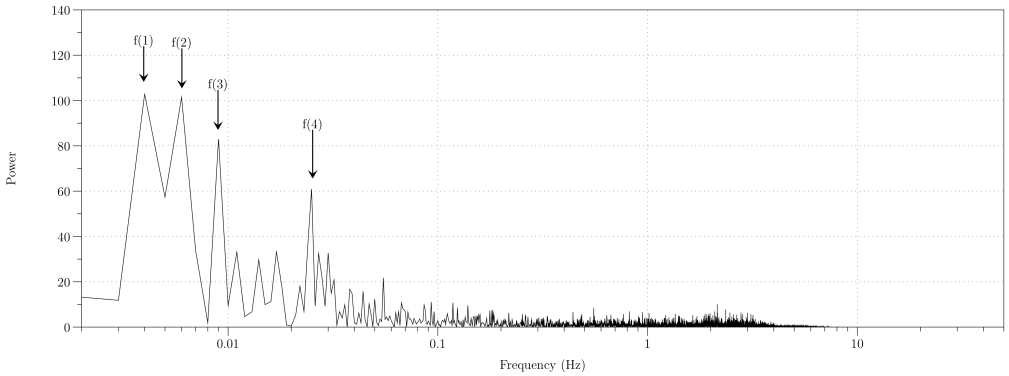

Figure 6.61: On-Road Frequency Power Spectrum of Yaw Angle.

Item	Frequency (Hz)	Period (s)
f(1)	0.004	250.0
f(2)	0.006	166.7
f(3)	0.009	111.0
f(4)	0.025	40.0

Table 6.24: On-Road Frequency Identification.

Run Number	$\overline{\beta}$	P1 (s)	P2 (s)	P3 (s)	P4 (s)
Run [1]	-9.9	202.8	100.3	53.1	38.7
Run [2]	10.5	202.0	144.5	92.1	75.8
Run [3]	2.2	247.0	125.5	99.8	66.8
Run [4b]	-3.9	250.0	166.7	111.0	40.0
Run [5b]	1.1	340.8	247.5	127.7	98.9
Run [6]	-2.2	196.8	102.7	83.1	54.8
Run [7]	-5.6	199.6	124.1	91.9	43.4
Run [8]	-4.8	327.4	248.7	143.5	111.2
Run [9]	-4.9	251.7	143.9	113.0	41.9
Run [10]	-2.2	334.4	125.2	99.6	70.8
Run [11]	2.3	330.4	124.4	70.9	35.6
Run [12]	3.2	255.8	171.8	113.0	40.0
Run [13]	-5.1	200.0	100.2	76.9	66.2
Run [14]	10.3	200.0	101.3	77.0	66.0
Run [15]	2.2	337.6	99.3	70.7	46.4
Average:	-0.45	238.4	141.7	94.9	53.1

Table 6.25: Test Route Frequency Statistics.

The resulting signal obtained was therefore approximated by a mean wind yaw angle ($\beta_{Average}$) perturbed by four frequencies: 0.004, 0007, 0.011 and 0.019 Hz. The mean direction ($\beta_{Average}$) for Run [4] was -3.9°, Fig.(6.62) shows a plot of ($\beta - \beta_{Average}$) for Run [4b].

The four frequencies associated with the perturbation are plotted for comparison of their effect on the signal.

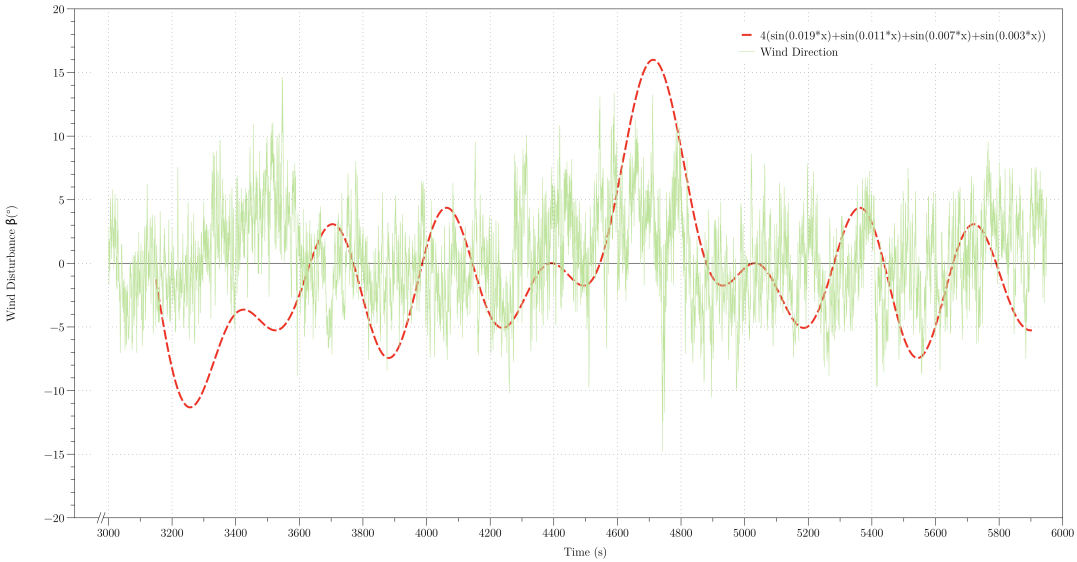

Figure 6.62: Wind Direction Offset.

From the frequency identification, it was apparent that the test routes had a similar frequency variation. Gaylard et.al [49] identified that "the greatest proportion of unsteadies encountered would be below 10 Hz". From the power spectrum obtained in Fig.(6.61) the majority of the unsteadies occurred below 0.1 Hz. Four key frequencies of 0.004, 0007, 0.011 and 0.019 Hz corresponded to periods of 238.4, 141.7, 94.9 and 53.1 seconds, respectively.

The dominating low frequencies were assumed to be due to environmental flow fields with perturbation by high frequency interference. Provided the sampling rate used for on-road tests is above the threshold frequency of 0.019 Hz and averaged over a time period up to 238.4 seconds, a sufficient estimation for the average yaw angle ($\beta_{Average}$) can be made. The average yaw angle required suitable filtering on the input data, this would enable accurate estimation of β_{Est} based only on β.

Due to the relatively high frequencies associated with the change in wind direction (53.1 seconds) compared to an average journey of approximately 2 hours (7,200 seconds), adjustment of the deflector cannot be made at such high frequencies. Calculations made in Sec.(5.3) imposed a critical frequency of 1.54 Hz (0.65 seconds)

on the deflector actuation. This was calculated by determining the minimum period between actuation cycles that would result in a net energy saving. The net energy saving was defined as the resultant saving due to the aerodynamic drag reduction minus the power required to actuate the movement.

Whilst the frequencies obtained from the analysis place the majority of frequencies well below this critical limit, adjustment of the deflector at 0.019 Hz would correspond to approximately 136 actuations per journey. Due to the human factors associated with the product, minimal actuation noise was required. The production controller therefore included an algorithm to estimate the mean yaw angle ($\beta_{Average}$) and adjust only if a significant change in the mean yaw angle was experienced over a significant time period.

6.3.5 Bluff Body Wakes in Freestream Velocity

Bluff body wakes have previously been investigated by Howell [92] and Barzanooni et al. [93], the notation used for bluff body wakes is shown in Fig.(6.63). The characteristic wake parameter is the velocity deficit (U_D) and it is given by

$$U_D = U_0 - U \tag{6.7}$$

It is defined as the difference between the feestream velocity (U_0) and the local velocity measurement in the wake (U). The velocity centre line defect is denoted by U_C and the wake size is defined as the distance between the points at which U_D has reduced to $U_C/2$.

Theoretical studies [94], [95] have shown that U_D decays as $x^{-2/3}$ and the wake width ($Y_{W1/2}$) grows as $x^{-2/3}$, where x is the longitudinal displacement behind the bluff body.

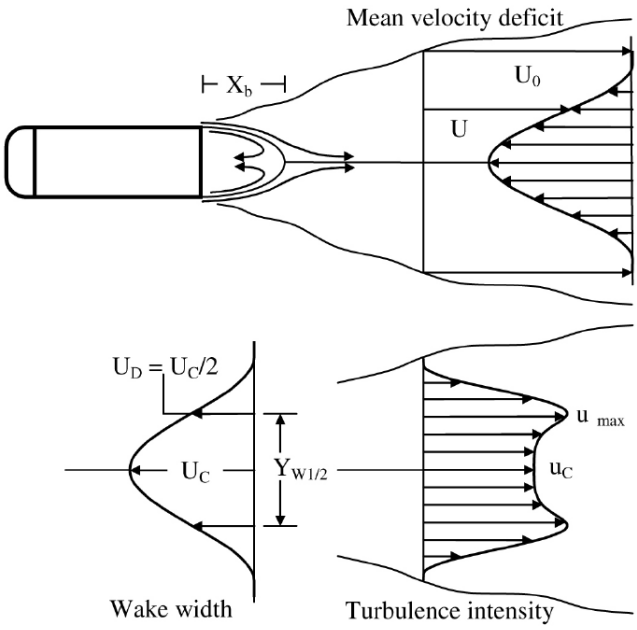

Figure 6.63: Bluff Body Wake Features and Definitions [92].

6.3.5.1 Bluff Body Model Dimensions

The bluff body notation used by Howell [92] applied to the 3D CFD model is shown in Fig.(6.64). The CFD simulation slices were extracted at a vertical height of 1.61 m in the y-axis equating to $(y/W = 0.5)$ and 1.25 m in the horizontal x-axis equating to $(x/W = 0.5)$ for the trailer width of 2.50 m. The slice extractions are shown in Fig.(6.65).

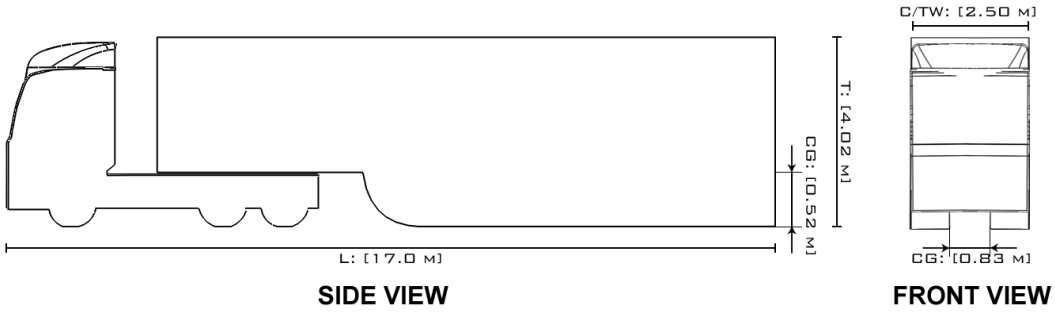

Figure 6.64: Bluff Body Model Notation.

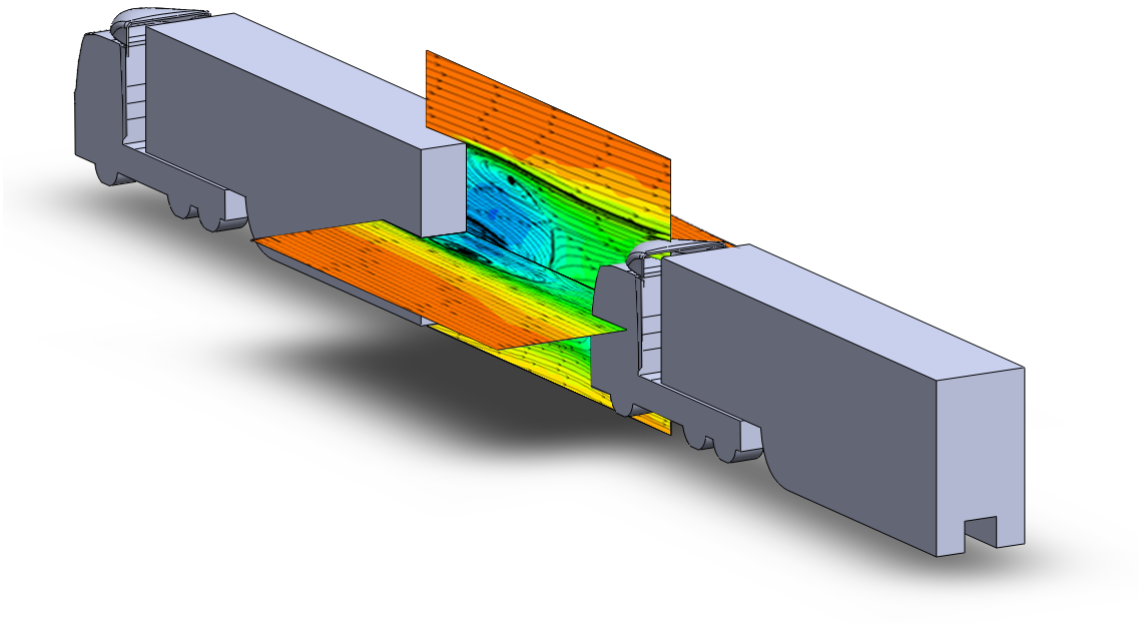

Figure 6.65: Time Averaged Trailer Wake Slice Extractions at y/W and $z/W = 0.5$.

An important difference between the models used by Howell [92], Barzanooni et al. [93] and the 3D CFD model is the addition of a trailer cavity shown in Fig.(6.64). Whilst the bluff bodies used in experimental testing had solid rear sections, the CFD model had a cavity section within the trailer, effectively reducing the height (T) to 3.5 m over a span of 0.83 m at the rear of the trailer.

It was expected that the effect of the addition of this cavity would be to produce asymmetric vortices in the vertical plane at the rear of the trailer. The rear of the trailer had a region of low pressure, high velocity air from the top of the trailer combining with slower moving, high pressure air exiting the rear of the trailer cavity. The velocity flow field on the rear of the trailer was therefore expected to be asymmetric with a greater recirculation occurring near the exit of the trailer cavity.

The CFD results illustrating the effect of the cavity on the vertical wake profile are shown pictorially in Fig.(6.66) with the velocity profile plotted in Fig.(6.67) in Sec.(6.3.5.2). The corresponding horizontal wake results are shown pictorially in Fig.(6.68) with the velocity profile plotted in Fig.(6.69) in Sec.(6.3.5.3). Whilst wake measurements of bluff bodies have been previously conducted by Johansson et al. [96], the research interest was focused at large downstream distances. Other investigations closer to the wake source tend to be conducted at lower R_e numbers [93], [97]. Limited experimental data conducted at high R_e (over 10^5) close to

the wake origin on bluff bodies exist.

6.3.5.2 Vertical Wake Profile (z/W)

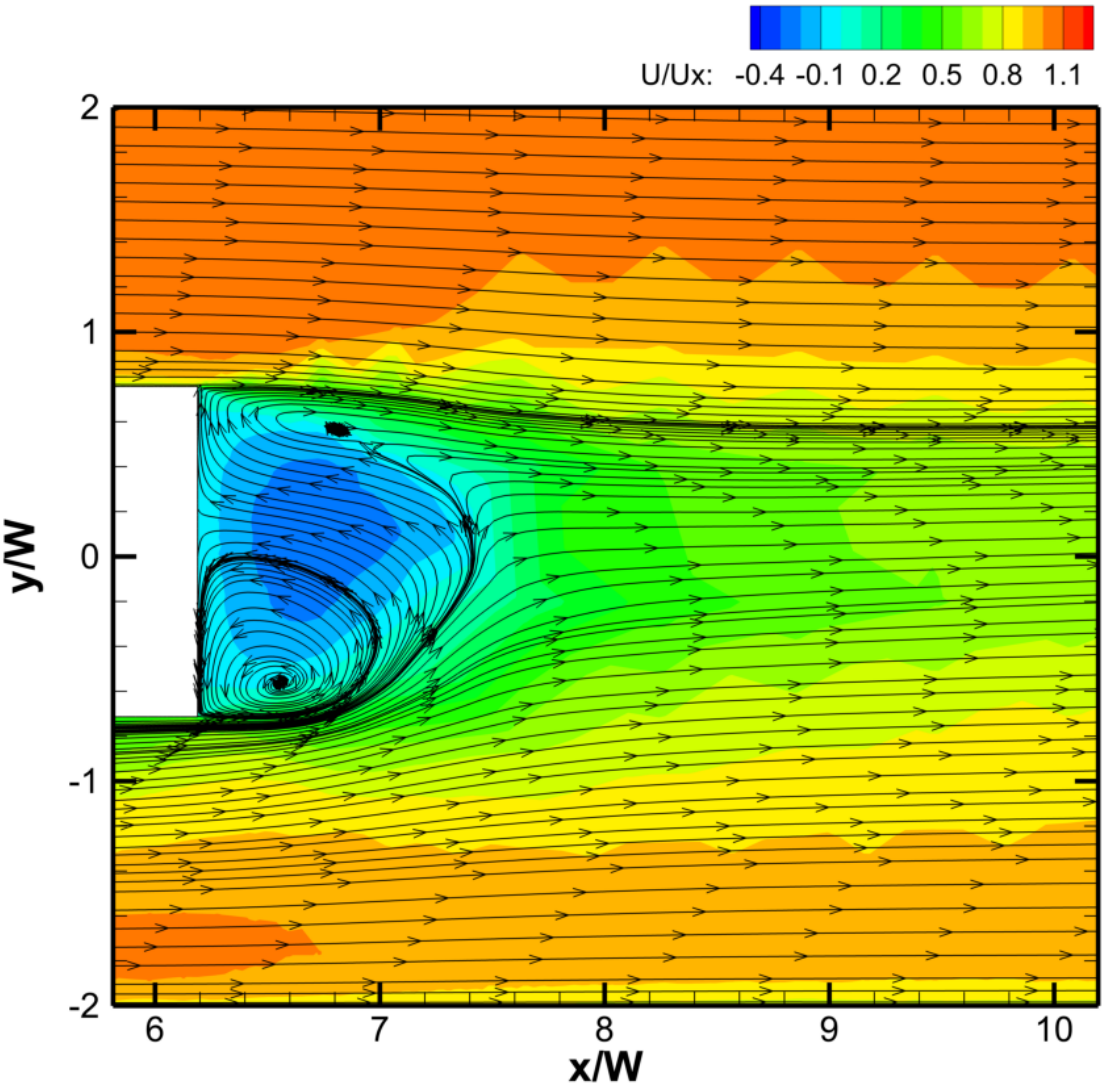

Figure 6.66: Time Averaged Trailer Wake, Normalised Velocity (U/U_X) and Slice Extracted at $z/W = 0.5$ at a Normalised Displacement Downstream of Trailer Rear $(x/W) = 3.8$.

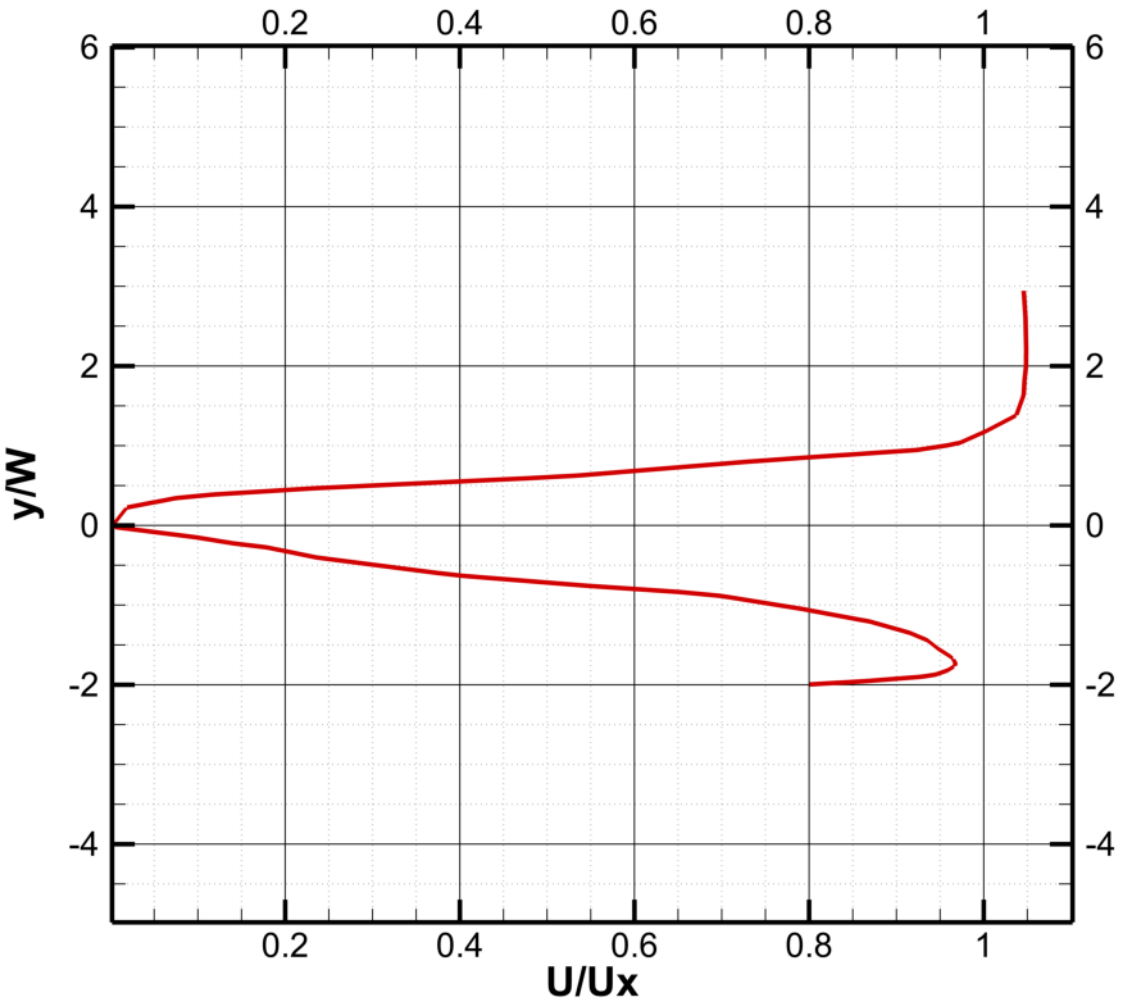

Figure 6.67: Time Averaged Trailer Wake Vertical Velocity Profile, Normalised Velocity (U/U_X) and Slice Extracted at $z/W = 0.5$ at a Normalised Displacement Downstream of Trailer Rear (x/W) = 3.8.

The CFD horizontal wake profile as a function of the downstream traverse (x/W) has been compared with the experimental data obtained by Barzanooni et al. [93] and is shown in Fig.(F.18) in Sec.(F.1.6) of Appendix F.

The difference between the vertical recirculation bubble length (X_b) of the trailer wake for the CFD vehicle and experimental bluff bodies is shown in Tab.(6.26).

B/T	X_b/T	C_D	R_e Number
0.71	0.74	0.568	5.0×10^6
1.00	1.00	0.390	2.0×10^6
2.00	1.37	0.390	2.0×10^6
3.00	1.70	0.440	2.0×10^6

Table 6.26: Reverse Flow Length as a Function of Bluff Body Geometry[4].

Table (6.26) highlights the difference between a simple bluff body and the CFD model of a heavy goods vehicle. The C_D of the CFD vehicle was higher than expected for a simple bluff body. This result was unsurprising due to the flow field from the cavity between the cab and trailer not being present on the experimental bluff body model. The CFD recirculation bubble length (X_b) was expected to be 0.90 based on extrapolation from the experimental data. The lower value of 0.74 is attributed to the lower Reynolds Number (R_e) used in the experiment. Gerrard [98] states: 'for bluff bodies, the length of the wake decreases as R_e increases'.

[4]Reproduced from Howell [92].

6.3.5.3 Horizontal Wake Profile (y/W)

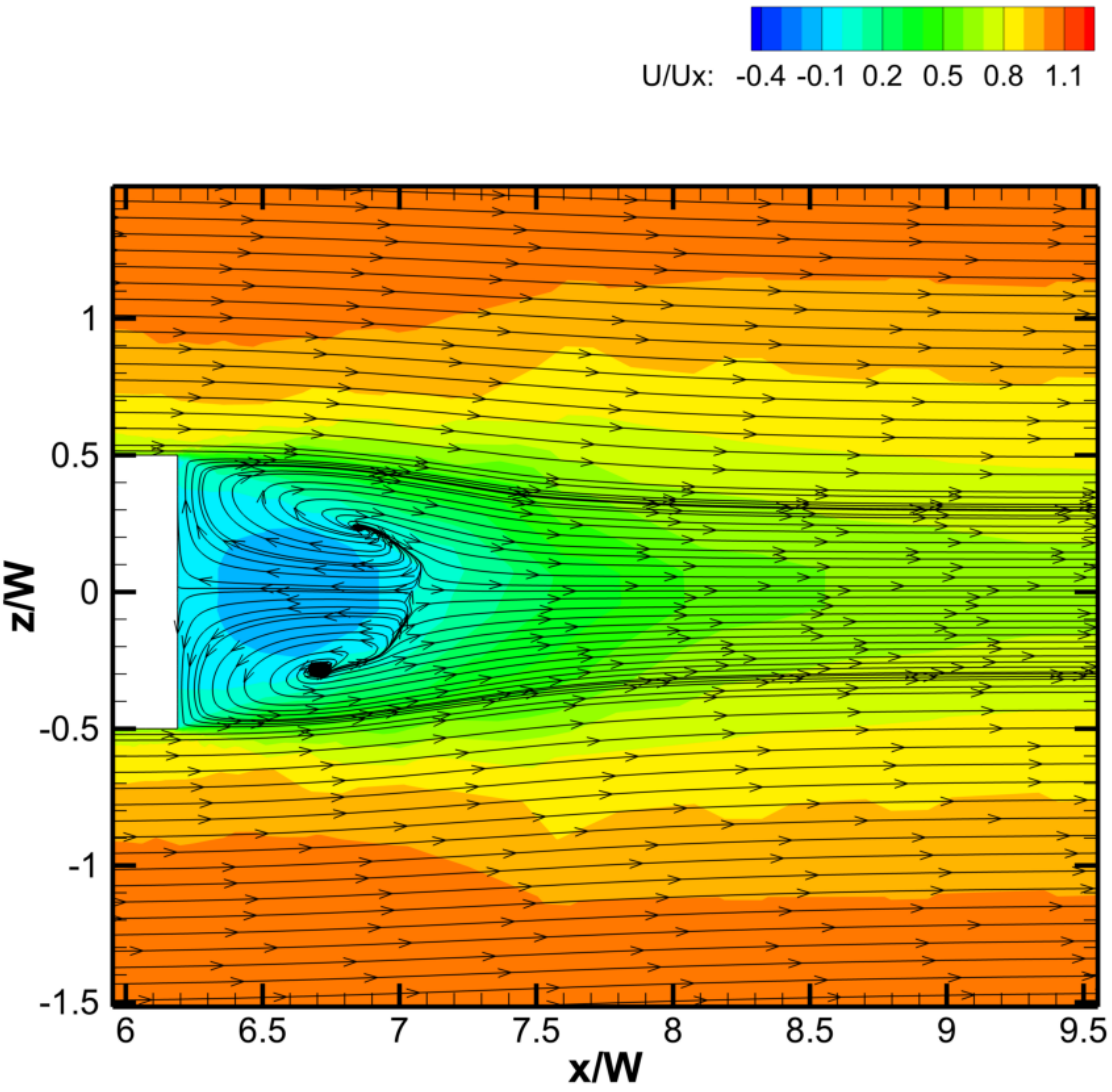

Figure 6.68: Time Averaged Trailer Wake, Normalised Velocity (U/U_X) and Slice Extracted at $y/W = 0.5$ at a Normalised Displacement Downstream of Trailer Rear (x/W) = 3.8.

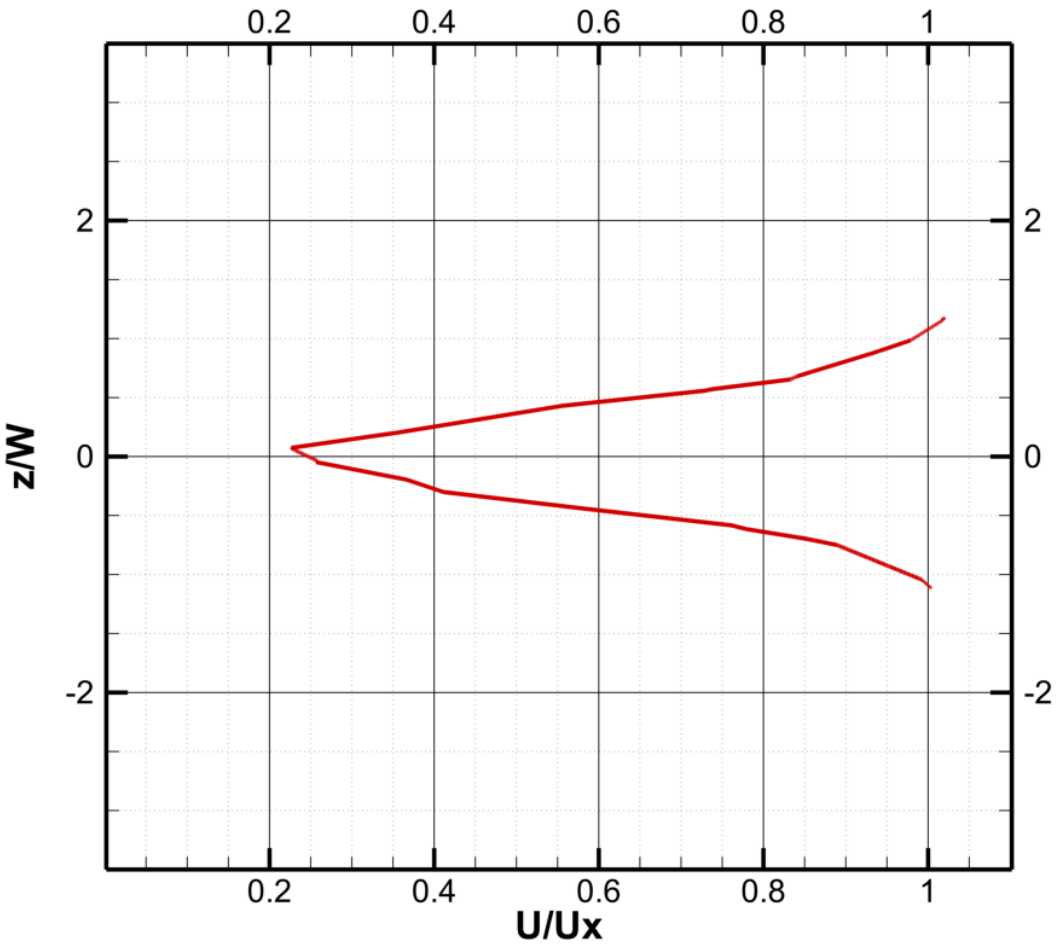

Figure 6.69: Time Averaged Trailer Wake Horizontal Velocity Profile, Normalised Velocity (U/U_X) and Slice Extracted at $y/W = 0.5$ at a Normalised Displacement Downstream of Trailer Rear (x/W) = 3.8.

The CFD horizontal wake profile as a function of the downstream traverse (x/W) has been compared with the experimental data obtained by Liu et al. [97] and is shown in Fig.(F.22) in Sec.(F.1.6) of Appendix F.

6.3.5.4 Freestream Wake Decay

The maximum velocity deficit ($U_0 - U$) for the CFD simulation as a function of the normalised distance downstream (x/T) is plotted in Fig.(6.70)

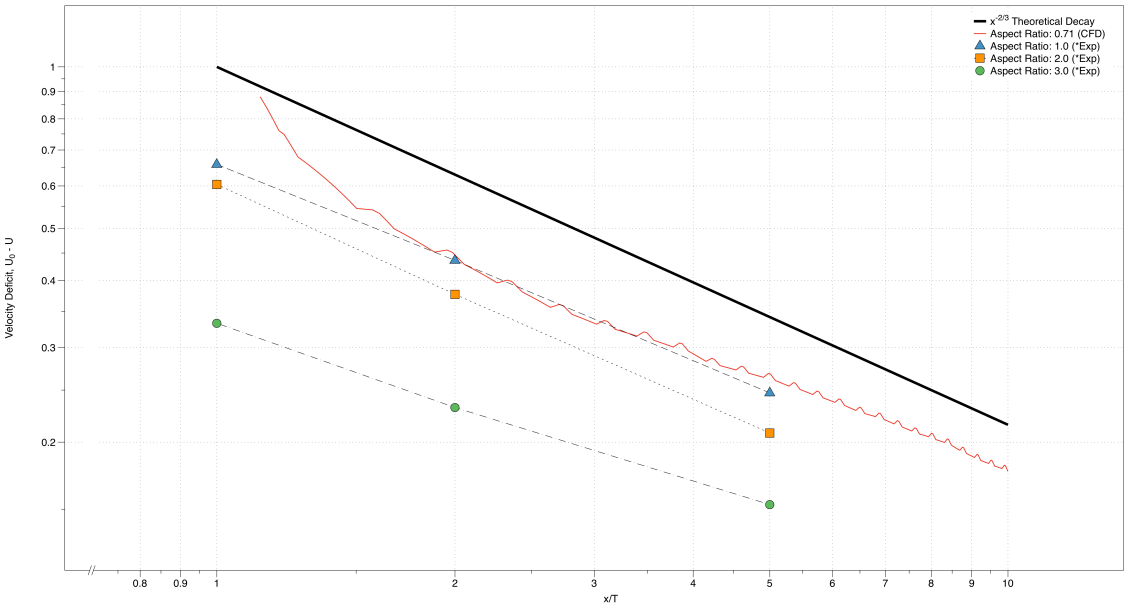

Figure 6.70: Time Averaged Decay of Maximum Velocity Deficit with Normalised Distance Downstream[6].

Fig.(6.70) shows that the CFD simulation is in good agreement with both the theoretical velocity decay of $x^{-2/3}$ and the experimental measurements obtained by Howell [92]. The CFD data contains oscillation in the wake decay due to the time averaging of the wake under RANS simulation. Whilst data exists for bluff bodies in freestream inlet velocity, currently no data exists for the effect of the leading bluff body wake on the trailing bluff body at high R_e.

6.3.6 The Effect of Bluff Body Wake on a Trailing Bluff Body

6.3.6.1 Vertical Wake Profile (z/W)

The vertical wake profile is shown pictorially in Fig.(6.71) with the vertical velocity defect vs. normalised displacement (x/W) plotted in Fig.(6.72). The data used in Fig.(6.72) is shown in Figs.(F.19 - F.21) of Appendix F. The area of recirculation ends at (x/W) = -4.5, with the trailing bluff body beginning at (x/W) = -2.5.

[6]Data Denoted with * Reproduced from Howell [92].

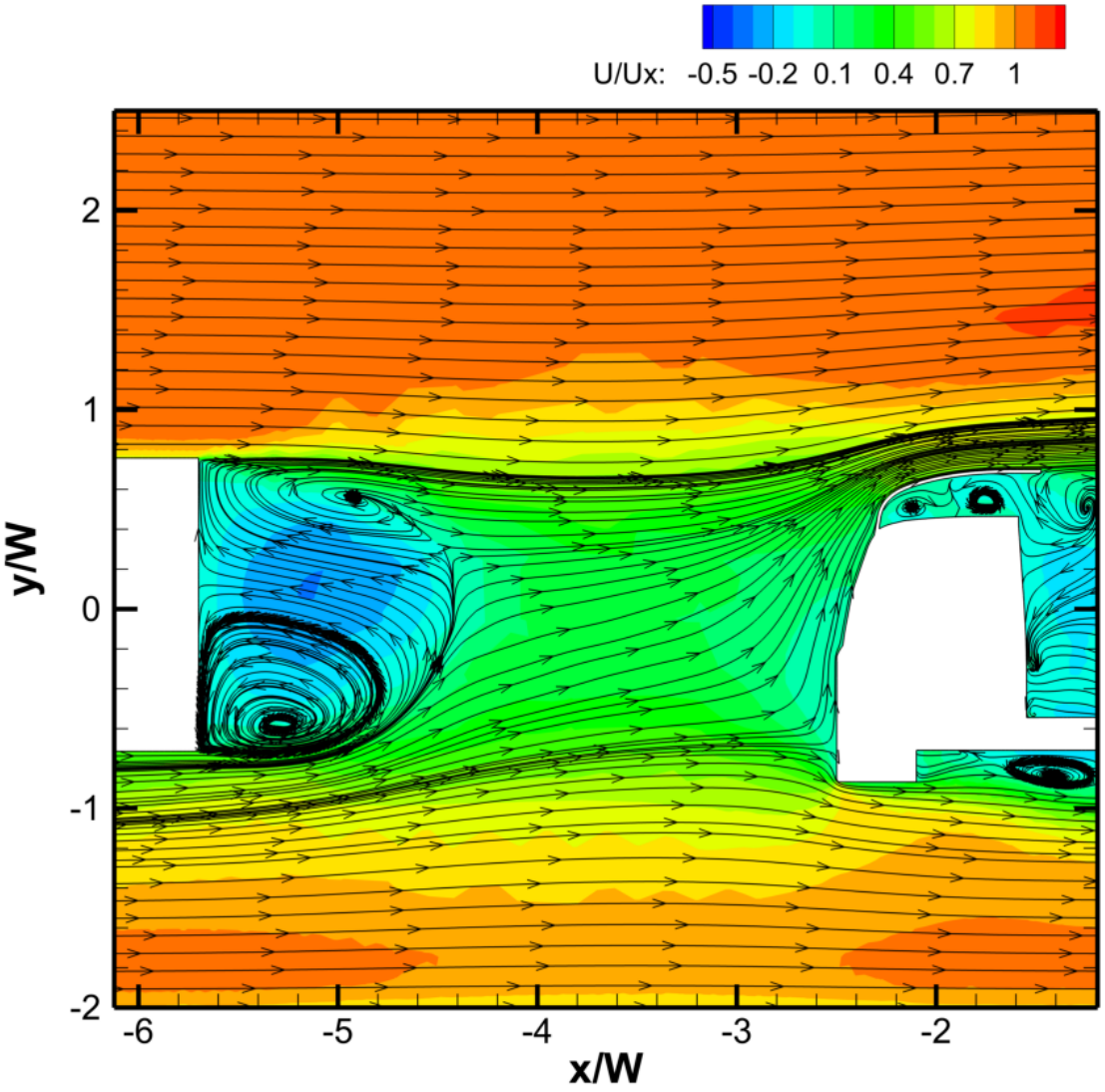

Figure 6.71: Time Averaged Trailer Wake, Normalised Velocity (U/U_X) and Slice Extracted at $y/W = 0.5$.

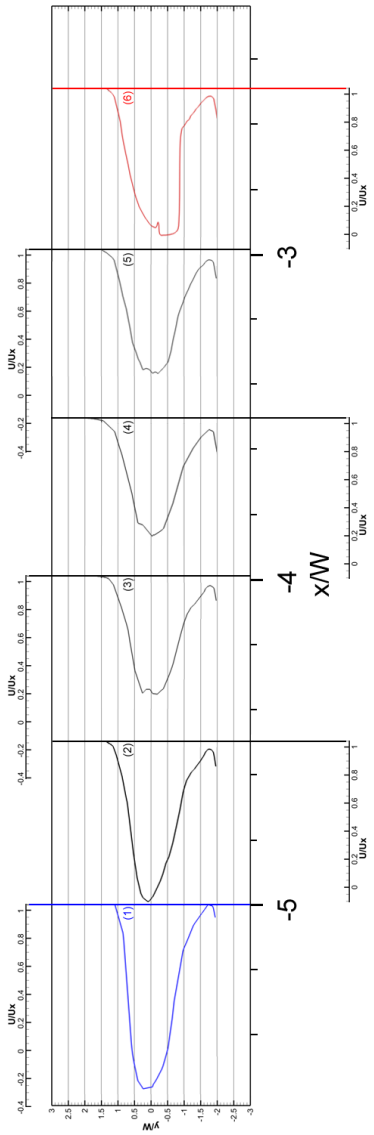

Figure 6.72: Time Averaged Vertical (y/W) Velocity Deficit (U_D) vs. Normalised Displacement (x/W).

6.3.6.2 Horizontal Wake Profile (y/W)

The horizontal wake profile is shown pictorially in Fig.(6.73) with the vertical velocity defect vs. normalised displacement (x/W) plotted in Fig.(6.74). The data used in Fig.(6.72) is shown in Figs.(F.23 - F.25) of Appendix F. The area of recirculation ends at (x/W) = -4.5, with the trailing bluff body beginning at (x/W) = -2.5.

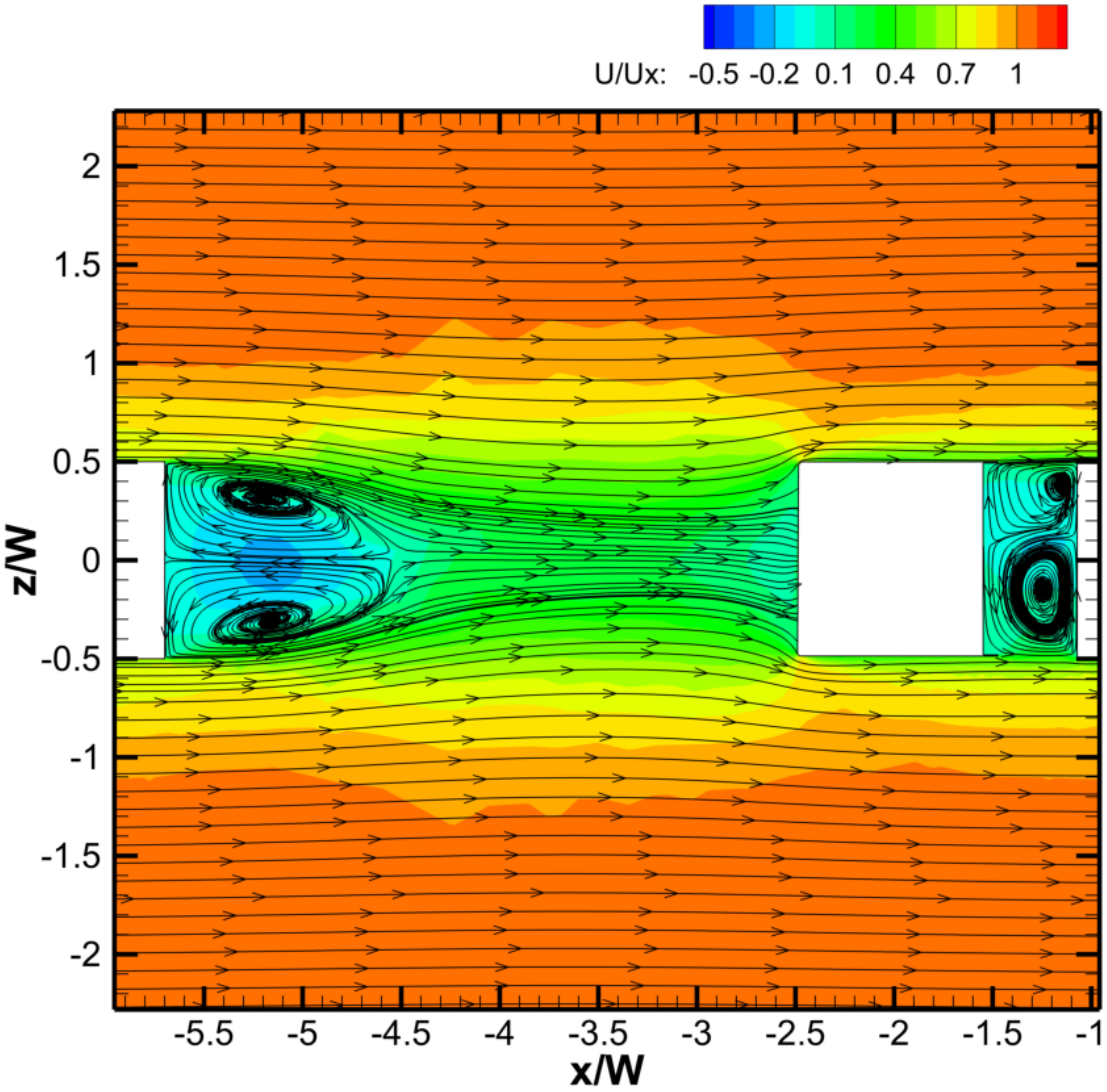

Figure 6.73: Time Averaged Trailer Wake, Normalised Velocity (U/U_X) and Slice Extracted at $y/W = 0.5$.

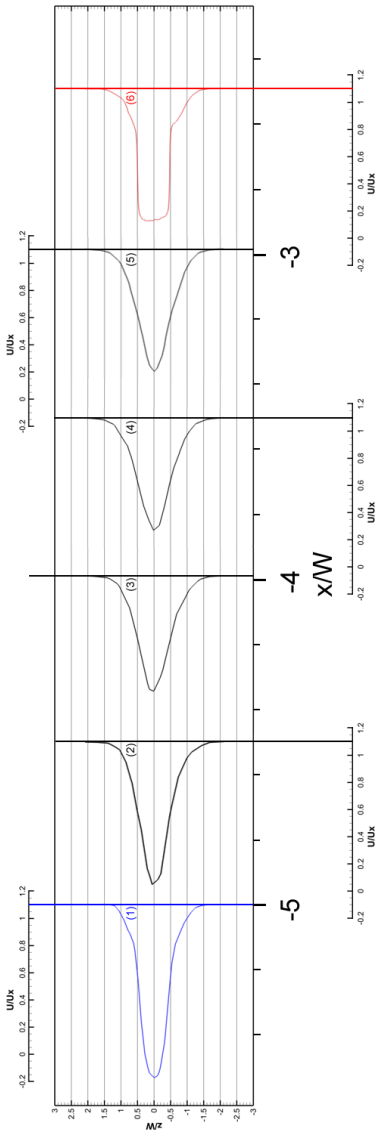

Figure 6.74: Time Averaged Horizontal Deficit (U_D) vs. Normalised Displacement (x/W).

6.3.7 Time Variation of Bluff Body Wake

From the frequency spectrum obtained from the on-road data, high frequency "noise" of high intensity was present. Fig.(6.61) shows the higher frequency noise present in the frequency range: (0.1 - 5 Hz). The relevant frequency range is shown enlarged in Fig.(6.75).

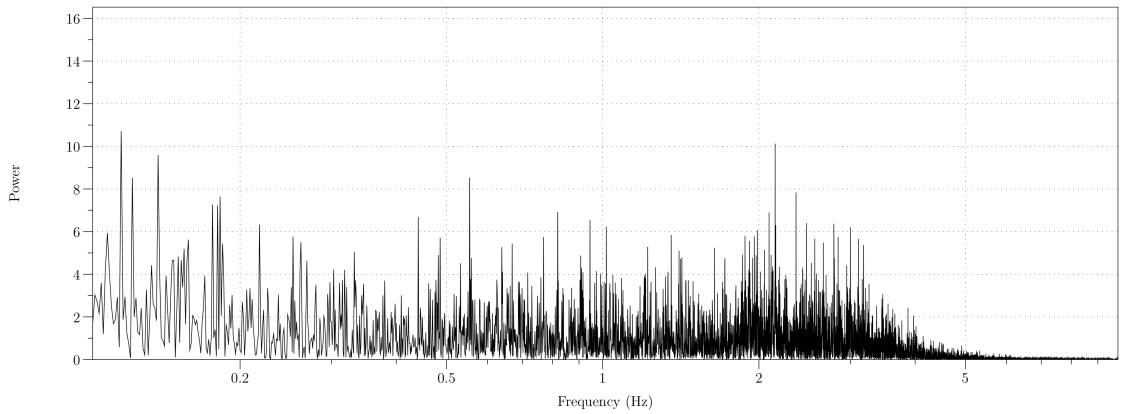

Figure 6.75: On-Road High Frequency Power Spectrum of Yaw Angle.

As a result of these higher frequency perturbations, investigation into unsteady Large Eddy Simulation (LES) was conducted. The simulation involved two tractor-trailer units in tandem separated by a non-dimensional gap separation $(g/L) = 0.38$, where g is the tractor-trailer gap and L is the length of the vehicle. The wind yaw angle (β) used for the simulations was 0°. The simulation was used to determine if there are any characteristic frequencies present in the trailer wake of the leading vehicle.

6.3.7.1 Trailer Wake Frequency Identification

For frequencies associated with bluff body vortex shedding, such as a Kármán vortex street, it is important to introduce the Strouhal number.

Strouhal Number

The Strouhal number is a dimensionless number describing oscillating flows and is given by

$$St = \frac{fD}{V} \tag{6.8}$$

where St is the Strouhal number, f is the characteristic frequency of shedding, D is the characteristic diameter and V the velocity of the freestream.

The Strouhal number can be empirically related to the Reynolds number of the flow for cylinders and bluff bodies [99] and is given by

$$St = \frac{fD}{V} = 0.198\left(1 - \frac{19.7}{Re}\right) \tag{6.9}$$

Rearranging for frequency gives

$$f = 0.198\left(1 - \frac{19.7}{Re}\right)\frac{V}{D} \tag{6.10}$$

for the CFD simulation, V = 35.0 ms^{-1}, D = 4.0 m and a corresponding Reynolds number (Re) of 50.2×10^6, giving

$$f = 0.198\left(1 - \frac{19.7}{50.2 \times 10^6}\right)\frac{35}{4} \tag{6.11}$$

this results in a predicted frequency of vortex shedding of: $f = 1.7$ Hz.

6.3.7.2 Trailer Wake Time Variation

The location of the CFD tappings used to determine ΔC_P are shown in Fig.(6.76) with the velocity stream traces for a time step shown in Fig.(6.77). The time variation of the trailer wake is shown in Fig.(6.80). The wake is shown for six time steps from 10.0 to 10.5 seconds with each step corresponding to 0.1 seconds, giving 0.6 seconds of flow visualisation. A vortex shedding frequency of 1.7 Hz equates to a period of 0.58 seconds. The starting slice at 10.0s is shown in Fig.(6.76). The time variation of the differential pressure coefficient (ΔC_P) and estimated wind direction (β_{Est}) are shown in Fig.(6.82 and 6.83), respectively.

The details for the computational simulation is shown in Chapter 4, with the experimental configuration for the tapping locations in Chapter 3.

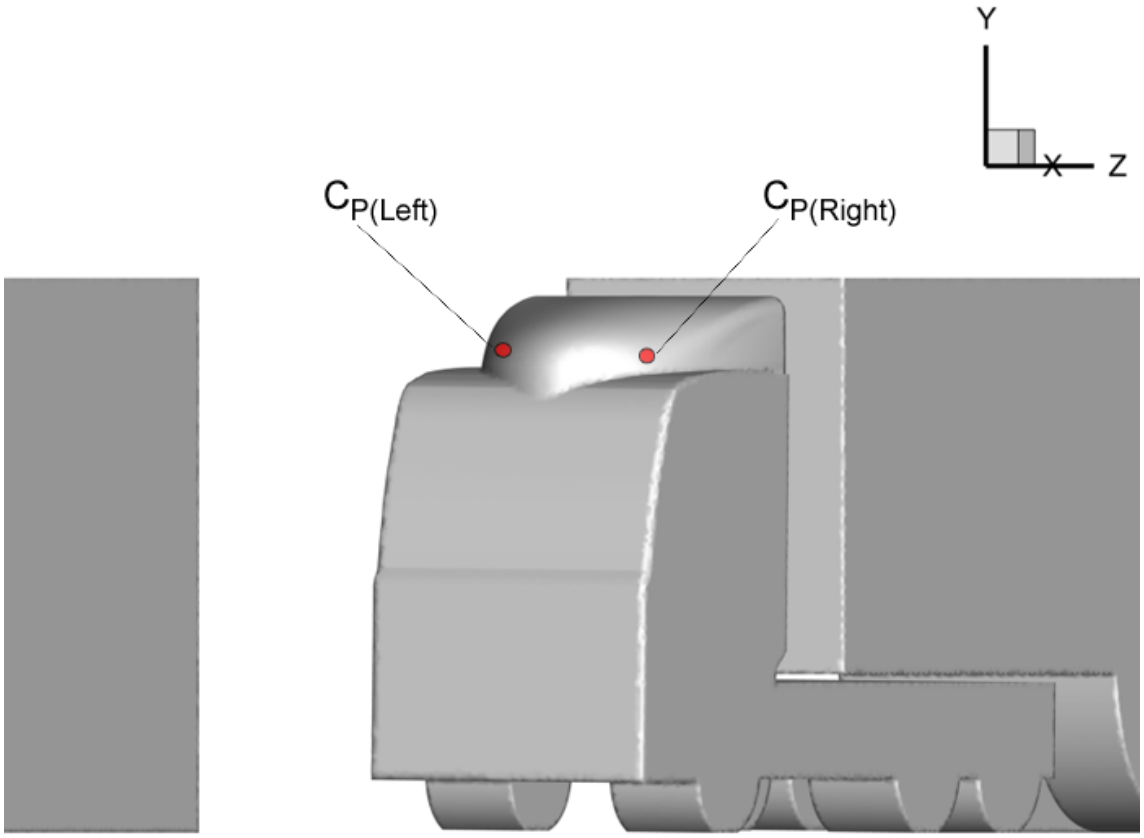

Figure 6.76: CFD Pressure Measurement Locations.

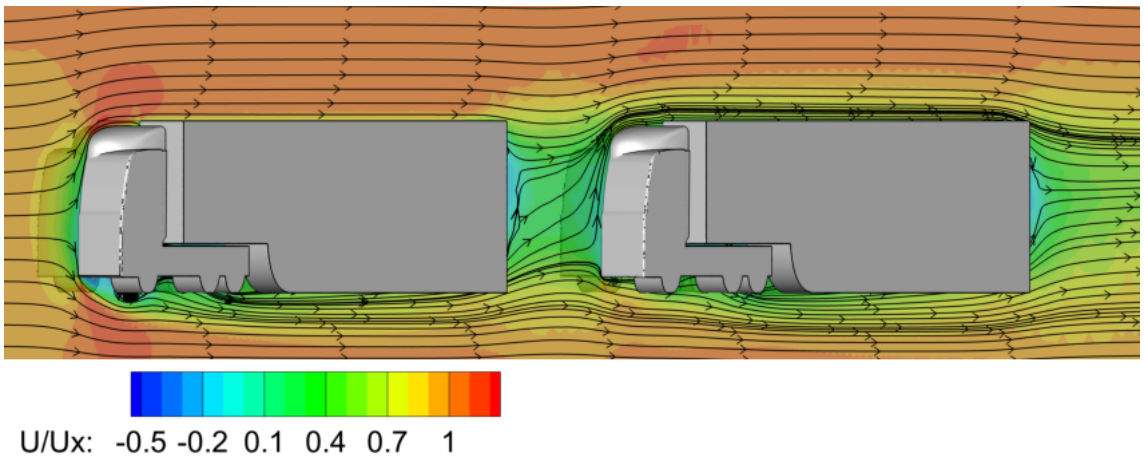

Figure 6.77: CFD Truck-Trailer in Tandem Velocity Streamtraces.

Accustom to CFD notation the time varying slices were extracted at a y - plane height that corresponded to 160% of the trailer width. The slice extraction location is shown in Fig.(6.78).

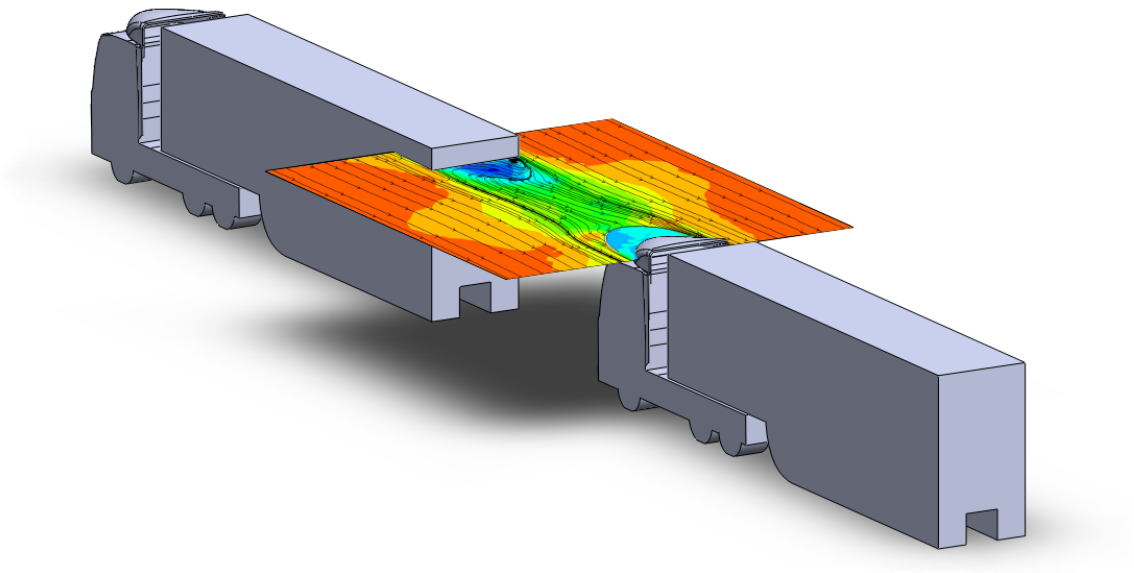

Figure 6.78: LES Trailer Wake Slice Extractions at $y/W = 1.6$.

An enlarged image of the extracted slice for t =10.0s is shown in Fig.(6.79), with the remaining time steps (t = 10.0s to t = 10.5s) shown in Fig.(6.80). The time step at 10.0 seconds corresponded to a horizontal displacement of 350 m travelled by the initial inlet particles (at t = 0.0s). The overall length of the domain was approximately 71 m, the time steps presented are therefore well within the time required to establish the lead vehicle to trailing vehicle flow field.

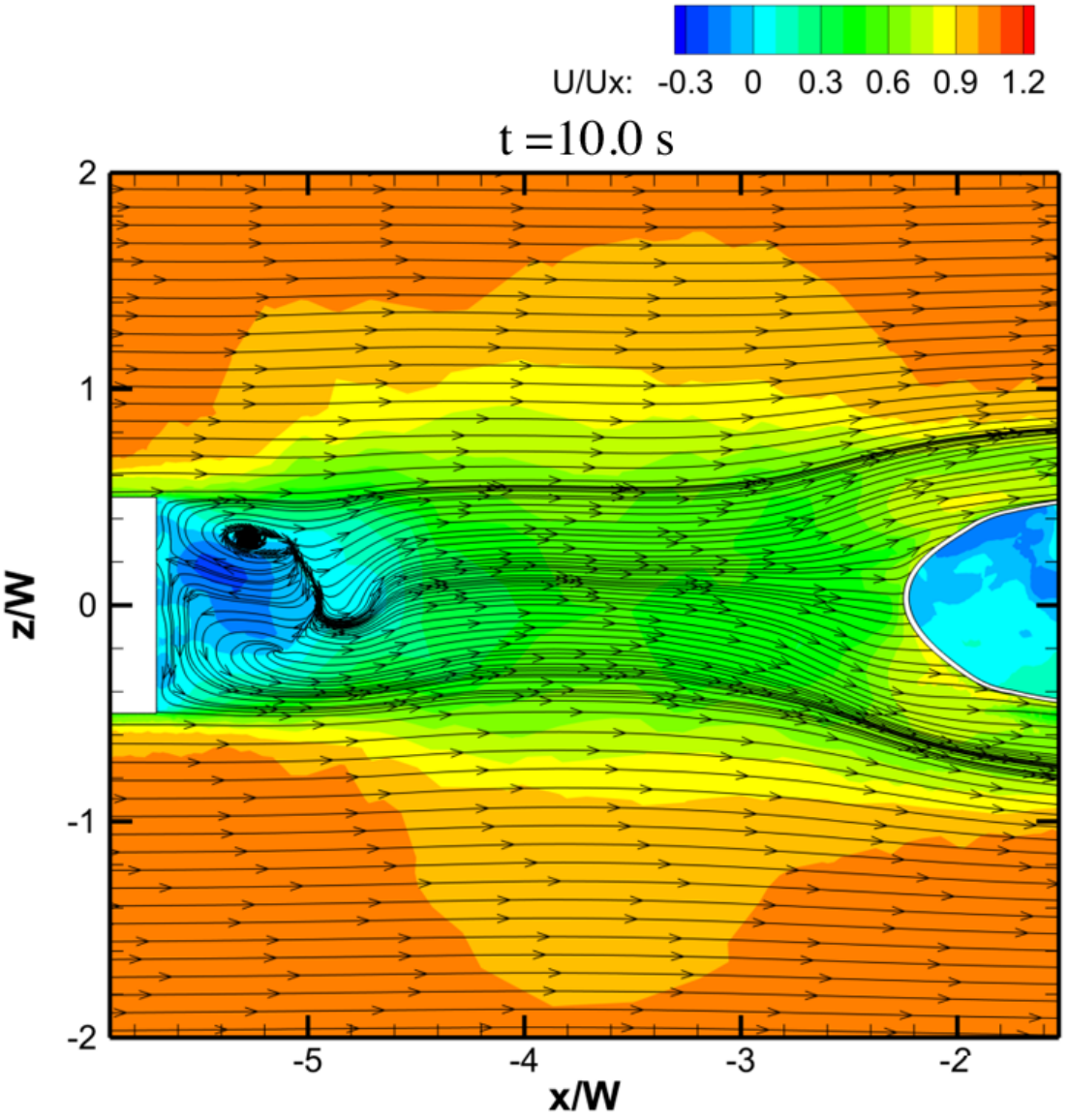

Figure 6.79: LES Trailer Wake Time Variation, (Left) Leading Trailer and (Right) Following Truck, Time = 10.0s, Slice Extracted at $y/W = 1.6$.

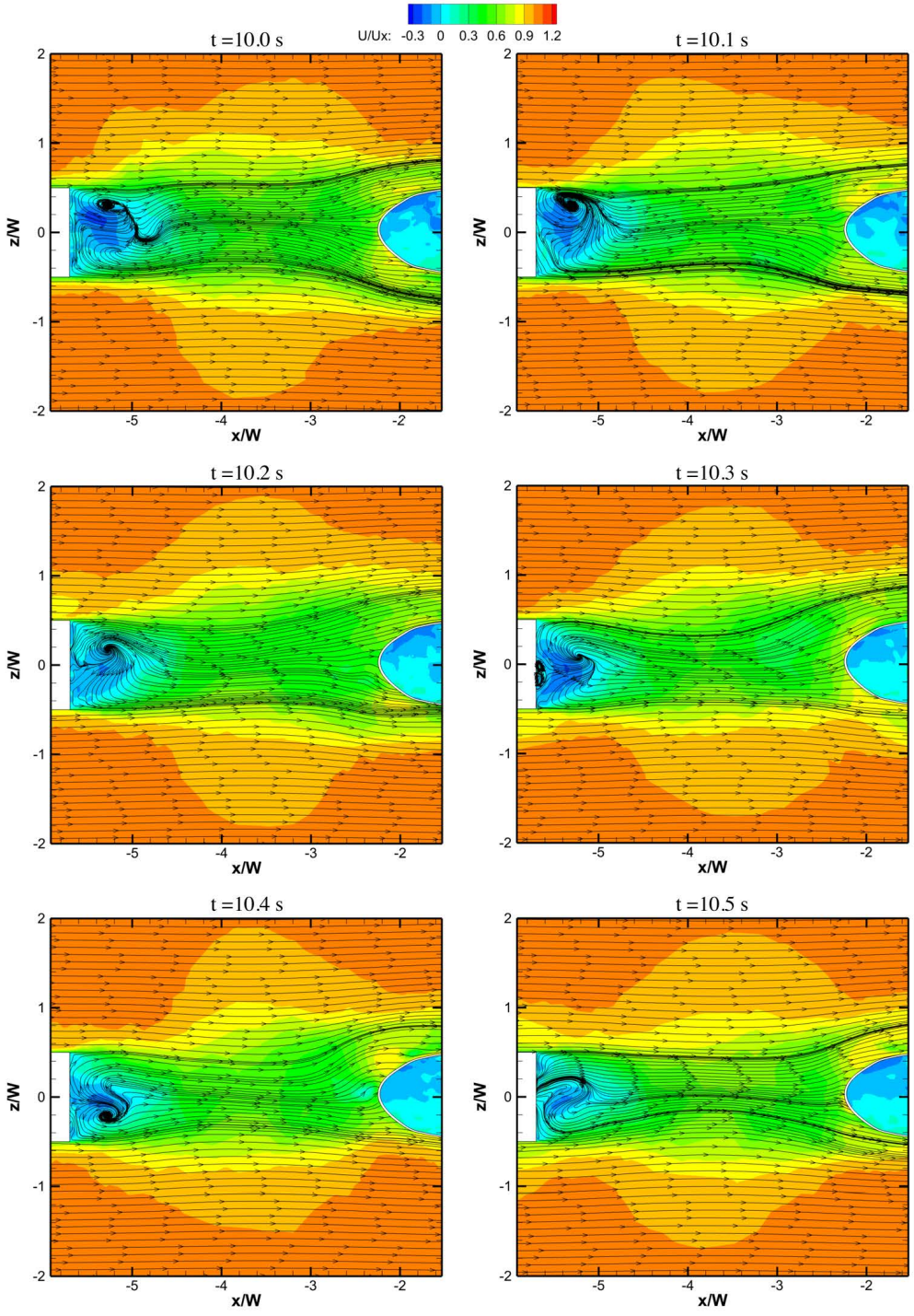

Figure 6.80: LES Trailer Wake Time Variation, (Left) Leading Trailer and (Right) Following Truck, Simulation Time from 10.0s to 10.5s, Slice Extracted at $y/W = 1.6$.

6.3.8 Angular Deviation in Bluff Body Wake

The angular deviation in the horizontal (x-z) plane from the trailer centre line is shown in Fig.(6.81). The data used in Fig.(6.81) is shown in Tab.(F.13) in Sec.(F.1.7) of Appendix F. The recirculation bubble ends at (x/W) = -4.5, with the trailing vehicle beginning a (x/W) = -2.5.

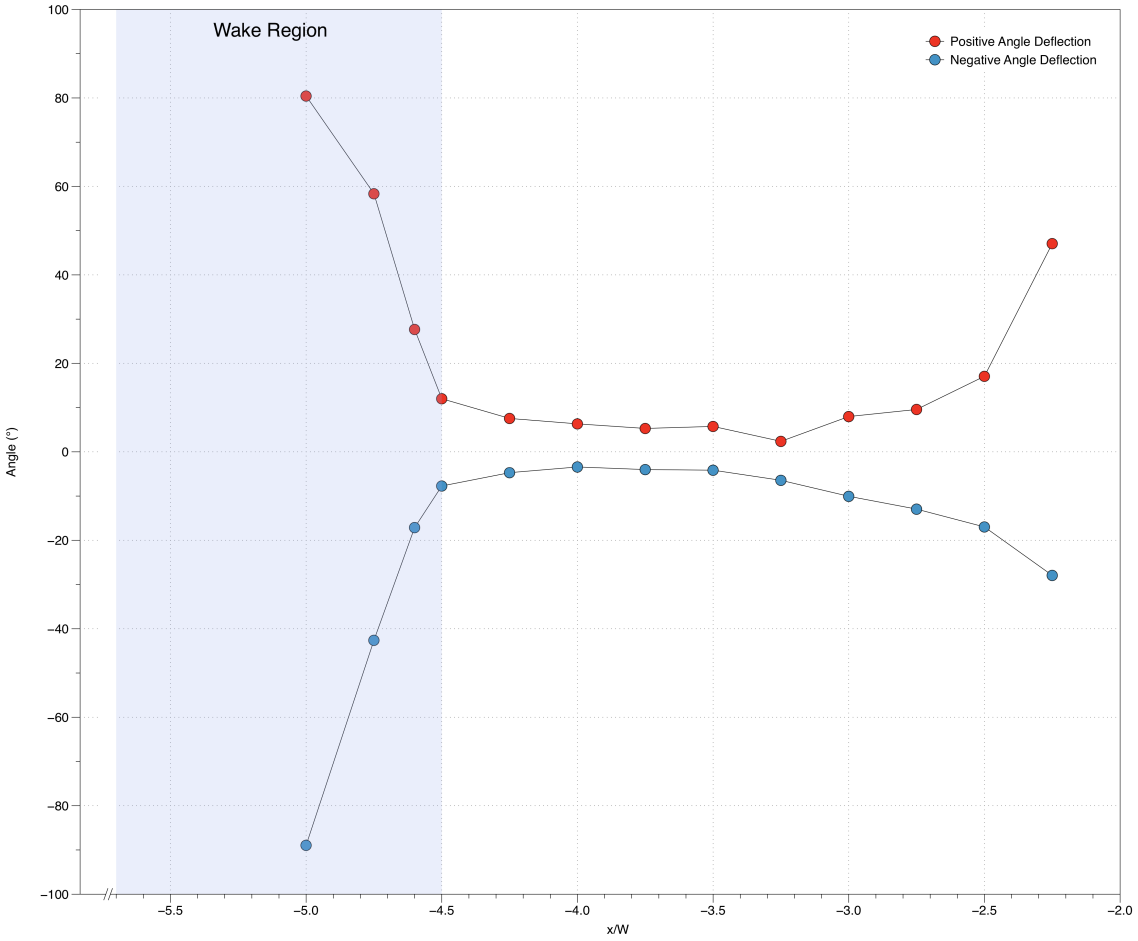

Figure 6.81: Angular Deviation (°) from Vehicle Centre Line vs. Normalised Distance (x/W), Slice Extractions at $y/W = 1.6$.

Fig.(6.81) shows a large angular fluctuation in the recirculation bubble $(x/W \leq -4.5)$ with a sharp decrease from ±80° to ±5°. This angular deviation is then fairly constant up to $(x/W$ = -3.0) where the flow field of the trailing vehicle begins to dominate. At the trailing vehicle $(x/W$ = -2.5) the centre line angular deviation is

±17°. The calibration factor used to account for instrument location in Sec.(6.1.11) was determined to be ±15°, however, this location was not along the centre line.

6.3.9 LES Predicted Variables

The time step of 0.01s used in the unsteady simulations corresponded to a sample frequency of 100 Hz, matching the on-road sampling rate. High frequency oscillations were present within the data shown in Fig.(6.82). The estimated yaw angle (β_{Est}), was obtained using Eq.(6.5) derived in Sec.(6.1.10). A comparison between the wind disturbance (the disturbances on the average yaw angle ($\overline{\beta}$)) is made in Fig.(6.84). The associated frequency spectrum for the LES is shown in Fig.(6.85).

6.3.9.1 LES Pressure Coefficient Differential (ΔC_P)

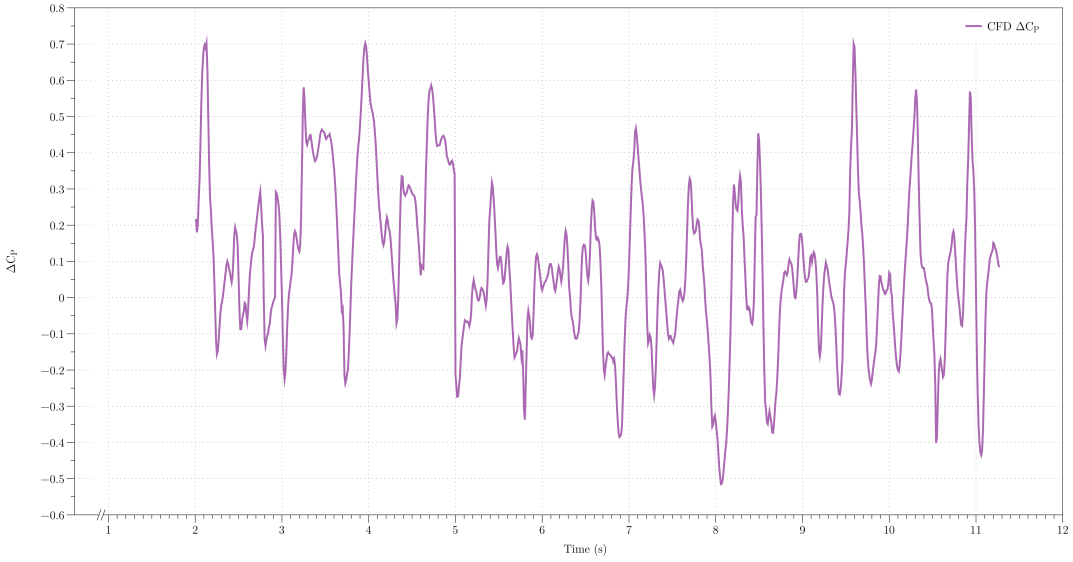

Figure 6.82: CFD Estimated Wind Pressure Coefficient Differential (ΔC_P) Time Variation.

The estimated wind direction (β_{Est}) generated from relating the ΔC_P, obtained from the LES simulation, to β is shown in Fig.(6.83).

6.3.9.2 LES Estimated Wind Direction (β_{Est})

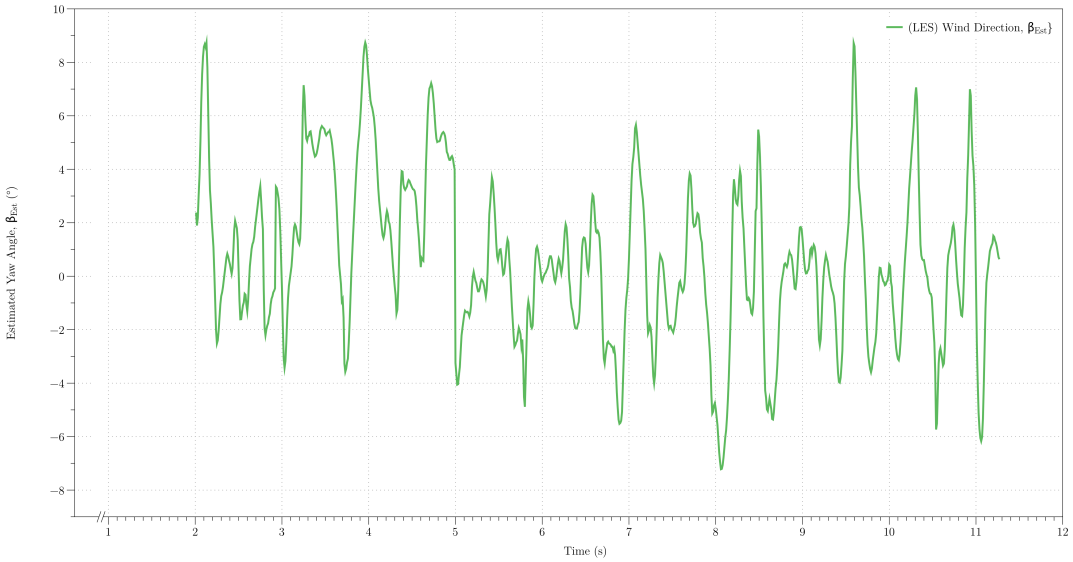

Figure 6.83: CFD Estimated Wind Yaw Angle (β_{Est}) Time Variation.

6.3.9.3 LES Simulation vs. On-Road Data

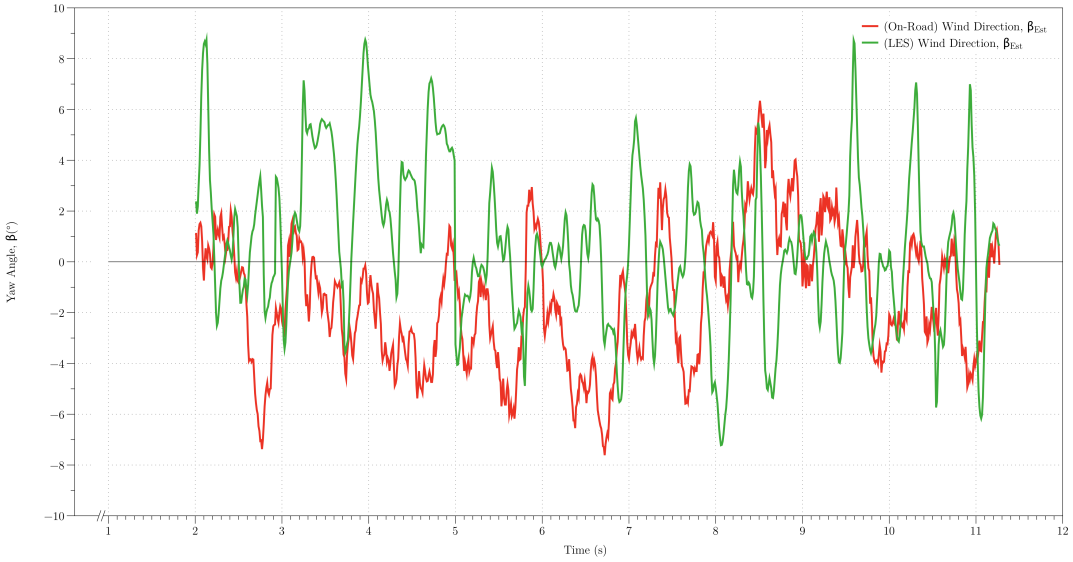

Figure 6.84: CFD vs. On-Road Estimated Wind Yaw Angle (β_{Est}) Variation with Time Variation.

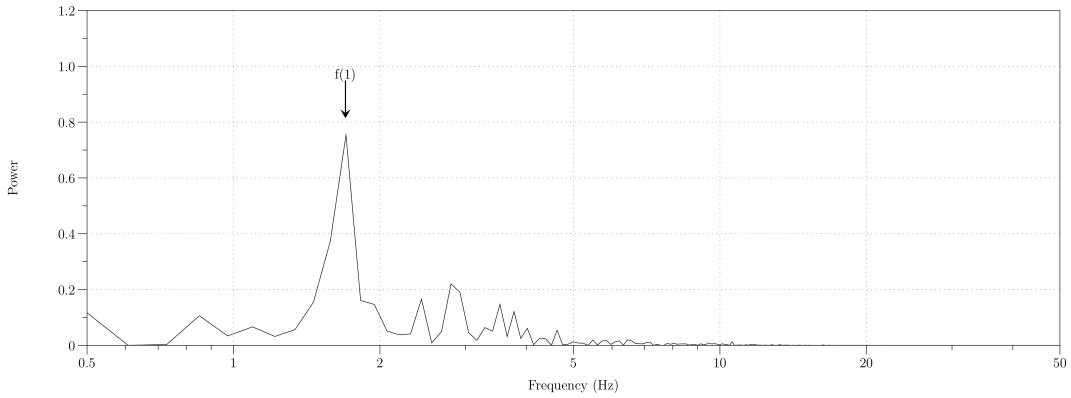

Figure 6.85: CFD Frequency Spectrum.

The LES data contained a high frequency maximum of f(1) = 1.7 Hz in exact agreement with the empirically predicted value from the Strouhal number. The magnitude of the high frequency disturbances occurred at a relative wind yaw angle of ±8° in both the simulated and on-road data. The LES data had a high frequency maximum of f(1) = 1.7 Hz, compared to the on-road high frequency maximum of 2.1 Hz (shown in Fig.(6.75)).

The large angular disturbance of ±8° on the estimated yaw angle imposed the requirement of data filtration. A suitable filter was required on the measured pressure data in order to reduce the effects of the vortex shedding.

6.3.10 Low-Pass Filter

A low-pass filter is an electronic filter that permits the passage of low frequency signals whilst greatly attenuating frequencies higher than the cut off frequency (f_c). The sampling rate of 100 Hz imposed a condition of $f_c = 50$ Hz to prevent aliasing (see Appendix E for sampling theorem). This resulted in analogue 50 Hz low-pass filters being added to the input channels of the data logger.

The results from the on-road and computational data indicated that higher frequency noise was present above 1.5 Hz. A frequency of 1.0 Hz was therefore chosen to as the cut-off frequency for the digital filter used for filtering the obtained data. To attenuate the higher frequencies, a 30 dB reduction was applied to frequencies greater than f_c. The magnitude response of the low-pass filter is shown in Fig.(G.66) in Sec.(G.7) of Appendix G.

6.3.11 Filtered Data

The effect of a low-pass filter applied to the sample data is shown in Fig.(6.86), with the smoothed response is shown in Fig.(6.87). To dampen the effects of lower frequency noise, a moving average filter was applied after the low-pass filter with an averaging period of 2.5 seconds (0.4 Hz). A moving average filter was chosen to remove random noise contained within the signal whilst retaining a sharp step responses.

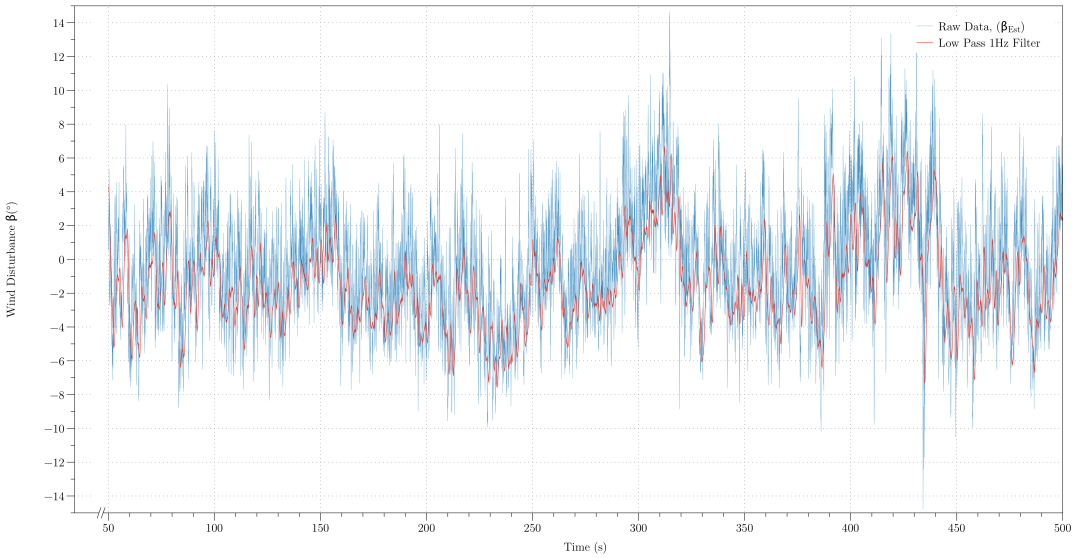

Figure 6.86: Low-Pass Filter Applied to Sampled Data.

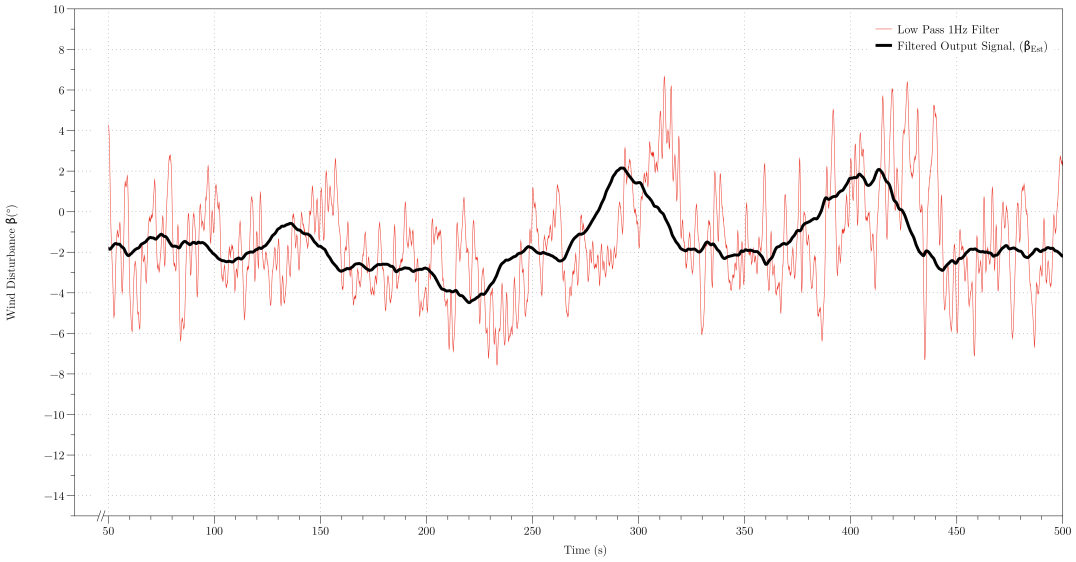

Figure 6.87: Smoothing Filter Applied to Sampled Data.

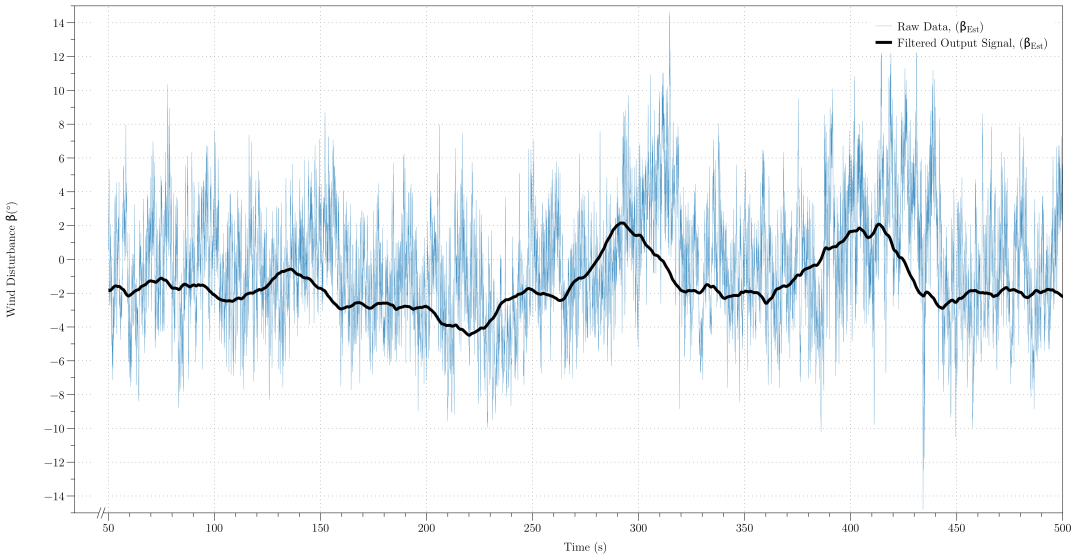

Figure 6.88: Output Signal from Sampled Data.

The resulting attenuation on the high frequency frequencies (shown in Fig.(6.88)) removed a significant proportion of the fluctuation in the wind disturbance (Fig.(6.86)). The wind disturbance range of $\pm 15°$ was reduced to $\pm 6°$. Further smoothing from the moving average filter reduced the disturbance range to around $\pm 3°$.

6.3.12 Accuracy of Yaw Estimation

An estimation of the accuracy of the measurement of the wind yaw angle ($|\beta_{Est.}|$) by the pressure differential ($|\Delta C_P|$) was made. This was achieved using a comparison between the measured $|\Delta C_P|$ and the wind yaw angle ($|\beta|$) measured by the wind vane. Filtered data from Run [4] was used for this comparison. The two variables ($|\beta_{Est.}|$ and $|\beta|$) were plotted against each other and the resulting graph is shown in Fig.(6.89).

Estimated Wind Direction (β_{Est})

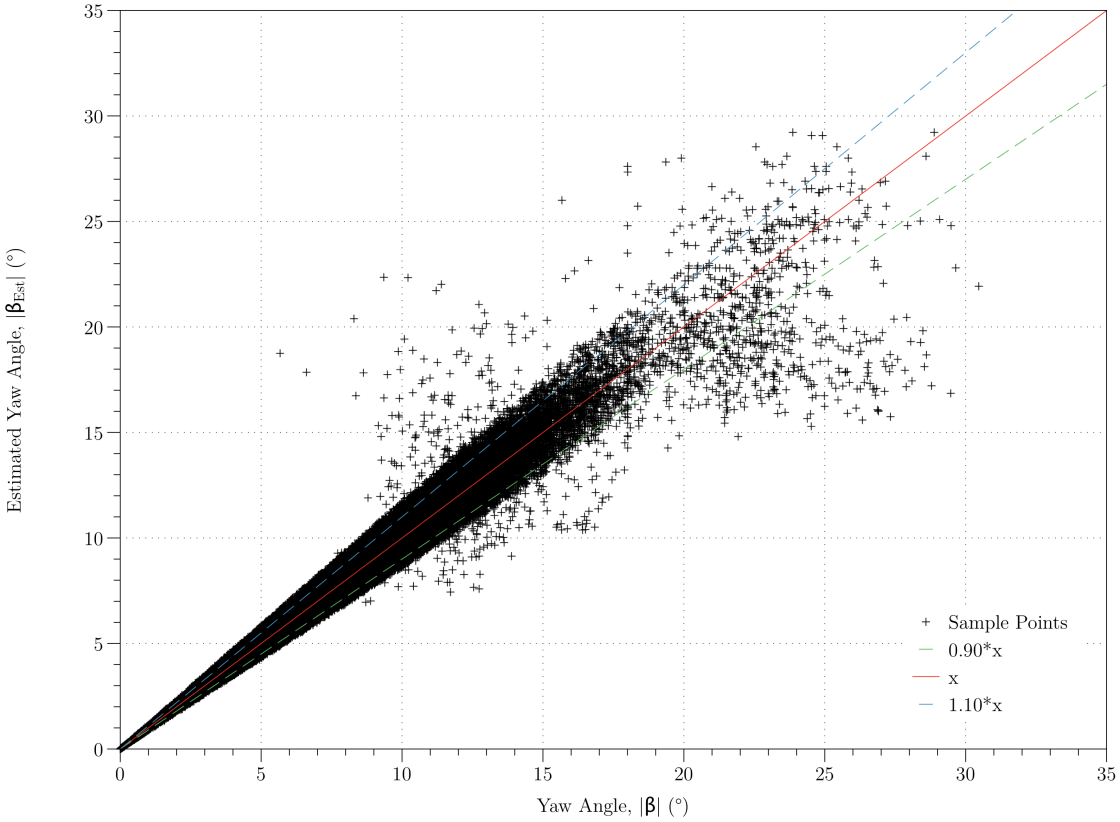

Figure 6.89: Estimated vs. Wind Yaw Angle.

Perfect correlation would be a 45° line and is represented in Fig.(6.89) by a solid red line (x) corresponding to 100% accuracy of the predicted yaw angle.

From the results obtained, 90% of the data was within 10% accuracy (dashed blue line) up to 8° yaw angle, corresponding to ±0.8° at 8°. Seventy-six percent (76%) of the data was within 10% accuracy (dashed blue line) from 10-15° yaw angle

corresponding to ±1.5° at 15°. Sixty-five percent (65%) of the data was within 10% accuracy (dashed blue line) from 10-15° yaw angle corresponding to ±2.5°. Eighty-one percent (81%) of the data was within 15% accuracy (dashed green line) at 25° yaw angle, corresponding to ±3.8° at 25°.

Two factors influenced the accuracy of β_{Est} compared to β. The first was that the linear relationship determined between β and ΔC_P was sufficient only for angles up to around ±18° yaw, as shown in Fig.(6.29) in Sec.(6.1.10). The accuracy of using the linear relationship was greatly reduced at the higher ($\geq 20°$).

The second reason was the effect of the pitch angle (α) on the linear relationship, due to the pressure differential relying on two pressure tappings effectively acting as a three-hole probe, it was not possible to correct for a pitch dependence of the flow. Figure (6.29) in Sec.(6.1.10) shows the strong relationship between α and the gradient of the associated (C_P/β) line. As a result of instrument simplification for commercial implementation an element of inbuilt inaccuracy was present in the measured values.

The average on-road yaw angle ($|\overline{\beta}_{Average}|$) from Sec.(6.3.2.2) was found to be 4.6°. This lower average value implies that the pressure transducers will be well within the linear range of the ΔC_P vs. β calibration chart and as a result will provide an accurate estimation of the yaw angle.

6.3.13 Subsection Summary

A test of approximately four weeks duration was conducted to obtain on-road measurements of the wind speed (V_{Wind}) and wind direction (β). Various delivery routes were taken across the UK spanning over 1,200 km. V_{Wind} and β, two pressure tappings (to determine ΔC_P) located on the vehicle and vehicle speed (V_{Truck}) were sampled at 100 Hz by an on-board data logger.

The data was sampled for close to 14h resulting in approximately 5×10^6 sample points. The resulting wind data established a mean V_{Wind} of 8.7 ms^{-1} at -0.46° wind yaw angle. The average magnitude of the wind yaw angle ($|\overline{\beta}|$) was found to be 4.6°, indication on average the wind will be at 8.7 ms^{-1} at a yaw angle of either ±4.6°.

Frequency investigation of the signal identified four key low frequencies of: 0.004, 0.006, 0.009 and 0.025 Hz corresponding to periods of 250.0, 166.7, 111.0 and 40.0 seconds respectively. CFD investigation revealed higher frequency (f > 1.0 Hz) disturbances were due to the flow field of the trailer wake. The resulting wind direction due to the macro environment was therefore established as being a mean yaw angle ($\beta_{Average}$) perturbed by higher frequency on-road turbulence. The angular deviation was found to be approximately ±5.0° within the centre line of separation. This value, however, rose sharply to ±80.0° within the recirculation bubble length

($X_b/T \leq 0.71$).

The horizontal and vertical velocity profiles for the freestream and vehicles in tandem were extracted. The wakes initially decayed in a similar manner to freestream decay, until interaction with the trailing vehicle occurred (approximately two trailer widths behind the lead vehicle).

Investigation into data filtering revealed significant removal of the high frequency on-road turbulence was obtained through use of a low-pass filter. A low-pass filter was used with $f_c = 1.0$ Hz and a smoothing filter with frequency 0.4 Hz further reduced the disturbance on $\beta_{Average}$. The effect of the filters was a reduction in the disturbance on $\beta_{Average}$ from $\pm 15^\circ$ to $\pm 3^\circ$.

The resulting β_{Est} was determined to have 65% of the data lie within $\pm$ 2.0% and 81% of the data lie within $\pm$ 3.8% of the data at the maximum (20 - 25)° yaw angle. The accuracy of the estimation was reduced due to the use of a linear relationship between β and ΔC_P. The relationship could only be considered linear for angles up to around $\pm 20^\circ$, above this critical angle, the efficiency of the relationship is greatly reduced.

As ΔC_P relied on two pressure tappings effectively acting as a three-hole probe, it was not possible to correct for any pitch variation within the flow. There was an even stronger relationship between α and the gradient of the associated (C_P/β) line. The result of instrumentation simplification for commercial implementation introduced an element of unaccountable inbuilt inaccuracy present within the measured values.

This page intentionally left blank.

6.4 Control Scheme

The control scheme chapter is divided into two sub sections, the Research Controller (TRL1 - TRL4) and the Production Controller (TRL7 - TRL9). The research controller focused on Extremum Seeking Control (ESC) applied to active aerodynamics. The benefit of the research controller over the production controller is that a priori knowledge about the plant (the vehicle) was not required. The research controller sought to reduce the aerodynamic drag of the vehicle by minimising the pressure measured at a tapping located on the vehicle. From an aerodynamic perspective, the advantage of the research controller over the production controller was that no information about the geometry or configuration of the tractor-trailer was required. This resulted in the research controller having a wider application than the production controller, which was model specific.

The production controller research focused on estimating the performance of the system over a static deflector. This was achieved by simulation using a numerical model for the on-road vehicle in conjunction with data obtained from the full scale on-road tests. From the simulation an optimal adjustment frequency of the actuators used to control the height of the deflector was determined. An estimation of the power saving (accounting for the power used during actuation) of an active deflector over a static deflector using the optimal adjustment frequency was then simulated. Section (1.6) gives further details about the ESC algorithm.

6.4.1 Research Controller (TRL1 - TRL4)

A flowchart to show the dependent variables required for the controller is shown in Fig.(1.8) in Sec.(1.6.1). The research controller model was designed to simulate the vehicle and the typical on-road environmental conditions the vehicle was subjected to. The overview of the symbolic notation for block diagrams used in control theory is shown in Sec.(2.5). The model of the heavy goods vehicle is shown in Fig.(5.2) in Sec.(5.1.2) and in *Simulink*® format in Fig.(5.3) in Sec.(5.1.2). The extremum seeking controller used for deflector adjustment is shown in Fig.(5.8) in Sec.(5.1.6).

6.4.1.1 Research Controller Simulation Variables

The variables used for the simulation are listed below. The reference velocity (V_{ref}) used for the vehicle cruise control was set to 23.0 ms^{-1} (approximately 51.4 mph).

General Simulation Variables:

m = 3,000.00 (Mass of the Vehicle (kg))
ρ = 1.22 (Air Density (kgm^{-3}))

A = 4.00 (Nominal Area (m^2))

μ = 0.80 (Coefficient of Friction for a Dry Surface.)

g = 9.81 (Gravity ms^{-2})

PID Controller Parameters:

K_P = 1.0 (Proportional Gain)

K_I = 1.0 (Integral Gain)

K_D = 1.0 (Differential Gain)

Extremum Seeking Controller Parameters:

k = 1.2, a = 0.03, ω = 2.0, ω_H = 0.01, ω_L = 0.01, ϕ = 0.7995, h_1= -0.01,

Actuator Parameters

ζ = 0.7, ω_{Lag} = 0.2, k_{Lag} = 1.

6.4.2 Aerodynamic Force Simulation for Constant V_W, β and α

The first simulation was conducted to investigate the effect of aerodynamic load on the vehicle for an extremum seeking controller vs. static deflector height. During the simulation the wind velocity (V_W), the wind direction (β) and the road gradient (α) were kept at a constant of 0°.

The vehicle velocity is shown in Fig.(6.90) and the associated aerodynamic force in Fig.(6.91). The results in Figs.(6.90 and 6.91) show the vehicle started with a velocity of 20 ms^{-1} (44.7 mph) and accelerated for 35 seconds until a terminal velocity of 23 ms^{-1} (51.4 mph) was achieved. The corresponding aerodynamic force for both the fixed deflector (δ_H = 0.936) and optimum deflector ratio (δ_{Hopt}) increased due to the increased velocity of the vehicle.

The optimal input (θ^*) for $\beta = 0°$ was δ_{Hopt} = 0.994, corresponding to a plant minimum ($f^*(t)$) of $C_{D(Min)}$ = 0.538 from Tab.(6.1) in Sec.(6.1.4).

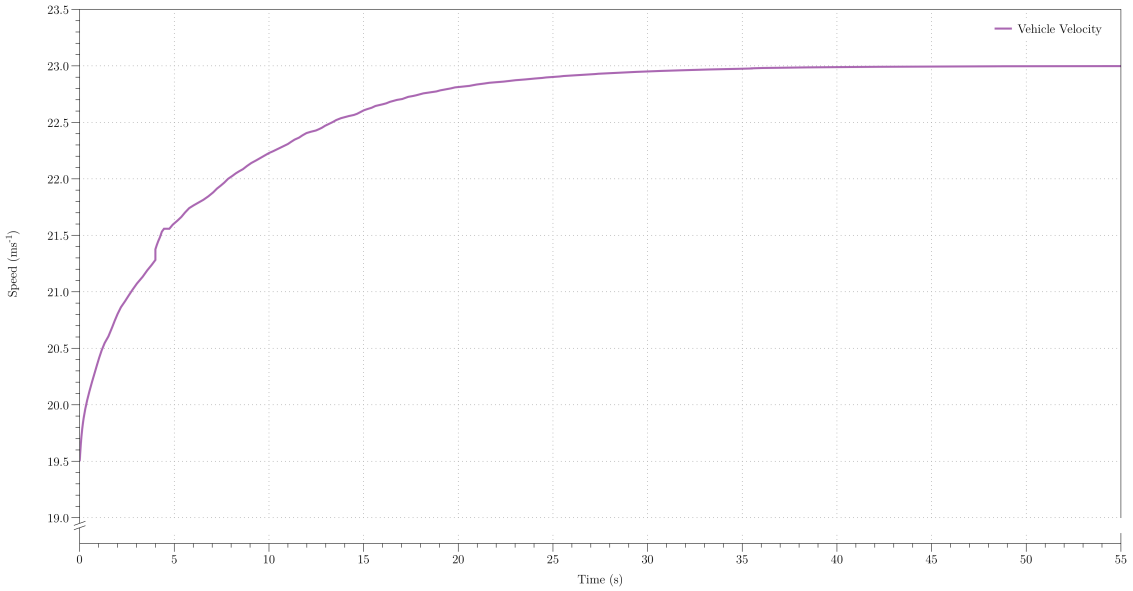

Figure 6.90: Vehicle Velocity vs. Time for (α, β) = 0°.

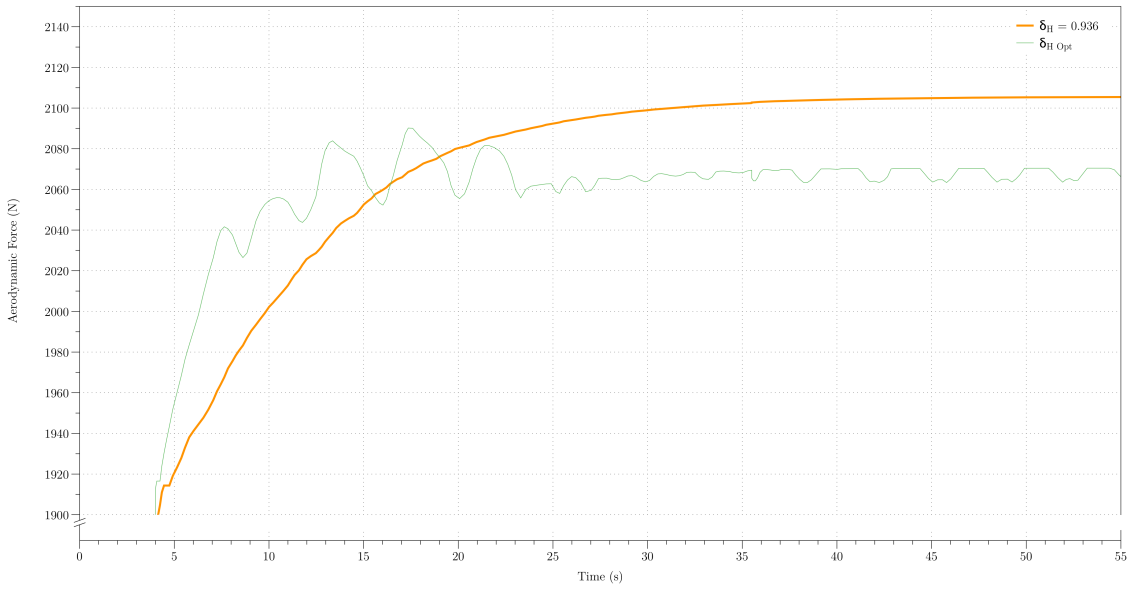

Figure 6.91: Aerodynamic Force vs. Time for (α, β) = 0° and δ_H = 0.936.

Figure (6.92) shows the time variation of $\theta^*(t)$ (δ_{Hopt}) and θ (δ_H) from the extremum seeking algorithm. Figure (6.93) shows the corresponding time variation of $f^*(t)$ ($C_{D(Min)}$) and y (C_D).

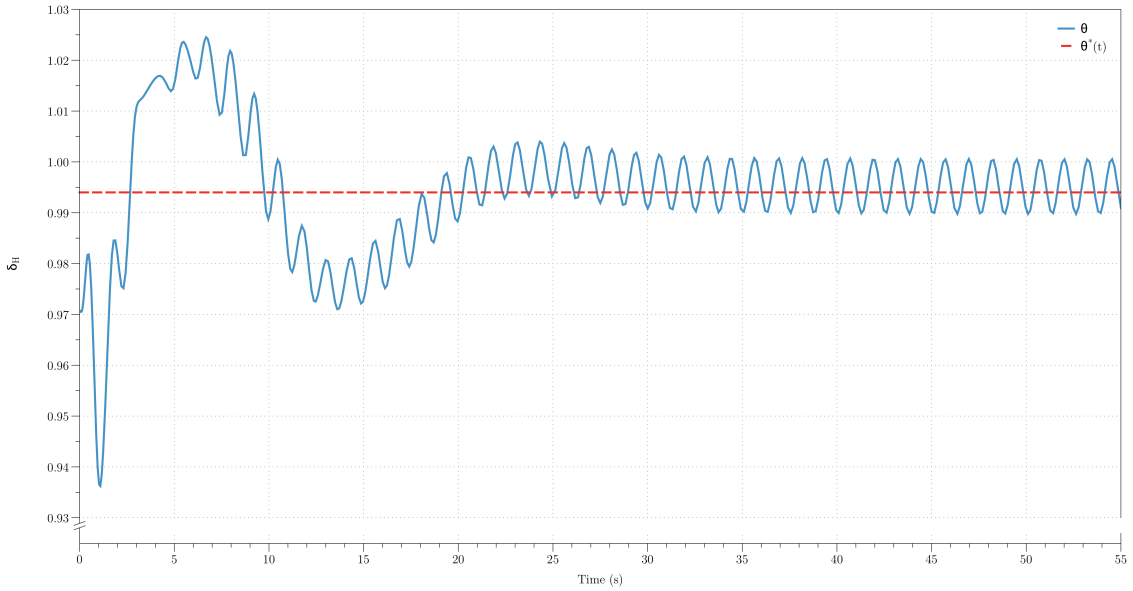

Figure 6.92: θ^* and θ vs. Time for $(\alpha, \beta) = 0°$.

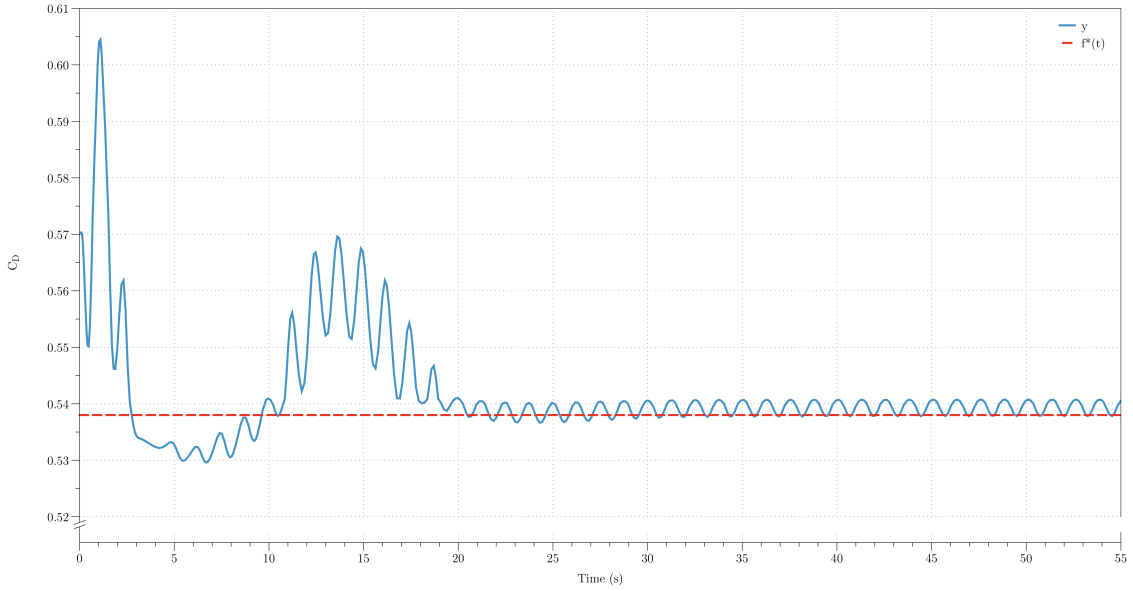

Figure 6.93: $f^*(t)$ and y vs. Time for $(\alpha, \beta) = 0°$.

The extremum seeking controller had an initial excitation perturbation that raised the C_D and corresponding aerodynamic force (shown in Fig.(6.91)). After the excitation perturbation the C_D/aerodynamic force dropped to the optimum

(lower) value and a residual sinusoidal oscillation remained (due to the sinusoidal perturbation used to determine the gradient information of the map f(θ)).

The controlled deflector had, as expected a lower final aerodynamic force due to the optimised height. The optimum deflector height (θ or δ_H) from the ESC algorithm oscillated between 0.990 and 1.000. The optimum deflector height determined from wind tunnel testing was 0.994. This resulted in the aerodynamic and total force oscillating towards the minimum possible value achievable due to deflector height adjustment.

Once the basic test case had been established, investigation into the variation of the aerodynamic force with a varying β was conducted.

6.4.3 Aerodynamic Force Simulation for Constant V_W and α

The yaw angle (β) was now allowed to vary with time. The time variation of β is shown in Fig.(6.94) and the model response in Fig.(6.95).

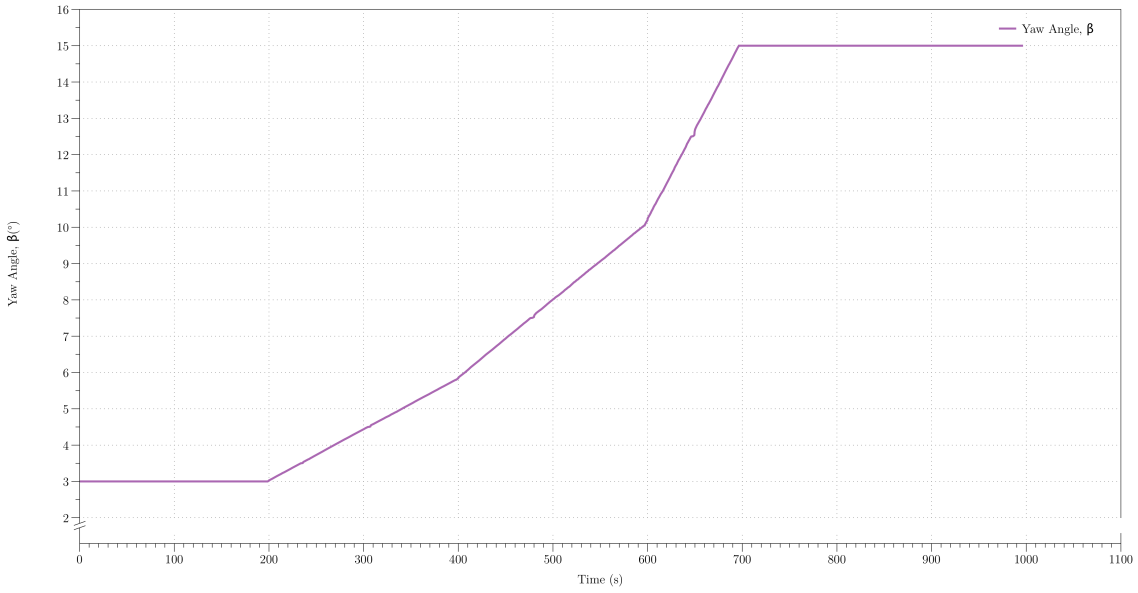

Figure 6.94: Yaw Angle (β) vs. Time.

Figure 6.95: Aerodynamic Force vs. Time.

The yaw angle varied through an angular range of: $+11° \rightarrow +15°$, corresponding to a δ_{Hopt} range of: $0.988 \rightarrow 0.965$. The extremum seeking controller again provided a lower total aerodynamic force on the vehicle due to the optimisation of δ_H. Variation in β again caused discrete plant disturbances followed by an oscillating sinusoidal residual.

The optimal plant input (θ^*) vs. θ is shown in Fig.(6.96) with the optimal output (f*) vs. y shown in Figs.(6.97 and 6.97).

The results showed fast convergence toward the optimal input (θ^* or δ_{Hopt}) after a plant disturbance. The convergence speed was, however, at the expense of an oscillation error. Upon convergence, θ (the plant feedback or C_D - $C_{D(Min)}$) oscillated between 0.990 and 0.978 (a 1.2% error on δ_H or a 4.9 cm full scale error). A disturbance was shown at around 500 seconds where β changes but the optimal input (θ^*) remained constant, such a response was expected from the extremum control scheme [57]. The resulting, optimal output (f^* or $C_{D(Min)}$), was tracked well by the extremum seeking control algorithm.

As a result of the simulations, the extremum seeking control algorithm provided fast adaptation for an unknown optimal input (θ^* or δ_{Hopt}) with good tracking of the minimum (f^* or $C_{D(Min)}$).

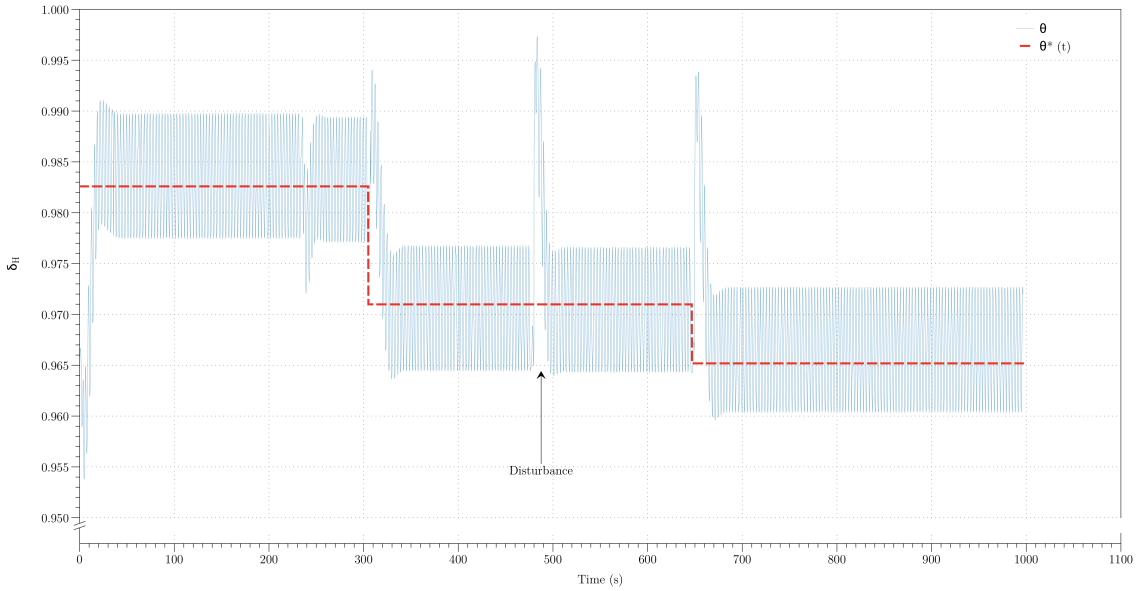

Figure 6.96: θ^* and θ vs. Time.

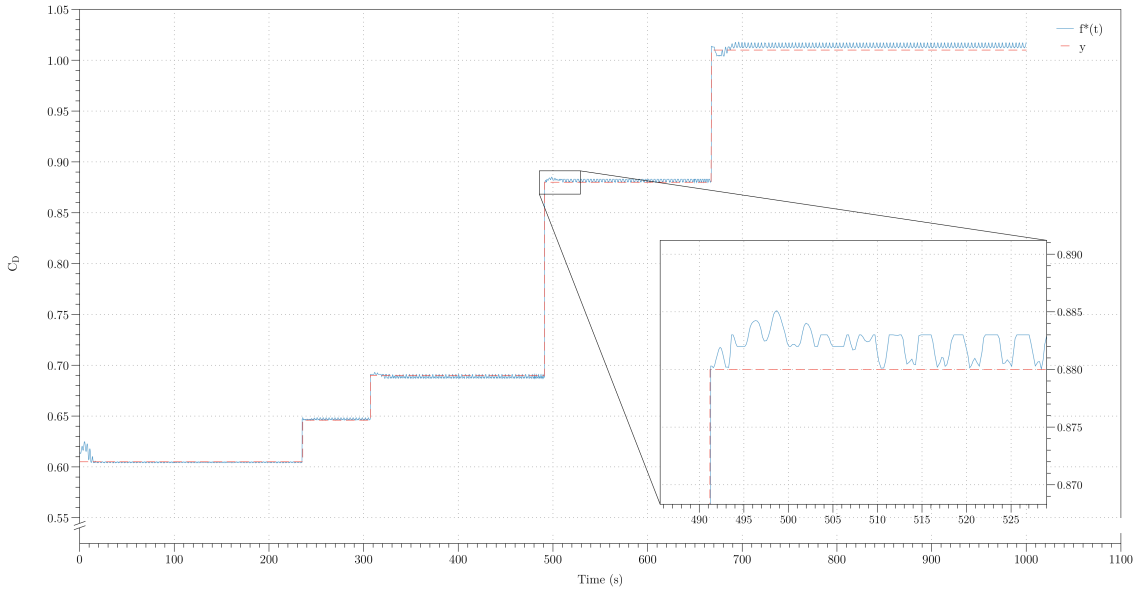

Figure 6.97: f^* and y vs. Time.

The downside of the control algorithm was that the engine force used in the simulations was difficult to practically measure on-road. The aerodynamic wind tunnel tests failed to provide a pressure location for an input parameter on the

control scheme. The lack of a suitable plant input to minimise using extremum seeking control meant the control scheme could not be used for the higher TRL controllers.

6.4.4 Production Controller (TRL7 - TRL9)

The flowchart to show the dependent variables required for the controller is presented in Fig.(1.10) in Sec.(1.6.3).

The uncompiled C-code used for the production controller is shown in Appendix E. The main focus of research for the production controller was the sampling frequency of the parameters and the adjustment frequency of the actuators. The actuator power expenditure was first investigated to determine the limit on the frequency of adjustment.

6.4.4.1 Optimal Adjustment Frequency

A short selection of on-road data was taken prior to permanent installation of the data logger into the vehicle. The resulting time variation for 1,000 seconds is shown in Fig.(6.98).

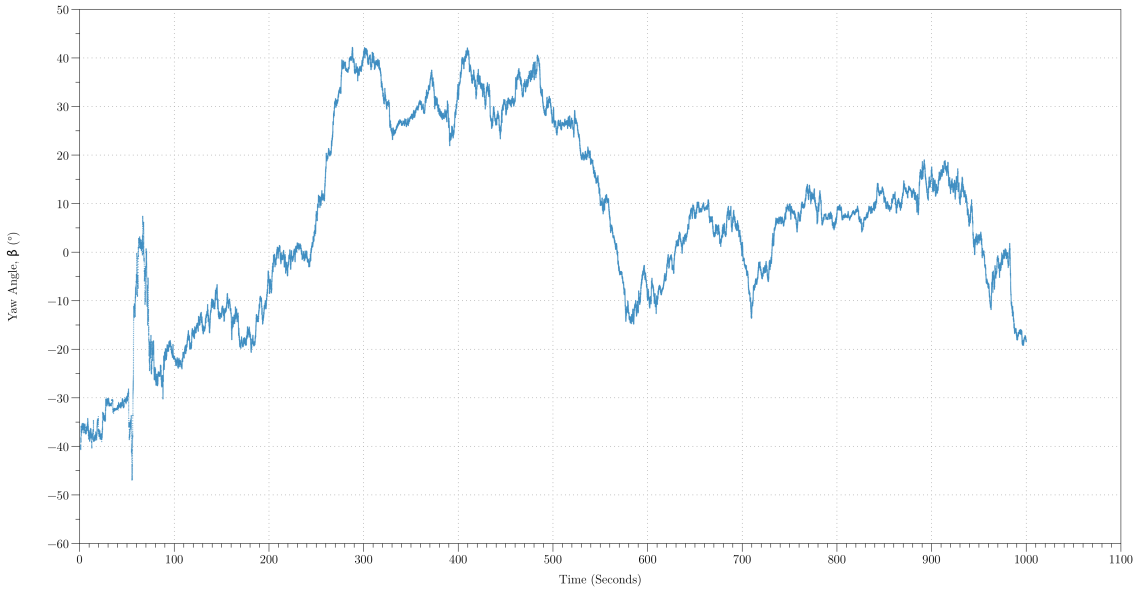

Figure 6.98: Sample Wind Yaw Angle.

The initial results showed a large variation in the yaw angle (β) over the tested time period. The results showed up to 90° change in the yaw angle over a time

period of 300 seconds. To determine if an optimal frequency of adjustment existed, the data was inserted into the *Simulink*® model shown in Fig.(5.17) in Sec.(5.3.1.2).

The adjustment frequency of the actuator was then varied from 100 Hz to 0.0010 Hz to determine if the efficiency reduced with a reduction in the frequency of deflector actuation. The adjustment frequencies of the actuator are shown in Fig.(6.99) with the efficiency reduction shown graphically in Fig.(6.99) and numerically in Tab.(6.27).

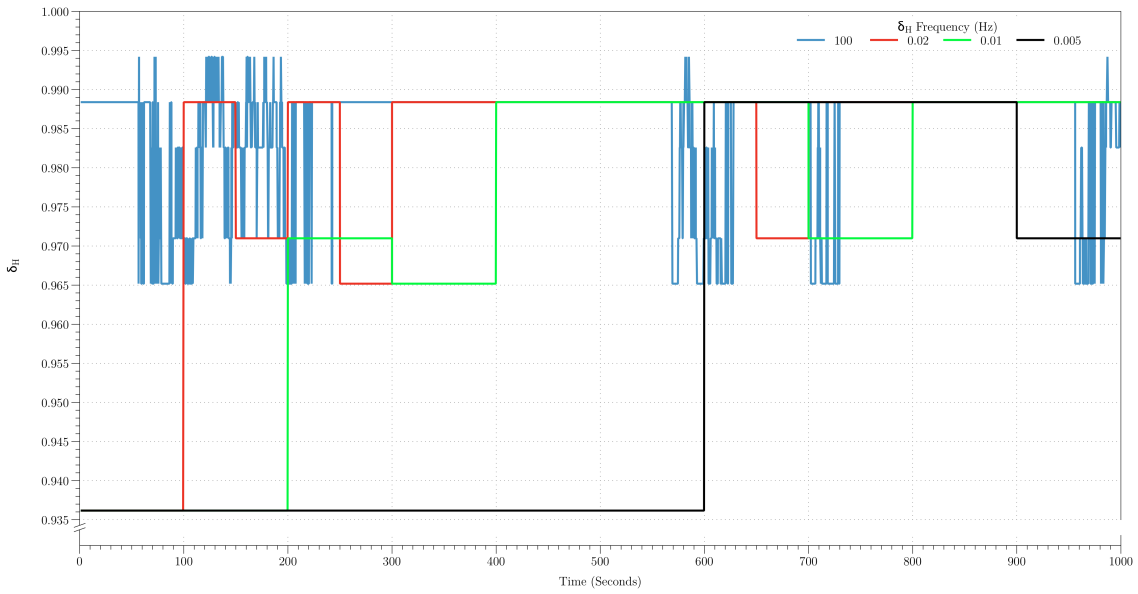

Figure 6.99: δ_H Adjustment Frequency.

The results indicated for a given test period a reduction in the efficiency of the control system was achieved when the actuation adjustment time was extended. A reduction in efficiency of over 64% was obtained for a 200 second adjustment period. Additional reduction in the actuator frequency resulted in a positive drag increase as the deflector was out of synchronisation with the wind yaw and was adjusting to a prior optimal height.

The result of the adjustment frequency having a large influence on the overall performance of the control system placed great emphasis on the selection of the actuator frequency. The actuator frequency chosen for the production controller was 300 seconds. Tab.(6.27) estimates a reduction in efficiency of 78.2%, however, the variation of β during alternate runs was much slower than for the run tested.

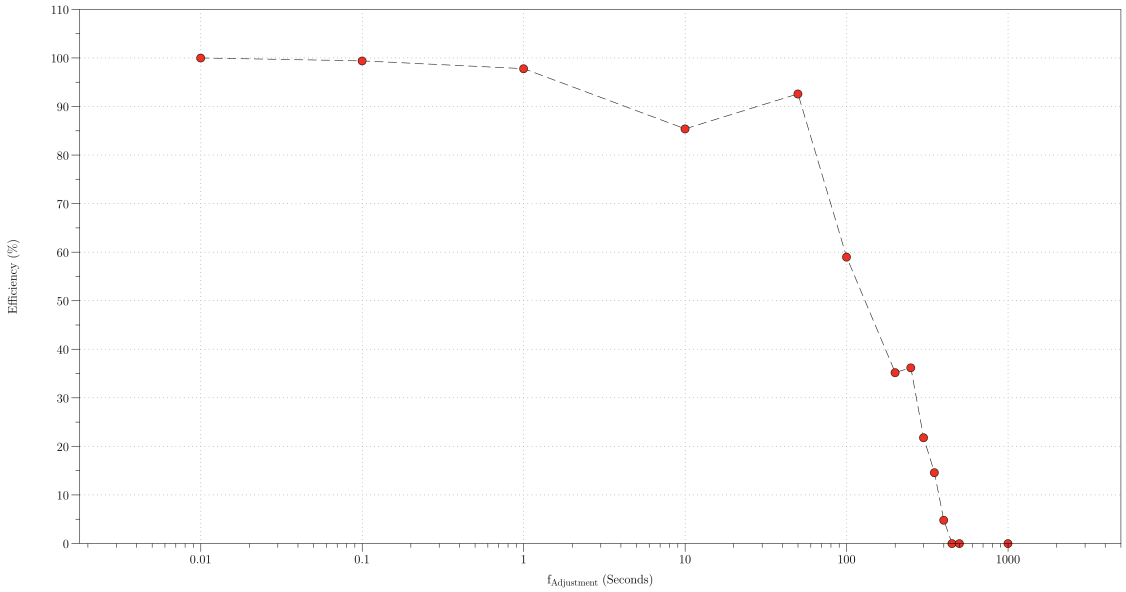

Figure 6.100: Adjustment Frequency Efficiency.

Frequency of Adjustment (Hz)/(Sec)	C_D (%)	Efficiency(%)
100/(0.01)	-3.15	100.0
10/(0.1)	-3.13	99.4
1/(1)	-3.08	97.8
0.1/(10)	-2.69	85.4
0.02/(50)	-2.92	92.6
0.01/(100)	-1.86	59.0
0.0050/(200)	-1.11	35.2
0.0040/(250)	-1.14	36.2
0.0033/(300)	-0.69	21.8
0.0028/(350)	-0.46	14.6
0.0025/(400)	-0.15	4.8
0.0022/(450)	+0.17	0.0
0.0020/(500)	+0.56	0.0
0.0010/(1000)	+0.56	0.0

Table 6.27: C_D % Saving vs. Frequency of Adjustment.

6.4.4.2 Estimation of Drag Reduction

In order to provide an estimation of the potential drag savings associated with the active system, the complete set of yaw angle data was inserted into the *Simulink*®

model, show in Fig.(5.17) in Sec.(5.3.1.2). From the results obtained earlier, an average yaw angle ($\beta_{Average}$) is present due to turbulence caused by from other vehicles on-road. The adjustment frequency of the deflector was therefore not as important as the determination of the average wind direction.

The adjustment frequency was removed and the deflector height ratio (δ_H) set to the $\pm 15^\circ$ value of 0.988, the sample rate of the yaw angle was reduced to 1.0 Hz and the simulation initialised. The simulation was repeated for the zero yaw optimised (ZYO) deflector height ratio of 0.994.

Run	C_{DMin}	C_{DMax}	$\overline{C_D}$	ΣC_D
δ_{HZYO}	0.5980	1.0320	1.0005	2.084×10^6
δ_{Hopt}	0.5700	1.0130	0.9814	2.044×10^6
$(\delta_{HZYO} - \delta_{Hopt})$	0.028	0.019	0.024	4×10^4

Table 6.28: Estimated C_D Saving, where $\overline{C_D}$ is the Average C_D Saving.

The results obtained from the simulation show for 4×10^4 sample points, a summation of the drag coefficient for the ZYO deflector height of 2.084×10^6.

For the active deflector, this value is reduced to 2.044×10^6. The simulations contained identical parameters for each run (wind speed/vehicle speed etc.), the only parameter allowed to vary between the runs was the deflector height (δ_H). A C_D reduction of 1.9% over the static ZYO deflector was achieved by the active system (including actuator power expenditure) for an adjustment frequency of 0.01 Hz (period of 100s).

An active system would therefore provide a total energy saving over an optimised static deflector.

6.4.4.3 Zero Yaw Optimised Deflector Performance Evaluation

During May 2013 an on-road test was conducted to estimate the performance of the zero-yaw optimised deflector. The specification of the heavy goods vehicle used for the on-road test is shown in Sec.(3.7). The data logger used to measure the fuel usage of the vehicle was supplied and installed by Mercedes-Benz and was a DATroniC 3 data acquisition system. The data logger was connected to the CAN bus of the vehicle and enabled measurement from the on-board sensors. Technical details about the logger are shown in Fig.(B.15) in Sec.(B.8) of Appendix B.

The test vehicle was connected to a 'Commercial Motors' supplied test trailer, used to evaluate the performance of production tractor units. The trailer unit used

was 4.0 m in height with a gap of 1.25 m equation to a g/d_2 ratio of 0.875. The deflector height ranged from: 3.87 m $\rightarrow$ 4.17 m, corresponding to $\delta_H = 0.968 \rightarrow 1.04$.

The trailer contained the maximum permissible load, brining the combined tractor-trailer unit to approximately 40 tonnes. The test vehicle and test trailer are shown in Figs.(6.101 and 6.102).

Figure 6.101: Front 3/4 View of Test Vehicle and Test Trailer.

Figure 6.102: Side View of Test Vehicle and Test Trailer.

The on-road test route comprised of a combination of Run [1] and Run [2] from Sec.(6.3). The combined route created a test loop of approximately 111.0 km (70.0 miles). Three runs over the test route were conducted using deflector heights of: 3.87 m, 4.00 m and 4.17 m equating to $\delta_H = 0.968$, 1.000 and 1.040, respectively. The on-board data logger recorded the vehicle speed and fuel usage for each run with the wind speed and direction obtained from a local weather station (station (i) from Tab.(G.1) in Sec.(G.2) of Appendix G).

An example output from the analysis software provided by Mercedes-Benz is shown in Fig.(6.103).

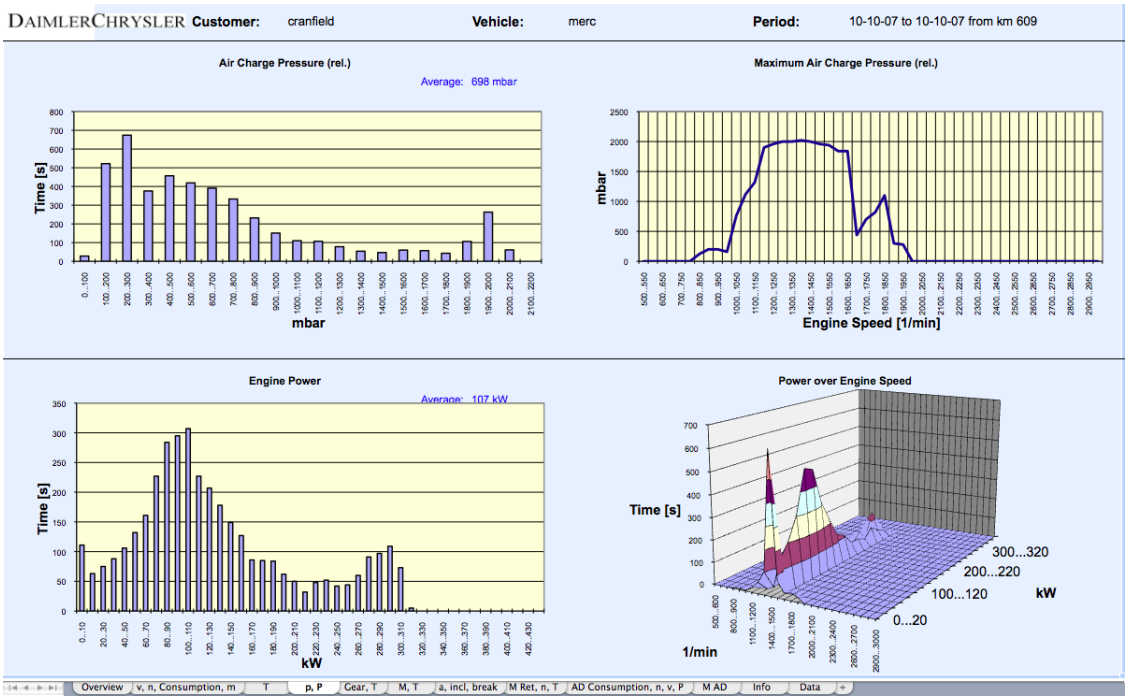

Figure 6.103: Mercedes-Benz Data Analysis Software.

The on-road meteorological data obtained from weather station (i) [91] recorded the wind direction (Φ_{Wind}) as: 180°, with an average wind speed (V_{Wind}) of 12.5 ms^{-1}. The test route used during the on-road testing had a loop to ensure the vehicle traversed the wind in both directions. The vehicle direction (Φ_{Truck}) was 311° for the northbound section and 131° for the southbound section. This corresponded to an angular difference between the truck and the wind direction ($|\varphi|)of41°$, the vehicle speed (V_{Truck}) was a consistent 24.4 ms^{-1} for the duration of the tests (the constant velocity was due to cruise control and a vehicle speed limiter).

Using Eq.(G.4) in Appendix G, this equated to a wind yaw angle magnitude ($|\beta|$) during the tests of 13.6°. The test route and wind direction (blue arrows) are shown in Fig.(6.104).

From Tab.(6.4), the optimum δ_H for $g/d_2 = 1.315$ at 15° wind yaw angle was 0.992. From the wind tunnel tests, the lowest drag configuration was estimated to be the zero yaw optimised case.

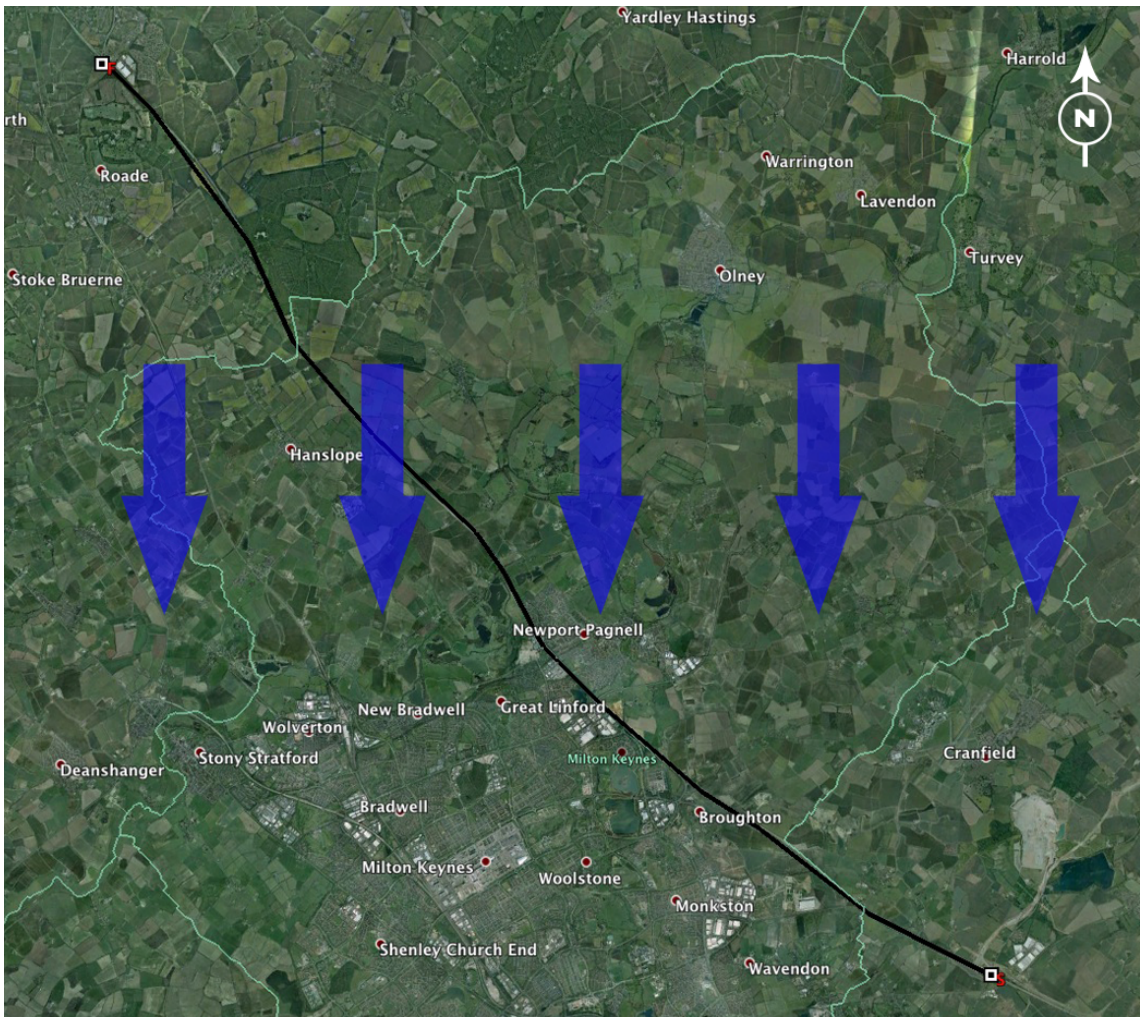

Figure 6.104: Performance Evaluation Test Route[7].

The results from the on-road performance test are shown in summarised form in Tab.(6.29).

δ_H	Distance (km)	Fuel Consumption (L/100 km)	MPG	Fuel Saving(%)
0.968	116.50	31.90	8.86	0.3
1.000	111.10	31.70	8.91	0.9
1.043	111.90	32.00	8.83	0.0

Table 6.29: Zero Yaw Optimised Performance Evaluation Test Results.

[7]Blue Arrows Denote Wind Direction.

The results from Tab.(6.29) show that the highest drag configuration tested was with $\delta_H = 1.043$. The fuel used during 100 km with this deflector height was approximately 32.0 litres. The maximum saving achieved was with the predicted δ_{Hopt} of 1.0, resulting in a percentage fuel saving of 0.9%. Using an empirical 3:1 ratio between drag saving : fuel saving, this equated to an estimated drag reduction of approximately 2.7%.

From the wind tunnel testing, at 15° yaw angle for a g/d_2 separation of 1.315, the difference in C_D between δ_{Hopt} and the maximum δ_H height tested was approximately 1.5%.

This value was in good agreement with the experimentally tested values, with a slight difference due to lack of wind tunnel data on the g/d_2 used for the on-road tests.

6.4.4.4 Prototype Controller Performance Evaluation

During June 2012 the prototype control system (see Sec.(1.6.2) for further information about the prototype controller) was tested at full scale at Millbrook Proving Ground. The test involved four trailers: a single deck curtain trailer, a refrigerated single deck trailer, a refrigerated double deck trailer and a refrigerated pillow double deck trailer. The height of the trailers used in the test were single deck (4.0 m), refrigerated single deck trailer (4.2 m) and refrigerated double deck (4.8 m). The "pillow" on the refrigerated double deck trailer refers to an aerodynamic add on trailer deflector used to remove the area of high pressure on the container forebody when a lower than optimal deflector height is used.

The full test report is shown in Sec.(G.8.2) with the trailer types used during the test shown in Sec.(G.8). The vehicle used for the testing was a 2011 Mercedes-Benz 2543, the specifications for the vehicle are shown in Sec.(3.7).

The test involved two days of testing. The initial day involved testing at 50 mph (22.4 ms^{-1}) for 20 laps (a 3.2 km circumference banked high speed circle shown in Fig.(6.105)) equating to a total test distance of approximately 64 km.

Figure 6.105: Aerial Photo of the Millbrook Proving Ground High Speed Circle [100].

The tests used the prototype controller ActiveFREDDIE deflector (height range of 4.2 - 4.5 m equating to $\delta_H = 0.938 \rightarrow 1.000$ on the 4.8 m trailer) and a static FREDDIE deflector (height fixed at 4.2 m equating to $\delta_H = 0.875$ on the 4.8 m trailer).

The second day of testing involved a repetition of the test conducted on the first day at a reduced speed of 40 mph (18.0 ms^{-1}).

The data obtained from the 50 mph data on day 1 is shown in Tab.(6.30) and the 40 mph data is shown in Sec.(G.8.3) of Appendix G.

The results obtained from the on-road testing are in good agreement with the wind tunnel results obtained in Sec.(6.1.4). There is an increase in fuel consumption of around 5% between the ActiveFREDDIE and static FREDDIE deflectors. This increase was anticipated as the deflector geometry was altered away from the optimum shape to allow for the deflector to adjust. The benefits of the active system can be seen in the remaining results, the single deck refrigerated trailer shows the active system contributed to a 3.9% saving over the static system. Section (6.1.4) estimated a maximum C_D saving of around 10.0%, using an empirical 3:1 ratio for C_D reduction : fuel saving, this equated to around 3.3%. There was expected to be an additional reduction in drag due to the refrigeration unit assisting in removing the pressure from the forebody of the trailer.

Single Deck Curtain Trailer						
Deflector	Distance (km)	Litres	KPL	MPG	Adjusted MPG	Fuel Saving(%)
Static	66.3	16.8	3.95	9.28	9.28	-
Active	65.8	17.5	3.76	8.84	8.84	-4.7
Refrigerated Single Deck Trailer						
Deflector	Distance (km)	Litres	KPL	MPG	Adjusted MPG	Fuel Saving(%)
Static	66.5	18.8	3.54	8.32	8.34	-
Active	66.6	18.5	3.60	8.47	8.67	3.9
Refrigerated Double Deck Trailer						
Deflector	Distance (km)	Litres	KPL	MPG	Adjusted MPG	Fuel Saving(%)
Static	66.7	21.7	3.07	7.23	7.05	-
Active	66.4	21.0	3.16	7.44	7.82	10.9
Refrigerated Pillow Double Deck Trailer						
Deflector	Distance (km)	Litres	KPL	MPG	Adjusted MPG	Fuel Saving(%)
Static	65.8	20.2	3.26	7.66	7.39	-
Active	66.5	20.0	3.33	7.82	7.92	7.1

Table 6.30: Millbrook ActiveFREDDIE Test Data [101] with Various Trailer Combinations, Test Conducted at 50 mph[9].

The larger trailer height of 4.8 m was not tested with the ActiveFREDDIE deflector in the wind tunnel. The results obtained from full scale testing, however, showed a large reduction in fuel of approximately to 11% equating to a C_D reduction of over 30%. The aerodynamic trailer "pillow" deflector, showed a 4.9% reduction in fuel for the static deflector and a 1.3% reduction for the active system. Due to the movement of the active system removing the area of high pressure from the forebody of the container, the effectiveness of the "pillow" was expected to be reduced when used in conjunction with ActiveFREDDIE.

The large fuel saving of over 30% highlights the benefits of an active system, due to various trailers used with a single tractor unit, switching between a refrigerated and non-refrigerated trailer is common. A result of this is a non-optimal tractor-trailer combination, which if left without adjustment of the deflector, leads to a high aerodynamic drag penalty.

From the independent tests conducted by Tesco Engineering [101], the official policy was to retro fit all existing Tesco cabs with ActiveFREDDIE and for all new Tesco cabs purchased to be fitted with the active system.

[9]Adjusted MPG Corresponds to Allowance for Atmospheric Conditions.

6.4.5 Subsection Summary

The results from the control system simulation concluded that the extremum seeking controller was a suitable algorithm for use in active flow control. The results showed fast convergence toward the optimal input (θ^*/δ_{Hopt}) after a plant disturbance. The convergence speed was, however, at the expense of the oscillation error. Upon convergence, (θ^*/δ_{Hopt}) oscillated between 0.990 and 0.978 (a 1.2% error on δ_H or a 4.9 cm full scale error). The resulting optimal output (f* or $C_{D(Min)}$) was tracked well by the extremum seeking control algorithm.

The extremum seeking controller could not, however, be used in the full scale production controller, as a suitable plant input was not found during wind tunnel testing. A plant input was required in order for the minimisation algorithm to function, the simulations assumed the vehicle drag could be measured or related to a measurable parameter. No such parameter was found in the experimental testing and as a result, the algorithm could not be used.

The full scale controller was designed to use data obtained from wind tunnel testing and from Computational Fluid Dynamics (CFD) simulations in a look-up table to adjust the deflector to the known optimum (δ_{Hopt}). Investigation into the optimal adjustment frequency of the actuators revealed that for normal operational velocities, any deflector adjustment at a frequency less than 1.5 Hz would result in a net energy saving. The efficiency was found to decrease as the adjustment frequency increased. A reduction in efficiency of over 64% was obtained for a 200 second adjustment period. Additional reduction in the actuator frequency resulted in a positive drag increase as the deflector became unsynchronised with changes in the wind yaw and was adjusting to a prior optimal height.

The on-road wind data was then inserted into a *Simulink*® model to estimate the additional saving over a zero yaw optimised (ZYO) deflector. The results obtained from the simulation indicated a reduction in the drag coefficient (C_D) of 2.4% could be obtained over $\delta_{H(ZYO)}$. This result indicated that an active system could provide addition drag reduction as $\delta_{H(ZYO)}$ could be established based on trailer height and length measurements, however, only on-road pressure measurement would enable δ_{Hopt} as a function of β to be determined.

Full scale on-road measurements of the zero yaw optimised deflector revealed a fuel saving of 0.9%, equating to an approximate C_D reduction of 2.7%. The on-road test validated at full scale the predictions made from the wind tunnel testing. Further testing of the prototype controller by Tesco Engineering [101] revealed the active system produced a fuel saving of between 3.9% -10.9% when used in conjunction with various trailer configurations. This test served to highlight the importance of active optimisation compared to the static systems fitted on most heavy goods vehicles.

The tests conducted by Tesco Engineering [101] concluded that (subject to field testing on the robustness of the prototype controller used for ActiveFREDDIE), the semi-active deflector was to be retro fitted to all existing Tesco cabs and for all new Tesco cabs purchased to be fitted with the semi-active system.

Chapter 7

Conclusions and Future Work

7.1 Conclusions

7.1.1 Initial Project Objectives

The project objectives performed in this research were identified as:

- To determine if for a given tractor-trailer configuration an optimum cab mounted deflector height (δ_{Hopt}) existed. The optimum deflector height was defined as the height at which the deflector reduced the vehicle's drag coefficient (C_D) to a minimum ($C_{D(Min)}$).

- If δ_{Hopt} existed, determine the variation of the optimum height with external variables. These variables were: the wind yaw angle (β) and the container separation (g/d_2).

- Determine a suitable input parameter for the control system for an 'active' deflector to minimise the aerodynamic drag on the vehicle. The basic requirement for the control scheme was to be able to relate the vehicle's C_D to a measurable parameter on the vehicle. Since the C_D of a vehicle is difficult to measure outside of a stable environment such as a wind tunnel, the C_D had to be related to a measurable parameter (such as a pressure measurement) that could be measured on-road.

  A suitable pressure measurement on the vehicle could not be related to the C_D, therefore an alternate control scheme was constructed. The alternate control scheme required direct measurement of the wind yaw angle (β), container separation (g/d_2) and the deflector height (δ_H).

- Determine measurement methods for the variables required for the control scheme: β, g/d_2 and δ_H.

- Construct a simplified numerical model of the vehicle together with an estimation of the on-road environment suitable with simulation within *Simulink*®. Due to the complexity of the on-road turbulence, on-road performance of the active system was estimated using simulation. The model used for simulation enables estimation of parameters required for the control scheme such as the optimum adjustment frequency for the deflector.

- Production of a full-scale prototype of the active system. This allowed for the testing of the semi-active component of the controller (adjustment to the zero yaw optimised (ZYO) height ($\delta_{H(ZYO)}$)).

- Design and implementation of a full scale test program to correlate parameters measured in the wind tunnel test with on-road data.

- CFD simulation of two commercial vehicles in tandem to attribute on-road signal 'noise' to a parameter associated with the steady-state operation of the full-scale vehicle. Due to the large amount of "noise" present within the on-road data, suitable filters were required to improve accuracy of the measured parameters.

- Production of a commercial active control system from the data obtained from wind tunnel, CFD, control simulations and on-road testing.

- Estimation of the performance of the active control device over the zero yaw optimised deflector using numerical simulation.

7.1.2 Summary of Project Findings

An optimum deflector height was found to exist that minimised the drag coefficient (C_D) of a heavy goods vehicle. The optimum height was expressed as an optimum deflector height ratio (δ_{Hopt}) between the cab and container height.

The optimum deflector height ratio was found from wind tunnel testing to be close to 1.0 for a standard tractor-trailer unit. The optimum deflector height ratio was also found to vary with the wind yaw angle (β) and the cab-container separation (g/d_2).

Surface static pressure tappings on the wind tunnel model located on the cab rear, deflector rear, trailer forebody and trailer centre line were unable to relate the C_D of the vehicle to a particular pressure measurement. The initial extremum seeking control (ESC) scheme sought to minimise the C_D of the vehicle and placed a requirement that the C_D (or a measurable parameter that related to the C_D) had to be measured on the vehicle. From this variable, the optimum deflector height could then be calculated. The complex 3D flow fields associated with the geometry meant that the container forebody pressure was the only location found to relate to the deflector height (δ_H). This tapping location, however, did not relate to δ_{Hopt}. The container forebody pressure was found to decrease as the deflector height increased, this trend, however, continued past δ_{Hopt}. If this pressure measurement had been used as a plant input for the ESC, the controller would simply have calculated δ_{Hopt} to be the highest deflector height (and therefore lowest container forebody pressure), this in turn would have lead to an increase in the vehicle's C_D and the C_D would not have been driven to a minimum.

The requirement from the control scheme to be able to measure the vehicle's C_D was based on the design of extremum seeking control. The extremum seeking controller was found to be a suitable control system for the theoretical problem. The controller showed fast convergence towards the optimal input (θ^* or δ_{Hopt}) even with plant disturbances (e.g. a change in β). Due to the lack of a suitable pressure location on the vehicle for use as an input to the system, the vehicle's engine force was instead used for the simulations. The engine force used, however, was impractical to measure on-road and therefore could not be used as an input for the production controller. Without a suitable pressure location on the vehicle relating to the C_D an alternate control scheme was created.

The alternative control scheme used data obtained from wind tunnel testing. δ_{Hopt} had been established to depend on β and g/d_2. These variables, therefore were the only required inputs parameters for the new control scheme. A 3D look-up table was generated to express δ_{Hopt} as a function of $\delta_{Hopt}(\beta, g/d_2)$. The container separation ratio (g/d_2) was measured using an infrared sensor and β was inferred using a linear relationship between a pressure differential (ΔC_P) located on the

vehicle. Wind tunnel testing revealed the ActiveFREDDIE deflector geometry acted as a three-hole probe. Pressure tappings located on either side of the static skirt of the deflector were found to provide a linear relationship between ΔC_P and β. The ability to measure the two variables required for the control scheme enabled a control algorithm to be designed.

The accuracy of data contained within the 3D look-up table directly related to the overall performance of the control scheme. Investigation into numerical simulation of the flow field via Computational Fluid Dynamics (CFD) around the geometry was conducted. The numerical simulation aimed at improving both the accuracy of the data and to increase the range of obtained data. Primary investigation was conducted into a simplified 2D geometry to determine the most suitable Reynolds-Averaged Navier-Stokes (RANS) turbulence model. Many RANS turbulence models exist and the most suitable for the research was defined as the model that most accurately predicted the ΔC_D associated with a variation in δ_H and g/d_2. The CFD simulation on the tractor-trailer unit revealed the optimum RANS model to be k-$\epsilon_{(Realizable)}$.

The RANS model chosen from the 2D geometry allowed continued investigation into a 3D geometry. A 3D geometry was required to accurately model the complex flow field associated with the cab-trailer gap. Extension into 3D with the k-$\epsilon_{(Realizable)}$ turbulence model showed strong agreement with the experimental data. The 3D CFD model predicted an increase in the C_D obtained for $g/d_2 = 1.056$, a larger container separation that could not be experimentally tested. The data obtained from the 3D CFD simulations using the k-$\epsilon_{(Realizable)}$ turbulence model was found to be suitable for predicting δ_{Hopt} for various tractor-trailer configurations.

An extensive full scale test program involving over 1,200 km of test route was conducted. The test program involved recording the vehicle speed (V_{Truck}), wind speed (V_{Wind}), wind direction (β) and the pressure tappings located on the vehicle (ΔC_P). The results showed an average wind speed of 8.7 ms^{-1}. The average yaw angle measured (β) was -0.5° with an average magnitude $|\beta|$ of 4.6°. Investigation into the time variation of β found there was a average wind angle containing four underlying frequencies of: 0.004, 0007, 0.011 and 0.019 Hz perturbed by relatively higher (> 1.0 Hz) frequencies. The four underlying frequencies were contained within all the runs tested and corresponded to periods of: 238.4, 141.7, 94.9 and 53.1 seconds, respectively.

Unsteady CFD simulation using Large Eddy Simulation (LES) was used for frequency analysis. Frequency analysis was conducted on the tractor-trailer wake of two vehicles traveling in tandem. The results indicated the higher frequency perturbations (f > 1.0), with an average direction fluctuation of around $|5°|$ obtained from the on-road testing, could be accounted for by the flow field present within the trailer wake.

Post-processing of the on-road data found the application of a low-pass numerical filter with cut-off frequency (f_c) of 1.0 Hz and use of a moving average filter with frequency 0.004 Hz to be optimal. The disturbance on the mean yaw angle was reduced from $\pm 15^\circ$ to $\pm 3^\circ$. The on-road yaw angle estimation obtained from the linear equation relating ΔC_P to β found that 65% of the data was within $\pm 2\%$ accuracy and 81% within $\pm 3.8\%$ accuracy at the maximum $\pm 25^\circ$ yaw angle. The wind vane was found, from experimental and CFD testing, to have a -15° offset at zero yaw angle. After correction factors had been applied the accuracy of the wind vane at $\pm 20^\circ$ was approximately 6%. The mounting location of the wind vane was found to account for the majority of this discrepancy.

The experimental and CFD results provided the data for the control algorithm and allowed programming of the micro controller. Results obtained from numerical *Simulink*® simulation allowed an estimation of the sampling frequency of the sensors and adjustment frequency of the actuators. The power expenditure from movement of the actuators imposed a critical frequency of adjustment of 1.54 Hz or 0.65 seconds. This high frequency implied that the adjustment time was not limited by the actuators. Simulation of the actuator adjustment time showed that the efficiency dropped as the adjustment frequency increased. A reduction in efficiency of over 85% was obtained as the time period increased from a few seconds to 350 seconds, with a critical period of 450 seconds before an increase in C_D over the zero yaw optimised deflector.

Full scale on-road testing was conducted to estimate the performance of varying δ_H on-road. The test vehicle was connected to a test trailer of height 4.00 m, g/d_2 ratio of 0.875. Three deflector heights (3.87, 4.00 and 4.17 m) were tested over a test loop of approximately 111 km. The deflector heights used corresponded to δ_H = 0.968, 1.000 and 1.043, respectively. The wind direction and speed was obtained from a local weather station and corresponded to $\Phi_{Wind} = 180^\circ$ and 12.5 ms^{-1}, respectively. The vehicle route gave a vehicle direction of $\Phi_{Truck} = 311^\circ$ for the northbound element of the journey and $\Phi_{Truck} = 131^\circ$ for the southbound. The average truck velocity of 24.4 ms^{-1} gave an effective wind yaw angle of $\pm 13.6^\circ$. Wind tunnel testing predicted the optimum δ_H to be close to 1.0 with an estimated 0.5% saving in fuel. The on-road tests concluded the optimum δ_H to be 1.0 resulting in a fuel saving of 0.9%, in good agreement with the experimental data.

The prototype controller designed in Sec.(5.2.3) was tested by Tesco Engineer [101] at Millbrook Proving Ground high speed oval. The tests involved two days of testing, the initial day involved testing at 50 mph (22.4 ms^{-1}) for 20 laps (a 3.2 km circumference banked high speed circle), equating to a total test distance of approximately 64 km. Three trailer heights were used in the test were single deck (4.0 m), refrigerated single deck trailer (4.2 m) and refrigerated double deck (4.8 m). The active deflector's heights range was: 4.2 - 4.5 m (equating to $\delta_H = 0.938 \rightarrow 1.0$ on

the 4.8 m trailer) and a static FREDDIE deflector (height fixed at 4.0 m equating to $\delta_H = 0.833$ on the 4.8 m trailer). The second day of testing involved a repetition of the test conducted on the first day at a reduced speed of 40 mph (18.0 ms^{-1}).

The active system produced a 3.9% saving over the static system on the single deck refrigerated trailer, (wind tunnel estimated 3.3% fuel saving,from Sec.(6.1)). There was an expected additional reduction in drag due to the refrigeration unit assisting in removing the area of high pressure from the forebody of the trailer.

The larger trailer height of 4.8 m was not tested with the ActiveFREDDIE deflector in the wind tunnel. The results obtained from full scale testing, however, showed a large reduction in fuel of close to 11% equating to a C_D reduction of over 30%. The aerodynamic trailer "pillow" deflector, showed a 4.9% reduction in fuel for the static deflector and a 1.3% reduction for the active system. Due to the movement of the active system removing the area of high pressure from the forebody of the container, the effectiveness of the "pillow" was expected to be reduced when used in conjunction with ActiveFREDDIE. The large fuel saving of over 30% highlights the benefits of an active system, due to various trailers used with a single tractor unit, switching between a refrigerated and non-refrigerated trailer is common. This results in a non-optimal tractor-trailer combination, which if left without deflector adjustment, leads to a high aerodynamic drag penalty. From the independent tests conducted by Tesco Engineering [101], the official policy (subject to field testing on the robustness of ActiveFREDDIE) was to retro fit all existing Tesco cabs with ActiveFREDDIE and for all new Tesco cabs to be fitted with the active system.

Simulink® simulation using on-road data of a vehicle model fitted with the ActiveFREDDIE profile deflector allowed an estimation of its on-road performance. Results indicated a zero yaw optimised deflector had a wind averaged saving of up to 7.4% (from Sec.(1.3), this equated to an annual fuel saving of £25.0 Million) over a non optimised, static deflector. A further saving of around 1.9% in the C_D (equating to an annual saving of £6.3 Million) over the zero yaw optimised (ZYO) deflector was estimated for the active deflector adjusting to the wind direction (β).

The ZYO deflector was used as the theoretical baseline for active comparison, however, in reality most HGVs operate with varying containers. The containers used by most fleet operators vary in both height and separation. This results in most fleet operators not adjusting or having the ability to adjust the deflector when the vehicle is connected to varying containers. The real world performance of the active system should therefore show an even larger drag reduction compared to static deflectors.

In conclusion, the thesis resulted in the production of full scale active deflector named 'ActiveFREDDIE'. ActiveFREDDIE is currently in commercial production with a computer simulated additional aerodynamic drag reduction of 1.9% over 'FREDDIE'. This resulted in an estimated annual saving of £6.3 Million.

7.1.3 Conclusions Summary

A summary of the unique results obtained within this thesis are:

- Determined a non dimensionalised optimum deflector height ratio (δ_{Hopt}) as a function of the wind yaw angle (β) and the container separation (g/d_2).
- Use of vehicle geometry to determine pressure tapping locations on a Heavy Goods Vehicle (HGV), the resulting pressure coefficient differential (ΔC_P) between these locations linearly related to the wind yaw angle (β). The resulting estimated yaw angle (β_{Est}) was generated from the linear relationship.
- Established k-$\epsilon_{(Realizable)}$ as a the most suitable Reynolds-Averaged Navier-Stokes (RANS) turbulence model for a 3D truck-trailer combination.
- Used 3D k-$\epsilon_{(Realizable)}$ turbulence model to predict container separations that were not possible to test in the wind tunnel due to test section size constraints.
- Full scale on-road testing of a HGV including high frequency measurement of the wind yaw angle (β), wind speed (V_{Wind}), truck speed (V_{Truck}), pressure differential (ΔC_P) and the estimated yaw angle (β_{Est}).
- Attribute on-road variation of β to a $\beta_{Average}$ perturbed by four fundamental frequencies.
- Identify the fundamental frequencies as: 0.004, 0.007, 0.011 and 0.019 Hz and design of a suitable filter to dampen their effects.
- Large Eddy Simulation (LES) of a truck-trailer configuration and comparison with on-road data. Results attributed the high frequency on-road perturbations to vortex shedding from lead vehicles when the vehicle is tandem.
- Prediction of the wake structure between bluff bodies in tandem using RANS simulation at a high (5×10^6) Reynolds number (Re).

- Generated model of a Heavy Goods Vehicle (HGV) using *Simulink*® in conjunction with on-road data to model a full scale, on-road vehicle.
- Implementation of Extremum Seeking Control (ESC) algorithm with HGV. Simulation of ESC applied to a HGV fitted with active deflector.
- Production of full scale prototype controller. Generation of embedded C/C++ code used for controller as well as construction of controller using prototyping board.
- Determined from simulation, the optimal adjustment frequency for actuators used in the active system.
- Full scale on-road and off-road testing of prototype controller. Fuel savings of between 3.3% - 11.0% were achieved depending on tractor unit used for testing. On-road results validated using wind tunnel data.
- Production of full scale controller ActiveFREDDIE used in commercial production with simulated active performance of 1.9% over the theoretical best static baseline.
- ActiveFREDDIE provided a 1.9% reduction in C_D over the ZYO 'FREDDIE' and generated a predicted annual saving of £6.3 Million.
- ActiveFREDDIE provided a 9.3% reduction in C_D over a non optimised 'FREDDIE' and generated a predicted annual saving of £93.0 Million.

7.2 Future Work

There is potential scope to extend the project further, primarily via improving the accuracy of data used within the control scheme and by testing alternate deflector geometries. The initial system was restricted by commercial limitation on the actuation method used in the active system. The deflector height (δ_H) used was therefore assumed to be the optimal shape for all deflection heights. A more commercially relaxed project would allow investigation into 3D variation of the geometry to determine how δ_H varies in three-dimensional space.

The control system designed in the project used an infrared signal measurement to determine gap to container height ratio (g/d_2). This same system could be used to determine the geometry of the container forebody/roof. The wind tunnel tests assumed a rectangular shaped container forebody, however, alternate designs of trailer units exist and are in commercial use. Use of an infrared sensor in this manner would allow the control system to be modified to note the distance of the trailer as a function of actuator height. This would allow an estimation of the trailer forebody/roof geometry to be made. This result in combination with 3D deflector geometry control could possibly result in a lower drag saving if an unconventional trailer is used with the tractor unit.

Further investigation using 3D Computational Fluid Dynamics (CFD) at non zero yaw would also provide additional data points for the look-up tables, the ultimate accuracy of the data determines the efficiency of the system, as a result the ability to numerically simulate the system at yaw would provide additional data points. CFD at non zero yaw angles would also allow for easier investigation into the possibility of a pressure signature located on the vehicle to allow use of the extremum seeking controller.

Further on-road testing would also provide useful information on the variation of sampled on-road data with varying climatic conditions. This would allow investigation into whether fundamental frequencies present within the wind yaw angle (β) vary throughout the year. The addition of a synchronised video recording system on the test vehicle would also help identify the on-road contributions to lower frequency disturbances. This could be used in conduction with Large Eddy Simulations (LES) of an overtaking vehicle to identify the wake structure. The effect of other passing heavy goods vehicles and local infrastructure could therefore be used to more effectively filter the measurement signals, further improving the yaw estimation.

The full scale performance evaluation of the system is also a large and challenging area. Most commercial operators have varying delivery routes and varying loads. Repeat runs with identical parameters are therefore almost impossible to obtain. Investigation into fleet operators running active and static deflectors on similar routes or through use of a closed test section would yield feedback on the accuracy of the

Simulink® simulation. This would in turn give a better estimation towards the real world performance via numerical simulation.

This page intentionally left blank.

This page intentionally left blank.

References

[1] Intrasolutions & Consulting. Permissible trailer heights in europe. http://www.internationaltradingsolutions.com, 2002.

[2] H.Gotz and G.Mayr. *Aerodynamics of Road Vehicles*, pages 417–434. SAE, 1998.

[3] ATS. Ats vehicle image. http://www.americantruckshowroomsatlanta.com, 2013.

[4] Cartwright. Manufacturers specification sheet. http://www.cartwrightrentals.com, 2012.

[5] F.Buckley, C.Marks, and W.Walston. A study of aerodynamic methods for improving truck fuel economy. Technical report, University of Maryland, 1978.

[6] Freight Transport Association. Fuel as a percentage of hgv operating costs. http://www.fta.co.uk/policy_and_compliance/fuel_prices_and_economy/fuel_prices/fuel_fractions.html, 2013.

[7] Department for Transport. Domestic road freight statistics. http://www.dft.gov.uk/statistics/series/road-freight, 2013.

[8] NASA. Technology readiness levels demystified. http://www.nasa.gov, 2010.

[9] K.Ogata. *System Dynamics*, pages 14–36. Prentice Hall, fourth edition, 2003.

[10] K.Cooper. Commercial vehicle aerodynamic drag reduction: Historical perspective as a guide. In *The Aerodynamics of Heavy Vehicles: Trucks, Buses and Trains*, page 9. Springer, 2002.

[11] Smithsonian's National Air and Space Museum. Drag around various objects. http://www.howthingsfly.si.edu/aerodynamics/pressure-drag, 2014.

[12] M.Hirz and S.Stadler. A new approach for the reduction of aerodynamic drag of long-distance transportation vehicles. *SAE*, 6(2), 2013.

[13] J.Anderson. *Fundamentals of Aerodynamics*, page 397. McGraw-Hill, 2005.

[14] W.Hucho. *Aerodynamics of Road Vehicles*, page 434. SAE, 1998.

[15] A.Sherwood. Wind tunnel test report no.85. Technical report, University of Maryland, 1953.

[16] S.Saunders. Apparatus for reducing linear and lateral wind resistance in a tractor-trailer combination vehicle. US Patent Ser. No. 341,622, 1966.

[17] A.Sherwood. Wind tunnel test report no.98. Technical report, University of Maryland, 1974.

[18] K.Ingram. The wind-average drag coefficient applied to heavy goods vehicles. Technical report, TRRL, 1978.

[19] B.Storms, J.Ross, J.Heineck, S.Walker, D.Driver, G.Zilliac, and D.Bencze. An experimental study of the ground transportation system (gts) model in the nasa ames 7- by 10-ft wind tunnel. Technical report, NASA Ames Research Centre, 2001.

[20] A.Ojima and K.Kamemoto. Numerical simulation of unsteady flow around three dimensional bluff bodies by an advanced vortex method. *Japan Society of Mechanical Engineers*, B43-2:127–135, 2000.

[21] 16th and Georgetown. Marlboro team penske racing truck. `http://www.16thandgeorgetown.wordpress.com/2008/08/20/323/`, 2012.

[22] K.Cooper. A wind tunnel investigation into the fuel savings available from the aerodynamic drag reduction of trucks. *DME/NAE*, 3, 1976.

[23] K.Cooper. The effect of front-edge rounding and rear edge shaping on the aerodynamic drag of bluff vehicles in ground proximity. *SAE Technical Paper Series*, 1985.

[24] W.Mason and P.Beebe. The drag related flow field characteristics of trucks and buses. aerodynamic drag mechanisms of bluff bodies and road vehicles. In *Symposium Held at the General Motors Research Laboratories*. Plenum Press, 1978.

[25] Uncredited. Evaluation and demonstration of practical devices/systems to reduce aerodynamic drag of tractor-semitrailer combination unit trucks. *TMA*, 2007.

[26] R.Englar. Advanced aerodynamic devices to improve the performance, economics, handling and safety of heavy vehicles. *SAE Technical Paper Series*, 2001.

[27] K.Salari. Heavy vehicle drag reduction devices, computational evaluation and design. *DOE Heavy Vehicle Systems Review*, 2006.

[28] A.Seifert, O.Stalnov, D.Sperber, G.Arwatz, V.Palei, S.David, I.Dayan, and I.Fono. Large truck drag reduction using active flow control. In *The Aerodynamics of Heavy Vehicles II: Trucks, Buses and Trains*, pages 115–133. Springer, 2009.

[29] W.Pointer. Evaluation of commercial cfd code capabilities for prediction of heavy vehicle drag coefficients. *34th AIAA Fluid Dynamics Conference and Exhibit*, 2004.

[30] Mercedes-Benz. 2012 mercedes-benz actros. `http://www2.mercedes-benz.co.uk/content/`, 2012.

[31] J.Leuschen and K.Cooper. Summary of full-scale wind tunel test of aerodynamic drag-reducing devices for tractor-trailers. Technical report, SAE, 2006.

[32] B.Khalighi, J.Johnson, and R.Lee K.Chen. Experimental characterization of the unsteady flow field behind two outside rear-view mirrors. Technical report, SAE, 2008.

[33] J.Urban. *The Aerodynamics of Heavy Vehicles: Trucks, Buses and Trains*, page 327. Springer, 2004.

[34] C.Beers. Air drag reducer for motor freight vehicles. US Patent Ser. No. US4047747 A, 1977.

[35] J.Lambie and P.Lisaaman. Air decelerator for truck cab. US Patent Ser. No. US3934923 A, 1977.

[36] Volvo Trucks. Test, evaluation and demonstration of practical devices / systems to reduce aerodynamic drag of tractor-semitrailer combination unit trucks. Technical report, TMA, 2007.

[37] R.Spivey, R.Hewitt, H.Othman, and T.Corke. Flow separation control on trailing edge radii using single dielectric barrier discharge plasma actuators, an application to vehicle drag control. In *The Aerodynamics of Heavy Vehicles II: Trucks, Buses and Trains*, pages 135–149. Springer, 2009.

[38] J.Heineck, S.Walker, and D.Satran. The measurement of wake and gap flows of the generic conventional truck model (gcm) using three-component piv. Technical report, NASA Ames Research Centre, 2006.

[39] M.Hammache and F.Browand. On the aerodynamics of tractor-trailers. In *The Aerodynamics of Heavy Vehicles: Trucks, Buses and Trains*, pages 186–205. Springer, 2002.

[40] J.Ortega, K.Salari, and B.Storms. Investigation of tractor base bleeding for heavy vehicle aerodynamic drag reduction. In *The Aerodynamics of Heavy Vehicles II: Trucks, Buses and Trains*, pages 161–178. Springer, 2005.

[41] Don-Bur. Trailer aerodynamic covering. `http://www.donbur.co.uk`, 2012.

[42] R. Pankajakshan, B. Mitchell, and D. Whitfield. Full-scale simulation of drag reduction devices for class 8 trucks. In *The Aerodynamics of Heavy Vehicles II: Trucks, Buses and Trains*, pages 339–348. Springer, 2009.

[43] K.Garry. Development of container-mounted devices for reducing the aerodynamic drag of commercial vehicles. *Journal of Wind Engineering and Industrial Aerodynamics*, 9, 1981.

[44] J.Coon and K.Visser. Drag reduction of a tractor-trailer using planar boat tail plates. In *The Aerodynamics of Heavy Vehicles: Trucks, Buses and Trains*, pages 249–265. Springer, 2002.

[45] L.Taubert and I.Wygnanski. *The Aerodynamics of Heavy Vehicles: Trucks, Buses and Trains*, pages 106–113. Springer, 2004.

[46] T.Sofu, F.Chang, R.Dupree, S.Malipeddi, S.Uppuluri, and S.Shapiro. *The Aerodynamics of Heavy Vehicles: Trucks, Buses and Trains*, pages 374–383. Springer, 2004.

[47] S.Watkins. *The Aerodynamics of Heavy Vehicles: Trucks, Buses and Trains*, pages 388–402. Springer, 2004.

[48] S.Watkins, J.Saunders, and P.Hoffmann. Comparison of road and wind-tunnel drag reductions for commercial vehicles. *Journal of Wind Engineering and Industrial Aerodynamics*, 49, 1993.

[49] A.Gaylard, N.Oettle, O.Mankowski, D.Sims-Williams, R.Dominy, and C.Freeman. Assessment of a vehicle's transient response. *SAE*, pages 1–17, 2012.

[50] S.Wordley and J.Saunders. On-road turbulence. Technical report, SAE, 2008.

[51] Wordpress. Pid control scheme. `http://www.radhesh.wordpress.com/2008/05/11/pid-controller-simplified`, 2013.

[52] R.Sehab and B.Barbedette. Fuzzy pid supervision for an automotive application: Design and implementation. Technical report, Ecole Suprieure des Techniques Aronautiques et de Construction Automobile, 2012.

[53] K.Astrom and B.Wittenmark. *Adaptive Control, 2^{nd} Edition*, pages 8–25. Addison-Wesley, 1995.

[54] M.Krstic, I.Kanelllakopoulous, and P.Kokotovic. *Nonlinear and Adaptive Control Design*, pages 25–36. Wiley, 1995.

[55] P.Blackman. *Extremum-Seeking Regulators*, pages 45–56. Macmillan Company, 1962.

[56] M.Leblanc. Sur l'électrification des chemins de fer au moyen de courants alternaitifs de fréquence elevee. *Revue Generale de l'Electricite*, 1922.

[57] K.Ariyur and M.Krstic. *Real-Time Optimization by Extremum-Seeking Control*, pages 3–20. Wiley, 2003.

[58] R.Muminovic, L.Henning, and R.King. Robust and model predictive drag control for a generic car model. In *AIAA 2008-3859 4th Flow Conference*, pages 100–138. AIAA, 2004.

[59] M.Pastoor, L.Henning, B.Noak, R.King, and G.Tadmor. Feedback shear layer control for bluff body drag reduction. *Journal of Fluid Mechanics*, 608, 2008.

[60] J.Beaudoin, O.Cadot, J.Aider, and J.Wesfreid. Bluff-body drag reduction by extremum-seeking control. *Journal of Fluids and Structures*, 2006.

[61] J.Barlow, W.Rae, and A.Pope. *Low-Speed Wind Tunnel Testing*, pages 1–17. Wiley-Interscience, third edition, 1999.

[62] SAE. Sae wind-tunnel test procedures for trucks and buses. Technical report, SAE, 1979.

[63] JR3. Jr3 load cell documentation. `http://www.jr3.com`, 2012.

[64] K.Cooper. A wind tunnel investigation into the fuel savings available from the aerodynamic drag reduction of trucks. Technical report, DME/NAE, 1976.

[65] SAE. Aerodynamic testing of road vehicles–testing methods and procedures. Technical report, SAE, 1993.

[66] University of Cambridge. 5 hole pressure probe. http://www-g.eng.cam.ac.uk/whittle/current-research/hph/pressure-probes/pressure-probes.html, 2013.

[67] T.Yasa and G.Paniagua. Robust procedure for multi-hole probe data processing. *Flow Measurement and Instrumentation*, 2012.

[68] Race Technology. Dl1 mk2 data logger. http://www.race-technology.com/dl1_2_27.html, 2012.

[69] InSpeed. Inspeed vortex wind sensor. http://www.inspeed.com/anemometers/Vortex_Wind_Sensor.asp, 2012.

[70] InSpeed. Inspeed vortex wind sensor. http://www.inspeed.com/anemometers/Vortex_Wind_Sensor.asp, 2012.

[71] Omega Engineering. Px138-0.3d5v. http://www.omega.com/pptst/PX138.html, 2014.

[72] United Sensor Corp. Kiel probe. http://www.unitedsensorcorp.com/kiel.html, 2014.

[73] S.Watkins, J.W.Saunders, and P.Hoffmann. Turbulence experienced by moving vehicles. part i. introduction and turbulence intensity. *Journal of Wind Engineering and Industrial Aerodynamics*, 57:1–17, 1995.

[74] R.Flay. *Structure of a Rural Atmospheric Boundary Layer Near the Ground*, pages 17–44. University of Canterbury, New Zealand, 1978. Ph.D. Thesis.

[75] ANSYS. User documentation. http://www.ansys.com/Products/Simulation+Technology/Fluid+Dynamics/, 2012.

[76] D.Pointer, T.Sofu, J.Chang, and D.Weber. *Applicability of Commercial CFD Tools for Assessment of Heavy Vehicle Aerodynamic Characteristics*, pages 349–361. The Aerodynamics of Heavy Vehicles: Trucks, Buses and Trains. Springer, 2004.

[77] VOSA. Speed limiter legislation. http://www.dft.gov.uk/vosa/, 2006.

[78] H.Naunheimer, B.Bertsche, J.Ryborz, and W.Novak. *Automotive Transmission: Fundamentals,Selection,Design and Application*, page 97. Springer, 2011.

[79] F.Pfeiffer. *Mechanical System Dynamics*, page 317. Springer, first edition, 2005.

[80] HIWIN. Hiwin las3 actuators. `http://www.hiwin.com`, 2014.

[81] Pi Innovo. M100 open ecu. `http://www.pi-innovo.com`, 2014.

[82] Devantech. Devantech md03 h bridge motor drive. `http://www.devantech.co.uk`, 2014.

[83] SHARP Electronics. Devantech md03 h bridge motor drive. `http://www.sharpsme.com`, 2014.

[84] K.Koenig and A.Roshko. An experimental study of geometrical effects on the drag and flow field of two bluff bodies separated by a gap. *Journal of Fluid Mechanics*, 156:167–204, 1985.

[85] K.Garry. A summary of the scale model wind tunnel measurements and full scale surface pressure tests on the leyland t45 and daf 3300 vehicles used for the trrl spray dispersion programme. Technical report, Cranfield University, 1987.

[86] A.Pisasale and N.Ahmed. A novel method for extending the calibration range of five-hole probe for highly three-dimensional flows. *Journal of Flow Measurement and Instrumentation*, 2002.

[87] A.Gilhaus, E.Hau, R.Kunstner, and J.Potthoff. Über den luftwiderstand von fernlastzügen ergebnisse aus modellmessungen im windkanal. Technical report, Automobil-Industrie, 1980.

[88] ETSU. Annual mean wind speed. `http://www.esru.strath.ac.uk/EandE/Web_sites/03-04/wind/content/ukwindspeedmap.html`, 2012.

[89] S.Zekai, A.Altunkaynak, and T.Erdik. Wind velocity vertical extrapolation by extended power law. *Advances in Meteorology*, 2012.

[90] M.Patel. Wind and solar power systems. *CRC Press*, 1999.

[91] Met Office. Historic weather data. `http://www.metoffice.gov.uk`, 2014.

[92] J.Howell. The decay of bluff body wakes. *SAE*, 4(1), 2011.

[93] V. Barzanooni and A. Khoshnevis. *Continuum Mechanics, Fluids, Heat*, pages 196–200. WSEAS Press, first edition, 2010.

[94] L.Swain. On the turbulent wake behind a body of revolution. *Proc. R. Soc*, 125(799):647–659, 1929.

[95] H.Schlichting. Boundary layer theory; part 2. Technical report, NACA TM, 1949.

[96] P.Johansson and W.George. The far downstream evolution of the high reynolds number axisymmetric wake behind a disk. part 1. single point statistics. *Journal of Fluid Mechanics*, 555:363–385, 2006.

[97] H.Liu, J.Wei, and Z.Qu. The interaction of porous material coating with the near wake of bluff body. *Journal of Fluids Engineering*, 136(2), 2013.

[98] J.Gerrard. The mechanics of the formation region of vortices behind bluff bodies. *Journal of Fluid Mechanics*, 25(2):401–413, 1966.

[99] U.Oteh. *Mechanics of Fluids*, page 413. AuthorHouse, 2009.

[100] Aerial F1. Millbrook aerial photo. `http://images.aerialf1.com/europe/uk`, 2014.

[101] A.Grigor. Performance evaluation of the ActiveFREDDIE system. Unpublished, 2012.

[102] UCCP. Ideal fluid flow through a pipe. `http://www.ucopenaccess.org`, 2012.

[103] SAE. Closed-test-section wind tunnel blockage corrections for road vehicles. Technical report, SAE, 1996.

[104] J.Barlow, W.Rae, and A.Pope. *Low-Speed Wind Tunnel Testing*, volume Third, pages 353–355. Wiley-Interscience, 1999.

[105] T.Dudzinski and L.Krause. Flow direction measurement with fixed probes. Technical report, NASA, 1969.

[106] Schaeffler Engineering. Datronic 3 - data acquisition system. `http://www.schaeffler-engineering.com`, 2014.

[107] J.Boussinesq. Essai sur la théorie des eaux courantes. In *Mémoires présentés par divers savants à l'Académie des Sciences*, pages 1–680, 1877.

[108] P.Spalart and S.Allmaras. A one-equation turbulence model for aerodynamic flows. *AIAA*, 1992.

[109] B.Launder and D.Spalding. The numerical computation of turbulent flows. *Computer Methods in Applied Mechanics and Engineering*, 3:269–289, 1974.

[110] PE micro. Usb-ml-12 multilink debugger. `http://www.pemicro.com/products`, 2014.

[111] K.Ingram. Wind tunnel tests on scale models of heavy goods vehicles. Technical report, TRRL, 1977.

[112] Physical Geography. Wind compass notation. http://www.physicalgeography.net, 2014.

This page intentionally left blank.

Appendix A

Control Theory

A.1 Extremum Seeking Algorithm

The extremum seeking algorithm applied to a model plant is shown in Fig.(A.1), with the mathematics for a static map shown in Eqs.(A.1 - A.12).

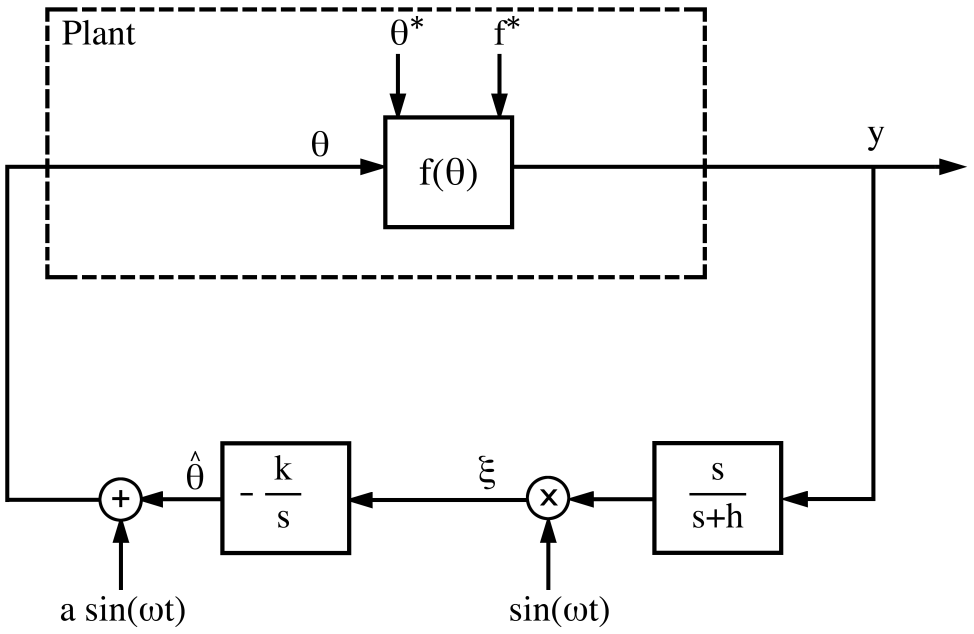

Figure A.1: Extremum Seeking Control Scheme [57].

Extremum Seeking for a Static Map

Expansion using the Taylor Series of a function, $f(\theta)$ about a point θ, towards a minimum at $\theta = \theta^*$ is defined as

$$f(\theta) = f(\theta^*) + f'(\theta^*)(\theta - \theta^*) + \frac{1}{2}f''(\theta^*)(\theta - \theta^*)^2 + O((\theta - \theta^*)^3) \tag{A.1}$$

if θ^* is a minimum, $f'(\theta) = 0$ and neglecting terms higher than second order, the function can be approximated by

$$f(\theta) = f(\theta^*) + \frac{1}{2}f''(\theta^*)(\theta - \theta^*)^2 \tag{A.2}$$

noting that the function evaluated at the minimum, $f(\theta^*)$ provides the minimum of the function, f^* and absorbing $f''(\theta^*)/2$ into the integrator gain (k), the function can therefore be approximated by

$$f(\theta) = f^* + (\theta - \theta^*)^2 \tag{A.3}$$

where f^* and θ^* can be viewed as disturbances inputs.

Washout Filter

The washout or high pass filter ($\frac{s}{s+h}$) when applied to the plant output (y) serves to remove f^*

$$\frac{s}{s+h}[y] = \frac{1}{2}f''(\theta^*)(\theta - \theta^*)^2 \tag{A.4}$$

the estimation error of the unknown optimal input (θ^*) is defined [54] by

$$\tilde{\theta} = \theta^* - \hat{\theta} \tag{A.5}$$

giving

$$\theta - \theta^* = a\sin(\omega t) - \tilde{\theta} \tag{A.6}$$

substituting into Eq.(A.4) gives

$$\frac{s}{s+h}[y] = \frac{1}{2}f''(\theta^*)(\tilde{\theta} - a\sin\omega t)^2 \tag{A.7}$$

expanding Eq.(A.7) and using the trigonometric identity: $2\sin^2\omega t = 1 - \cos(2\omega t)$ gives

$$\frac{s}{s+h}[y] \approx \frac{f''}{2}\tilde{\theta}^2 - af''\tilde{\theta}\sin(\omega t) + \frac{a^2 f''}{4}\cos(2\omega t) \tag{A.8}$$

Demodulation

Demodulation is achieved through multiplication of the output filter by $\sin(\omega t)$, giving

$$\varepsilon \approx \frac{f''}{2}\tilde{\theta}^2 \sin(\omega t) - af''\tilde{\theta}\sin^2(\omega t) + \frac{a^2 f''}{4}\cos(2\omega t)\sin(\omega t) \tag{A.9}$$

applying the identities: $2\sin^2 \omega t = 1 - \cos(2\omega t)$ and $2\cos(2\omega t)\sin(\omega t) = \sin(3\omega t) - \sin(\omega t)$ gives

$$\varepsilon \approx -\frac{af''}{2}\tilde{\theta} + \frac{af''}{2}\tilde{\theta}\cos(2\omega t) + \frac{a^2 f''}{8}(\sin(\omega t) - \sin(3\omega t)) + \frac{f''}{2}\tilde{\theta^2}\sin(\omega t) \tag{A.10}$$

Gain Compensator

Applying Gain Compensation to the demodulated signal and noting $(\dot{\tilde{\theta}} = -\dot{\hat{\theta}})$

$$\tilde{\theta} \approx \frac{k}{s}\left[-\frac{af''}{2}\tilde{\theta} + \frac{af''}{2}\tilde{\theta}\cos(2\omega t) + \frac{a^2 f''}{8}(\sin(\omega t) - \sin(3\omega t)) + \frac{f''}{2}\tilde{\theta^2}\sin(\omega t)\right] \tag{A.11}$$

from Eq.(A.11) we can neglect the last term due to being quadratic in $\tilde{\theta}$ and the second and third terms are high frequency signals, the integrator will greatly attenuate them and can also be ignored, therefore

$$\dot{\tilde{\theta}} = \frac{-kaf''}{2}\tilde{\theta} \tag{A.12}$$

since $kf'' > 0$, $\tilde{\theta} \to 0$ or $\hat{\theta}(t)$ converges to θ^*.

This page intentionally left blank.

Appendix B

Experimental Details

The equations used for low speed experimental calculations are shown in Eqs.(B.1 - B.24) in Secs.(B.1.1 - B.1.6). The experimental wind tunnel details and arrangement are shown in Sec.(B.2). The application of the equations derived in Secs.(B.1.1 - B.1.6) to the wind tunnel data is shown in Secs.(B.3 - B.6.2).

Calibration of the five hole pressure probe used in the wind tunnel test is shown in Sec.(B.7).

The specification sheets for the vehicle used for on-road testing is shown in Sec.(B.8) with the equipment used for the on-road testing shown in Sec.(B.9). The data analysis code used to automate the data processing is shown in Sec.(B.10), with the error analysis on the measured parameters shown in Sec.(B.11).

B.1 Experimental Equations

B.1.1 Conservation of Mass

$$\frac{\partial p}{\partial t} + \nabla \cdot (\rho V) = 0 \tag{B.1}$$

B.1.2 Newton's Second Law

$$\rho \left(\frac{DV}{Dt} \right) = \rho F_B + F_S \tag{B.2}$$

B.1.3 Energy Equation

$$\rho\frac{\partial}{\partial t}\left(C_vT+\frac{V^2}{2}\right)+\rho V\cdot\nabla\left(C_vT+\frac{V^2}{2}\right)=\rho g\cdot V-\nabla\cdot pV+ \\ \nabla\cdot\left[2\mu\nabla\left(\frac{V^2}{2}\right)+\mu(\nabla\times V)\times V-\frac{2}{3}\mu(\nabla\cdot V)V\right]+\nabla\cdot k\nabla T \tag{B.3}$$

B.1.4 Bernoulli's Equation

Bernoulli's Equation for incompressible flow is given by

$$\frac{v^2}{2}+gz+\frac{p}{\rho}=constant \tag{B.4}$$

with Bernoulli's Equation for equipotential flow given by

$$P_1+\frac{1}{2}\rho v_1^2=P_2+\frac{1}{2}\rho v_2^2 \tag{B.5}$$

B.1.5 Continuity Equation

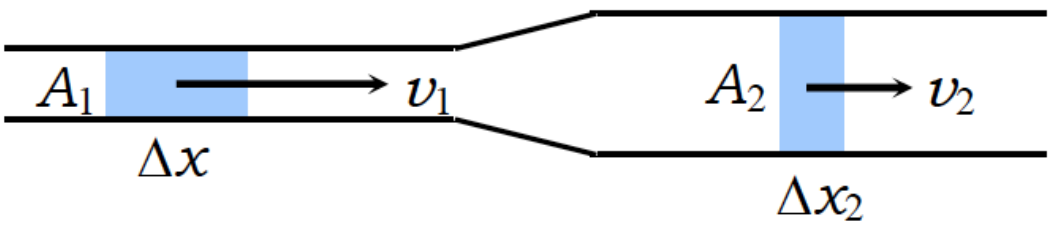

Figure B.1: Ideal Fluid Flow Through a Pipe [102].

For an ideal fluid the Continuity Equation for mass flow is defined as

$$\dot{m_{in}}=\dot{m_{out}} \tag{B.6}$$

where

$$\dot{m}=\rho v\cdot A \tag{B.7}$$

giving the alternate version

$$\rho_1 v_1 A_1 = \rho_2 v_2 A_2 \tag{B.8}$$

where $\rho_1 = \rho_2$ for incompressible flow, rearranging gives

$$v_2 = \frac{A_1}{A_2} v_1 \tag{B.9}$$

rearranging Eq. B.5 gives

$$P_2 - P_1 = \frac{1}{2}\rho \left(v_2^2 - v_1^2\right) \tag{B.10}$$

and substituting Eq. B.9 into Eq. B.10 gives

$$P_2 - P_1 = \frac{1}{2}\rho v_1^2 \left(\frac{A_2^2}{A_1^2} - 1\right) \tag{B.11}$$

where the pressure difference $(\Delta P) = P_2 - P_1$, $q = \frac{1}{2}\rho_\infty v^2$ and $k = \left(\frac{A_2^2}{A_1^2} - 1\right)$, giving the final relationship between ΔP and q to be

$$\Delta P \propto q \tag{B.12}$$

B.1.6 Navier-Stokes Equations

The Navier-Stokes equations are the governing equations of fluid motion. They arise by assuming the fluid is a continuum and the application of Newton's Second Law (Eq.(B.2)) of fluid motion.

The Continuity Equation can be rewritten in three dimensions as:

$$\left[\frac{\partial u}{\partial x} + \frac{\partial v}{\partial y} + \frac{\partial w}{\partial z}\right] = 0 \tag{B.13}$$

where u, v, w are the velocities in the x, y and z direction respectively. The viscosity of the fluid requires the tangential and normal stress are shown in Eqs.(B.14 - B.19).

Tangential Stress:

$$\tau_{xy} = \tau_{yx} = \mu \left[\frac{\partial v}{\partial x} + \frac{\partial u}{\partial y}\right] \tag{B.14}$$

$$\tau_{yz} = \tau_{zy} = \mu \left[\frac{\partial w}{\partial y} + \frac{\partial v}{\partial z}\right] \tag{B.15}$$

$$\tau_{xz} = \tau_{zy} = \mu \left[\frac{\partial u}{\partial z} + \frac{\partial w}{\partial x}\right] \tag{B.16}$$

Normal Stress:

$$\tau_{xx} = 2\mu\frac{\partial u}{\partial x} \tag{B.17}$$

$$\tau_{yy} = 2\mu\frac{\partial v}{\partial y} \tag{B.18}$$

$$\tau_{zz} = 2\mu\frac{\partial w}{\partial z} \tag{B.19}$$

where μ is the viscosity coefficient. The time dependent change of momentum equations for the fluid are defined by

X - Momentum:

$$\rho\frac{\partial u}{\partial t} = \rho g_x - \frac{\partial p}{\partial x} + \mu\left[\frac{\partial^2 u}{\partial x^2} + \frac{\partial^2 u}{\partial y^2} + \frac{\partial^2 u}{\partial z^2}\right] \tag{B.20}$$

Y - Momentum:

$$\rho\frac{\partial v}{\partial t} = \rho g_y - \frac{\partial p}{\partial x} + \mu\left[\frac{\partial^2 v}{\partial x^2} + \frac{\partial^2 v}{\partial y^2} + \frac{\partial^2 v}{\partial z^2}\right] \tag{B.21}$$

Z - Momentum:

$$\rho\frac{\partial w}{\partial t} = \rho g_y - \frac{\partial p}{\partial x} + \mu\left[\frac{\partial^2 w}{\partial x^2} + \frac{\partial^2 w}{\partial y^2} + \frac{\partial^2 w}{\partial z^2}\right] \tag{B.22}$$

where μ is the dynamic viscosity, ρ is the density and g_x, g_y, g_z are the gravitational forces in the x, y, z direction, respectively.

The Navier-Stokes equations for incompressible fluids, written in tensor notation can be expressed as

$$\frac{\partial u_i}{\partial x_i} = 0 \tag{B.23}$$

$$\frac{\partial u_i}{\partial t} + u_j\frac{\partial u_i}{\partial x_j} = f_i - \frac{1}{\rho}\frac{\partial p}{\partial x_i} + v\frac{\partial^2 u_i}{\partial x_j \partial x_j} \tag{B.24}$$

B.2 Cranfield Wind Tunnel Details

8' x 6' AIRCRAFT AERODYNAMICS WIND TUNNEL

Wind Tunnel Layout
Closed working section, closed return.

Working Section Dimensions (metres)
height 1.82
width 2.43
length 5.18
mean height/width of corner fillets 0.3

Speed Range (metres/sec)
55 max - 3 min (depending on model geometry)

Flow Velocity Uniformity
+/- 0.7% over 93% of horizontal centre line.
+/- 1.1% over 91% of vertical centre line.

Longitudinal Turbulence Intensity
0.09% on working section centre line at 40 m/s

Flow Angularity
max - 0.25 deg. yaw
max - 0.75 deg. pitch
on working section centre line in the range 5 - 60 m/s.

Static Pressure Gradient
Negligible along the effective operational length of the working section.

Balance Layout
Electro-mechanical 6 component balance mounted above a 360 degree turntable, measuring wind axis forces and moments. Data returned on line to a microcomputer system for analysis. Additional 5 and 6 component sting balances available.

for further details contact:

Professor Kevin P. Garry
Aerodynamics, Cranfield University, Cranfield Bedford MK43 OAL UK
Tel. +44(0)1234 750111 Ext. 5135/8211.
k.p.garry@cranfield.ac.uk

Figure B.2: Cranfield 8′ x 6′ Low Speed Wind Tunnel Specification Sheet.

B.2.1 Cranfield Wind Tunnel Arrangement

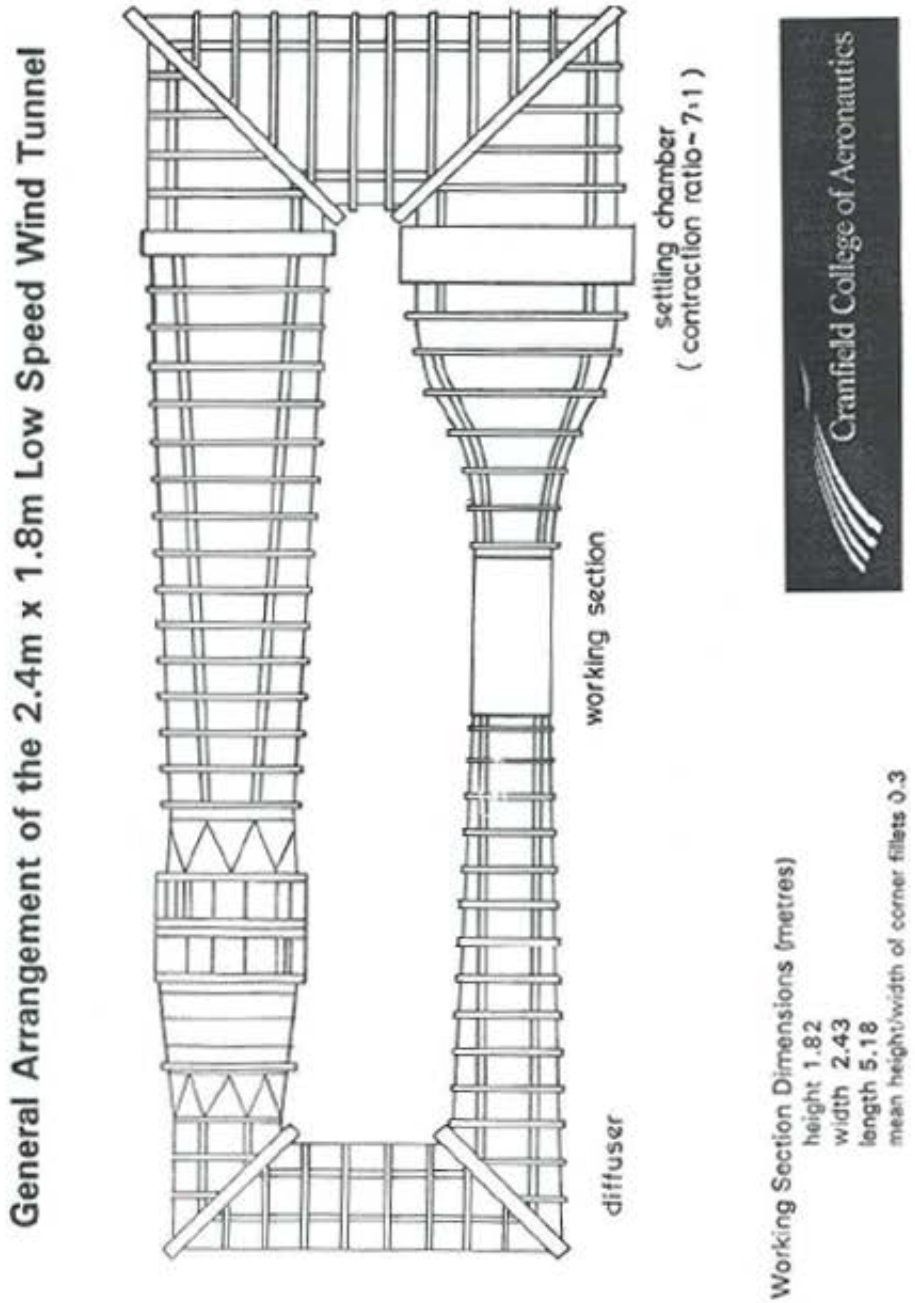

Figure B.3: Cranfield 8′ x 6′ Low Speed Wind Tunnel.

B.2.2 Cranfield Wind Tunnel Yaw Notation

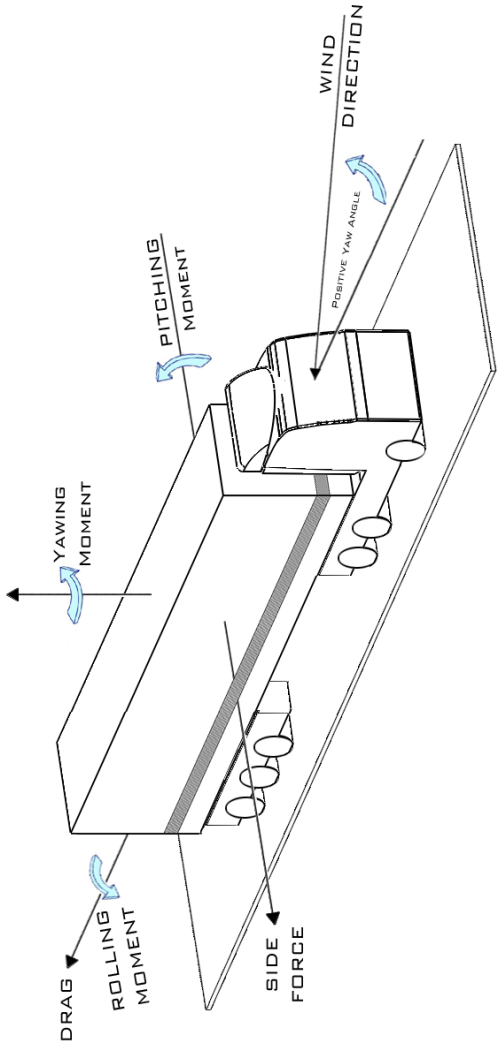

Figure B.4: Cranfield 8′ x 6′ Force and Moment Orientation.

B.3 Force Measurement

The drag force on an object is given by

$$F_D = \frac{1}{2}\rho_\infty V_\infty^2 C_D A \tag{B.25}$$

the force (F_D) is measured directly by the force torque sensors. A dimensionless force can be defined by dividing the measured force by the dynamic pressure (q) and reference area (A). Similarly, dimensionless force and moment coefficients can be defined by dividing by q, A and the characteristic length (l). The reference area (A) is defined as (trailer width x trailer height) when (deflector height $<$ trailer height). For (deflector height $>$ trailer height), A is defined as (trailer width x deflector height). All the heights were measured with respect to vertical distance above the ground board.

The characteristic length is the model's track width of 312 mm for the rolling moment and the model's wheelbase value of 1827 mm for the yaw and pitching moment.

$$\text{Force Coefficient} = \frac{\text{Force}}{qA} \tag{B.26}$$

$$\text{Moment Coefficient} = \frac{\text{Moment}}{qAl} \tag{B.27}$$

B.4 Pressure Measurements

Determining the speed of a wind tunnel with a model present cannot be achieved using a pitot-static tube. Placement of a pitot-static tube or other measuring device into the test section to measure the dynamic pressure would cause "induced flow". Induced flow is the difference in flow velocity obtained with respect to an empty working section. As a result of the inability to use a pitot-static tube with a model present in the working section, a calibration run must be performed prior to testing with a model. The calibration run uses a calibrated pitot-static tube to determine the freestream dynamic pressure (p_∞). Two static tappings, one located ahead of the settling chamber (P_1) and one located downstream of the contraction (P_2) are used to measure the pressure differential (ΔP).

The pressure differential between P_2 and P_1 can be related to the freestream dynamic pressure (q_∞) as follows

$$\Delta P \propto q \tag{B.28}$$

where $\Delta P = (P_2 - P_1)$ and the value of k is a constant of proportionality relating to the wind tunnel layout and design, giving

$$k = \frac{q_\infty}{\Delta P} \tag{B.29}$$

By conducting several runs at various tunnel velocities, the value of k can be calculated. The pressure differential (ΔP) measured between P_2 and P_1 can therefore be used to determine the freestream dynamic pressure (q_∞) without use of a probe within the wind tunnel.

The pressure difference (ΔP) is measured using a Furness FC016 differential pressure transducer.

The standard definition of dynamic pressure is

$$q_\infty = \frac{1}{2}\rho_\infty V_\infty^2 \tag{B.30}$$

where the gas is assumed to be ideal and therefore obey the ideal gas law. Therefore ρ_∞ can be calculated by

$$\rho_\infty = \frac{P}{RT} \tag{B.31}$$

The temperature of the freestream air is measured in the settling chamber and the pressure by a Druck DPI 261 barometer in a thermally isolated chamber located above the working section. The velocity of the freestream fluid (V_∞) can therefore be calculated by

$$V_\infty = \sqrt{\frac{2q_\infty}{\rho_\infty}} \tag{B.32}$$

This enables real-time monitoring of the wind speed within the wind tunnel. Tappings located on the model were measured by a Furness FC018 differential pressure transducers referenced to the upstream static pressure. The pressure coefficient (C_P) can therefore be calculated by

$$C_P = \frac{p - p_\infty}{\frac{1}{2}\rho_\infty V_\infty^2} \tag{B.33}$$

B.5 Data Acquisition

National Instruments LabVIEW® was used in order to automate the data acquisition and wind tunnel program. Five thousand data points were sampled and averaged for each yaw angle tested.

Initial corrections to the measured freestream dynamic pressure (q_∞) are made in accordance with the method outlined in SAE article: "Closed-Test-Section Wind Tunnel Blockage Corrections for Road Vehicles" [103].

$$q_{corrected} = q_\infty \left[1 + 0.5 \left(\frac{\text{Vehicle Frontal Area}}{\text{Working Section Area}} \right)^2 \right] \tag{B.34}$$

The model is measured to determine the Vehicle Front Area and the Working Section Area for the Cranfield 8′ x 6′ Low Speed Wind Tunnel is 4.42 m^2 [B.3]. A correction to the measured dynamic pressure is required as there is a reduction in the effective working area. In accordance with the Continuity Equation, Eq.(B.9), a reduction in the working area will result in an increase in flow velocity over the model. The blockage effect is simply a function of the dimensions of the model [104]

The Reynolds number can be calculated from the standard definition

$$Re = \frac{\rho V_\infty l}{\mu} \tag{B.35}$$

where the characteristic length for a HGV is the model's wheelbase of 1,827 mm [62]. The dynamic viscosity as a function of temperature, μ, is determined using Sutherland's law for an ideal gas by

$$\mu = \mu_0 \frac{T_0 + C}{T + C} \left(\frac{T}{T_0} \right)^{\frac{3}{2}} \tag{B.36}$$

where μ_0 and T_0 are the reference viscosity and temperature respectively, measured in a thermally isolated chamber and T is measured in the settling chamber.

A correction to the reference pressure is then required. The pressure data recorded is the change in pressure between the pressure at the tappings (p_3) and the upstream static pressure ring (p_2). The static pressure ring is not equal to the freestream pressure (p_∞) in the test section.

The adjustment to the coefficient is therefore given by

$$C_P = C_{P(uncorrected)} - \frac{p_\infty - p_2}{q_\infty} \tag{B.37}$$

where

$$C_{P(uncorrected)} = \frac{p_3 - p_2}{q_\infty} \tag{B.38}$$

for the Cranfield 8′×6′ Low Speed Wind Tunnel the correction value was found to be -0.05, giving

$$C_P = \frac{p_3 - p_2}{q_\infty} + 0.05 \tag{B.39}$$

B.6 Error Analysis

Experimental measurements due to finite resolution are subject to measurement errors. The following errors were present within the experimental apparatus, shown in Tab.(B.1).

Item	Error
R3 Component Balance	±0.0125(%)
Furness FC016 PressureTransducer	±1.0(%)
Furness FC018 PressureTransducer	±0.5(%)
Druck DPI 261 Barometer	±0.04(%)
RS Thermometer	±0.1(%)
Yaw Angle Measurement	±0.25(°)
Model Dimension Measurements	±0.5(mm)

Table B.1: Experimental Errors on Test Equipment.

B.6.1 Error Propagation

For a measured quantity 'R′, the uncertainty in the measurement (δR) is defined for some common functions by Eqs.(B.49 - B.53).

B.6.2 Application to Measured Data

Using the data in Table B.1 along with the propagation formulas defined in Eqs.(B.49 - B.53), gives the following values:

- Constant of Proportionality (k):

$$\frac{\delta k}{k} = \sqrt{(\delta p_1)^2 + (\delta p_2)^2} = \sqrt{(0.5)^2 + (-0.5)^2} = 0.7\% \tag{B.40}$$

- Dynamic Pressure (q_∞):

$$\frac{\delta q_\infty}{q_\infty} = \sqrt{(k)^2 + (\delta p_2)^2} = \sqrt{(0.007)^2 + (1.0)^2} = 1.0\% \tag{B.41}$$

- Drag Force (F_D):

$$\frac{\delta F_D}{F_D} = \left(\frac{2.06}{165.4}\right) = 0.0125\% \tag{B.42}$$

- Drag Coefficient (C_D):

$$\frac{\delta C_D}{C_D} = \sqrt{\left(\frac{\delta D}{D}\right)^2 + \left(\frac{\delta q_\infty}{q_\infty}\right)^2 + \left(\frac{\delta h}{h}\right)^2 + \left(\frac{\delta w}{w}\right)^2}$$

$$\frac{\delta C_D}{C_D} = \sqrt{\left(\frac{2.06}{165.4}\right)^2 + \left(\frac{1.0}{960.5}\right)^2 + \left(\frac{0.5}{569}\right)^2 + \left(\frac{0.5}{312}\right)^2} = 1.26\% \tag{B.43}$$

- Pressure Coefficient (C_P):

$$\frac{\delta C_P}{C_P} = \sqrt{\left(\frac{\delta p}{p}\right)^2 + \left(\frac{\delta p_\infty}{p_\infty}\right)^2 + \left(\frac{\delta \rho_\infty}{\rho_\infty}\right)^2 + \left(\frac{\delta V_\infty}{V}\right)^2}$$

From Equation 3.4, $V_\infty = \sqrt{\frac{2q_\infty}{\rho_\infty}}$, therefore:

$$\frac{\delta C_P}{C_P} = \sqrt{\left(\frac{\delta p}{p}\right)^2 + 2 \cdot \left(\left(\frac{\delta p_\infty}{p_\infty}\right)^2 + \left(\frac{\delta \rho_\infty}{\rho_\infty}\right)^2\right)} = \sqrt{\left(\frac{3.0}{601.7}\right)^2 + 2 \cdot \left(\left(\frac{1.0}{960.5}\right)^2 + \left(\frac{0.01}{1.225}\right)^2\right)}$$

$$\frac{\delta C_P}{C_P} = 1.3\% \tag{B.44}$$

B.7 Five Hole Probe Calibration

Due to the requirement of mounting sensors to the test vehicle for full scale testing, measurements of the local velocity and flow angle at the sensor location were made. Evaluation of the mounting locations was required to ensure the sensor position was suitable for the measurement and any correction factors for calibration were applied prior to testing.

Many methods exist for flow field measurements such as Particle Imaging Velocimetry (PIV), however, such methods require intensive post-processing. The method that enables fast measurement of varying locations is the use of a calibrated five-hole pressure probe. The five-hole pressure probe used in the experimental testing is shown in Fig.(B.5).

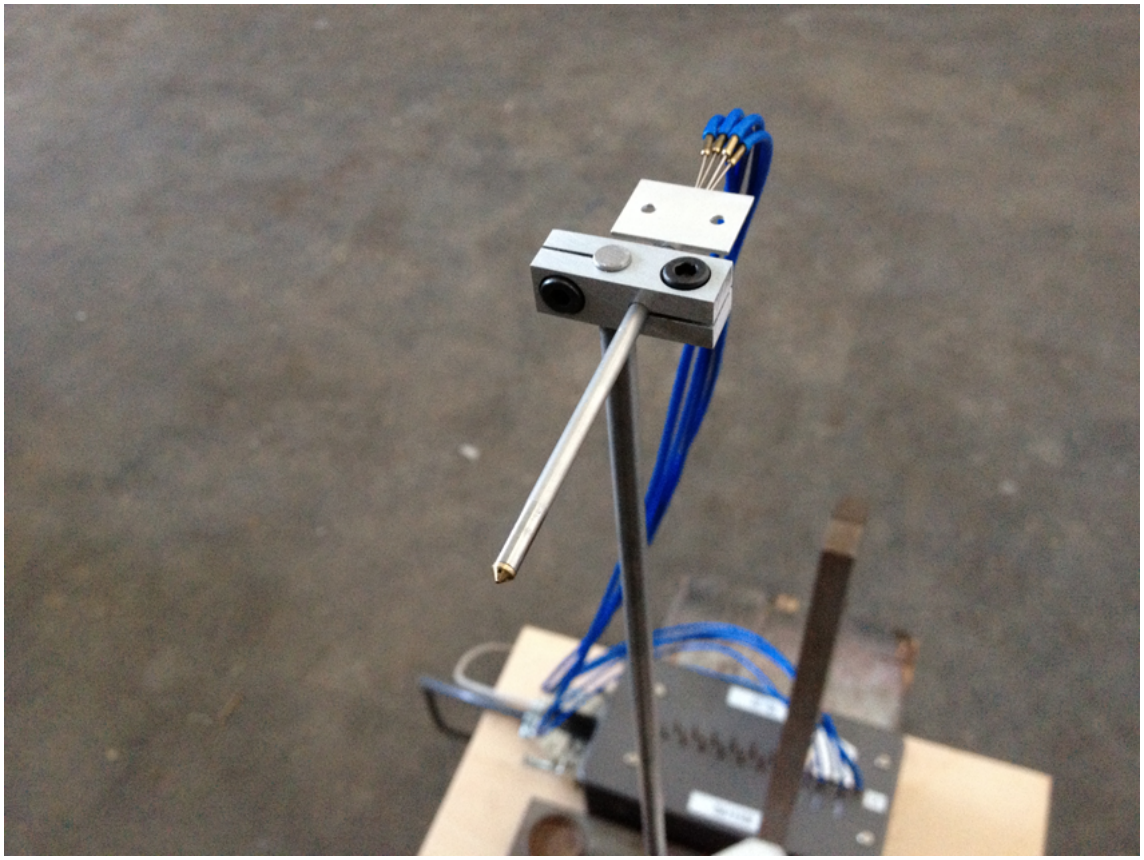

Figure B.5: Cranfield Five Hole Pressure Probe.

The role of five-hole pneumatic pressure probe is to carry out steady-state measurements of the three components of velocity, static and total pressure simultane-

ously at any test point within the sample fluid. Prior to using the probe for flow measurements, the probe must be calibrated.

The notation used to non-dimensionalise the pressure coefficients is the technique outline by Dudzindki et al. [105]. The nomenclature used in the equations is shown in Fig.(B.6).

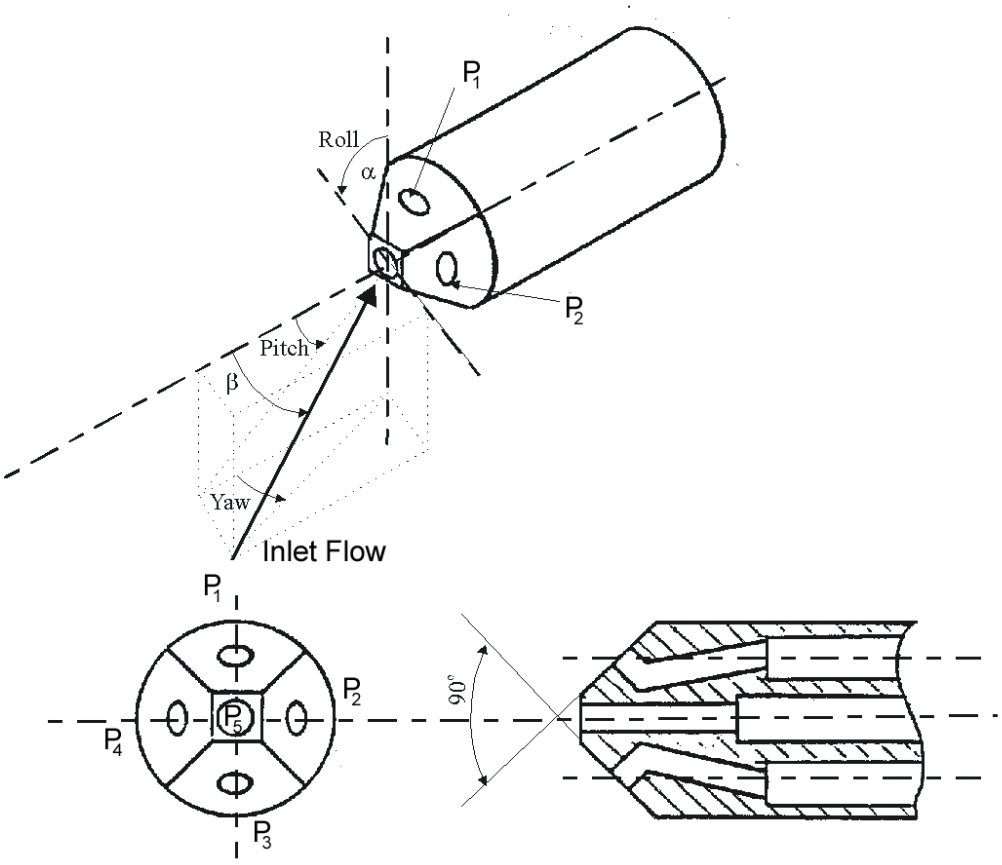

Figure B.6: Five Hole Pressure Probe [66].

$$C_{P\alpha} = \frac{P_1 - P_3}{P_5 - \overline{P}} \tag{B.45}$$

$$C_{P\beta} = \frac{P_2 - P_4}{P_5 - \overline{P}} \tag{B.46}$$

$$C_{PTotal} = \frac{P_5 - P_{Total}}{P_5 - \overline{P}} \tag{B.47}$$

$$C_{PStatic} = \frac{\overline{P} - P_{Static}}{P_5 - \overline{P}} \tag{B.48}$$

where $\overline{P} = \frac{(P_1+P_2+P_3+P_4)}{4}$

The probe was placed into a quadrant rig, with a pitch adjustment range of (-40° $\leq \alpha \leq$ +40°) and yaw range of (-40° $\leq \beta \leq$ +40°). The probe was then placed in an open working section blower tunnel shown in Fig.(B.7). Three wind tunnel velocities of: 20, 25 and 30 ms^{-1} were used to determine if any Reynolds number effects were present with the sensor. The sensor was rotated through a yaw angle range of: (β = -40°, -35°, -30°, -25°, -20°, -15°, -10°, -8°, -6°,- 4°, -2°, 0°, +2°, +4°, +6°, +8°, +10°, +15°, +20°, +25°, +30°, +35°, +40°) and over the same pitch (α) angle range. The resulting 23×23 calibration array was produced for the sensor (see Tab.(B.2 - B.5) for summarised data and Figs.(B.8 - B.11) for the full calibration plots).

Figure B.7: Five Hole Pressure Probe Calibration Experiment.

B.7.1 $C_{P(\alpha)}$ Calibration

B.7.1.1 $C_{P(\alpha)}$ Calibration Map

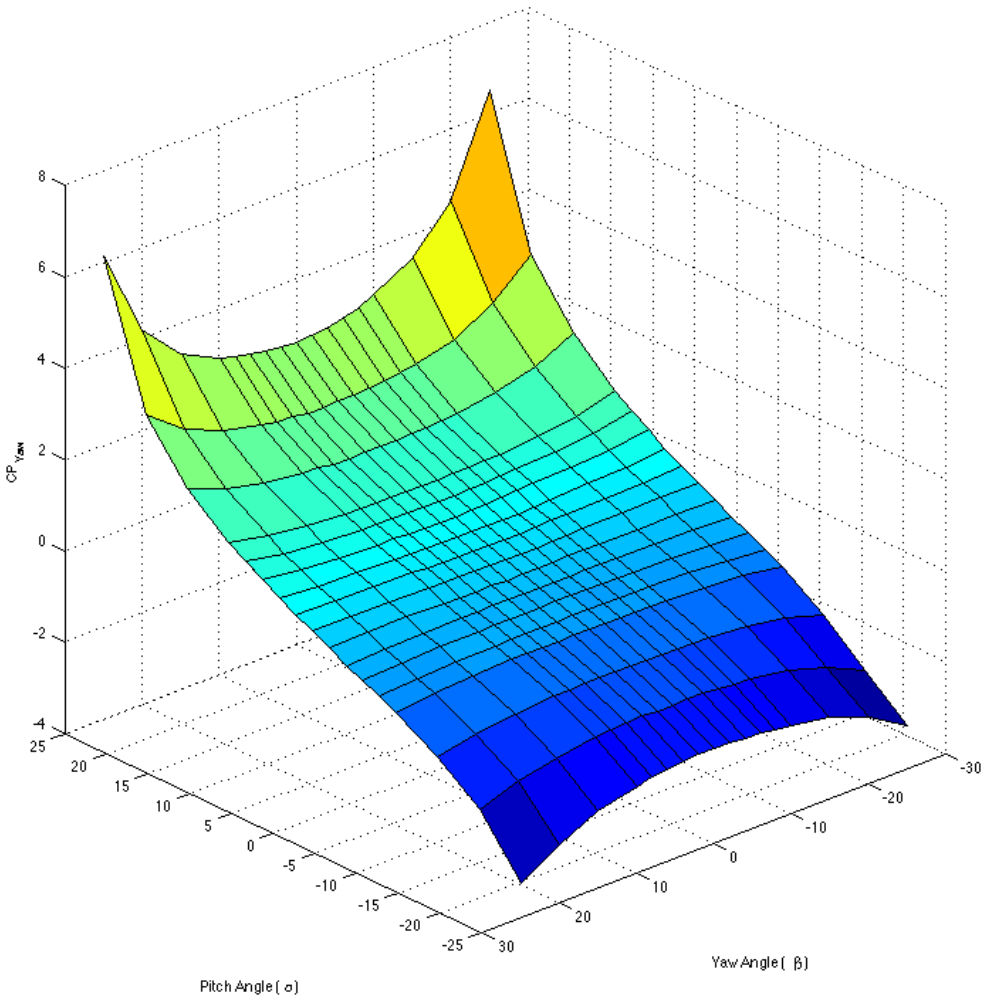

Figure B.8: $C_{P(Yaw)}$ Configuration Map for Yaw and Pitch Angle.

B.7.1.2 $C_{P(\alpha)}$ Calibration Table

	Pitch Angle (α)								
(β)	-25	-10	-8	-2	0	2	8	10	25
-25	3.669	2.319	2.273	2.217	3.062	2.308	2.546	2.701	6.610
-10	1.072	0.634	1.019	0.643	0.801	0.636	0.640	0.679	1.192
-8	0.849	0.634	0.606	0.475	0.620	0.482	0.482	0.499	0.879
-2	0.251	0.176	0.185	0.048	0.222	0.055	0.032	0.048	0.124
0	-0.062	-0.089	-0.099	-0.100	-0.095	-0.092	-0.119	-0.093	-0.111
2	-0.126	-0.240	-0.219	-0.225	-0.250	-0.201	-0.254	-0.257	-0.353
8	-0.722	-0.680	-0.663	-0.657	-0.744	-0.615	-0.697	-0.703	-1.126
10	-0.957	-0.827	-0.828	-0.799	-0.921	-0.759	-0.864	-0.865	-1.402
25	-3.631	-2.462	-2.366	-2.280	-3.081	-2.317	-2.655	-2.708	-6.810

Table B.2: $C_{P(\alpha)}$ Configuration Map for Yaw and Pitch Angle.

B.7.2 $C_{P(\beta)}$ Calibration

B.7.2.1 $C_{P(\beta)}$ Calibration Map

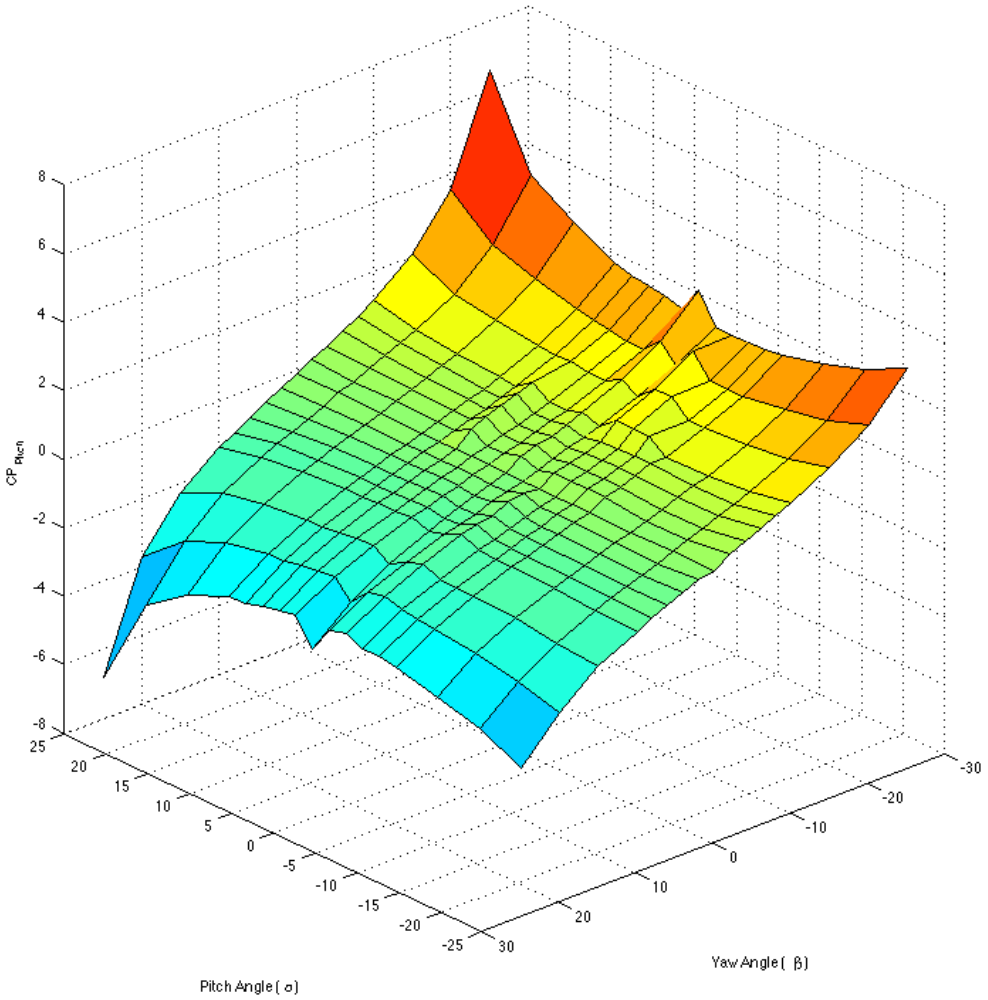

Figure B.9: $C_{P(\beta)}$ Configuration Map for Yaw and Pitch Angle.

B.7.2.2 $C_{P(\beta)}$ Calibration Table

	Pitch Angle (α)								
(β)	-25	-10	-8	-2	0	2	8	10	25
-25	-3.072	-0.893	-0.701	-0.136	0.063	0.260	0.955	1.228	6.494
-10	-2.087	-0.656	-0.513	-0.111	0.044	0.191	0.654	0.817	3.005
-8	-2.037	-0.660	-0.525	-0.119	0.029	0.186	0.635	0.814	2.820
-2	-1.934	-0.627	-0.501	-0.115	0.024	0.165	0.608	0.778	2.640
0	-1.922	-0.618	-0.500	-0.117	0.028	0.174	0.610	0.777	2.621
2	-1.919	-0.622	-0.504	-0.120	0.035	0.174	0.623	0.792	2.632
8	-2.047	-0.643	-0.496	-0.104	0.042	0.189	0.638	0.796	2.828
10	-2.115	-0.642	-0.507	-0.095	0.067	0.215	0.636	0.812	2.928
25	-3.255	-0.822	-0.638	-0.097	0.089	0.273	0.922	1.165	6.132

Table B.3: $C_{P(\beta)}$ Configuration Map for Yaw and Pitch Angle.

B.7.3 $C_{P(Static)}$ Calibration

B.7.3.1 $C_{P(Static)}$ Calibration Map

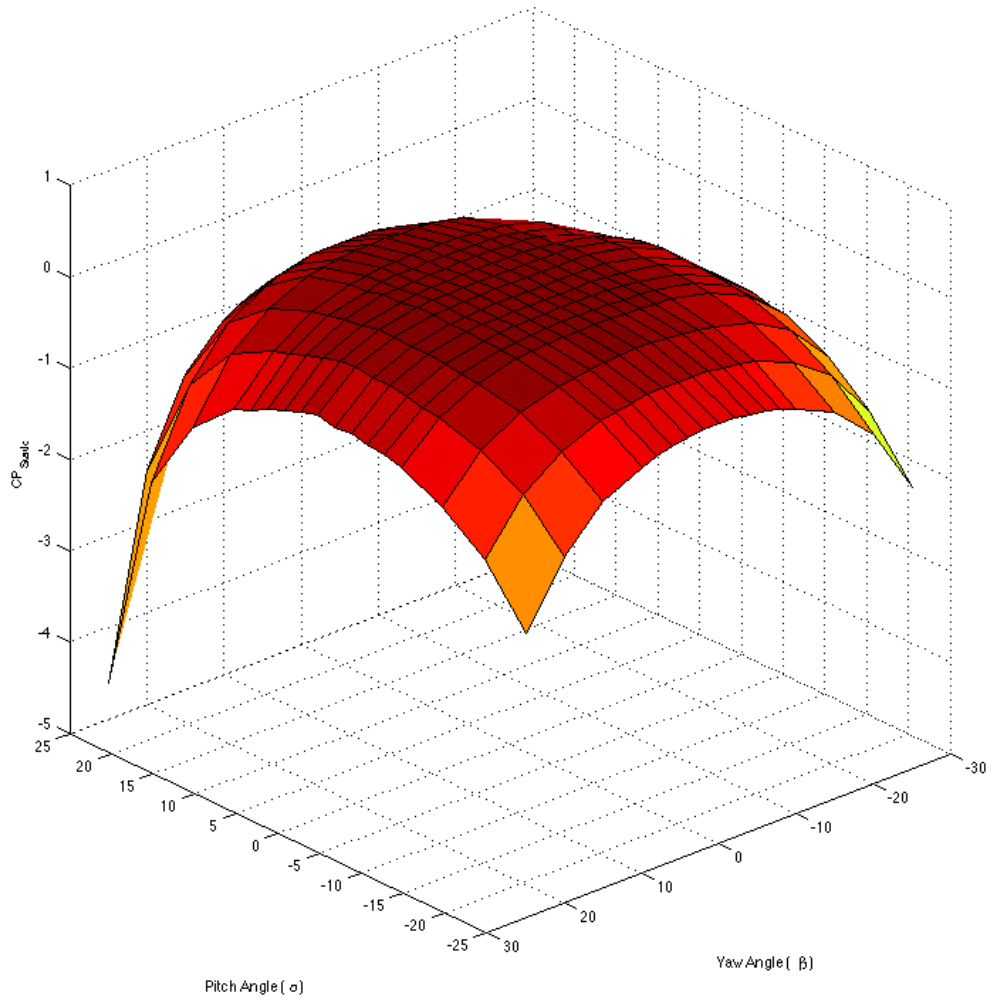

Figure B.10: $C_{P(Static)}$ Configuration Map for Yaw and Pitch Angle.

B.7.3.2 $C_{P(Static)}$ Calibration Table

	Pitch Angle (α)								
(β)	-25	-10	-8	-2	0	2	8	10	25
-25	-1.928	-0.699	-0.671	-0.612	-0.623	-0.690	-0.671	-1.001	-4.659
-10	-0.577	-0.023	-0.014	0.013	0.021	0.009	-0.014	-0.089	-1.155
-8	-0.517	-0.013	0.001	0.027	0.033	0.027	0.001	-0.065	-1.025
-2	-0.417	0.020	0.027	0.033	0.035	0.035	0.027	-0.019	-0.866
0	-0.407	0.023	0.029	0.029	0.034	0.037	0.029	-0.018	-0.852
2	-0.409	0.020	0.028	0.037	0.039	0.036	0.028	-0.023	-0.856
8	-0.508	-0.013	0.003	0.023	0.024	0.030	0.003	-0.058	-1.022
10	-0.565	-0.023	-0.019	0.007	0.019	0.015	-0.019	-0.085	-1.123
25	-1.892	-0.735	-0.679	-0.636	-0.595	-0.645	-0.679	-0.960	-4.614

Table B.4: $C_{P(Static)}$ Configuration Map for Yaw and Pitch Angle.

B.7.4 $C_{P(Total)}$ Calibration

B.7.4.1 $C_{P(Total)}$ Calibration Map

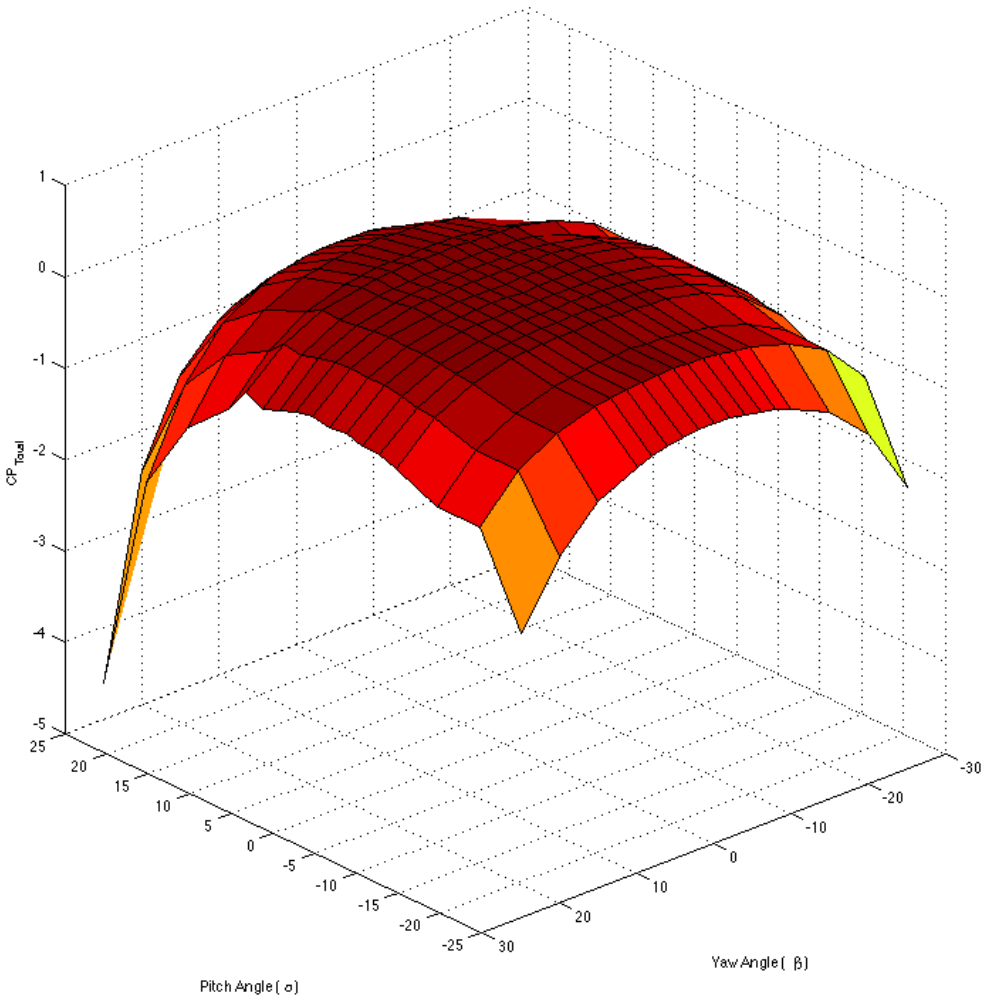

Figure B.11: $C_{P(Total)}$ Configuration Map for Yaw and Pitch Angle.

B.7.4.2 $C_{P(Total)}$ Calibration Table

	Pitch Angle (α)								
(β)	-25	-10	-8	-2	0	2	8	10	25
-25	-1.924	-0.696	-0.668	-0.609	-0.621	-0.688	-0.911	-0.998	-4.652
-10	-0.574	-0.021	-0.012	0.015	0.023	0.011	-0.066	-0.087	-1.152
-8	-0.515	-0.011	0.003	0.029	0.035	0.029	-0.037	-0.063	-1.022
-2	-0.415	0.021	0.029	0.035	0.037	0.037	-0.006	-0.017	-0.863
0	-0.405	0.025	0.030	0.031	0.036	0.039	-0.003	-0.016	-0.850
2	-0.406	0.022	0.030	0.039	0.041	0.038	-0.008	-0.021	-0.853
8	-0.506	-0.011	0.005	0.025	0.026	0.032	-0.028	-0.056	-1.019
10	-0.563	-0.021	-0.017	0.009	0.021	0.017	-0.066	-0.083	-1.120
25	-1.888	-0.732	-0.677	-0.634	-0.593	-0.643	-0.893	-0.957	-4.608

Table B.5: $C_{P(Total)}$ Configuration Map for Yaw and Pitch Angle.

B.8 On-Road Test Vehicle

B.8.1 Test Vehicle Specification Sheet

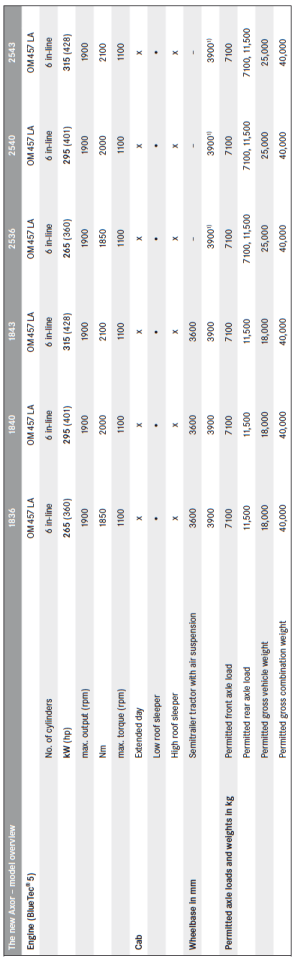

The new Axor – model overview		1836	1840	1843	2536	2540	2543
Engine (BlueTec® 5)		OM 457 LA	OM 457 LA	OM 457 LA	OM 457 LA	OM 457 LA	OM 457 LA
	No. of cylinders	6 in-line	6 in-line	6 in-line	6 in-line	6 in-line	6 in-line
	kW (hp)	265 (360)	295 (401)	315 (428)	265 (360)	295 (401)	315 (428)
	max. output (rpm)	1900	1900	1900	1900	1900	1900
	Nm	1850	2000	2100	1850	2000	2100
	max. torque (rpm)	1100	1100	1100	1100	1100	1100
Cab	Extended day	x	x	x	x	x	x
	Low roof sleeper	•	•	•	•	•	•
	High roof sleeper	x	x	x	x	x	x
Wheelbase in mm	Semitrailer tractor with air suspension	3600	3600	3600	–	–	–
		3900	3900	3900	3900[1]	3900[1]	3900[1]
Permitted axle loads and weights in kg	Permitted front axle load	7100	7100	7100	7100	7100	7100
	Permitted rear axle load	11,500	11,500	11,500	7100, 11,500	7100, 11,500	7100, 11,500
	Permitted gross vehicle weight	18,000	18,000	18,000	25,000	25,000	25,000
	Permitted gross combination weight	40,000	40,000	40,000	40,000	40,000	40,000

• Standard x Optional – Not available [1] Available with 22.5" midlift axle or lightweight 17.5" midlift axle

Figure B.12: Mercedes-Benz Axor Specification Sheet.

B.8.2 Test Vehicle Cab Specification Sheet

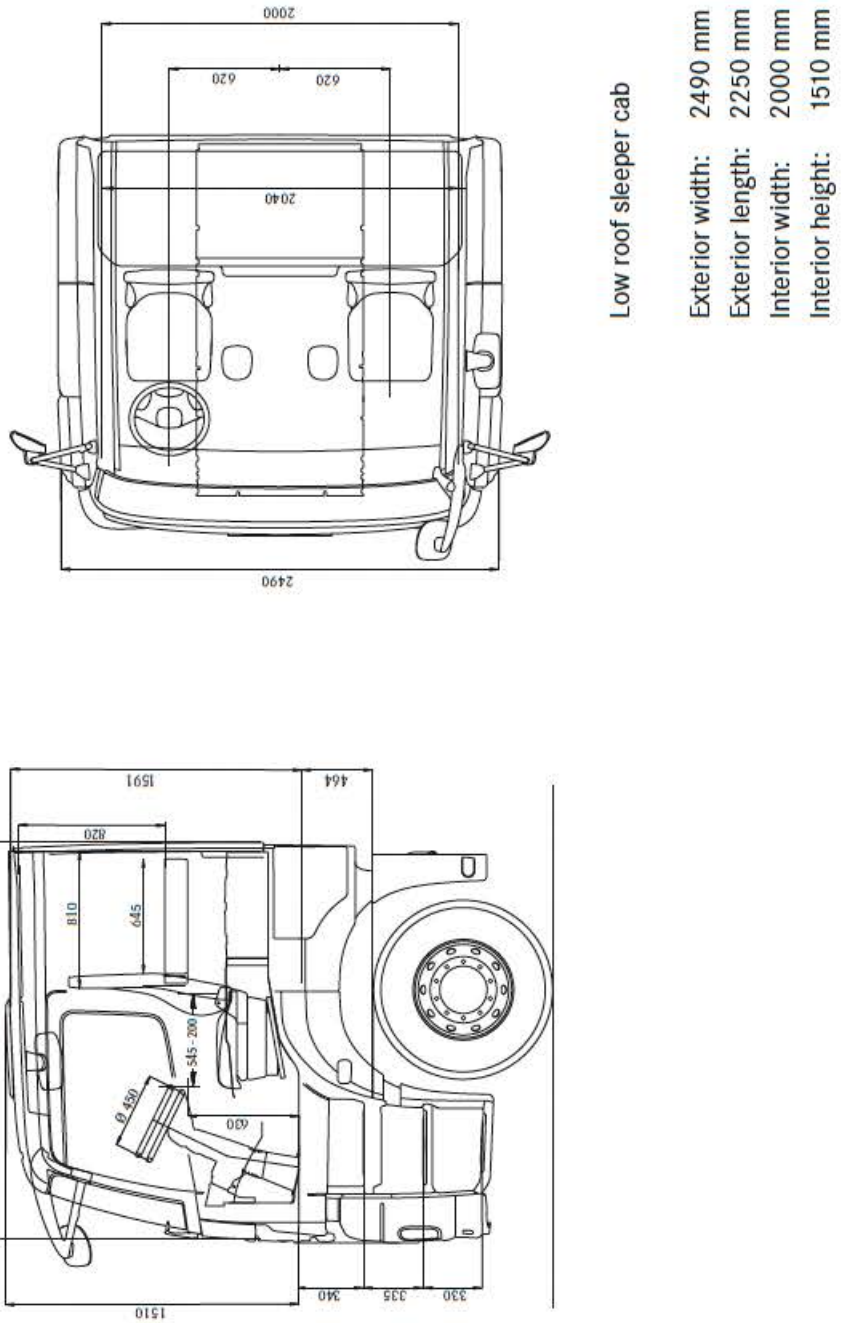

Figure B.13: Mercedes-Benz Axor Cab Specification Sheet.

B.9 On-Road Test Equipment

B.9.1 Data Logger

Technical Specification

Memory	Compact flash type I. Data in FAT16 PC format. Minimum card size 32MB, maximum card size 2GB (limited by FAT16), or larger if formatted in DOS
GPS	Outputs position, speed, position accuracy and speed accuracy every 100ms with no interpolation. GPS tracking loops optimised for applications up to approximately 4g. Tracking of all satellites in view.
GPS antenna	Magnetic base, 3.3v active antenna with SMA connector
Analogue Inputs	8 external inputs, all 12 bit resolution. All 0-12V scale. All inputs are protected to twice maximum input voltage.
Frequency Inputs	4 external frequency inputs with a maximum input frequency >2kHz. Hardware dividers of 4 or 16 to average readings if required. Triggering voltage requires a low input of <1v and a high input of >4v and 15v maximum.
Lap Beacon Input	Triggering voltage requires a low input of <1v and a high input of >4v and 15v maximum.
Start Sample Input/Output	Input requires grounding to start sampling and again to stop sampling. Open collector output with a maximum current of 50mA
Power Supply Requirements	12v nominal input, minimum of 10v, maximum of 15v. Current consumption of about 180mA including GPS, dependant on compact flash card size
+5v Reference Out	Maximum current draw 100mA, tolerance 1%.
Ignition In Signal (High Level)	Triggered by fast voltage transients. Can be connected directly to the low tension side of the ignition coil, or capacitively coupled to the high-tension side.
Ignition In Signal (Low Level)	Triggering voltage requires a low input of <1v and a high input of >4v up to 15v maximum. Suitable for connection directly to most ECU tacho outputs. Maximum input frequency >300Hz.
Case Construction	Extruded aluminium anodised black, nominal case thickness 2mm. End panels CNC cut carbon fibre. Overall dimensions (excluding connectors) 107mm x 68mm x 29mm
Connector Type	Weidmuller spring retention type, 24 way. 2 part unplugable connector
Main Processor	24MHz RISC with embedded flash program memory
GPS Serial Port	User configurable for baud rate and messages. Factory set at 4800 baud and outputting NMEA messages of $GPRMC and $GPGGA,
DL1 Serial Port	2 separate ports. Port 1 fixed at a baud rate of 115200 baud. Whilst logging outputs all data from all channels at 100Hz. Also used for re flashing, diagnostics and configuration. Port 2 used for inputting RS232 data for storage during a run, from an ECU, OBDII adapter or any other compatible device.
Accelerometers	3-axis, precision digital output. Guaranteed 2g minimum full scale on both axes. Resolution of 0.005g. Upgrade 6g available.
Vibration	Factory tested at 25g, 50Hz sinusoid for 5 minutes (without compact flash card inserted).
Temperature	Factory tested from -20°C to +70°C

Race Technology Ltd. VAT 715 9671 09
UK Tel +44 (0)1773 537620 Fax +44 (0)1773 537621
US Tel +1 804 358 7289 Fax +1 804 359 6694
Email: sales@race-technology.com

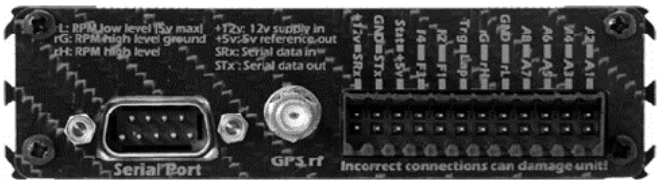

Figure B.14: Race Technology DL1 MK2 Data Logger Specification Sheet.

B.9.2 Mercedes-Benz Supplied Data Logger

DATroniC 3 BlueLAN
Technical Data

Rev.-No. 2009-04-21

DATroniC is a classification data logger, which is connected to the vehicle CAN-bus for recording specific vehicle parameters and operating statuses.

Example:
Operating data acquisition unit for long-term and short-term data acquisition in heavy-duty vehicles*

I. Technical Data

System Data

• Operating Voltage:	8 V to 32 V DC
• Temperature Range:	-40 °C to +85 °C
• Device Connectors:	
◦ Vehicle / Supply	14-pin ODU G51MC7-P14QC00-A060
◦ USB	Mini-USB
◦ Ethernet	RJ45
• Displays:	5 LEDs for operating mode and device status
• Housing:	
◦ Dimensions	111.5 mm x 35.5 mm x 70 mm (W x H x D)
◦ Material	Aluminium ALMGSi 0.5 acc. to EN AW 6060
◦ Colour	Blue anodised / front and rear aluminium
◦ IP Protection Class	IP50
• Weight:	225 g

CPU

• Processor:	Freescale MC9S12XDP512 (40 MHz)
• Memory:	Flash: 512 kByte (µController internal) 4 MByte (µController external) RAM: 1 MByte external (32 KByte µController internal) EEPROM: 4 KByte (µController internal)

Communication Interfaces

• CAN:	2 x High-Speed-CAN (2.0B Full-CAN, ISO DIS 11898) 1 x Low-Speed-CAN (ISO DIS 11992)
• PC Connection:	
◦ USB	USB2.0 Full Speed compatible
◦ Ethernet	10Base-T / 100Base-TX (Auto-Sensing); TCP/IP, HTTP and AutoIP; Link and Activity Indicator
◦ Bluetooth®	Class-2 (Bluetooth 1.2) with internal ceramic chip antenna (can be switched off)

II. Software

- Recording of all configured CAN signals via classification operations
- Long-term data storage for large complete-course recordings
- Storage of up to 40 daily data sets (counter start depending on date or, alternatively, after 12 hours)
- Windows-based configuration and analysis software
- Online display of most important vehicle parameters in parallel to data recording
- Online display via PDA (wireless via Bluetooth®, for devices with Windows Mobile 5 and Windows Mobile 6)
- Future-oriented through possibility of Firmware updates
- Pre-configured display of recorded classification values in Microsoft Excel (from Version 2002 onwards)

Delivery includes vehicle-specific connection adaptor, connector power supply with exchangeable travel plug adaptors for Europe, United Kingdom, Australia and USA / Japan, as well as connector cables for USB and Ethernet.

For further information on ***DATroniC*** and other AFT products as well as a current price list, please contact us at:
info@aft-werdohl.de

* The specific configuration and selection of the CAN signals to be recorded is realised after consultation with the customer.

AFT Atlas Fahrzeugtechnik GmbH
www.aft-werdohl.de

Gewerbestr. 14
58791 WERDOHL
GERMANY
Tel: +49 23 92 8 09-0
Fax: +49 23 92 8 09-1 00

P.O. Box 11 07
58771 WERDOHL

Deutsche Bank AG Baden-Baden
Account No.: 06 63 120
Sort Code: 662 700 01

VAT-No.: DE123836977

President: Helmut Schilly, Dr. Peter Gutzmer
Registered in Germany No. HRB 5275
Registration Office: Iserlohn, Germany

Figure B.15: DATroniC 3 Data Acquisition Specification Sheet [106].

B.9.3 GPS Receiver

	Speed Errors	
	DL2 – 20Hz	DL2 – 5Hz
Test 1	0.008kph	-0.015 kph
Test 2	-0.028 kph	-0.1 kph
Test 3	0.066 kph	0.151 kph
Test 4	0.007 kph	0.007 kph
Test 5	0.044 kph	-0.031 kph
Test 6	-0.087 kph	-0.277 kph

Figure B.16: Race Technology 20 Hz GPS Receiver Specification Sheet.

B.9.4 Wind Anemometer

SENSOR TYPE	Anemometer utilizes a 3-Cup rotor. Reed switch/magnet provide 1 pulse per rotation.
ROTOR DIAMETER	approx. 6 in (150 mm)
SPEED RANGE	approx. 3 mph to 125+ mph (~5 kph to over 200 kph)
MOUNTING BRACKET	Supplied with an aluminum mounting bracket with 2 holes for screws. Designed to be mounted on top of a pole or bracket. Custom brackets available up request (offset, for example)
WIRE	Standard length is 25 feet (8m) Custom lengths available upon request - tested OK to over 1,500 feet The wire is provided stripped and unterminated
DISPLAY	Removable LCD Digital Display is a Cateye Velo8 bicycle computer. **Dual Display** simutaneously shows CURRENT SPEED (top display)plus: MAX, AVERAGE, KM/MILES, or several other (bicycle-related) functions. Select **mph** or **km/h** (**knots** too if you wish - see **Owners Instructions** for details) Water-resistant (not waterproof). Provided with high strength self-adhesive Velcro pads for mounting the display
POWER	CR2032 Coin Battery located in the display - not the rotor/head Battery life 1 to 3 years of intermittent, occasional use. A few months to a year of continuous use, depending on wind conditions and mode of use (Display goes to low power mode when the wind speed drops to zero, or if removed from the bracket when not in use)
SPEED RESOLUTION	Top Anemometer Display (Current Speed): 0.5 mph Bottom Anemometer Display (Max, Average, etc.): 0.01 mph
DIGIT SIZE	Top Display (Current Speed): 10mm (approx. 1/2") Bottom Display (Max, Average, etc.): 5mm (approx. 1/4")
UPDATE RATE	Approximately 1Hz (1 second)
ACCURACY	0.5 mph from 4 to 10 mph +/-4% from 10 to 50 mph estimated within 4% above 50 mph
	A further note on accuracy We sent an original Vortex anemometer to a certified lab to check its accuracy. The results are shown in the graph below. It can be seen that the Vortex anemometer is within a few percent from about 10 to about 50 mph. From 5 to 10 the readout is the limiting factor, with a resolution of 0.5 mph. Above 50 mph the anemometer still works fine, although we do not have accuracy data in that region. Nevertheless, we believe it to be quite accurate to speeds well over 100 mph. 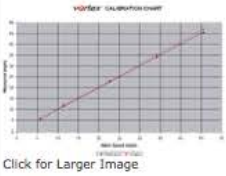 Click for Larger Image **Maximum Speed** The maximum wind speed that can be measured by a Vortex anemometer is over 150 mph (~240 kph). See note below on accuracy. **Minimum Speed** Approx. 3 to 4 mph (~6 kph) **Accuracy:** +/-4% from ~10 to ~50 mph +/- a few tenths of a mph from ~4 to ~10 mph The accuracy above 50 mph is presumed to be excellent (based on data from the rotor manufacturer), but no precise laboratory calibration has been obtained. The Vortex™ anemometer is NOT sensitive to how it is held in the wind, provided the head is held horizontal and the air flow is not obstructed by the user (i.e. you do not have to face into the wind). **IMPORTANT NOTE ABOUT AVERAGE WIND SPEED:** Since bicyclists do not want their average speed to be diminished when they come to a stop, **the computer will only record and average when the wind is blowing. It stops recording below approximately 1 mph**. That means that if the wind blows for 2 hours at 20 mph and 2 hours at zero, the average shown will be **20**, not **10**! Please keep this in mind for your desired use of the Vortex anemometer. **WORKAROUND :** if you want to know the real average wind speed - even with spells near zero, do the following: reset the computer, note the time. When desired, simply divide the total number of wind "miles" on the display by the number of hours since reset.

Figure B.17: InSpeed Vortex Wind Speed Specification Sheet.

B.9.5 Wind Vane

SENSOR TYPE	Balanced wind vane connected to an active, non-contact, zero friction Hall Effect sensor Sealed magnetic Hall Effect sensor. Magnet hovers over the sensor to provide ~0-5VDC output
SENSOR RANGE	Full 360 degrees , zero deadband
ACCURACY/LINEARITY	+/-0.3 to 0.5% of signal range
RESOLUTION	12 bit or 0.025 degrees
ELECTRICAL	3 wire flying leads. Supply voltage 4.5 to 5.5 VDC Current 15 mA typical Output 5% to 95% of input voltage (0.25 to 4.75VDC) Length of wire: optional (standard lengths provided - click to order to view options)
MOUNTING	The E-Vane is provided with an offset aluminum bracket with 2 mounting holes. The mounting is compatible with Inspeed Vortex Wind Sensors (the 2 holes match).
DIMENSIONS	Directional Vane approximately 8 inches
COMPATIBILITY	The Inspeed e-Vane is compatible with Inspeed WindWorks It is not compatible with Inspeed Windware software (which provides wind speed only)

Figure B.18: InSpeed Wind Direction Specification Sheet.

B.9.6 Pressure Transducers

- **Available for Differential, Gage, or Absolute Measurement**
- **Precision 5V Output Span**
- **Precise Temperature Compensation**
- **Constant Voltage Excitation**
- **For Clean, Dry Gas**

The PX138 Series pressure transducer uses state-of-the-art micro-machined silicon sensors with stress-free packaging techniques to provide highly accurate, temperature-compensated pressure measurements for the most demanding applications. When operating from an 8 Vdc regulated power source, the PX138 transducer provides a 1 to 6 Vdc output. Other regulated voltages from 7 to 16V can be used but the output will change in proportion to the excitation.

SPECIFICATIONS

Excitation Voltage: 8 Vdc (7 to 16 Vdc limits)
Output: 1 to 6 Vdc (@ 8 Vdc exc.)
Linearity and Hysteresis: ±0.1% FS typical, 0.5% max (0.5% typ. 1% max for ±0.3 psi range)
Repeatability: ±0.1% FS typical, 0.3% max
Zero Balance: 3.5 ±0.05 Vdc diff.; 1 ±0.1 Vdc abs.
Storage Temperature: -40 to 125°C (-40 to 257°F)
Compensated Temp Range: 0 to 50°C (32 to 122°F)
Zero Temp Effects: ±0.5% FS (±1% FS for 0.3 psi)
Span Temp Effects: ±0.5% FS (±1% FS for 0.3 psi)
Proof Pressure: >3x FS pressure
Burst Pressure: >5x FS pressure
Common Mode Press: 50 psi
Media Compatibility: For use with gases compatible with silicon, glass-filled nylon and alumina ceramic
Mating Connector: CX136-4 (sold separately)

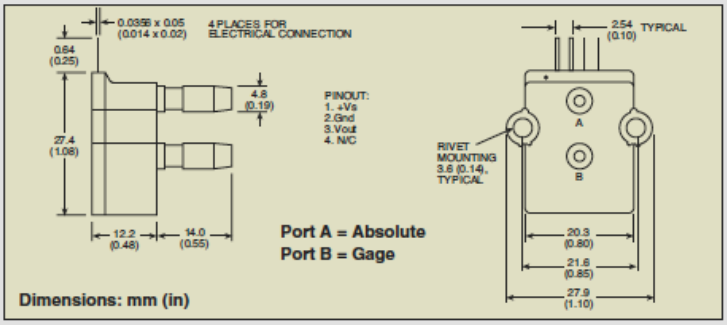

To Order *Visit omega.com/px138 for Pricing and Details*

GAGE/DIFF PRESSURE		MODEL NO.	COMPATIBLE METERS
±0.3 psi	0.02 bar	**PX138-0.3D5V**	DP24-E, DP25B-E, DP41-E
±1 psi	0.069 bar	**PX138-001D5V**	DP24-E, DP25B-E, DP41-E
±5 psi	0.34 bar	**PX138-005D5V**	DP24-E, DP25B-E, DP41-E
±15 psi	1.0 bar	**PX138-015D5V**	DP24-E, DP25B-E, DP41-E
ABSOLUTE PRESSURE RANGES			
0 to 15 psia	0 to 1.0 bar	**PX138-015A5V**	DP24-E, DP25B-E, DP41-E
0 to 30 psia	0 to 2.1 bar	**PX138-030A5V**	DP24-E, DP25B-E, DP41-E

Comes complete with operator's manual.
***Ordering Example: PX138-001D5V,** voltage output silicon pressure sensor with a gage/differential range of ±1 psi.*

ACCESSORIES

MODEL NO.	DESCRIPTION
PST-8	8 Vdc power supply
CX136-4	4-contact connector

Figure B.19: Omega Engineering PX138-0.3D5V Differential Pressure Transducer Specification Sheet.

B.9.7 Kiel Probe

B.9.7.1 Kiel Probe Specification Sheet

Ordering Part Number	Sensing Head Description	Probe Diameter h	Probe Length a	Yaw Range **	Pitch Range **	Time† Constant (Sec.)
KRC-"a"	1/4" Dia. High Range Type KR 	1/8"	Standard Probe Lengths are 6" 8" 12" 24"	±54°	±49°	0.6
KRF-"a"		1/4"				
KEC-"a"	3/8" Dia. Venturi Type KE	1/8"		±63°	±58°	0.3
KEE-"a"-W		3/16"				
KEF-"a'		1/4"				
KFF-"a"	3/4" Dia. Venture Type KF 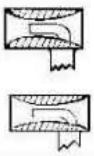	1/4"		±67°	±61°	0.3

Type KR:

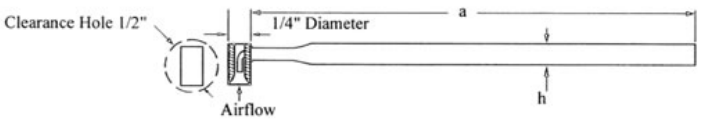

Type KE:

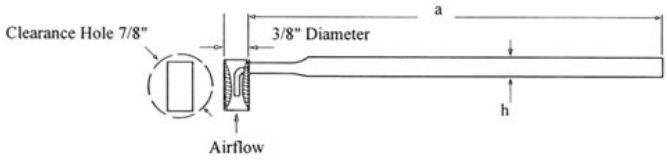

Type KF:

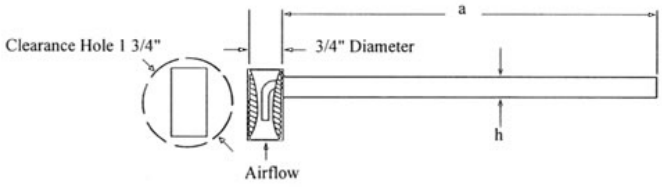

Figure B.20: United Sensor Corp. Kiel Probe Specification Sheet.

B.9.7.2 Kiel Probe Technical Drawing

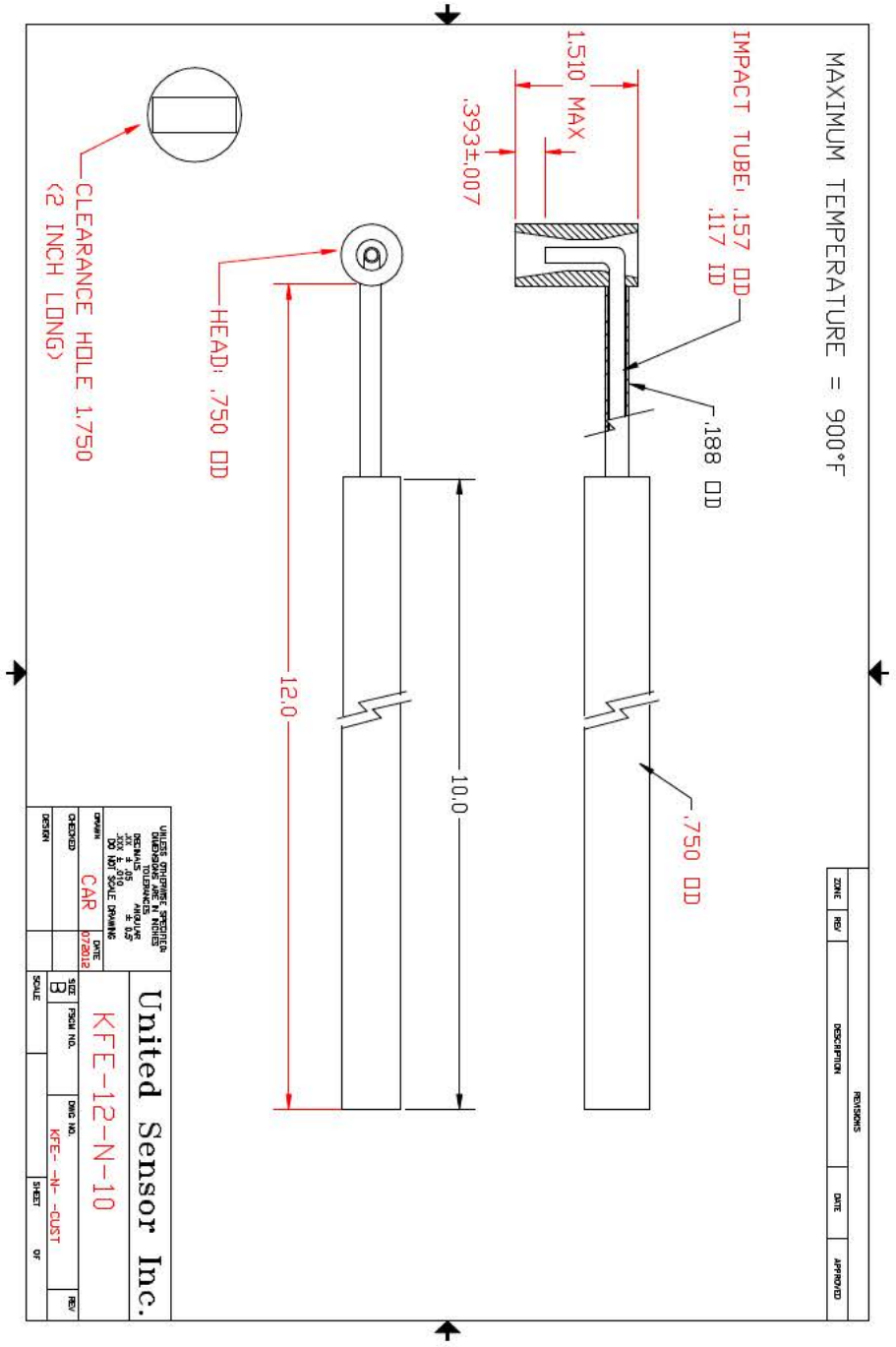

Figure B.21: United Sensor Corp. Kiel Probe Technical Drawing.

B.9.8 Actuators

• **LAS3 Specifications**

Model	Thrust max. (N)	Pulling max. (N)	Holding max. (N)	Speed (mm/s) Load=Max./Load=0		Standard stroke (mm) : S					Duty cycle %	Current max. (A) 12VDC	Current max. (A) 24VDC	Optical Sensor Resolution (mm/pulse)	Potentiometer Resolution (Ohm/mm)
LAS3-1	1200	1200	800	8	12	50	100	150	200	250	10	6	2.5	0.3175	21
LAS3-2	600	600	300	16	25	50	100	150	200	250	10	6	3	0.635	10.5

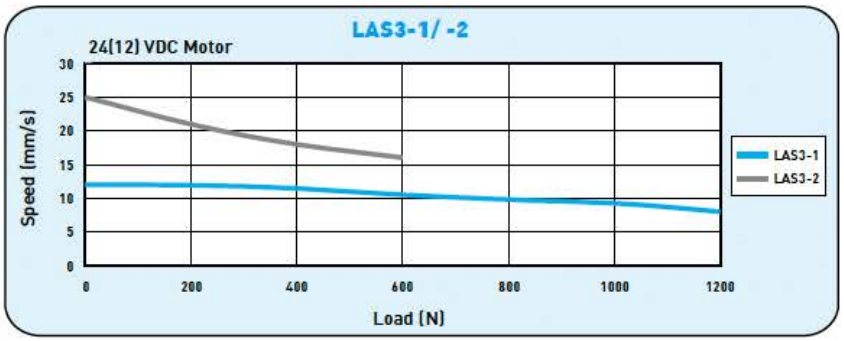

**Note: The test results are obtained by using the 24VDC power supply.

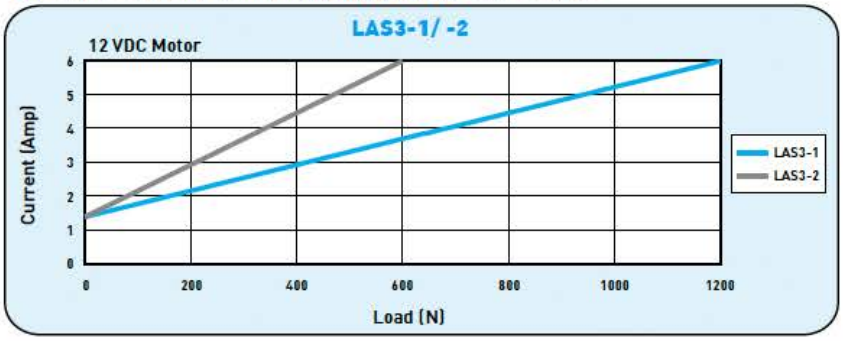

**Note: The test results are obtained by using the 12VDC power supply.

HIWIN.
A99LE18-1107

Figure B.22: Hiwin LAS3 Actuator Specification Sheet.

B.9.9 Engine Control Unit

openecu

Pi SHURLOK

M100 VEHICLE CONTROL MODULE

Overview

The M100 module is a compact electronics module, designed to full automotive specifications. It is available ex-stock for use in prototype vehicle development, or in volume (customized as required) for production programs.

2 CAN Interfaces, 16 standard input/output functions and 8 uncommitted LED indicators are provided.

Typical applications include communications gateways and ancillary function control.

Two levels of customization are available. Level 1 provides customer selection of certain components e.g. pull up and pull down resistors, but without change to functionality. Level 2 allows custom designed circuitry to be added via a daughter board to provide new functionality for input and output pins.

A software platform library to access functions can be integrated with customer applications, alternatively Pi Shurlok can supply custom application software.

Module Characteristics

SIZE	85mm by 65mm by 32mm
HOUSING	ABS, flame retardant, black spark finish
CONNECTOR 1	24 way AMP 1318853-2 (mating connector 24 way AMP 1318917-2)
CONNECTOR 2	8 way AMP 1376350-2 (mating connector 8 way AMP 1376352-2)
OPERATING TEMP.	-40°C to +85°C
ENVIRONMENTAL	Designed for in-cab location
SUPPLY VOLTAGE	6.5 – 16V ≤2mA quiescent current Protection against reverse supply connection Meets ISO 7637-2 : 1990 up to 40V 200ms load dump
INPUT OUTPUT PROTECTION	Input protection to supply voltage, outputs protected against short to supply or ground
OUTPUT CURRENT	4 x 1A plus 4 x 0.5A (total output current 2.5A max @ 80°C , 1.5A max @ 85°C)

Figure B.23: Pi Innovo M100 ECU Specification Sheet.

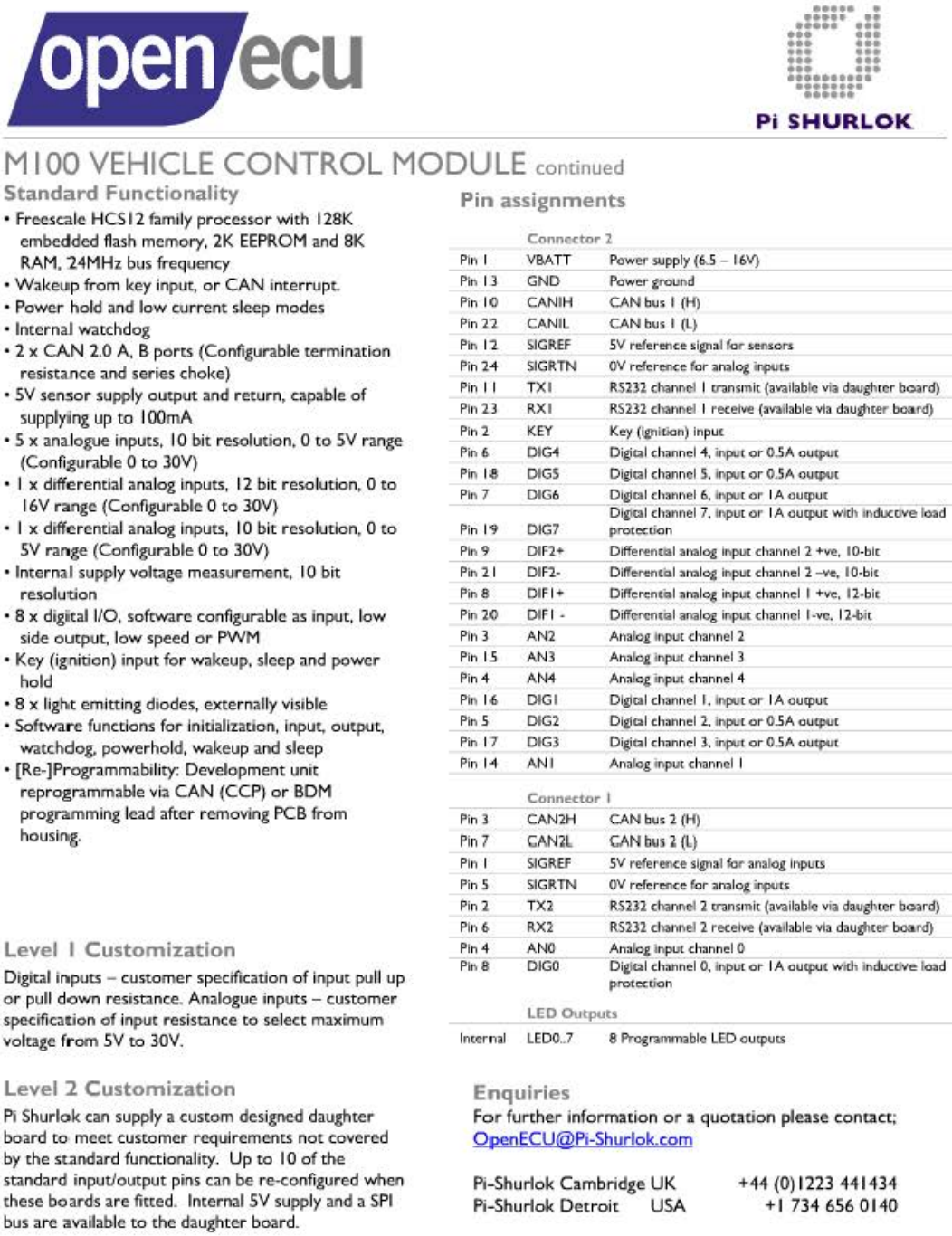

openecu

Pi SHURLOK

M100 VEHICLE CONTROL MODULE continued

Standard Functionality

- Freescale HCS12 family processor with 128K embedded flash memory, 2K EEPROM and 8K RAM, 24MHz bus frequency
- Wakeup from key input, or CAN interrupt.
- Power hold and low current sleep modes
- Internal watchdog
- 2 x CAN 2.0 A, B ports (Configurable termination resistance and series choke)
- 5V sensor supply output and return, capable of supplying up to 100mA
- 5 x analogue inputs, 10 bit resolution, 0 to 5V range (Configurable 0 to 30V)
- 1 x differential analog inputs, 12 bit resolution, 0 to 16V range (Configurable 0 to 30V)
- 1 x differential analog inputs, 10 bit resolution, 0 to 5V range (Configurable 0 to 30V)
- Internal supply voltage measurement, 10 bit resolution
- 8 x digital I/O, software configurable as input, low side output, low speed or PWM
- Key (ignition) input for wakeup, sleep and power hold
- 8 x light emitting diodes, externally visible
- Software functions for initialization, input, output, watchdog, powerhold, wakeup and sleep
- [Re-]Programmability: Development unit reprogrammable via CAN (CCP) or BDM programming lead after removing PCB from housing.

Level 1 Customization

Digital inputs – customer specification of input pull up or pull down resistance. Analogue inputs – customer specification of input resistance to select maximum voltage from 5V to 30V.

Level 2 Customization

Pi Shurlok can supply a custom designed daughter board to meet customer requirements not covered by the standard functionality. Up to 10 of the standard input/output pins can be re-configured when these boards are fitted. Internal 5V supply and a SPI bus are available to the daughter board.

Pin assignments

		Connector 2
Pin 1	VBATT	Power supply (6.5 – 16V)
Pin 13	GND	Power ground
Pin 10	CANIH	CAN bus 1 (H)
Pin 22	CANIL	CAN bus 1 (L)
Pin 12	SIGREF	5V reference signal for sensors
Pin 24	SIGRTN	0V reference for analog inputs
Pin 11	TX1	RS232 channel 1 transmit (available via daughter board)
Pin 23	RX1	RS232 channel 1 receive (available via daughter board)
Pin 2	KEY	Key (ignition) input
Pin 6	DIG4	Digital channel 4, input or 0.5A output
Pin 18	DIG5	Digital channel 5, input or 0.5A output
Pin 7	DIG6	Digital channel 6, input or 1A output
Pin 19	DIG7	Digital channel 7, input or 1A output with inductive load protection
Pin 9	DIF2+	Differential analog input channel 2 +ve, 10-bit
Pin 21	DIF2-	Differential analog input channel 2 –ve, 10-bit
Pin 8	DIF1+	Differential analog input channel 1 +ve, 12-bit
Pin 20	DIF1 -	Differential analog input channel 1-ve, 12-bit
Pin 3	AN2	Analog input channel 2
Pin 15	AN3	Analog input channel 3
Pin 4	AN4	Analog input channel 4
Pin 16	DIG1	Digital channel 1, input or 1A output
Pin 5	DIG2	Digital channel 2, input or 0.5A output
Pin 17	DIG3	Digital channel 3, input or 0.5A output
Pin 14	AN1	Analog input channel 1
		Connector 1
Pin 3	CAN2H	CAN bus 2 (H)
Pin 7	CAN2L	CAN bus 2 (L)
Pin 1	SIGREF	5V reference signal for analog inputs
Pin 5	SIGRTN	0V reference for analog inputs
Pin 2	TX2	RS232 channel 2 transmit (available via daughter board)
Pin 6	RX2	RS232 channel 2 receive (available via daughter board)
Pin 4	AN0	Analog input channel 0
Pin 8	DIG0	Digital channel 0, input or 1A output with inductive load protection
		LED Outputs
Internal	LED0..7	8 Programmable LED outputs

Enquiries

For further information or a quotation please contact;
OpenECU@Pi-Shurlok.com

Pi-Shurlok Cambridge UK +44 (0)1223 441434
Pi-Shurlok Detroit USA +1 734 656 0140

Figure B.24: Pi Innovo M100 ECU Specification Sheet (Cont).

B.9.10 Devantech H bridge Controller

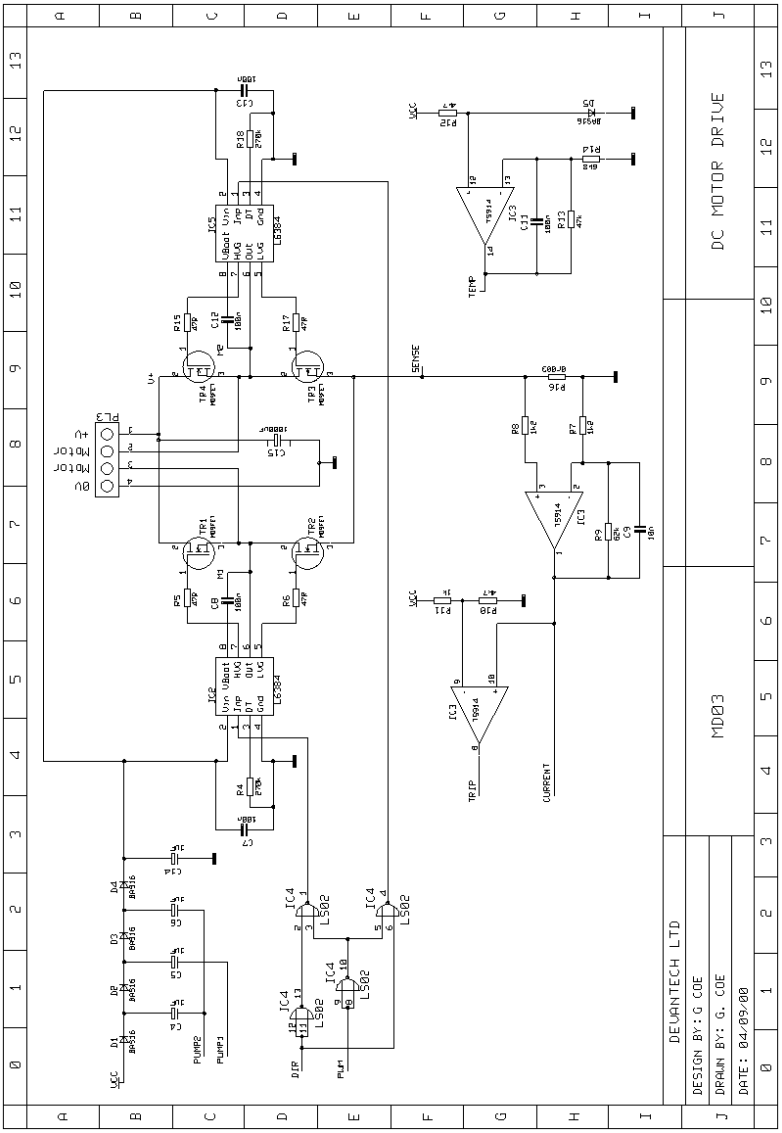

Figure B.25: Devantech MD03 24V 20A H Bridge Motor Drive Circuit Diagram.

B.9.11 Sharp Infrared Range Finder

B.9.11.1 Sharp IR Sensor Specification Sheet

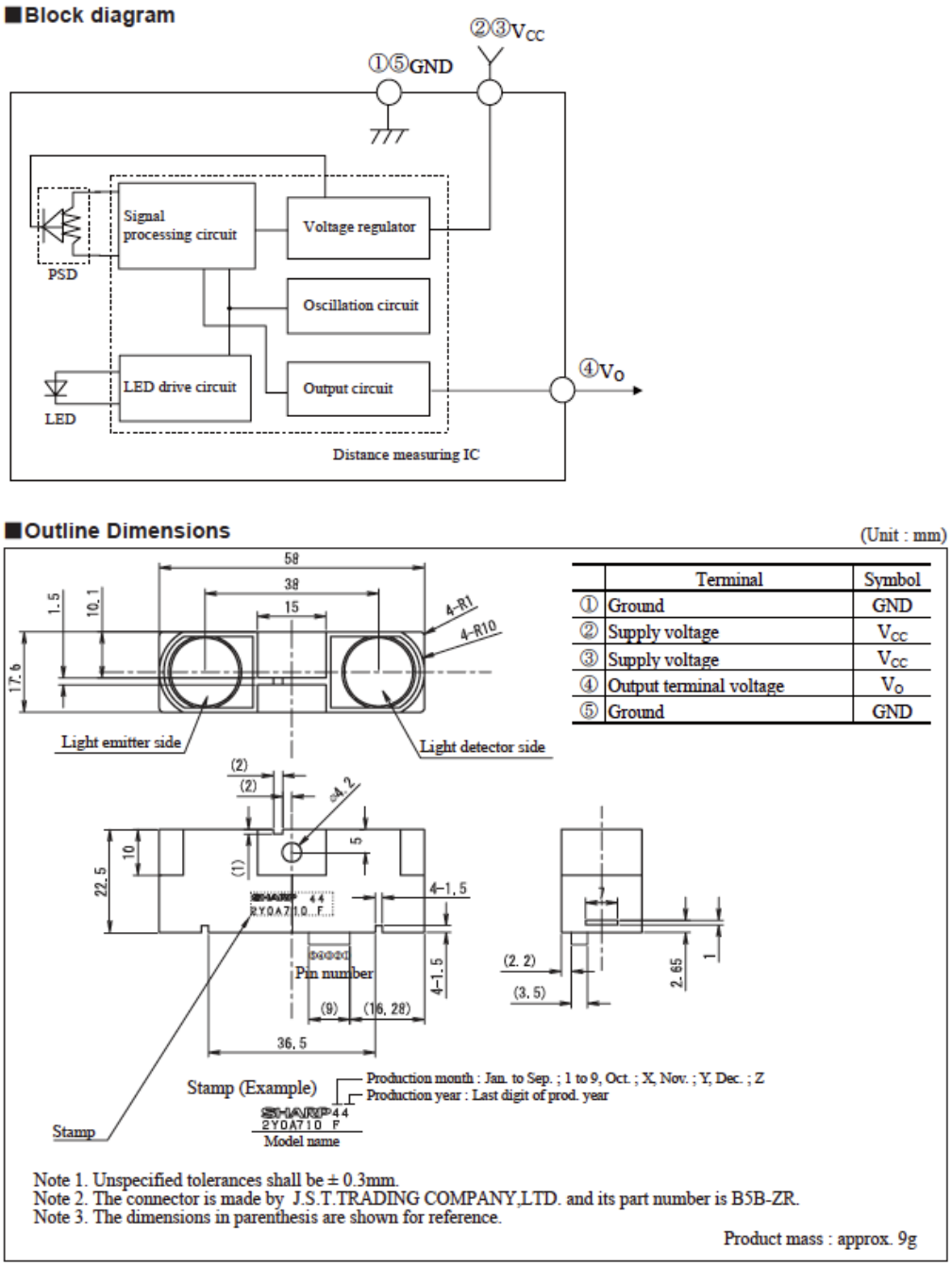

Figure B.26: Sharp GP2Y0A710K0F IR Range Finder Technical Specification Sheet.

B.9.11.2 Sharp IR Sensor Calibration Sheet

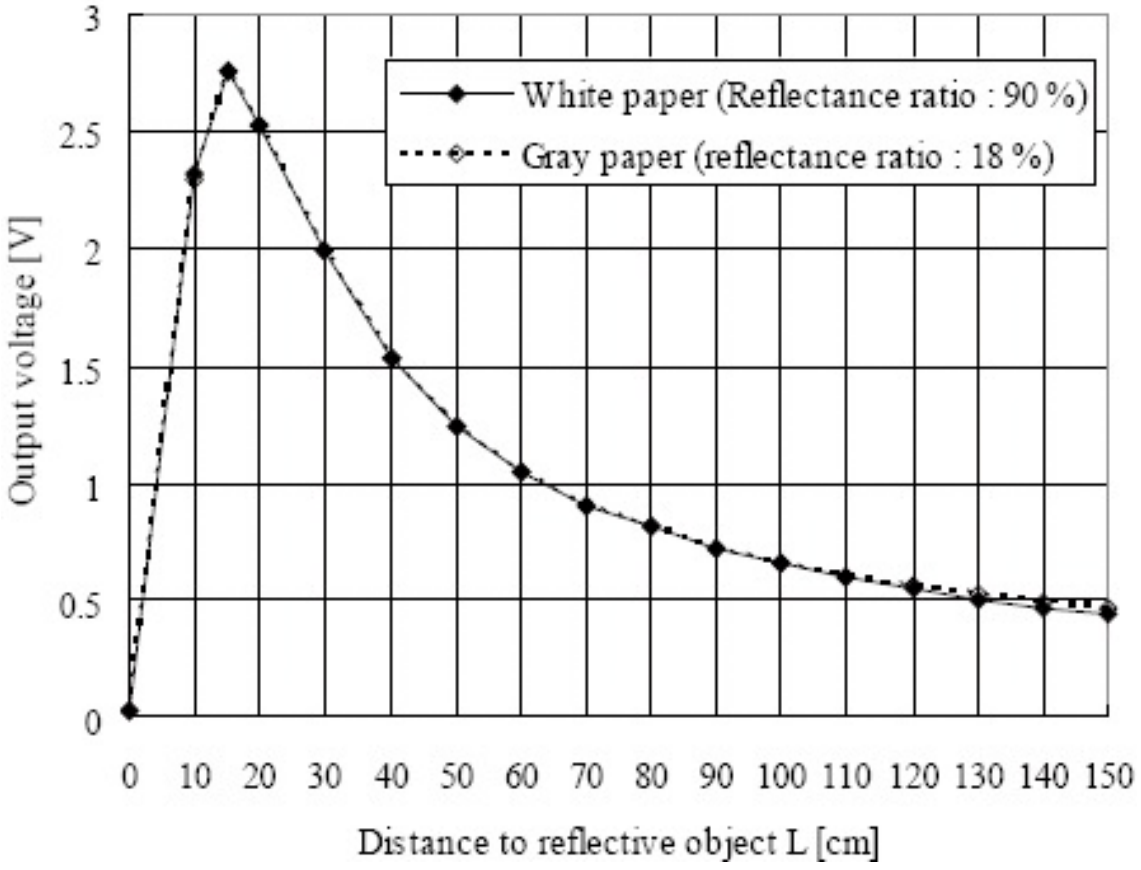

Figure B.27: Sharp GP2Y0A710K0F IR Range Finder Calibration Sheet.

B.10 On-Road Data Analysis

Due to the large quantity of data produced from the testing, data extraction and processing of the raw voltages for conversion to numerical values was achieved using *Mathematica*®, the processing code is show in Fig.(B.10.1).

B.10.1 On-Road Data Processing Code

```
Import Data;

(* Import All Data *)
dataImport=Import["/Users/jasonbarden/Desktop/CSV_Road_Data/full_dataset_2.csv"];
data2=Drop[Flatten[dataImport],{1,6}];

(*--------------- IMPORT PRE - EVALUATED DATA SECOND RUN - PART [1] ---------------*)

(* RECALC'D PRESSURES *)
DeltaPSelect= Flatten[Import["../DeltaPSelect.csv"]];
(* RECALC'D Angle *)
BetaDSelect= Flatten[Import["../BetaDSelect.csv"]];
(* K Values *)
kvaluesSelect= Flatten[Import["../kvaluesSelect.csv"]];

(*--------------- IMPORT PRE - EVALUATED DATA SECOND RUN - PART [2] ---------------*)


(* RECALC'D PRESSURE *)
DeltaPSelect2= Flatten[Import["...DeltaPSelect2.csv"]];
(* RECALC'D Angle *)
BetaDSelect2= Flatten[Import["../BetaDSelect2.csv"]];
(* K Values *)
kvaluesSelect2= Flatten[Import["../kvaluesSelect2.csv"]];

(*-------------------------------------------------------------------------------------*)


(* CONSTANTS *)

ms=0.44704; (* Convert Mph to m/s *)
freq=2.5; (* Frequency of cup anemometer to mph *)
TransLZero=4.832; (* Transducer zero shift *)
TransRZero=4.841;(* Transducer zero shift 3.778 *)
Deg2Rads=Pi/180;
Rads2Deg=180/Pi;
TransLVolts2PSI=0.3/TransLZero;
TransRVolts2PSI=0.3/TransRZero;
PSItoPa=6894.75729;

(* Over Sample Time, ZeroBalance & Pressures will drop! *)


Main Calculations - Second Run ;

(* Strip From Main DataSet *)
requiredlength=811933;
samplelength=requiredlength*6;
TimeF=Take[data2,{1,samplelength,6}];
TSmphF=Take[data2,{2,samplelength,6}];
BetaVoltF=Take[data2,{3,samplelength,6}];
TransLVoltF=Take[data2,{4,samplelength,6}];
TransRVoltF=Take[data2,{5,samplelength,6}];
WSVoltF=Take[data2,{6,samplelength,6}];
TransLVoltMax=Max[TransLVoltF];
TransRVoltMax = Max[TransRVoltF];
TSF=TSmphF*ms;
WSF=(Abs[(WSVoltF*freq)-TSF]+0.3)*ms;
SpeedF=TSF+WSF;
MinBetaVolt=Min[BetaVoltF];
MaxBetaVolt=Max[BetaVoltF];


Second Run - First Selection
```

```
(* Adjust Selection - TS is at operating velocity... *)
SelectionStart=8000;
SelectionEnd=21000;
TimeSelect=Take[TimeF,{SelectionStart,SelectionEnd}];
TSmphSelect=Take[TSmphF,{SelectionStart,SelectionEnd}];
BetaVoltSelect=Take[BetaVoltF,{SelectionStart,SelectionEnd}];
TransLVoltSelect=Take[TransLVoltF,{SelectionStart,SelectionEnd}];
TransRVoltSelect=Take[TransRVoltF,{SelectionStart,SelectionEnd}];
WSVoltSelect=Take[WSVoltF,{SelectionStart,SelectionEnd}];
TSSelect=TSmphSelect*ms;
WSSelect=(Abs[(WSVoltSelect*freq)-TSSelect]+0.3)*ms;
SpeedSelect=TSSelect+WSSelect;
TotalDirSelect=(((BetaVoltSelect-MinBetaVolt)/MaxBetaVolt)*360);
TransLPaSelect=(TransLVoltSelect-TransLZero)*TransLVolts2PSI;
TransLSelect=TransLPaSelect*PSItoPa;
TransRPaSelect=(TransRVoltSelect-TransRZero)*TransRVolts2PSI;
TransRSelect=TransRPaSelect*PSItoPa;
GaugeLPaSelect=TransLSelect;
GaugeRPaSelect=TransRSelect;
DeltaCPSelect=DeltaPSelect/(0.5*1.22*(SpeedSelect^2));
TimeLengthSelect=Dimensions[TimeSelect]/100;
xSelect=Flatten[{0,TimeLengthSelect}];
DeltaPNormSelect=(Flatten[DeltaPSelect]/Mean[kvaluesSelect]);
Run Second-First Selection


Export Data;

(*-------------------------------- EXPORT VARIABLES --------------------------------*)

(* Yaw Angles *)
Export[".../BetaDSelect.csv",Flatten[BetaDSelect],"CSV"];
(* Transducer L Pressure *)
Export[".../GaugeLPaSelect.csv",Flatten[GaugeLPaSelect],"CSV"];
(* Transducer R Pressure *)
Export[".../GaugeRPaSelect.csv",Flatten[GaugeRPaSelect],"CSV"];
(* DeltaP Pressure *)
Export[".../DeltaPSelect.csv",Flatten[DeltaPSelect],"CSV"];
(* Wind Speed *)
Export[".../WSSelect.csv",Flatten[WSSelect],"CSV"];
(* Truck Speed *)
Export[".../TSSelect.csv",Flatten[TSSelect],"CSV"];
(* Time *)
Export[".../TimeSelect.csv",Flatten[TimeSelect],"CSV"];
(* k Values *)
Export[".../kvaluesSelect.csv",Flatten[kvaluesSelect],"CSV"];

(*-----------------------------------------------------------------------------------------------------------*)

Second Run - Second Selection
Run Second-Second Selection

(* Correct voltages due to battery pack.. *)
vLCorrect1=Table[0,{12930}];
vLCorrect2=Table[.3,{39102}];
vLCorrect3=Table[0,{3969}];
vLCorrect4=Flatten[AppendTo[vLCorrect1,vLCorrect2]];
vLCorrect=Flatten[AppendTo[vLCorrect4,vLCorrect3]];

vRCorrect1=Table[0,{12928}];
vRCorrect2=Table[.3,{39102}];
vRCorrect3=Table[0,{3969}];
vRCorrect4=Flatten[AppendTo[vLCorrect1,vLCorrect2]];
vRCorrect=Flatten[AppendTo[vLCorrect4,vLCorrect3]];



(* Adjust Selection - TS is at operating velocity... *)

vLCorrect1=Table[0,{12930}];
vLCorrect2=Table[.5,{24603}];
vLCorrect3=Table[0.3,{18468}];
vLCorrect4=Flatten[AppendTo[vLCorrect1,vLCorrect2]];
vLCorrect=Flatten[AppendTo[vLCorrect4,vLCorrect3]];

SelectionStart2=40000;
SelectionEnd2=600000;

Samplerate=10;
TimeSelect2=Take[TimeF,{SelectionStart2,SelectionEnd2,Samplerate}];
TSmphSelect2=Take[TSmphF,{SelectionStart2,SelectionEnd2,Samplerate}];
BetaVoltSelect2=Take[BetaVoltF,{SelectionStart2,SelectionEnd2,Samplerate}];
TransLVoltSelect2UM=Take[TransLVoltF,{SelectionStart2,SelectionEnd2,Samplerate}];
```

```
TransLVoltSelect2=TransLVoltSelect2UM+vLCorrect;
TransRVoltSelect2UM=Take[TransRVoltF,{SelectionStart2,SelectionEnd2,Samplerate}];
TransRVoltSelect2=TransRVoltSelect2UM+vLCorrect;
WSVoltSelect2=Take[WSVoltF,{SelectionStart2,SelectionEnd2,Samplerate}];
TSSelect2=TSmphSelect2*ms;
WSSelect2=(Abs[(WSVoltSelect2*freq)-TSSelect2]+0.3)*ms;
SpeedSelect2=TSSelect2+WSSelect2;
TotalDirSelect2=(((BetaVoltSelect2-MinBetaVolt)/MaxBetaVolt)*360);
TransLPaSelect2=(TransLVoltSelect2-TransLZero)*TransLVolts2PSI;
TransLSelect2=TransLPaSelect2*PSItoPa;
TransRPaSelect2=(TransRVoltSelect2-TransRZero)*TransRVolts2PSI;
TransRSelect2=TransRPaSelect2*PSItoPa;
GaugeLPaSelect2=TransLSelect2;
GaugeRPaSelect2=TransRSelect2;
DeltaCPSelect2=DeltaPSelect2/(0.5*1.22*(SpeedSelect2^2));
TimeLengthSelect2=Dimensions[TimeSelect2]/100;
xSelect2=Flatten[{0,TimeLengthSelect2}];
DeltaPNormSelect2=(Flatten[DeltaPSelect2]/Mean[kvaluesSelect2]);

Export Data;
(*------------------------------ EXPORT VARIABLES ------------------------------*)

(* Yaw Angles *)
Export["...BetaDSelect2.csv",Flatten[BetaDSelect2],"CSV"];
(* Transducer L Pressure *)
Export[".../GaugeLPaSelect2.csv",Flatten[GaugeLPaSelect2],"CSV"];
(* Transducer R Pressure *)
Export[".../GaugeRPaSelect2.csv",Flatten[GaugeRPaSelect2],"CSV"];
(* DeltaP Pressure *)
Export["...DeltaPSelect2.csv",Flatten[DeltaPSelect2],"CSV"];
(* Wind Speed *)
Export["...WSSelect2.csv",Flatten[WSSelect2],"CSV"];
(* Truck Speed *)
Export[".../TSSelect2.csv",Flatten[TSSelect2],"CSV"];
(* Time *)
Export[".../TimeSelect2.csv",Flatten[TimeSelect2],"CSV"];
(* k Values *)
Export["...kvaluesSelect2.csv",Flatten[kvaluesSelect2],"CSV"];

(*------------------------------------------------------------------------------*)
```

B.11 Full Scale Errors Analysis

Experimental measurements due to finite resolution are subject to measurement errors. The following errors were present within the full scale experimental apparatus shown below in Tab.(B.6).

Item	Error
Inspeed Vortex Wind Speed Sensor	±4.0 (%)
Inspeed Wind Direction Sensor	±0.5(%)
Omega PX138-0.3D5V Differential Pressure Transducers	±0.5(%)
Race Technology 20 Hz GPS Receiver	±0.075 ms^{-1}

Table B.6: Full Scale Experimental Errors on Test Equipment.

B.11.1 Full Scale Error Propagation

For a measured quantity 'R', the uncertainty in the measurement (δR) is defined for some common functions by Eqs.(B.53 - B.53).

B.11.2 Error Propagation

- Addition or Subtraction ($R = X + Y - Z$):

$$\delta R = \sqrt{(\delta X)^2 + (\delta Y)^2 + (\delta Z)^2} \tag{B.49}$$

- Multiplication or Division ($R = \frac{X \cdot Y}{Z}$):

$$\delta R = |R| \cdot \sqrt{\left(\frac{\delta X}{X}\right)^2 + \left(\frac{\delta Y}{Y}\right)^2 + \left(\frac{\delta Z}{Z}\right)^2} \tag{B.50}$$

- Multiplication by a Constant ($R = c \cdot X$):

$$\delta R = |R| \cdot \delta X \tag{B.51}$$

- Polynomial Functions ($R = X^n$):

$$\delta R = |n| \cdot \frac{\delta X}{X} \cdot |R| \tag{B.52}$$

- General Functions: $(R = R(X, Y, ..N))$:

$$\delta R = |R| \cdot \sqrt{\left(\frac{\partial R}{\partial X} \cdot \delta X\right)^2 + \left(\frac{\partial R}{\partial Y} \cdot \delta Y\right)^2 + ... \left(\frac{\partial R}{\partial N} \cdot \delta N\right)^2} \tag{B.53}$$

B.11.3 Application to Measured Data

Using the data in Table B.6 along with the propagation formulas defined in Eqs.(B.49 - B.53), gives the following values:

- Total Velocity $(V_{(Total)})$:

$$\frac{\delta V}{V} = \sqrt{\left(\delta V_{(Truck)}\right)^2 + \left(\delta V_{(Wind)}\right)^2} = \sqrt{(0.4)^2 + (0.5)^2} = 0.6\% \tag{B.54}$$

- Pressure Coefficient (ΔC_P):

$$\frac{\delta C_P}{C_P} = \sqrt{\left(\frac{\delta P_{(left)}}{P}\right)^2 + \left(\frac{\delta P_{(right)}}{p}\right)^2 + \left(\frac{\delta V_\infty}{V}\right)^2} \tag{B.55}$$

$$\frac{\Delta C_P}{C_P} = \sqrt{(0.5)^2 + (0.5)^2 + (0.6)^2} = 0.9\% \tag{B.56}$$

This page intentionally left blank.

Appendix C

Computational Fluid Dynamics

C.1 Reynolds-Averaged Navier-Stokes

Reynolds-Averaged Navier-Stokes (RANS) equations are time averaged equations for the motion of fluid flow. They arise from a Reynolds decomposition whereby an instantaneous quantity is decomposed into its time-averaged and time varying quantitates. RANS equations are not a closed set and as a result it is not possible to solve for Reynolds stresses directly. Turbulence models are therefore required to represent the Reynolds stresses. RANS models are the current most widely applied algorithms used in commercial code. Extensive testing and validation with fast implementation make them the perfect solution for both Education and Industry.

The RANS model is based on Reynolds decomposition where the flow is divided into a mean and fluctuating part given by

$$\tilde{P} = \overline{P} + p \tag{C.1}$$

$$\tilde{u_i} = \overline{U_i} + u_i \tag{C.2}$$

$$\tilde{\Phi} = \overline{\Phi} + \phi \tag{C.3}$$

where p is the pressure, u is the velocity and Φ can be another quantity in the flow field such as temperature. These modified variables are then substituted into the Navier-Stokes Equations and averaged in time.

Substituting into the Navier-Stokes equations (Eq. B.24) and taking an ensemble average, yields the Reynolds-Averaged Navier-Stokes equations

$$\frac{\partial \overline{u_i}}{\partial x_i} = 0 \tag{C.4}$$

$$\frac{\partial \overline{u_i}}{\partial t} + \overline{u_j}\frac{\partial \overline{u_i}}{x_j} + \overline{u'_j \frac{\partial u'_i}{\partial x_j}} = \overline{f_i} - \frac{1}{\rho}\frac{\partial \overline{p}}{\partial x_i} + v\frac{\partial^2 \overline{u_i}}{\partial x_j \partial x_j} \tag{C.5}$$

Defining the mean rate of stress tensor by

$$\overline{S_{ij}} = \frac{1}{2}\left(\frac{\partial \overline{u_i}}{\partial x_j} + \frac{\partial \overline{u_j}}{\partial x_i}\right) \tag{C.6}$$

Substituting (Eq. C.6) into (Eq. C.5) and removing the time dependence of resulting terms yields

$$\rho\frac{\partial \overline{u}_j \overline{u}_i}{\partial x_j} = \rho\overline{f_i} + \frac{\partial}{\partial x_j}\left[-\overline{p}\delta_{ij} + 2\mu\overline{S}_{ij} - \rho\overline{u'_i u'_j}\right] \tag{C.7}$$

The above equations are unclosed because they contain terms of unknown fluctuating components. The Reynolds stresses contained within these fluctuating components must therefore be modelled in order to solve the equations. Boussinesq [107] employed a hypothesis to relate the Reynolds stress to the mean velocity gradients given by

$$-\rho\overline{u'_i u'_j} = \mu_t\left(\frac{\partial u_i}{\partial x_j} + \frac{\partial u_j}{\partial x_i}\right) - \frac{2}{3}\left(\rho k + \mu_t\frac{\partial u_k}{\partial x_k}\right) \tag{C.8}$$

where μ_t is the turbulent viscosity. The Boussinesq hypothesis is used in the Spalart-Allmaras model, the k-ϵ models, and the k-ω models.

RANS models can be classified into three main categories:

- Linear eddy - viscosity models
  - Algebraic (zero equation models)
  - Single equation models
  - Two equation models
- Non - linear eddy viscosity
- Second moment closure models (SMCM)

C.2 RANS One Equation Model

C.2.1 Spalart-Allmaras Model

The Spalart-Allmaras model [108] is a one equation turbulence model that solves the transport equation for a viscosity-like variable ($\tilde{\nu}$). The model incorporates a destructive term dependent on the distance to the wall. The modified viscosity-like variable ($\tilde{\nu}$) is similar to the turbulent kinematic viscosity except for near wall treatment where viscous effects dominate.

The one-equation model is given by

$$\frac{\partial(\rho\tilde{\nu})}{\partial t}+\frac{\partial(\rho\tilde{\nu}u_i)}{\partial x_i}=G_\nu+\frac{1}{\sigma\tilde{\nu}}\left[\frac{\partial}{\partial x_j}\left[(\mu+\rho\tilde{\nu})\frac{\partial\tilde{\nu}}{\partial x_j}\right]+C_{b2}\rho\left(\frac{\partial\tilde{\nu}}{\partial x_j}\right)^2\right]-Y_\nu+S_{\tilde{\nu}} \quad \text{(C.9)}$$

where G_ν = Turbulent viscosity production, Y_ν = Turbulent viscosity destruction, near wall, $S_{\tilde{\nu}}$ = Source term, $\sigma_{\tilde{\nu}}$ and C_{b2} are constants. The turbulent viscosity is computed by

$$\mu_t=\rho\tilde{\nu}f_{\nu1} \quad \text{(C.10)}$$

where $f_{v1}=\frac{\chi^3}{\chi^3+C_{\nu1}^3}$ and $\chi=\frac{\tilde{\nu}}{\nu}$ and the production of turbulent viscosity is given by

$$G_\nu=C_{b1}\rho\tilde{S}\tilde{\nu} \quad \text{(C.11)}$$

$$\tilde{S}\equiv S+\frac{\tilde{\nu}}{k^2d^2}f_{\nu2} \quad \text{(C.12)}$$

$$S=\sqrt{2\Omega_{ij}\Omega_{ij}} \quad \text{(C.13)}$$

$$\Omega_{ij}=\frac{1}{2}\left(\frac{\partial u_i}{\partial x_j}-\frac{\partial u_j}{\partial x_i}\right) \quad \text{(C.14)}$$

$$f_{\nu2}=1-\frac{\chi}{1+\chi f_{\nu1}} \quad \text{(C.15)}$$

where d = distance from the field point to the nearest wall, C_{b1} and k are constants. The destruction of turbulent viscosity is given by

$$Y_\nu=C_{w1}\rho f_w\left(\frac{\tilde{\nu}}{d}\right)^2 \quad \text{(C.16)}$$

where:

$$f_w = g\left[\frac{1+c_{w3}^6}{g^6+C_{w3}^6}\right] \tag{C.17}$$

$$g = r + C_{w2}\left(r^6 - r\right) \tag{C.18}$$

$$r = \frac{\nu}{\tilde{S}k^2d^2} \tag{C.19}$$

where C_{w1}, C_{w2} and C_{w3} are constants.

C.3 RANS Two Equation Models

Computational Fluid Dynamics used within industry focuses on the families contained within the two equation models. The two equation models use the Boussinesq assumption to compute the local conditions for the Reynolds stresses. In reality, the Reynolds stresses could be convected by both the mean and the fluctuating velocities. The two equation models are used despite their known limitations as they offer reduced computational cost over the second moment closure models (SMCM).

The two main families of the two equation models are k-ϵ and k-ω. Details about the performance and limitation of each family are listed below.

C.3.1 k-ϵ

One of the more common families of turbulence models is the k-ϵ model. Two extra equations are solved to represent the flow turbulence. The two transported variables are k and ϵ, the turbulent kinetic energy and the turbulent dissipation, respectively.

The k-ϵ family consists of three sub models: Standard, RNG and Realizable. The Standard model was the primary model developed and is widely used in engineering calculations due to its robustness.

The RNG model contains an additional term in the turbulent dissipation equation enabling higher accuracy in strained flows.

The Realizable model is the latest model to be developed, it introduces a newer formulation for turbulent viscosity and dissipation rate. The Realizable k-ϵ model more accurately models the spreading rate of both planar and round jets. In addition it also performs well in flows containing rotation, separation, recirculation or boundary layers under strong adverse pressure gradients.

Results from Pointer et al. [76] have shown that the k-ϵ family of turbulence models can predict the drag coefficient on a generic car geometry to within 3% of the experimental value.

The k-ϵ model is the baseline model for solving k (turbulent energy production term) and ϵ (turbulent energy dissipation term). Coefficients within the model are empirically derived. The model is valid for fully turbulent flows.

- Advantages: Robust, widely used, suitable for initial iterations and initial screening of alternative designs.

- Disadvantages: Performs poorly for complex flows involving sever pressure gradients, separation and strong streamline curvature.

Transport Equation

The transport equation for the Standard k-ϵ model is given by

$$\frac{\partial(\rho k)}{\partial t} + \frac{\partial(\rho k u_j)}{\partial x_j} = \frac{\partial}{\partial x_i}\left[\left(\mu + \frac{\mu_t}{\sigma_k}\right)\frac{\partial k}{\partial x_j}\right] + G_k + G_b - \rho\epsilon - Y_M + S_k \tag{C.20}$$

$$\frac{\partial(\rho\epsilon)}{\partial t} + \frac{\partial(\rho\epsilon u_j)}{\partial x_j} = \frac{\partial}{\partial x_j}\left[\left(\mu + \frac{\mu_t}{\sigma_\epsilon}\right)\frac{\partial \epsilon}{\partial x_j}\right] + C_{1\epsilon}\frac{\epsilon}{k}(G_k + C_{3\epsilon}G_b) - C_{2\epsilon}\rho\frac{\epsilon^2}{k} + S_\epsilon \tag{C.21}$$

C.3.2 Standard k-ϵ

The transport equation for the Standard k-ϵ model is given by

$$\frac{\partial(\rho k)}{\partial t} + \frac{\partial(\rho k u_j)}{\partial x_j} = \frac{\partial}{\partial x_i}\left[\left(\mu + \frac{\mu_t}{\sigma_k}\right)\frac{\partial k}{\partial x_j}\right] + G_k + G_b - \rho\epsilon - Y_M + S_k \tag{C.22}$$

$$\frac{\partial(\rho\epsilon)}{\partial t} + \frac{\partial(\rho\epsilon u_j)}{\partial x_j} = \frac{\partial}{\partial x_j}\left[\left(\mu + \frac{\mu_t}{\sigma_\epsilon}\right)\frac{\partial \epsilon}{\partial x_j}\right] + C_{1\epsilon}\frac{\epsilon}{k}(G_k + C_{3\epsilon}G_b) - C_{2\epsilon}\rho\frac{\epsilon^2}{k} + S_\epsilon \tag{C.23}$$

with constants: $C_{1\epsilon} = 1.44$, $C_{2\epsilon} = 1.92$ and turbulent Prandtl Numbers: $\sigma_\epsilon = 1.3$, $\sigma_k = 1.0$. Where S_ϵ and S_k are the source terms. G_k is the production of turbulent kinetic energy, defined by

$$G_k = -\rho\overline{u_i' u_j'}\frac{\partial u_j}{\partial x_i} = \mu_t S^2 \tag{C.24}$$

where S is the strain-rate tensor: $S = \sqrt{2S_{ij}S_{ij}}$ and the turbulent viscosity (μ_t) is calculated using

$$\mu_t = \rho C_\mu \frac{k^2}{\epsilon} \tag{C.25}$$

with constant $C_\mu = 0.09$ and Y_M accounts for compressibility effects and is modelled by

$$Y_M = 2\rho\epsilon M_t^2 \tag{C.26}$$

where M_t is the turbulent Mach number defined as: $M_t = \sqrt{\frac{k}{a^2}}$.

C.3.2.1 k-ϵ RNG

The k-ϵ RNG model is a variant of the standard k-ϵ model. Equations and coefficients are derived analytically. Significant changes are made to ϵ to improve the ability to model highly strained flows. Additional option within the model to account for low Re flows.

- Advantages: Improved accuracy for complex shear flows involving rapid strain, moderate swirl, vortices and locally transition flows.

The k-ϵ RNG model is a variant of the standard k-ϵ model. The 'realizable' term accounts for mathematical constraints placed on the turbulence model.

- Advantages: Slightly more accurate and faster convergence than RNG.
- Disadvantages: Subjected to limitations due to isotropic eddy viscosity assumptions.

Transport Equation

The transport equations for the Realizable k-ϵ model are given by

$$\frac{\partial(\rho k)}{\partial t} + \frac{\partial(\rho k u_j)}{\partial x_j} = \frac{\partial}{\partial x_i}\left[\left(\mu + \frac{\mu_t}{\sigma_k}\right)\frac{\partial k}{\partial x_j}\right] + G_k + G_b - \rho\epsilon - Y_M + S_k \qquad \text{(C.27)}$$

$$\frac{\partial(\rho\epsilon)}{\partial t}+\frac{\partial(\rho\epsilon u_j)}{\partial x_j} = \frac{\partial}{\partial x_j}\left[\left(\mu + \frac{\mu_t}{\sigma_\epsilon}\right)\frac{\partial \epsilon}{\partial x_j}\right]+\rho C_1 S_\epsilon-\rho C_2 S_\epsilon-\rho C_2\frac{\epsilon^2}{k+\sqrt{\nu\epsilon}}+C_{1\epsilon}\frac{\epsilon}{k}C_{3\epsilon}G_b+S_\epsilon \qquad \text{(C.28)}$$

C.3.3 Realizable k-ϵ

The transport equations for the Realizable k-ϵ model are given by

$$\frac{\partial(\rho k)}{\partial t} + \frac{\partial(\rho k u_j)}{\partial x_j} = \frac{\partial}{\partial x_i}\left[\left(\mu + \frac{\mu_t}{\sigma_k}\right)\frac{\partial k}{\partial x_j}\right] + G_k + G_b - \rho\epsilon - Y_M + S_k \qquad \text{(C.29)}$$

$$\frac{\partial(\rho\epsilon)}{\partial t}+\frac{\partial(\rho\epsilon u_j)}{\partial x_j} = \frac{\partial}{\partial x_j}\left[\left(\mu + \frac{\mu_t}{\sigma_\epsilon}\right)\frac{\partial \epsilon}{\partial x_j}\right]+\rho C_1 S_\epsilon-\rho C_2 S_\epsilon-\rho C_2\frac{\epsilon^2}{k+\sqrt{\nu\epsilon}}+C_{1\epsilon}\frac{\epsilon}{k}C_{3\epsilon}G_b+S_\epsilon \qquad \text{(C.30)}$$

where:

$$S = \sqrt{2S_{ij}S_{ij}} \tag{C.31}$$

$$C_1 = \max\left[0.43, \frac{\eta}{\eta+5}\right] \tag{C.32}$$

$$\eta = S\frac{k}{\epsilon} \tag{C.33}$$

G_k represents the generation of turbulent kinetic energy due to mean velocity gradients. K_b is the generation of turbulent kinetic energy due to buoyancy, both are calculated in the same manner as k-$\epsilon_{(Standard)}$ model.

The turbulent viscosity is modelled by

$$\mu_t = \rho C_\mu \frac{k^2}{\epsilon} \tag{C.34}$$

where:

$$C_\mu = \frac{1}{A_0 + A_S\frac{kU*}{\epsilon}} \tag{C.35}$$

$$A_0 = 4.04 \tag{C.36}$$

$$U* = \sqrt{S_{ij}S_{ij} + \tilde{\Omega_{ij}}\tilde{\Omega_{ij}}} \tag{C.37}$$

$$\tilde{\Omega_{ij}} = \Omega_{ij} - 2\epsilon_{ijk}\omega_k \tag{C.38}$$

$$\Omega_{ij} = \overline{\Omega_{ij}} - \epsilon_{ijk}\omega_k \tag{C.39}$$

$$A_s = \sqrt{6}cos(\phi) \tag{C.40}$$

$$\phi = \frac{1}{3}cos^{-1}(\sqrt{6W}) \tag{C.41}$$

$$W = \frac{S_{ij}S_{jk}S_{ki}}{\tilde{S}^3} \tag{C.42}$$

$$\tilde{S} = \sqrt{2S_{ij}S_{ij}} \tag{C.43}$$

$$S_{ij} = \frac{1}{2}\left(\frac{\partial u_i}{\partial x_j} - \frac{\partial u_j}{\partial x_i}\right) \tag{C.44}$$

C.3.4 k-ω

The second most common family of turbulence models is the k-ω model. Two equations are again solved to represent the flow turbulence. The two transported variables are k, the turbulent kinetic energy and (ω/k), the specific dissipation rate. The k-ω family consists of two sub models: Standard and SST.

The Standard model was the primary model developed and is widely used in engineering calculations for internal flows due to its superior performance of wall-bounded flows.

The SST model contains a blending function that combines near wall flow modelled as k-ω and k-ϵ away from the wall. This has the added benefit over k-ω at reducing the prediction of early separation.

C.3.4.1 Standard k-ω

The k-ω model is the baseline model for solving k and ω. The default k-ω model demonstrates superior performance for wall bounded and low-Re flows. Improved prediction over k-ϵ for transitions and model options to include transitional and free shear flows.

- Advantages: Superior performance of wall-bounded boundary layers. Suitable for complex boundary layer flows under adverse pressure gradients and separation.

- Disadvantages: Predicts separation excessive and early.

C.3.4.2 SST k-ω

The SST k-ω model is a variant of the standard k-ω model. It uses the standard k-ω model for near walls and the standard k-ϵ away from walls using a blending function.

- Advantages: Similar benefits as standard k-ω with improved performance on separation prediction.

- Disadvantages: Not available for compressible flows, less suitable for free shear flows.

C.4 RANS SMCM

Unlike the two equation models which use the Boussinesq assumption to compute the local conditions for the Reynolds stresses, the Second moment closure models (SMCM) such as the Reynolds Stress Model (RSM) solve the stresses directly with the transport equations. As a result, isotropic viscosity assumptions about the flow are avoided. A quadratic pressure-strain option improves the performance for many basic shear flows.

- Advantages: Most theoretically sound RANS model. Avoids isotropic eddy viscosity assumption. Suitable for complex 3D flows with strong streamline curvature, swirl and rotation.

- Disadvantages: Computationally intensive, tougher to converge due to close coupling of equations.

C.5 Large Eddy Simulation

Kolmogrov proposed that turbulent flow contained varying sized "eddies". Large eddies are unstable and eventually break up to form smaller eddies, kinetic energy is transferred from the larger to the smaller eddies. Resolution of all of these turbulence lengths can be achieved via Direct Numerical Simulation (DNS). DNS, however, is computationally intensive, even for small domains with simple geometry. Large Eddy Simulation (LES) therefore filters the spatial field $\overline{\phi(x)}$ to remove smaller length scales. The analogy of the process is to add a low-pass filter to a DNS domain. The process allows higher fidelity than RANS, however, LES still models the sub-grid scale turbulence of the solution, rather than resolving them. LES does not time average the varying flow fields and hence allows for time dependent effects of the flow to be investigated.

The filter spatial filter used by Fluent is given by

$$\overline{\phi}(x) = \int_D \phi x' G(x, x') dx' \tag{C.45}$$

where D is the fluid domain and G is the filter function that determines the length scale of the resolved eddies.

The finite-volume discretisation improves the filtering operation, given by

$$\overline{(x)} = \frac{1}{V} \int_\nu \phi(x') dx', x' \in \nu \tag{C.46}$$

where V is the volume of a computational cell. The filter function $G(x, x')$ is defined by

$$G(x, x') = \begin{cases} 1/V, & \text{x}' \in \nu \\ 0, & \text{x}' \text{ otherwise} \end{cases} \tag{C.47}$$

The filter applied to the Navier-Stokes equation yields:

$$\frac{\partial p}{\partial t} + \frac{\partial}{\partial x_i}(\rho \overline{u_i}) = 0 \tag{C.48}$$

and

$$\frac{\partial}{\partial t}(\rho \overline{u_i}) + \frac{\partial}{\partial x_j}(\rho \overline{u_i u_j}) = \frac{\partial}{\partial x_j}(\sigma_{ij}) - \frac{\partial \overline{p}}{\partial x_i} - \frac{\partial \tau_{ij}}{\partial x_j} \tag{C.49}$$

where σ_{ij} is the stress tensor due to molecular viscosity defined by

$$\sigma_{ij} \equiv \left[\mu\left(\frac{\partial\overline{u_i}}{\partial x_j} + \frac{\partial\overline{u_j}}{\partial x_i}\right)\right] - \frac{2}{3}\mu\frac{\partial\overline{u_l}}{\partial x_l}\delta_{ij} \tag{C.50}$$

and the subgrid-scale stress (τ_{ij}) defined by

$$\tau_{ij} \equiv \rho\overline{u_i u_j} - \rho\overline{u_i}\,\overline{u_j} \tag{C.51}$$

The subgrid-scale stresses resulting from the filtration operation are unknown and require modelling. The subgrid-scale turbulent stresses are commuted in the same manner as the RANS approach mentioned earlier. The subgrid-scale turbulent flux of a scalar ϕ is modelled using a subgrid-scale turbulent Prandtl number given by

$$q_j = \frac{\mu_t}{\sigma_t}\frac{\partial\phi}{\partial x_j} \tag{C.52}$$

where q_j is the subgrid-scale flux. The subgrid-scale eddy viscosity (μ_t) has a variety of models, the most applicable of which is the "Dynamic Kinetic Energy Subgrid-Scale Model" available in Fluent. In this model μ_t is defined by

$$\mu_t = C_k k_{sgs}^{1/2}\Delta_f \tag{C.53}$$

where k_{sgs} is the subgrid-scale kinetic energy, given by

$$k_{sgs} = \frac{1}{2}\left(\overline{u_k^2} - \overline{u_k}^2\right) \tag{C.54}$$

where Δ_f is the filter size, determined by $\Delta_f \equiv V^{1/3}$

The subgrid-scale stress can therefore be written as:

$$\tau_{ij} - \frac{2}{3}k_{sgs}\delta_{ij} = -2C_k k_{sgs}^{1/2}\Delta_f\overline{S_{ij}} \tag{C.55}$$

and k_{sys} is obtained by solving the transport equation:

$$\frac{\partial\overline{k_{sgs}}}{\partial_t} + \frac{\partial\overline{u_j}\,\overline{k_{sgs}}}{\partial x_j} = -\tau_{ij}\frac{\partial\overline{u_i}}{\partial x_j} - C_\varepsilon\frac{k_{sgs}^{3/2}}{\Delta_f} + \frac{\partial}{\partial x_j}\left(\frac{\mu_t}{\sigma_k}\frac{\partial k_{sgs}}{\partial x_j}\right) \tag{C.56}$$

where C_k and C_ε are model constants determined dynamically and σ_k is fixed at a value of 1.0

C.6 Commercial Numerical Solvers

ANSYS Fluent has a variety of Reynolds-Averaged Navier-Stokes (RANS) turbulence models. Fluent provides different sub models for each solver as well as different methods for wall treatment. The solvers used in this project for modelling the fluid flow are: Spalart-Allmaras and Realizable k-ϵ, details of the solver are listed in Sec.(C.1). The full list of numerical solvers available is shown in the Fluent User's Manual [75]

C.7 Standard Wall Function

Fluent has the ability to use a wall function to eliminate the need to modify the turbulence models to account for the presence of the wall. The standard wall function is based on a method proposed by Launder [109].

For the velocity contained within the logarithmic region, the law-of-the-wall for mean velocity yields:

$$U^* = \frac{1}{k} ln\left(Ey^*\right) \tag{C.57}$$

$$U^* = \frac{U_p C_\mu^{1/4} k_p^{1/2}}{\tau_\omega/\rho} \tag{C.58}$$

$$y^* = \frac{\rho C_\mu^{1/4} k_p^{1/2} y_p}{\mu} \tag{C.59}$$

where $k = 0.4187$ is the von Karman constant, $E = 9.793$, U_p = Mean velocity of the fluid, k_p = Turbulent kinetic energy at point P, y_p = Distance from the wall to point P and μ is the dynamic viscosity.

The law above applies for the region: $30 < y^* < 300$. For $y^* < 11.225$ Fluent applies a laminar stress-strain relationship.

C.8 Upwind Discretisation Scheme

By default, Fluent stores discrete values of the cell-centred value (ϕ) at the cell centre. For convection terms face values (ϕ_f) are required. Interpolation over cell centre values are therefore conducted. This is achieved through the use of an upwind discretisation scheme. An upwind discretisation scheme derives the face value (ϕ_f) from the upwind cells relative to the normal velocity (v_n).

For second order accuracy, the cell faces are computed using a multidimensional linear reconstruction.

High-order accuracy is achieved via a Taylor series expansion of the cell-centred solution about the cell centroid.

ϕ_f for second-order unwinding is computed by

$$\phi_{f,SOU} = \phi + \nabla\phi \cdot \overrightarrow{r} \tag{C.60}$$

where ϕ and $\nabla\phi$ are the cell-centred value and upstream cell gradient and $\overrightarrow{r}$ is the displacement vector from the upstream cell centroid to the face centroid. $\nabla\phi$ is maxima/minima limited such that no new extremum values are introduced.

C.9 SIMPLE Pressure - Velocity Coupling

SIMPLE or Semi-Implicit Method for Pressure-Linked Equations is an iterative algorithm designed to relate velocity and pressure corrections to enforce mass conservation and obtain the pressure field. This correction is required for non-compressible flows where pressure does not explicitly appear in the continuity equation. The algorithm is designed to calculate the pressure and velocity at different nodes in the control volume. The calculation at different nodal points removes the effect that a non-uniform pressure field can act like a uniform one. As a result, the scalar variables such as pressure and density at ordinary points but with velocity components on staggered grids centred on the cell face.

C.10 2D Meshes

Enlarged images of the 2D geometry used for the CFD simulations is shown in Secs.(C.10.1 - C.10.4). The images contain each of the three mesh densities used for the 2D simulations: 20,000, 40,000 and 80,000 cells.

C.10.1 20k Frontal Section

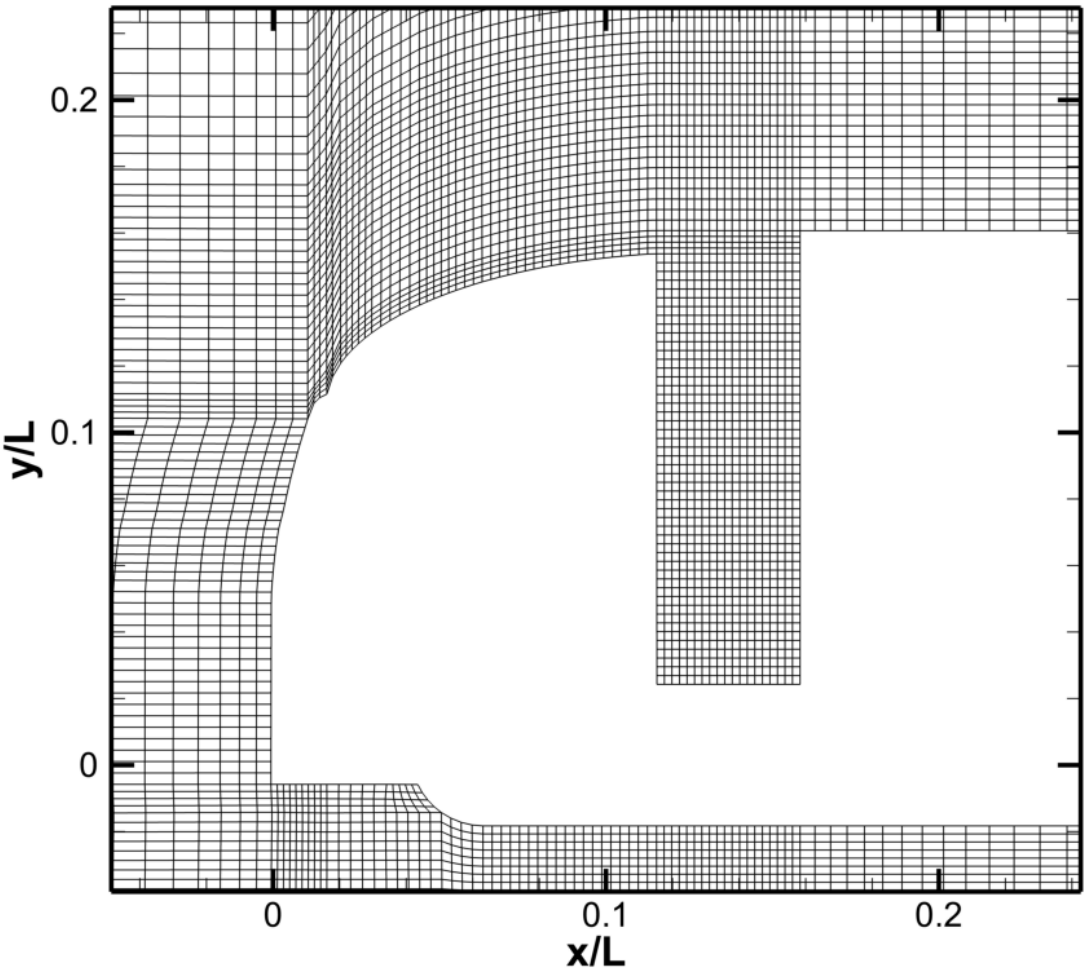

Figure C.1: Enlarged Frontal Section of 20k Grid Cell Mesh.

C.10.2 40k Frontal Section

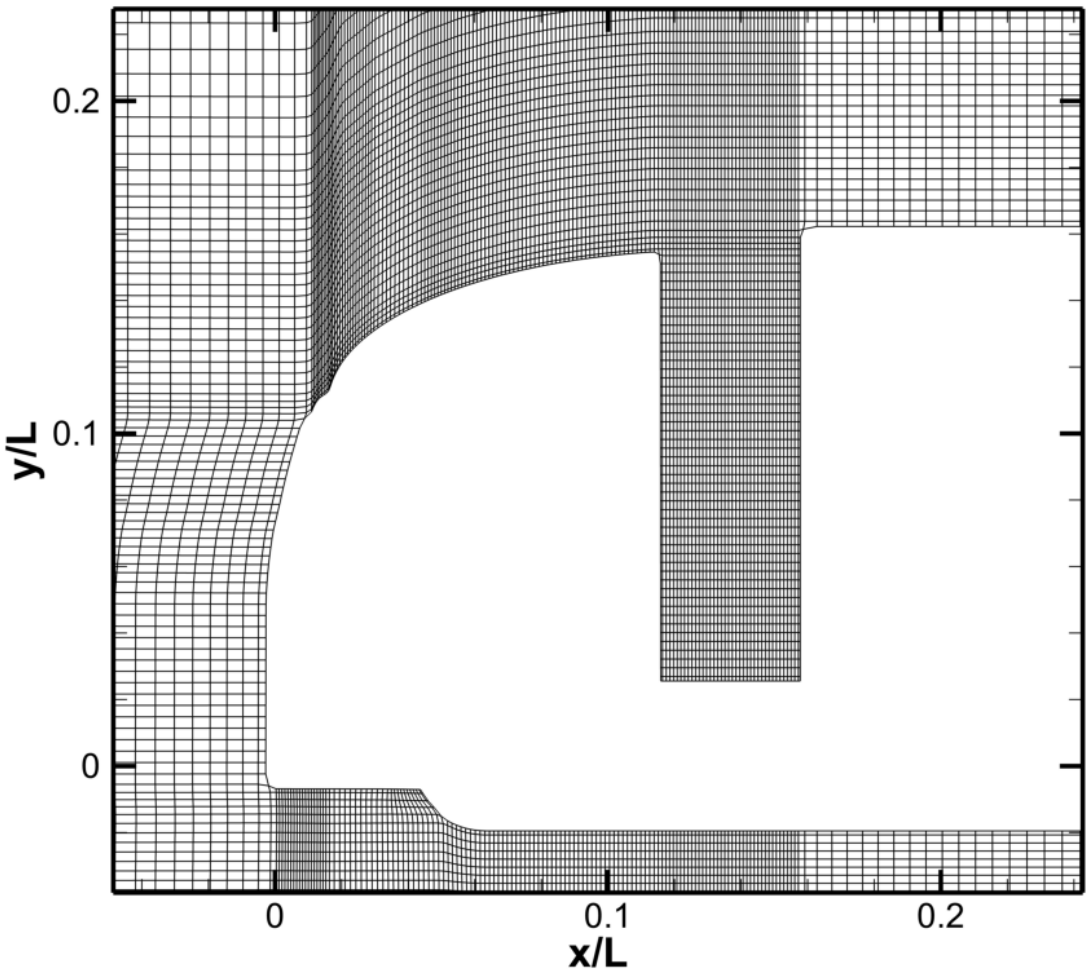

Figure C.2: Enlarged Frontal Section of 40k Grid Cell Mesh.

C.10.3 80k Frontal Section

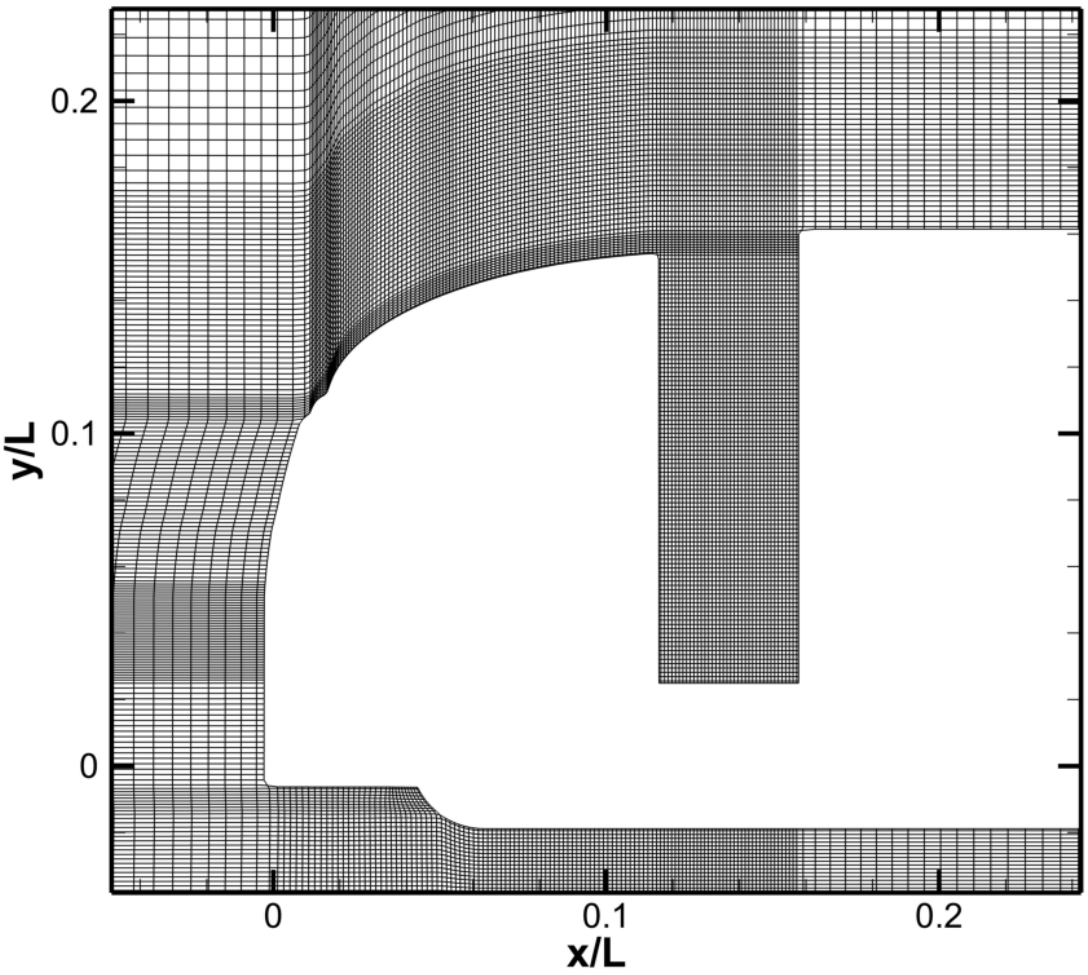

Figure C.3: Enlarged Frontal Section of 80k Grid Cell Mesh.

C.10.4 20k Rear Sections

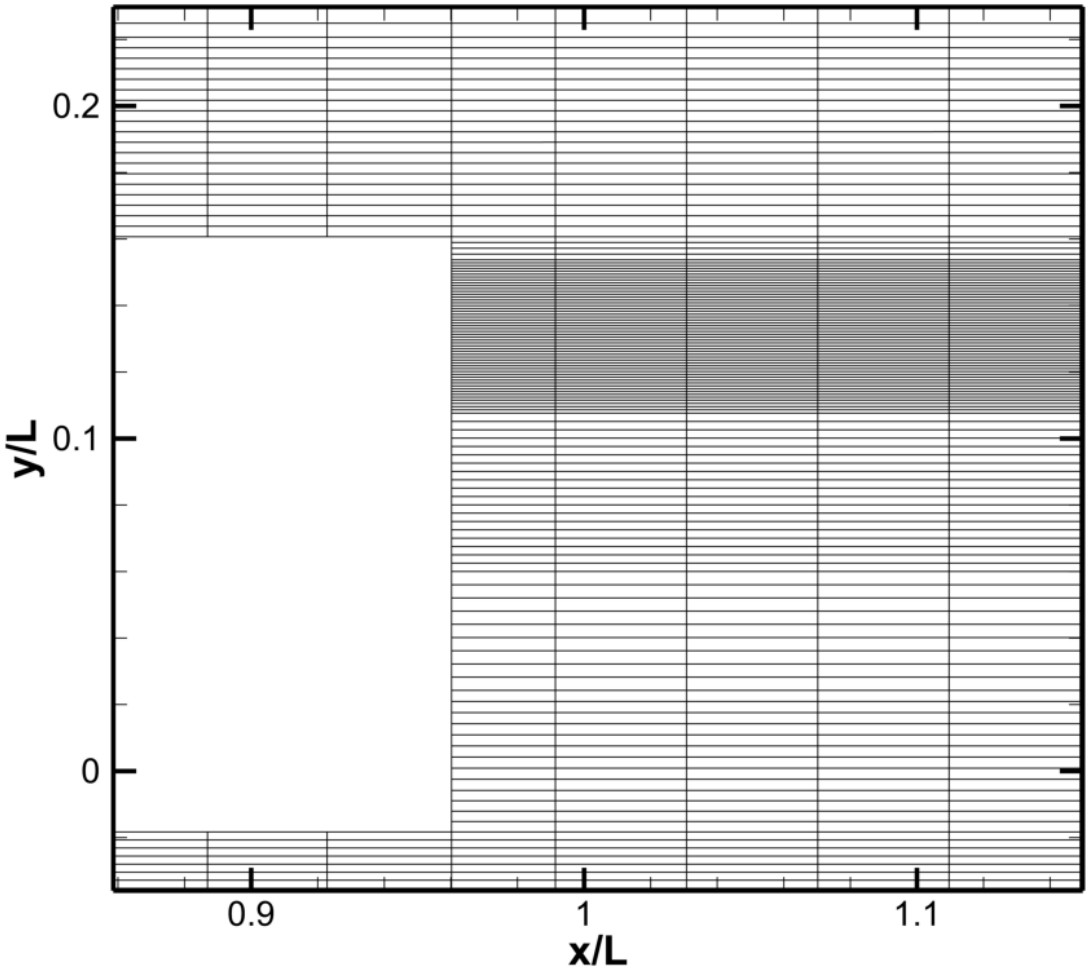

Figure C.4: Enlarged Rear Section of 20k Grid Cell Mesh.

C.10.5 40k Rear Sections

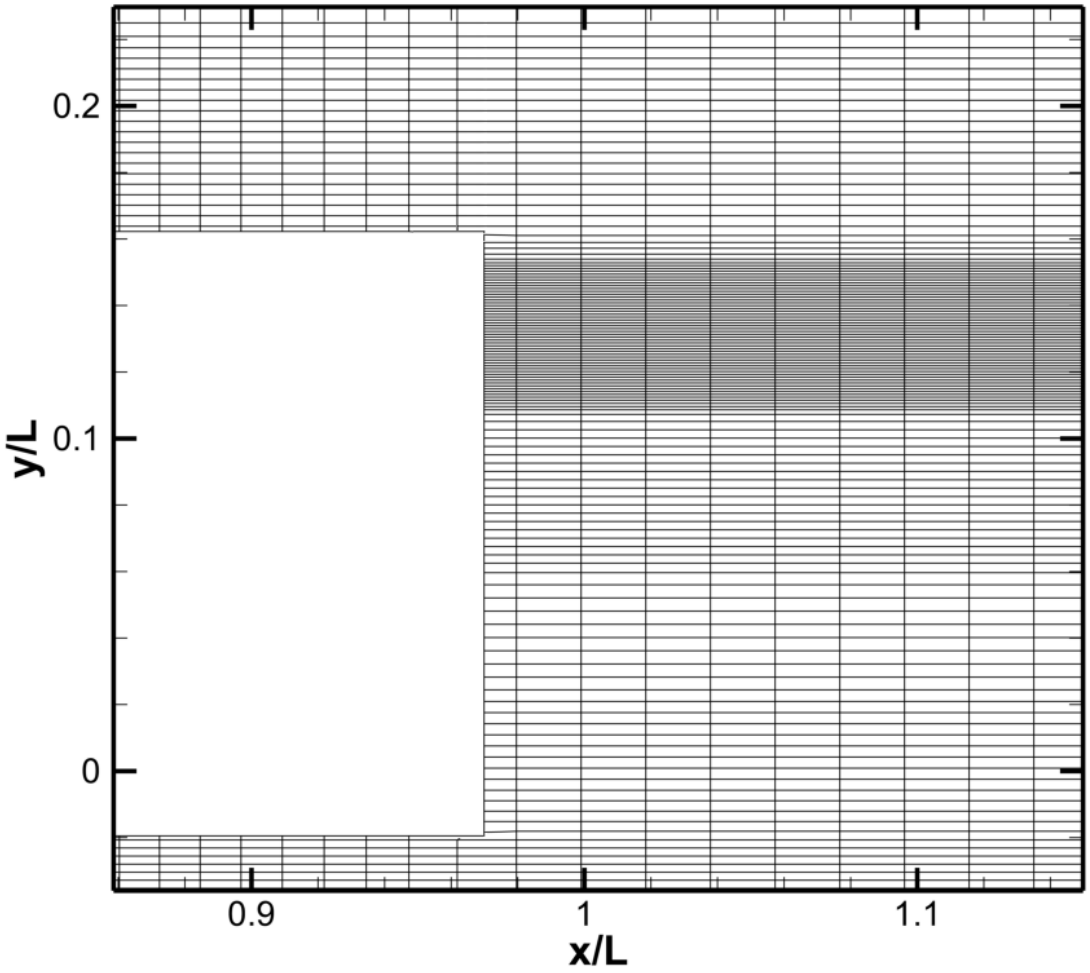

Figure C.5: Enlarged Rear Section of 40k Grid Cell Mesh.

C.10.6 80k Rear Sections

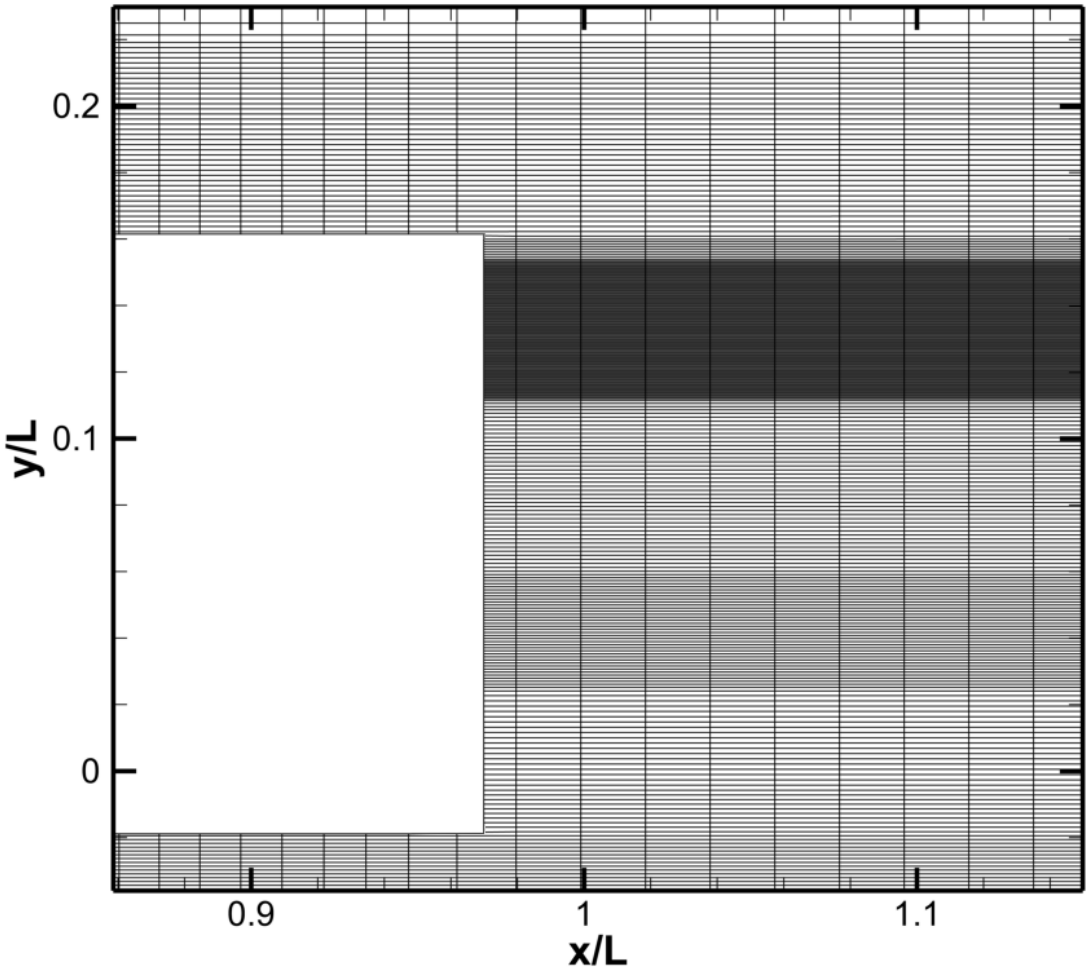

Figure C.6: Enlarged Rear Section of 80k Grid Cell Mesh.

C.11 CFD Submission Scripts

The submission scripts used to automate the running of the commercial solver on Cranfield's supercomputer (Astral II) is shown in Sec.(C.11.1). Sec.(C.11.2) shows the script used by Fluent to automate the execution of the solver.

C.11.1 Fluent Submission Script

```
#! /bin/bash
#
#
#PBS -N 121_sep
#PBS -l select=4:ncpus=16:mpiprocs=16
#PBS -l place=exclhost
#PBS -l cfd_base=1
#PBS -l cfd_hpc=60
#PBS -k oe
#PBS -q short
#PBS -m abe -M j.p.barden@cranfield.ac.uk

#
# Load module environment
. /etc/profile.d/modules.sh

# Load application environment
module load fluent/14.0

#
# Change to working directory
cd $PBS_O_WORKDIR

# Calculate number of CPUs.
cpus=$( cat $PBS_NODEFILE | wc -l )


# Run FLUENT solver

fluent 3ddp -ssh -g -pinfiniband -mpi=intel -t${cpus} -cnf=$PBS_NODEFILE < 484_502_121_10mil_ke.inp
```

C.11.2 Fluent Input File

```
;Import the mesh
/file/read 484_502_121_10mil.msh

;Change length scale of mesh - Convert from mm to m
/mesh/scale 0.001 0.001 0.001

;Define solver model k-e Realizable
/define/models/viscous/ke-realizable? yes

;Define boundary conditions, inlet velocity.
/define/boundary-conditions/velocity-inlet inlet no no yes yes no 5 no 0 yes no 1 no 1

;Specify the Reference Values
/report/reference-values/compute/velocity-inlet/inlet
/report/reference-values/area/10.5
/report/reference-values/length/22.5
/report/reference-values/zone/air.5

;Initialize the calcs
/solve/initialize/compute-defaults/velocity-inlet inlet
/solve/iterate 100

;Write initial output
file/write-case-data "484_502_121_10mil-100its.dat.gz"

;Solution Methods (switch to second order)
/solve/set/discretization-scheme/pressure 12
/solve/set/discretization-scheme/mom 1

;Specify update frequency for saving longer calcs.
/file/binary-files no
/file/confirm-overwrite no
/files/auto-save/retain-most-recent-files/yes
/file/auto-save/data-frequency/1000
/file/auto-save/case-frequency if

;Begin Iteration
/solve/iterate 15000

;Output Solution
/file/write-case-data "484_502_121_10mil-end.dat.gz"

;EXIT
exit
yes
exit
```

Appendix D

Control Code

The ActiveFREDDIE control code is shown in Sec.(D.1). The code was compiled using CodeWarrior, an integrated development environment (IDE) enabling the creation and development of embedded software. CodeWarrior was supplied by Freescale Semiconductor ™.

The core code used to run the M100 microcontroller was created by Pi Shurlok [81], with the ActiveFREDDIE control code written by the author. Once the code had been compiled and debugged using CodeWarrior, it was transferred to the M100 microcontroller by a PE micro USB debugger shown in Fig.(D.1).

Figure D.1: USB BDM Multilink Debugger [110].

The code in Sec.(D.1) was used for the prototype controller and is reproduced in its entirety except for the "lut.h" header file. The header file contained the aerodynamic wind tunnel data for δ_H as a function of $\Delta C_P/\beta$ and g/d_2.

D.1 ActiveFREDDIE Prototype Control Code

```
/*
 ******************************************************************************
 *
 *  Project:        OpenECU 16-bit C-API
 *  Version:            $Id: app.c 8317 2009-11-05 16:54:09Z dcarsky $
 *  File:                       $URL: https://apple.ps.local/$
 *
 *
 *  Copyright (C) 2008 Pi Shurlok
 *  This document (program) contains proprietary information
 *  which is the property of Pi Shurlok
 *  The contents of this document (program) must not be copied
 *  or disclosed to a third party without the prior agreement
 *  of an authorised officer of Pi Shurlok
 *
 *  Notes:
 *
 *  $NoKeywords: $  ** Do not remove **
 *
 ******************************************************************************
 */

/********* Includes *********/
#include        "std_def.h"
#include        "main.h"
#include        "ccp.h"
#include        "app.h"
#include        "pdx.h"
#include        "rs232.h"
#include        "can.h"
#include        "ain.h"
#include        "pin.h"
#include        "ipp.h"
#include            "spi.h"
#include        "config_nvm.h"
#include            "psy.h"
#include        "config.h"
#include        "pbt_common.h"
#include        "scheduler.h"
#include        "lut.h"         //Look-Up Table Header file.

/********* These macros can be changed *********/
#define J5_FITTED       (TRUE)


/* Standard things to specify in all applications: */
#define APP_MS_BEFORE_RESET_COUNTER_DEC  60000UL /* 1 minute */



/********* These macros must not be changed *********/
#define NUM_CYCLES_IN_50MS  ((U32)50 * 1000 / cfg->schc_period_usec)


#define NUM_CYCLES_IN_500MS ((U32)500 * 1000 / cfg->schc_period_usec)


#define NUM_PDIO                    (8u)    /* number of PDIO outputs */

#define CAN_MSG_ELLAPSED_TIME   (0x00000700)
#define CAN_MSG_GET_PWM_IP              (0x00000701)
#define CAN_MSG_GET_ANALOG_IP   (0x00000702)
#define CAN_MSG_CAN_TRANSLATE   (0x00000703)
#define CAN_MSG_SPI_ECHOED              (0x00000704)
#define CAN_MSG_CONFIG_DAT              (0x00000705)
#define CAN_MSG_ERROR_REP               (0x00000706)
#define CAN_MSG_DIAG_REP                (0x00000707)
#define CAN_MSG_GET_PERIOD_IP   (0x00000708)
#define CAN_MSG_CAN_SCALE               (0x82000000 | CAN_EXTENDED_ID_BIT)
#define CAN_ID                                  (0x80000000)
//#define CAN_EXTENDED_ID_BIT
```

```
/********* Static Structure Definitions *********/

/********* LED Definitions *********/
#define led_1_on  (pdx_digital_output(DOT_PIN_PA0,1,TRUE))
#define led_2_on  (pdx_digital_output(DOT_PIN_PA1,1,TRUE))
#define led_3_on  (pdx_digital_output(DOT_PIN_PA2,1,TRUE))
#define CSV_Found (pdx_digital_output(DOT_PIN_PA3,1,TRUE))
#define led_5_on  (pdx_digital_output(DOT_PIN_PA4,1,TRUE))
#define LAH_Fail  (pdx_digital_output(DOT_PIN_PA5,1,TRUE))
#define YAS_Fail  (pdx_digital_output(DOT_PIN_PA6,1,TRUE))
#define CSV_Fail  (pdx_digital_output(DOT_PIN_PA7,1,TRUE))
// LED off
#define led_1_off  (pdx_digital_output(DOT_PIN_PA0,0,TRUE))
#define led_2_off  (pdx_digital_output(DOT_PIN_PA1,0,TRUE))
#define led_3_off  (pdx_digital_output(DOT_PIN_PA2,0,TRUE))
#define led_4_off  (pdx_digital_output(DOT_PIN_PA3,0,TRUE))
#define led_5_off  (pdx_digital_output(DOT_PIN_PA4,0,TRUE))
#define led_6_off  (pdx_digital_output(DOT_PIN_PA5,0,TRUE))
#define led_7_off  (pdx_digital_output(DOT_PIN_PA6,0,TRUE))
#define led_8_off  (pdx_digital_output(DOT_PIN_PA7,0,TRUE))

/********* LED Definitions *********/


/********* Actuator Definitions *********/
//Raise Act
#define act_raise  (pdx_digital_output(DOT_PIN_PP7, 1, 1))
#define act_raise_2 (pdx_digital_output(DOT_PIN_PP2, 0, 1))

//Lower Act

#define act_lower (pdx_digital_output(DOT_PIN_PP7, 1, 1)) //SDA
#define act_lower_2 (pdx_digital_output(DOT_PIN_PP2, 1, 1))

//Turn off Act
#define act_off (pdx_digital_output(DOT_PIN_PP7, 0, 1))

/********* Actuator Definitions *********/

/********* Static Prototypes *********/
static void error_messages(void);
static void app_elapsed_time(U16 ticks);
static void app_read_inputs(void);
static void app_can_receive(void);
static void app_set_dot(can_raw_message_t *rx_msg);
static void app_set_pwm(can_raw_message_t *rx_msg);
static void graceful_shutdown_periodic();
static void app_get_pwm(void);
static void app_get_period(void);
static void app_sensor_yaw_failure();
static void app_sensor_lah_failure();
static void get_YAS();
static void calc_DH();
static void get_CHS();
static void app_schedule();
static void get_ODHS();
static void get_aveYAS();
extern drive_act();
static void act_limits();
static void app_can_msg_translate(U8 *data, CAN_BUS_ENUM_T bus);
static void app_scale_value(can_raw_message_t *rx_msg);
static void app_spi_echo(can_raw_message_t *rx_msg);
static void app_config_data(can_raw_message_t *rx_msg);
static void app_error_report(void);
static void app_get_dop_diagnostics(void);
static void app_report_diagnostics(void);
static void app_pwm_ip_detect(void);
static void app_can_rx_detect(void);


/********* Global Variable Instantiations *********/

#pragma CONST_SEG CALIBRATION
/* These may be monitored, manipulated and modified using a calibration tool such as ATI Vision */


#pragma CONST_SEG DEFAULT

const U16 sys_int_bus_clk = ((APP_EXT_CLK_FREQ_MHZ * APP_BUS_FREQ_MULT) / APP_BUS_FREQ_DIV);

const U16 put_major_ver_num = 1;
const U16 put_minor_ver_num = 0;
```

```
const U16 put_sub_minor_ver_num = 0;
const U8  put_model_name[] = "model_name_undefined";
const U8  put_model_desc[] = "model_description_undefined";
const U8  put_model_copyright[] = "model_copyright_undefined";

/********* Static Variables *********/
static U8       apps_Counter;
// static U8    apps_PortA_State;
static U8       apps_PDIO_Diag[NUM_PDIO];
static U8       apps_ErrReport[ERR_TOTAL];
static BOOL apps_can_msg_received;

/********* Unit Test Support *********/

#ifdef EMBED_DECLARATIONS
EMBED_DECLARATIONS
#endif

/*****************************************************************************/
/* START OF DECLARATION SECTION                                              */
/*                                                                           */
/* The following declarations of arrays and constants which are application- */
/* dependent and are used by other files in the platform library. The        */
/* platform is likely to work incorrectly if these definitions are modified. */
/* Leave them as-is unless directed to change them by Pi Shurlok.            */
/*****************************************************************************/

/************************************************/
/* RS232 code moved for Object File compatibility */
/************************************************/

/* This is a buffer where received character are written,
 * in a circular fashion.
 */
volatile U8 app_rs232_rx_buf[RS232_RX_BUF_SIZE];

/* varible holder for RS232_RX_BUF_SIZE */
const U8 app_rs232_rx_buf_size = RS232_RX_BUF_SIZE;

/* varible holder for RS232_BAUD_RATE */
const U16 app_rs232_baud_rate = RS232_BAUD_RATE;

/************************************************/
/* CAN code moved for Object File compatibility */
/************************************************/

/* varible holder for CAN_MAX_RX_DATA_ENTRIES */
const U16 app_can_num_rx_entries = CAN_MAX_RX_DATA_ENTRIES;

/* Contains information about received CAN data. can_rx_data_info[0] corresponds
 * to the first entry in cfg->can_rx_data_cfg[], can_rx_data_info[1] corresponds
 * to the second entry, etc.*/
volatile CAN_RX_DATA_INFO_STRUCT_T app_can_rx_data_info[CAN_MAX_RX_DATA_ENTRIES];

/* Array where recieved CAN parameter values are stored */
U16 app_can_rx_data[CAN_MAX_RX_DATA_ENTRIES];

/************************************************/
/* IPP code moved for Object File compatibility */
/************************************************/

/* An array of history information for each filtered analogue input. */
IPP_ANALOG_HISTORY_T ipp_analog_history[IPP_NUM_INPUTS];

/* An array of history information for each filtered digital input (from analogue). */
IPP_DIGITAL_HISTORY_T ipp_digital_history[IPP_NUM_INPUTS];

/* An array of history information for each filtered digital input (from digital). */
IPP_DIGITAL_HISTORY_T ipp_ddigital_history[IPP_NUM_INPUTS];

/* An array of history information for each pwm input. */
IPP_PWM_HISTORY_T ipp_pwm_history[PIN_NUM_INPUTS];

/* varible holder for IPP_NUM_INPUTS */
const U8 app_ipp_num_inputs = IPP_NUM_INPUTS;

/************************************************/
/* PIN code moved for Object File compatibility */
/************************************************/

/* The timing info for the PWM inputs */
volatile PIN_TIMING_T pin_timing[PIN_NUM_INPUTS];
```

```
/* varible holder for PIN_NUM_INPUTS */
const U8 app_pin_num_inputs = PIN_NUM_INPUTS;

/*********************************************/
/* SPI code moved for Object File compatibility */
/*********************************************/

volatile SPI_DEVICE_RX_DATA_BUFFER_T spi_rx_data_buffer[SPI_NUM_DEVICES];

/* varible holder for SPI_NUM_DEVICES */
const U8 app_spi_num_devices = SPI_NUM_DEVICES;


/* Application responsibility to handle reset counter when it has been running
 * OK for a reasonable time:
 */
static U32 app_ms_since_start = 0u;
static BOOL app_reset_counter_decd = FALSE;

/*****************************************************************************/
/* END OF DECLARATION SECTION                                                */
/*****************************************************************************/



/*****************************************************************************************/
oooooo0-----------------------------------------------
oo----oo-oo-ooo---ooooo---oooo---oo-ooo---ooooo--oo-oo-oo--
oo----oo-ooo---o-oo---oo-oo--oo--ooo---o-oo---oo-ooo-oo--o-
oooooo---oo------oo---oo-oo---o--oo------oo---oo-oo--oo--o-
oo-------oo------oo---oo--oooooo-oo------oo---oo-oo--oo--o-
oo-------oo-------ooooo--o----oo-oo-------oooo-o-oo------o-
--------------------------ooooo----------------------------
/*****************************************************************************************/




 /*
 ***************************************************************************
 *  Function:       error_messages
 *  Purpose:        Sets the state of LEDs on Port A
 *  Returns:        Nothing.
 *  Pre-condition:  None.
 *  Post-condition: None.
 *  Notes:          None.
 ***************************************************************************
*/
 #ifndef ERROR_MESSAGES
static void error_messages(void)
{

/* Notes..
CSV_Fail = led_8_on; // CSVFail - Failure of the IR sensor.
YAS_Fail = led_7_on; // YASFail - Failure of the YAS sensor..
LAH_Fail = led_6_on; // LAHFail - Failure of the Linear Actuator.
CSV_Found = led_4_on; // CSV_Found - Container Found.
*/

//Normal Operating LEDs - check everything is ok.
if(LAH_soft_limit == TRUE){
//led_1_on;
//led_3_on;
//led_5_on;
}

// Switch everything ON.
if(led_on == TRUE){
//led_1_on;
led_2_on;
led_3_on;
CSV_Found;
led_5_on;
LAH_Fail;
YAS_Fail;
CSV_Fail;
}
//Switch everything OFF.
if(led_on == FALSE){
led_1_off;
led_2_off;
led_3_off;
```

```
led_4_off;
led_5_off;
led_6_off;
led_7_off;
led_8_off;
}


}
#endif /* #ifdef ERROR_MESSAGES */



/*
 ******************************************************************************
 *  Function:        app_init
 *  Purpose:         Initialise the application prior to starting its periodics.
 *  Returns:         Nothing.
 *  Pre-condition:   None.
 *  Post-condition:  None.
 *  Notes:           Initialise after OPP module.
 ******************************************************************************
 */
#ifndef DUMMY_APP_INIT
void app_init(void)
{
        led_on = TRUE;
        error_messages();
        elapTime = 0.0;
        aveYAS = 0;
        apps_Counter = 0;
    apps_can_msg_received = FALSE;

(void) pdx_digital_output(DOT_PIN_PB7,0,1); // CAN 1 (outside)
(void) pdx_digital_output(DOT_PIN_PB6,0,1); // CAN 2 (outside)

}
#endif /* #ifdef DUMMY_APP_INIT */
#ifndef DUMMY_APP_IS_OK_TO_REFLASH
BOOL app_is_ok_to_reflash(void)
{
    return TRUE;
}
#endif


/*
 ******************************************************************************
 *  Function:        app_background
 *  Purpose:         Called from the main background loop, a hook to allow the
 *                   application to perform processing in the background.
 *  Returns:         None.
 *  Pre-condition:   None.
 *  Post-condition:  None.
 *  Notes:           Only call from the background loop!
 ******************************************************************************
 */
#ifndef DUMMY_APP_BACKGROUND
void app_background(void)
{
}
#endif /* #ifdef DUMMY_APP_BACKGROUND */


/*
 ******************************************************************************
 *  Function:        app_periodic
 *  Purpose:         Handle the periodic update to the module.
 *  Returns:         Nothing.
 *  Pre-condition:   None.
 *  Post-condition:  None.
 *  Notes:           None.
 ******************************************************************************
 */
#ifndef DUMMY_APP_PERIODIC
void app_periodic(void)
{

    BOOL IsIgnON;
    static U16  u16CycleCounter = 0;
        static BOOL     WDogState = 0;
        U16 FctTiming;
        static U16  u16CycleOffCounter = 0;
```

```
FctTiming = lib_get_timer();

(void) pdx_digital_input(DOT_PIN_PE0, &IsIgnON, 0);
    act_limits();

    if (IsIgnON || J5_FITTED)
    {
            u16CycleCounter++;
            apps_Counter++;

            /* Toggle the PSU watchdog */

            WDogState = !WDogState;
            if (pdx_digital_output(DOT_PIN_PB3, WDogState, TRUE))
            {
                    apps_ErrReport[ERR_DIG_OP] |= 0x10;
            }
            else
            {
                    apps_ErrReport[ERR_DIG_OP] &= 0x0F;


            }

            if(graceful_shutdown == 1){
                    graceful_shutdown_periodic();

                    led_on = FALSE;
            }
            else{
            get_aveYAS();
            get_ODHS();
            }

            drive_act();
            app_schedule();
            get_CHS();
            calc_DH();
            get_YAS();
            error_messages();
            app_sensor_yaw_failure();
    app_can_rx_detect();
            app_can_receive();
            app_get_dop_diagnostics();
            app_report_diagnostics();


    if ((u16CycleCounter \% (2 * NUM_CYCLES_IN_50MS)) == 0)
            {
                    /* Look for PWM input signal - we get here every 100 ms */
        app_get_pwm();
        app_get_period();
                    app_pwm_ip_detect();
            }
            else
            {
                    /* do nothing */
            }

            /* Calculating the time taken for app_periodic to execute */
            app_elapsed_time(lib_get_timer() - FctTiming);

            elapTime += 1.0 / (20 * NUM_CYCLES_IN_50MS);

            app_error_report();
    }
    else
    {
    u16CycleCounter = NUM_CYCLES_IN_500MS;
            /*
             * ignition has been turned OFF, do clean up (saving parameters etc.)
             * and turn itself OFF - just demonstrating this concept by turning
             * all LEDs ON for 500ms before turning unit off
             */
            //              apps_PortA_State = 0xFF;

            u16CycleOffCounter++;
            if ((u16CycleOffCounter \% u16CycleCounter) == 0){
                    int counter_lower_act = 0;
                            if (counter_lower_act == 0){
                                    if(DHS != 0){
```

```
                        pdx_digital_output(DOT_PIN_PP3, 0, 1); // PDIO 5 - LOW
                        pdx_pwm_output(POT_PWM45,512,1,TRUE); // PDIO 6 - HIGH PWM
                                        counter_lower_act = 0;
                                }
                                else{counter_lower_act = 1;
                                }
                        }

                        /*
                         * turn OFF microcontroller - this will only work if jumper J5
                         * is not fitted - WILL NEED TO ADD CODE TO LOWER ACTUATOR TO MIN HEIGHT
                         */
                        (void) pdx_digital_output(DOT_PIN_PB5, 0, 1);
                }
        }



    /*
     * Integrity checks -- must be done in all applications
     */

    /* Decrement reset counter once if we have been running OK for a while */
    app_ms_since_start += sch_periodic_time; /* allow to wrap, harmless */
    if (!app_reset_counter_decd && (app_ms_since_start >= APP_MS_BEFORE_RESET_COUNTER_DEC))
    {
        if (pbt_reset_counter > 0)
        {
            pbt_reset_counter--;
        }
        app_reset_counter_decd = TRUE;
    }

    /*
         */
    main_prog_flow |= MAIN_APP_RUNNING;
}


#endif /* #ifdef DUMMY_APP_PERIODIC */



/*
 ******************************************************************************
 *  Function:        app_elapsed_time
 *  Purpose:         Calculates and transmits the elapsed time in us.
 *  Returns:         Nothing.
 *  Pre-condition:   None.
 *  Post-condition:  None.
 *  Notes:           None.
 ******************************************************************************
 */
#ifndef DUMMY_ELAPSED_TIME
static void app_elapsed_time(U16 ticks)
{
        U16 Time_us;
        can_raw_message_t message;

        message.id = CAN_MSG_ELLAPSED_TIME;
        message.length = 2;
        Time_us = lib_timer_to_us(ticks);
        message.payload[0] = (U8)(Time_us >> 8);
        message.payload[1] = (U8)(Time_us);
        apps_ErrReport[ERR_CAN_TX] &= 0xF0;     /* clearing previous return value */
        apps_ErrReport[ERR_CAN_TX] |= can_q_tx_raw_msg(&message, CAN_BUS_0);
}
#endif /* #ifdef DUMMY_ELAPSED_TIME */


/*
 ******************************************************************************
 *  Function:        app_schedule.
 *  Purpose:         Schedule startup items
 *  Returns:         CHS.
 *  Pre-condition:   None.
 *  Post-condition:  None.
 *  Notes:           None.
 ******************************************************************************
 */
```

```
#ifndef DUMMY_read_CHS
static void app_schedule() {
        if (elapTime <= (act_innit_period)) {
                counter = 0;
                updateCounter = TRUE;
        }
        else if(elapTime <= (act_innit_period * 2)) {
                counter = 1;
                updateCounter = TRUE;
        }
        else{
                counter = 2;
                updateCounter = TRUE;
        }
}

#endif /* #ifdef DUMMY_read_CHS */
```

```
/*
:'######::'########:'##::: ##::'######:::'########::'########:::::
'##... ##: ##.....:: ###:: ##:'##... ##:'##.... ##: ##.... ##::::
 ##:::..:: ##::::::: ####: ##: ##:::..:: ##:::: ##: ##:::: ##::::
. ######:: ######::: ## ## ##:. ######:: ##:::: ##: ########:::::
:..... ##: ##...:::: ##. ####::..... ##: ##:::: ##: ##.. ##::::::
'##::: ##: ##::::::: ##:. ###:'##::: ##: ##:::: ##: ##::. ##:::::
. ######:: ########: ##::. ##:. ######:: ########:: ##:::. ##::::
:......:::........::..::::..:::......:::........:::..:::::..:::::
'########::'########::::'###::::'########::'####:'##::: ##::'######::::
 ##.... ##: ##.....::::'## ##::: ##.... ##:. ##:: ###:: ##:'##... ##:::
 ##:::: ##: ##::::::::'##:. ##:: ##:::: ##:: ##:: ####: ##: ##:::..::::
 ########:: ######:::'##:::. ##: ##:::: ##:: ##:: ## ## ##: ##::'####::
 ##.. ##::: ##...:::: #########: ##:::: ##:: ##:: ##. ####: ##::: ##:::
 ##::. ##:: ##::::::: ##.... ##: ##:::: ##:: ##:: ##:. ###: ##::: ##::
 ##:::. ##: ########: ##:::: ##: ########::'####: ##::. ##:. ######::::
..:::::..::........::..:::::..::........:::....::..::::..:::......:::::
*/
```

```
/*
 ***************************************************************************
 *  Function:        get_CHS
 *  Purpose:         Converts the IR sensor voltage to Distance.
 *  Returns:         None.
 *  Pre-condition:   None.
 *  Post-condition:  None.
 *  Notes:           None.
 ***************************************************************************
 */

#ifndef get_CHS
static void get_CHS() {

        apps_ErrReport[ERR_ANLG_IP] = pax_adc_input(AIN_PIN_1, &CS, FALSE);

        if (!apps_ErrReport[ERR_ANLG_IP])
                {
        CSvoltage =  (float)((U16)CS) * (5.0 / 409.6);
                }

                //Converts Input Voltage to distance based on manufacturers spec.

        if (CSvoltage >= 3.0 && CSvoltage < 3.4){CSout = 5.0;}
        else if (CSvoltage >= 2.9){CSout = 6.4;}
        else if (CSvoltage >= 2.8){CSout = 6.6;}
        else if (CSvoltage >= 2.7){CSout = 6.9;}
        else if (CSvoltage >= 2.6){CSout = 7.3;}
        else if (CSvoltage >= 2.5){CSout = 7.7;}
        else if (CSvoltage >= 2.4){CSout = 8.1;}
        else if (CSvoltage >= 2.3){CSout = 8.6;}
        else if (CSvoltage >= 2.2){CSout = 9.1;}
        else if (CSvoltage >= 2.1){CSout = 9.6;}
        else if (CSvoltage >= 2.0){CSout = 10.3;}
        else if (CSvoltage >= 1.9){CSout = 11.0;}
        else if (CSvoltage >= 1.8){CSout = 11.8;}
        else if (CSvoltage >= 1.7){CSout = 12.7;}
        else if (CSvoltage >= 1.6){CSout = 13.7;}
        else if (CSvoltage >= 1.5){CSout = 15.0;}
        else if (CSvoltage >= 1.4){CSout = 16.4;}
```

```
        else if (CSvoltage >= 1.3){CSout = 18.1;}
        else if (CSvoltage >= 1.2){CSout = 20.1;}
        else if (CSvoltage >= 1.1){CSout = 25.5;}
        else if (CSvoltage >= 1.0){CSout = 29.3;}
        else if (CSvoltage >= 0.9){CSout = 34.1;}
        else if (CSvoltage >= 0.8){CSout = 40.7;}
        else if (CSvoltage >= 0.7){CSout = 50.0;}
        else if (CSvoltage >= 0.6){CSout = 63.2;}
        else if (CSvoltage >= 0.5){CSout = 63.2;}

}

#endif /* #ifdef get_CHS */



/*
 ***************************************************************************
 *  Function:       get_YAS
 *  Purpose:        Reads yaw angle and converts to voltage for look-up table.
 *  Returns:        Nothing.
 *  Pre-condition:  None.
 *  Post-condition: None.
 *  Notes:          None.
 ***************************************************************************
 */
#ifndef GET_YAS
static void get_YAS()
{
calc_DH();
/***************************** For reference ****************************/
                //PWM OUTPUT CHANNELS
                // POT_PWM01 = PDIO 7
                // POT_PWM23 = PDIO 5
                // POT_PWM45 = PDIO 6
                // POT_PWM67 = PDIO 3

                //DIGITAL CHANNELS
                // DOT_PIN_PP0 = PDIO 0
                // DOT_PIN_PP4 = PDIO 1
                // DOT_PIN_PP2 = PDIO 2
                // DOT_PIN_PP7 = PDIO 3
                // DOT_PIN_PT7 = PDIO 4
                // DOT_PIN_PP3 = PDIO 5
                // DOT_PIN_PP5 = PDIO 6
                // DOT_PIN_PP1 = PDIO 7
/***************************** /For reference ***************************/



        if (counter == 2) {
                CSoutsave = CSout; //3D LUT if CS is a factor.

        //apps_ErrReport[ERR_ANLG_IP] = pax_adc_input(AIN_PIN_0, &Yaw, FALSE);
        //Yaw Sensor


                if (!apps_ErrReport[ERR_ANLG_IP])
                {
                        // 10 bit input
                        voltage = (float)((U16)get_aveyas) * (5.0 / 4092);


                /*  Assign Yaw to Voltage in */

        }
}
}
#endif /* #ifdef GET_YAS */



/*
 ***************************************************************************
 *  Function:       get_DHS
 *  Purpose:        Reads dhs and converts to voltage for look-up table.
 *  Returns:        Nothing.
 *  Pre-condition:  None.
 *  Post-condition: None.
 *  Notes:          None.
 ***************************************************************************
 */
```

```
//#ifndef GET_DHS
//static void get_DHS(){

//DHS = DH;

        /* Get DHS */
//      apps_ErrReport[ERR_ANLG_IP] = pax_adc_input(AIN_PIN_4, &Lah, FALSE);
//Linear Actuator Height
//      DHS = (float)((U16)Lah) * (5.0 / 4092);
//      DHSmm = (float)((U16)Lah) * (5.0 / 409.2);
//      DHSint = (int) (DHS + 0.5);
//      DHSintmm = (int) (DHSmm + 0.5);



//}
//#endif /* #ifdef GET_YAS */




/*
 ******************************************************************************
 *  Function:       app_read_averageYAS
 *  Purpose:        Average of periodic reading of YAS.
 *  Returns:        None.
 *  Pre-condition:  None.
 *  Post-condition: None.
 *  Notes:          None.
 ******************************************************************************
 */
#ifndef get_aveYAS
static void get_aveYAS(){
        static int avgCounter = 0;
        static int sampleCounter = 0;
        static int numSamples = 0;
        get_YAS();

        if (elapTime >= act_YAS_period*sampleCounter) {
                apps_ErrReport[ERR_ANLG_IP] = pax_adc_input(AIN_PIN_0, &Yaw, FALSE);
                //Yaw Sensor
                aveYAS += Yaw;
                sampleCounter++;
                numSamples++;
        }
        if (counter == 2 && elapTime >= act_YAS_aveperiod*avgCounter) {
        //      pdx_digital_output(DOT_PIN_PA1,1,TRUE);
                led_on = FALSE;
                //led_1_on;
                get_aveyas = aveYAS / numSamples;
                updatePWM = TRUE;
                aveYAS = 0;
                numSamples = 0;

                avgCounter++;
        }
}


#endif /* #ifdef DUMMY_read_aveYAS */




/*
:'#######::'########::'##::::'##::'######::
'##.... ##: ##.... ##: ##:::: ##:'##... ##:
 ##:::: ##: ##:::: ##: ##:::: ##: ##:::..::
 ##:::: ##: ##:::: ##: ##########:. ######::
 ##:::: ##: ##:::: ##: ##.... ##::.....  ##:
 ##:::: ##: ##:::: ##: ##:::: ##:'##::: ##:
. ########:: ########:: ##:::: ##:. ######::
:........::::.....::::..:::::..:::......:::
*/
```

```
/*
 ******************************************************************************
 *  Function:        get_ODHS
 *  Purpose:         Calculation of ODHS
 *  Returns:         None.
 *  Pre-condition:   None.
 *  Post-condition:  None.
 *  Notes:           None.
 ******************************************************************************
 */
#ifndef get_ODHS
static void get_ODHS(){
        calc_DH();
        get_aveYAS();
        CHSint = (int)((CHS/10.0) + 0.5);


//First Voltage {Zero Yaw}
                if(voltage <= 1.5){
                        aveYAScalc = 0;
                        ODHS = CHS;

                }

//Second Voltage {1 Degree Yaw}
                else if(voltage <= 2.0){
                        aveYAScalc = 1;
                        ODHS = LUT[CHSint][aveYAScalc];
                }

//Third Voltage {2 Degree Yaw}
                else if(voltage <= 2.5){
                        aveYAScalc = 2;
                        ODHS = LUT[CHSint][aveYAScalc];
                }

//Fourth Voltage {3 Degree Yaw}
                else if(voltage <= 3.0){
                        aveYAScalc = 3;
                        ODHS = LUT[CHSint][aveYAScalc];
                }

//Fifth Voltage {4 Degree Yaw}
                else if(voltage <= 3.5){
                        aveYAScalc = 4;
                        ODHS = LUT[CHSint][aveYAScalc];
                }

//Sixth Voltage {5 Degree Yaw}
                else if(voltage <= 4.0){
                        aveYAScalc = 5;
                        ODHS = LUT[CHSint][aveYAScalc];
                }

//Seventh Voltage {10 Degree Yaw}
                else if(voltage <= 4.5){
                        aveYAScalc = 10;
                        ODHS = LUT[CHSint][aveYAScalc];
                }

//Eight Voltage {15 Degree Yaw}
                else if(voltage <= 5.0){
                        aveYAScalc = 15;
                        ODHS = LUT[CHSint][aveYAScalc];
                }


//Begin Actuation
                if(counter == 2) {
                //      updatePWM = FALSE;

                        if(DHSintmm > ODHS && !goingUp) {
                                goingUp = TRUE;
                                goingDown = FALSE;
                                act_lower;
                                act_lower_2;
                                //led_2_on;

                        }

                        if(DHSintmm < ODHS && !goingDown){
```

```
                                goingDown = TRUE;
                                goingUp = FALSE;
                                act_raise;
                                act_raise_2;
                                //led_1_on;
                        }

                        if(ODHS == DHSintmm){
                                act_off;
                                //led_1_on;
                                //led_2_on;
                                //led_3_on;
                        }
                }

}
#endif /* #ifdef get_ODHS */



/*
:::'###::::::'######::'########:'##::::'##::::'###::::'########::'#######::'########::
::'## ##:::'##... ##:... ##..:: ##:::: ##:::'## ##::: ##.....::'##.... ##: ##.... ##:
:'##:. ##:: ##:::..::::: ##:::: ##:::: ##::'##:. ##:: ##::::::: ##:::: ##: ##:::: ##:
'##::. ##: ##:::::::::: ##:::: ##:::: ##:'##::. ##:: ##::::::: ##:::: ##: ########::
 #########: ##:::::::::: ##:::: ##:::: ##: #########:: ##::::::: ##:::: ##: ##.. ##:::
 ##.... ##: ##::: ##:::: ##:::: ##:::: ##: ##.... ##:: ##::::::: ##:::: ##: ##::. ##::
 ##:::: ##:. ######::::: ##::::. #######:: ##:::: ##:: ##::::::::. #######:: ##:::. ##:
..:::::..:::......::::::..::::::.......:::..:::::..:::..::::::::::.......:::..:::::..::
*/



 /*
 ******************************************************************************
 *  Function:        drive_act
 *  Purpose:         Drive actuators (PWM) before beginning app_periodic
 *  Returns:         Nothing.
 *  Pre-condition:   None.
 *  Post-condition:  None.
 *  Notes:           None.
 ******************************************************************************
 */
#ifndef DRIVE_ACT
extern drive_act() {
        get_CHS();

        if (updateCounter == TRUE) {
                updateCounter = FALSE;

                if (counter == 0) {
                        led_on = FALSE;
                        act_raise;
                        act_raise_2;
                        //led_5_on;

                        /* safety limits on actuators startup - Max height */
                        if(DHSintmm >= (DHSmaxH_int_limit)){
                                //led_1_on;
                                //led_3_on;
                                //led_5_on;
                                act_off;
                                updateCounter = FALSE;
                        }
                }
                else if (counter == 1) {
                        if(CSvoltage < 1.0) {
                                led_on = FALSE;
                                act_lower;
                                act_lower_2;
                        }
                        else if(CSvoltage >= 1.0) {
                                CSV_Found;
                                act_off;
                                act_height = 0.0;
                                CHS = DHSintmm;
                                //return CHS;
                                }
                        /* safety limits on actuators startup - Min height */
                         if(DHSintmm <= (DHSminH_int_limit)){
                                //led_2_on;
```

```
                                act_off;
                                updateCounter = FALSE;
                        }
                }
}

#endif /* #ifdef APP_DRIVE_ACT */
}


// ACTUATOR CALCULATION

/*
 ******************************************************************************
 *  Function:        calc_DHS
 *  Purpose:         raise act
 *  Returns:         None.
 *  Pre-condition:   None.
 *  Post-condition:  None.
 *  Notes:           None.
 ******************************************************************************
 */
#ifndef calc_DH
static void calc_DH(){

if(goingUp = TRUE)
{
//Calc Height of Actuator.
elapTime2 += 1.0 / (20 * NUM_CYCLES_IN_50MS);
period2height = lib_timer_to_us(pin_get_raw_period(PIN_PIN_2));
DH_Calc = period2height*elapTime2*conversion_factor;
DH = DH+DH_Calc;
}

if(goingDown = TRUE)
{
//Calc Height of Actuator.
elapTime2 += 1.0 / (20 * NUM_CYCLES_IN_50MS);
period2height = lib_timer_to_us(pin_get_raw_period(PIN_PIN_2));
DH_Calc = period2height*elapTime2*conversion_factor;
DH = DH-DH_Calc;
}

}


#endif /* #ifdef calc_DH */
```

```
/*
:::'###:::::'######::'########:'##::::'##::::'###::::'########::'#######::'########::
::'## ##:::'##... ##:... ##...:: ##:::: ##:::'## ##::: ##.....::'##.... ##: ##.... ##:
:'##:. ##:: ##:::..::::: ##:::: ##:::: ##::'##:. ##:: ##::::::: ##:::: ##: ##:::: ##:
'##::::. ##: ##:::::::::: ##:::: ##:::: ##:'##::::. ##: ##::::::: ##:::: ##: ########::
 #########: ##:::::::::: ##:::: ##:::: ##: #########::: ##::::::: ##:::: ##: ##.. ##:::
 ##.... ##: ##::: ##::: ##:::: ##:::: ##: ##.... ##:::: ##::::::: ##:::: ##: ##::. ##::
 ##:::: ##:. ######:::::: ##:::: #######:: ##:::: ##:::: ##::::::: #######:: ##:::. ##:
..:::::..:::......:::::::..:::::.......::..:::::..:::::..::::::::.......:::..:::::..::
'##::::::'####:'##::::'##:'####:'########::'######::
 ##:::::::. ##:: ###::'###:. ##:::... ##..::'##... ##:
 ##::::::::: ##:: ####'####:: ##::::: ##::::: ##::..::
 ##::::::::: ##:: ## ### ##:: ##::::: ##::::. ######::
 ##::::::::: ##:: ##. #: ##:: ##::::: ##:::::..... ##:
 ##::::::::: ##:: ##:.:: ##:: ##::::: ##::::'##::: ##:
 ########:'####: ##::::: ##:'####:::: ##::::. ######::
.........::....::..::::::..::....:::::..::::::......:::
*/


/*
 ******************************************************************************
 *  Function:        act_limits
 *  Function:        act_limits
 *  Purpose:         Defines the limits of the actuators under normal working conditions.
 *  Returns:         Nothing.
 *  Pre-condition:   None.
 *  Post-condition:  None.
```

```
 *  Notes:          None.
 ************************************************************************
 */
#ifndef ACT_LIMITS
static void act_limits(){
/* safety limits on actuators Normal Operation */

 if(counter == 2){
        /* prevents stopping if int actuator is raised */
        if(DHSintmm >= DHSmaxH || DHSintmm <= DHSminH){
                        LAH_soft_limit = TRUE;
                        act_off;
                }

        }
}
#endif /* #ifdef ACT_LIMITS */



/*
'########::::'###::::'####:'##::::::::'##::::'##:'########::'########:
 ##.....::::'## ##:::. ##:: ##::::::::  ##::::##: ##.... ##: ##.....::
 ##::::::::'##:. ##::: ##:: ##::::::::  ##::::##: ##:::: ##: ##:::::::
 ######:::'##:::. ##:: ##:: ##::::::::  ##::::##: ########:: ######:::
 ##...:::: #########:: ##:: ##::::::::  ##::::##: ##.. ##::: ##...::::
 ##::::::: ##.... ##:: ##:: ##::::::::  ##::::##: ##::. ##:: ##:::::::
 ##::::::: ##:::: ##:'####: ########:.  ########:: ##:::. ##: ########:
.:::::::::.:::::..::....::........::::........:::..:::::..::........::
'##::::'##::'#######::'########::'########::'######::
 ###::'###:'##.... ##: ##.... ##: ##.....::'##... ##:
 ########: ##:::: ##: ##:::: ##: ##::::::: ##:::..::
 ## ### ##: ##:::: ##: ##:::: ##: ######:::. ######::
 ##. #: ##: ##:::: ##: ##:::: ##: ##...::::.....  ##:
 ##:.:: ##: ##:::: ##: ##:::: ##: ##::::::'##::: ##:
 ##:::: ##:. #######:: ########:: ########:. ######::
..:::::..:::.......:::........:::........:::......:::
*/


/*
 ************************************************************************
 *  Function:       app_sensor_yaw_failure
 *  Purpose:        Check YAS works otherwise throw error.
 *  Returns:        Nothing.
 *  Pre-condition:  None.
 *  Post-condition: None.
 *  Notes:          None.
 ************************************************************************
 */
#ifndef APP_SENSOR_YAW_FAILURE
static void app_sensor_yaw_failure() {
        get_YAS();
        if(voltage > 5.5) //Lower limit is 0V. (negative voltage?)
        {
                YAS_Fail;
                /* lower acts to min */
                updatePWM = TRUE;
                graceful_shutdown = 1;
        }


#endif /* #ifdef APP_SENSOR_YAW_FAILURE */
}



/*
 ************************************************************************
 *  Function:       app_sensor_lah_failure
 *  Purpose:        Check LAH works otherwise throw error.
 *  Returns:        Nothing.
 *  Pre-condition:  None.
 *  Post-condition: None.
 *  Notes:          Needs seriousn rework for multi actuators.
 ************************************************************************
 */
#ifndef APP_SENSOR_LAH_FAILURE
static void app_sensor_lah_failure() {
        get_YAS();
        if(Lah >= 12.0) //check
        {
        //Need to kill it, not shut_down as we do not know the height of actuator.
```

```
        LAH_Fail;
        act_off;
        }

#endif /* #ifdef APP_SENSOR_LAH_FAILURE */
}



/*
:'######::'##::::'##:'##::::'##:'########:
'##... ##: ##:::: ##: ##:::: ##:... ##..::
 ##::::..:: ##:::: ##: ##:::: ##::::: ##::::
. ######:: ########:: ##:::: ##::::: ##::::
:..... ##: ##.... ##: ##:::: ##::::: ##::::
'##::: ##: ##:::: ##: ##:::: ##::::: ##::::
. ######:: ##:::: ##:. #######:::::: ##::::
:......:::..:::::..:::.......::::::..:::::
'########:::'#######::'##::::'##:'##::: ##:
 ##.... ##:'##.... ##: ##:'##: ##: ###:: ##:
 ##::::: ##: ##:::: ##: ##: ##: ##: ####: ##:
 ##::::: ##: ##:::: ##: ##: ##: ##: ## ## ##:
 ##::::: ##: ##:::: ##: ##: ##: ##: ##. ####:
 ##::::: ##: ##:::: ##: ##: ##: ##: ##:. ###:
 ########::. #######::. ###. ###:: ##::. ##:
........::::.......::::...:::...::..::::..::
*/



/*
 ******************************************************************************
 *  Function:        graceful_shutdown_periodic
 *  Purpose:         Shut down the periodic application & lower acts to min height.
 *  Pre-condition:   None.
 *  Post-condition:  None.
 *  Notes:           None.
 ******************************************************************************
 */ // Drive actuators to lowest position due to a fault/sensor error etc.

#ifndef graceful_shutdown_periodic
static void graceful_shutdown_periodic(){
calc_DH();

        if(updatePWM == TRUE) {
                updatePWM = FALSE;

                if(DHSintmm >= DHSmaxH_limit){
                        act_lower;
                        act_lower_2;
                        //led_on = TRUE;
                }
                if(DHSintmm <= DHSminH_limit){
                        act_off;
                }
        }

}
#endif /* #ifdef graceful_shutdown_periodic */


/*
:'######::::::'###::::'##::: ##::::::::'##::'######::'########::'####:
'##... ##:::'## ##::: ###:: ##::::::::'##::'##... ##: ##.... ##:. ##::
 ##::::..:::'##:. ##:: ####: ##::::::'##::: ##::..:::: ##:::: ##:: ##::
 ##:::::::'##:::. ##: ## ## ##:::::'##:::::. ######:: ########::: ##::
 ##::::::: #########: ##. ####::::'##:::::::.....##: ##.....:::: ##::
 ##::: ##: ##.... ##: ##:. ###:::'##::::::'##::: ##: ##::::::::: ##::
. ######:: ##:::: ##: ##::. ##::'##:::::::. ######:: ##::::::::'####:
:......:::..:::::..::..::::..::..:::::::::.......:::..:::::::::....::

*/

/*
 ******************************************************************************
 *  Function:        app_can_receive
 *  Purpose:         Actions any CAN messages that we are interested in.
 *  Returns:         Nothing.
 *  Pre-condition:   None.
 *  Post-condition:  None.
```

```
 *  Notes:          None.
 ******************************************************************************
 */
#ifndef DUMMY_APP_CAN_RECEIVE
static void app_can_receive(void)
{
   // can_raw_message_t rx_msg;

 //    apps_can_msg_received = TRUE;

        //if (can_get_raw_msg(CAN_MSG_SET_DIGITAL_OP, &rx_msg))
   // {
        /* set the digital output state */
  //      app_set_dot(&rx_msg);
  //  }
//      else if (can_get_raw_msg(CAN_MSG_SET_PWM_OP, &rx_msg))
 //   {
        /* set the pwm output signal */
 //       app_set_pwm(&rx_msg);
 //   }
//      else if (can_get_raw_msg(CAN_MSG_SCALE_DATA, &rx_msg))
  //  {
        /* get the scaled data */
 //       app_scale_value(&rx_msg);
 //   }
        //else if (can_get_raw_msg(CAN_MSG_SPI_ECHO, &rx_msg))
  //  {
        /* echo data via the low-side driver IC */
 //       app_spi_echo(&rx_msg);
  //  }
/*      if (can_get_raw_msg(CAN_VEL_RS, &rx_msg))
    {
       /* read or save configuration data
      app_config_data(&rx_msg);

    }
        else
        {
                // no message of interest has been received
       apps_can_msg_received = FALSE;
          // led_1_on;
           led_5_on;

        }
*/
}
#endif /* #ifdef DUMMY_APP_CAN_RECEIVE */


/*
 ******************************************************************************
 *  Function:       app_set_dot
 *  Purpose:        Set the digital output state
 *  Returns:        Nothing.
 *  Pre-condition:  None.
 *  Post-condition: None.
 *  Notes:          None.
 ******************************************************************************
 */
#ifndef DUMMY_SET_DIGITAL_OUTPUT
static void app_set_dot(can_raw_message_t *rx_msg)
{
/*
         PDIO[1] connects to PortP[4]
        if (pdx_digital_output(DOT_PIN_PP4, rx_msg->payload[0], FALSE))
        {
                apps_ErrReport[ERR_DIG_OP] |= 0x01;
        }
        else
        {
                apps_ErrReport[ERR_DIG_OP] &= 0xF0;

        if (rx_msg->payload[0])
                {
                //      apps_PortA_State |= (0x01 << LED_DIG_OP);
                        cfg_nvm.app.DOP_State = TRUE;
                }
                else
                {
                        //apps_PortA_State &=~(0x01 << LED_DIG_OP);
                        cfg_nvm.app.DOP_State = FALSE;
                }
        }
```

```
        */
}
#endif /* #ifdef DUMMY_SET_DIGITAL_OUTPUT */


/*
 ******************************************************************************
 *  Function:        app_set_pwm
 *  Purpose:         Sets the PWM Output signal - frequency and duty cycle
 *  Returns:         Nothing.
 *  Pre-condition:   None.
 *  Post-condition:  None.
 *  Notes:           None.
 ******************************************************************************
 */
#ifndef DUMMY_SET_PWM_OUTPUT
static void app_set_pwm(can_raw_message_t *rx_msg)
{
        /*
         * Assigning PWM values to the config data
         * This is actually a copy of the config data and resides in RAM
         * hence unless it is explicitly saved the data will be lost on switch off
         */
        /*cfg_nvm.app.PWM_Freq = ((U16)(rx_msg->payload[0]) << 8) + rx_msg->payload[1];
        cfg_nvm.app.PWM_Duty = ((U16)(rx_msg->payload[2]) << 8) + rx_msg->payload[3];
        apps_ErrReport[ERR_PWM_OP] =
        pdx_pwm_output(POT_PWM67, cfg_nvm.app.PWM_Freq, cfg_nvm.app.PWM_Duty, FALSE);*/
}
#endif /* #ifdef DUMMY_SET_PWM_OUTPUT */


/*
 ******************************************************************************
 *  Function:        app_get_pwm
 *  Purpose:         Retrieves the PWM Input 2 data and reports it via a CAN message
 *  Returns:         Nothing.
 *  Pre-condition:   None.
 *  Post-condition:  None.
 *  Notes:           None.
 ******************************************************************************
 */
#ifndef DUMMY_GET_PWM_INPUT
static void app_get_pwm(void)
{
/*
        PIN_PWM_DATA_T  pwm_data;
        can_raw_message_t message;

        message.id = CAN_MSG_GET_PWM_IP;
        message.length = 6;

        if (pin_get_pwm_data(PIN_PIN_2, &pwm_data))
        {
                apps_ErrReport[ERR_PWM_IP] = 1;

                // send raw period first
                message.payload[0] = (U8)(pwm_data.pin_raw_period >> 24);
                message.payload[1] = (U8)(pwm_data.pin_raw_period >> 16);
                message.payload[2] = (U8)(pwm_data.pin_raw_period >> 8);
                message.payload[3] = (U8)(pwm_data.pin_raw_period);
                // duty cycle after
                message.payload[4] = (U8)(pwm_data.pin_duty_cycle >> 8);
                message.payload[5] = (U8)(pwm_data.pin_duty_cycle);
        }
        else
        {
                apps_ErrReport[ERR_PWM_IP] = 0;

                // PWM acquire returned error, thus no frequency info
                message.payload[0] = 0;
                message.payload[1] = 0;
                message.payload[2] = 0;
                message.payload[3] = 0;
                //
                 // although PWM returned error, the duty cycle data may still be valid
                 // i.e. for duty cycle = 0\% or 100\%

                message.payload[4] = (U8)(pwm_data.pin_duty_cycle >> 8);
                message.payload[5] = (U8)(pwm_data.pin_duty_cycle);
        }

        apps_ErrReport[ERR_CAN_TX] &= 0xF0;     /* clearing previous return value
        apps_ErrReport[ERR_CAN_TX] |= can_q_tx_raw_msg(&message, CAN_BUS_0);
```

```
        */
}
#endif /* #ifdef DUMMY_GET_PWM_INPUT */


/*
 ******************************************************************************
 *  Function:       app_get_period
 *  Purpose:        Retrieves the period Input 6 data and reports it via a CAN message
 *  Returns:        Nothing.
 *  Pre-condition:  None.
 *  Post-condition: None.
 *  Notes:          None.
 ******************************************************************************
 */
#ifndef DUMMY_GET_PERIOD_INPUT
static void app_get_period(void)
{
/*
        PIN_PWM_DATA_T  pwm_data;
        can_raw_message_t message;
    U32 tempPeriod;

        message.id = CAN_MSG_GET_PERIOD_IP;
        message.length = 4;

    tempPeriod = pin_get_raw_period(PIN_PIN_6);

         send raw period first
        message.payload[0] = (U8)(tempPeriod >> 24);
        message.payload[1] = (U8)(tempPeriod >> 16);
        message.payload[2] = (U8)(tempPeriod >> 8);
        message.payload[3] = (U8)(tempPeriod);

        apps_ErrReport[ERR_CAN_TX] &= 0xF0;     // clearing previous return value
        apps_ErrReport[ERR_CAN_TX] |= can_q_tx_raw_msg(&message, CAN_BUS_0);
        */
}
#endif /* #ifdef DUMMY_GET_PWM_INPUT */
```

This page intentionally left blank.

Appendix E

Wind Tunnel Data

E.1 Yaw Angle (β) vs. Deflector Height (δ_H)

	Deflector Height Ratio, δ_H										
$\beta(^\circ)$	0.936	0.942	0.948	0.954	0.959	0.965	0.971	0.977	0.983	0.988	0.994
-5	0.719†	0.713	0.712	0.705	0.701	0.696*	0.699	0.702	0.703	0.703	0.706
-3	0.653†	0.647	0.644	0.640	0.636	0.630	0.624*	0.626	0.626	0.625	0.626
0	0.598†	0.591	0.588	0.581	0.576	0.570	0.559	0.549	0.541	0.540	0.538*
1	0.600†	0.593	0.590	0.583	0.578	0.571	0.561	0.544	0.544	0.540*	0.544
2	0.615†	0.607	0.605	0.598	0.594	0.588	0.579	0.571	0.567*	0.567*	0.568
3	0.640†	0.634	0.631	0.625	0.620	0.615	0.608	0.605	0.604*	0.605	0.605
4	0.672†	0.667	0.665	0.657	0.655	0.650	0.646*	0.647	0.646*	0.648	0.650
5	0.709†	0.704	0.701	0.695	0.693	0.688	0.687*	0.691	0.691	0.691	0.693
10	0.898†	0.894	0.892	0.889	0.885	0.880*	0.883	0.883	0.882	0.882	0.884
15	1.032†	1.027	1.028	1.023	1.018	1.013	1.013	1.010	1.007	1.004*	1.005

Table E.1: C_D Coefficients[2]vs. Yaw Angle (β) for Various Deflector Heights (δ_H) with $g/d_2 = 1.335$.

[2]* Denotes Lowest and † Denotes Highest C_D Value Obtained Respectively. Zero Yaw Optimised (ZYO) Deflector Height = 0.994.

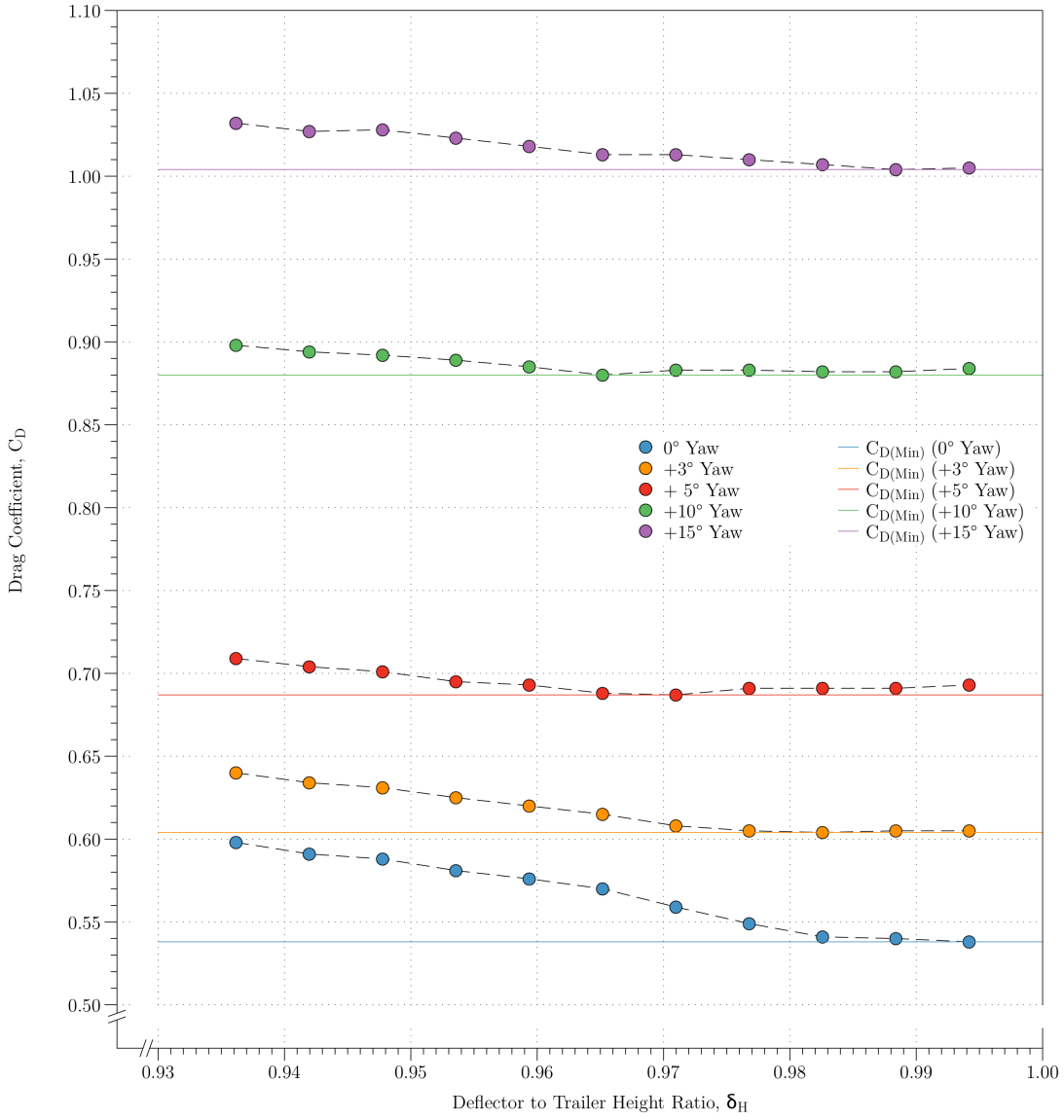

Figure E.1: C_D Variation with Deflector Height Ratio (δ_H) for $\beta = 0°$, $+5°$, $+10°$ and $+15°$.

E.2 The Effect of g/d_2 on δ_{Hopt}

E.2.1 C_D Variation with β and δ_H for Various g/d_2

	0° Yaw Deflector Height Ratio, δ_H										
g/d_2	0.968	0.974	0.980	0.986	0.992	0.998	1.004	1.010	1.016	1.022	1.028
1.315	0.598†	0.588	0.578	0.574	0.570*	0.571	0.572	0.572	0.571	0.574	0.575
1.600	0.584	0.579	0.579	0.574*	0.577	0.577	0.580	0.581	0.581	0.584	0.587†
1.676	0.583	0.579*	0.580	0.581	0.580	0.582	0.585	0.585	0.588	0.590	0.593†
	+5° Yaw										
1.315	0.699	0.699	0.699	0.700	0.698*	0.700	0.702	0.705	0.706	0.709	0.711†
1.600	0.732*	0.733	0.733	0.734	0.738	0.742	0.744	0.744	0.746	0.744	0.746†
1.676	0.739*	0.740	0.742	0.746	0.754	0.758	0.758	0.765	0.766	0.766	0.767†
	+10° Yaw										
1.315	0.855†	0.851	0.846	0.841*	0.843	0.845	0.845	0.849	0.847	0.853	0.853
1.600	0.932	0.927	0.927	0.925*	0.929	0.938	0.942	0.942	0.942	0.941	0.943†
1.676	0.963*	0.973	0.978	0.990	0.993†	0.989	0.984	0.977	0.976	0.979	0.977
	+15° Yaw										
1.315	0.957†	0.943	0.942	0.938*	0.939	0.942	0.944	0.948	0.948	0.951	0.955
1.600	1.090†	1.085	1.085	1.087	1.086	1.084	1.084	1.085	1.079	1.076*	1.077
1.676	1.164	1.174	1.178	1.180	1.183†	1.177	1.176	1.170	1.169	1.146	1.120*
	+17.5° Yaw										
1.315	0.980	0.970	0.970	0.966*	0.967	0.970	0.973	0.979	0.980	0.981	0.987†
1.600	1.144†	1.143	1.143	1.142	1.142	1.140	1.137	1.134	1.125	1.120	1.115*
1.676	1.229	1.235	1.241†	1.236	1.241	1.236	1.234	1.231	1.233	1.227	1.207*

Table E.2: C_D Coefficients[3]vs. g/d_2, Various δ_H Values.

[3]Denotes Lowest and † Denotes Highest C_D Value Obtained Respectively.

E.2.2 C_D Variation with β and δ_H for g/d_2 = 1.315

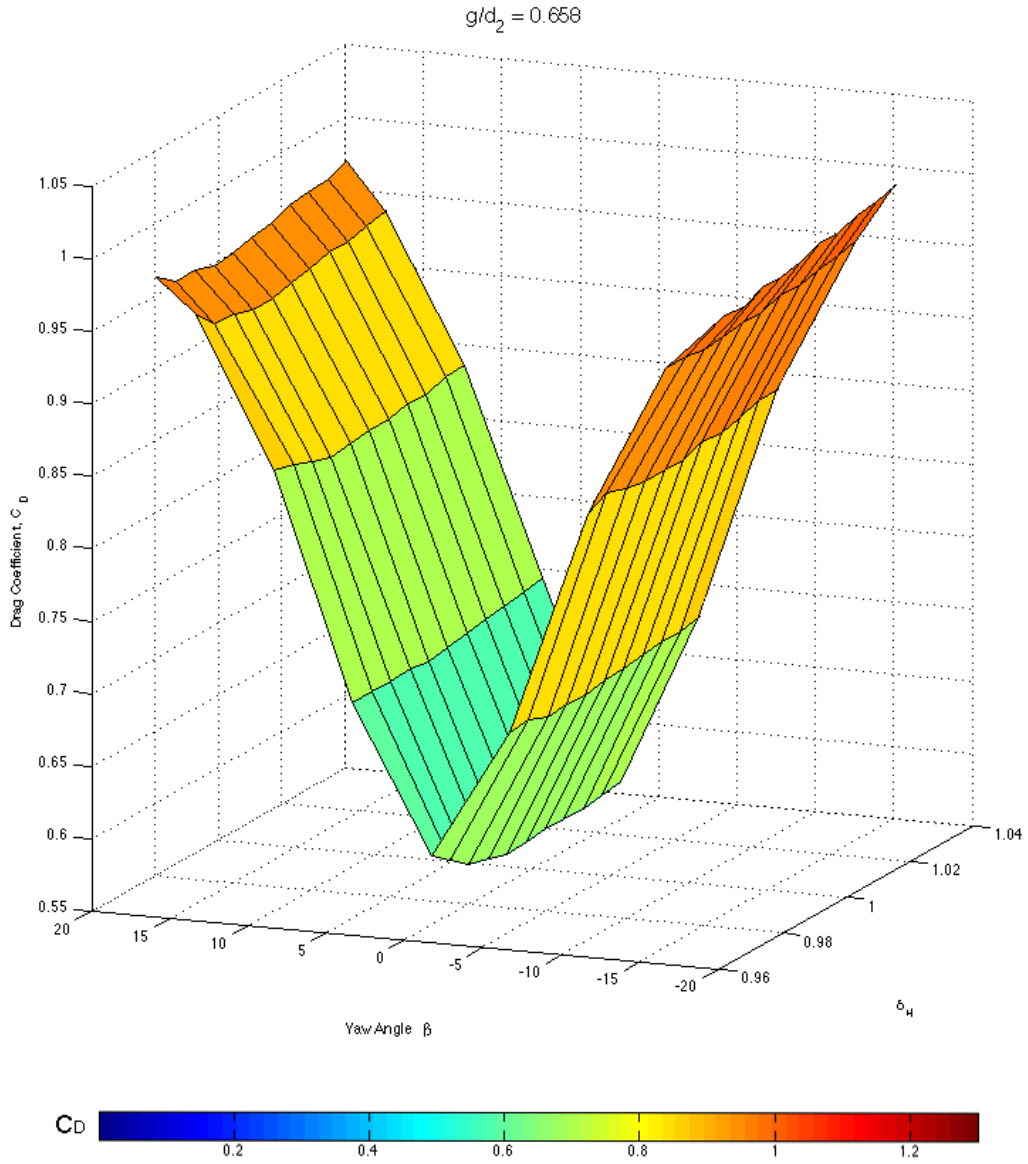

Figure E.2: Tractor-Trailer C_D Variation with Yaw Angle (β) and Deflector Height Ratio (δ_H) for g/d_2 = 1.315.

E.2.3 C_D Variation with β and δ_H for g/d_2 = 1.600

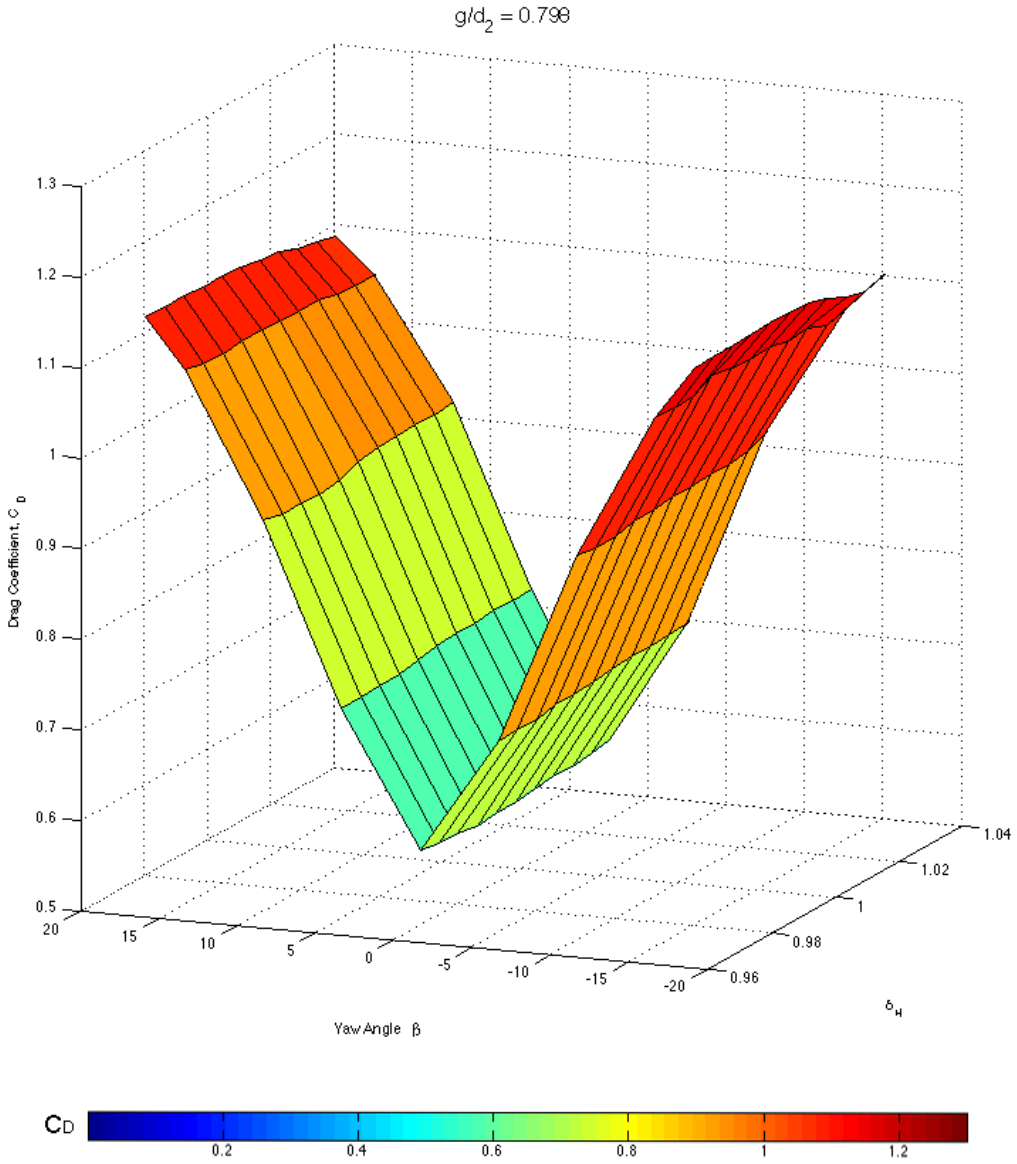

Figure E.3: Tractor-Trailer C_D Variation with Yaw Angle (β) and Deflector Height Ratio (δ_H) for g/d_2 = 1.600.

E.2.4 C_D Variation with β and δ_H for g/d_2 = 1.676

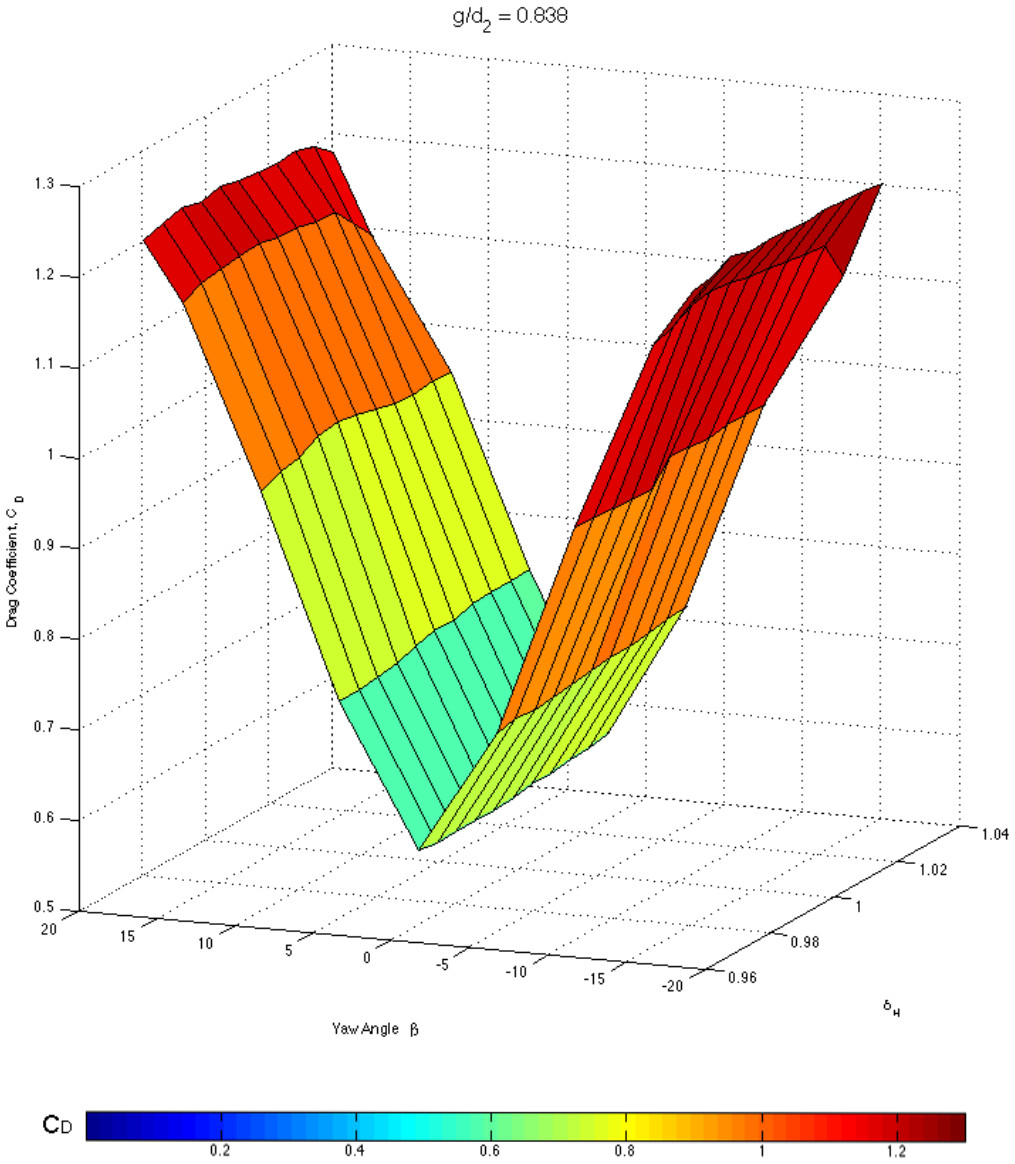

Figure E.4: Tractor-Trailer C_D Variation with Yaw Angle (β) and Deflector Height Ratio (δ_H) for g/d_2 = 1.676.

E.3 Deflector C_P Variation with δ_H and β

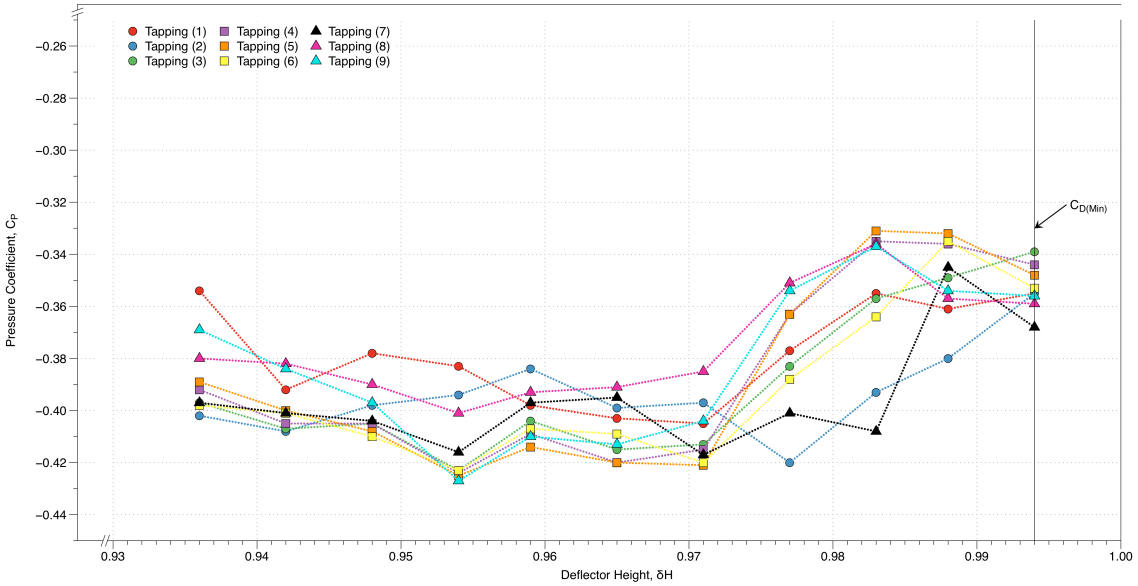

Figure E.5: C_P Distribution on Rear of Deflector for $\beta = 0°$.

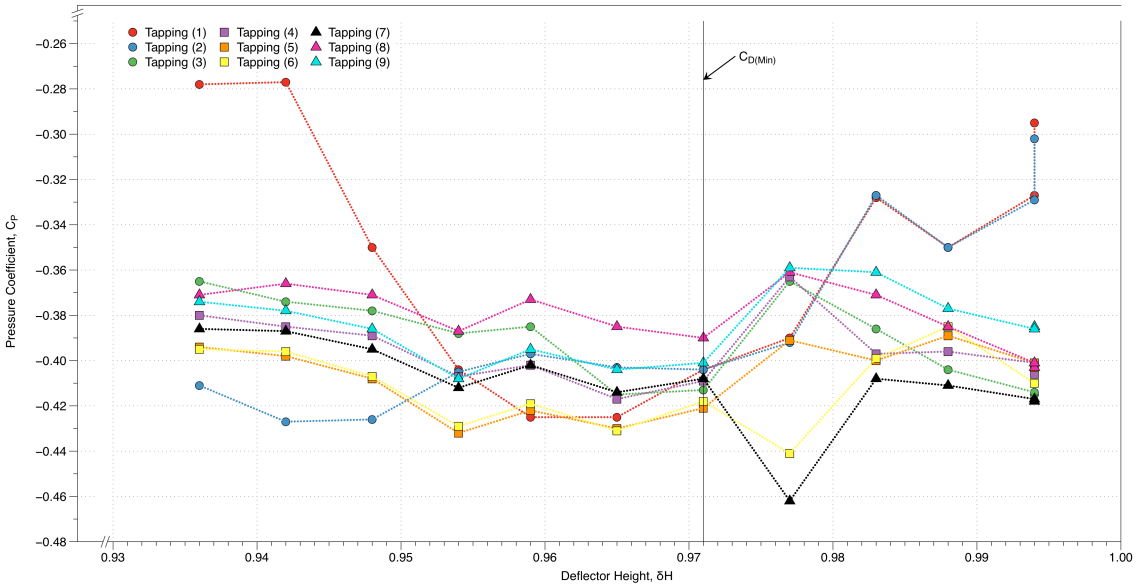

Figure E.6: C_P Distribution on Rear of Deflector for $\beta = +5°$.

E.4 Centre Line C_P Variation with β

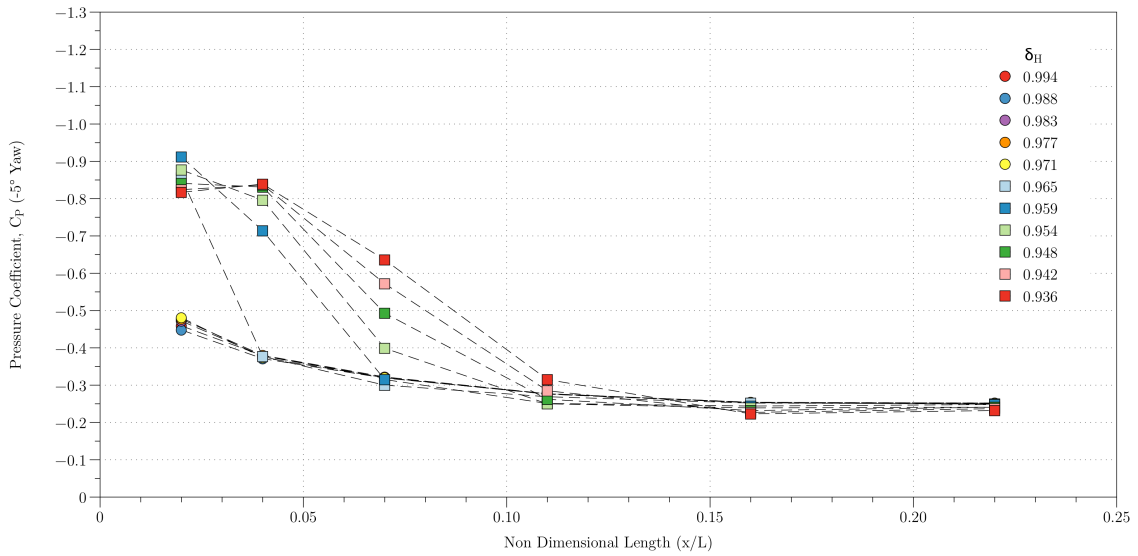

Figure E.7: C_P Variation vs. Displacement Along Trailer Centre Line for $\beta = -5°$.

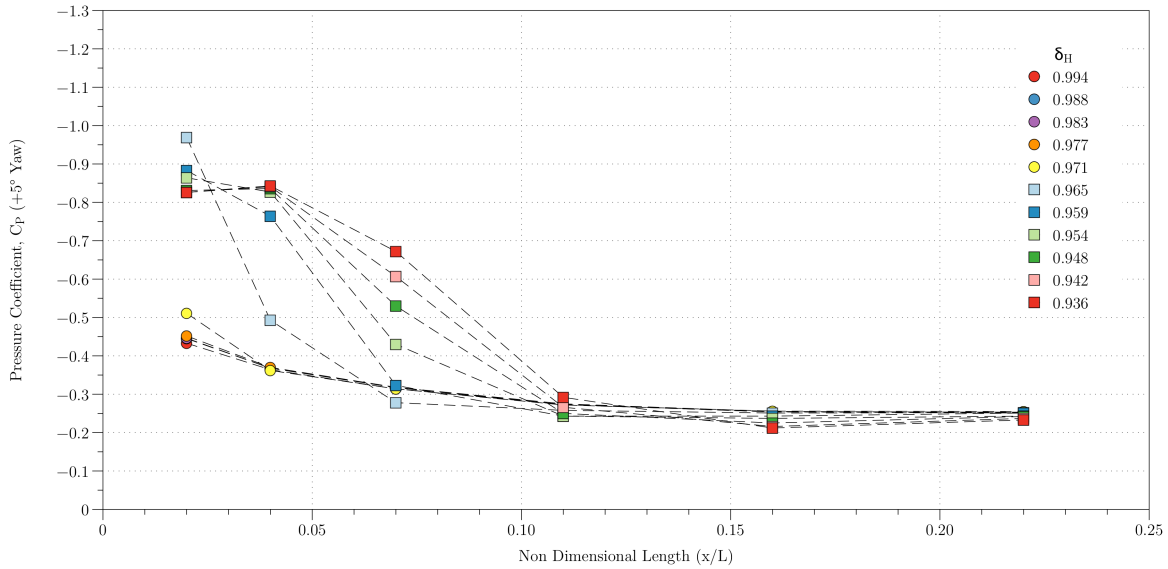

Figure E.8: C_P Variation vs. Displacement Along Trailer Centre Line for $\beta = +5°$.

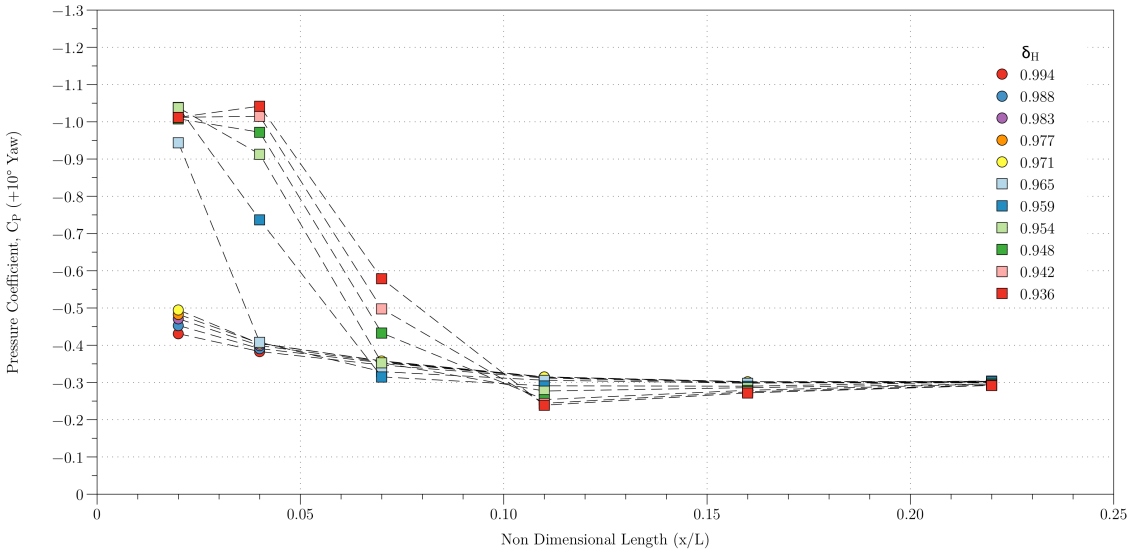

Figure E.9: C_P Variation vs. Displacement Along Trailer Centre Line for $\beta = +10°$.

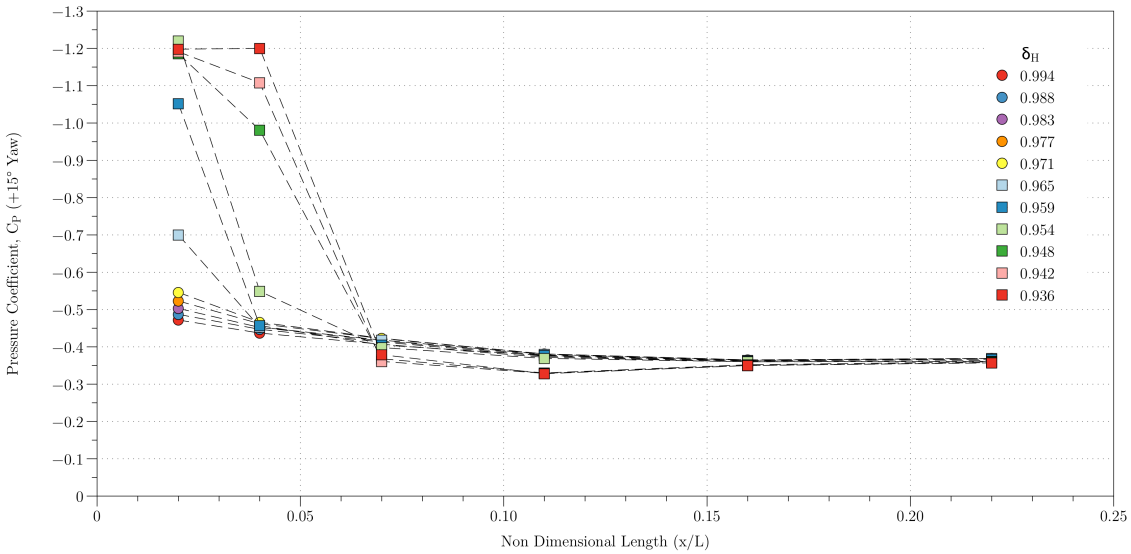

Figure E.10: C_P Variation vs. Displacement Along Trailer Centre Line for $\beta = +15°$.

E.5 Wind Averaged Drag Coefficient

Assuming a heavy goods vehicle is travelling with speed (V_{Truck}) and the wind has a velocity (V_W) at an angle (ϕ) (shown in Fig.(E.11)), the resultant velocity of the air relative to the vehicle is given by Eq.(E.1), where the probability distribution is symmetric about the vehicle centre line.

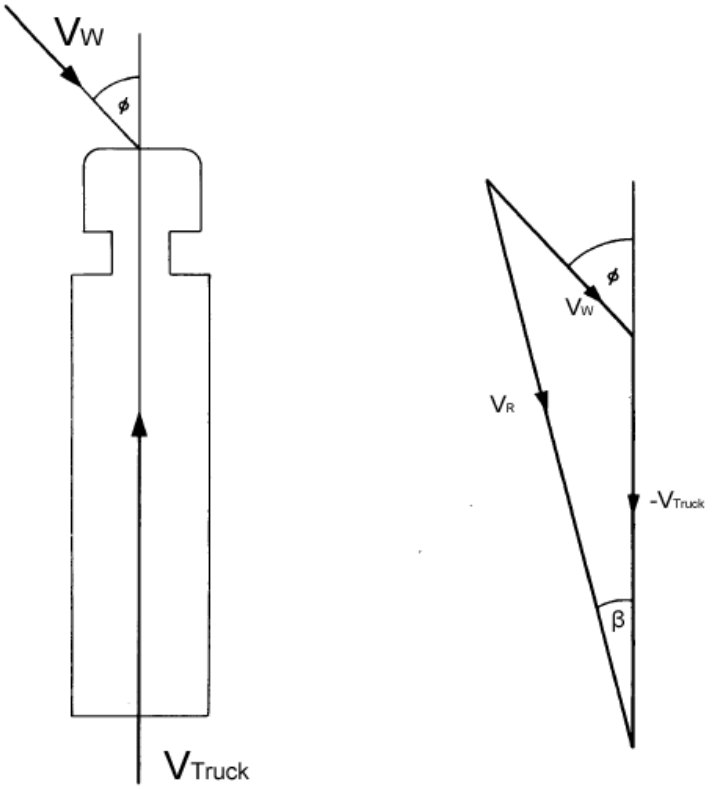

Figure E.11: On-Road Relative Wind Vector Diagrams for a Heavy Goods Vehicle [18].

$$V_R = V_{\text{Truck}}\sqrt{1 + (V_W/V_{\text{Truck}})^2 + 2(V_W/V_{\text{Truck}})\cos(\phi)} \tag{E.1}$$

The yaw angle (β) is therefore given by

$$\tan(\beta) = [(V_W/V_{\text{Truck}})\sin(\phi)] \,/\, [1 + (V_W/V_{\text{Truck}})\cos(\phi)] \tag{E.2}$$

where the aerodynamic drag force is given by

$$F_D = \frac{1}{2}\rho(V_R)^2 C_D(\beta) A \tag{E.3}$$

where ρ is the density of the air, A is the reference area of the vehicle and $C_D(\beta)$ is the drag coefficient of the vehicle at the yaw angle.

Substituting Eq.(E.1) into Eq.(E.3) gives the wind averaged drag force ($\overline{D}$) given by

$$\overline{D} = \frac{\rho V_{\text{Truck}}^2 A}{2} \int_0^{2\pi} \int_0^{V_{W\text{Max}}} C_D(\beta) \left[1 + (V_W/V_{\text{Truck}})^2 + 2(V_W/V_{\text{Truck}})\cos(\phi)\right] p(V_W, \phi) \mathrm{d}\phi \mathrm{d}V_W \tag{E.4}$$

where V_{Truck} is assumed constant with respect to the wind speed V_W and $p(V, \beta)$ is the probability of V_W blowing at an angle ϕ relative to the vehicle.

The wind averaged drag coefficient (WADC) can therefore be defined [18] as

$$\overline{C_D} = \int_0^{2\pi} \int_0^{V_{W(\text{Max})}} C_D(\beta) \left[1 + (V_W/V_{\text{Truck}})^2 + 2(V_W/V_{\text{Truck}})\cos(\phi)\right] p(V_W, \phi) \mathrm{d}\phi \mathrm{d}V_W \tag{E.5}$$

If V_W is replaced by an average wind speed (V_{Ave}), assumed to be equally probable from all directions with the vehicle assumed symmetric about the longitudinal axis, Eq.(E.5) can be reduced to Eq.(E.6):

$$\overline{C_D} = \frac{1}{\pi} \int_0^{\pi} C_D(\beta) \left[1 + (V_{Ave}/V_{\text{Truck}})^2 + 2(V_{Ave}/V_{\text{Truck}})\cos(\phi)\right] p(V_{Ave}, \phi) \mathrm{d}\phi \tag{E.6}$$

Whilst Eq.(E.6) is an approximation to Eq.(E.6) it is commonly used in academic research [5], [111]. This report, however, used the more accurate form given in Eq.(E.5).

The data required to calculate $\overline{C_D}$ was $C_D(\beta)$ (obtained from wind tunnel data) and $p(V_W, \phi)$ wind statistics used by Ingram [18].

E.5.1 Probability of On-Road Wind Direction

The on-road wind direction probabilities ($p(\phi)$) calculated by Ingram [18] are shown in Tab.(E.3) and Fig.(E.12) where $p(\phi)$ is symmetric about the longitudinal axis of the vehicle.

Wind Direction (ϕ) (°)	Probability (p(ϕ))
16-45	0.168
46-75	0.170
76-105	0.169
106-135	0.171
136-165	0.167
166-15	0.155

Table E.3: On-Road Wind Direction Distribution Data [18].

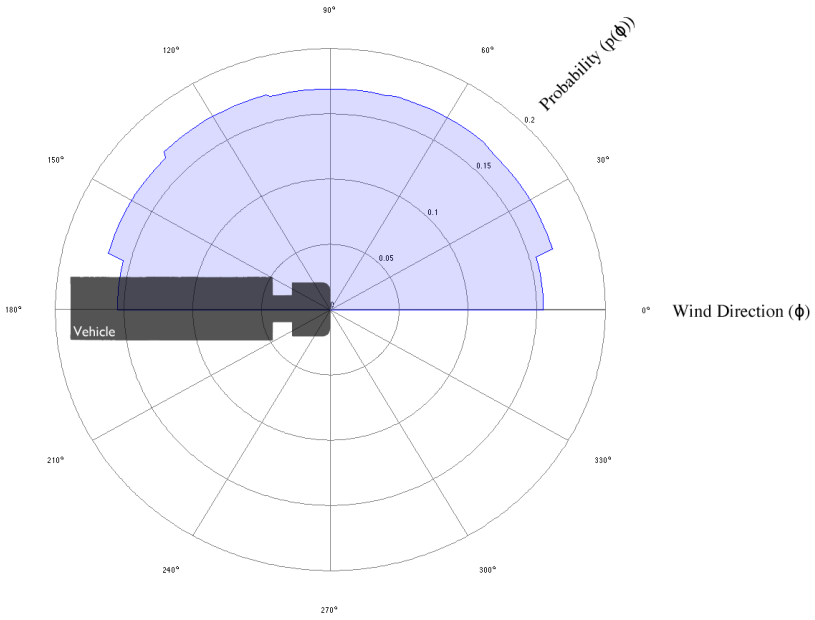

Figure E.12: Polar Plot of On-Road Wind Direction Distribution [18]

E.5.2 Probability of On-Road Wind Speed

The on-road wind speed probabilities ($p(V_W)$) calculated by Ingram [18] are shown in Tab.(E.4) and Fig.(E.13).

Wind Speed (V_W)	Probability (p(V_W))
0.00 - 0.49	0.000
0.50 - 0.99	0.004
1.00 - 1.49	0.021
1.50 - 1.99	0.075
2.00 - 2.49	0.149
2.50 - 2.99	0.241
3.00 - 3.49	0.485
3.50 - 3.99	0.445
4.00 - 4.49	0.315
4.50 - 4.99	0.145
5.00 - 5.49	0.069
5.50 - 5.99	0.031
6.00 - 6.49	0.014
6.50 - 6.99	0.006

Table E.4: On-Road Speed Probability Distribution Data [18].

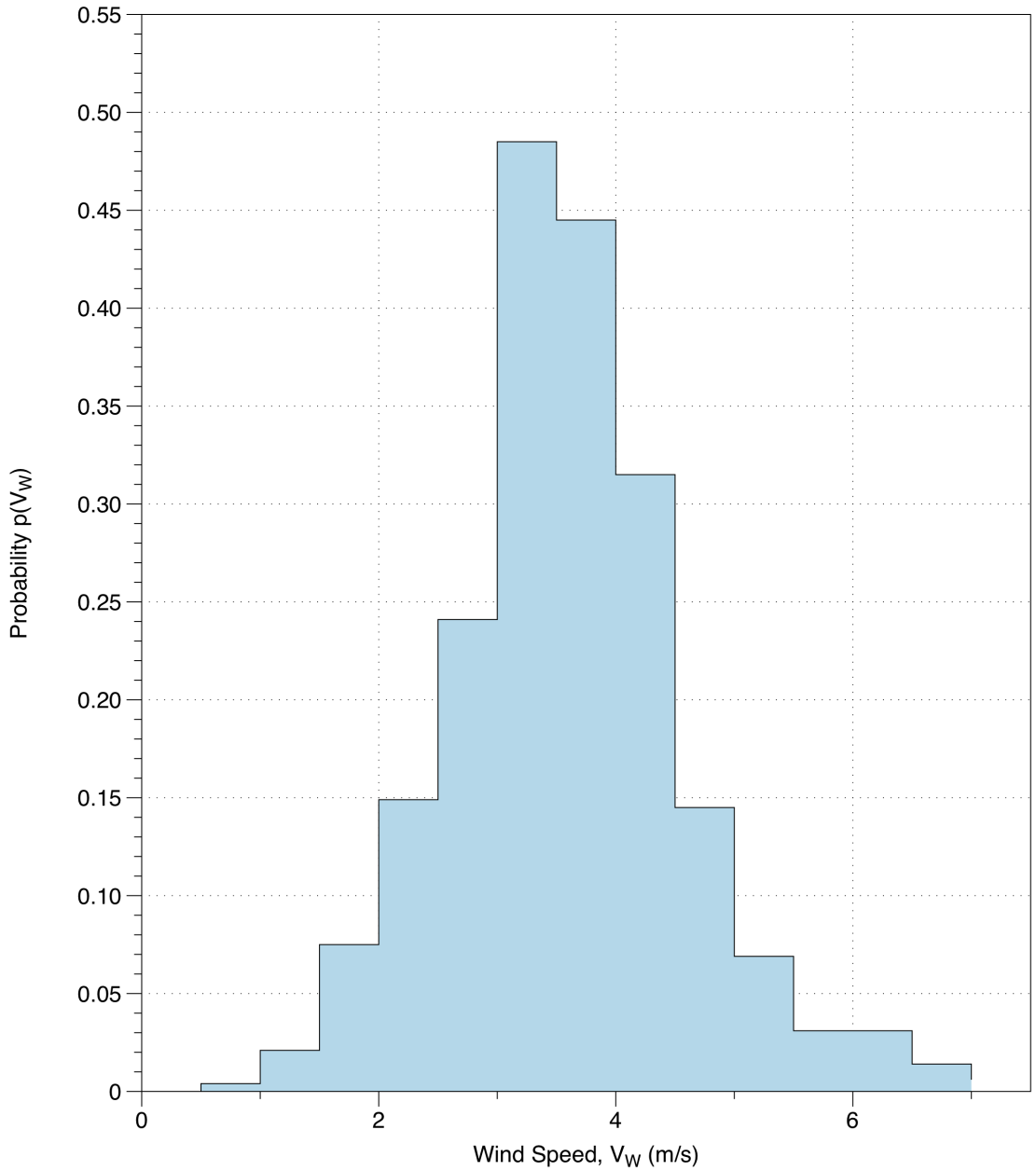

Figure E.13: Probability Plot of On-Road Wind Speeds [18].

E.5.3 WADC Applied to Measured Data

Due to the $C_D(\beta)$ requiring a range of: $0° < \beta \leq 180°$ (the vehicle is assumed symmetric about the longitudinal centre line), linear interpolation of $C_D(\beta)$ was performed. The interpolation of one set of data used is shown in Fig.(E.14).

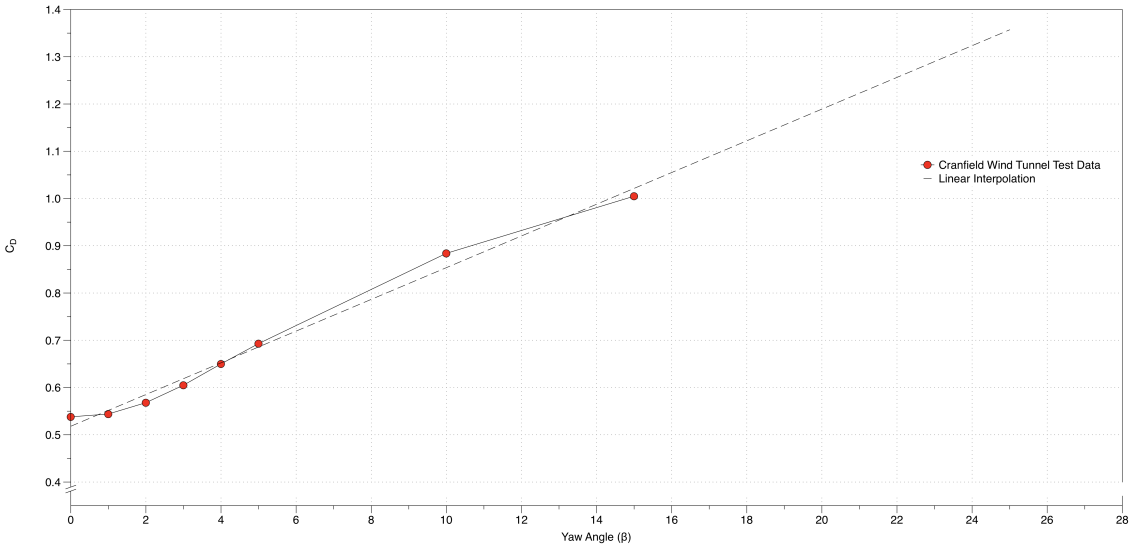

Figure E.14: Linear Interpolation of Wind Tunnel Data ($\delta_H = 0.994$).

From Eq.(E.5) and noting $C_D(-\beta) = C_D(-\beta)$ and under the assumption $p(V_W, \phi)$ can be decomposed into the product of two independent probabilities $p(V_W)p(\phi)$, the integral to calculate the WADC is shown in Eq.(E.7):

$$\overline{C_D} = \int_0^{\pi} \int_0^{V_{W(\mathrm{Max})}} C_D(\beta) \left[1 + (V_W/V_{\mathrm{Truck}})^2 + 2(V_W/V_{\mathrm{Truck}}) \cos(\phi)\right] p(V_W)p(\phi)\mathrm{d}\phi\mathrm{d}V_W \tag{E.7}$$

Eq.(E.7) was evaluated using Monte Carlo simulation to approximate the integral. *Mathematica*® was used for the numerical simulation, the processing code created to calculate the WADC is shown in Sec.(E.5.3.1).

E.5.3.1 WADC *Mathematica*® Processing Code

```
(* Wind Average Drag Coefficient Calculation *)

(* Wind Angle Probability *)
e = 16;
f = 29;
PPhi[x_] := 0.0775/e /; 0 <= x <= 15
PPhi[x_] := 0.16/f /; 15 < x <= 45
PPhi[x_] := 0.170/f /; 45 < x <= 75
PPhi[x_] := 0.169/f /; 75 < x <= 105
PPhi[x_] := 0.171/f /; 105 < x <= 135
PPhi[x_] := 0.167/f /; 135 < x <= 165
PPhi[x_] := 0.0775/e /; 165 < x <= 180
Plot[PPhi[x], {x, 0, 180}]
Sum[PPhi[x], {x, 0, 180, 1}];


(* Wind Velocity Probability *)
p = 2;
r = 3;
PV[x_] := 0.001/r /; 0 <= x <= 0.5
PV[x_] := 0.002286/p /; 0.5 < x <= 1
PV[x_] := 0.02571/p /; 1 < x <= 1.5
PV[x_] := 0.074286/p /; 1.5 < x <= 2.0
PV[x_] := 0.150857/p /; 2.0 < x <= 2.5
PV[x_] := 0.24/p /; 2.5 < x <= 3.0
PV[x_] := 0.486857/p /; 3.0 < x <= 3.5
PV[x_] := 0.4435/p /; 3.5 < x <= 4.0
PV[x_] := 0.313143/p /; 4.0 < x <= 4.5
PV[x_] := 0.14172/p /; 4.5 < x <= 5.0
PV[x_] := 0.068571/p /; 5.0 < x <= 5.5
PV[x_] := 0.029714/p /; 5.5 < x <= 6.0
PV[x_] := 0.011429/p /; 6.0 < x <= 6.5
PV[x_] := 0.004571/p /; 6.5 < x <= 7.0
PV[x_] := 0.001/r /; 7 < x
Vmax = 7.0;
Plot[PV[x], {x, 0, 7}]

(* Wind Tunnel Cd's *)
Cd = {0.5380, 0.5440, 0.5680, 0.6050, 0.6500, 0.6930, 0.8841,1.0050};
YawAngle = {0, 1, 2, 3, 4, 5, 10, 15};

(* Combine and Plot *)
CdYaw = Partition[Riffle[Flatten[YawAngle], Flatten[Cd]], 2];
ListPlot[CdYaw, Joined -> True, PlotRange -> {{0, 15}, {0.5, 1.2}}]

(*  Linear Interpolation of Data: Y = 0.5181 + 0.033556 X *)
CdYawInterp = Interpolation[CdYaw, InterpolationOrder -> 1];
Plot[CdYawInterp[x], {x, 0, 20}]

(* Monte Carlo Approximation to Numerical Integral *)
SimAns = 0;
Do[SimAns += (1/24)*NIntegrate[CdYawInterp[beta]*((1 + (Vw/Vt)^2) + (2*(Vw/Vt)*cos[beta]))*
PPhi[beta]*PV[Vw], {beta, 0, 180}, {Vw, 0, Vmax}, Method -> "MonteCarlo"], {Vt, 8.0, 30, 1}]
SimAns = 1.395
```

E.6 Wind Vane and Wind Anemometer Sensor Positioning

(β)	P_1	P_2	P_3	P_4	P_5	$\overline{P}$	$C_{P(\alpha)}$
-17.5	735.803	-202.493	-173.002	-87.029	223.315	68.320	5.863
-15	745.659	-167.746	-211.534	-169.687	247.058	49.173	4.837
-10	740.440	-32.328	-345.544	-339.869	289.010	5.675	3.833
-5	671.293	61.362	-573.866	-583.622	225.320	-106.208	3.756
-4	650.675	80.987	-622.757	-633.023	208.006	-131.029	3.756
-3	627.764	97.897	-671.537	-688.023	187.705	-158.475	3.753
-2	603.084	110.429	-723.758	-742.333	161.522	-188.145	3.795
-1	577.947	120.689	-776.096	-796.933	133.320	-218.598	3.848
0	561.560	132.444	-815.563	-840.351	113.924	-240.478	3.886
1	538.237	141.793	-862.429	-885.842	83.789	-267.060	3.992
2	507.724	153.283	-903.878	-929.195	57.635	-293.016	4.026
3	479.149	166.321	-944.351	-967.919	27.454	-316.700	4.136
4	445.773	180.889	-984.818	-1008.046	-0.023	-341.551	4.189
5	411.886	195.371	-1026.305	-1046.299	-28.176	-366.337	4.253
10	221.109	244.916	-1268.446	-1276.174	-227.298	-519.649	5.095
15	13.966	298.613	-1497.203	-1480.608	-425.223	-666.308	6.268
17.5	-121.283	327.826	-1631.910	-1594.522	-548.389	-754.973	7.312

Table E.5: $C_{P(\alpha)}$ Wind Vane and Wind Anemometer Sensor Positioning.

This page intentionally left blank.

Appendix F

Computational Data

Primary investigation was conducted on a 2D geometry to determine the most accurate Reynolds-Averaged Navier-Stokes (RANS) turbulence model for the geometry. The geometry was then replaced by a 3D version to investigate the accuracy of the chosen RANS model with the obtained experimental results. More information on the model arrangement and computational methodology is shown in Chapter 4.

F.1 2D Grid Convergence Study

Initially a series of three meshes (shown with data summarised in Tab.(F.1)) were developed to conduct a grid convergence study. The purpose of the study was to investigate the effects of grid refinement on the accuracy of the computational results. The chosen mesh size was therefore sufficiently accurate to model the problem, but sufficiently coarse that the simulation times are within permissible execution time.

The Spalart-Allmaras solver was chosen as it is a single equation model, providing the lowest execution time for convergence.

Case Number	Mesh Size (Cells)	C_D
Case 1	21132	0.613
Case 2	42929	0.624
Case 3	84528	0.625

Table F.1: Spalart-Allmaras Grid Convergence Study.

From the results obtained from the convergence study, the initial mesh of approximately 21k grid cells varied in C_D by 1.8% to the next finer mesh of 43k. Further refinement of the 43k mesh to 85k grid cells revealed a reduction in the drag

coefficient by 0.2%. From the result of the grid convergence study, Case 2 (42929 Grid Cells) provided a sufficient balance between refinement and execution time and was chosen for the simulations.

F.1.1 2D RANS Model Selection

F.1.1.1 2D RANS ΔC_D Model Prediction

Due to the difference in turbulence modelling present within the various RANS models, a model comparison study was conducted to determine which numerical model best captured the flow physics. The initial drag coefficient (C_D) values for gap to trailer separations (g/d_2) of 0.658, 0.798 and 0.838 were investigated for a fixed deflector height ratio (δ_H) of 0.968. The RANS model results are shown in Tab.(F.2 and F.3) and the experimental results shown in Tab.(F.4).

Model	δ_h	g/d_2	C_D	ΔC_D
S-A	0.968	0.658	0.624	
S-A	0.968	0.798	0.609	-2.4%
S-A	0.968	0.838	0.604	-0.8%
k-$\epsilon_{(\text{Standard})}$	0.968	0.658	0.650	
k-$\epsilon_{(\text{Standard})}$	0.968	0.798	0.625	-3.8%
k-$\epsilon_{(\text{Standard})}$	0.968	0.838	0.623	-0.3%
k-$\epsilon_{(\text{Realizable})}$	0.968	0.658	0.575	
k-$\epsilon_{(\text{Realizable})}$	0.968	0.798	0.545	-5.2%
k-$\epsilon_{(\text{Realizable})}$	0.968	0.838	0.544	-0.2%
k-$\epsilon_{(\text{RNG})}$	0.968	0.658	0.533	
k-$\epsilon_{(\text{RNG})}$	0.968	0.798	0.522	-2.1%
k-$\epsilon_{(\text{RNG})}$	0.968	0.838	0.520	-0.4%

Table F.2: C_D Prediction Using S-A and the k-ϵ Family of Numerical Solvers.

Model	δ_h	g/d_2	C_D	ΔC_D
k-$\omega_{(\text{Standard})}$	0.968	0.658	0.898	
k-$\omega_{(\text{Standard})}$	0.968	0.798	0.945	+5.2%
k-$\omega_{(\text{Standard})}$	0.968	0.838	0.950	+0.5%
k-$\omega_{(\text{SST})}$	0.968	0.658	0.655	
k-$\omega_{(\text{SST})}$	0.968	0.798	0.633	-3.4%
k-$\omega_{(\text{SST})}$	0.968	0.838	0.636	+0.5%
$\text{Trans}_{(SST)}$	0.968	0.658	0.658	
$\text{Trans}_{(SST)}$	0.968	0.798	0.653	-0.8%
$\text{Trans}_{(SST)}$	0.968	0.838	0.652	-0.1%
$\text{Trans}_{(k-kl-\omega)}$	0.968	0.658	0.722	
$\text{Trans}_{(k-kl-\omega)}$	0.968	0.798	0.702	-2.8%
$\text{Trans}_{(k-kl-\omega)}$	0.968	0.838	0.734	+4.6%

Table F.3: C_D Prediction Using the k-ω and $Trans$ Families of Numerical Solvers.

δ_h	g/d_2	C_D	ΔC_D
0.968	0.658	0.598	
0.968	0.798	0.584	-2.3%
0.968	0.838	0.583	-0.2%

Table F.4: C_D Wind Tunnel Results for Various g/d_2.

The results obtained from the RANS model comparison showed a wide variation in the initial C_D prediction or the $g/d_2 = 0.658$ case. The predicted C_D varied from 0.533 to 0.898, compared to the experimental value of 0.598. Due to the simplification of the geometry, comparison of the baseline drag coefficient for the 2D CFD cases against the 3D experimental data was not conducted. Comparison of the change in the C_D for varying g/d_2 at 0° yaw (ΔC_D) yielded a more accurate comparison term. The improvement in the comparison term was due to the differences in baseline configurations being accounted for by the turbulence model. The turbulence model correctly predicted the change in drag coefficient due solely to the change in geometry.

The models that correctly predicted a decrease in C_D for an increase in g/d_2 from 0.658 to 0.798 and 0.838 were: S-A, k-$\epsilon_{(Standard)}$, k-$\epsilon_{(Realizable)}$, k-$\epsilon_{(RNG)}$ and $\text{Trans}_{(SST)}$. The models that predicted the closest values of the ΔC_D were S-A and k-$\epsilon_{(RNG)}$. Investigation into the container roofline pressure distribution was then made to further establish which model best represented the flow physics.

F.1.1.2 2D Container Centre Line Pressure Distribution

The pressure distribution along the centre line of the container top has previously been investigated by Gilhaus et al. [87]. The pressure distribution obtained by Gilhaus et al. was for an unfaired cab. As a result the centre line pressure distribution near the leading edge of the trailer was expected to differ. The experimental data obtained from the wind tunnel testing is therefore presented for the leading edge of the container. The results are shown in Fig.(F.2). The simulation centre line pressures for the models that most accurately predicted the ΔC_D are shown in Fig.(F.3). Comparison of all the models is shown in Fig.(F.1).

The experimental results obtained by Gilhaus et al. [87] showed a pressure coefficient (C_P) value of around -0.8 at (x/L = 0), rising to -0.05 at around (x/L = 0.5), the value then rose to close to the freestream pressure until an increase to -0.2 at (x/L = 1). The overall pressure distribution trend obtained from the simulation, however, matched poorly with the experimental data.

The C_P values close to the leading edge were not predicted accurately by any of the RANS models. The experimental data for the faired cab had a container C_P dropping from around -1.0 to close to -0.2 over a short length (x/L = 0.1). The difference in centre line pressures originates from the simplified geometry and lack of 3D cavity effects. The lower predicted C_P of -1.0 at (x/L = 0) compared with the data obtained by Gilhaus et al. [87] indicated a smoother transition between cab and trailer, the difference arising due to the presence of a cab mounted roof deflector present on the numerical model. Fig.(6.22) shows an experimental C_P value of -0.95 can be achieved at (x/L = 0) with a cab mounted roof deflector. The drop in C_P for the experimental results to approximately -0.23 until around (x/L = 0.22). The 2D CFD case does not take into account any 3D effects and therefore overpredicted the centre line velocity which resulted in a lower C_P along the centre line. The RANS models used did predict a raise in the C_P towards the rear of the container due the interference of the near wake flow field.

Due to all the tested RANS models predicting similar pressures on the trailer centre line, which did not match the experimental data, investigation continued into the accuracy of the predicted wake structure.

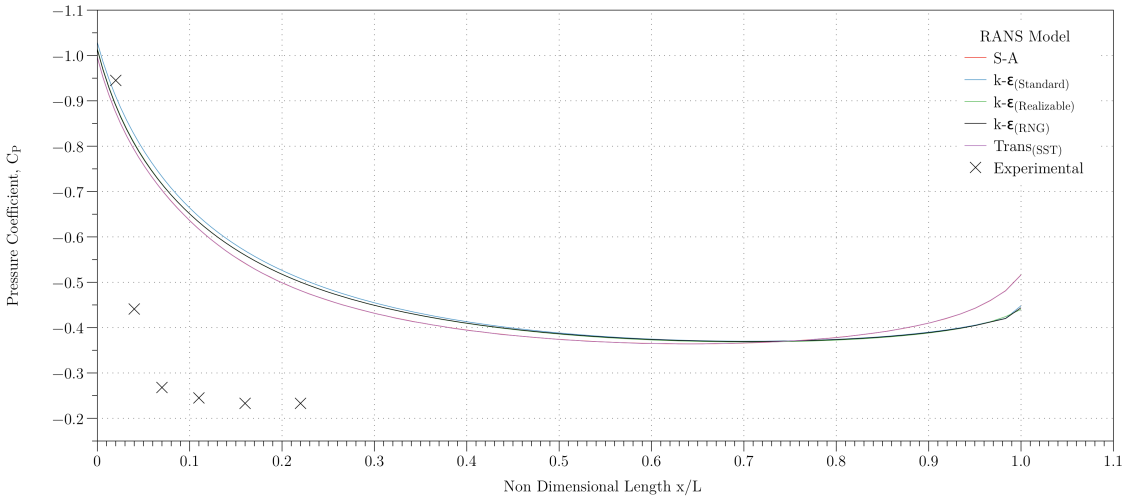

Figure F.1: Computationally Predicted Truck Centre Line Pressure Distribution.

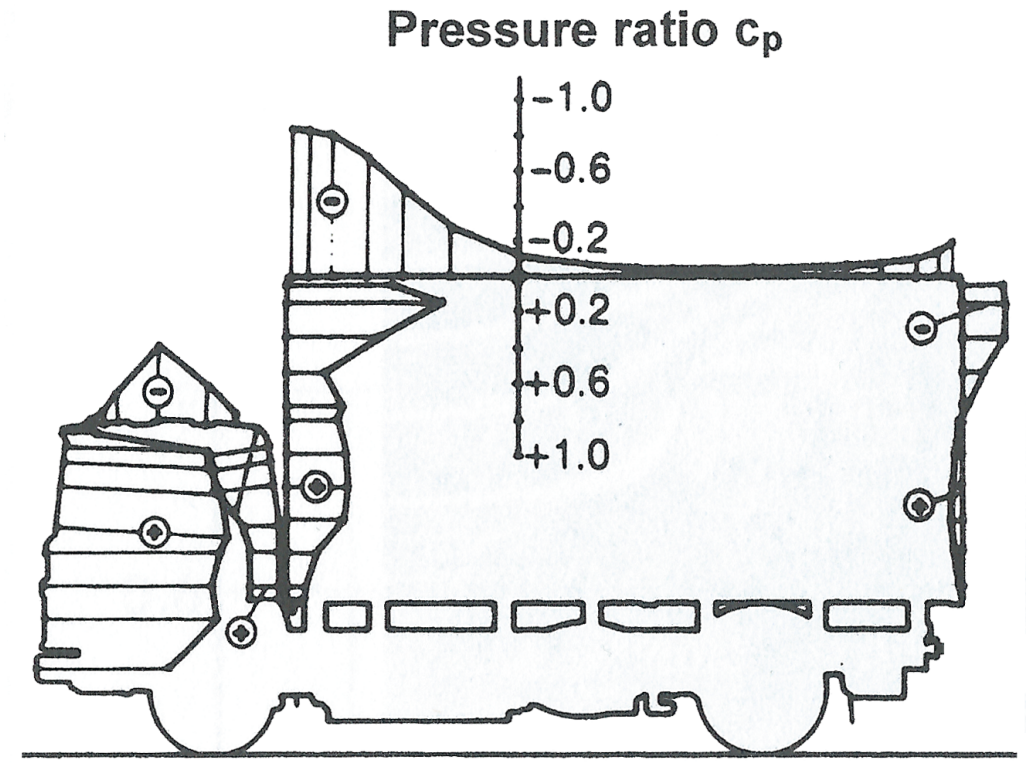

Figure F.2: Experimental Truck Centre Line Pressure Distribution [87].

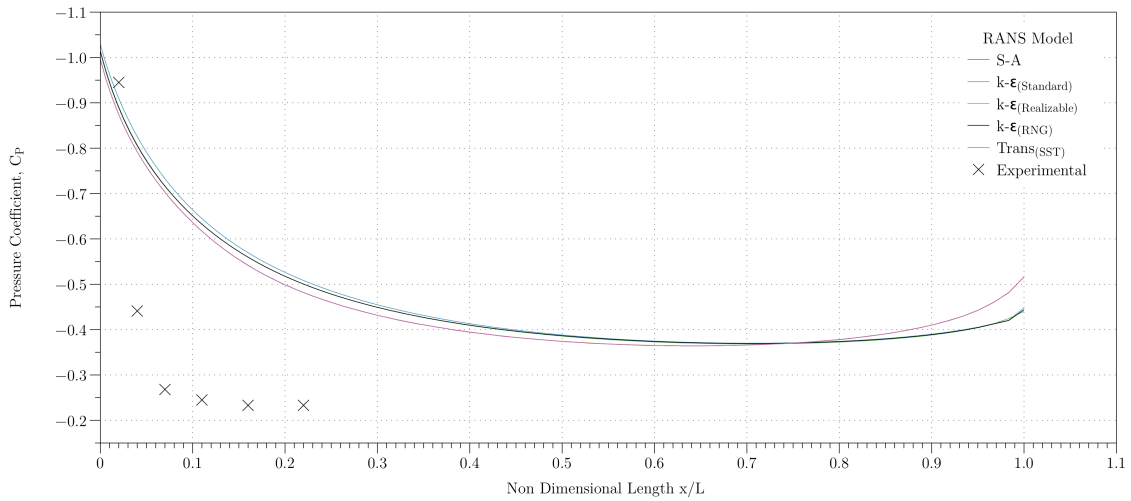

Figure F.3: 2D Computationally Predicted Trailer Centre Line Pressure Distribution.

F.1.1.3 2D Trailer Wake Prediction

Prior experimental work has been conducted to investigate the trailer wake. Particle Image Velocimetry had been used on the rear wake of a simplified tractor-trailer geometry by Heineck et al. [19]. The experimental data is shown in Fig.(F.4), with the computational results shown in Figs.(F.5 - F.9). Where x/W, y/W and z/W are the normalised displacements in the x, y and z directions, respectively and are normalised with respect to the trailer width (W).

The k-$\epsilon_{(Realizable)}$ was chosen based from the structure of the wake vortices produced that most closely matched the experimental data. The k-$\epsilon_{(RNG)}$ model that most accurately predicted the ΔC_D added an additional recirculation region to the lower side of the tractor (shown in Fig.(F.8)). The k-$\epsilon_{(Realizable)}$ was therefore chosen as the RANS solver that most accurately modelled the flow over the vehicle. This was as a result of the model correctly predicting the rear wake and closely predicting the ΔC_D.

The k-$\epsilon_{(Realizable)}$ model should offer better performance over both k-ϵ and k-$\epsilon_{(RNG)}$ as it satisfies mathematical constraints on the Reynolds stresses consistent with the flow physics of turbulent flows. As a result it should offer better performance over k-ϵ and k-$\epsilon_{(RNG)}$ for separating and recirculating flows.

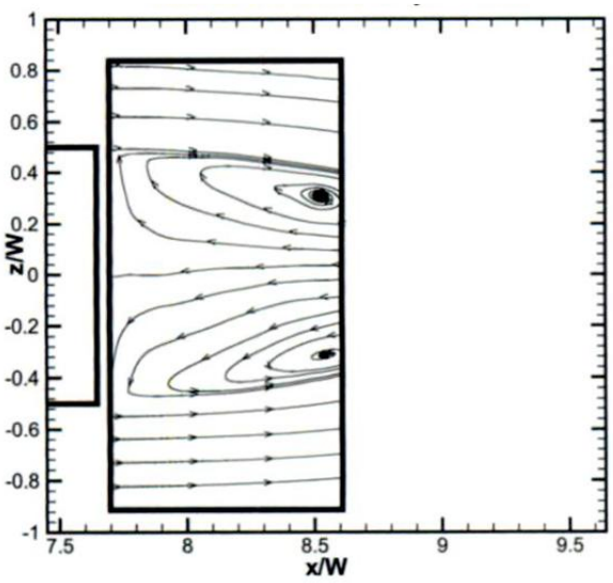

Figure F.4: Experimental PIV Streamlines of Trailer Wake [19].

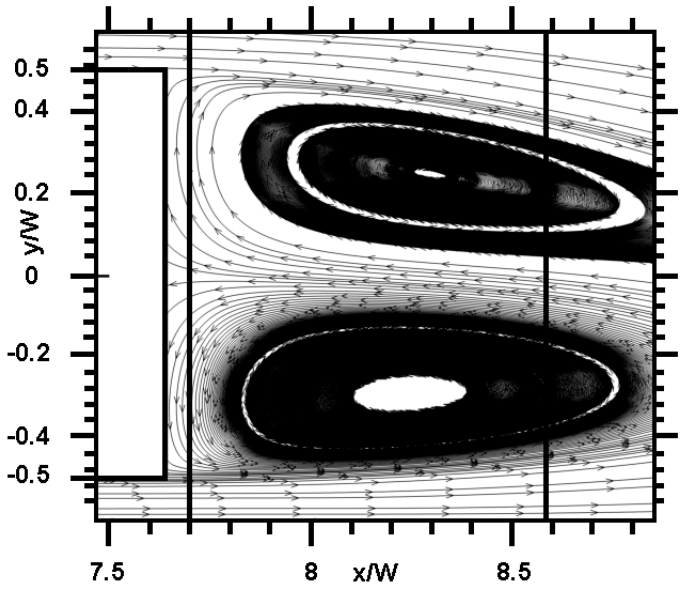

Figure F.5: S-A Computational Prediction of Trailer Wake.

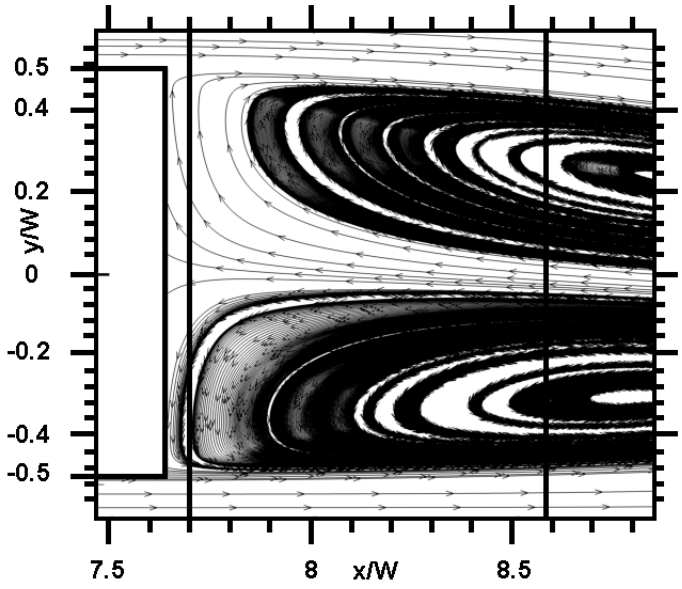

Figure F.6: k-ϵ Computational Prediction of Trailer Wake.

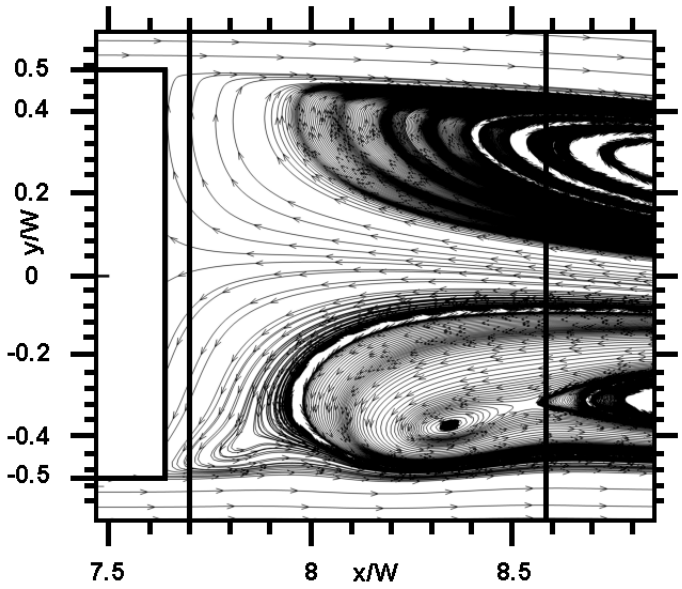

Figure F.7: k-$\epsilon_{(Realizable)}$ Computational Prediction of Rear Trailer Wake.

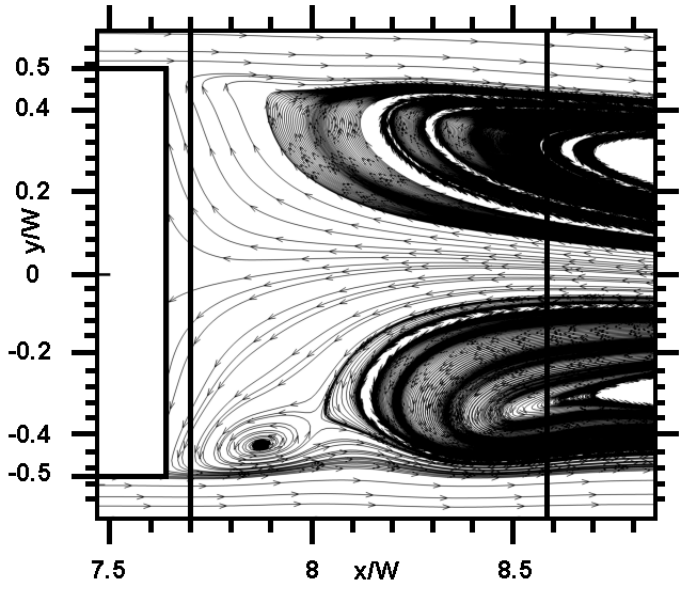

Figure F.8: k-$\epsilon_{(RNG)}$ Computational Prediction of Trailer Wake.

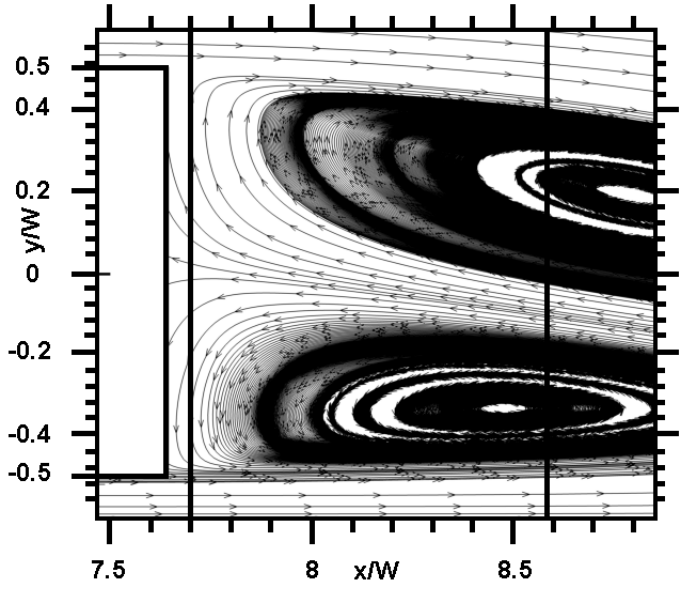

Figure F.9: $TRANS_{(SST)}$ Computational Prediction of Trailer Wake.

F.1.2 k-$\epsilon_{(Realizable)}$ Prediction of ΔC_D vs. δ_H

The wind tunnel data obtained earlier in Chapter 6 is shown in Tab.(F.5 and F.6), the corresponding k-$\epsilon_{(Realizable)}$ predicted C_D and ΔC_D are shown in Tab.(F.7 and F.8) respectively. The data is presented in graphical format in Fig.(F.10).

	g/d_2			
δ_H	0.658	0.798	0.838	1.056
0.968	0.598	0.584	0.583	-
δ_{Hopt}	0.570	0.574	0.579	-
1.028	0.575	0.587	0.593	-

Table F.5: Wind Tunnel C_D Results Summary.

	g/d_2			
δ_H	0.658	0.798	0.838	1.056
0.968	+4.9%	+1.7%	+0.7%	-
δ_{Hopt}	-	-	-	-
1.028	+0.9%	+2.3%	+2.4%	-

Table F.6: Wind Tunnel ΔC_D Results Summary.

	g/d_2			
δ_H	0.658	0.798	0.838	1.056
0.968	0.574	0.569	0.568	0.547
δ_{Hopt}	0.567	0.568	0.568	0.547
1.028	0.584	0.578	0.578	0.581

Table F.7: k-$\epsilon_{(Realizable)}$ C_D Prediction.

	g/d_2			
δ_H	0.658	0.798	0.838	1.056
0.968	+1.2%	+0.2%	0%	0%
δ_{Hopt}	-	-	-	-
1.028	+2.9%	+2.3%	+1.8%	+6.2%

Table F.8: k-$\epsilon_{(Realizable)}$ ΔC_D Predication.

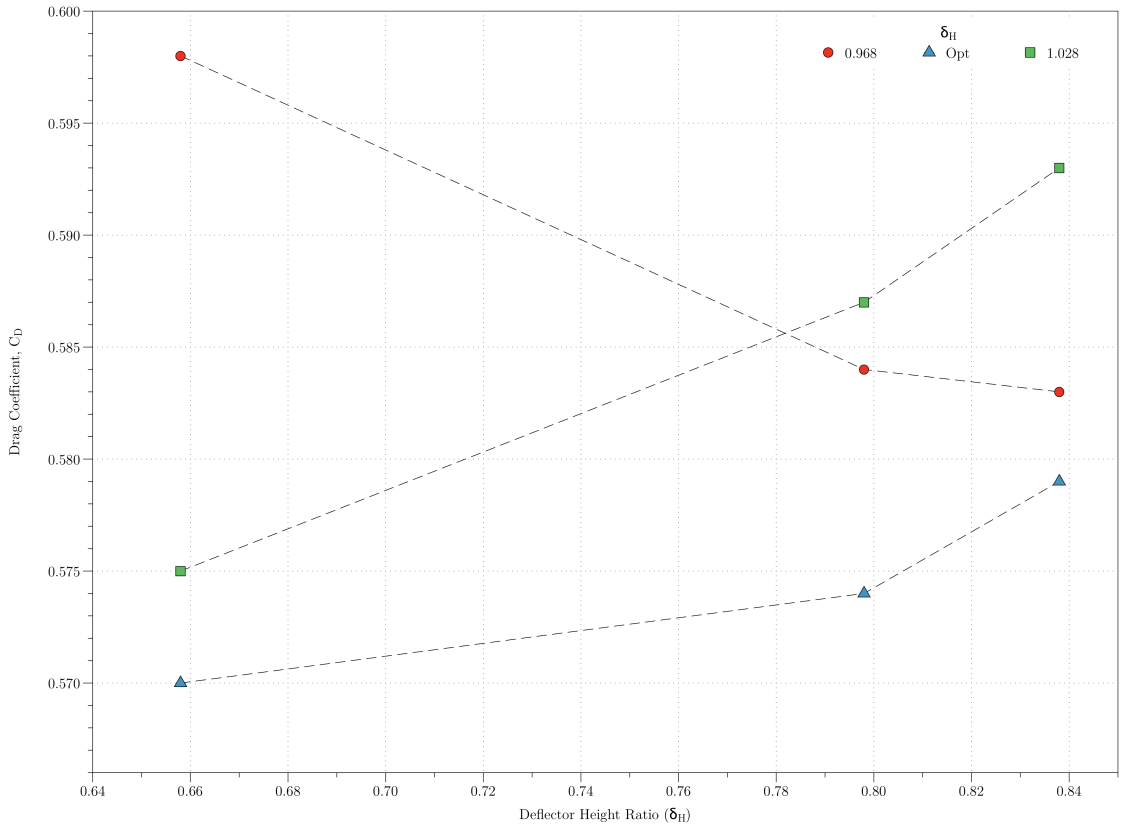

Figure F.10: Experiment and CFD ΔC_D Results.

The k-$\epsilon_{(Realizable)}$ provided accurate estimation to the increase in C_D for non optimal δ_H ratios. The model also correctly predicted a decrease in the ΔC_D for an increase in g/d_2 for $\delta_H = 0.968$. The decrease in ΔC_D is due to δ_{Hopt} decreasing with increasing g/d_2. The model underpredicted the drag increase for $\delta_H = 0.968$ for the lowest separation of $g/d_2 = 0.658$ and over predicted the drag increase for $\delta_H = 1.028$.

The velocity streamtraces for the three δ_H heights are shown in the following section.

F.1.3 2D Flow-Field Visualisation of Optimum δ_H

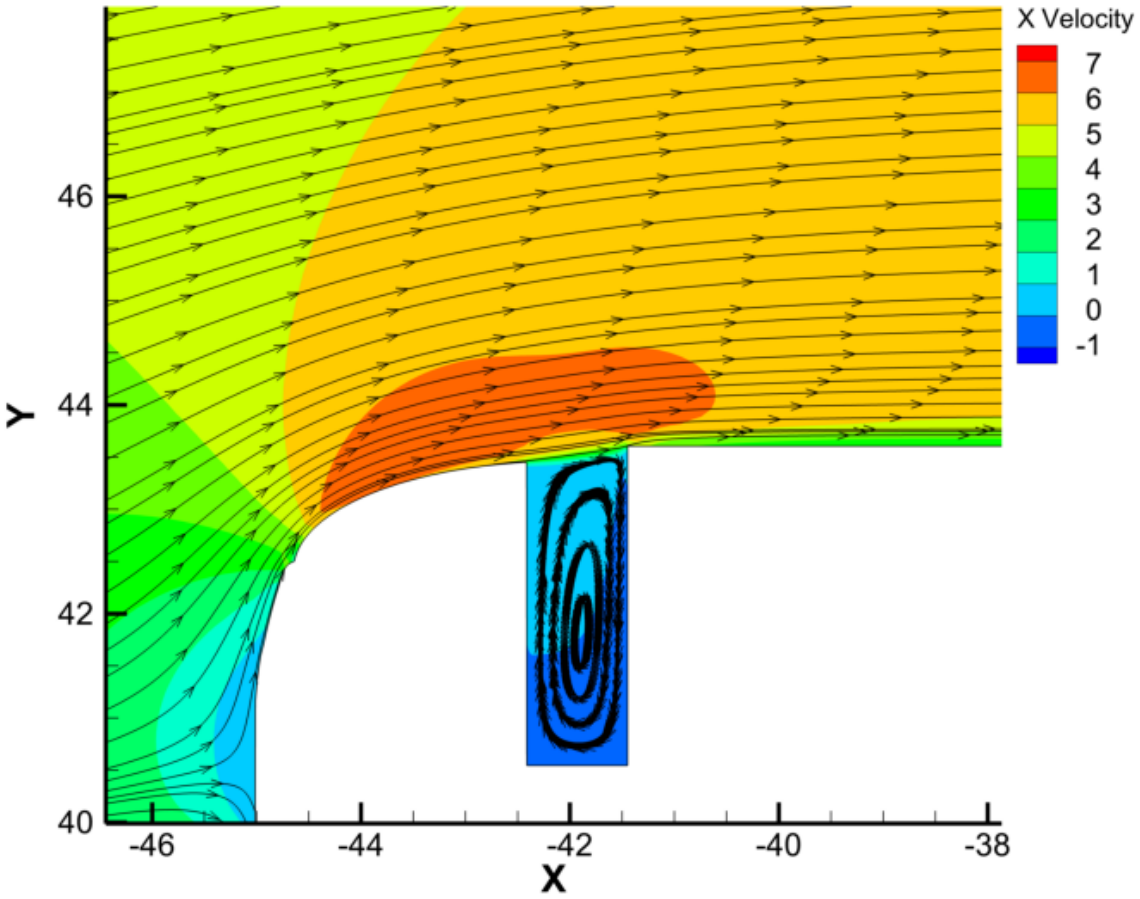

Figure F.11: 2D CFD Velocity Flow-Field, $\delta_H = 0.968$ and $g/d_2 = 0.838$.

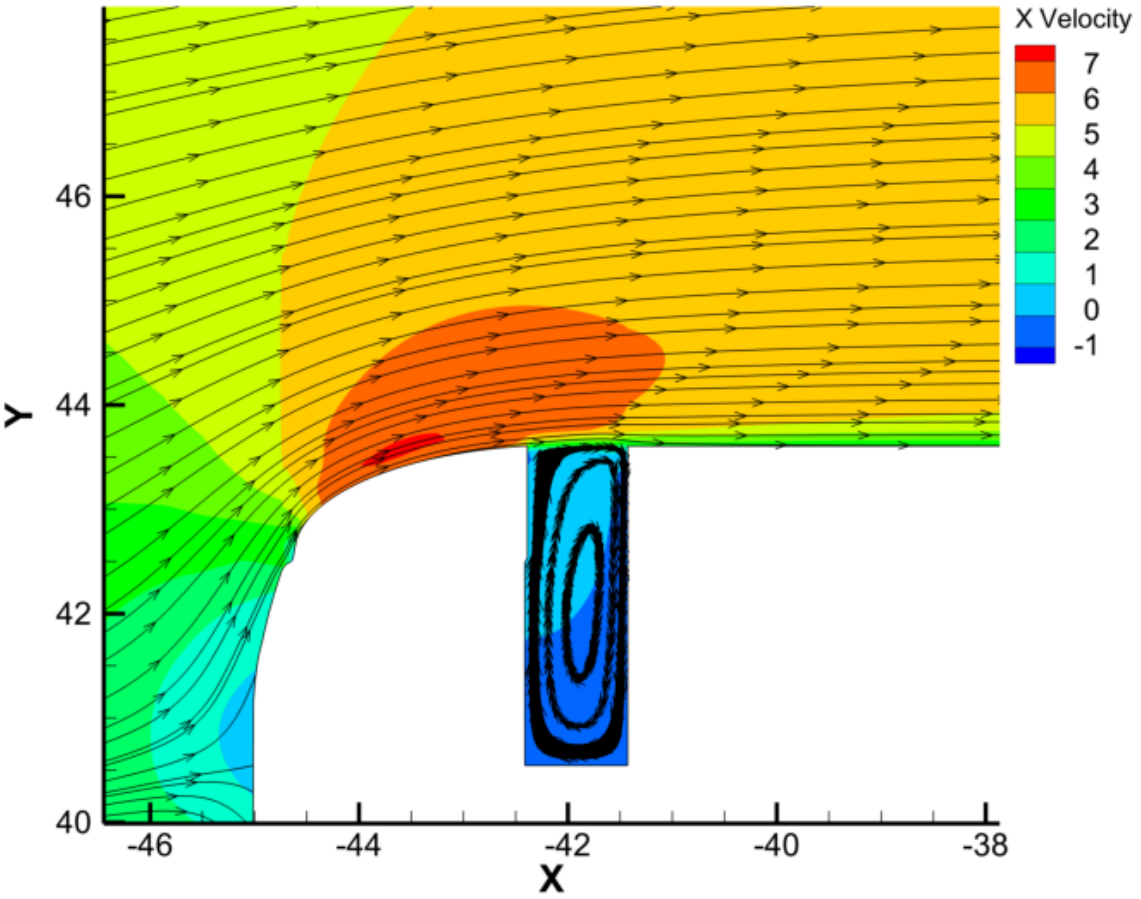

Figure F.12: 2D CFD Velocity Flow-Field, δ_{Hopt} and $g/d_2 = 0.838$.

The velocity streamtraces from the simulation show that when $\delta_H < \delta_{Hopt}$ (shown in Fig.(F.11)) there was an area of low velocity/high pressure on the upper container forebody. This is due to the height mismatch causing flow stagnation. When $\delta_H = \delta_{Hopt}$ (shown in Fig.(F.12)), this area of low velocity/high pressure is removed and a smoother transition is produced.

The velocity on the deflector also increased from 5 ms^{-1} to 7 ms^{-1} due to the additional positive velocity gradient provided by from additional deflection height. For $\delta_H > \delta_{Hopt}$ the velocity profile on the deflector was extended increasing the velocity over the cavity. The associated increase in velocity over the cavity caused an increase recirculation strength within in the cavity (shown in Fig.(F.13)).

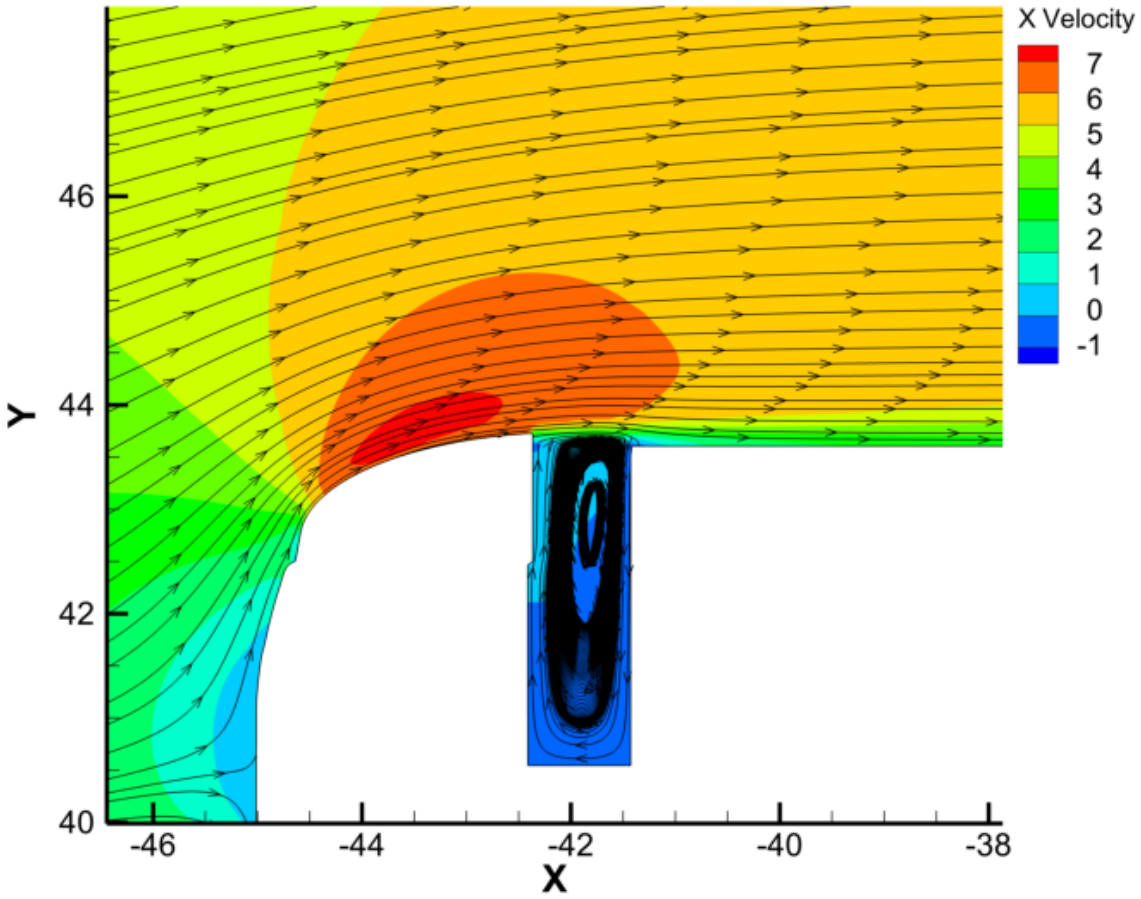

Figure F.13: 2D CFD Velocity Flow-Field, $\delta_H = 1.028$ and $g/d_2 = 0.838$.

F.1.4 k-$\epsilon_{(Realizable)}$ Prediction of ΔC_D vs. g/d_2

The wind tunnel data from Chapter 6 is shown in Tab.(F.9 and F.10). The associated k-$\epsilon_{(Realizable)}$ predicted C_D and ΔC_D are shown in Tab.(F.11 and F.12) respectively.

	g/d_2			
δ_H	0.658	0.798	0.838	1.056
0.968	0.598	0.584	0.583	-

Table F.9: Wind Tunnel C_D Results Summary for $\delta_H = 0.968$.

	g/d_2			
δ_H	0.658	0.798	0.838	1.056
0.968	-	-2.3%	-2.5%	-

Table F.10: Wind Tunnel ΔC_D Results Summary for $\delta_H = 0.968$.

	g/d_2			
δ_H	0.658	0.798	0.838	1.056
0.968	0.574	0.569	0.568	0.547

Table F.11: k-$\epsilon_{(Realizable)}$ C_D Prediction for $\delta_H = 0.968$.

	g/d_2			
δ_H	0.658	0.798	0.838	1.056
0.968	-	-0.9%	-1.0%	-4.7%

Table F.12: k-$\epsilon_{(Realizable)}$ ΔC_D Prediction for $\delta_H = 0.968$.

The velocity streamtraces for the four g/d_2 separations are shown in the following section.

F.1.5 2D Flow-Field Visualisation for Varying g/d_2

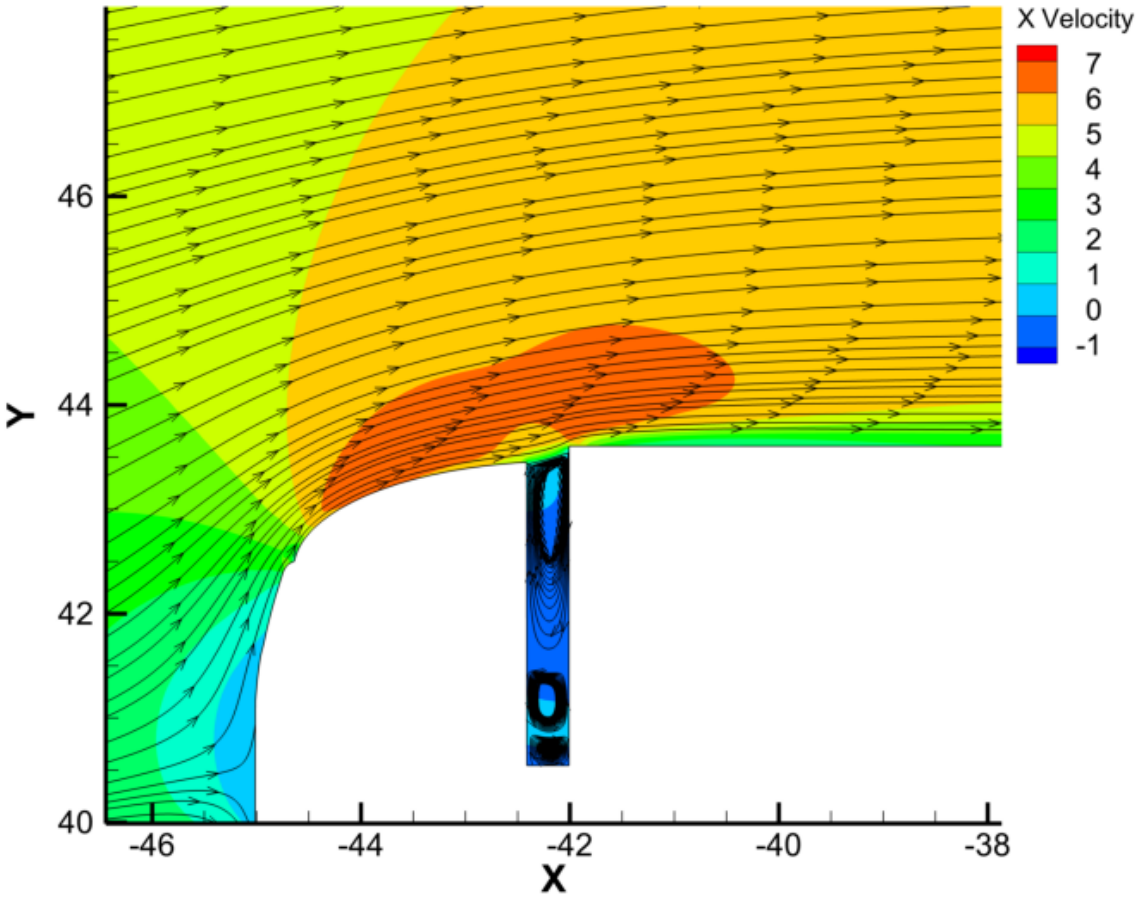

Figure F.14: CFD Velocity Flow-Field, $\delta_H = 0.968$ and $g/d_2 = 0.658$.

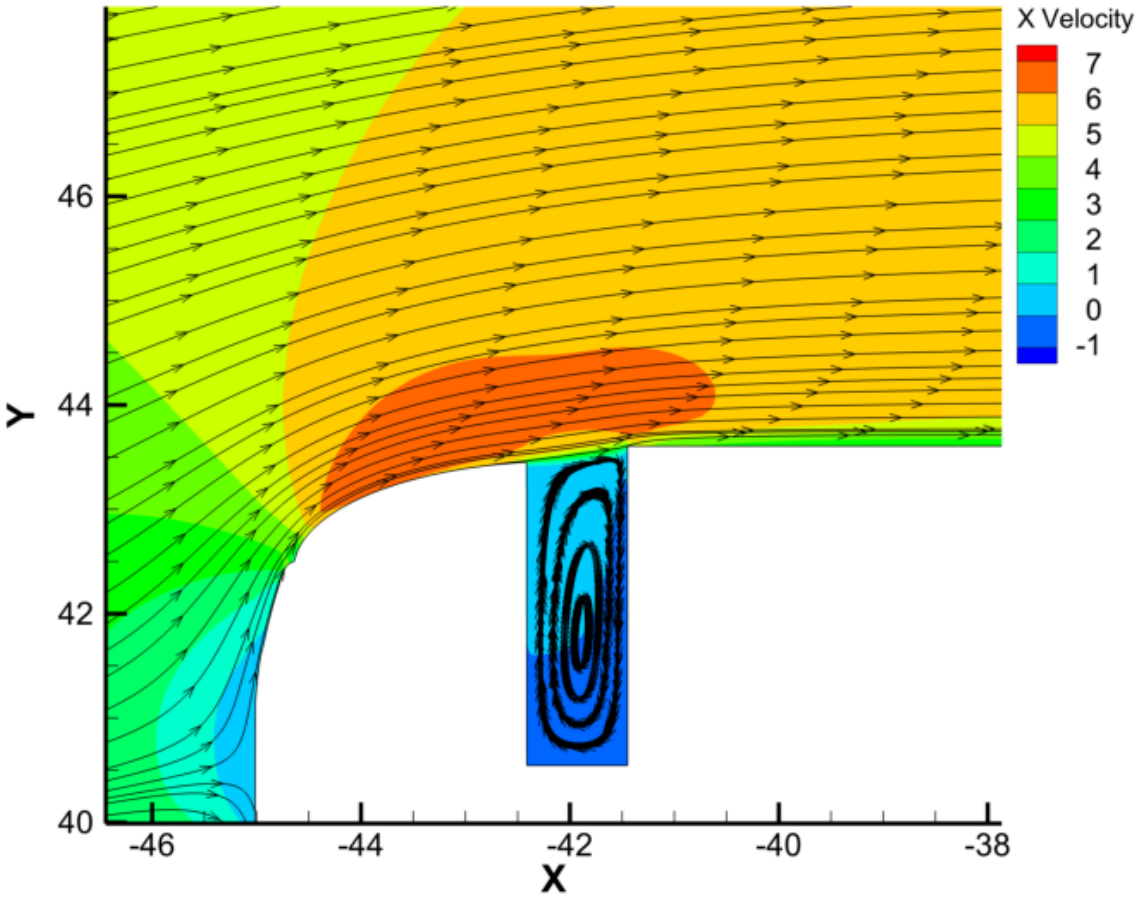

Figure F.15: CFD Velocity Flow-Field, $\delta_H = 0.968$ and $g/d_2 = 0.798$.

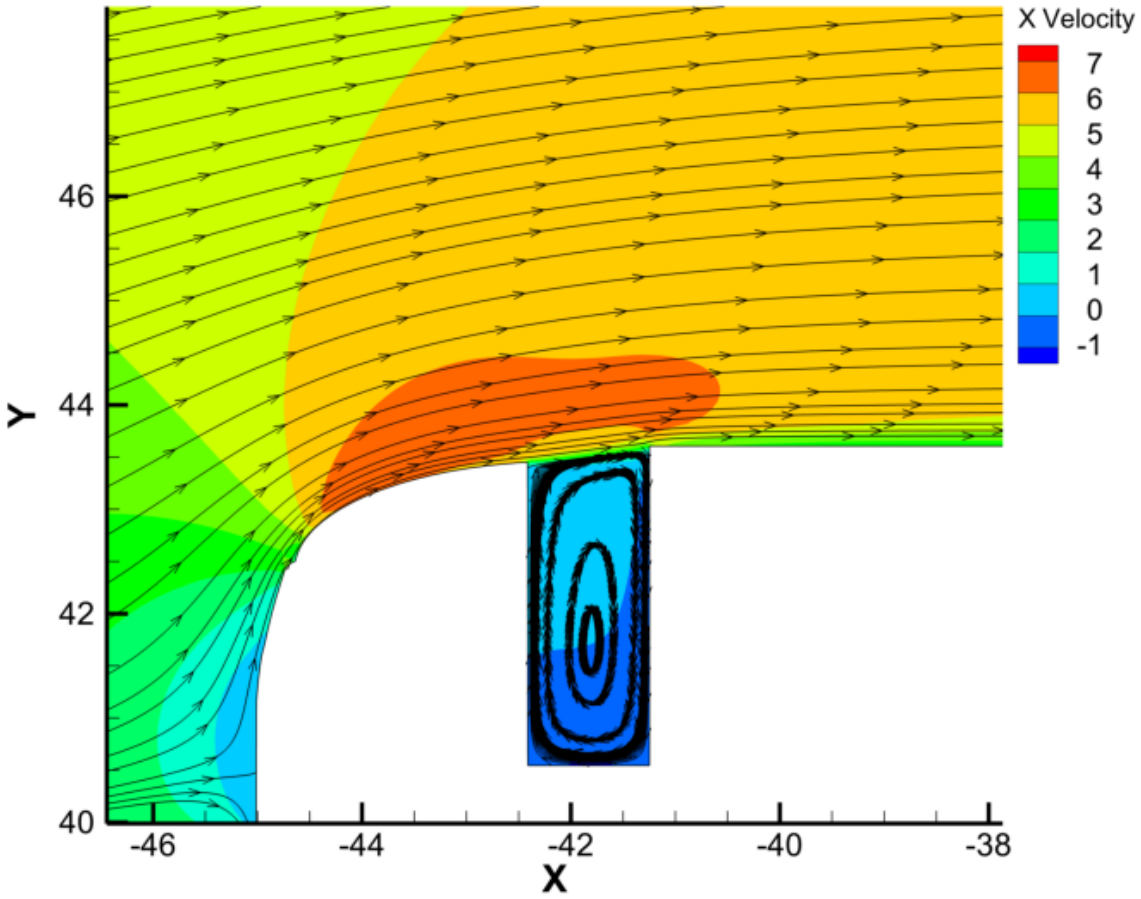

Figure F.16: CFD Velocity Flow-Field, $\delta_H = 0.968$ and $g/d_2 = 0.838$.

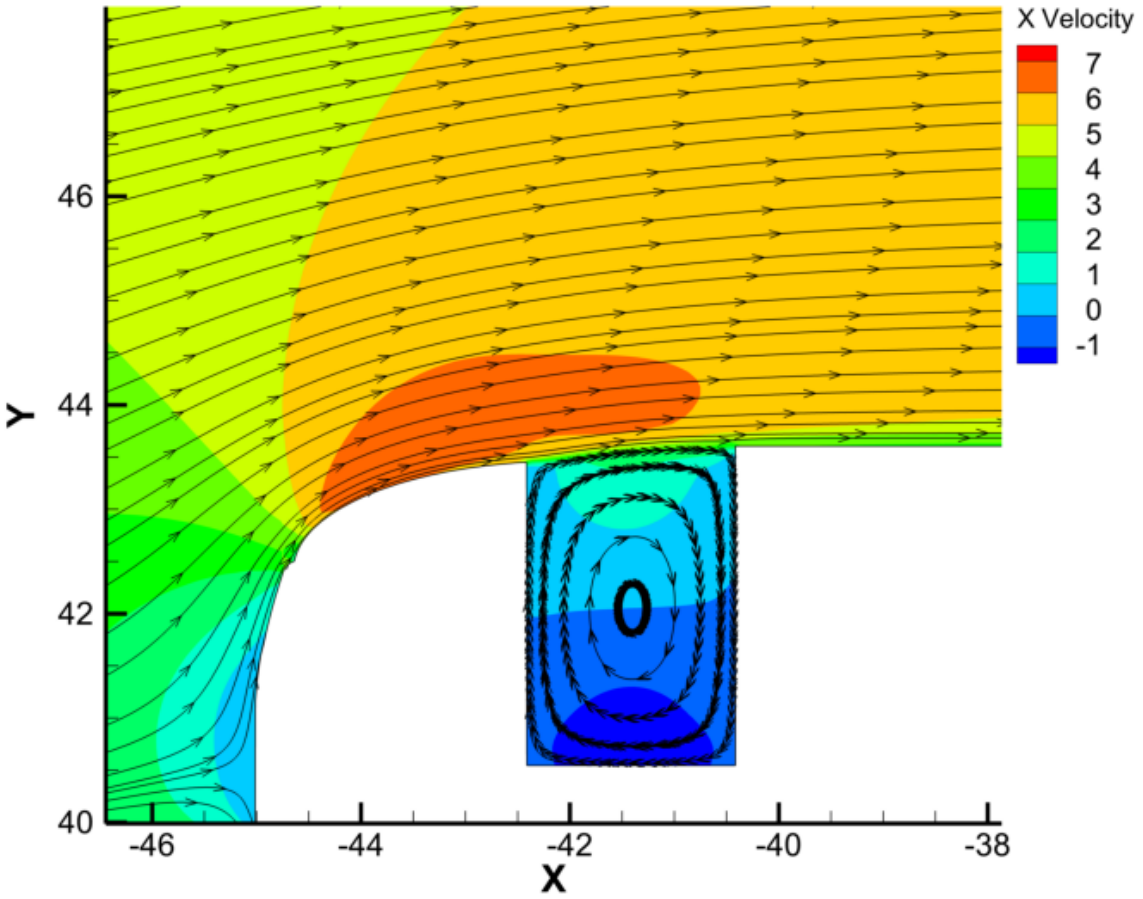

Figure F.17: CFD Velocity Flow-Field, $\delta_H = 0.968$ and $g/d_2 = 1.056$.

The velocity streamtraces showed that for the lowest deflector height ratio of $\delta_H = 0.968$, the optimal trajectory for the flow was achieved at increasing g/d_2, until the maximum g/d_2 of 1.056 (the effects are shown in Figs.(F.14 - F.17)). The increase in cavity recirculation within the cavity is a predominantly 3D effect. The prediction that the drag continues to decrease with increased separation implies the 2D geometry was not sufficient for modelling the flow at higher cavity separations.

F.1.6 RANS Wake Velocity Profiles

F.1.6.1 Vertical Velocity Profiles

The RANS velocity profile for a single heavy goods vehicle in freestream is shown in Fig.(F.18). The downstream evolution of the vertical velocity profile for two vehicles in tandem are shown in Figs.(F.19 - F.21).

Fig.(F.19) (blue line) shows the vertical velocity profile within the recirculation bubble. Fig.(F.20) (black line) shows the vertical velocity profile at the mid point between the two vehicles. Fig.(F.21) (red line) shows the vertical velocity profile close to the truck following. The recirculation bubble ends at x/W = -4.5 and the forebody of the truck in tandem begins at x/W = -2.5.

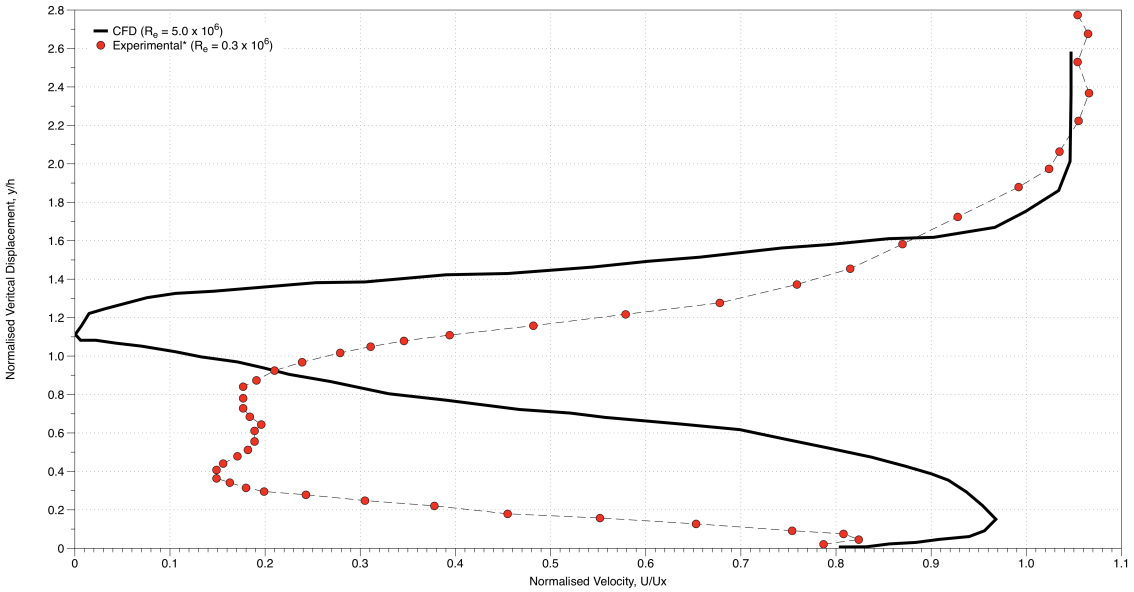

Figure F.18: Time Averaged Trailer Wake Vertical Velocity Profile, Normalised Velocity (U/U_X) and Slice Extracted at Displacement (x/L) = 0.2 Behind Trailer[2].

[2]Data Denoted * Reproduced from [93].

F.1.6.2 Vertical Velocity Profile vs. Displacement

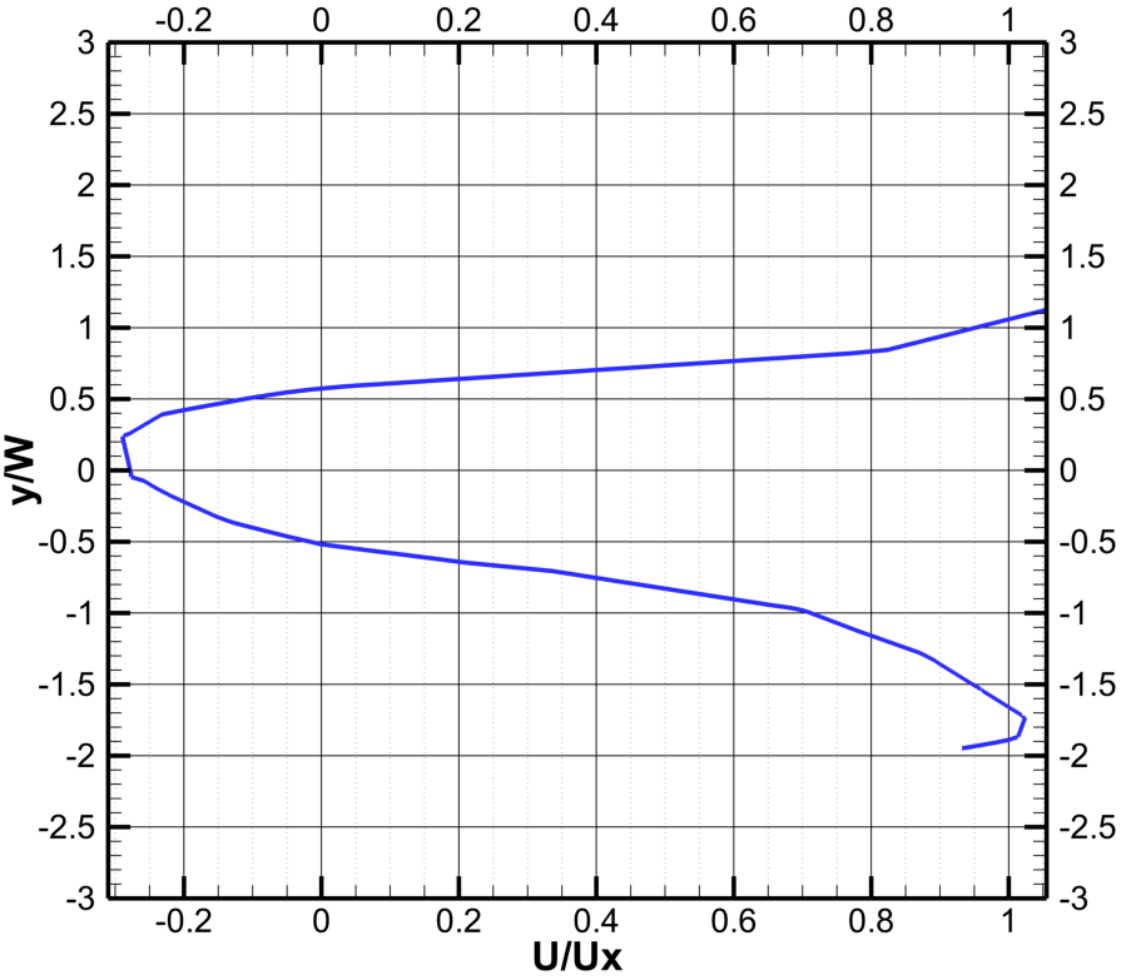

Figure F.19: Time Averaged Trailer Vertical Wake Slice (1), Normalised Velocity (U/U_X) and Slice Extracted at z/W = 0.5 at a Normalised Displacement Length Downstream of the Recirculation Bubble (x/W) = -0.5.

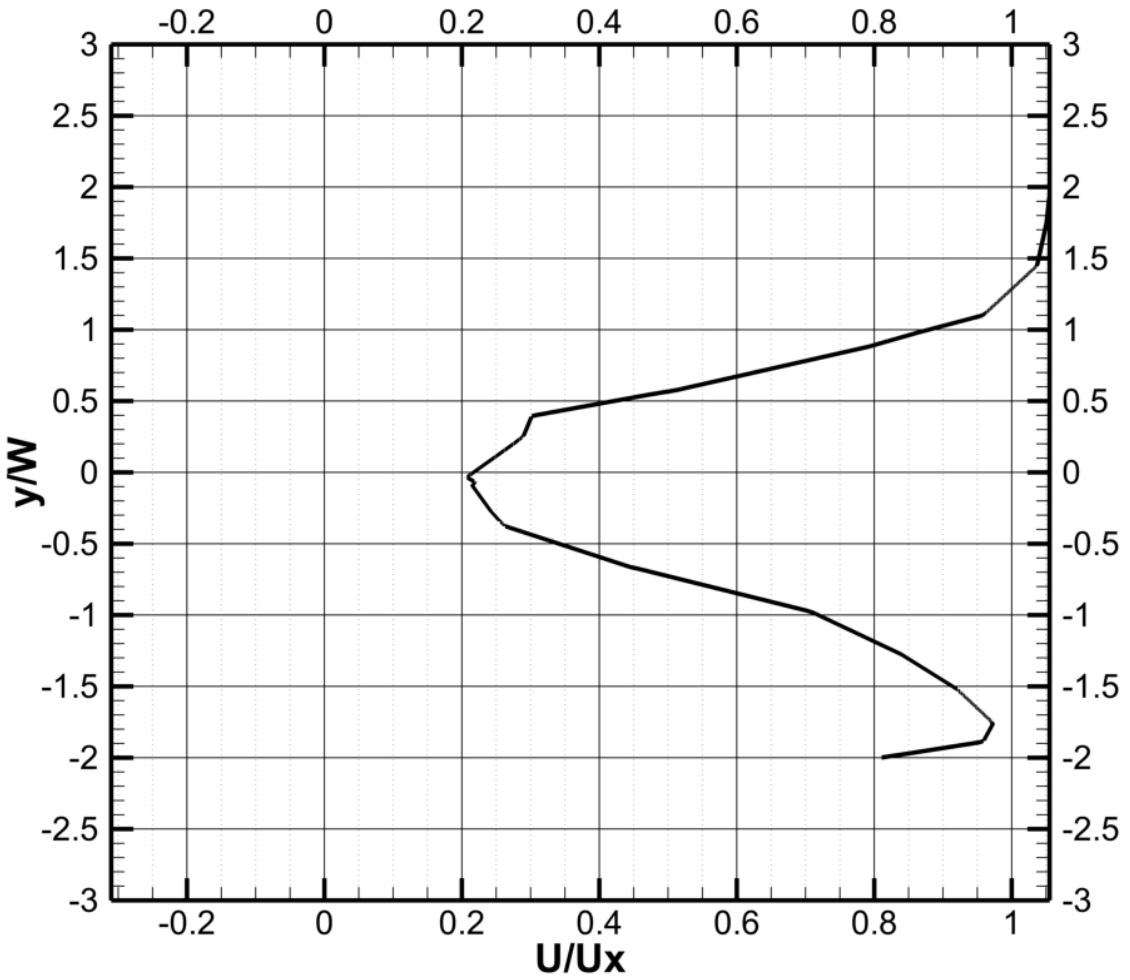

Figure F.20: Time Averaged Trailer Vertical Wake Slice (3), Normalised Velocity (U/U_X) and Slice Extracted at $z/W = 0.5$ at a Normalised Displacement Length Downstream of the Recirculation Bubble (x/W) = 0.5.

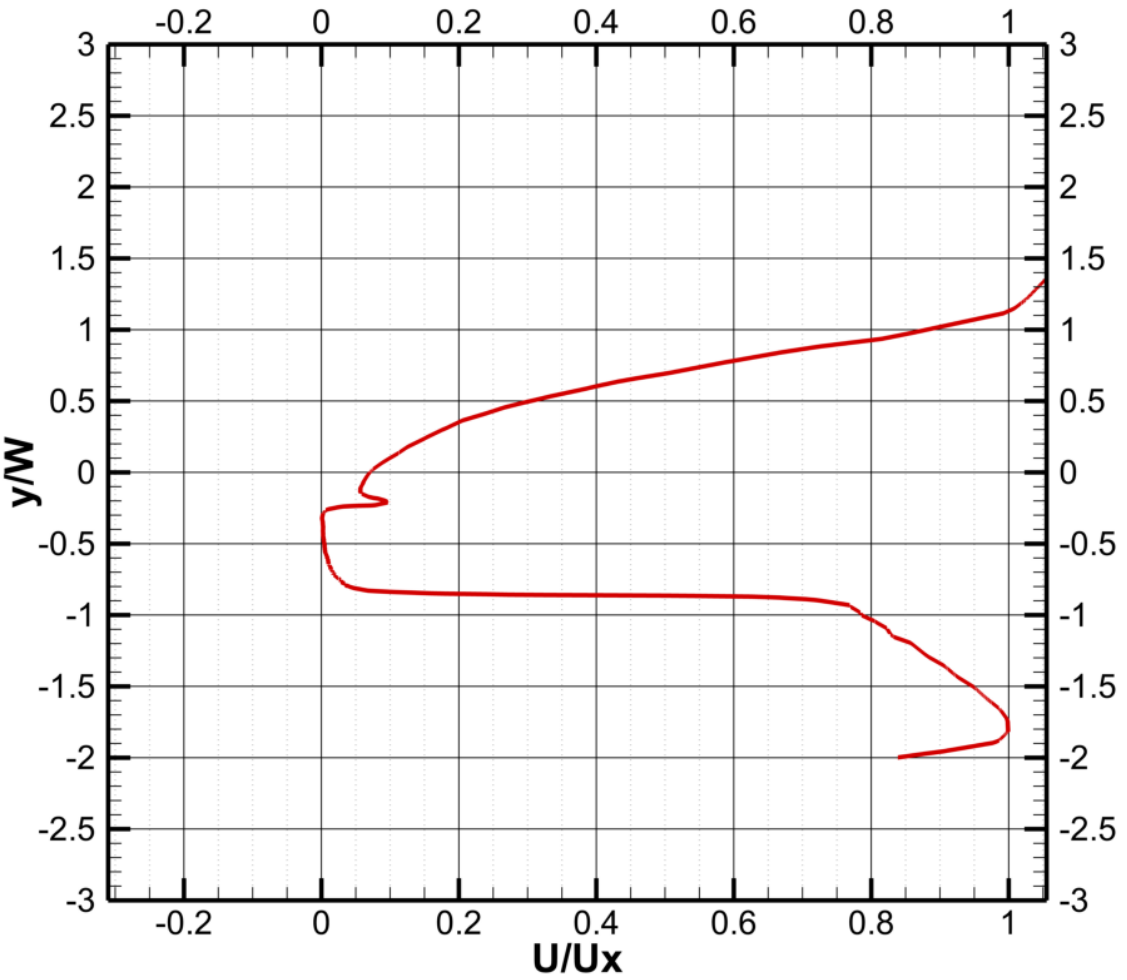

Figure F.21: Time Averaged Trailer Vertical Wake Slice (6), Normalised Velocity (U/U_X) and Slice Extracted at $z/W = 0.5$ at a Normalised Displacement Length Downstream of the Recirculation Bubble (x/W) = 2.0.

F.1.6.3 Horizontal Velocity Profiles

The RANS horizontal profile for a single heavy goods vehicle in freestream air is shown in Fig.(F.22). The downstream evolution of the horizontal velocity profile for two vehicles in tandem are shown in Figs.(F.23 - F.25). Fig.(F.23) (blue line) shows the horizontal velocity profile within the recirculation bubble. Fig.(F.24) (black line) shows the horizontal velocity profile at the mid point between the two vehicles. Fig.(F.25) (red line) shows the horizontal velocity profile close to the truck following.

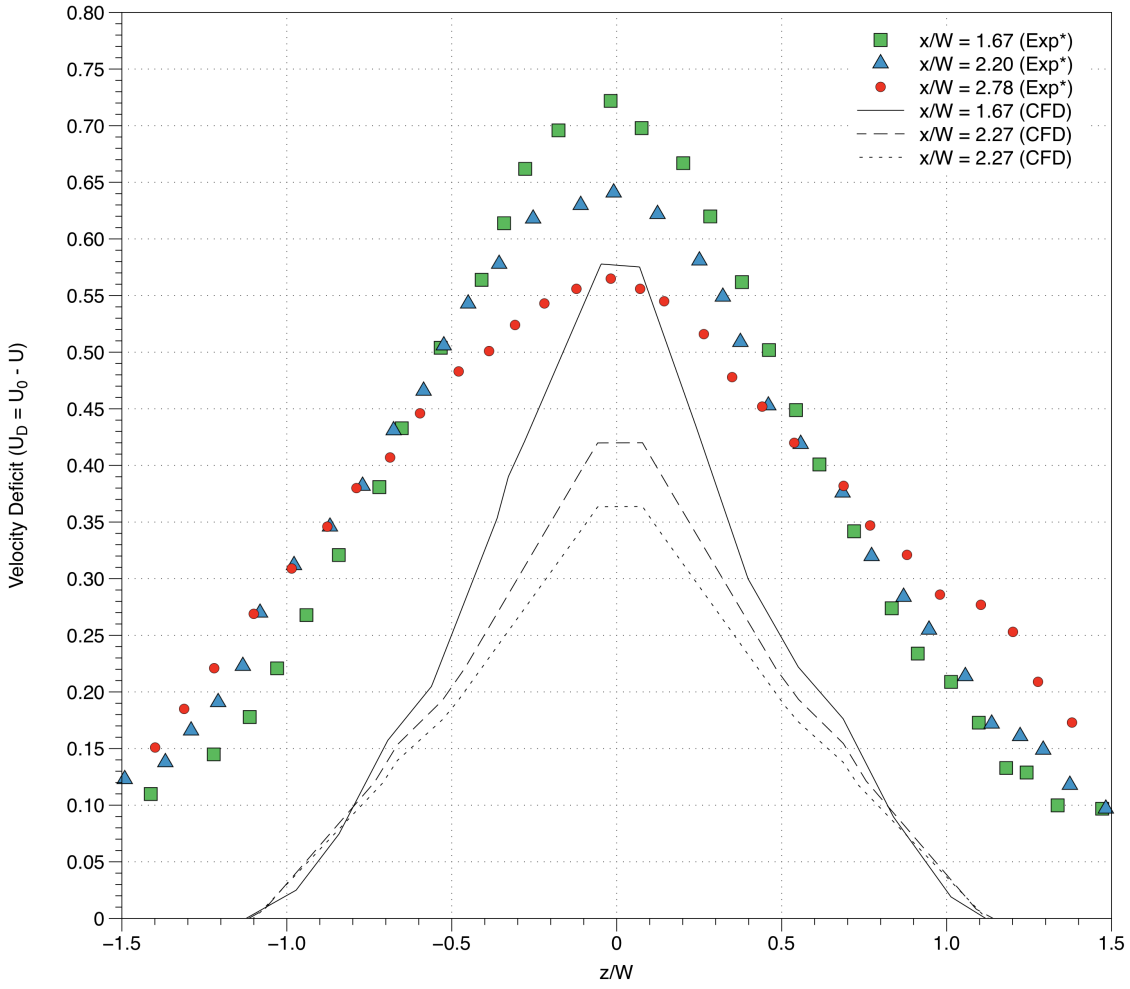

Figure F.22: Velocity Deficit[4](U_D) vs. Horizontal Traverse (x/W). Experimental $R_e \sim 10^4, CFD \sim 10^6$.

[4]Data Denoted * Reproduced from [97]

F.1.6.4 Horizontal Velocity Profile vs. Displacement

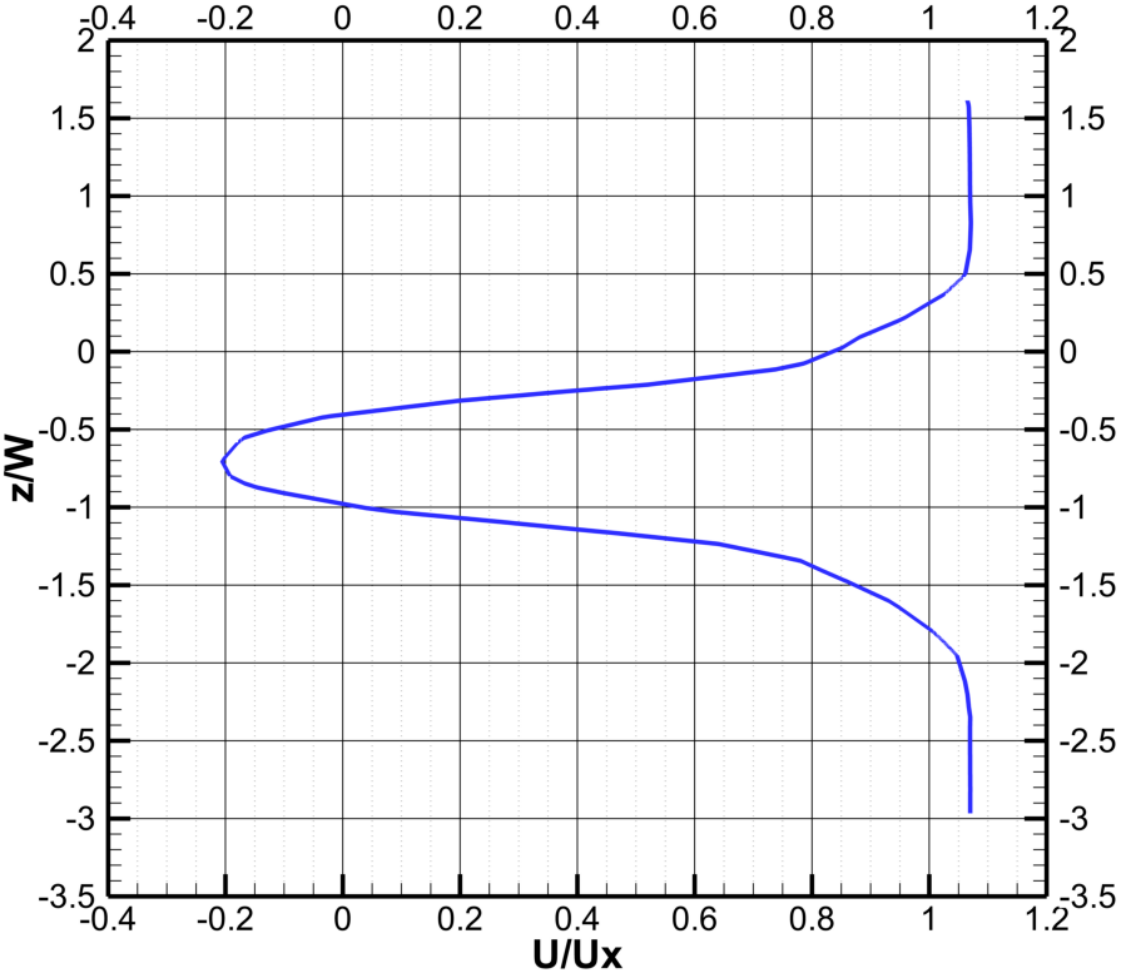

Figure F.23: Time Averaged Trailer Horizontal Wake Slice (1), Normalised Velocity (U/U_X) and Slice Extracted at y/W = 0.5 at a Normalised Displacement Length Downstream of the Recirculation Bubble (x/W) = -0.5.

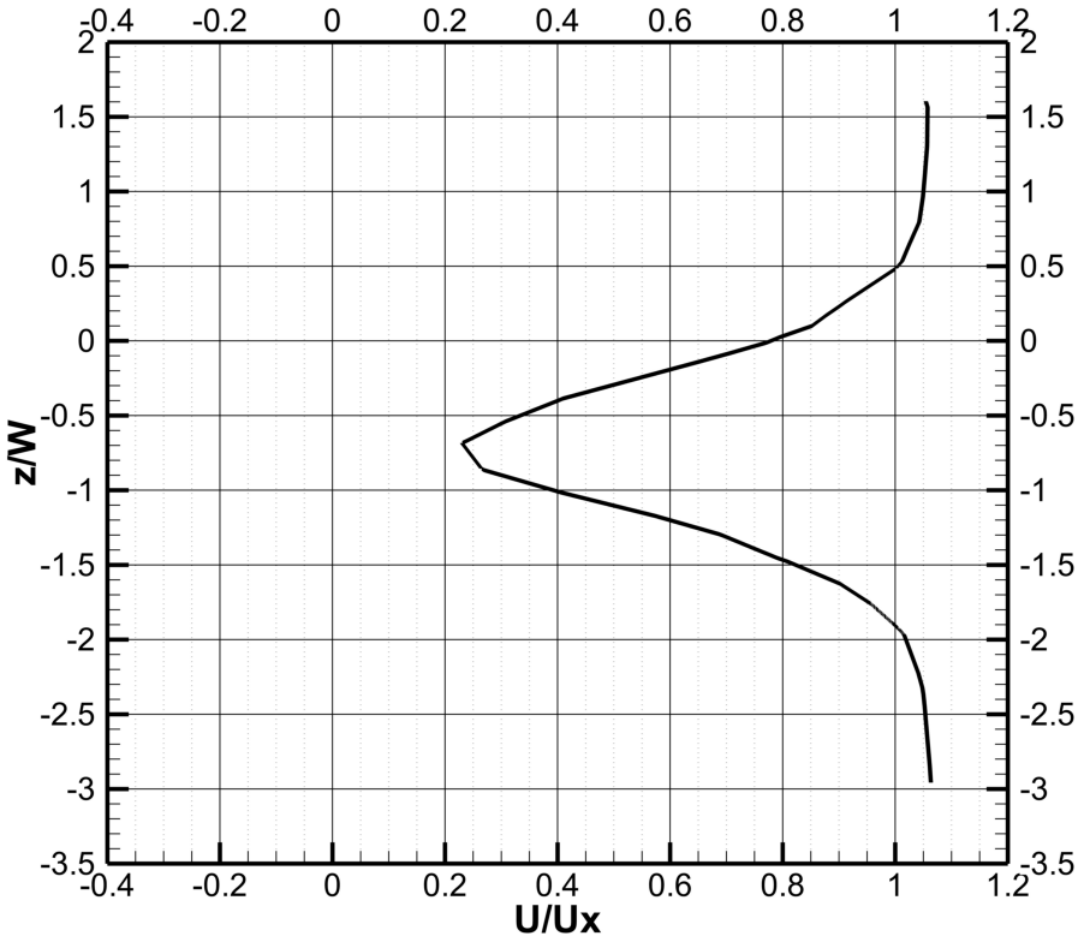

Figure F.24: Time Averaged Trailer Horizontal Wake Slice (3), Normalised Velocity (U/U_X) and Slice Extracted at $y/W = 0.5$ at a Normalised Displacement Length Downstream of the Recirculation Bubble (x/W) = 0.5.

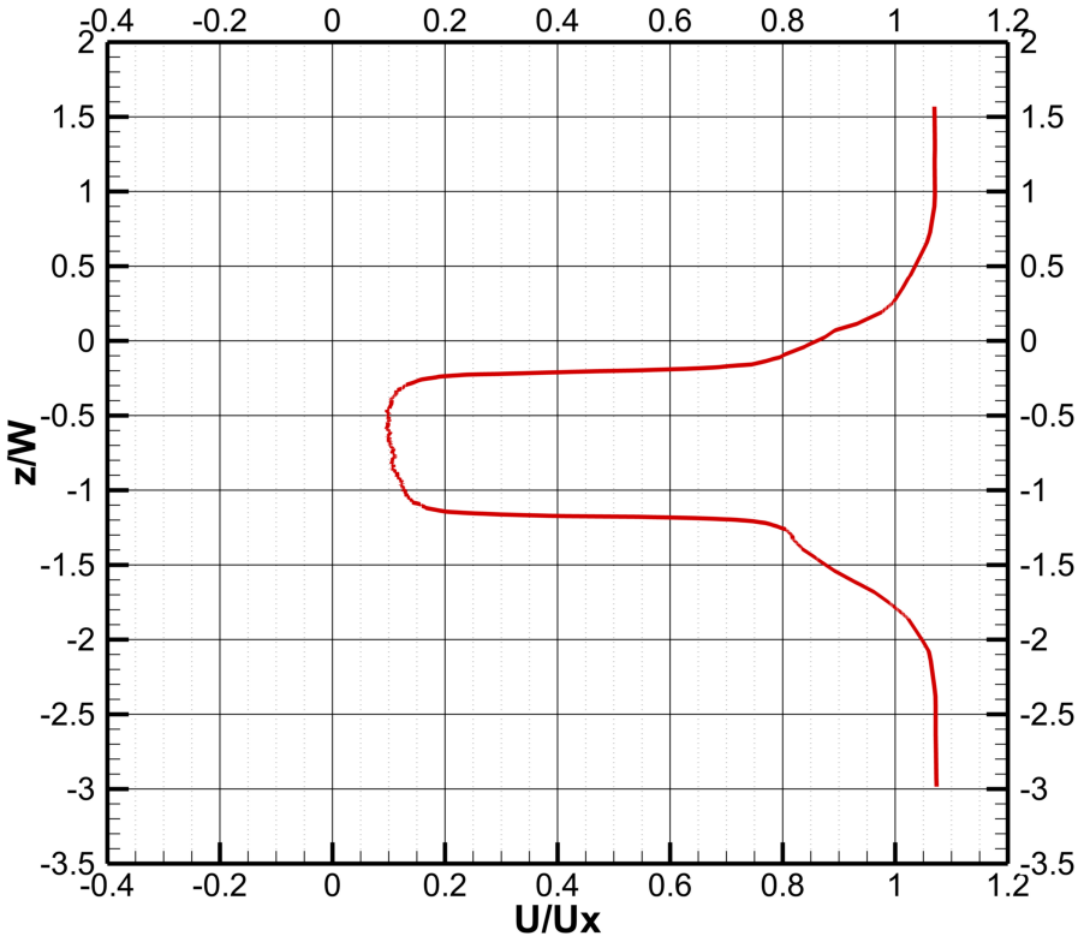

Figure F.25: Time Averaged Trailer Horizontal Wake Slice (6), Normalised Velocity (U/U_X) and Slice Extracted at $y/W = 0.5$ at a Normalised Displacement Length Downstream of the Recirculation Bubble (x/W) = 2.0.

F.1.7 LES Angular Deviation Along Centre Line

Table (F.13) shows the maximum and minimum angular deviation along the centre line between the two vehicles in tandem. Six time steps (equating to a time range of 10.0s to 10.5s) were used to calculate the angular deviation. The recirculation bubble ends at x/W = -4.5 and the forebody of the truck in tandem begins at x/W = -2.5.

Distance (x/W)	Max Angle (°)	Min Angle (°)
-5.00	80.45	-88.95
-4.75	58.36	-42.59
-4.60	27.67	-17.12
-4.50	12.01	-7.72
-4.25	7.55	-4.71
-4.00	6.33	-3.42
-3.75	5.29	-4.01
-3.50	5.75	-4.14
-3.25	2.37	-6.44
-3.00	7.98	-10.05
-2.75	9.58	-12.95
-2.50	17.08	-16.97
-2.25	47.08	-27.93

Table F.13: Angular Deviation from Vehicle Centre Line vs. Normalised Distance (x/W).

Appendix G

On-Road Data

An example of the type of routes experienced by the vehicle during the full scale on-road testing are shown in Sec.(G.1). The location of the weather stations used for data comparison of the on-road wind speed (V_W) and direction (β) are shown in Sec.(G.2). An example calculation on how the data from the weather station was used to calculate the effective wind yaw angle (β) is shown in Sec.(G.3). An example of the data obtained from the weather station is shown in Sec.(G.3.1).

The on-road data with the effective yaw angle for each run calculated is shown in Sec.(G.3).

Detailed information about data recorded from the on-road runs (Run [1] - Run [15]) are shown in Secs.(G.4.2 - G.4.14.1), respectively. The details behind the Fourier Transform used for frequency identification within the obtained data is shown in Sec.(G.5). The magnitude response of the filter designed to improve the estimated yaw angle (β_{Est}) is shown in Sec.(G.7).

The full scale test on the prototype ActiveFREDDIE controller is shown in Sec.(G.8), with the Millbrook Proving Grounds test report shown in Sec.(G.8.2). The 40 mph and 50 mph Millbrook test data on the prototype ActiveFREDDIE controller is shown in Sec.(G.8.3).

G.1 Vehicle Route Examples

G.1.1 Typical UK Motorway

Figure G.1: Example of a Typical UK Motorway (M1).

G.1.2 Typical UK Dual Carriageway

Figure G.2: Example of a Typical UK Dual Carriageway (A14).

G.2 Location of Weather Stations

The list of ten weather stations used for comparison against the on-road data is shown in Tab.(G.1). The stations are commercial airports and as a result have a International Civil Aviation Organisation (ICAO) airport code used for unique identification. The test routes are shown in conjunction with the weather station positions in Fig.(G.3).

Run Number	Station	Name	ICAO	Latitude	Longitude
Run [1]	(i)	Cranfield	EGTC	52°4'13.08"N	0°37'36.12"W
Run [2]	(i)	Cranfield	EGTC	52°4'13.08"N	0°37'36.12"W
Run [3a]	(i)	Cranfield	EGTC	52°4'13.08"N	0°37'36.12"W
Run [4b]	(ii)	Birmingham	EGBB	52°27'0.00"N	-1°43'48.00"W
Run [5b]	(iii)	Leeds Bradford	EGNM	54°31'12.00"N	-1°38'60.00"W
Run [6]	(iv)	RAF Mildenhall	EGSC	52°22'12.00"N	0°28'48.00"E
Run [7]	(v)	Cambridge	EGXT	52°12'0.00"N	0°10'48.00"E
Run [8]	(vi)	RAF Wittering	EGNX	52°37'12.00"N	0°28'12.00"W
Run [9]	(vii)	East Midlands	EGNH	52°49'48.00"N	-1°19'48.00"W
Run [10]	(viii)	Blackpool	EGNH	53°46'12.00"N	-3°1'48.00"W
Run [11]	(viii)	Blackpool	EGCC	53°46'12.00"N	-3°1'48.00"W
Run [12]	(ix)	Manchester	EGCN	53°21'0.00"N	-2°16'12.00"W
Run [13]	(x)	Doncaster	EGCM	53°28'31.00"N	-1°00'15.00"W
Run [14]	(iii)	Leeds Bradford	EGNM	54°31'12.00"N	-1°38'60.00"W
Run [15]	(x)	Doncaster	EGCN	53°28'31.00"N	-1°00'15.00"W

Table G.1: Name, Number, ICAO Identifier and Location of Weather Stations.

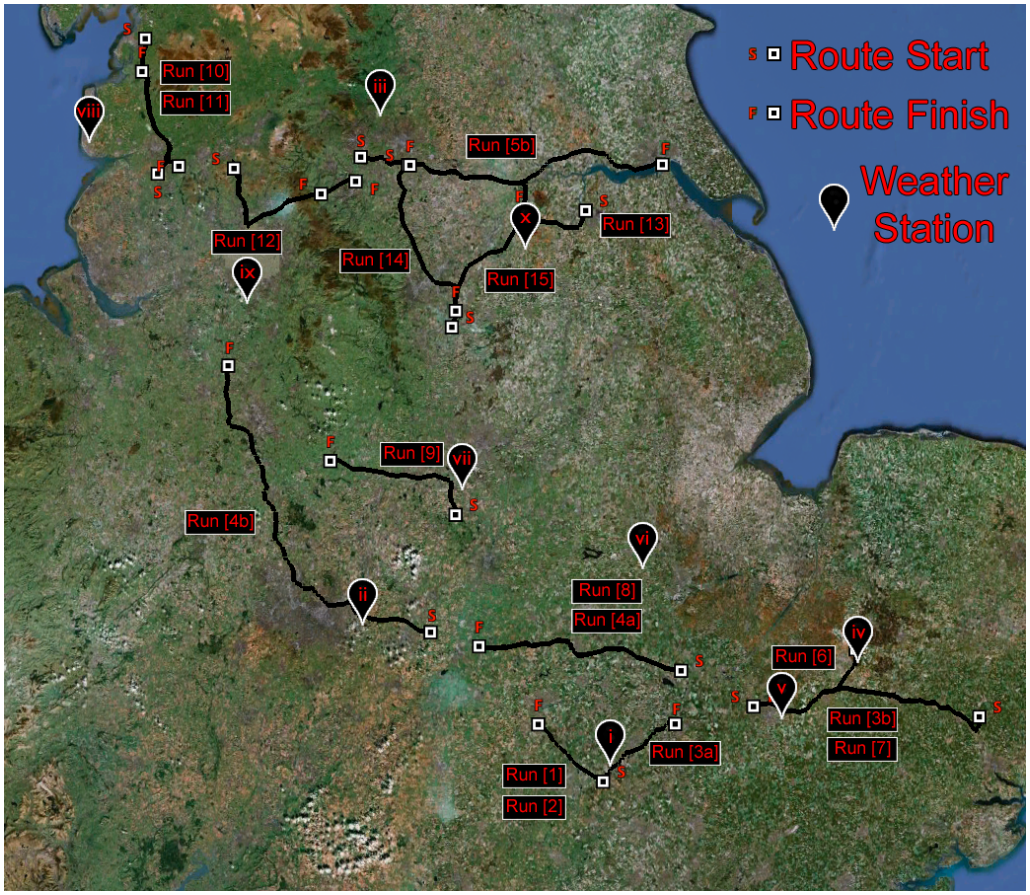

Figure G.3: Map of Weather Stations and Vehicle Routes.

Station Number	Name	ICAO
(i)	Cranfield	EGTC
(ii)	Birmingham	EGBB
(iii)	Leeds Bradford	EGNM
(iv)	RAF Mildenhall	EGSC
(v)	Cambridge	EGXT
(vi)	RAF Wittering	EGNX
(vii)	East Midlands	EGNH
(viii)	Blackpool	EGNH
(ix)	Manchester	EGCN
(x)	Doncaster	EGCM

Table G.2: Weather Station Information.

G.3 Example Calculation

Run [13] is used for the example wind yaw calculation, the data obtained from weather station: (x) located in Doncaster is shown in Figs.(G.6 and G.7). The average vehicle direction of the vehicle is represented by a red line, with the average wind direction (Φ) represented by a blue line in Fig.(G.4). The notation used to describe the wind direction (Φ) is shown in Fig.(G.5).

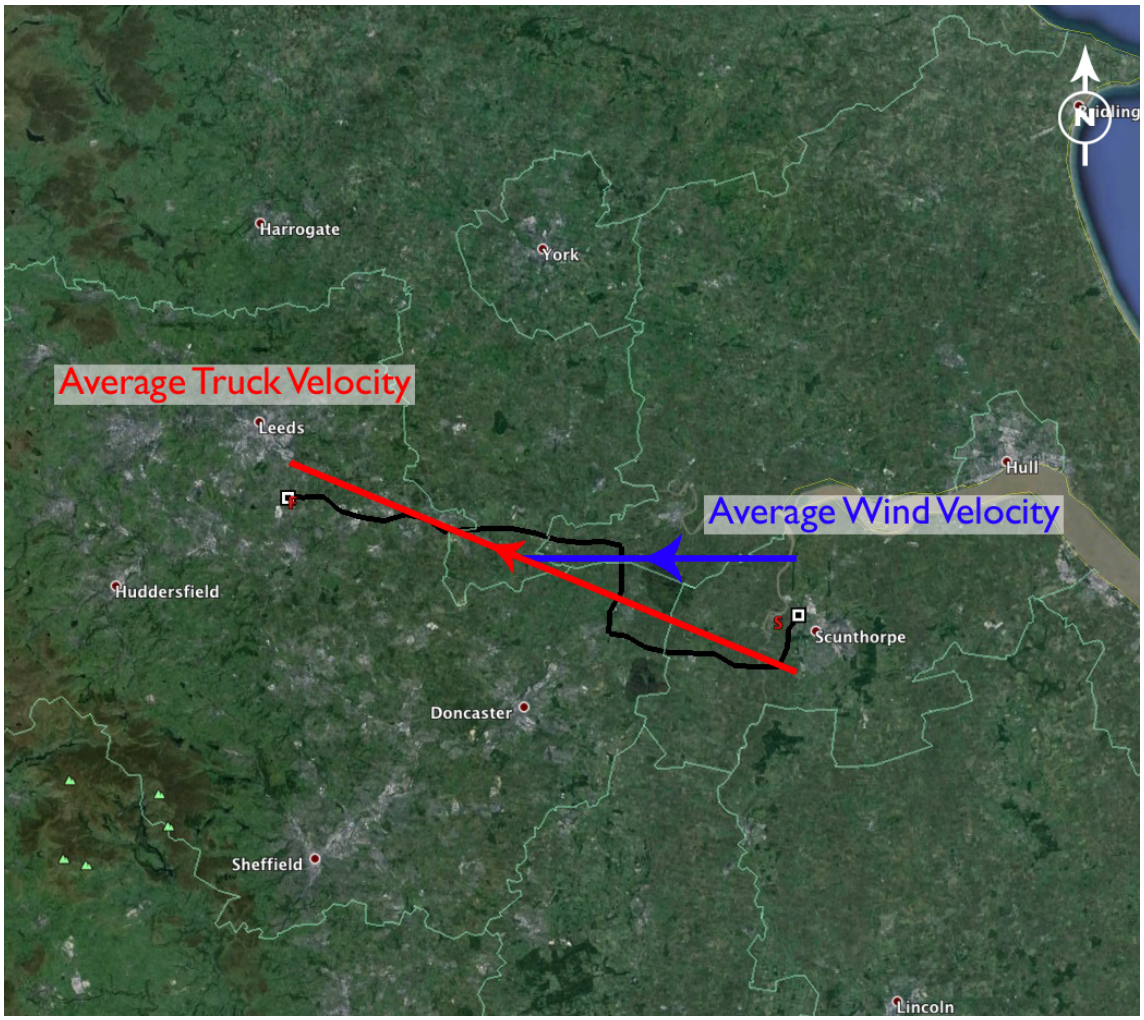

Figure G.4: Run [13] Example Calculation.

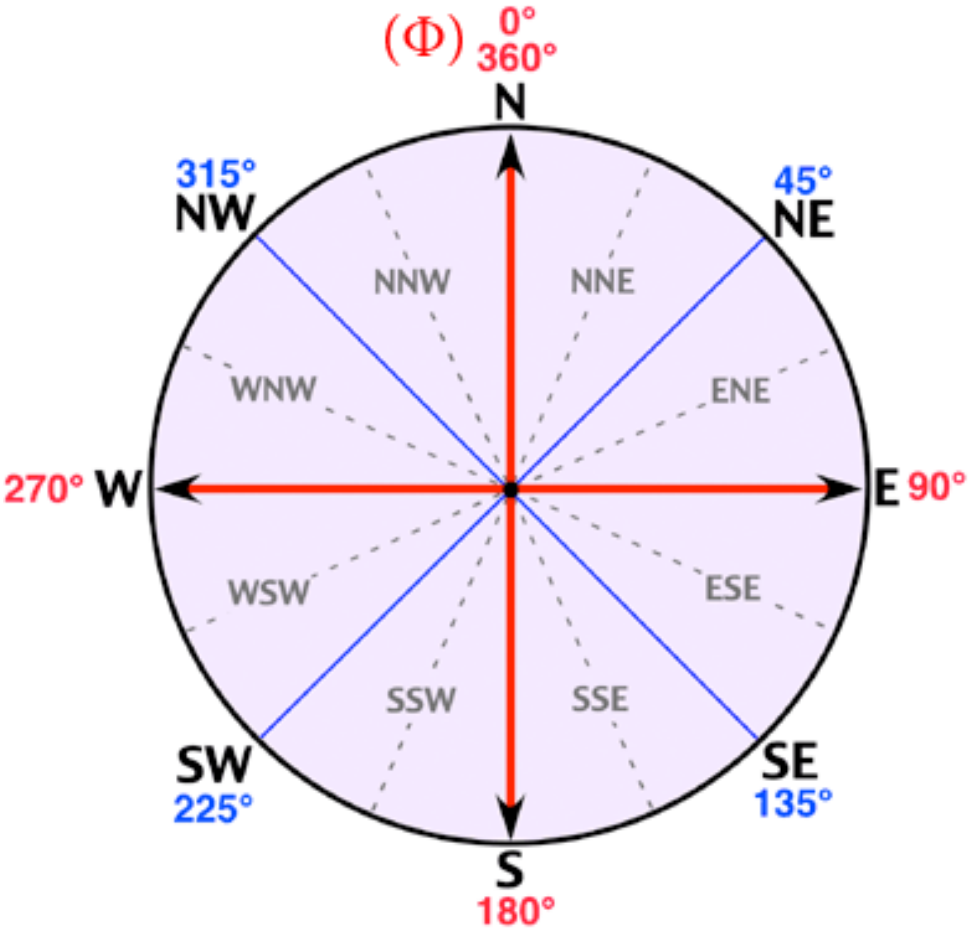

Figure G.5: Wind Direction Notation [112].

From the data in Fig.(G.7) and Tab.(G.5) at the time of vehicle operation, the variables were known:

- Average Wind Direction (Φ): 270.0°
- Average Wind Speed: 8.2 ms^{-1}
- Average Vehicle Direction (Φ): 292.5°
- Average Vehicle Speed: 18.5 ms^{-1}

The resulting vector diagram is shown in Fig.(G.8).

G.3.1 Example Data

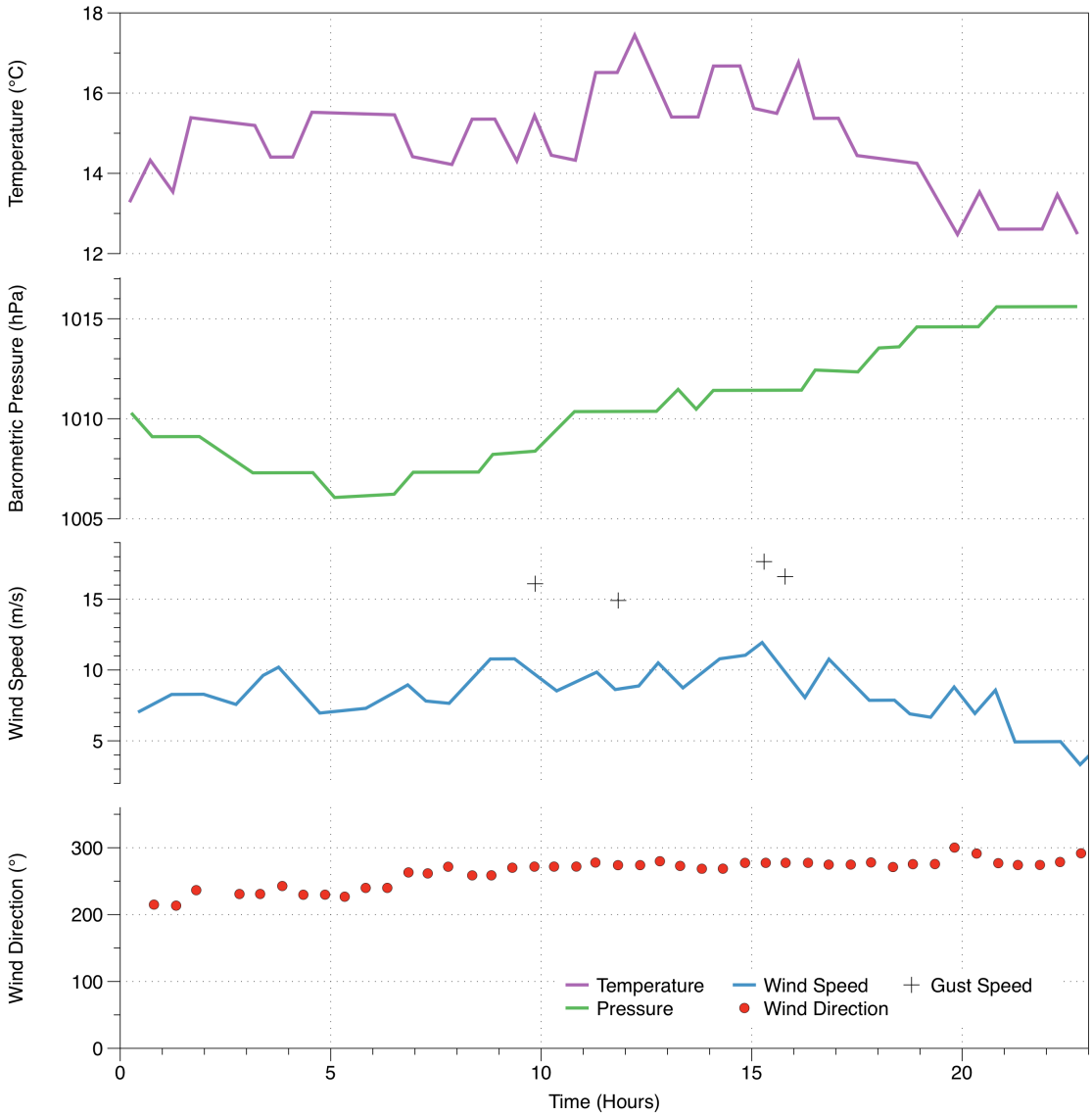

Figure G.6: Wind Data Obtained from Doncaster Station (x).

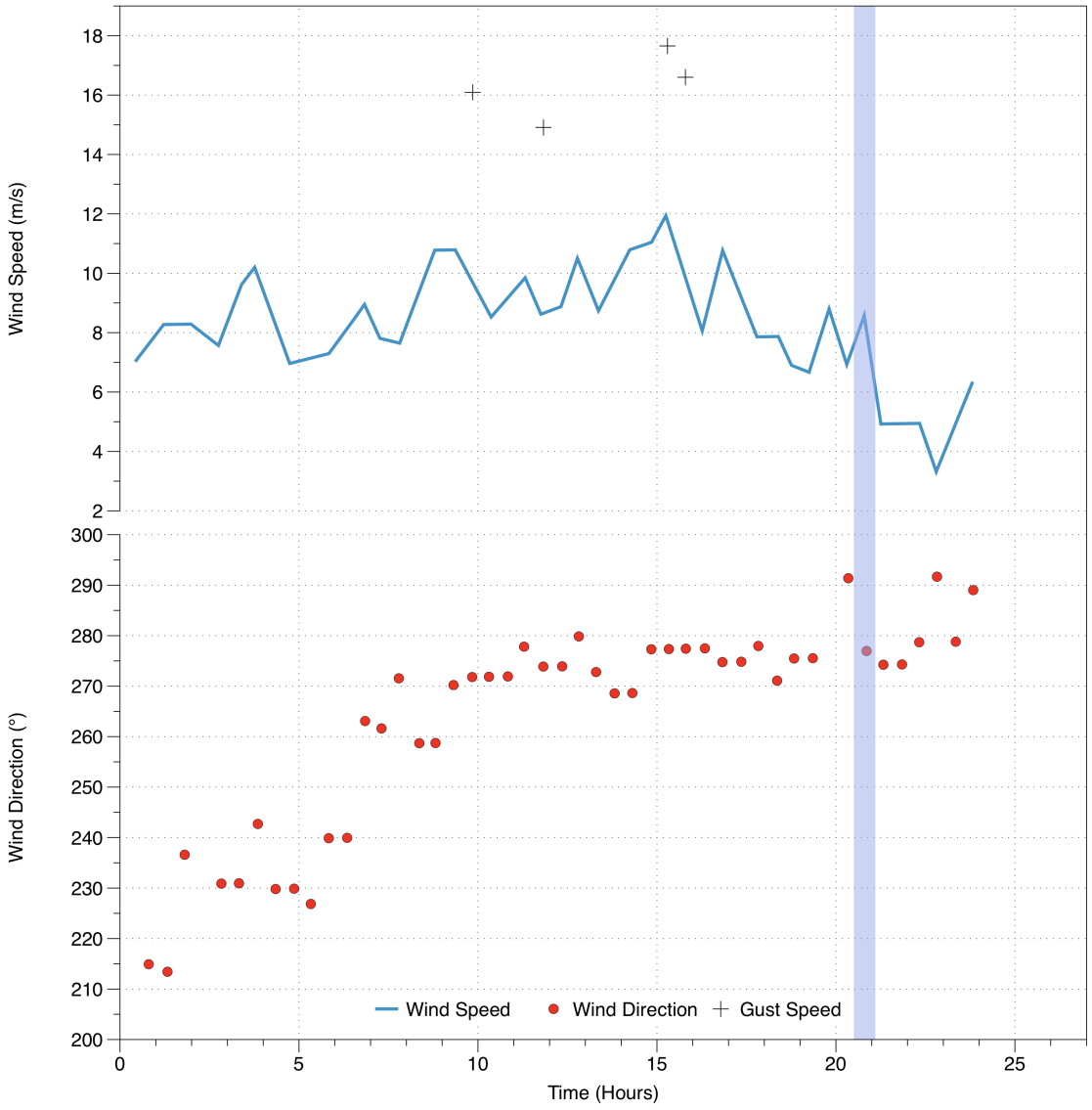

Figure G.7: Wind Data Obtained from Doncaster Station (x) with Applicable Run Data Highlighted.

After an angular rotation (Φ) of -22.5° to centre the notation along the longitudinal centre line of the vehicle, the resulting vector diagram is shown in Fig.(G.8).

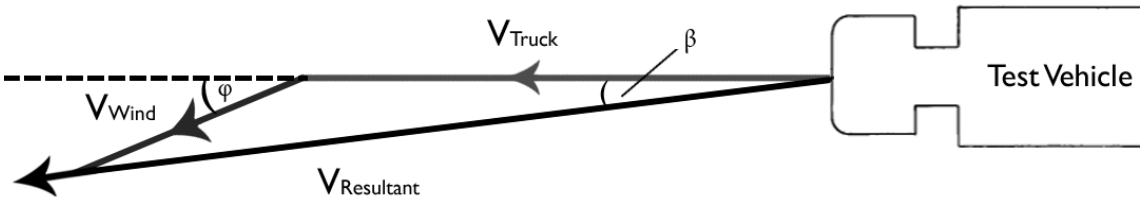

Figure G.8: Run [13] Example Calculation.

where $\varphi = 22.5°$ and $\overline{V}_{Wind} = 8.2$ ms^{-1}. This equates to a x-component (along longitudinal centre line of vehicle) $\overline{V}_{Wind}$ of 7.8 ms^{-1} and a y-component $\overline{V}_{Wind}$ of -3.1 ms^{-1}, calculated using Eqs.(G.1 and G.2):

$$\overline{V}_{(x)Wind} = \overline{V}_{Wind}\cos(\varphi) \tag{G.1}$$

$$\overline{V}_{(y)Wind} = \overline{V}_{Wind}\sin(\varphi) \tag{G.2}$$

The effective yaw angle (β) was calculated by

$$\beta = \tan^{-1}\left[\frac{\overline{V}_{(y)Wind}}{\overline{V}_{(x)Wind} + \overline{V}_{Truck}}\right] \tag{G.3}$$

giving

$$\beta = \tan^{-1}\left[\frac{-3.1}{8.2 + 18.5}\right] \tag{G.4}$$

resulting in an estimate for the yaw angle: $\beta = -7.0°$. The remaining calculations for the tested routes are shown in Tab.(G.3).

G.4 On-Road Route Data and Statistics

The summarised wind data from all runs tested is shown in Tab.(G.3), the individual analysis of each run is shown in Secs.(G.4.2 - G.4.14.1)

G.4.1 On-Road Data - All Runs

Run Number	Φ_{Truck} (°)	V_{Truck}	Φ_{Wind} (°)	φ_{Wind} (°)	V_{Wind}	$\overline{V}_{(x)Wind}$	$\overline{V}_{(y)Wind}$	β
Run [1]	311.0	10.1	282.0	-29.0	6.2	5.4	-3.0	-11.0
Run [2]	131.0	9.6	282.0	29.0	6.2	5.4	3.0	11.3
Run [3a]	45.0	24.5	232.0	7.0	7.4	7.3	0.9	2.0
Run [4b]	325.0	24.5	200.0	-55.0	5.1	2.9	-4.2	-8.7
Run [5b]	90.0	23.3	270.0	0.0	7.7	7.7	0.0	0.0
Run [6]	60.0	24.7	0.0	-30.0	7.2	6.2	-3.6	-6.6
Run [7]	90.0	22.3	45.0	-45.0	6.7	4.7	-4.7	-9.9
Run [8]	275.0	24.5	250	-25.0	6.7	6.1	-2.8	-5.2
Run [9]	275.0	23.6	227.0	-48.0	7.2	4.8	-5.4	-10.7
Run [10]	350.0	24.0	270.0	-10.0	8.2	8.1	-1.4	-2.5
Run [11]	170.0	24.0	270.0	10.0	6.7	6.6	1.2	2.3
Run [12]	76.0	24.4	270.0	14.0	7.2	7.0	1.7	3.1
Run [13]	292.5	18.5	270.0	-22.5	8.2	7.8	-3.1	-7.0
Run [14]	157.5	18.5	270.0	22.5	10.0	9.2	3.8	8.0
Run [15]	202.5	24.8	270.0	22.5	9.3	8.6	3.6	6.2

Table G.3: Vehicle Test Route Estimated Yaw Angles (β).

G.4.2 Run [1] and Run [2]

G.4.2.1 Location Data: Run [1] and Run [2]

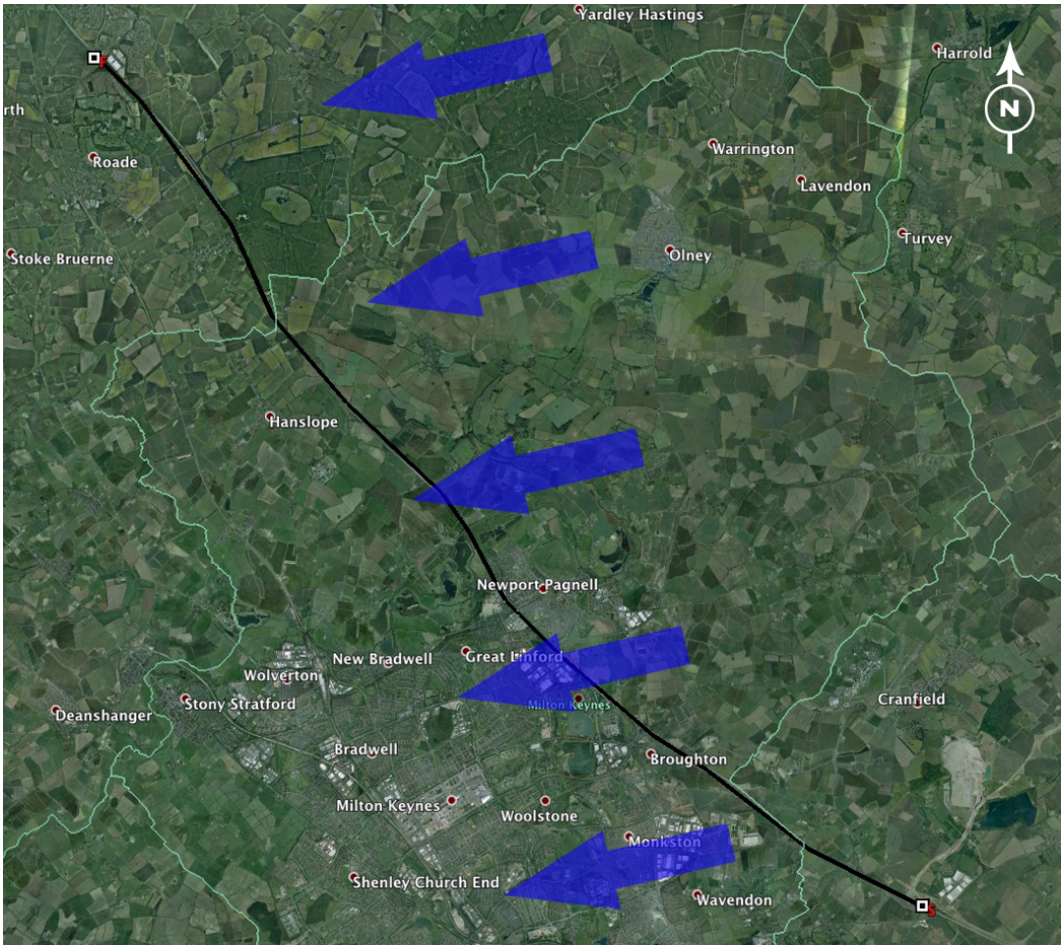

Figure G.9: Vehicle Test Route: Run [1] and [2][1].

Run Number	Latitude [Start]	Longitude [Start]	Latitude [Finish]	Longitude [Finish]
Run [1]	52°1'35.45"N	0°36'9.73"W	52°11'5.27"N	0°53'40.37"W
Run [2]	52°11'5.27"N	0°53'40.37"W	52°1'35.45"N	0°36'9.73"W

Table G.4: Vehicle Test Route Start and Finish Locations: Run [1] and Run [2].

[1]Blue Arrows Denote $\overline{\Phi}_{Wind}$ Measured from Weather Station (i).

G.4.2.2 Wind Speed and Direction Data: Run [1 and 2]

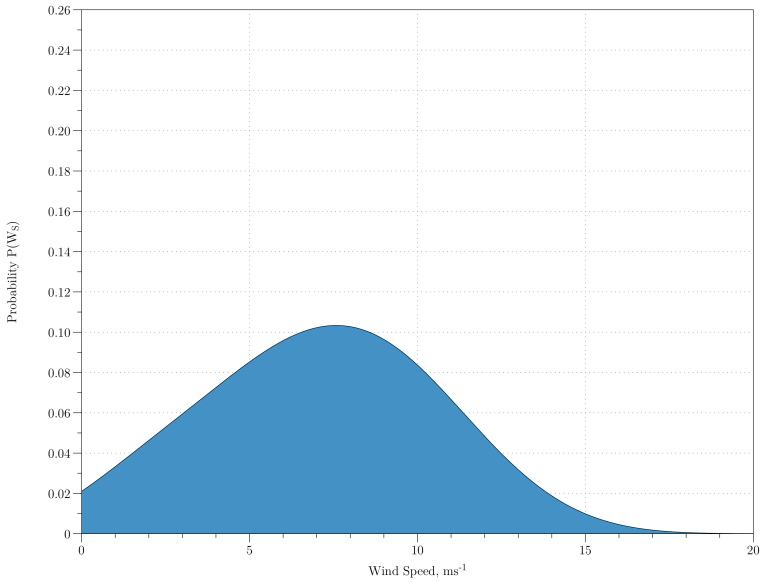

Figure G.10: Wind Speed Histogram of Run [1 and 2].

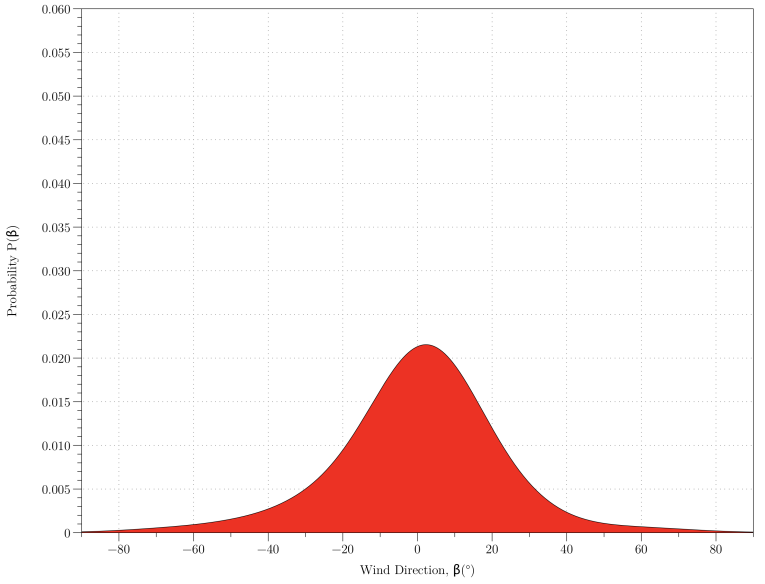

Figure G.11: Wind Direction Histogram of Run [1 and 2].

Run Number	$\overline{\beta}$ (°)	$\overline{V}_W$ (ms^{-1})	$\overline{V}_{Truck}$ (ms^{-1})	$\overline{\beta}(°)[W.S]$	$\overline{V}_W[W.S]$
Run [1]	-9.9	6.0	10.1	-11.0	6.2
Run [2]	10.5	8.5	9.6	11.3	6.2

Table G.5: Vehicle Average Wind Direction (β), Wind Speed (V_W) and Vehicle Speed (V_{Truck}): Run [1] and Run [2].

G.4.2.3 Wind Frequency Data: Run [1] and Run [2]

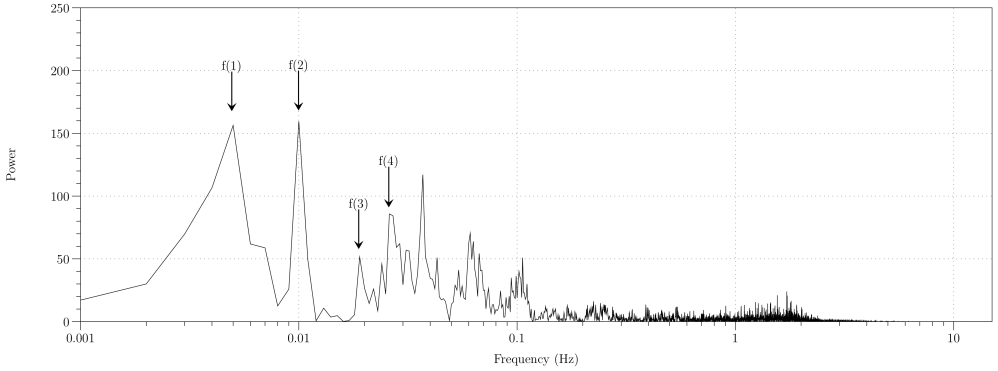

Figure G.12: FFT Power Spectrum of Run [1].

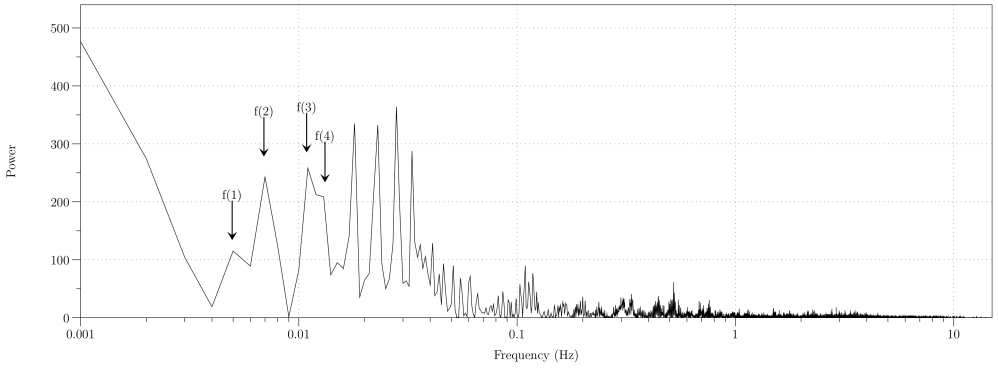

Figure G.13: FFT Power Spectrum of Run [2].

Run Number	$\overline{\beta}$ (°)	P1(s)	P2 (s)	P3 (S)	P4 (S)
Run [1]	-9.9	202.8	100.3	53.1	38.7
Run [2]	10.5	202.0	144.5	92.1	75.8

Table G.6: Vehicle Test Route Frequency Statistics: Run [1] and Run [2].

G.4.3 Run [3]

G.4.3.1 Location Data: Run [3a]

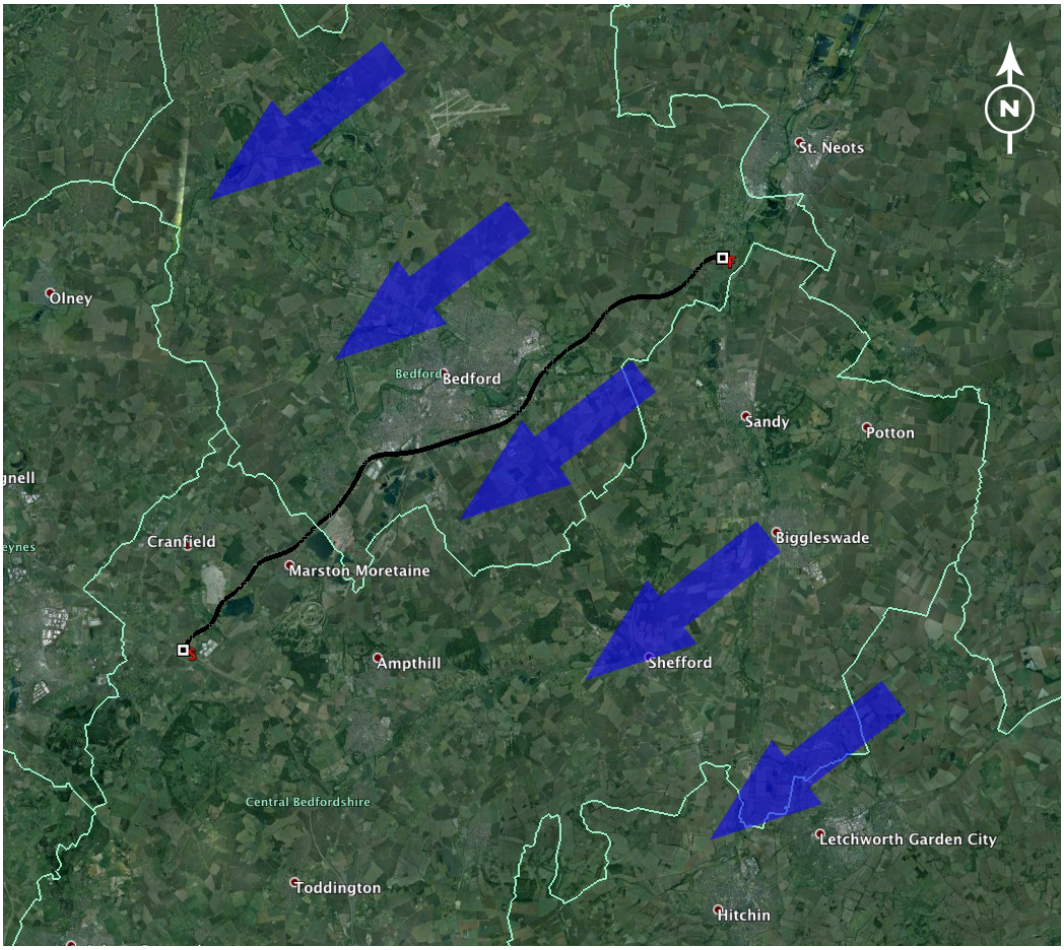

Figure G.14: Vehicle Test Route: Run [3a][2].

Run Number	Latitude [Start]	Longitude [Start]	Latitude [Finish]	Longitude [Finish]
Run [3]	52°1'48.79"N	0°36'26.35"W	52°8'51.86"N	1°4'41.35"E

Table G.7: Vehicle Test Route Start and Finish Location: Run [3a].

[2]Blue Arrows Denote $\overline{\Phi}_{Wind}$ Measured from Weather Station (i).

G.4.3.2 Wind Speed and Direction Data: Run [3a]

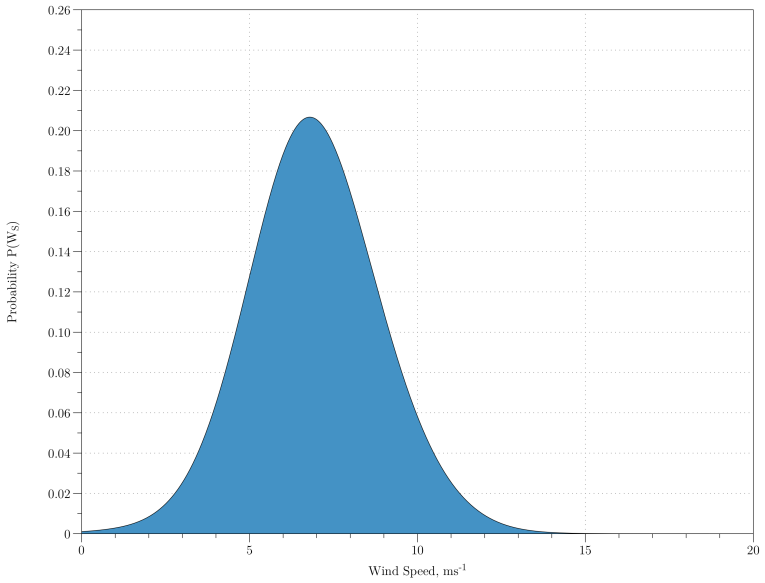

Figure G.15: Wind Speed Histogram of Run [3a].

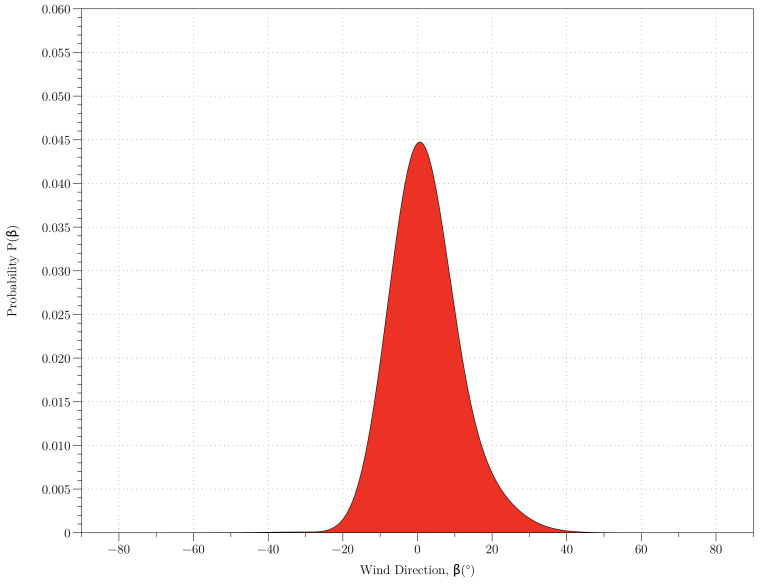

Figure G.16: Wind Direction Histogram of Run [3a].

Run Number	$\overline{\beta}$ (°)	$\overline{V}_W$ (ms^{-1})	$\overline{V}_{Truck}$ (ms^{-1})	$\overline{\beta}(°)[W.S]$	$\overline{V}_W[W.S]$
Run [3]	2.2	7.0	24.6	2.0	7.4

Table G.8: Vehicle Average Wind Direction (β), Wind Speed (V_W) and Vehicle Speed (V_{Truck}): Run [3a].

G.4.3.3 Wind Frequency Data: Run [3a]

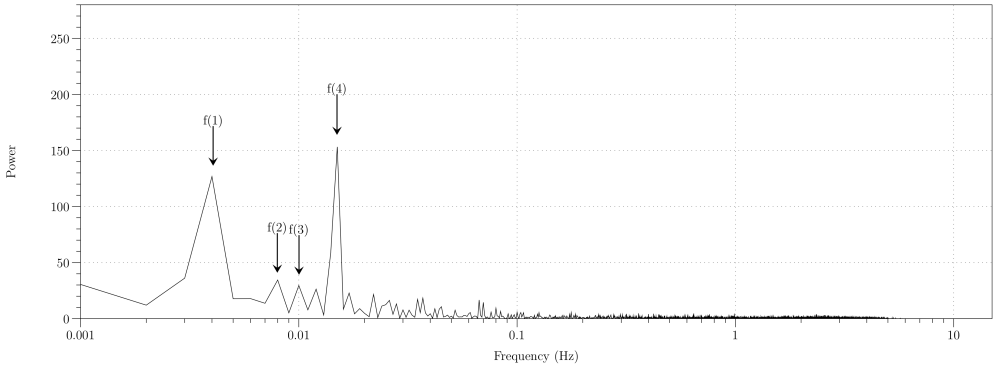

Figure G.17: FFT Power Spectrum of Run [3a]

Run Number	$\overline{\beta}$ (°)	P1(s)	P2 (s)	P3 (S)	P4 (S)
Run [3]	2.2	247.0	125.5	99.8	66.8

Table G.9: Vehicle Test Route Frequency Statistics: Run [3a].

G.4.4 Run [4]

G.4.4.1 Location Data: Run [4b]

Figure G.18: Vehicle Test Route: Run [4b][3].

Run Number	Latitude [Start]	Longitude [Start]	Latitude [Finish]	Longitude [Finish]
Run [4b]	52°19'56.93"N	0°14'56.66"W	53° 8'14.36"N	2°20'11.40"W

Table G.10: Vehicle Test Route Start and Finish Location: Run [4b].

[3]Blue Arrows Denote $\overline{\Phi}_{Wind}$ Measured from Weather Station (ii).

G.4.4.2 Wind Speed and Direction Data: Run [4b]

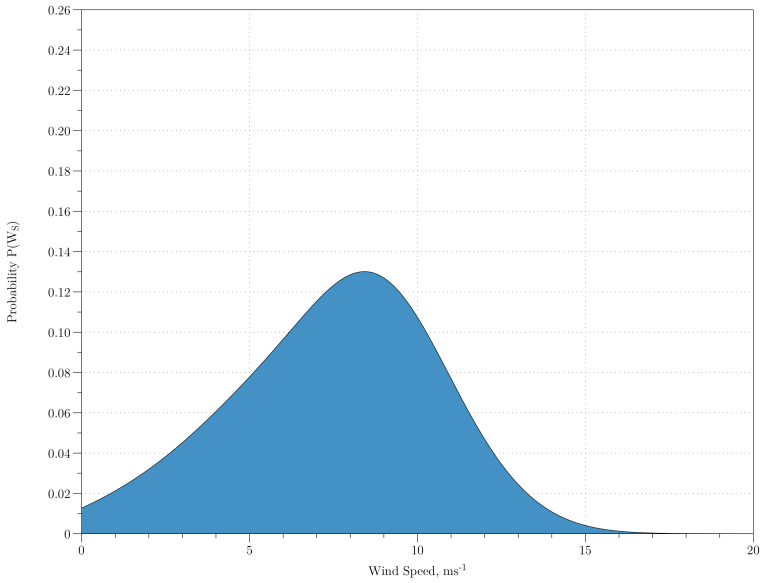

Figure G.19: Wind Speed Histogram of Run [4b].

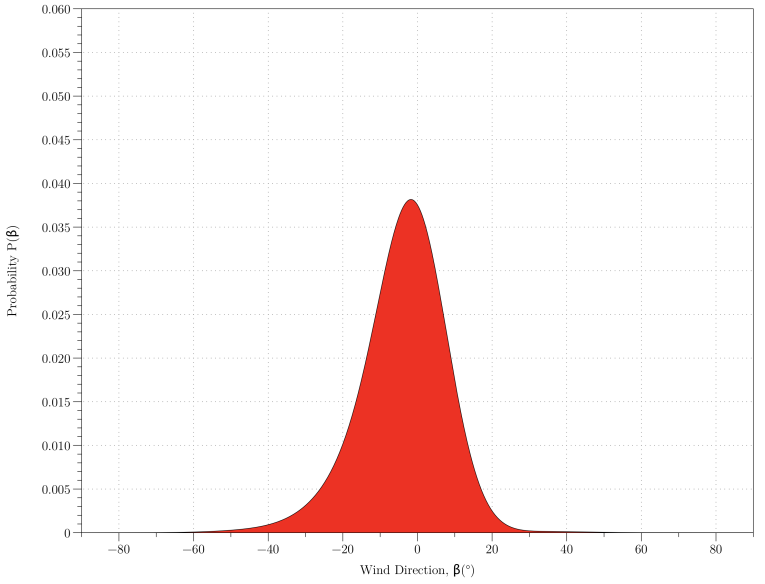

Figure G.20: Wind Direction Histogram of Run [4b].

Run Number	$\overline{\beta}$ (°)	$\overline{V}_W$ (ms^{-1})	$\overline{V}_{Truck}$ (ms^{-1})	$\overline{\beta}(°)[W.S]$	$\overline{V}_W[W.S]$
Run [4b]	-3.9	7.4	24.6	-8.7	5.1

Table G.11: Vehicle Average Wind Direction (β), Wind Speed (V_W) and Vehicle Speed (V_{Truck}): Run [4b].

G.4.4.3 Wind Frequency Data: Run [4b]

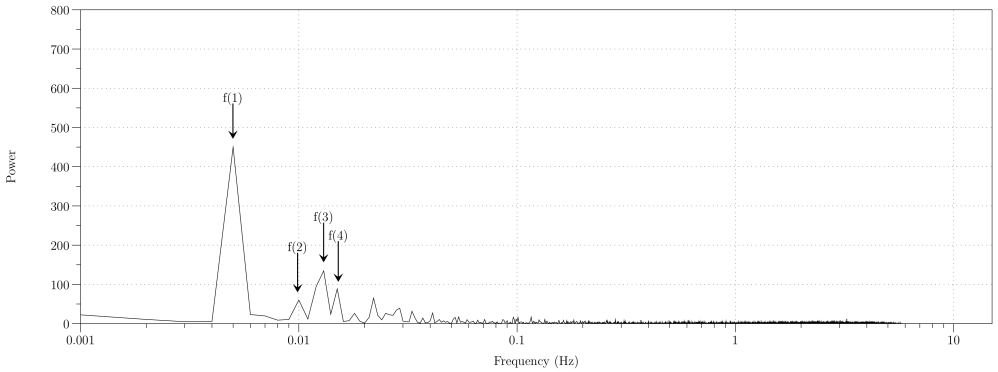

Figure G.21: FFT Power Spectrum of Run [4b].

Run Number	$\overline{\beta}$ (°)	P1(s)	P2 (s)	P3 (S)	P4 (S)
Run [4b]	-3.9	250.0	166.7	111.0	40.0

Table G.12: Vehicle Test Route Frequency Statistics: Run [4b].

G.4.5 Run [5]

G.4.5.1 Location Data: Run [5b]

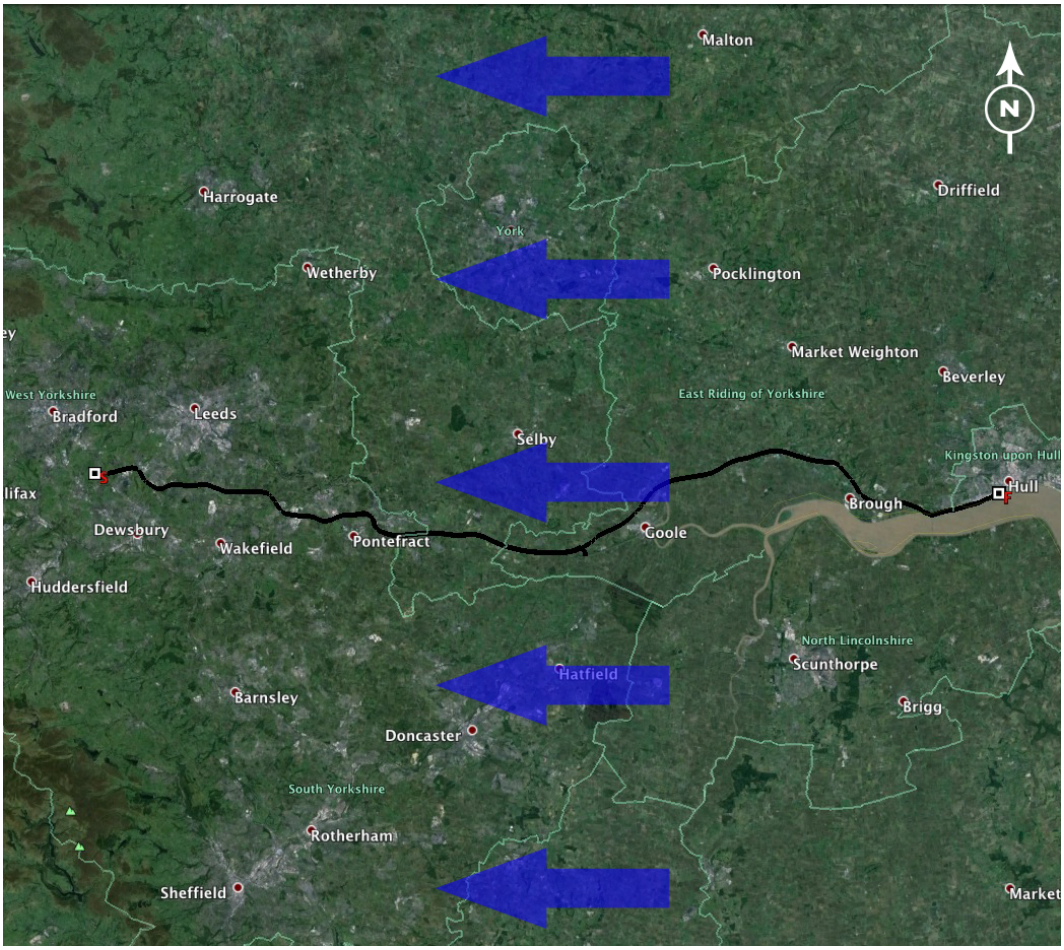

Figure G.22: Vehicle Test Route: Run [5b][4].

Run Number	Latitude [Start]	Longitude [Start]	Latitude [Finish]	Longitude [Finish]
Run [5b]	53°43'50.35"N	2°20'29.93"W	53° 44'12.98"N	0°21'18.77"W

Table G.13: Vehicle Test Route Start and Finish Location: Run [5b].

[9]Blue Arrows Denote $\overline{\Phi}_{Wind}$ Measured from Weather Station (iii).

G.4.5.2 Wind Speed and Direction Data: Run [5b]

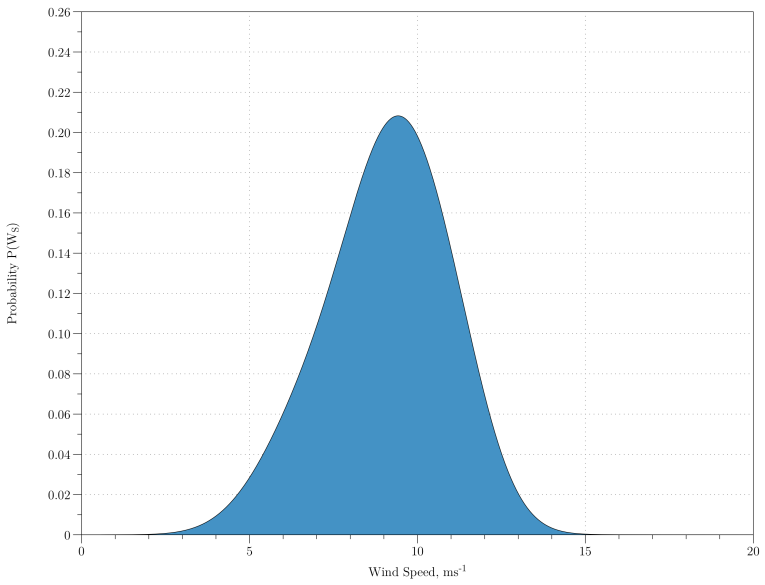

Figure G.23: Wind Speed Histogram of Run [5b].

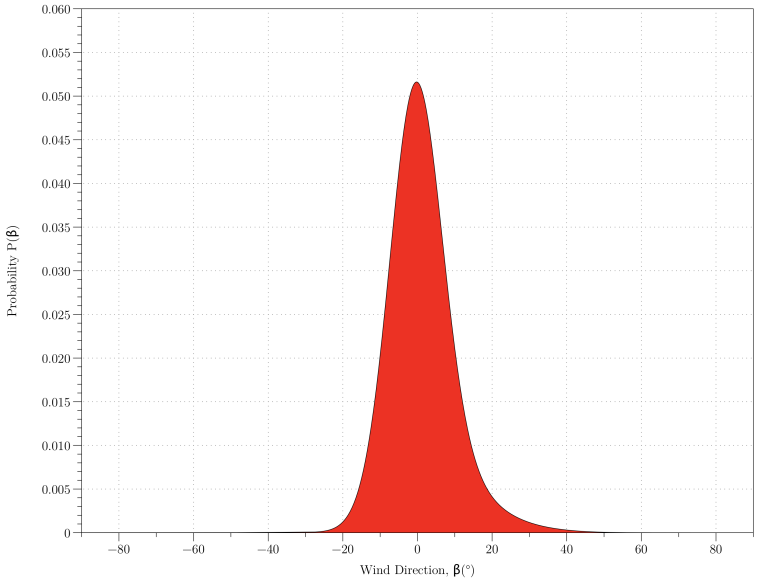

Figure G.24: Wind Direction Histogram of Run [5b].

Run Number	$\overline{\beta}$ (°)	$\overline{V}_W$ (ms^{-1})	$\overline{V}_{Truck}$ (ms^{-1})	$\overline{\beta}(°)[W.S]$	$\overline{V}_W[W.S]$
Run [5b]	1.1	9.0	23.3	0.0	7.7

Table G.14: Vehicle Average Wind Direction (β), Wind Speed (V_W) and Vehicle Speed (V_{Truck}): Run [5b].

G.4.5.3 Wind Frequency Data: Run [5b]

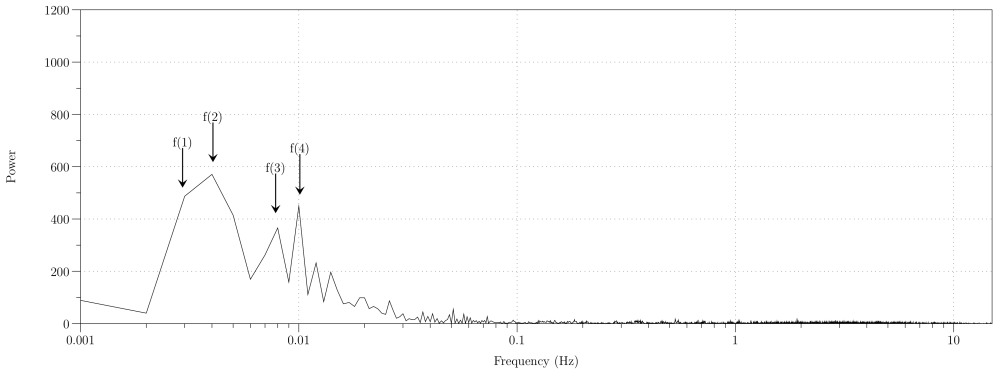

Figure G.25: FFT Power Spectrum of Run [5b].

Run Number	$\overline{\beta}$ (°)	P1(s)	P2 (s)	P3 (S)	P4 (S)
Run [5b]	1.1	340.8	247.5	127.7	98.9

Table G.15: Vehicle Test Route Frequency Statistics: Run [5b].

G.4.6 Run [6]

G.4.6.1 Location Data: Run [6]

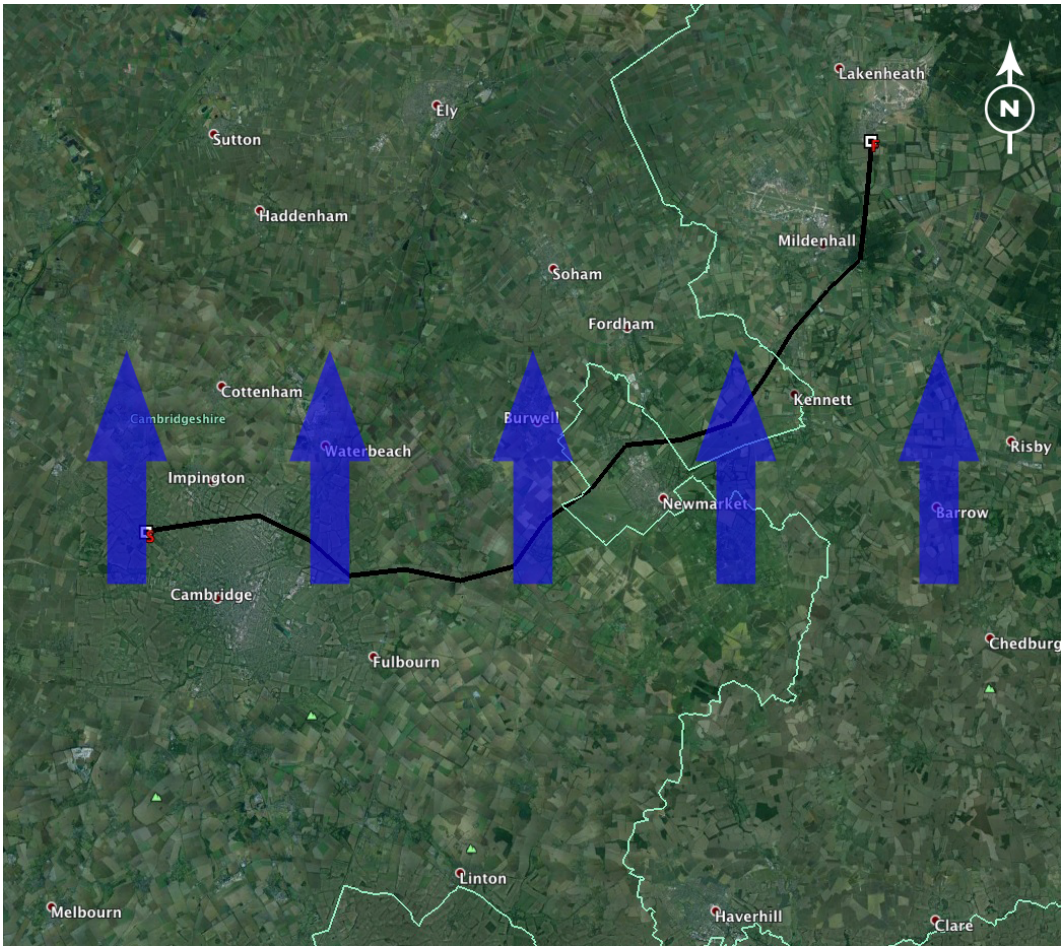

Figure G.26: Vehicle Test Route: Run [6][5].

Run Number	Latitude [Start]	Longitude [Start]	Latitude [Finish]	Longitude [Finish]
Run [6]	52°13'54.39"N	0°4'35.64"E	52° 23'7.53"N	0°32'33.60"E

Table G.16: Vehicle Test Route Start and Finish Location: Run [6].

[5]Blue Arrows Denote $\overline{\Phi}_{Wind}$ Measured from Weather Station (iv).

G.4.6.2 Wind Speed and Direction Data: Run [6]

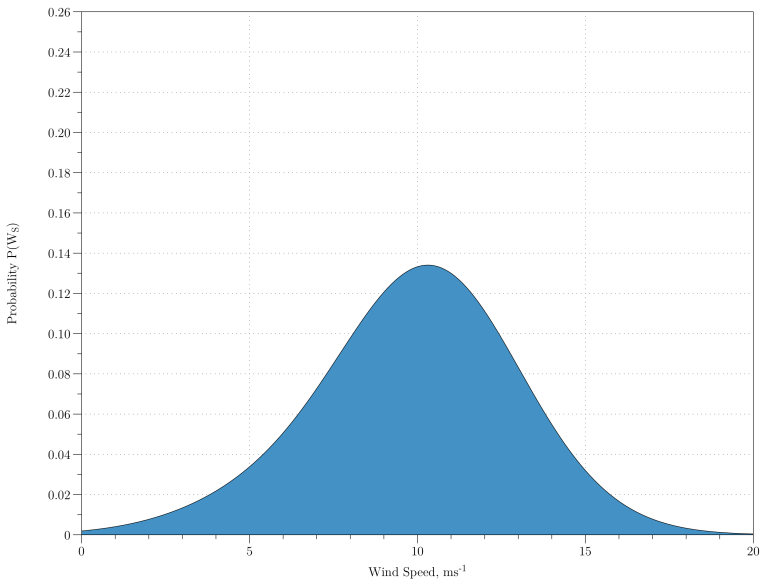

Figure G.27: Wind Speed Histogram of Run [6].

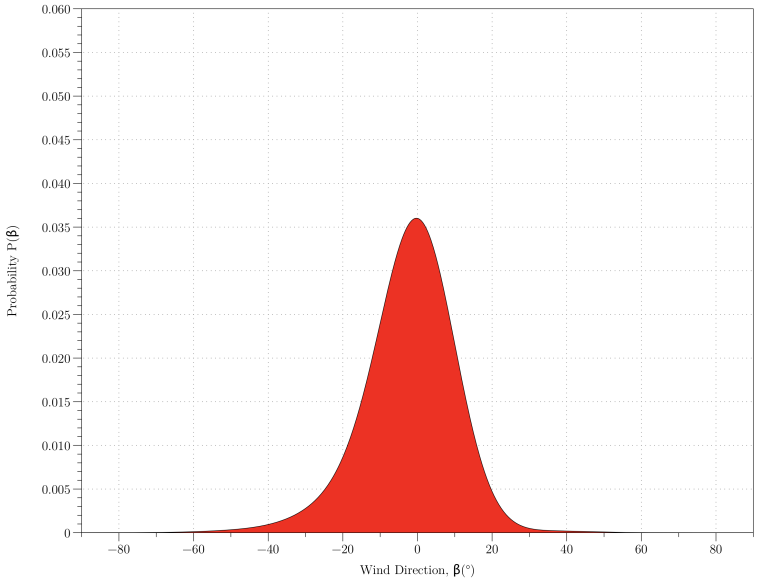

Figure G.28: Wind Direction Histogram of Run [6].

Run Number	$\overline{\beta}$ (°)	$\overline{V}_W$ (ms^{-1})	$\overline{V}_{Truck}$ (ms^{-1})	$\overline{\beta}(°)[W.S]$	$\overline{V}_W[W.S]$
Run [6]	-2.2	9.9	24.7	-6.6	7.2

Table G.17: Vehicle Average Wind Direction (β), Wind Speed (V_W) and Vehicle Speed (V_{Truck}): Run [6].

G.4.6.3 Wind Frequency Data: Run [6]

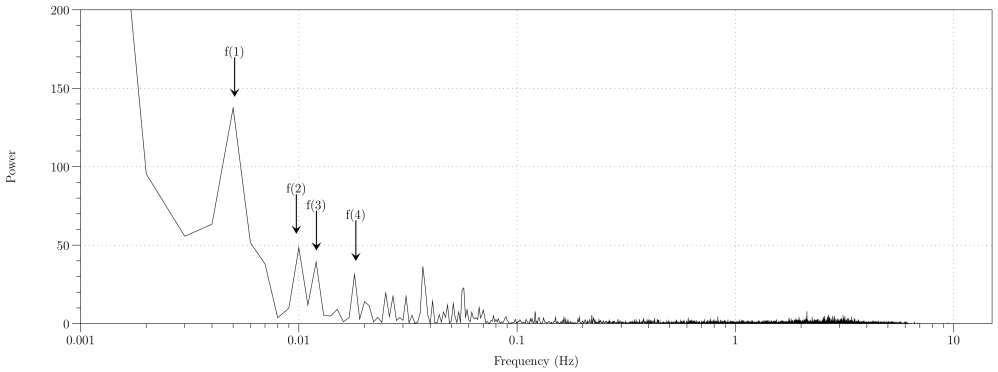

Figure G.29: FFT Power Spectrum of Run [6].

Run Number	$\overline{\beta}$ (°)	P1(s)	P2 (s)	P3 (S)	P4 (S)
Run [6]	-2.2	196.8	102.7	83.1	54.8

Table G.18: Vehicle Test Route Frequency Statistics: Run [6].

G.4.7 Run [7]

G.4.7.1 Location Data: Run [7]

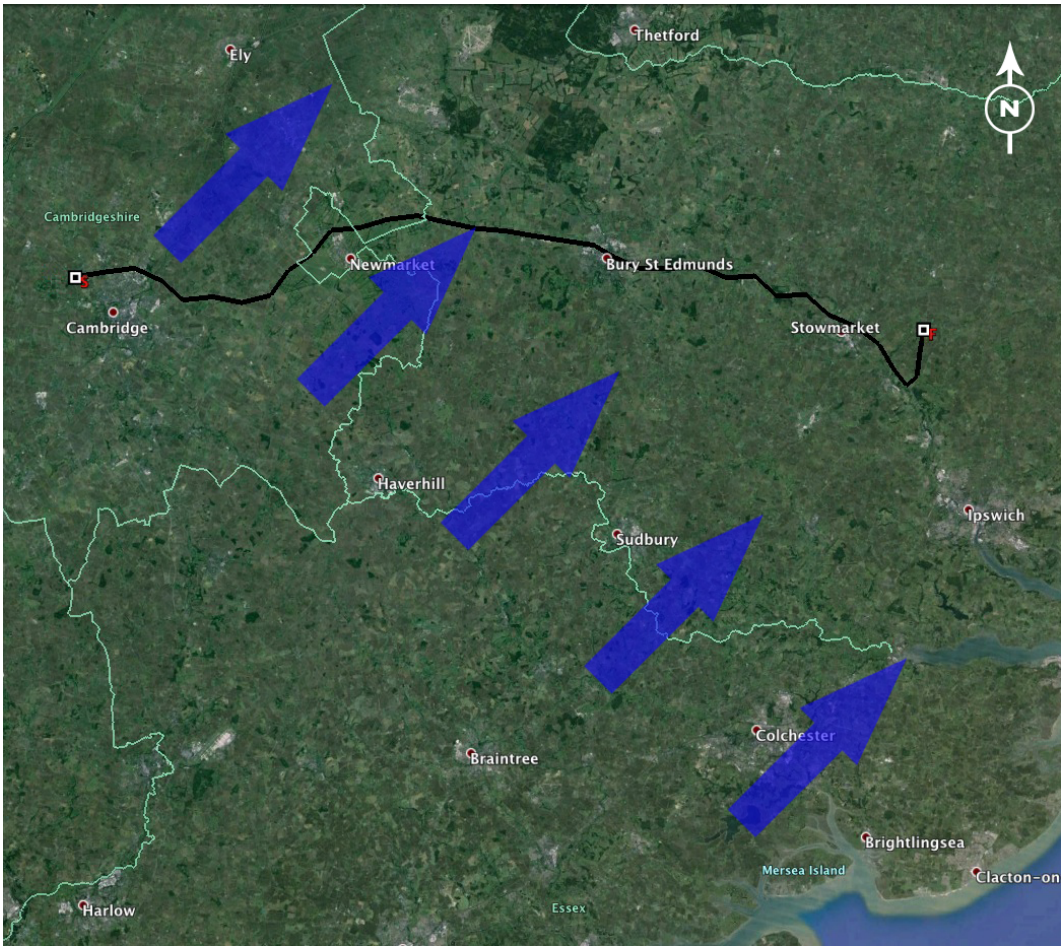

Figure G.30: Vehicle Test Route: Run [3b] and [7][6].

Run Number	Latitude [Start]	Longitude [Start]	Latitude [Finish]	Longitude [Finish]
Run [7]	52° 13'54.60"N	0° 4'36.33"E	52°11'26.79"N	1°5'51.80"E

Table G.19: Vehicle Test Route Start and Finish Location: Run [7].

[6]Blue Arrows Denote $\overline{\Phi}_{Wind}$ Measured from Weather Station (v).

G.4.7.2 Wind Speed and Direction Data: Run [7]

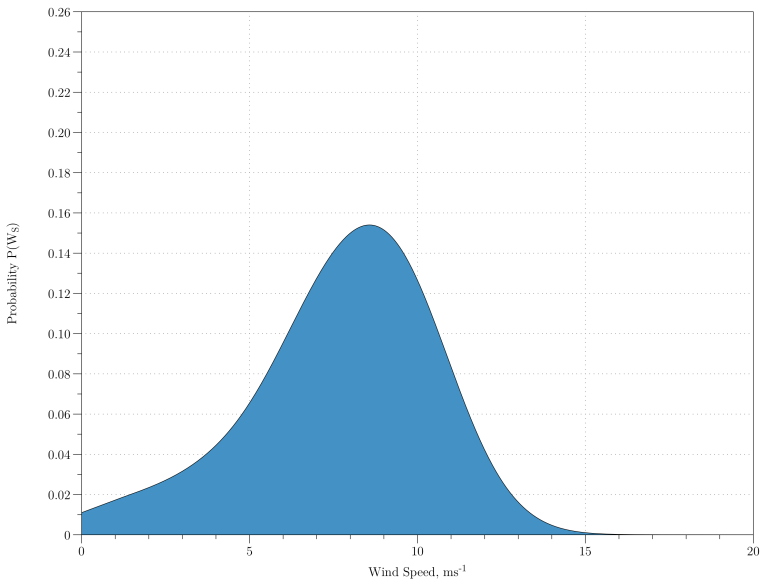

Figure G.31: Wind Speed Histogram of Run [7].

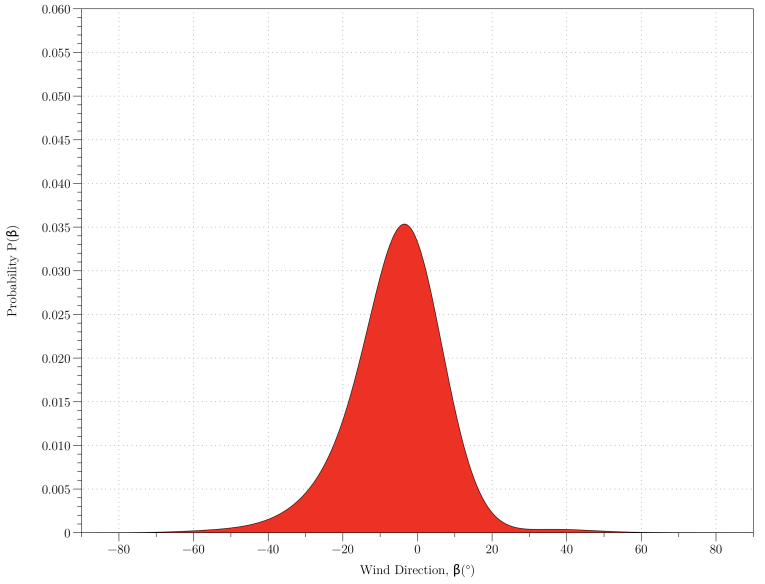

Figure G.32: Wind Direction Histogram of Run [7].

Run Number	$\overline{\beta}$ (°)	$\overline{V}_W$ (ms^{-1})	$\overline{V}_{Truck}$ (ms^{-1})	$\overline{\beta}$(°)[W.S]	$\overline{V}_W$[W.S]
Run [7]	-5.6	7.7	22.3	-9.9	6.7

Table G.20: Vehicle Average Wind Direction (β), Wind Speed (V_W) and Vehicle Speed (V_{Truck}): Run [7].

G.4.7.3 Wind Frequency Data: Run [7]

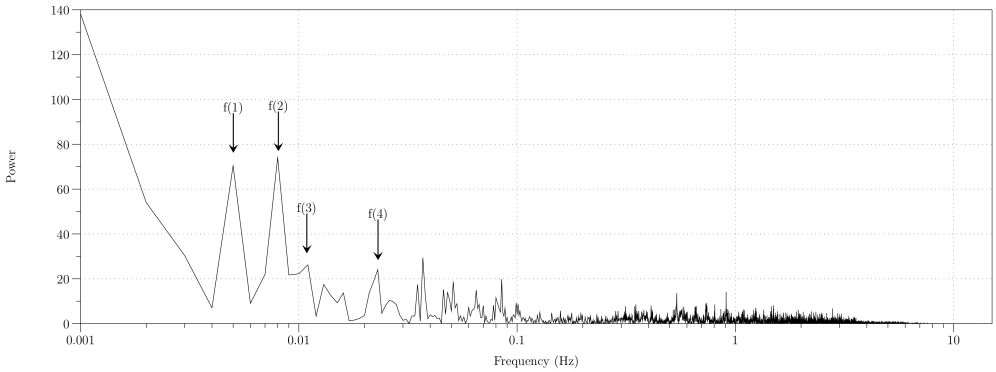

Figure G.33: FFT Power Spectrum of Run [7].

Run Number	$\overline{\beta}$ (°)	P1(s)	P2 (s)	P3 (S)	P4 (S)
Run [7]	-5.6	199.6	124.1	91.9	43.4

Table G.21: Vehicle Test Route Frequency Statistics: Run [7].

G.4.8 Run [8]

G.4.8.1 Location Data: Run [8]

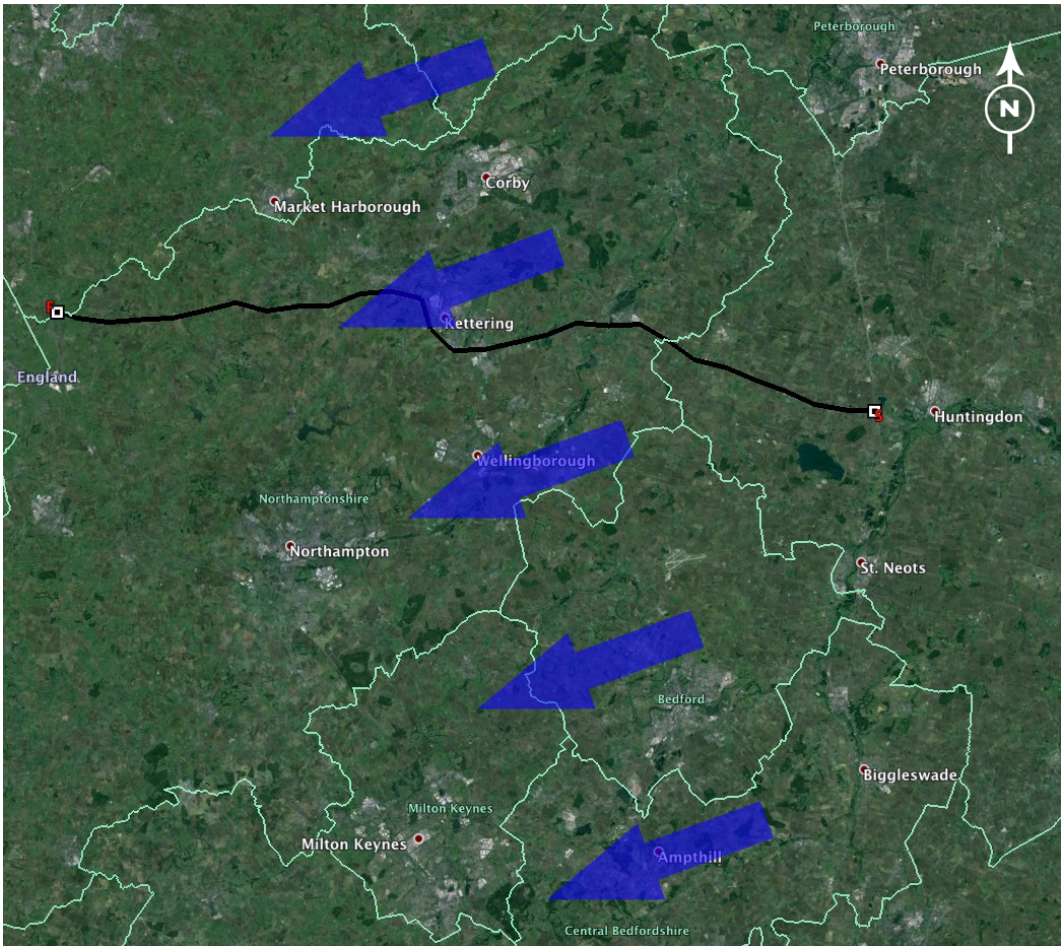

Figure G.34: Vehicle Test Route: Run [4a] and [8][7].

Run Number	Latitude [Start]	Longitude [Start]	Latitude [Finish]	Longitude [Finish]
Run [4a and 8]	52°20'2.87"N	0°14'56.15"W	52°24'5.44"N	1° 9'51.97"W

Table G.22: Vehicle Test Route Start and Finish Location: Run [8].

[7]Blue Arrows Denote $\overline{\Phi}_{Wind}$ Measured from Weather Station (vi).

G.4.8.2 Wind Speed and Direction Data: Run [8]

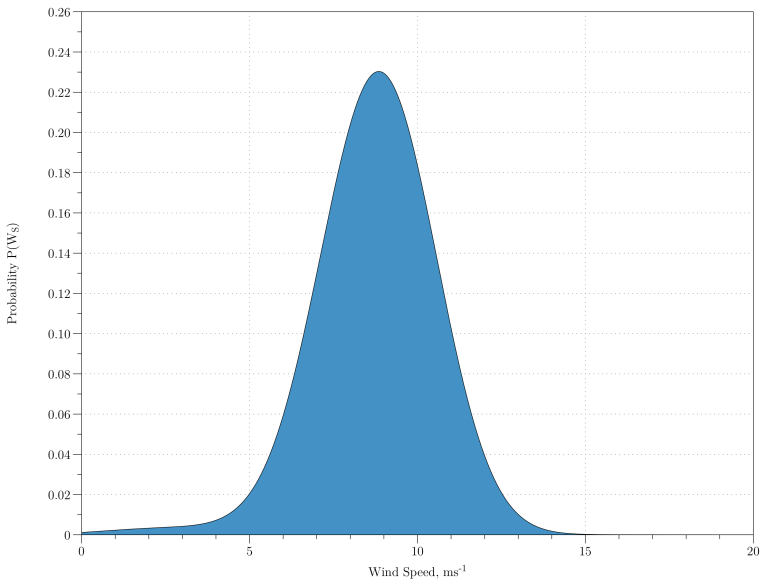

Figure G.35: Wind Speed Histogram of Run [8].

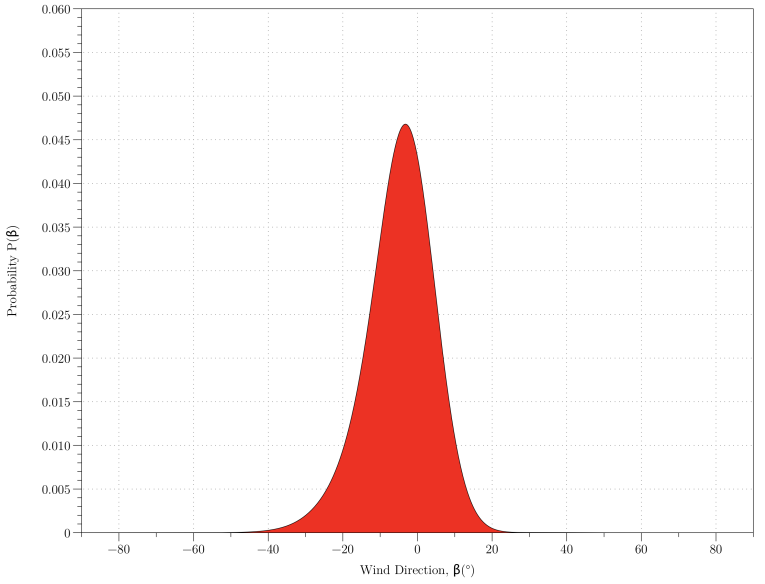

Figure G.36: Wind Direction Histogram of Run [8].

Run Number	$\overline{\beta}$ (°)	$\overline{V}_W$ (ms^{-1})	$\overline{V}_{Truck}$ (ms^{-1})	$\overline{\beta}(°)[W.S]$	$\overline{V}_W[W.S]$
Run [8]	-4.8	8.7	24.5	-5.2	6.7

Table G.23: Vehicle Average Wind Direction (β), Wind Speed (V_W) and Vehicle Speed (V_{Truck}): Run [8].

G.4.8.3 Wind Frequency Data: Run [8]

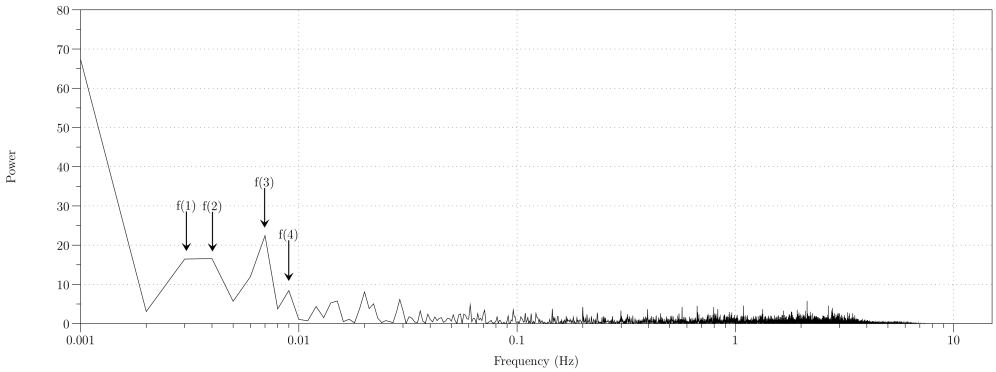

Figure G.37: FFT Power Spectrum of Run [8].

Run Number	$\overline{\beta}$ (°)	P1(s)	P2 (s)	P3 (S)	P4 (S)
Run [8]	-4.8	324.7	248.7	143.5	111.2

Table G.24: Vehicle Test Route Frequency Statistics: Run [8].

G.4.9 Run [9]

G.4.9.1 Location Data: Run [9]

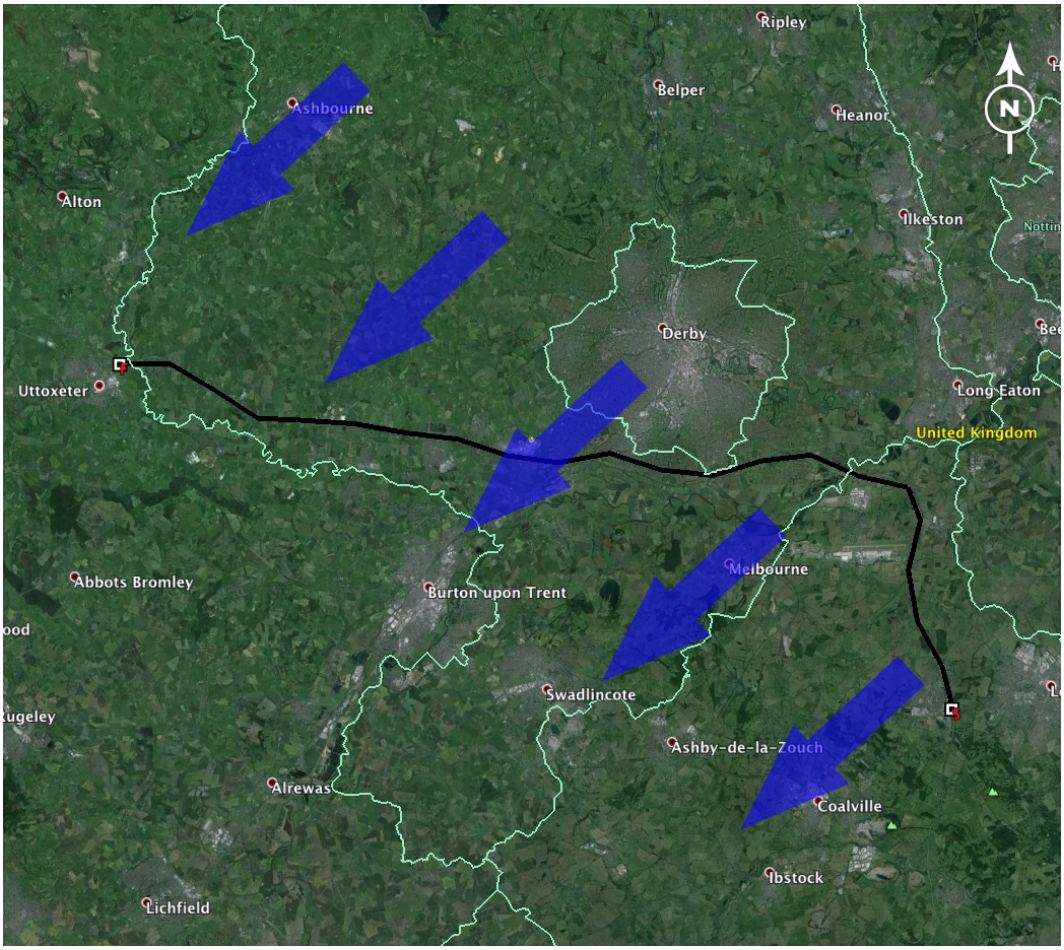

Figure G.38: Vehicle Test Route: Run [9][8].

Run Number	Latitude [Start]	Longitude [Start]	Latitude [Finish]	Longitude [Finish]
Run [9]	52°45'42.82"N	1°16'30.26"W	52°54'20.72"N	1°51'3.79"W

Table G.25: Vehicle Test Route Start and Finish Locations: Run [9].

[8]Blue Arrows Denote $\overline{\Phi}_{Wind}$ Measured from Weather Station (vii).

G.4.9.2 Wind Speed and Direction Data: Run [9]

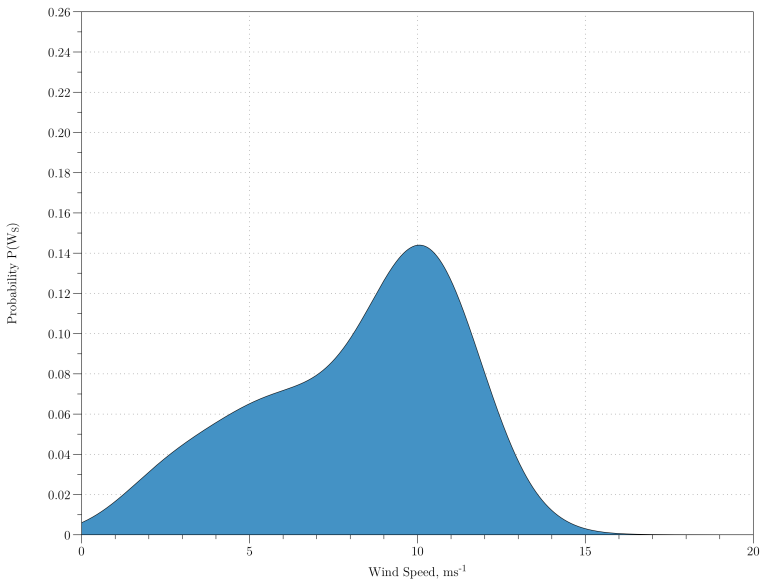

Figure G.39: Wind Speed Histogram of Run [9].

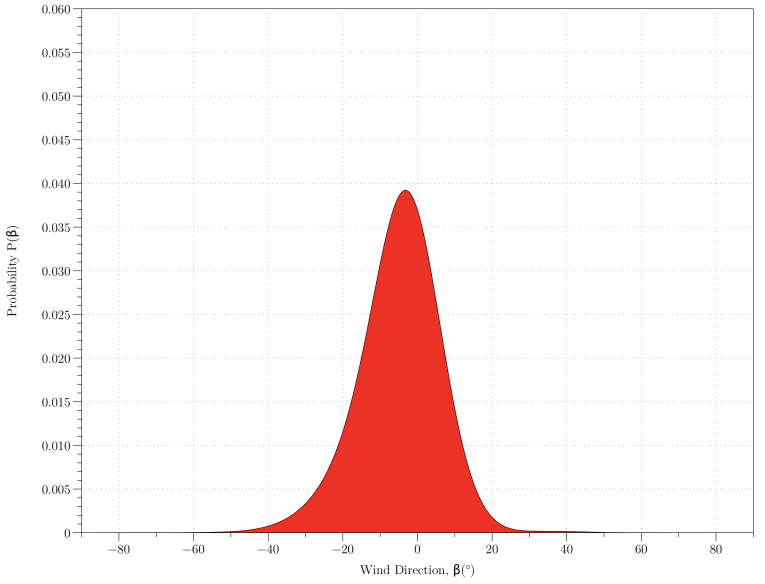

Figure G.40: Wind Direction Histogram of Run [9].

Run Number	$\overline{\beta}$ (°)	$\overline{V}_W$ (ms^{-1})	$\overline{V}_{Truck}$ (ms^{-1})	$\overline{\beta}(°)[W.S]$	$\overline{V}_W[W.S]$
Run [9]	-4.9	8.1	23.6	-10.7	7.2

Table G.26: Vehicle Average Wind Direction (β), Wind Speed (V_W) and Vehicle Speed (V_{Truck}): Run [9].

G.4.9.3 Wind Frequency Data: Run [9]

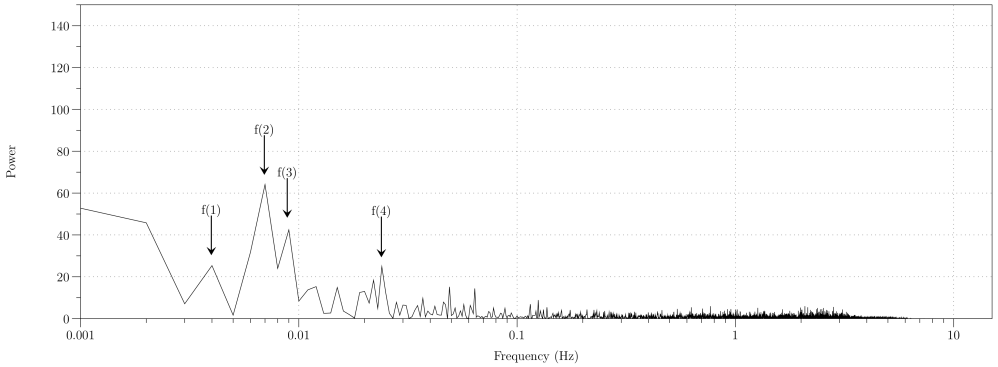

Figure G.41: FFT Power Spectrum of Run [9].

Run Number	$\overline{\beta}$ (°)	P1(s)	P2 (s)	P3 (S)	P4 (S)
Run [9]	-4.9	251.7	143.9	113.0	41.9

Table G.27: Vehicle Test Route Frequency Statistics: Run [9].

G.4.10 Run [10] and Run [11]

G.4.10.1 Location Data: Run [10] and Run [11]

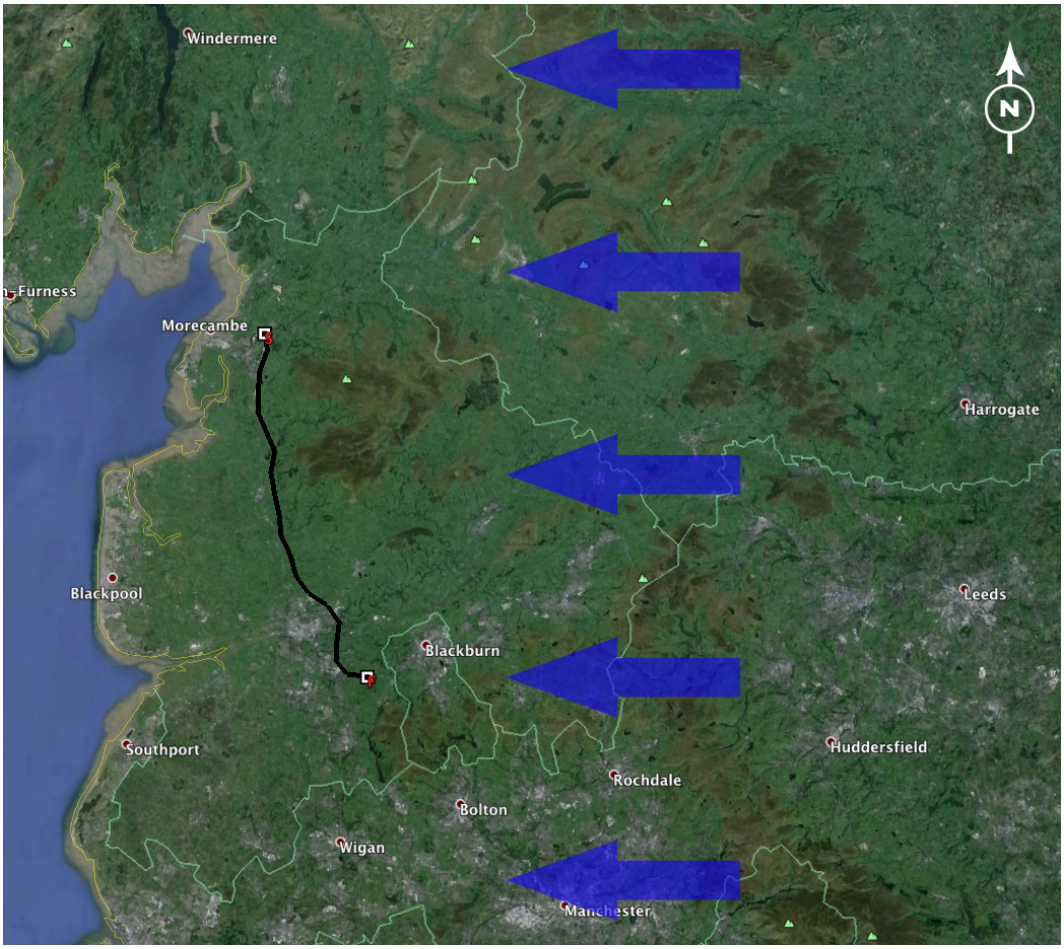

Figure G.42: Vehicle Test Route: Run [10] and [11][9].

Run Number	Latitude [Start]	Longitude [Start]	Latitude [Finish]	Longitude [Finish]
Run [10]	54°4'31.38"N	2°46'10.38"W	53°43'16.60"N	2°35'16.09"W
Run [11]	53°43'16.60"N	2°35'16.09"W	54° 4'31.38"N	2°46'10.38"W

Table G.28: Vehicle Test Route Start and Finish Locations: Run [10] and Run [11].

[9]Blue Arrows Denote $\overline{\Phi}_{Wind}$ Measured from Weather Station (viii).

G.4.10.2 Wind Speed and Direction Data: Run [10 and 11]

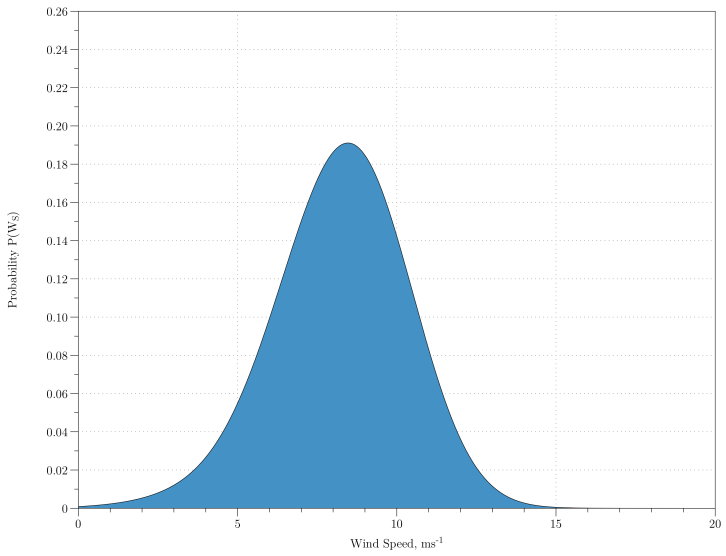

Figure G.43: Wind Speed Histogram of Run [10 and 11].

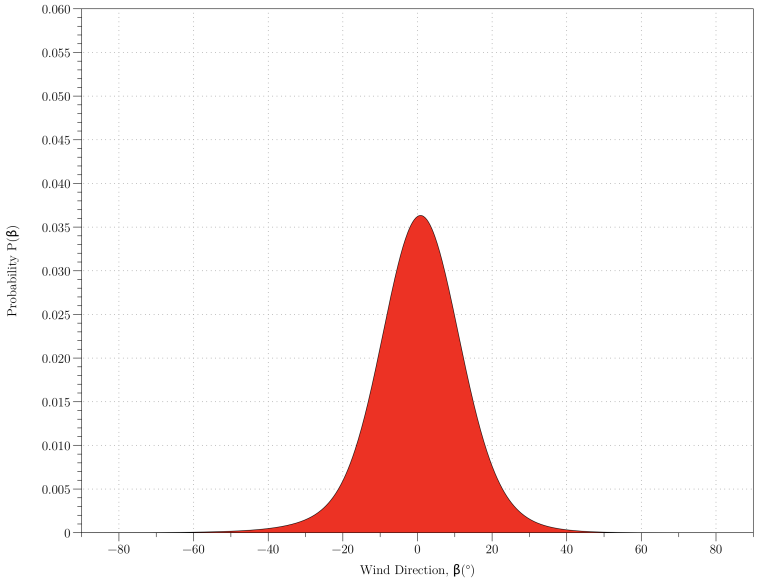

Figure G.44: Wind Direction Histogram of Run [10 and 11].

Run Number	$\overline{\beta}$ (°)	$\overline{V}_W$ (ms^{-1})	$\overline{V}_{Truck}$ (ms^{-1})	$\overline{\beta}(°)[W.S]$	$\overline{V}_W[W.S]$
Run [10]	-2.2	8.6	24.0	-2.5	8.2
Run [11]	2.3	8.6	24.0	2.3	6.7

Table G.29: Vehicle Average Wind Direction (β), Wind Speed (V_W) and Vehicle Speed (V_{Truck}): Run [10 and 11].

G.4.10.3 Wind Frequency Data: Run [10] and Run [11]

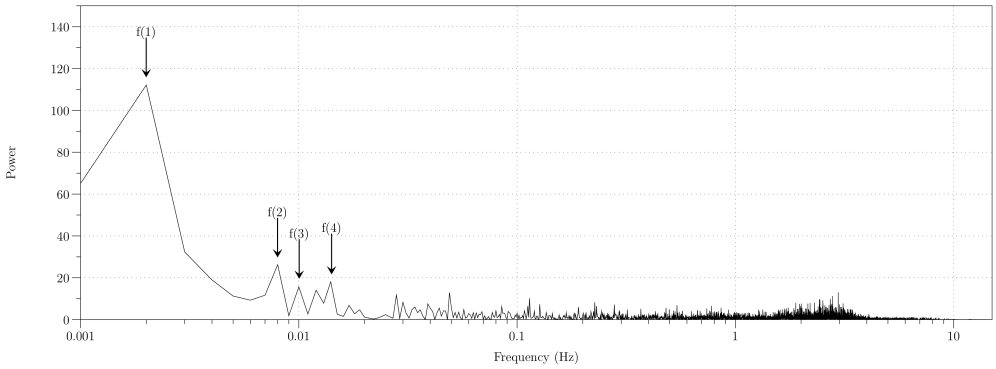

Figure G.45: FFT Power Spectrum of Run [10].

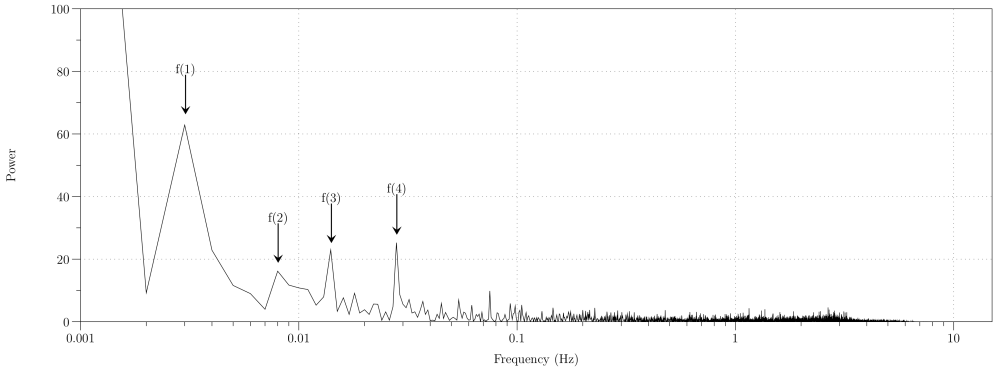

Figure G.46: FFT Power Spectrum of Run [11].

Run Number	$\overline{\beta}$ (°)	P1(s)	P2 (s)	P3 (S)	P4 (S)
Run [10]	-2.2	334.4	125.2	99.6	70.8
Run [11]	2.3	330.4	124.4	70.9	35.6

Table G.30: Vehicle Test Route Frequency Statistics: Run [10] and Run [11].

G.4.11 Run [12]

G.4.11.1 Location Data: Run [5a] and Run [12]

Figure G.47: Vehicle Test Route: Run [5a] and [12][10].

Run Number	Latitude [Start]	Longitude [Start]	Latitude [Finish]	Longitude [Finish]
Run [5a and12]	53°42'44.35"N	2°19'40.34"W	53°38'45.93"N	1°54'59.03"W

Table G.31: Vehicle Test Route Start and Finish Location: Run [5a and 12].

[10]Blue Arrows Denote $\overline{\Phi}_{Wind}$ Measured from Weather Station (ix).

G.4.11.2 Wind Speed and Direction Data: Run [12]

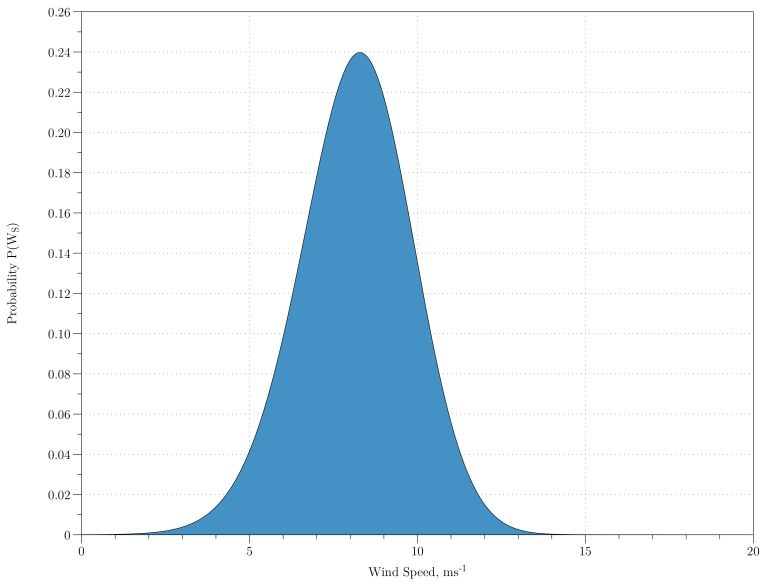

Figure G.48: Wind Speed Histogram of Run [12].

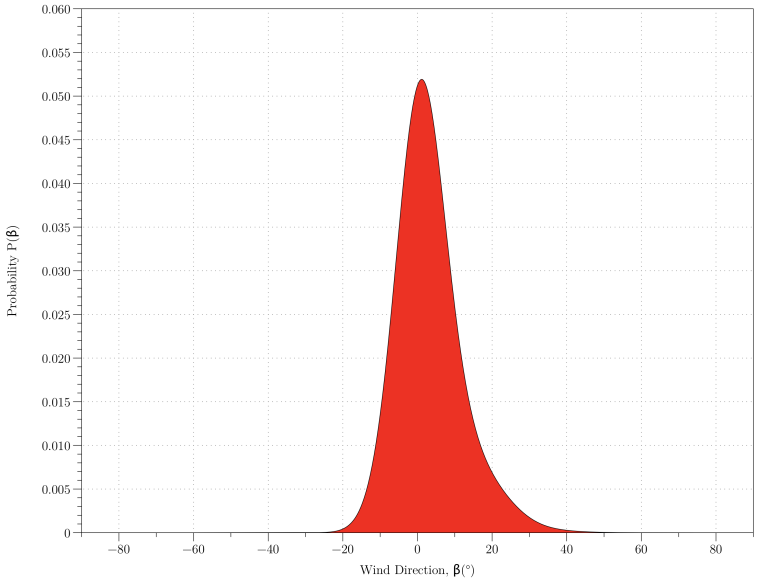

Figure G.49: Wind Direction Histogram of Run [12].

Run Number	$\overline{\beta}$ (°)	$\overline{V}_W$ (ms^{-1})	$\overline{V}_{Truck}$ (ms^{-1})	$\overline{\beta}(°)[W.S]$	$\overline{V}_W[W.S]$
Run [12]	3.2	8.1	24.4	3.1	7.2

Table G.32: Vehicle Average Wind Direction (β), Wind Speed (V_W) and Vehicle Speed (V_{Truck}): Run [12].

G.4.11.3 Wind Frequency Data: Run [12]

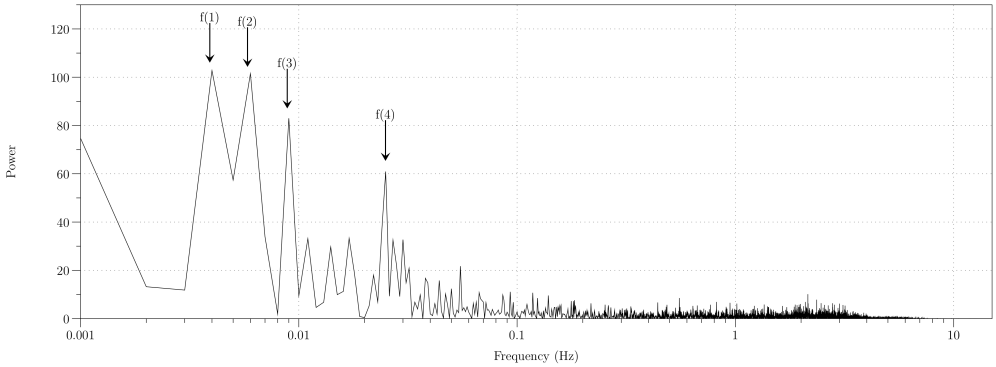

Figure G.50: FFT Power Spectrum of Run [12].

Run Number	$\overline{\beta}$ (°)	P1(s)	P2 (s)	P3 (S)	P4 (S)
Run [12]	3.2	255.8	171.8	113.0	40.0

Table G.33: Vehicle Test Route Frequency Statistics: Run [12].

G.4.12 Run [13]

G.4.12.1 Location Data: Run [13]

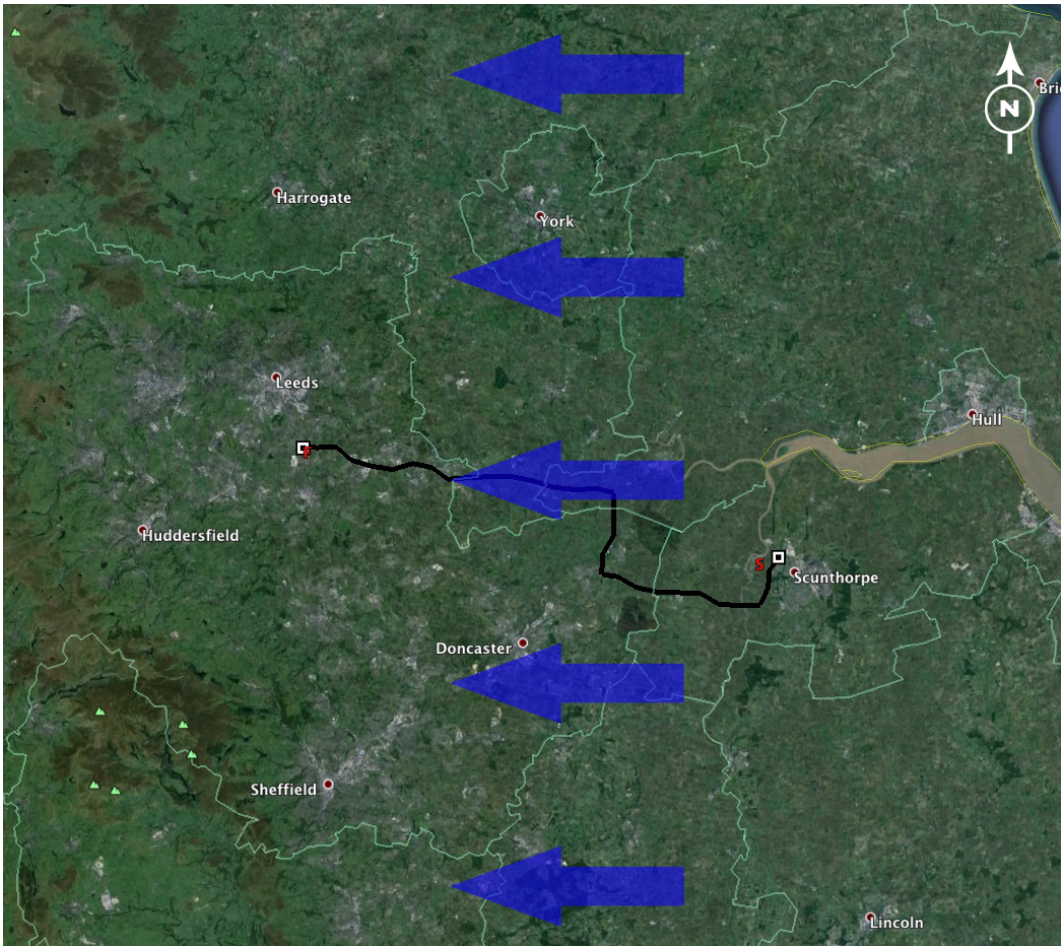

Figure G.51: Vehicle Test Route: Run [13][11].

Run Number	Latitude [Start]	Longitude [Start]	Latitude [Finish]	Longitude [Finish]
Run [13]	53°36'12.50"N	0°40'52.57"W	53°43'37.20"N	1°30'11.49"W

Table G.34: Vehicle Test Route Start and Finish Location: Run [13].

[11]Blue Arrows Denote $\overline{\Phi}_{Wind}$ Measured from Weather Station (x).

G.4.12.2 Wind Speed and Direction Data: Run [13]

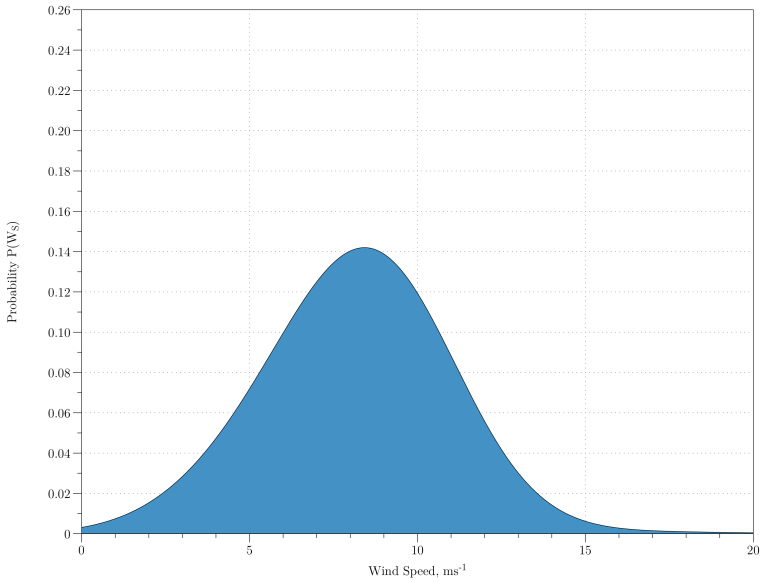

Figure G.52: Wind Speed Histogram of Run [13].

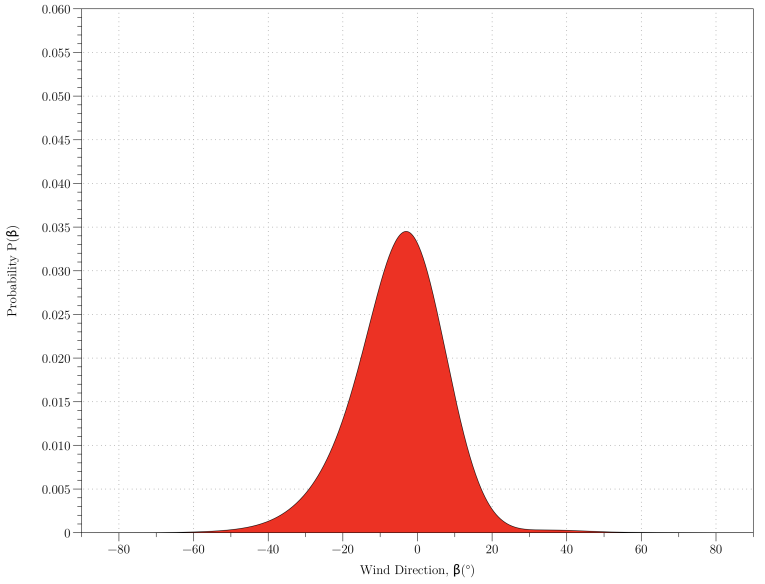

Figure G.53: Wind Direction Histogram of Run [13].

Run Number	$\overline{\beta}$ (°)	$\overline{V}_W$ (ms^{-1})	$\overline{V}_{Truck}$ (ms^{-1})	$\overline{\beta}$(°)[W.S]	$\overline{V}_W$[W.S]
Run [13]	-5.1	8.2	18.5	-7.0	8.2

Table G.35: Vehicle Average Wind Direction (β), Wind Speed (V_W) and Vehicle Speed (V_{Truck}): Run [13].

G.4.12.3 Wind Frequency Data: Run [13]

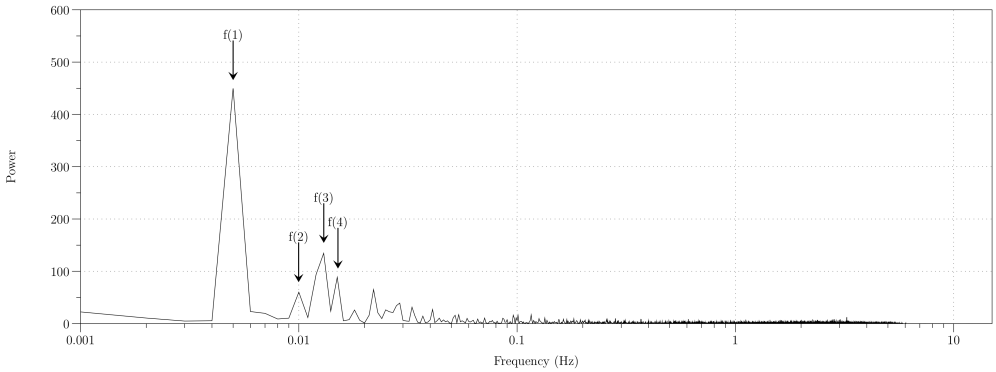

Figure G.54: FFT Power Spectrum of Run [13].

Run Number	$\overline{\beta}$ (°)	P1(s)	P2 (s)	P3 (S)	P4 (S)
Run [13]	-5.1	200.0	100.2	76.9	66.2

Table G.36: Vehicle Test Route Frequency Statistics: Run [13].

G.4.13 Run [14]

G.4.13.1 Location Data: Run [14]

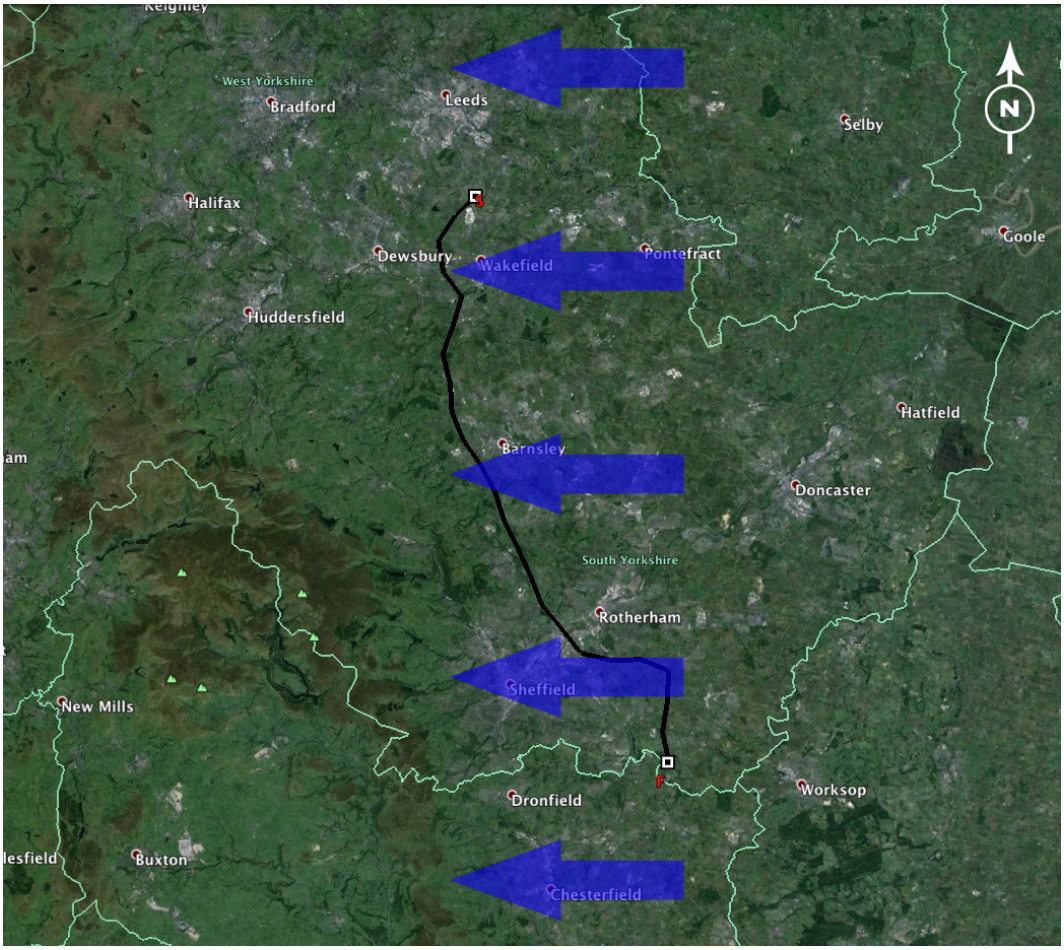

Figure G.55: Vehicle Test Route: Run [14][12].

Run Number	Latitude [Start]	Longitude [Start]	Latitude [Finish]	Longitude [Finish]
Run [14]	53°43'42.35"N	1°30'46.95"W	53°19'19.25"N	1°17'0.61"W

Table G.37: Vehicle Test Route Start and Finish Location: Run [14].

[12]Blue Arrows Denote $\overline{\Phi}_{Wind}$ Measured from Weather Station (iii).

G.4.13.2 Wind Speed and Direction Data: Run [14]

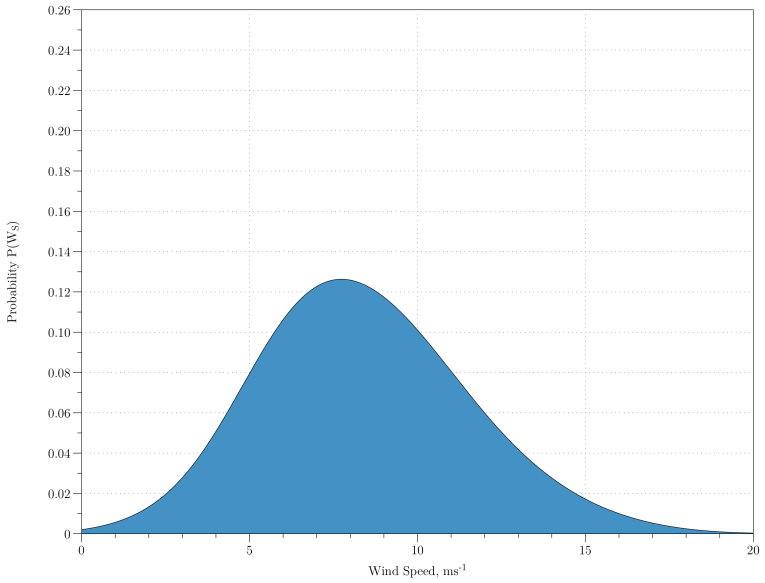

Figure G.56: Wind Speed Histogram of Run [14].

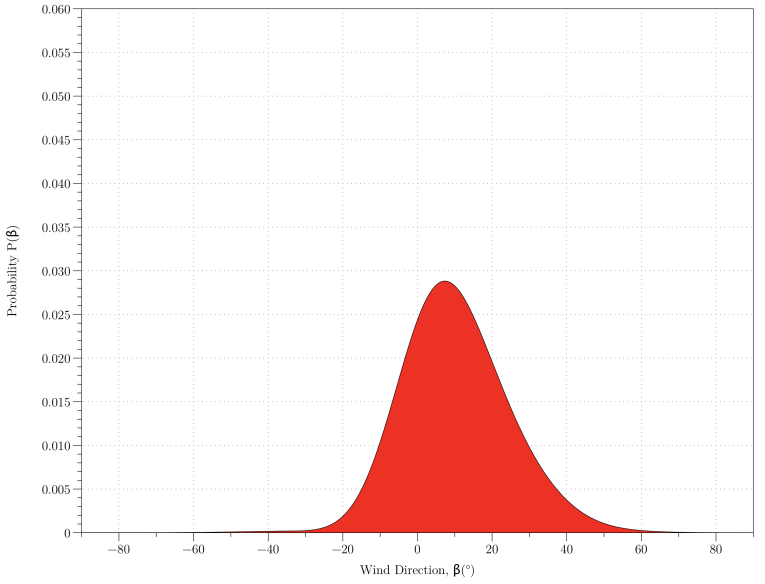

Figure G.57: Wind Direction Histogram of Run [14].

Run Number	$\overline{\beta}$ (°)	$\overline{V}_W$ (ms^{-1})	$\overline{V}_{Truck}$ (ms^{-1})	$\overline{\beta}(°)[W.S]$	$\overline{V}_W[W.S]$
Run [14]	10.3	8.4	24.7	8.0	10.0

Table G.38: Vehicle Average Wind Direction (β), Wind Speed (V_W) and Vehicle Speed (V_{Truck}): Run [14].

G.4.13.3 Wind Frequency Data: Run [14]

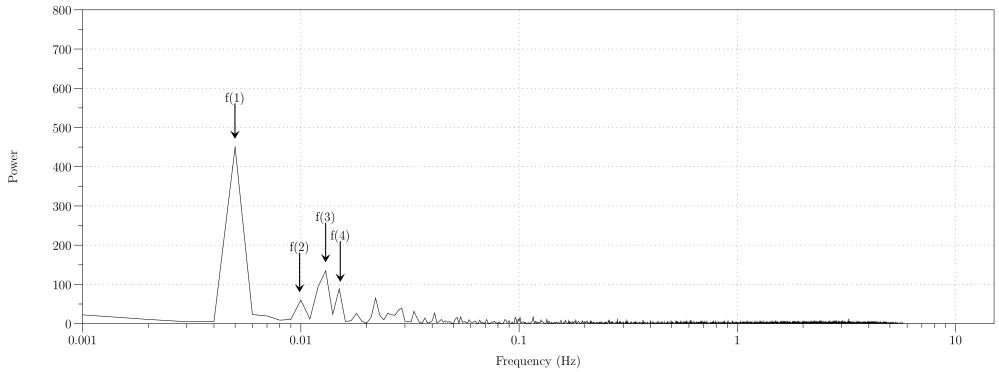

Figure G.58: FFT Power Spectrum of Run [14].

Run Number	$\overline{\beta}$ (°)	P1(s)	P2 (s)	P3 (S)	P4 (S)
Run [14]	10.3	200.0	101.3	77.0	66.0

Table G.39: Vehicle Test Route Frequency Statistics: Run [14].

G.4.14 Run [15]

G.4.14.1 Location Data: Run [15]

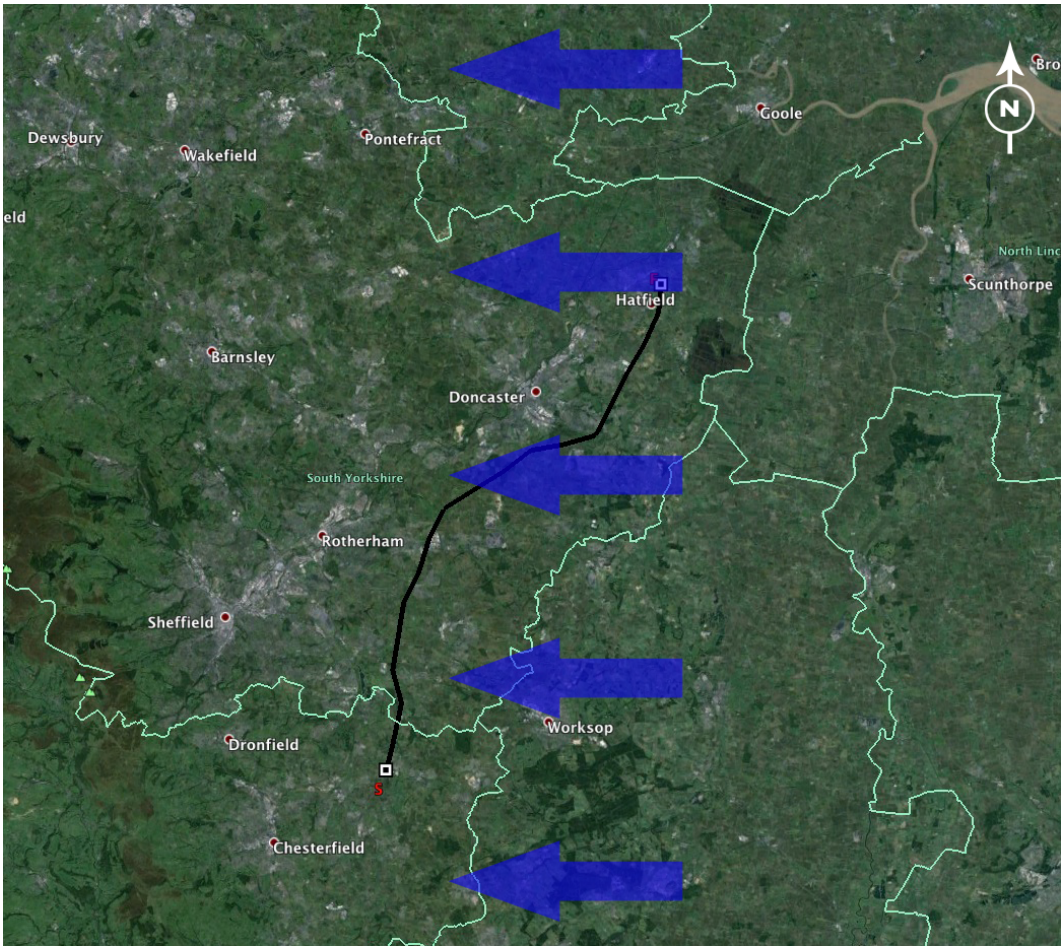

Figure G.59: Vehicle Test Route: Run [15][13].

Run Number	Latitude [Start]	Longitude [Start]	Latitude [Finish]	Longitude [Finish]
Run [15]	53°16'49.79"N	1°17'56.33"W	53°35'26.92"N	0°59'21.56"W

Table G.40: Vehicle Test Route Start and Finish Location: Run [15].

[13]Blue Arrows Denote $\overline{\Phi}_{Wind}$ Measured from Weather Station (x).

G.4.14.2 Wind Speed and Direction Data: Run [15]

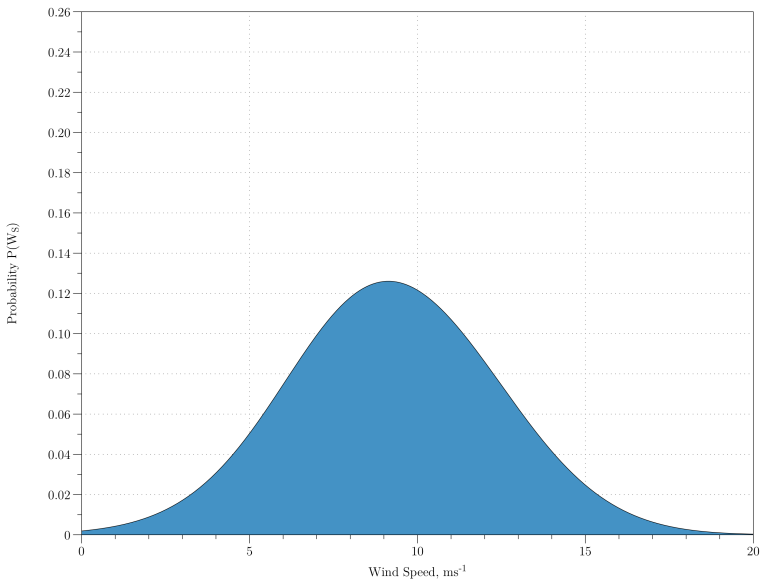

Figure G.60: Wind Speed Histogram of Run [15].

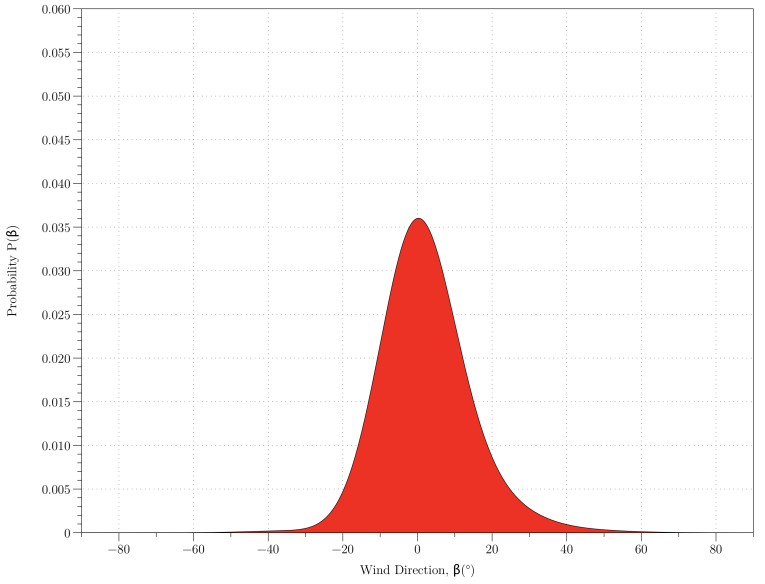

Figure G.61: Wind Direction Histogram of Run [15].

Run Number	$\overline{\beta}$ (°)	$\overline{V}_W$ (ms^{-1})	$\overline{V}_{Truck}$ (ms^{-1})	$\overline{\beta}(°)[W.S]$	$\overline{V}_W[W.S]$
Run [15]	2.2	9.3	24.8	6.2	24.8

Table G.41: Vehicle Average Wind Direction (β), Wind Speed (V_W) and Vehicle Speed (V_{Truck}): Run [15].

G.4.14.3 Wind Frequency Data: Run [15]

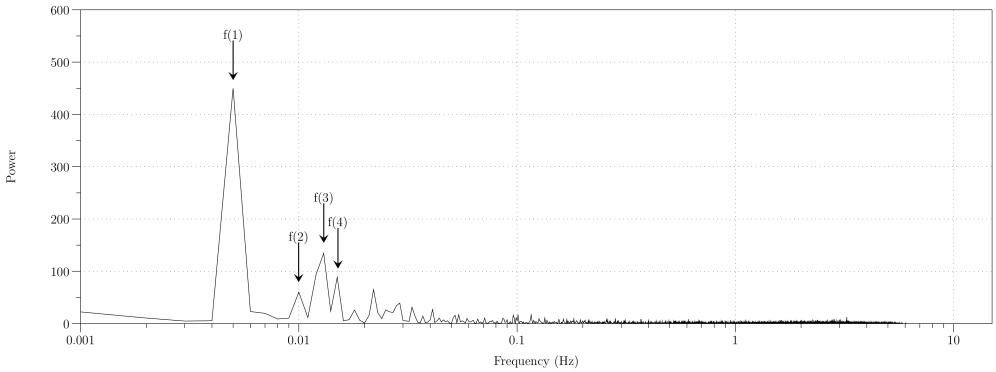

Figure G.62: FFT Power Spectrum of Run [15].

Run Number	$\overline{\beta}$ (°)	P1(s)	P2 (s)	P3 (S)	P4 (S)
Run [15]	2.2	337.6	99.3	70.7	46.4

Table G.42: Vehicle Test Route Frequency Statistics: Run [15].

G.5 Fourier Transform

The continuous Fourier transform is a mathematical transformation that converts a signal from a time domain into a frequency domain. The transformation is defined by

$$F(s) \equiv \int_{-\infty}^{\infty} f(x) \exp^{-2\pi i s x} \, dx \tag{G.5}$$

for discreetly sampled data, with N uniformly sampled data points, the Discrete Fourier Transform (DFT) is given by

$$X_k = \sum_{j=0}^{N-1} x_j \exp^{-2\pi i j k/N} \tag{G.6}$$

where the continuos variable s has been replaced with the discrete variable k.

The power spectrum of a series contains no phase information on the original time series. The power spectrum contains the power information as a function of frequency and is given by

$$\int_{-\infty}^{\infty} |f(x)|^2 dx = \int_{-\infty}^{\infty} |F(s)|^2 ds \tag{G.7}$$

where

$$|F(s)|^2 = \overline{F(s)} F(s) \tag{G.8}$$

G.5.1 Frequency Analysis Applied to Measured Data

The Discrete Fourier Transform (DFT) applied to a series converts the discrete signal from the time domain to the frequency domain. A sample input signal is shown below to illustrate the effect of the DFT applied to sample data.

DFT Example

A sinusoidal wave free from noise disturbance can be expressed by

$$y(t) = A \sin(2\pi f t + \phi) \tag{G.9}$$

where A is the amplitude, f is the frequency and ϕ is the phase.

For a single with zero phase shift ($\phi = 0$), amplitude (A =1) and a period of 250.0 seconds ($f = 4{\times}10^{-3}$ Hz), Eq.(G.9) reduces to

$$y(t) = \sin(0.025t) \tag{G.10}$$

where 0.025 is the angular frequency ($\omega = 2\pi f$), the resulting input signal is shown in Fig.(G.63).

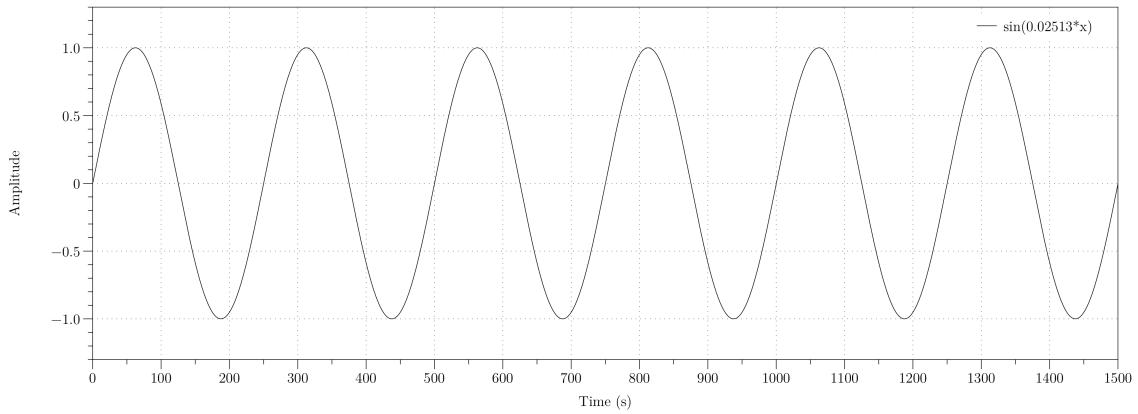

Figure G.63: Sinusoidal Signal Input Signal ($f = 4{\times}10^{-3}$ Hz).

Addition of random noise with ($f_{Noise} = 10Hz$) gives a resulting signal shown in Fig.(G.64).

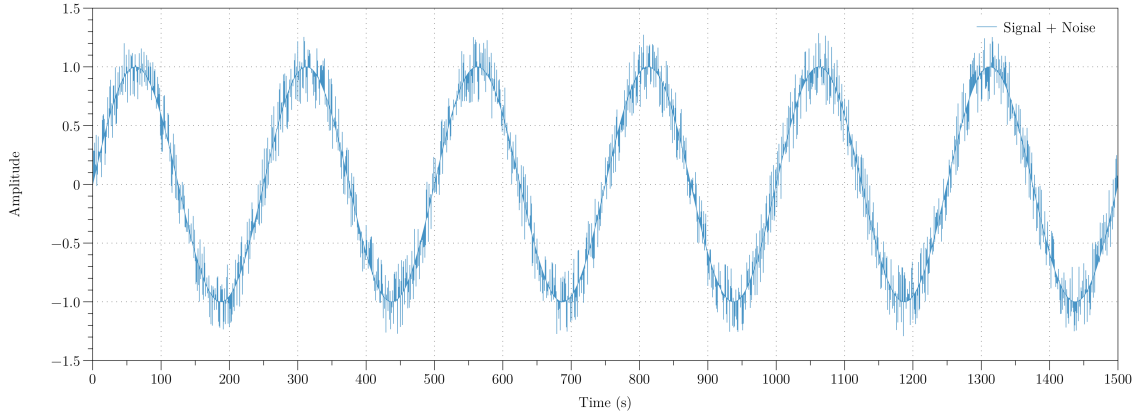

Figure G.64: Sinusoidal Signal Input Signal with Random Noise.

The input signal contains 1,800 seconds (30 minutes) of sample points, the underlying signal has a period of 250 seconds. Application of the DFT on the input signal gives the resulting power spectrum shown in Fig.(G.65).

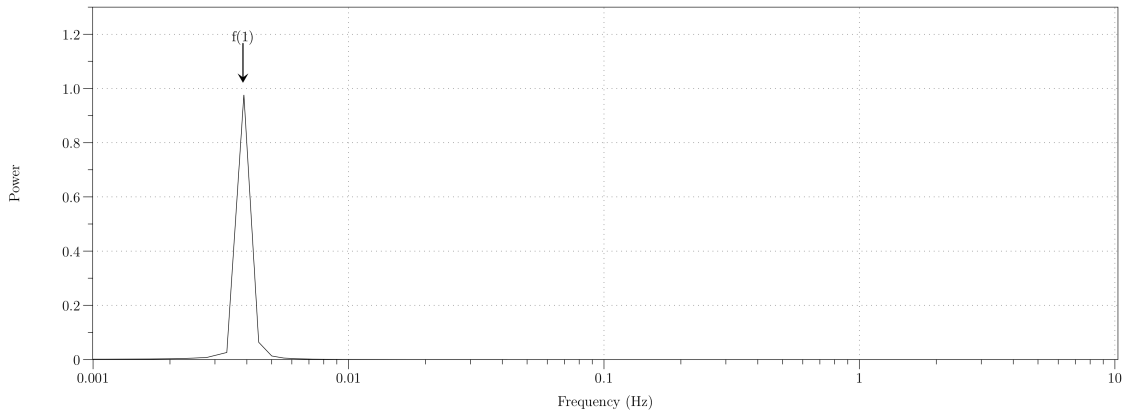

Figure G.65: Power Spectrum of a Noisy Sinusoidal Input Signal.

where f(1) = 0.00389 Hz, giving a predicted signal period of 257.1 seconds.

G.6 Sampling Theorem

The Sampling Theorem created by Nyquist-Shannon states that any continuous baseband signal may be reconstructed if the sampling frequency is at least twice the bandwidth of the signal. The critical sampling rate ($1/\Delta$t) is known as the Nyquist rate. The Nyquist frequency is given by

$$\nu_{N/2} = 1/(2\Delta t) \tag{G.11}$$

where the Nyquist frequency is the cut-off frequency for the system. Any frequencies higher than the Nyquist frequency will be aliased to other lower frequencies.

G.7 Low-Pass Filter

The magnitude response of the low-pass filter designed to remove high frequency "noise" attributed to vortex shedding of leading vehicles is shown in Fig.(G.66).

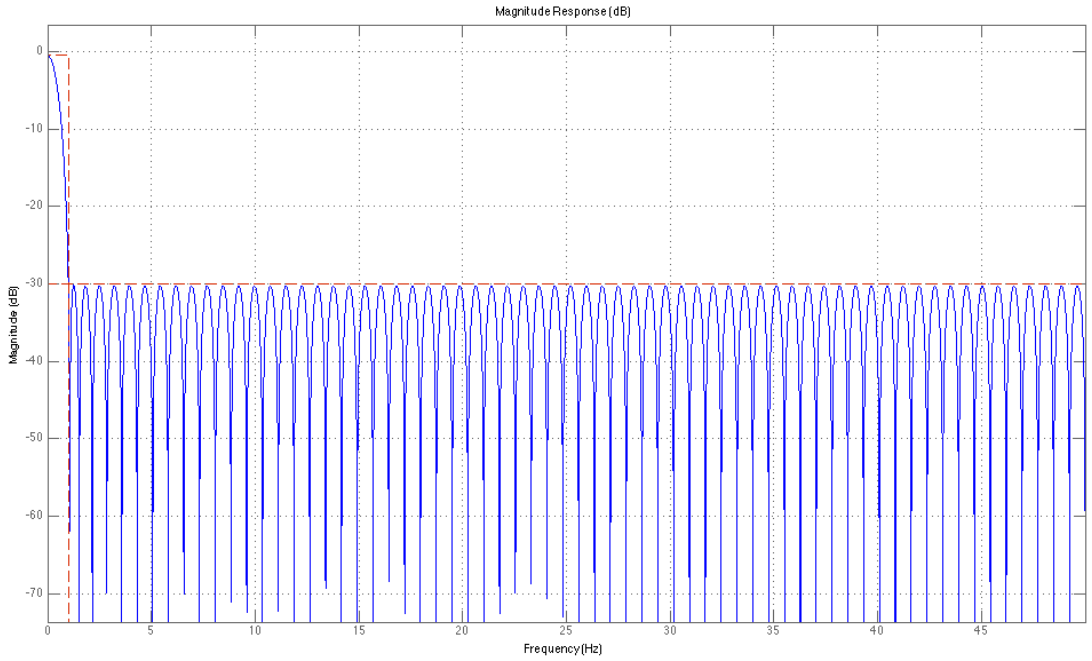

Figure G.66: Low-Pass Filter Magnitude Response (dB).

G.8 ActiveFREDDIE Prototype Full Scale Test

Examples of the trailers used for the full scale prototype ActiveFREDDIE controller are shown in Figs.(G.67 - G.69). The Millbrook post-test report is shown in Sec.(G.8.2) with the test data shown in Sec.(G.8.3).

G.8.1 Test Trailers

Figure G.67: Standard Single Deck 4.0 m Curtain Trailer.

Figure G.68: Standard Single Deck 4.2 m Refrigerated Trailer.

Figure G.69: Standard Double Deck 4.8 m Refrigerated Trailer.

G.8.2 Millbrook Test Report

TESCO Engineering

Hatcher – Active Freddie Tractor Unit
Air Deflector
&
New Actros Stream-Space with Active Freddie

Axor– Sleeer Cab
Freddie (1)

New Actros – Stream-space
Active-Freddie (3)

Axor– Sleeer Cab
Active-Freddie (2)

Created by : Andrew Grigor – Engineering Development Manager

Central Engineering Development Project's

TESCO Engineering

Active Freddie Air Deflector

Management Summary

What - Testing of the new Active Freddie Air Deflector and the new Mercedes Actros with the Active Freddie around the Millbrook Proving Ground

Why - Test to confirm whether there is a fuel and CO_2 saving on current Freddie Air Defector that Tesco fit by changing to the Active Freddie and to measure if there is any fuel benefit with the New Actros.

Who - Test will be complete by Tesco Engineering, Tesco Test Drivers, Mercedes and Hatcher

When - Test completed on 11th and 12th June 2012

Where - Test completed at Millbrook Proving Ground

Result Summary

- Active Freddie showed a benefit on a Single Deck fridge trailer of 0.58% at 40mph this was then reduced by 30% to 0.41% for the cost analysis to take into account expected operational findings
- Active Freddie showed a benefit on a Double Deck fridge trailer of 7.64% at 40mph this was then reduced by 30% to 5.34% for the cost analysis to take into account expected operational findings
- New Euro 5 Actros vehicle showed a benefit of 5% overall compared to the current Euro 5 Axor vehicle.

Central Engineering Development Project's

TESCO Engineering

Active Freddie Air Deflector

Contents of Presentation

- Overview
- Objective
- Scope
- Involved Parties
- Methodology
- Results – Data
- Analysis
- Overall Results
- Costs
- Summary / Recommendations
- Next Steps
- Project Review

TESCO Engineering

Active Freddie Air Deflector

Overview

- Hatcher have developed a New Freddie Air Defector that automatically changes height depending on the trailer height and also changes depending on the Yaw angle of the wind to give the best aerodynamic properties of tractor unit and trailer combination.

- Decision was taken to performance a fuel trial at Millbrook on the fuel test circuit to confirm fuel saving and also to explore the if there is any benefit in the New Actros which has a new Euro 6 engine that is Euro 5 compliant. Mercedes expect this to have a 4 - 6% fuel benefit over the current Euro 5 engine.

Operational & Technical Feasibility

Available on new bodies and easily done on production line and there will be no change to operation. Also available as a retrofit.

Environmental Benefit

Fuel improvement identified and therefore reduction in CO_2

Central Engineering Development Project's

TESCO
Engineering
Active Freddie Air Deflector
HATCHER
COMPONENTS
Europe's cab conversion and aerodynamic specialists
Hatcher Components Ltd
Broadwater Road, Framlingham,
Suffolk IP13 9LL
t: +44 (0) 1728 723675
f: +44 (0) 1728 724475
e: sales@hatchercomp.co.uk
www.hatchercomp.co.uk
BS EN ISO 9001 : 2008 Approved
When turning on the ignition, the spoiler will be lowered automatically by the actuators to it's lowest height (this process takes 10 seconds when the spoiler is at its highest).
If the height sensor doesn't detect a trailer it will not adjust the height of the spoiler, it will remain at the lowest height.
If the height sensor detects a trailer, it will adjust according to the height of it.
On the road, the spoiler will adjust depending on the wind speed and angle
Actuator
Height Sensor
Lowest Height
Maximum Height
Central Engineering Development Project's

TESCO Engineering

Active Freddie Air Deflector

Objectives

- To measure the performance of the new Active Freddie against the current Freddie air deflector that Tesco fit as standard
- Measure the performance of the New Actros (New Euro 5 engine) against the current Euro 5 engine and Axor model.

TESCO Engineering

Active Freddie Air Deflector

In-Scope

- Future Tractor unit purchases
- Retro-fit to existing vehicles

Out-Scope

- Trailer fleet

TESCO Engineering

Active Freddie Air Deflector

Involved Parties

- Site – Millbrook Proving Ground
- Operators – Stuart Bown; Simon D Smith;
- Drivers - Paul Moran and Steve Charles
- OEM's – Mercedes – Brian Kellow; Hatcher – Brian Getley
- Engineering Team – Andrew Grigor – Engineering Development Manager
- Outside Agencies – Millbrook

Central Engineering Development Project's

TESCO Engineering

Active Freddie Air Deflector

Training needed for Project

- None required as Drivers - Paul Moran and Steve Charles are trained on the Mercedes vehicles

Risk Assessment's for Project

- None required as previously done

Health and Safety Requirements for Project

- None required

Central Engineering Development Project's

TESCO Engineering

Active Freddie Air Deflector

Methodology – Millbrook Road Performance Test

Each test run will consist of 20 laps. Day 1 at 50mph and Day 2 same tests at 40mph

Runs will be measured via Telematics; manual data capture and from the on-board dashboard system.

	Tractor unit	Description	Trailer
Test 1	YS61 WWH	Current Freddie CONTROL	Single Deck Curtain
	YS61 WWJ	Current Freddie	Single Deck Curtain
	YP61 XNO	Active Freddie Axor	Single Deck Curtain
Test 2	YS61 WWH	Current Freddie CONTROL	Single Deck Curtain
	YS61 WWJ	Current Freddie	Std - Double Deck
	YP61 XNO	Active Freddie Axor	Fridge Single Deck
Test 3	YS61 WWH	Current Freddie CONTROL	Single Deck Curtain
	YS61 WWJ	Current Freddie	Fridge Single Deck
	YP61 XNO	Active Freddie Axor	Std - Double Deck
Test 4	YS61 WWH	Current Freddie CONTROL	Single Deck Curtain
	YP61 XNO	Active Freddie Axor	Pillow Concept - Double Deck
	YR12 FFY	Active Freddie Actros	Single Deck Curtain
Test 5	YS61 WWH	Current Freddie CONTROL	Single Deck Curtain
	YS61 WWJ	Current Freddie	Pillow Concept - Double Deck
	YR12 FFY	Active Freddie Actros	Fridge Single Deck

Central Engineering Development Project's

TESCO
Engineering

Hatcher – Active Freddie Tractor Unit
Air Deflector
&
New Actros Stream-Space with Active Freddie

Axor– Sleeer Cab
Freddie (1)

New Actros – Stream-space
Active-Freddie (3)

Axor– Sleeer Cab
Active-Freddie (2)

Created by : Andrew Grigor – Engineering Development Manager

Central Engineering Development Project's

TESCO Engineering

Active Freddie Air Deflector

Methodology – Millbrook Road Performance Test - Setup

- Bandvulc visit Millbrook on the morning of trial to measure tread depths and put tyre pressures to 120 PSI on front axle and 90 PSI on rear axle and all axles of the trailers at 125 PSI on Single deck and 120 on Double deck trailer.
- Anti-siphon device to be removed to give clear access to maintain same level of fuel filling with filling point identified
- All brakes checked for binding – Completed by Wentworth Park (Mercedes) before delivery in
- Wheel alignment checked – Completed by Wentworth Park (Mercedes) before delivery in
- Air conditioning switched off during test runs; adblue tank full and fridge red diesel tank full with fridge off.
- Additional person in each vehicle to count laps and collect data.

TESCO Engineering

Active Freddie Air Deflector

Methodology – Trial – Data Capture Sheet for each run

Millbrook test data capture form - Slipstream Trial

Date		Time		Test Number		Driver name	
Total number of planned laps			Test speed			Test or control combination?	
Weather description							
Vehicle information						Trailer information	
Vehicle reg.						Fleet number	
Make						Make	
Model						Model	
Gearbox							
Total combination laden weight				Number of concrete weights loaded			
Vehicle check list						Trailer check list	
Wheel alignment	Yes	Note: carried out at Wentworth Park				Wheel alignment	
Front axle tread depth	N/S	O/S					
Front axle tread depth						Front axle tread depth	
Rear axle tread depth	N/S Inner	N/S Outer	O/S Inner	O/S Outer			
Rear axle tread depth						Centre axle tread depth	
Front axle tyre pressures	N/S	O/S					
Front axle tyre pressures						Rear axle tread depth	
Rear axle tyre pressures	N/S Inner	N/S Outer	O/S Inner	O/S Outer			
Rear axle tyre pressures						Front axle tyre pressures	
All brakes checked for binding	Yes	Note: carried out at Wentworth Park				Centre axle tyre pressures	
Air conditioning switched off	Yes					Rear axle tyre pressures	
Windows closed	Yes					All brakes checked for binding	Yes
Adblue tank full	Yes					Fridge fuel tank full	Yes
Fuel information						Fridge off	Yes
Fuel added prior to test		Fill to mark on filler neck (anti syphon removed)				Concrete blocks adequately restrained	Yes
Fuel added post test							
Fuel used for test							
Mileage information		Note: All mileage readings taken at refueling point					
Odo reading prior to test							
Odo reading post test							
Total kms run							
MPG calculation		Note:Convert kms into miles divide by 1.6093. Convert litres into gallons divide by 4.546					
Fleetboard information							
Total travelled mileage							
MPG calculation							
Litres used							

Central Engineering Development Project's

TESCO Engineering

Active Freddie Air Deflector

Results - Data

- Summary of data collated

20 Laps @ 50 mph	Tractor unit	Description	Trailer	KMs	Litres	KPL	MPG	Control vs Test	Condition Adjustment	Comparasion MPG to be used
Test 1	YS61 WWH	Current Freddie CONTROL	Single Deck Curtain	66.2	17.1	3.87	9.11		0.00%	
	YS61 WWJ	Current Freddie	Single Deck Curtain	66.3	16.8	3.95	9.28	-1.90%	0.00%	
	YP61 XNO	Active Freddie Axor	Single Deck Curtain	65.8	17.5	3.76	8.84	2.96%	0.00%	
Test 2	YS61 WWH	Current Freddie CONTROL	Single Deck Curtain	66.2	17	3.89	9.16		-0.59%	
	YS61 WWJ	Current Freddie	Std - Double Deck	66.7	21.7	3.07	7.23	-1.90%	-0.59%	7.05
	YP61 XNO	Active Freddie Axor	Fridge Single Deck	66.6	18.5	3.60	8.47	2.96%	-0.59%	8.67
Test 3	YS61 WWH	Current Freddie CONTROL	Single Deck Curtain	66.3	17.4	3.81	8.96		2.15%	
	YS61 WWJ	Current Freddie	Fridge Single Deck	66.5	18.8	3.54	8.32	-1.90%	2.15%	8.34
	YP61 XNO	Active Freddie Axor	Std - Double Deck	66.4	21	3.16	7.44	2.96%	2.15%	7.82
Test 4	YS61 WWH	Current Freddie CONTROL	Single Deck Curtain	66.3	17.1	3.88	9.12		-1.75%	
	YP61 XNO	Active Freddie Axor	Pillow - Double Deck	66.5	20	3.33	7.82	2.96%	-1.75%	7.92
	YR12 FFY	Active Freddie Actros	Single Deck Curtain	66.3	16.2	4.09	9.63			
Test 5	YS61 WWH	Current Freddie CONTROL	Single Deck Curtain	65.4	16.6	3.94	9.27		-1.61%	
	YS61 WWJ	Current Freddie	Pillow - Double Deck	65.8	20.2	3.26	7.66	-1.90%	-1.61%	7.39
	YR12 FFY	Active Freddie Actros	Fridge Single Deck	65.4	16	4.09	9.61		-5.15%	9.12

Central Engineering Development Project's

G.8.3 Millbrook Test Data

The 40 mph data obtained from the full scale test on the prototype ActiveFREDDIE controller is shown in Tab.(G.43), with the 50 mph data shown in Tab.(G.44).

G.8.3.1 40 mph Test Data

Single Deck Curtain Trailer						
Deflector	Distance (km)	Litres	KPL	MPG	Adjusted MPG	Fuel Saving(%)
Static	67.1	13.8	4.86	11.44	11.44	-
Active	67.0	14.0	4.79	11.26	11.26	-1.6
Refrigerated Single Deck Trailer						
Deflector	Distance (km)	Litres	KPL	MPG	Adjusted MPG	Fuel Saving(%)
Static	66.5	18.8	3.54	8.32	8.34	-
Active	66.6	18.5	3.60	8.47	8.67	3.9
Refrigerated Double Deck Trailer						
Deflector	Distance (km)	Litres	KPL	MPG	Adjusted MPG	Fuel Saving(%)
Static	66.7	21.7	3.07	7.23	7.05	-
Active	66.4	21.0	3.16	7.44	7.82	10.9
Refrigerated Pillow Double Deck Trailer						
Deflector	Distance (km)	Litres	KPL	MPG	Adjusted MPG	Fuel Saving(%)
Static	65.8	20.2	3.26	7.66	7.39	-
Active	66.5	20.0	3.33	7.82	7.92	7.1

Table G.43: Millbrook ActiveFREDDIE Test Data [101] with Various Trailer Combinations, Test Conducted at 40 mph[15].

[15]Adjusted MPG Corresponds to Allowance for Atmospheric Conditions.

G.8.3.2 50 mph Test Data

Single Deck Curtain Trailer						
Deflector	Distance (km)	Litres	KPL	MPG	Adjusted MPG	Fuel Saving(%)
Static	66.3	16.8	3.95	9.28	9.28	-
Active	65.8	17.5	3.76	8.84	8.84	-4.7
Refrigerated Single Deck Trailer						
Deflector	Distance (km)	Litres	KPL	MPG	Adjusted MPG	Fuel Saving(%)
Static	66.5	18.8	3.54	8.32	8.34	-
Active	66.6	18.5	3.60	8.47	8.67	3.9
Refrigerated Double Deck Trailer						
Deflector	Distance (km)	Litres	KPL	MPG	Adjusted MPG	Fuel Saving(%)
Static	66.7	21.7	3.07	7.23	7.05	-
Active	66.4	21.0	3.16	7.44	7.82	10.9
Refrigerated Pillow Double Deck Trailer						
Deflector	Distance (km)	Litres	KPL	MPG	Adjusted MPG	Fuel Saving(%)
Static	65.8	20.2	3.26	7.66	7.39	-
Active	66.5	20.0	3.33	7.82	7.92	7.1

Table G.44: Millbrook ActiveFREDDIE Test Data [101] with Various Trailer Combinations, Test Conducted at 50 mph[17].

[17]Adjusted MPG Corresponds to Allowance for Atmospheric Conditions.

This page intentionally left blank.

This page intentionally left blank.